

Magnetic, electronic, and structural characterization of mass-selected mono and multinuclear transition metal complexes

Am Fachbereich Chemie der Technischen Universität Kaiserslautern zur Erlangung
des akademischen Grades "Doktor der Naturwissenschaften" genehmigte

Dissertation

(D386)

vorgelegt von

Dipl.-Chem. Michael Lembach

Betreuer: Prof. Dr. Dr. G. Niedner-Schatteburg

Tag der wissenschaftlichen Aussprache: 10.11.2022

Technische Universität Kaiserslautern 2022

Die vorliegende Arbeit wurde im Zeitraum von August 2017 bis Oktober 2021 im Fachbereich Chemie der Technischen Universität Kaiserslautern unter Betreuung von Prof. Dr. Dr. G. Niedner-Schatteburg angefertigt.

Datum des Antrages auf Eröffnung des Promotionsverfahrens: 22.04.2021

Promotionskommission:

Vorsitzender	Prof. Dr. A. Pierik
1. Berichterstatter	Prof. Dr. Dr. G. Niedner-Schatteburg
2. Berichterstatter	Jun. Prof. Dr. J. Meyer

FÜR MEINE ELTERN

*„'Cause I'm tired of the fear that I can't control this
I'm tired of feeling like every next step's hopeless
I'm tired of being scared what I build might break apart
I don't want to know the end, all I want is a place to start “*

Mike Shinoda

Kurzfassung

Diese Arbeit gliedert sich in sieben verschiedene Forschungsprojekte über ein- und mehrkernige Übergangsmetallkomplexe als gespeicherte Ionen in der Gasphase sowie ein Kapitel über die Entwicklung einer neuen Ionenquelle, die den Zugang zu katalytischen Prozessen über Coadsorption ermöglicht.

Bei der Elektrospray-Ionisierung (ESI) werden Ionen für massenspektrometrische Untersuchungen aus der Lösung in die Gasphase überführt, was eine breite Palette experimenteller Methoden ermöglicht, um grundlegende Einblicke in die molekularen Eigenschaften isolierter Komplexe ohne Lösungsmittel-, Kristallgitter-, Festkörper- oder unterstützende Oberflächeneffekte zu erhalten.

Die kollisionsinduzierte Dissoziation (CID) erforscht molekulare Fragmentierungsmechanismen und ihre relative Gasphasenstabilität bei Raumtemperatur. Laserexperimente wie die Infrarot (Mehrfach) Photonen Dissoziation und die Ultraviolet Photonen Dissoziation liefern Informationen über die Bindungsmotive, die zu Molekülstrukturen und deren elektronischen Grundzuständen führen. Wenn quantenchemische Berechnungen unter Verwendung der Dichtefunktionaltheorie (DFT) und der zeitabhängigen Dichtefunktionaltheorie (TD-DFT) mit aufgenommenen Spektren verglichen werden, ist ein besseres und tieferes Verständnis der strukturellen Eigenschaften und der elektronischen Grundzustände von Übergangsmetallkomplexen möglich.

Röntgenmagnetischer Zirkulardichroismus (XMCD) ist eine Technik, die die magnetischen Eigenschaften isolierter und gespeicherter Ionen unter kryogenen Temperaturen innerhalb eines extern angelegten Magnetfeldes mit hoch energetischen polarisierten Röntgenphotonen in Verbindung mit einem Massenspektrometer analysiert. Die elementselektive Technik, kombiniert mit der Summenanalyse, ermöglicht die Zerlegung der Gesamtmagnetischen Momente in deren Spin- und Bahnmomente in verschiedenen Metallzentren. Eine Bestimmung der magnetischen Kopplungen zwischen verschiedenen Metallzentren in mehrkernigen Komplexen ist über den Broken Symmetry Ansatz in Kombination mit dem Röntgenmagnetischen Zirkulardichroismus (XMCD) möglich.

Abstract

This thesis is separated into seven distinct research projects on mono and multinuclear transition metal complexes as trapped ions in gas phase, as well as one chapter on focusing on the development of a new ion source to enable access to catalytic processes via coadsorption.

ElectroSpray Ionization (ESI) transfers ions from solution to gas phase for mass spectrometric investigations, allowing a broad variety of experimental methods to obtain fundamental insights into the molecular properties of isolated complexes devoid of solvent, crystal lattice, bulk, or supporting surface effects.

Collision Induced Dissociation (CID) researches molecular fragmentation mechanisms and their relative gas phase stabilities at room temperature. Laser experiments such as InfraRed (Multiple) Photon dissociation and Ultraviolet Photon dissociation offer information on the bonding motifs, resulting in molecular structures and their electronic ground states. When quantum chemical calculations utilizing Density Functional Theory (DFT) and Time Dependent Density Functional Theory (TD-DFT) are combined with monitored spectra, a better and deeper understanding of the structural properties and electronics of transition metal complexes is possible.

X-ray magnetic circular dichroism (XMCD) is a technique that analyzes the magnetic properties of isolated and trapped ions at cryogenic temperatures inside an externally applied magnetic field using high brilliant polarized X-ray photons in conjunction with a mass spectrometer. The element selective technique, combined with sum analysis, allows for the decomposition of the total magnetic moments in their spin and orbital magnetic moments in various metal centers. A determination of the magnetic couplings between distinct metal centers in multinuclear complexes is possible via Broken symmetry approach in combination with X-ray Magnetic Circular Dichroism (XMCD).

Content

1	Introduction	1
1.1	References	8
2	Experimental setup	1
2.1	Ion Sources	1
2.1.1	Apollo II ESI Source	1
2.1.2	ESI source of the Schlathölder group	2
2.1.3	ESI source of the Lau group	3
2.1.4	Laser vaporization source (LVAP)	4
2.2	Mass Spectrometric Instrumentation	5
2.2.1	AmaZon mass spectrometer (Speed, SL, ETD)	6
2.2.2	Ion Trap mass spectrometer	10
2.2.3	GERTI (General Electrospray Time of flight Instrument)	13
2.3	Light Sources	14
2.3.1	Optical Parametric Oscillator/Amplifier IR Laser system	14
2.3.2	X-ray Synchrotron Radiation at BESSY II (UE52–PGM beamline)	17
2.3.3	Wyvern KMLaps system	19
2.4	References	20
3	Methods	23
3.1	Electrospray Ionization process	23
3.2	Time of flight mass spectrometry (TOF-MS)	25
3.3	Collision Induced Dissociation (CID)	26
3.4	Electron Transfer Dissociation (ETD)	29
3.5	InfraRed (Multiple) Photon Dissociation (IR(M)PD)	31
3.6	Ultra Violet Photon Dissociation (UVPD)	33
3.7	X-ray Absorption and X-ray Magnetic Circular Dichroism (XMCD)	34
3.7.1	X-ray absorption spectroscopy (XAS)	34
3.7.2	X-ray magnetic circular magnetism (XMCD)	37
3.8	References	45
4	Computational methods	49
4.1	Density Functional Theory	49
4.1.1	Geometry optimization	50

4.1.2	Vibrational Frequencies.....	51
4.2	Non covalent Interactions (NCI)	52
4.3	TD-DFT calculation.....	53
4.4	Broken symmetry	54
4.5	XA Simulations.....	55
4.6	References.....	56
5	Magnetic properties and their correlation to the electronics of isolated trinuclear 3d spin frustrated complexes.....	59
5.1	Preamble	59
5.2	Abstract	60
5.3	Introduction.....	60
5.4	Experimental setup and methods	63
5.5	Computational methods.....	66
5.6	Results and Discussion.....	67
5.6.1	Results I: X-ray magnetic circular dichroism.....	67
5.6.2	Discussion I: X-ray magnetic circular dichroism	68
5.6.3	Results II: Ultra Violet Photon Dissociation	80
5.6.4	Discussion II: Ultra Violet Photon Dissociation.....	81
5.6.5	Discussion III: Opto- magnetic correlation	83
5.7	Conclusions.....	92
5.8	Acknowledgment.....	94
5.9	References.....	94
5.10	Supplementary material.....	101
6	IR(M)PD studies of isolated spin frustrated trimetallic μ-oxo bridged 4d complexes	143
6.1	Preamble	143
6.2	Abstract	144
6.3	Introduction.....	144
6.4	Experimental setup and methods	147
6.4.1	Collision Induced Dissociation	147
6.4.2	InfraRed (Multiple) Photon Dissociation (IR(M)PD)	148
6.5	Computational methods.....	150
6.6	Results and Discussion.....	150
6.6.1	Collision Induced Dissociation (CID)	150
6.6.2	InfraRed (Multiple) Photon Dissociation (IR(M)PD)	153

6.6.3	Spin magnetic determination via Broken symmetry.....	164
6.7	Conclusion	170
6.8	Acknowledgment.....	171
6.9	References.....	171
6.10	Supplementary material.....	177
7	Opto-magnetic correlation of a mass-selected monometallic spin-crossover iron complex ..	199
7.1	Preamble	199
7.2	Abstract	200
7.3	Introduction.....	200
7.4	Experimental setup and methods	203
7.5	Computational methods.....	207
7.6	Results and Discussion.....	208
7.6.1	Results I: X-ray magnetic circular dichroism (XMCD)	208
7.6.2	Results II: Collision Induced Dissociation (CID) and InfraRed (Multiple) Photon Dissociation (IR(M)PD).....	216
7.6.3	Results III: UV/VIS and XMCD correlation.....	223
7.7	Conclusions.....	227
7.8	Acknowledgment.....	229
7.9	References.....	229
7.10	Supplementary material.....	235
8	Temperature dependent X-ray magnetic circular dichroic studies of a trinuclear Manganese SMM complex in isolation.....	267
8.1	Preamble	267
8.2	Abstract	268
8.3	Introduction.....	268
8.4	Experimental Setup and Methods.....	271
8.5	Computational methods.....	274
8.6	Results and Discussion.....	275
8.6.1	Collision Induced Dissociation (CID)	275
8.6.2	X-ray magnetic dichroism (XMCD).....	278
8.7	Conclusion	290
8.8	Acknowledgment.....	291
8.9	References.....	292
8.10	Supplementary material.....	297

9 IR(M)PD studies on a series of isolated trimetallic single molecule magnets containing 3d metals and Lanthanides	315
9.1 Preamble	315
9.2 Abstract	316
9.3 Introduction.....	316
9.4 Experimental setup and methods	318
9.5 Computational methods.....	322
9.6 Results	322
9.6.1 Collision Induced Dissociation (CID)	322
9.6.2 InfraRed (Multiple) Photon Dissociation (IR(M)PD)	329
9.6.3 Theoretical approximation of the XA spectra and UV correlation	337
9.7 Conclusion	344
9.8 Acknowledgment.....	345
9.9 References.....	345
9.10Supplementary material.....	349
10 Comment: X-ray Magnetic Circular Dichroism Spectroscopy Applied to Nitrogenase and Related Models: Experimental Evidence for a Spin-Coupled Molybdenum(III) Center.....	381
10.1 Preamble	381
10.2 Introduction.....	382
10.3 Results	382
10.4 Acknowledgment.....	395
10.5 References	396
11 First Investigations of a heptanuclear homoleptic Manganese complex with single molecular magnetic behavior.....	397
11.1 Preamble	397
11.2 Abstract	398
11.3 Introduction.....	398
11.4 Experimental setup and methods	400
11.5 Computational methods.....	401
11.6 Results and Discussion.....	402
11.7 Conclusion	417
11.8 Acknowledgment.....	418
11.9 References	418

12 Development of a new ion source for aggregation of small molecules on cluster surfaces ...	423
12.1 Preamble	423
12.2 Introduction.....	423
12.3 Results	424
12.4 Conclusion	439
12.5 References.....	440
Summary and outlook	441
Zusammenfassung und Ausblick	449
Appendices	459
Appendix I: IR(M)PD and CID investigations on a trimetallic Rhodium complex in isolation.	459
Appendix II: Investigation of the auto oxidation in a neutral trinuclear palladium complex to a monocationic complex in isolation	475
Appendix III: Repairing an RF contact failure in an AmaZon Paul trap mass spectrometer	487
Appendix IV: Reanimation of the MALDI ULTRAFLEX TOF mass spectrometer	497
Curriculum Vitae	505
Lebenslauf	507
Contribution to conferences: Oral, Poster Presentations and Beamtime proposals.....	509
Research visits	513
Danksagung	515
Eidesstattliche Erklärung	519

Abbreviations

SCO	Spin-crossover
SMM	Single molecule magnet
LS	Low spin
HS	High spin
MOF	Metal organic framework
MALDI	Matrix assisted Laser desorption
ESI	Electrospray ionization
CID	Collision Induced Dissociation
DFT	Density functional theory
IR(M)PD	InfraRed (Multiple) Photon Dissociation
UVPD	Ultraviolet photon dissociation
XMCD	X-ray magnetic circular dichroism
UV/VIS	Ultraviolet/visible
XA	X-ray absorption
TD-DFT	Time dependent density functional theory
ETD	Electron Transfer Dissociation
kV	Kilo volt
V	Volt
RF	Radio frequency
kHz	kilohertz
MS	Mass spectrometer
DC	Direct current
TM	Transition metal
LVAP	Laser vaporization
GERTI	General electrospray time of flight instrument
Hz	Hertz
mbar	millibar
ms	Milli second
FWHM	Full width of half maximum
T	Tesla

MHz	Megahertz
K	Kelvin
GaAs	Gallium Arsenid
meV	Milli electron volt
TOF	Time of flight
MCP	Multi channel plate
ReTOF	Reflectron time of flight
LinTOF	Linear time of flight
HV	High voltage
PL	plate
OPO	Optical parametric oscillator
OPA	Optical parametric amplifier
SHG	Second harmonic generation
KTA	Potassium titanyl arsenate
AgGaSe ₂	Silver Gallium diselenoide
DFM	Difference frequency mixing
KTP	Potassium titanyl phosphate
cm ⁻¹	wavenumber
nm	Nanometer
GeV	Giga electron volt
mA	Milli ampere
AE	Appearance energy
CI	Chemical ionization
M	Methane
F	Flouranthene
IVR	Internal vibrational redistribution
ns	Nanosecond
IR	Infrared
IC	Internal conversion
HDvV	Heisenberg Dirac van Vleck Hamiltonian
[Fe ₃ O(OAc) ₆ (py) _n] ⁺	Hexakis[μ-(acetato-κO:κO')]triaqua-μ ₃ -oxotriiron

OAc	Acetate
py	pyridine
H ₂ O	Water
HZB	Helmholtz zentrum Berlin
Å	Angström
a.u.	Arbitrary units
pDOS	Projected Density of States
cm ³	Cubic centimetre
mol	Amount of substance
μ _B	Bohr's magneton
BR	Branching ratio
SOC	Spin orbit coupling
ELF	Electron localized field
NCI	Non covalent interaction
DORI	differential overlap region interaction
HOMO	Highest occupied molecular orbital
LUMO	Lowest occupied molecular orbital
amu	Atomic mass unit
μm	Micrometer
L	Litre
min	Minute
μL	Microliter
h	hour
μJ	Microjoule
TS	Tanabe sugano
exp	experimental
J	Exchange coupling constant
DMF	dimethylformamid
[Ru ₃ O(OAc) ₆ (py) _n] ⁺	Hexakis[μ-(acetato-κO:κO')]triaqua-μ ₃ -oxotriruthenium
km	kilometer
kJ	Kilo Joule

btpa	<i>N,N,N',N'</i> -Tetrakis(2-pyridylmethyl)-6,6'-bis(aminomethyl)-2,2'-bipyridine)
S	Total spin
L	Total orbital Moment
MLCT	Metal to ligand charge transfer
X_m	Molar susceptibility
dpa	<i>N, N'</i> -bis(2-pyridylmethyl)-6,6'-bis(aminomethyl)-2,2'-bipyridine)
$[\text{Fe}(\text{dpa})]^{2+}$	<i>N,N'</i> -bis(2-pyridylmethyl)-6,6'-bis(aminomethyl)-2,2'-bipyridine)iron(II)
HCN	Hydrogencyanate
Bz	Benzyl
sym	Symmetric
calc.	Calculated
H ₃ cht	cis,cis 1,3,5-cyclohexanetriol, Bipy = bipyrimidyl
Bipy	bipyrimidyl
Vab	2-[(2-hydroxymethyl-phenylimino)-methyl]-6-methoxy-phenol
$ \phi\rangle$	valence final state
$ \iota\rangle$	initial core state
$\langle S_L \rangle$	expectation value of the orbital angular momentum
$\langle S_J \rangle$	expectation value of the total angular momentum
$\langle S_Z \rangle$	expectation value of the spin
$\langle T_Z \rangle$	expectation value of the spin magnetic dipole operator
μ^-	XA spectrum recorded with negative circularly polarized light; $q = -\hbar$
μ^+	XA spectrum recorded with positive circularly polarized light; $q = +\hbar$
μ_0	magnetic permeability of the free space
μ_0	XA spectrum recorded with linearly polarized light; $q = 0$
μ_B	Bohr magneton
μ_r	relative magnetic permeability of a given material
APPLE	Advanced Planar Polarized Light Emitter
B	magnetic flux density
BLYP	functional by Becke Lee Yang and Parr

J	total angular momentum, $J = L + S$
L	total orbital angular momentum
M	magnetization, transition matrix element
m_e	electron mass
m_L	orbital magnetic moment
$m_L^{(z)}$	projection of the orbital magnetic moment onto the quantization axis (magnetization)
m_S	spin magnetic moment
$m_S^{(z)}$	projection of the spin magnetic moment onto the quantization axis (magnetization)
m_{tot}	total magnetic moment
$m_{\text{tot}}^{(z)}$	projection of the total magnetic moment onto the quantization axis (magnetization)
n_h	number of holes in the final state / shell ($= 4l_f + 2 - n$)
$\rho(\epsilon_f)$	density of final states per unit energy
σ^-	left-handed circularly polarized light, $q = -1$
σ^+	right-handed circularly polarized light, $q = +1$
σ^{abs}	absorption cross section
χ	susceptibility

1 Introduction

Transition metal (TM) complexes provide properties that are of high interest since antiquity^[1-4], and found application in different areas^[5, 6]. They catalyze chemical reactions^[7-11] through homogeneous or heterogeneous catalysis by activating small molecules in order to functionalize them^[12-16]. Transition metal complexes have become prominent in pharmaceutical treatments, e.g., cancer^[17-25] or malaria infection^[26-29]. The wide variety of mono and multinuclear complexes leads to different research fields focusing on their properties. Paramagnetic transition metal complexes enable access to intrinsic magnetic properties with fascinating properties^[30]. There are various magnetic phenomena in these complexes, such as spin-crossover^[31-36] (SCO), spin frustration^[37-41], and single molecule magnetic (SMM) behavior^[42-47].

Spin-crossover complexes find application in electronic devices as molecular switches^[34, 48, 49], memory devices^[50], rectifiers^[51, 52], and other electrical parts such as transistors or wires^[53-55]. Spin-crossover processes usually occur by thermal excitation from a low spin (LS) state to a high spin (HS) state^[34]. Several research groups performed experiments in order to determine the spin-crossover process in mono and multinuclear transition metal complexes^[31-36, 49, 56, 57]. The most commonly utilized transition metal seems to be the Fe²⁺ ion. The excitation occurs from an (e_g)⁶(t_{2g})⁰ electronic state to an (e_g)⁴(t_{2g})² state by elongation of the bonding distances^[34] and crystal field splitting energies smaller than the actual spin pairing energy^[58, 59]. This redistribution can be achieved by changing the temperature, the pressure, or by photon irradiation.

Spin frustrated complexes do not allow for a single spin configuration that would lead to the most favorable and energetic convenient structure^[60, 61]. Instead, these complexes establish a spin configuration, which do not obtain an alternating manner of “spin up” and “spin down” electrons in a specific structure. Complexes with such remarkable properties serve as model compounds in metal organic frameworks (MOF)^[62-66], quantum computing^[67-72], spin trionics^[73-76], metalloenzymes^[77], and catalysis^[66, 78-81]. The spin arrangement of such oligonuclear complexes leads to unique magnetic properties through the interaction of adjacent transition metals, which is impossible in mononuclear complexes because of the lack of such exchange couplings of multiple metal centers.

Upon application of an external magnetic field, some TM complexes show an intrinsic long living magnetization and hysteresis, which indicates single molecule magnetic (SMM) behavior^[82]. These unique properties arise from the molecule itself and show prospects for a great variety of applications, e.g., data storage^[67, 83] or quantum computing^[67, 69, 84, 85]. Such transition metal complexes acquire a high spin ground state combined with a sizeable anisotropic barrier^[30, 75, 86-88]. The first discovered molecule with such behavior was an Mn₁₂-acetate complex synthesized by Lis^[89]. Nowadays, for the design of improved SMM molecules, the combination of 3d transition metals in a high spin configuration with 4f lanthanides provides enhanced magnetic anisotropies^[43, 45, 46, 90-95]. Besides the combination of 3d and 4f ions, the design of multimetallic 3d transition metal complexes are in focus because of the high availability of the metal ions^[96-101].

Multimetallic complexes allow for investigation of cooperative effects that occur through the interaction of metal centers in such complexes, which represents a very active field of research^[102-108], e.g., in magnetism, reactivity, or functional applications. There are cooperative effects of multimetallic transition metal complexes in their catalytic^[109-118], optical^[112, 119-128], and magnetic^[129-135] properties, which helps to understand such cooperative effects.

Most investigations of the above mentioned properties in TM complexes were performed either in solution or in the bulk phase. However, gas phase investigations seem necessary in order to recognize effects by solvation or packing effects through crystalline interactions.

Matrix-assisted Laser Desorption/Ionization^[136-138] (MALDI) and Electrospray Ionization^[139-141] (ESI) have been established as the most common ion sources for the soft ionization of transition metal complexes and enable the transfer into vacuum and isolation. Mass spectrometric analysis^[142-145] determines the mass to charge (m/z) ratio of the complex of interest and allows the specific selection by their m/z selection. Subsequent irradiation of TM complexes with various light sources, the “action spectroscopy” approach^[146], can be performed. The ion density is lower within the ion trap than in condensed phase samples in classical absorption experiments. The irradiation of isolated TM complexes with light sources thus needs to cause changes in the mass spectrum, e.g., dissociation. Collisions with buffer gas in an ion trap may provide further information on the complex of interest. By such

collisions, the complex cannot transfer its energy to the background gas and starts fragmentation, providing information about the stability of the molecule and its fragmentation or reaction pathways. Action spectroscopy and molecular collisions have been established as two common and powerful tools^[147-149] for the investigation of properties in isolated TM complexes. With these experimental methods it is possible to extract information of several molecular properties, such as geometrical structure^[150-152], reaction barriers^[153, 154], bonding strengths^[155, 156], fragmentation pathways^[115, 157] and magnetism^[158-164]. Combining the different experimental methods with quantum chemical calculations^[165, 166] supports the experimental data interpretation and helps gain fundamental insights into the TM complexes of interest.

Collision Induced Dissociation^[167, 168] (CID) is performed by collisions of trapped ions and the background gas molecules, converting the kinetic energy of the trapped ions into internal energy^[169]. For Transition metal complexes, this technique is beneficial to investigate the activation barrier of ligand binding energies^[170-172] and their fragmentation pathways^[173, 174]. Comparing the experimental results with DFT modeled geometries of parent, fragments and transition state structures provides fundamental insights into the intramolecular fragmentation pathways of isolated molecules^[175-177].

InfraRed (Multiple) Photon Dissociation (IR(M)PD) gives an insight into the geometrical structure and bonding motif of isolated transition metal complexes^[178-181]. By resonant absorption of the infrared photons, an intramolecular vibrational redistribution^[182] (IVR) process transfers the excess energy into the internal vibrational degree of freedom. When the internal energy reaches the dissociation threshold^[183, 184], the ion of interest starts fragmentation. High dissociation thresholds or inefficient IVR processes might lead to inefficient fragmentation, occasionally resulting in the absence of some vibrational bands^[185, 186]. DFT calculated geometries and their calculated IR spectra have been proven suitable for accurate interpretation and analysis of the experimental IR(M)PD spectra^[187, 188].

Ultra Violet Photon Dissociation^[106, 125, 189-191] (UVPD) provides information on the electronic ground state of isolated molecules. With this kind of action spectroscopy, it is possible to obtain knowledge of the electronic ground state without external effects such as solvation. This technique may provide access to coordinatively unsaturated complexes, which would not

be available in the condensed phase (cf. chapter 5). Compared with time-dependent DFT (TD - DFT) modeling, an interpretation of the UV/VIS spectra is possible.

X-ray Magnetic Circular Dichroism^[192] (XMCD) is an element selective spectroscopy, which enables the investigation of magnetic properties of nanoparticles^[193, 194], thin films^[195-197] and isolated molecules^[160-164, 194-197]. With sum rule analysis^[198-200], it is possible to determine the spin and orbital contributions of the investigated compound of interest. Therefore, XMCD spectra of isolated molecules give access to intrinsic magnetic properties void of external effects as, e.g., crystal packing effects, surface induced effects, or solvatochromy. The results of the XMCD experiments can be compared with DFT modeling in a Broken Symmetry^[201, 202] approach to determine the exchange coupling between transition metal ions in the isolated complex.

This thesis comprises studies on mass-selected mononuclear and multinuclear transition metal complexes. The presented complexes are investigated in gas phase by ESI infusion to various mass spectrometers. The molecular properties, as mentioned above, are explored by combining several experimental and computational methods (cf. Fig. 1). The thesis contains seven research studies (chapters 5-11) using IR(M)PD, UVPD, CID, and XMCD techniques combined with DFT modeling and XA simulations. All chapters provide an independent introduction, a brief description of the experimental setup and theoretical methods, a discussion, and a conclusion, thus formatted as a draft manuscript.

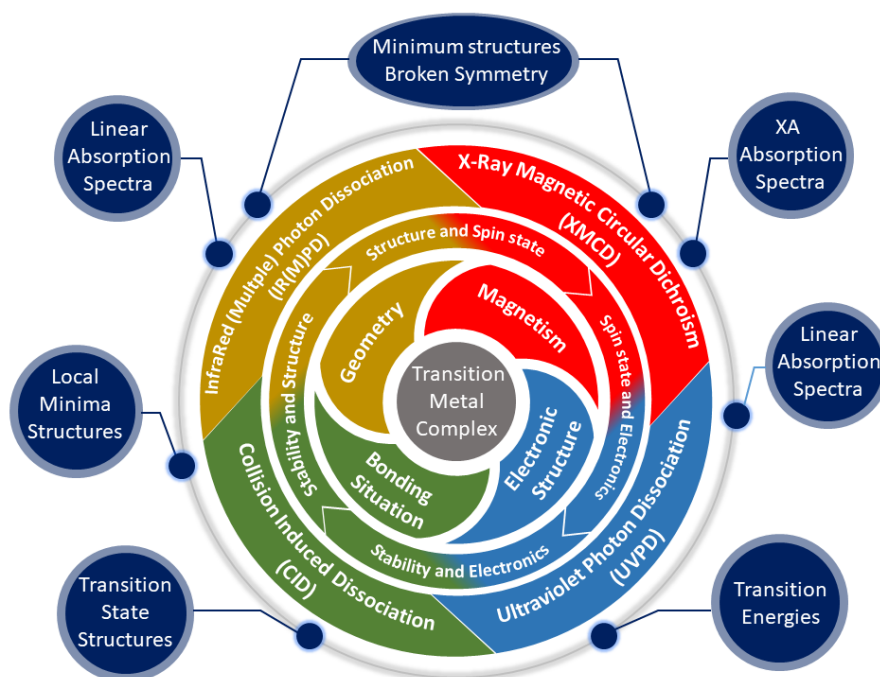


Fig. 1: The employed experimental and computational methods that serve to investigate isolated transition metal complexes as utilized in this thesis.

In more detail, the results documenting chapters of this thesis are as follows: Chapter 5 reports the change of an antiferromagnetic exchange coupled trinuclear iron (III) μ -oxo acetate complex $[\text{Fe}_3\text{O}(\text{OAc})_6]^+$ complex to a ferromagnetic exchange coupled complex with the coordination of pyridine to the complex. The chapter presents polarized dependent XA spectra and their corresponding XMCD spectra for the complexes $[\text{Fe}_3\text{O}(\text{OAc})_6(\text{py})_{0-3}]^+$ in comparison with DFT modeling and XA simulations. Geometrical changes in the angles of the Fe_3O core directly correlate with the magnetic moments per atom in this series of complexes, elucidating the change of the ground state by coordinating pyridine to the trinuclear μ -oxo acetate complex $[\text{Fe}_3\text{O}(\text{OAc})_6]^+$. The presented UVPD spectra reveal a small redshift by coordinating pyridine to the complex and a blueshift by coordinating three pyridines to the complex, resulting in a restoration of the symmetry.

At least an Opto magnetic correlation of the complex $[\text{Fe}_3\text{O}(\text{OAc})_6(\text{py})_{0-3}]^+$ is established. The XA spectra and the corresponding UVPD spectra reveal the same trend of shifting in both spectra. Compared with the Tanabe-Sugano diagram for a d^5 high spin atom, a correlation between the absorption energies in the UVPD spectra and the crystal field splitting from the XA spectra is possible. Compared with DFT modeling, the change of the bridging ligand has a minor influence on both properties (e.g., magnetic moments and absorption energies). The complex is more affected by non covalent interactions and the central oxygen atom.

Chapter 6 is built up from earlier IR(M)PD studies of $[\text{Fe}_3\text{O}(\text{OAc})_6]^{+}$ ^[203, 204] and focuses on the change from Fe(III) high spin atoms to Ru(III) low spin atoms. The IR(M)PD spectra, in combination with DFT calculations, point out that the complex does not feature restoration of the symmetry in the complex by coordinating three pyridines to the complex, as with Fe(III)^[203, 204]. Broken symmetry calculations hint no change in the magnetic properties, and this complex still shows antiferromagnetic exchange coupling with every coordination of pyridine to the complex.

Chapter 7 reports temperature dependent XA investigations of a mononuclear spin-crossover complex $[\text{Fe}(\text{btpa})]^{2+}$. The experimental magnetic values presented in this chapter reveal a change in the magnetic moments by raising the temperature. DFT modeling leads to three different minimum structures of the complex. The XA spectra hint three other geometrical complexes, e.g., two high spin complexes and one low spin complex. The IR(M)PD spectra also point out three different structures combined with DFT modeling two octahedral complexes and one quasi heptagonal coordinated complex are observed. Transition state calculations reveal a change from the low spin to the high spin by these structures. The correlation between XA spectra and their corresponding UV/VIS spectra of $[\text{Fe}(\text{btpa})]^{2+}$ hints that different crystal field splittings lead to two various absorption bands. In combination with TD-DFT modeling, these absorption bands can be assigned to the different high spin complexes.

Chapter 8 reports the investigation of a trimetallic Manganese complex with single molecule magnetic behavior. The temperature dependent XA spectra and their corresponding XMCD spectra reveal lower magnetic moments by raising the temperature. Broken Symmetry calculation also predicts a spin flip from one “spin up” electron to a “spin down” electron.

Chapter 9 reports the structure determination of complexes with the structure $[\text{M}_2\text{Ln}(\text{HVab})(\text{Vab})_3(\text{NO}_3)]^{2+}$ ($\text{M} = \text{Co}, \text{Cu}$; $\text{Ln} = \text{Dy}, \text{Gd}, \text{Nd}, \text{Sm}, \text{Tb}$) with single molecule magnetic behavior. The presented IR(M)PD spectra reveal two different isomers for this series of complexes. This series of complexes obtains a high symmetry as a result of fewer vibrational bands in the spectra. This study explains the influence of the transition metal on the lanthanide and their single molecule magnetic behavior.

Chapter 10 is a comment to a publication of Kowalska et al.^[205], which reports the nitrogenase process investigation with a spin coupled Molybdenum atom in a $[\text{MoFe}_3\text{S}_4]$ core. The delocalized electron is more located at the Fe^{3+} ion in the cubane system, and by X-ray absorption behaves like a Fe^{2+} atom. The assumed anti Hund'sche rule configuration in the Molybdenum atom could not be confirmed with DFT modeling.

Chapter 11 presents the first investigations of a single molecule magnet with the structure $[\text{Mn}_7(\text{Vab})_6]^{2+}$. The mass spectra and CID breakdown curves show a fairly stable complex that begins fragmentation by losing one methyl group. TD-DFT calculations reveal weak MLCT transitions, allowing the Tanabe-Sugano diagram to approximate the crystal field splitting in Mn^{2+} ions. Broken symmetry calculations reveal almost similar energies for the antiferromagnetically coupled structures, implying a degenerated system. The anisotropic tensors show a higher value for an antiferromagnetically coupled system than for the ferromagnetically coupled complex.

Chapter 12 reports developing a new ion source and troubleshooting on an existing home built mass spectrometer. The First test of the new ion source showed pure transition metal clusters with different metals. Next, the aggregation of Nitrogen to Tantalum clusters is reported and proved by comparing with previously measured mass spectra of Nitrogen adsorbed Tantalum clusters at the FRITZ instrument^[206-208].

The appendix AI provides a brief characterization of a trinuclear Rhodium complex via CID and IR(M)PD experiments combined with DFT calculations of the minimum structure and the corresponding linear absorption spectrum.

Appendix All serves as a starting point for the auto-oxidation investigation in a neutral trinuclear Palladium complex to a mono cationic complex. CID experiments point out that the investigated complex is present as a parent and not as a fragment, indicating that a Redox reaction occurs during the ESI process. DFT modeling of the neutral and the cationic complex reveals that the cationic complex is more favored than the neutral one.

In the appendix, AIII gives a detailed description of a common problem with the RF voltages in the amazon mass spectrometer. The conductance problems of the RF voltages lead to laborious actions to fix this problem. This description prevents a time loss for this problem and avoids more damage to other parts of the mass spectrometers.

Appendix AIV briefly reports the repair process of a commercially bought time of flight mass spectrometer called ultraflex II (bruker, daltonics). The reported chapter includes several steps for replacing defective parts of the mass spectrometer and maintaining the software package to provide a working instrument.

At least appendix AV comprises the scientific proposals to request beam time at the Helmholtz Zentrum Berlin für Materialien und Energie (BESSY II). The reviewers high ranked all these proposals, but some beam times were canceled due to other groups in resubmissions. We granted three beam times with a full time allocation of two weeks and one beam time with a time allocation of one week.

This thesis comprises different experimental techniques for investigating paramagnetic mono- and multinuclear TM complexes in combination with computational methods to gain a better insight into complexes with magnetic properties. Combining these techniques leads to a different point of view of the investigated complex, resulting in a more detailed understanding of how magnetic properties are influenced by structural or electronic properties and vice versa (cf. Fig. 1).

1.1 References

- [1] A. T. Baker, and S. E. Livingstone, Historical Sketch: The early history of coordination chemistry in Australia, *Polyhedron*, 4, 1337-1351, 1985.
- [2] R. A. H. K.R. Dunbar, Chemistry of Transition Metal Cyanide Compounds: Modern Perspectives, *John Wiley & Sons*, 2007.
- [3] G. B. Kauffman, Coordination Chemistry: History, in Encyclopedia of Inorganic Chemistry, *John Wiley & Sons*, 2006.
- [4] G. A. Lawrance, Introduction to coordination Chemistry, *John Wiley & Sons*, 41-82, 2009.
- [5] C. Elschenbroich, Organometallics, *Teubner*, 2005.
- [6] E. A. K. J.E. Huheey, R.L. Keiter, Inorganic Chemistry: Principles of Structure and Reactivity *Pearson Education*, 2000.
- [7] P. N. A.Behr, Applied Homogenous Catalysis, *Wiley*, 2012.
- [8] E. M. Beccalli, G. Brogini, M. Martinelli, and S. Sottocornola, C–C, C–O, C–N Bond Formation on sp² Carbon by Pd(II)-Catalyzed Reactions Involving Oxidant Agents, *Chem. Rev.*, 107, 5318-5365, 2007.
- [9] J. A. Labinger, and J. E. Bercaw, Understanding and exploiting C–H bond activation, *Nature*, 417, 507-514, 2002.

- [10] M. Lersch, and M. Tilset, Mechanistic Aspects of C–H Activation by Pt Complexes, *Chem. Rev.*, 105, 2471-2526, 2005.
- [11] V. Ritleng, C. Sirlin, and M. Pfeffer, Ru-, Rh-, and Pd-Catalyzed C–C Bond Formation Involving C–H Activation and Addition on Unsaturated Substrates: Reactions and Mechanistic Aspects, *Chem. Rev.*, 102, 1731-1770, 2002.
- [12] M. Aresta, Carbon Dioxide Reduction and Uses as Chemical Feedstock, in *Activation of Small Molecules, Wiley-VCH Verlag GmbH & Co. KGaA*, 1-41, 2006.
- [13] L. M. Berreau, Water Activation: Catalytic Hydrolysis, in *Activation of Small Molecules, Wiley-VCH Verlag GmbH & Co. KGaA*, 287-317, 2006.
- [14] M. S. S. C.N. Cornell, Molecular Oxygen Binding and Activation: Oxidation Catalysis, in *small molecules, Wiley-VCH Verlag GmbH & Co. KGaA*, 159-186, 2006.
- [15] H. Tanaka, K. Arashiba, S. Kuriyama, A. Sasada, K. Nakajima, K. Yoshizawa, and Y. Nishibayashi, Unique behaviour of dinitrogen-bridged dimolybdenum complexes bearing pincer ligand towards catalytic formation of ammonia, *Nature Communications*, 5, 3737, 2014.
- [16] N. Xiong, G. Zhang, X. Sun, and R. Zeng, Metal-Metal Cooperation in Dinucleating Complexes Involving Late Transition Metals Directed towards Organic Catalysis, *Chin. J. Chem.* 38, 185-201, 2020.
- [17] L. H. Einhorn, Treatment of testicular cancer: a new and improved model, *J. Clinical Oncology*, 8, 1777-1781, 1990.
- [18] M. Galanski, V. B. Arion, M. A. Jakupec, and B. K. Keppler, Recent Developments in the Field of Tumor-Inhibiting Metal Complexes, *Current Pharmaceutical Design*, 9, 2078-2089, 2003.
- [19] E. R. Jamieson, and S. J. Lippard, Structure, Recognition, and Processing of Cisplatin–DNA Adducts, *Chem. Rev.*, 99, 2467-2498, 1999.
- [20] H. M. Keys, B. N. Bundy, F. B. Stehman, L. I. Muder spach, W. E. Chafe, C. L. Suggs, J. L. Walker, and D. Gersell, Cisplatin, Radiation, and Adjuvant Hysterectomy Compared with Radiation and Adjuvant Hysterectomy for Bulky Stage IB Cervical Carcinoma, *New England J. Medicine*, 340, 1154-1161, 1999.
- [21] A. Leonidova, V. Pierroz, R. Rubbiani, J. Heier, S. Ferrari, and G. Gasser, Towards cancer cell-specific phototoxic organometallic rhenium(i) complexes, *Dalt. Trans*, 43, 4287-4294, 2014.
- [22] P. J. Loehrer, and L. H. Einhorn, Cisplatin, *Annals of Internal Medicine*, 100, 704-713, 1984.
- [23] P. G. Rose, B. N. Bundy, E. B. Watkins, J. T. Thigpen, G. Deppe, M. A. Maiman, D. L. Clarke-Pearson, and S. Insalaco, Concurrent Cisplatin-Based Radiotherapy and Chemotherapy for Locally Advanced Cervical Cancer, *New England J. Medicine*, 340, 1144-1153, 1999.
- [24] E. Shaili, Platinum Anticancer Drugs and Photochemotherapeutic Agents: Recent Advances and Future Developments, *Sci. Prog.*, 97, 20-40, 2014.
- [25] C. X. Zhang, and S. J. Lippard, New metal complexes as potential therapeutics, *Curr. Opin. Chem. Biol.*, 7, 481-489, 2003.
- [26] J. Adediji, E. Olayinka, M. Adebayo, and O. Babatunde, Antimalarial mixed ligand metal complexes: Synthesis, physicochemical and biological activities, *Int. J. Phys. Sciences*, 4, 2009.
- [27] P. A. Ajibade, and G. A. Kolawole, Synthesis, characterization and in vitro antiprotozoal studies of iron(III) complexes of some antimalarial drugs, *J. Coord. Chem.*, 61, 3367-3374, 2008.
- [28] T. J. Hubin, P. N. A. Amoyaw, K. D. Roewe, N. C. Simpson, R. D. Maples, T. N. Carder Freeman, A. N. Cain, J. G. Le, S. J. Archibald, S. I. Khan, B. L. Tekwani, and M. O. F. Khan, Synthesis and antimalarial activity of metal complexes of cross-bridged tetraazamacrocyclic ligands, *Biorg. Med. Chem.*, 22, 3239-3244, 2014.
- [29] N. Wasi, H. B. Singh, A. Gajanana, and A. N. Raichowdhary, Synthesis of metal complexes of antimalarial drugs and in vitro evaluation of their activity against plasmodium falciparum, *Inorg. Chim. Acta*, 135, 133-137, 1987.
- [30] J. V. R.S.D. Gatteschi, *Molecular Nanomagnets, Oxford University Press*, 2006.
- [31] Y. Garcia, P. J. van Koningsbruggen, E. Codjovi, R. Lapouyade, O. Kahn, and L. Rabardel, Non-classical FeII spin-crossover behaviour leading to an unprecedented extremely large apparent thermal hysteresis of 270 K: application for displays, *J. Mater. Chem.*, 7, 857-858, 1997.
- [32] P. Gütllich, Y. Garcia, and H. A. Goodwin, Spin crossover phenomena in Fe(I) complexes, *Chem. Soc. Rev.*, 29, 419-427, 2000.
- [33] P. Gütllich, H. A. Goodwin, and Y. Garcia, *Spin Crossover in Transition Metal Compounds I*: Springer, 2004.
- [34] H.-J. Krüger, Spin transition in octahedral metal complexes containing tetraazamacrocyclic ligands, *Coord. Chem. Rev.*, 253, 2450-2459, 2009.
- [35] V. Niel, J. M. Martinez-Agudo, M. C. Muñoz, A. B. Gaspar, and J. A. Real, Cooperative Spin Crossover Behavior in Cyanide-Bridged Fe(II)–M(II) Bimetallic 3D Hofmann-like Networks (M = Ni, Pd, and Pt), *Inorg. Chem.*, 40, 3838-3839, 2001.

- [36] M. Schmitz, M. Seibel, H. Kelm, S. Demeshko, F. Meyer, and H.-J. Krüger, How Does a Coordinated Radical Ligand Affect the Spin Crossover Properties in an Octahedral Iron(II) Complex?, *Angew. Chem. Int. Ed.*, 53, 5988-5992, 2014.
- [37] B. Kintzel, M. Böhme, J. Liu, A. Burkhardt, J. Mrozek, A. Buchholz, A. Ardavan, and W. Plass, Molecular electronic spin qubits from a spin-frustrated trinuclear copper complex, *Chem. Commun.*, 54, 12934-12937, 2018.
- [38] D. MasPOCH, D. Ruiz-Molina, K. Wurst, C. Rovira, and J. Veciana, A very bulky carboxylic perchlorotriphenylmethyl radical as a novel ligand for transition metal complexes. A new spin frustrated metal system, *Chem. Commun.*, 2958-2959, 2002.
- [39] R. Shaw, R. H. Laye, L. F. Jones, D. M. Low, C. Talbot-Eeckelaers, Q. Wei, C. J. Milios, S. Teat, M. Helliwell, J. Raftery, M. Evangelisti, M. Affronte, D. Collison, E. K. Brechin, and E. J. L. McInnes, 1,2,3-Triazolate-Bridged Tetradecametallic Transition Metal Clusters [M₁₄(L)₆O₆(OMe)₁₈X₆] (M = FeIII, CrIII and VIII/IV) and Related Compounds: Ground-State Spins Ranging from S = 0 to S = 25 and Spin-Enhanced Magnetocaloric Effect, *Inorg. Chem.*, 46, 4968-4978, 2007.
- [40] P. Zhang, and P. J. Sadler, Redox-Active Metal Complexes for Anticancer Therapy, *Eur. J. Inorg. Chem.*, 2017, 1541-1548, 2017.
- [41] W.-X. Zhang, W. Xue, J.-B. Lin, Y.-Z. Zheng, and X.-M. Chen, 3D geometrically frustrated magnets assembled by transition metal ion and 1,2,3-triazole-4,5-dicarboxylate as triangular nodes, *Cryst. Eng. Comm.*, 10, 1770-1776, 2008.
- [42] J. M. Clemente-Juan, E. Coronado, A. Forment-Aliaga, A. Gaita-Ariño, C. Giménez-Saiz, F. M. Romero, W. Wernsdorfer, R. Biagi, and V. Corradini, Electronic and Magnetic Study of Polycationic Mn₁₂ Single-Molecule Magnets with a Ground Spin State S = 11, *Inorg. Chem.*, 49, 386-396, 2010.
- [43] A. Dey, S. Das, V. Mereacre, A. K. Powell, and V. Chandrasekhar, Butterfly-shaped, heterometallic, hexanuclear, [FeII₂LnIII₄] (LnIII = GdIII, TbIII, DyIII and HoIII) Complexes: Syntheses, structure and magnetism, *Inorg. Chim. Acta*, 486, 458-467, 2019.
- [44] J. Dreiser, K. S. Pedersen, A. Schnegg, K. Holldack, J. Nehr Korn, M. Sigrist, P. Tregenna-Piggott, H. Mutka, H. Weihe, V. S. Mironov, J. Bendix, and O. Waldmann, Three-Axis Anisotropic Exchange Coupling in the Single-Molecule Magnets NEt₄[MnIII₂(5-Brsalen)₂(MeOH)₂MIII(CN)₆] (M=Ru, Os), *Chemistry – A European Journal*, 19, 3693-3701, 2013.
- [45] P. Hahn, S. Ullmann, J. Klose, Y. Peng, A. K. Powell, and B. Kersting, Dinuclear Tb and Dy complexes supported by hybrid Schiff-base/calixarene ligands: synthesis, structures and magnetic properties, *Dalt. Trans*, 2020.
- [46] R. Modak, Y. Sikdar, A. E. Thuijs, G. Christou, and S. Goswami, Coll₄, Coll₇, and a Series of Coll₂LnIII (LnIII = NdIII, SmIII, GdIII, TbIII, DyIII) Coordination Clusters: Search for Single Molecule Magnets, *Inorg. Chem.*, 55, 10192-10202, 2016.
- [47] A. V. Paliy, S. M. Ostrovsky, S. I. Klokishner, B. S. Tsukerblat, C. P. Berlinguette, K. R. Dunbar, and J. R. Galán-Mascarós, Role of the Orbitally Degenerate Mn(III) Ions in the Single-Molecule Magnet Behavior of the Cyanide Cluster {[MnII(tmphen)₂]₃[MnIII(CN)₆]₂} (tmphen = 3,4,7,8-tetramethyl-1,10-phenanthroline), *J. Am. Chem. Soc.*, 126, 16860-16867, 2004.
- [48] J.-F. Létard, Photomagnetism of iron(ii) spin crossover complexes—the T(LIESST) approach, *J. Mater. Chem.*, 16, 2550-2559, 2006.
- [49] J.-F. Létard, P. Guionneau, and L. Goux-Capes, "Towards Spin Crossover Applications," *Spin Crossover in Transition Metal Compounds III*, P. Gütllich and H. A. Goodwin, eds., pp. 221-249, Berlin, Heidelberg: Springer Berlin Heidelberg, 2004.
- [50] W. E. I. Lu, and C. M. Lieber, "Nanoelectronics from the bottom up," *Nanoscience and Technology*, pp. 137-146: Co-Published with Macmillan Publishers Ltd, UK, 2009.
- [51] R. M. Metzger, Unimolecular Electrical Rectifiers, *Chem. Rev.*, 103, 3803-3834, 2003.
- [52] R. M. Metzger, Unimolecular rectifiers: Methods and challenges, *Anal. Chim. Acta*, 568, 146-155, 2006.
- [53] J. K. Gimzewski, and C. Joachim, Nanoscale Science of Single Molecules Using Local Probes, *Science*, 283, 1683, 1999.
- [54] D. K. James, and J. M. Tour, "Molecular Wires," *Molecular Wires and Electronics*, pp. 33-62, Berlin, Heidelberg: Springer Berlin Heidelberg, 2005.
- [55] J. M. Tour, M. Kozaki, and J. M. Seminario, Molecular Scale Electronics: A Synthetic/Computational Approach to Digital Computing, *J. Am. Chem. Soc.*, 120, 8486-8493, 1998.
- [56] P. Gütllich, A. Hauser, and H. Spiering, Thermal and Optical Switching of Iron(II) Complexes, *Angew. Chemie Int. Ed.*, 33, 2024-2054, 1994.

- [57] M. Mörtel, A. Witt, F. W. Heinemann, S. Bochmann, J. Bachmann, and M. M. Khusniyarov, Synthesis, Characterization, and Properties of Iron(II) Spin-Crossover Molecular Photoswitches Functioning at Room Temperature, *Inorg. Chem.*, 56, 13174-13186, 2017.
- [58] G. B. Kaufman, Inorganic chemistry: principles of structure and reactivity, 4th ed. (Huheey, James E.; Keiter, Ellen A.; Keiter, Richard L.), *J. Chem. Educ.*, 70, A279, 1993.
- [59] L. H. Gade, Koordinationschemie, 2013.
- [60] G. Filoti, J. Bartolome, D. P. E. Dickson, C. Rillo, I. Prisecaru, T. Jovmir, V. Kuncser, and C. Turta, Intermediate frustration in [Fe₃O(CH₃COO)₆(H₂O)₃] NO₃ · 4(H₂O) trinuclear cluster, *J. Magn. Magn. Mater.*, 196-197, 561-563, 1999.
- [61] A. N. Georgopoulou, Y. Sanakis, and A. K. Boudalis, Magnetic relaxation in basic iron(III) carboxylate [Fe₃O(O₂CPh)₆(H₂O)₃]ClO₄·py, *Dalt. Trans.*, 40, 6371-6374, 2011.
- [62] G. Férey, M. Latroche, C. Serre, F. Millange, T. Loiseau, and A. Percheron-Guégan, Hydrogen adsorption in the nanoporous metal-benzenedicarboxylate M(OH)(O₂C-C₆H₄-CO₂) (M = Al³⁺, Cr³⁺), MIL-53, *Chem. Commun.*, 2976-2977, 2003.
- [63] G. Férey, C. Mellot-Draznieks, C. Serre, F. Millange, J. Dutour, S. Surblé, and I. Margiolaki, A Chromium Terephthalate-Based Solid with Unusually Large Pore Volumes and Surface Area, *Science*, 309, 2040, 2005.
- [64] G. Férey, C. Serre, C. Mellot-Draznieks, F. Millange, S. Surblé, J. Dutour, and I. Margiolaki, A Hybrid Solid with Giant Pores Prepared by a Combination of Targeted Chemistry, Simulation, and Powder Diffraction, *Angew. Chem. Int. Ed.*, 43, 6296-6301, 2004.
- [65] S. Uchida, M. Hashimoto, and N. Mizuno, A Breathing Ionic Crystal Displaying Selective Binding of Small Alcohols and Nitriles: K₃[Cr₃O(OOCH)₆(H₂O)₃][α-SiW₁₂O₄₀]·16 H₂O, *Angew. Chem. Int. Ed.*, 41, 2814-2817, 2002.
- [66] S. Uchida, and N. Mizuno, Unique Guest-Inclusion Properties of a Breathing Ionic Crystal of K₃[Cr₃O(OOCH)₆(H₂O)₃][α-SiW₁₂O₄₀]·16 H₂O, *Chemistry – A European Journal*, 9, 5850-5857, 2003.
- [67] G. Aromí, D. Aguilà, P. Gamez, F. Luis, and O. Roubeau, Design of magnetic coordination complexes for quantum computing, *Chem. Soc. Rev.*, 41, 537-546, 2012.
- [68] J. Ferrando-Soria, Samantha A. Magee, A. Chiesa, S. Carretta, P. Santini, Iñigo J. Vitorica-Yrezabal, F. Tuna, George F. S. Whitehead, S. Sproules, Kyle M. Lancaster, A.-L. Barra, Grigore A. Timco, Eric J. L. McInnes, and Richard E. P. Winpenny, Switchable Interaction in Molecular Double Qubits, *Chem*, 1, 727-752, 2016.
- [69] M. N. Leuenberger, and D. Loss, Quantum computing in molecular magnets, *Nature*, 410, 789-793, 2001.
- [70] T. N. Nguyen, W. Wernsdorfer, M. Shiddiq, K. A. Abboud, S. Hill, and G. Christou, Supramolecular aggregates of single-molecule magnets: exchange-biased quantum tunneling of magnetization in a rectangular [Mn₃]₄ tetramer, *Chemical Science*, 7, 1156-1173, 2016.
- [71] M. Trif, F. Troiani, D. Stepanenko, and D. Loss, Spin-Electric Coupling in Molecular Magnets, *Phys. Rev. Lett.*, 101, 217201, 2008.
- [72] J. P. S. Walsh, S. B. Meadows, A. Ghirri, F. Moro, M. Jennings, W. F. Smith, D. M. Graham, T. Kihara, H. Nojiri, I. J. Vitorica-Yrezabal, G. A. Timco, D. Collison, E. J. L. McInnes, and R. E. P. Winpenny, Electronic Structure of a Mixed-Metal Fluoride-Centered Triangle Complex: A Potential Qubit Component, *Inorg. Chem.*, 54, 12019-12026, 2015.
- [73] S. Bi, C. Liu, and H. Hu, Theoretical Study on Magnetostructural Correlation in Unsymmetrical Oxamidocopper(II) Complexes, *J. Phys. Chem. B*, 106, 10786-10792, 2002.
- [74] T. Cauchy, E. Ruiz, and S. Alvarez, Magnetostructural Correlations in Polynuclear Complexes: The Fe₄ Butterflies, *J. Am. Chem. Soc.*, 128, 15722-15727, 2006.
- [75] D. Gatteschi, and R. Sessoli, Quantum Tunneling of Magnetization and Related Phenomena in Molecular Materials, *Angew. Chem. Int. Ed.*, 42, 268-297, 2003.
- [76] S. M. Gorun, and S. J. Lippard, Magnetostructural correlations in magnetically coupled (μ-oxo)diiron(III) complexes, *Inorg. Chem.*, 30, 1625-1630, 1991.
- [77] Y.-W. Lin, Rational design of metalloenzymes: From single to multiple active sites, *Coord. Chem. Rev.*, 336, 1-27, 2017.
- [78] J.-L. Chen, L.-Y. Zhang, L.-X. Shi, H.-Y. Ye, and Z.-N. Chen, Syntheses, characterization and redox properties of di- and poly-phosphine linked oligomeric complexes of oxo-centered triruthenium clusters, *Inorg. Chim. Acta*, 359, 1531-1540, 2006.
- [79] M. Lu, T. Chen, M. Wang, G. Jiang, T. Lu, G. Jiang, and J. Du, A new μ₃-oxo-centered tri-nuclear carboxyl bridged iron (III) complex with thio-methyl groups in the periphery: Structural, spectroscopic and electrochemical studies, *J. Mol. Struct.*, 1060, 131-137, 2014.

- [80] S. Uchida, and N. Mizuno, Zeotype Ionic Crystal of Cs₅[Cr₃O(OOCH)₆(H₂O)₃][α-CoW₁₂O₄₀]-7.5H₂O with Shape-Selective Adsorption of Water, *J. Am. Chem. Soc.*, 126, 1602-1603, 2004.
- [81] S. T. Wilson, R. F. Bondurant, T. J. Meyer, and D. J. Salmon, OXIDATION STATE PROPERTIES OF DELOCALIZED, LIGAND-BRIDGED METAL COMPLEXES. (RU₃O(CH₃CO₂)₆L₃)N⁺ AND THE PYRAZINE-BRIDGED, CLUSTER-CLUSTER DIMER, (RU₃O(CH₃CO₂)₆(PY)₂)₂PYZM⁺, 1975.
- [82] G. Christou, D. Gatteschi, D. N. Hendrickson, and R. Sessoli, Single-Molecule Magnets, *MRS Bull.*, 25, 66-71, 2011.
- [83] R. Winnpenny volume editor, and G. Aromi with contributions by, *Single-molecule magnets and related phenomena*: Berlin ; New York : Springer, 2006.
- [84] M. Mannini, F. Pineider, P. Saintavitt, C. Danieli, E. Otero, C. Sciancalepore, A. M. Talarico, M.-A. Arrio, A. Cornia, D. Gatteschi, and R. Sessoli, Magnetic memory of a single-molecule quantum magnet wired to a gold surface, *Nature Materials*, 8, 194-197, 2009.
- [85] K. V. Raman, A. M. Kamerbeek, A. Mukherjee, N. Atodiresei, T. K. Sen, P. Lazić, V. Caciuc, R. Michel, D. Stalke, S. K. Mandal, S. Blügel, M. Münzenberg, and J. S. Moodera, Interface-engineered templates for molecular spin memory devices, *Nature*, 493, 509-513, 2013.
- [86] D. G. A. Caneschi, R. Sessoli, A. L. Barra, L. C. Brunel, M. Guillot Alternating-current susceptibility high-field magnetization and millimeter band EPR evidence for a ground S=10 in M₁₂(CH₃COO)₁₆(H₂O)₄ 2CH₃COOH 4H₂O, *J. Am. Chem. Soc.*, 113, 5873, 1991.
- [87] R. Sessoli, D. Gatteschi, A. Caneschi, and M. A. Novak, Magnetic bistability in a metal-ion cluster, *Nature*, 365, 141-143, 1993.
- [88] W. Wernsdorfer, E. B. Orozco, B. Barbara, A. Benoît, and D. J. P. B.-c. M. Maily, Classical and quantum magnetisation reversal studied in single nanometer-sized particles and clusters using micro-SQUIDS, 280, 264-268, 2000.
- [89] T. Lis, Preparation, structure, and magnetic properties of a dodecanuclear mixed-valence manganese carboxylate, *AcCrB*, 36, 2042-2046, 1980.
- [90] T. Glaser, Rational design of single-molecule magnets: a supramolecular approach, *Chem. Commun.*, 47, 116-130, 2011.
- [91] P.-E. Car, M. Perfetti, M. Mannini, A. Favre, A. Caneschi, and R. Sessoli, Giant field dependence of the low temperature relaxation of the magnetization in a dysprosium(iii)-DOTA complex, *Chem. Commun.*, 47, 3751-3753, 2011.
- [92] Y.-N. Guo, G.-F. Xu, P. Gamez, L. Zhao, S.-Y. Lin, R. Deng, J. Tang, and H.-J. Zhang, Two-Step Relaxation in a Linear Tetranuclear Dysprosium(III) Aggregate Showing Single-Molecule Magnet Behavior, *J. Am. Chem. Soc.*, 132, 8538-8539, 2010.
- [93] I. J. Hewitt, J. Tang, N. T. Madhu, C. E. Anson, Y. Lan, J. Luzon, M. Etienne, R. Sessoli, and A. K. Powell, Coupling Dy₃ Triangles Enhances Their Slow Magnetic Relaxation, *Angew. Chem. Int. Ed.*, 49, 6352-6356, 2010.
- [94] N. Ishikawa, M. Sugita, T. Ishikawa, S.-y. Koshihara, and Y. Kaizu, Lanthanide Double-Decker Complexes Functioning as Magnets at the Single-Molecular Level, *J. Am. Chem. Soc.*, 125, 8694-8695, 2003.
- [95] E. Moreno-Pineda, C. Godfrin, F. Balestro, W. Wernsdorfer, and M. Ruben, Molecular spin qubits for quantum algorithms, *Chem. Soc. Rev.*, 47, 501-513, 2018.
- [96] G. Arom, S. M. J. Aubin, M. A. Bolcar, G. Christou, H. J. Eppley, K. Folting, D. N. Hendrickson, J. C. Huffman, R. C. Squire, H.-L. Tsai, S. Wang, and M. W. Wemple, Manganese carboxylate clusters: from structural aesthetics to single-molecule magnets, Dedicated to Professor Jack Lewis on the occasion of his 70th birthday, *Polyhedron*, 17, 3005-3020, 1998.
- [97] F. Liedy, J. Eng, R. McNab, R. Inglis, T. J. Penfold, E. K. Brechin, and J. O. Johansson, Vibrational coherences in manganese single-molecule magnets after ultrafast photoexcitation, *Nature Chemistry*, 12, 452-458, 2020.
- [98] M. Murugesu, M. Habrych, W. Wernsdorfer, K. A. Abboud, and G. Christou, Single-Molecule Magnets: A Mn₂₅ Complex with a Record S = 51/2 Spin for a Molecular Species, *J. Am. Chem. Soc.*, 126, 4766-4767, 2004.
- [99] C. Rojas-Dotti, N. Moliner, F. Lloret, and J. Martínez-Lillo, Hexanuclear manganese(III) single-molecule magnets based on oxime and azole-type ligands, *Polyhedron*, 170, 223-231, 2019.
- [100] C.-I. Yang, W. Wernsdorfer, G.-H. Lee, and H.-L. Tsai, A Pentanuclear Manganese Single-Molecule Magnet with a Large Anisotropy, *J. Am. Chem. Soc.*, 129, 456-457, 2007.

- [101] J. Yoo, E. K. Brechin, A. Yamaguchi, M. Nakano, J. C. Huffman, A. L. Maniero, L.-C. Brunel, K. Awaga, H. Ishimoto, G. Christou, and D. N. Hendrickson, Single-Molecule Magnets: A New Class of Tetranuclear Manganese Magnets, *Inorg. Chem.*, 39, 3615-3623, 2000.
- [102] K. Balinski, L. Schneider, J. Wöllermann, A. Buling, L. Joly, C. Piamonteze, H. L. C. Feltham, S. Brooker, A. K. Powell, B. Delley, and K. Kuepper, Element specific determination of the magnetic properties of two macrocyclic tetranuclear 3d–4f complexes with a Cu₃Tb core by means of X-ray magnetic circular dichroism (XMCD), *Phys. Chem. Chem. Phys.*, 20, 21286-21293, 2018.
- [103] D. Garnier, A. Mondal, Y. Li, P. Herson, L.-M. Chamoreau, L. Toupet, M. Buron Le Cointe, E. M. B. Moos, F. Breher, and R. Lescouëzec, Tetranuclear [FeII₂FeIII₂]²⁺ molecular switches: [FeII(bik)₂(N–)₂] spin-crossover complexes containing [FeIII(Tp)(CN)₃][–] metalloligands as N-donor, *Comptes Rendus Chimie*, 22, 516-524, 2019.
- [104] A. W. Jones, C. K. Rank, Y. Becker, C. Malchau, I. Funes-Ardoiz, F. Maseras, and F. W. Patureau, Accelerated Ru–Cu Trinuclear Cooperative C–H Bond Functionalization of Carbazoles: A Kinetic and Computational Investigation, *Chemistry – A European Journal*, 24, 15178-15184, 2018.
- [105] N. Kazeminejad, L. Münzfeld, M. T. Gamer, and P. W. Roesky, Mono- and bimetallic amidinate samarium complexes – synthesis, structure, and hydroamination catalysis, *Dalt. Trans.*, 48, 8153-8160, 2019.
- [106] S. V. Kruppa, C. Groß, X. Gui, F. Böppler, B. Kwasigroch, Y. Sun, R. Diller, W. Klopfer, G. Niedner-Schatteburg, C. Riehn, and W. R. Thiel, Photoinitiated Charge Transfer in a Triangular Silver(I) Hydride Complex and Its Oxophilicity, *Chemistry – A European Journal*, 25, 11269-11284, 2019.
- [107] G. Niedner-Schatteburg, "Cooperative Effects in Clusters and Oligonuclear Complexes of Transition Metals in Isolation."
- [108] Y. Peng, C. E. Anson, and A. K. Powell, A W-Shaped Ga-Dy-Dy-Dy-Ga Cluster: Synthesis, Characterization, and Magnetic Properties, *ChemPlusChem*, 83, 676-681, 2018.
- [109] X.-Q. Hu, Z. Hu, A. S. Trita, G. Zhang, and L. J. Gooßen, Carboxylate-directed C–H allylation with allyl alcohols or ethers, *Chemical Science*, 9, 5289-5294, 2018.
- [110] S. Becker, U. Behrens, and S. Schindler, Investigations Concerning [Cu₄O₆L₄] Cluster Formation of Copper(II) Chloride with Amine Ligands Related to Benzylamine, *Eur. J. Inorg. Chem.*, 2015, 2437-2447, 2015.
- [111] S. Becker, M. Dürr, A. Miska, J. Becker, C. Gawlig, U. Behrens, I. Ivanović-Burmazović, and S. Schindler, Copper Chloride Catalysis: Do μ -4-Oxido Copper Clusters Play a Significant Role?, *Inorg. Chem.*, 55, 3759-3766, 2016.
- [112] E. Deck, K. Reiter, W. Klopfer, and F. Breher, A Dinuclear Gold(I) Bis(Carbene) Complex Based on a Ditopic Cyclic (Aryl)(Amino)Carbene Framework, *Z. Anorg. Allg. Chem.*, 642, 1320-1328, 2016.
- [113] A. Feyrer, M. K. Armbruster, K. Fink, and F. Breher, Metal Complexes of a Redox-Active [1]Phosphaferrocenophane: Structures, Electrochemistry and Redox-Induced Catalysis, *Chemistry – A European Journal*, 23, 7402-7408, 2017.
- [114] M. Gaffga, I. Munstein, P. Müller, J. Lang, W. R. Thiel, and G. Niedner-Schatteburg, Multistate-Mediated Rearrangements and FeCl₂ Elimination in Dinuclear FePd Complexes, *J. Phys. Chem. A*, 119, 12587-12598, 2015.
- [115] J. Lang, M. Cayir, S. P. Walg, P. Di Martino-Fumo, W. R. Thiel, and G. Niedner-Schatteburg, Intermetallic Competition in the Fragmentation of Trimetallic Au–Zn–Alkali Complexes, *Chemistry – A European Journal*, 22, 2345-2355, 2016.
- [116] S. Löw, J. Becker, C. Würtele, A. Miska, C. Kleeberg, U. Behrens, O. Walter, and S. Schindler, Reactions of Copper(II) Chloride in Solution: Facile Formation of Tetranuclear Copper Clusters and Other Complexes That Are Relevant in Catalytic Redox Processes, *Chemistry – A European Journal*, 19, 5342-5351, 2013.
- [117] F. Schön, M. Leist, A. Neuba, J. Lang, C. Braun, Y. Sun, G. Niedner-Schatteburg, S. Bräse, and W. R. Thiel, A direct access to heterobimetallic complexes by roll-over cyclometallation, *Chem. Commun.*, 53, 12016-12019, 2017.
- [118] F. Walz, E. Moos, D. Garnier, R. Köppe, C. E. Anson, and F. Breher, A Redox-Switchable Germylene and its Ligating Properties in Selected Transition Metal Complexes, *Chemistry – A European Journal*, 23, 1173-1186, 2017.
- [119] M. Grupe, F. Böppler, M. Theiß, J. M. Busch, F. Dietrich, D. Volz, M. Gerhards, S. Bräse, and R. Diller, Real-time observation of molecular flattening and intersystem crossing in [(DPEPhos)Cu(i)(PyrTet)] via ultrafast UV/Vis- and mid-IR spectroscopy on solution and solid samples, *Phys. Chem. Chem. Phys.*, 22, 14187-14200, 2020.

- [120] F. Böppler, M. Zimmer, F. Dietrich, M. Grupe, M. Wallesch, D. Volz, S. Bräse, M. Gerhards, and R. Diller, Photophysical dynamics of a binuclear Cu(i)-emitter on the fs to μ s timescale, in solid phase and in solution, *Phys. Chem. Chem. Phys.*, **19**, 29438-29448, 2017.
- [121] C. Braun, E. Spuling, N. B. Heine, M. Cakici, M. Nieger, and S. Bräse, Efficient Modular Synthesis of Isomeric Mono- and Bispyridyl[2.2]paracyclophanes by Palladium-Catalyzed Cross-Coupling Reactions, *Adv. Synth. Catal.*, **358**, 1664-1670, 2016.
- [122] J.-F. Greisch, M. E. Harding, B. Schäfer, M. Ruben, W. Klopfer, M. M. Kappes, and D. Schooss, Characterization of Nonanuclear Europium and Gadolinium Complexes by Gas-Phase Luminescence Spectroscopy, *J. Phys. Chem. Lett.*, **5**, 1727-1731, 2014.
- [123] B. Kern, J.-F. Greisch, D. Strelnikov, P. Weis, A. Böttcher, M. Ruben, B. Schäfer, D. Schooss, and M. M. Kappes, Photoluminescence Spectroscopy of Mass-Selected Electrosprayed Ions Embedded in Cryogenic Rare-Gas Matrixes, *Anal. Chem.*, **87**, 11901-11906, 2015.
- [124] S. V. Kruppa, F. Böppler, W. Klopfer, S. P. Walg, W. R. Thiel, R. Diller, and C. Riehn, Ultrafast excited-state relaxation of a binuclear Ag(i) phosphine complex in gas phase and solution, *Phys. Chem. Chem. Phys.*, **19**, 22785-22800, 2017.
- [125] S. V. Kruppa, Y. Nosenko, M.-O. Winghart, S. P. Walg, M. M. Kappes, and C. Riehn, Fragmentation pathways of dianionic $[\text{Pt}_2(\mu\text{-P}_2\text{O}_5\text{H}_2)_4\text{X}_2\text{Y}]^{2-}$ ($\text{X}, \text{Y} = \text{H}, \text{K}, \text{Ag}$) species in an ion trap induced by collisions and UV photoexcitation, *Int. J. Mass spectrom.*, **395**, 7-19, 2016.
- [126] Y. Schmitt, K. Chevalier, F. Rupp, M. Becherer, A. Grün, A. M. Rijs, F. Walz, F. Breher, R. Diller, M. Gerhards, and W. Klopfer, In-depth exploration of the photophysics of a trinuclear palladium complex, *Phys. Chem. Chem. Phys.*, **16**, 8332-8338, 2014.
- [127] K. Senthil Kumar, B. Schäfer, S. Lebedkin, L. Karmazin, M. M. Kappes, and M. Ruben, Highly luminescent charge-neutral europium(iii) and terbium(iii) complexes with tridentate nitrogen ligands, *Dalt. Trans.*, **44**, 15611-15619, 2015.
- [128] M. Zimmer, F. Rupp, P. Singer, F. Walz, F. Breher, W. Klopfer, R. Diller, and M. Gerhards, Time-resolved IR spectroscopy of a trinuclear palladium complex in solution, *Phys. Chem. Chem. Phys.*, **17**, 14138-14144, 2015.
- [129] M. Gysler, F. El Hallak, L. Ungur, R. Marx, M. Hakl, P. Neugebauer, Y. Rechkemmer, Y. Lan, I. Sheikin, M. Orlita, C. E. Anson, A. K. Powell, R. Sessoli, L. F. Chibotaru, and J. van Slageren, Multitechnique investigation of Dy³⁺ – implications for coupled lanthanide clusters, *Chemical Science*, **7**, 4347-4354, 2016.
- [130] G. Peng, V. Mereacre, G. E. Kostakis, J. A. Wolny, V. Schünemann, and A. K. Powell, Enhancement of Spin Relaxation in an FeDy₂Fe Coordination Cluster by Magnetic Fields, *Chemistry – A European Journal*, **20**, 12381-12384, 2014.
- [131] V. Mereacre, M. Schlageter, A. Eichhöfer, T. Bauer, J. A. Wolny, V. Schünemann, and A. K. Powell, Unusual metal-ligand charge transfer in ferrocene functionalized $\mu_3\text{-O}$ iron carboxylates observed with Mössbauer spectroscopy, *J. Magn. Magn. Mater.*, **407**, 87-91, 2016.
- [132] T. O. Bauer, M. Schmitz, M. Graf, H. Kelm, H. J. Krüger, and V. Schünemann, Determination of electronic ground state properties of a dinuclear iron(II) spin crossover complex, *Hyperfine Interact.*, **237**, 78, 2016.
- [133] M. Yadav, V. Mereacre, S. Lebedkin, M. M. Kappes, A. K. Powell, and P. W. Roesky, Mononuclear and Tetranuclear Compounds of Yttrium and Dysprosium Ligated by a Salicylic Schiff-Base Derivative: Synthesis, Photoluminescence, and Magnetism, *Inorg. Chem.*, **54**, 773-781, 2015.
- [134] Y. Peng, V. Mereacre, C. E. Anson, Y. Zhang, T. Bodenstein, K. Fink, and A. K. Powell, Field-Induced Co(II) Single-Ion Magnets with mer-Directing Ligands but Ambiguous Coordination Geometry, *Inorg. Chem.*, **56**, 6056-6066, 2017.
- [135] Y. Peng, V. Mereacre, C. E. Anson, and A. K. Powell, Multiple superhyperfine fields in a {DyFe₂Dy} coordination cluster revealed using bulk susceptibility and ⁵⁷Fe Mössbauer studies, *Phys. Chem. Chem. Phys.*, **18**, 21469-21480, 2016.
- [136] S. Berkenkamp, F. Kirpekar, and F. Hillenkamp, Infrared MALDI Mass Spectrometry of Large Nucleic Acids, *Science*, **281**, 260, 1998.
- [137] K. Dreisewerd, S. Berkenkamp, A. Leisner, A. Rohlfig, and C. Menzel, Fundamentals of matrix-assisted laser desorption/ionization mass spectrometry with pulsed infrared lasers, *Int. J. Mass spectrom.*, **226**, 189-209, 2003.
- [138] M. Karas, and R. Krüger, Ion Formation in MALDI: The Cluster Ionization Mechanism, *Chem. Rev.*, **103**, 427-440, 2003.

- [139] J. B. Fenn, Electrospray Wings for Molecular Elephants (Nobel Lecture), *Angew. Chem. Int. Ed.*, 42, 3871-3894, 2003.
- [140] M. Yamashita, and J. B. Fenn, Negative ion production with the electrospray ion source, *J. Phys. Chem.*, 88, 4671-4675, 1984.
- [141] M. Yamashita, and J. B. Fenn, Electrospray ion source. Another variation on the free-jet theme, *J. Phys. Chem.*, 88, 4451-4459, 1984.
- [142] W. N. Delgass, and R. G. Cooks, Focal Points in Mass Spectrometry, *Science*, 235, 545, 1987.
- [143] R. Łobiński, D. Schaumlöffel, and J. Szpunar, Mass spectrometry in bioinorganic analytical chemistry, *Mass Spectrom. Rev.*, 25, 255-289, 2006.
- [144] R. E. March.
- [145] W. Paul, Electromagnetic traps for charged and neutral particles, *Rev. Mod. Phys.*, 62, 531-540, 1990.
- [146] T. Baer, and R. C. Dunbar, Ion spectroscopy: Where did it come from; where is it now; and where is it going?, *J. Am. Soc. Mass. Spectrom.*, 21, 681-693, 2010.
- [147] D. Scuderi, V. Lepere, G. Piani, A. Bouchet, and A. Zehnacker-Rentien, Structural Characterization of the UV-Induced Fragmentation Products in an Ion Trap by Infrared Multiple Photon Dissociation Spectroscopy, *J. Phys. Chem. Lett.*, 5, 56-61, 2014.
- [148] A. K. Shukla, and J. H. Futrell, Tandem mass spectrometry: dissociation of ions by collisional activation, *J. Mass Spectrom.*, 35, 1069-1090, 2000.
- [149] L. Sleno, and D. A. Volmer, Ion activation methods for tandem mass spectrometry, *J. Mass Spectrom.*, 39, 1091-1112, 2004.
- [150] A. Fielicke, G. Meijer, and G. von Helden, Infrared multiple photodissociation spectroscopy of transition metal oxide cluster cations, *The European Physical Journal D - Atomic, Molecular, Optical and Plasma Physics*, 24, 69-72, 2003.
- [151] N. Heine, M. R. Fagiani, M. Rossi, T. Wende, G. Berden, V. Blum, and K. R. Asmis, Isomer-Selective Detection of Hydrogen-Bond Vibrations in the Protonated Water Hexamer, *J. Am. Chem. Soc.*, 135, 8266-8273, 2013.
- [152] N. C. Polfer, J. Oomens, D. T. Moore, G. von Helden, G. Meijer, and R. C. Dunbar, Infrared spectroscopy of phenylalanine Ag(I) and Zn(II) complexes in the gas phase, *J. Am. Chem. Soc.*, 128, 517-525, 2006.
- [153] E. Schneider, K. Brendle, P. Jäger, P. Weis, and M. M. Kappes, Ion Mobility Measurements of Multianionic Metalloporphyrin Dimers: Structural Changes Induced by Counterion Exchange, *J. Am. Soc. Mass. Spectrom.*, 29, 1431-1441, 2018.
- [154] X.-N. Wu, H.-T. Zhao, J. Li, M. Schlangen, and H. Schwarz, Highly regioselective hydride transfer, oxidative dehydrogenation, and hydrogen-atom abstraction in the thermal gas-phase chemistry of [Zn(OH)]⁺/C₃H₈, *Phys. Chem. Chem. Phys.*, 16, 26617-26623, 2014.
- [155] P. B. Armentrout, The power of accurate energetics (or thermochemistry: what is it good for?), *J. Am. Soc. Mass. Spectrom.*, 24, 173-185, 2013.
- [156] K. M. Ervin, and P. B. Armentrout, Energy dependence, kinetic isotope effects, and thermochemistry of the nearly thermoneutral reactions N+(3P)+H₂(HD,D₂)→NH+(ND⁺)+H(D), *J. Chem. Phys.*, 86, 2659-2673, 1987.
- [157] K. Levsen, and H. Schwarz, Collisional Activation Mass Spectrometry—A New Probe for Determining the Structure of Ions in the Gas Phase, *Angew. Chem. Int. Ed.*, 15, 509-519, 1976.
- [158] A. Langenberg, "Magnetische Momente freier, massenselektierter Eisen-, Cobalt- und Nickelcluster," Doctoral Thesis, Technische Universität Berlin, Fakultät II - Mathematik und Naturwissenschaften, Technische Universität Berlin, Berlin, 2013.
- [159] A. Langenberg, K. Hirsch, A. Ławicki, V. Zamudio-Bayer, M. Niemeyer, P. Chmiela, B. Langbehn, A. Terasaki, B. v. Issendorff, and J. T. Lau, Spin and orbital magnetic moments of size-selected iron, cobalt, and nickel clusters, *Phys. Rev. B*, 90, 184420, 2014.
- [160] J. T. Lau, A. Achleitner, H. U. Ehrke, U. Langenbuch, M. Reif, and W. Wurth, Ultrahigh vacuum cluster deposition source for spectroscopy with synchrotron radiation, *Rev. Sci. Instrum.*, 76, 063902, 2005.
- [161] J. T. Lau, A. Föhlich, R. Nietubyċ, M. Reif, and W. Wurth, Size-Dependent Magnetism of Deposited Small Iron Clusters Studied by X-Ray Magnetic Circular Dichroism, *Phys. Rev. Lett.*, 89, 057201, 2002.
- [162] V. Zamudio-Bayer, K. Hirsch, A. Langenberg, A. Ławicki, A. Terasaki, B. v. Issendorff, and J. T. Lau, Electronic ground states of Fe²⁺ and Co²⁺ as determined by x-ray absorption and x-ray magnetic circular dichroism spectroscopy, *J. Chem. Phys.*, 143, 244318, 2015.
- [163] V. Zamudio-Bayer, L. Leppert, K. Hirsch, A. Langenberg, J. Rittmann, M. Kossick, M. Vogel, R. Richter, A. Terasaki, T. Möller, B. v. Issendorff, S. Kümmel, and J. T. Lau, Coordination-driven magnetic-to-nonmagnetic transition in manganese-doped silicon clusters, *Phys. Rev. B*, 88, 115425, 2013.

- [164] V. Zamudio-Bayer, R. Lindblad, C. Bülow, G. Leistner, A. Terasaki, B. V. Issendorff, and J. T. Lau, Electronic ground state of Ni 2 +, *J. Chem. Phys.*, 145, 2016.
- [165] M. C. H. W. Koch, The Kohn-Sham Approach, in *Chemist's Guide to Density Functional Theory*, Wiley-VCH Verlag GmbH & Co. KGaA, 41-44, 2016.
- [166] T. Ziegler, Approximate density functional theory as a practical tool in molecular energetics and dynamics, *Chem. Rev.*, 91, 651-667, 1991.
- [167] K. Biemann, and H. A. Scoble, Characterization by tandem mass spectrometry of structural modifications in proteins, *Science*, 237, 992-8, 1987.
- [168] K.R.Jennings, The changing impact of the collision-induced decomposition of ions on mass spectrometry, *Int. J. Mass spectrom.*, 200, 479-493, 2000.
- [169] S. A. McLuckey, and D. E. Goeringer, SPECIAL FEATURE: TUTORIAL Slow Heating Methods in Tandem Mass Spectrometry, *J. Mass Spectrom.*, 32, 461-474, 1997.
- [170] B. R. Bzdek, J. W. DePalma, D. P. Ridge, J. Laskin, and M. V. Johnston, Fragmentation Energetics of Clusters Relevant to Atmospheric New Particle Formation, *J. Am. Chem. Soc.*, 135, 3276-3285, 2013.
- [171] D. R. Carl, B. K. Chatterjee, and P. B. Armentrout, Threshold collision-induced dissociation of Sr²⁺(H₂O)_x complexes (x=1–6): An experimental and theoretical investigation of the complete inner shell hydration energies of Sr²⁺, *J. Chem. Phys.*, 132, 044303, 2010.
- [172] F. Falvo, L. Fiebig, F. Dreiocker, R. Wang, P. B. Armentrout, and M. Schäfer, Fragmentation reactions of thiourea- and urea-compounds examined by tandem MS-, energy-resolved CID experiments, and theory, *Int. J. Mass spectrom.*, 330-332, 124-133, 2012.
- [173] G. E. Johnson, T. Priest, and J. Laskin, Size-dependent stability toward dissociation and ligand binding energies of phosphine ligated gold cluster ions, *Chemical Science*, 5, 3275-3286, 2014.
- [174] J. Laskin, R. P. W. Kong, T. Song, and I. K. Chu, Effect of the basic residue on the energetics and dynamics of dissociation of phosphopeptides, *Int. J. Mass spectrom.*, 330-332, 295-301, 2012.
- [175] K. V. Barylyuk, K. Chingin, R. M. Balabin, and R. Zenobi, Fragmentation of benzylpyridinium "thermometer" ions and its effect on the accuracy of internal energy calibration, *J. Am. Soc. Mass Spectrom.*, 21, 172-177, 2010.
- [176] E.-L. Zins, C. Pepe, D. Rondeau, S. Rochut, N. Galland, and J.-C. Tabet, Theoretical and experimental study of tropylium formation from substituted benzylpyridinium species, *J. Mass Spectrom.*, 44, 12-17, 2009.
- [177] E.-L. Zins, D. Rondeau, P. Karoyan, C. Fosse, S. Rochut, and C. Pepe, Investigations of the fragmentation pathways of benzylpyridinium ions under ESI/MS conditions, *J. Mass Spectrom.*, 44, 1668-1675, 2009.
- [178] J. Mohrbach, J. Lang, S. Dillinger, M. Proscenc, P. Braunstein, and G. Niedner-Schatteburg, Vibrational fingerprints of a tetranuclear cobalt carbonyl cluster within a cryo tandem ion trap, *J. Mol. Spectrosc.*, 332, 103-108, 2017.
- [179] J. Oomens, B. G. Sartakov, G. Meijer, and G. von Helden, Gas-phase infrared multiple photon dissociation spectroscopy of mass-selected molecular ions, *Int. J. Mass spectrom.*, 254, 1-19, 2006.
- [180] J. Seo, J. Jang, S. Warnke, S. Gewinner, W. Schöllkopf, and G. von Helden, Stacking Geometries of Early Protoporphyrin IX Aggregates Revealed by Gas-Phase Infrared Spectroscopy, *J. Am. Chem. Soc.*, 138, 16315-16321, 2016.
- [181] F. X. Sunahori, G. Yang, E. N. Kitova, J. S. Klassen, and Y. Xu, Chirality recognition of the protonated serine dimer and octamer by infrared multiphoton dissociation spectroscopy, *Phys. Chem. Chem. Phys.*, 15, 1873-1886, 2013.
- [182] E. R. Grant, P. A. Schulz, A. S. Sudbo, Y. R. Shen, and Y. T. Lee, Is Multiphoton Dissociation of Molecules a Statistical Thermal Process?, *Phys. Rev. Lett.*, 40, 115-118, 1978.
- [183] S. L. Chin, and N. R. Isenor, Multiphoton ionization in atomic gases with depletion of neutral atoms, *Can. J. Phys.*, 48, 1445-1447, 1970.
- [184] M. Q. D.W. Lupo, IR-Laser Photochemistry, *Am. Chem. Soc.*, 87, 181-216, 1986.
- [185] D. Schröder, H. Schwarz, P. Milko, and J. Roithová, Dissociation Routes of Protonated Toluene Probed by Infrared Spectroscopy in the Gas Phase, *J. Phys. Chem. A*, 110, 8346-8353, 2006.
- [186] A. Simon, C. Joblin, N. Polfer, and J. Oomens, Infrared Spectroscopy of [XFeC₂₄H₁₂]⁺ (X = C₅H₅, C₅(CH₃)₅) Complexes in the Gas Phase: Experimental and Computational Studies of Astrophysical Interest, *J. Phys. Chem. A*, 112, 8551-8560, 2008.
- [187] I. Ciofini, and C. A. Daul, DFT calculations of molecular magnetic properties of coordination compounds, *Coord. Chem. Rev.*, 238-239, 187-209, 2003.
- [188] F. Neese, Prediction of molecular properties and molecular spectroscopy with density functional theory: From fundamental theory to exchange-coupling, *Coord. Chem. Rev.*, 253, 526-563, 2009.

- [189] D. Imanbaew, J. Lang, M. F. Gelin, S. Kaufhold, M. G. Pfeffer, S. Rau, and C. Riehn, Pump-Probe Fragmentation Action Spectroscopy: A Powerful Tool to Unravel Light-Induced Processes in Molecular Photocatalysts, *Angew. Chem. Int. Ed.*, 56, 5471-5474, 2017.
- [190] S. V. Kruppa, F. Böppler, C. Holzer, F. Dietrich, R. Diller, W. Klopper, and C. Riehn, Excited state vibrational coherence in a binuclear metal adduct: wave packet phase dependant molecular fragmentation under variation of ligand size, *EPJ Web Conf.*, 205, 2019.
- [191] S. V. Kruppa, F. Böppler, C. Holzer, W. Klopper, R. Diller, and C. Riehn, Vibrational Coherence Controls Molecular Fragmentation: Ultrafast Photodynamics of the [Ag₂Cl]⁺ Scaffold, *J. Phys. Chem. Lett.*, 9, 804-810, 2018.
- [192] A. Scherz, H. Wende, and K. Baberschke, Fine structure of X-ray magnetic circular dichroism for early 3d transition metals, *Appl. Phys. A*, 78, 843-846, 2004.
- [193] J. Bansmann, A. Kleibert, M. Getzlaff, A. F. Rodríguez, F. Nolting, C. Boeglin, and K.-H. Meiwes-Broer, Magnetism of 3d transition metal nanoparticles on surfaces probed with synchrotron radiation – from ensembles towards individual objects, *physica status solidi (b)*, 247, 1152-1160, 2010.
- [194] J. T. Lau, A. Föhlich, M. Martins, R. Nietubyc, M. Reif, and W. Wurth, Spin and orbital magnetic moments of deposited small iron clusters studied by x-ray magnetic circular dichroism spectroscopy, *Nuclear Phys.*, 4, 98-98, 2002.
- [195] K. W. Edmonds, N. R. S. Farley, T. K. Johal, G. van der Laan, R. P. Campion, B. L. Gallagher, and C. T. Foxon, Ferromagnetic moment and antiferromagnetic coupling in (Ga,Mn)As thin films, *Phys. Rev. B*, 71, 064418, 2005.
- [196] J. Grabis, A. Bergmann, A. Nefedov, K. Westerholt, and H. Zabel, Element-specific x-ray circular magnetic dichroism of Co₂MnGe Heusler thin films, *Phys. Rev. B*, 72, 024437, 2005.
- [197] J. Stöhr, X-ray magnetic circular dichroism spectroscopy of transition metal thin films, *J. Electron. Spectrosc. Relat. Phenom.*, 75, 253-272, 1995.
- [198] P. Carra, B. T. Thole, M. Altarelli, and X. Wang, X-ray circular dichroism and local magnetic fields, *Phys. Rev. Lett.*, 70, 694-697, 1993.
- [199] C. T. Chen, Y. U. Idzerda, H. J. Lin, N. V. Smith, G. Meigs, E. Chaban, G. H. Ho, E. Pellegrin, and F. Sette, Experimental Confirmation of the X-Ray Magnetic Circular Dichroism Sum Rules for Iron and Cobalt, *Phys. Rev. Lett.*, 75, 152-155, 1995.
- [200] B. T. Thole, P. Carra, F. Sette, and G. van der Laan, X-ray circular dichroism as a probe of orbital magnetization, *Phys. Rev. Lett.*, 68, 1943-1946, 1992.
- [201] E. M. V. Kessler, S. Schmitt, and C. van Wüllen, Broken symmetry approach to density functional calculation of zero field splittings including anisotropic exchange interactions, *J. Chem. Phys.*, 139, 184110, 2013.
- [202] S. Schmitt, "Berechnung der Magnetischen Anisotropie mit Hilfe von ein- und zweikomponentigen dichtefunktionaltheoretischen Rechnungen: Weiterentwicklung vorhandener Methoden und Anwendung auf mehrkernige Übergangsmetallkomplexe," 2015.
- [203] J. Lang, J. M. Hewer, J. Meyer, J. Schuchmann, C. van Wüllen, and G. Niedner-Schatteburg, Magnetostructural correlation in isolated trinuclear iron(III) oxo acetate complexes, *Phys. Chem. Chem. Phys.*, 20, 16673-16685, 2018.
- [204] J. Lang, J. Mohrbach, S. Dillinger, J. M. Hewer, and G. Niedner-Schatteburg, Vibrational blue shift of coordinated N₂ in [Fe₃O(OAc)₆(N₂)_n]⁺: "non-classical" dinitrogen complexes, *Chem. Commun.*, 53, 420-423, 2017.
- [205] J. K. Kowalska, J. T. Henthorn, C. Van Stappen, C. Trncik, O. Einsle, D. Keavney, and S. DeBeer, X-ray Magnetic Circular Dichroism Spectroscopy Applied to Nitrogenase and Related Models: Experimental Evidence for a Spin-Coupled Molybdenum(III) Center, *Angew. Chem. Int. Ed.*, 58, 9373-9377, 2019.
- [206] L. Barzen, "Metal cluster aggregates of the composition Nbn^{+/-}, Con^{+/-} and [ConPtm]^{+/-} as model systems for catalytic C-H activation and structural determination of selected metal peptide complexes of the molecules aspartame (Asp-PheOMe) and Asp-Phe," 2013.
- [207] S. Dillinger, "Cryo Spectroscopy and Kinetics of Isolated Transition Metal Clusters and Complexes," 2017.
- [208] J. Mohrbach, "Cryo Tagging Infrared Spectroscopy and Temperature Controlled Kinetic Studies in a Tandem Trap Mass Spectrometer," 2017.

2 Experimental setup

This chapter summarizes the experimental setups used in this thesis. This chapter is divided into three sections. The first section points out different ion sources to create the ions of interest for various investigations. The second section briefly points out the used mass spectrometer in this thesis. Finally, the third section briefly introduces the different light sources for investigating the ions in their geometrical, optical, and magnetic properties.

2.1 Ion Sources

2.1.1 Apollo II ESI Source

The Bruker Apollo II ESI source (cf. Fig. 1) is used in combination with three different mass spectrometers from the AmaZon series (Speed, SL, and ETD) explained in chapter 2.2.1. The ESI sprayer (1) houses the ESI capillary. A gas-tight syringe (Hamilton™) connection and a peek capillary (inner diameter of 0.13 mm) to a syringe pump continuously infers the solution sample into the ESI capillary. The syringe pump is usually operated with a constant solution flow rate of 100–180 $\mu\text{L}/\text{min}$. A continuous nitrogen flow along the spray needle serves as nebulizer gas (pressure: ~ 400 mbar, flow rate: 2.5 L/min). The nebulizer gas supports the formation of tiny aerosol particles in the spray chamber (2). A high voltage between 3.5 kV and 4.5 kV is applied to the spray shield (3). For the electrostatic gradient, it is necessary to ground the spray needle. The transfer capillary (4) serves as an entrance to the mass spectrometer. Both ends of this capillary are metal-coated (platinum coating) to apply a DC voltage gradient for better ion guiding. Heated Nitrogen gas is provided by a gas heater (5) with a temperature between 180 °C and 220 °C and a flow rate of 4-6 L/min. Heated Nitrogen gas flows against the direction of the droplet stream and supports the desolvation of the droplets. An electrostatic DC potential between the spray shield and the transfer capillary leads to a focus of the ions onto the mass spectrometer entrance.

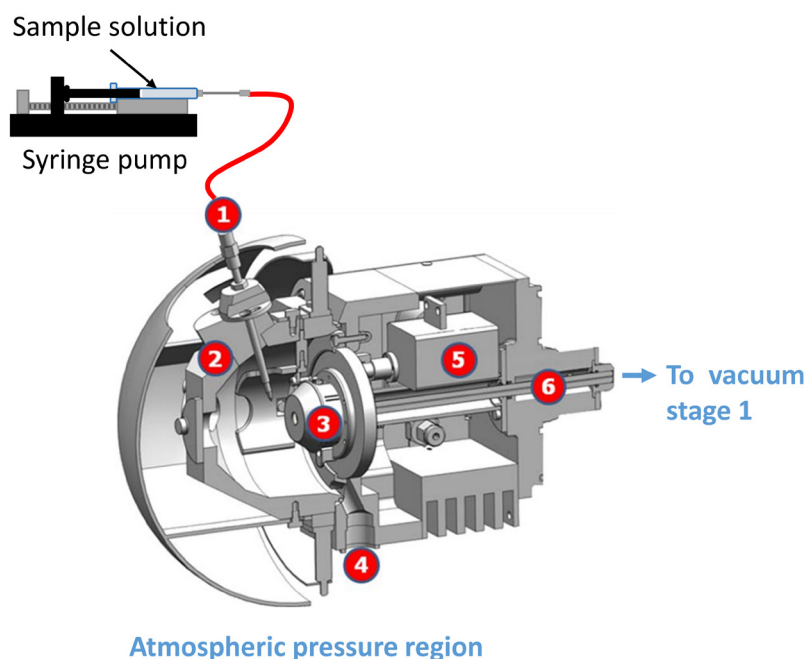


Fig. 1: Schematic overview of the Bruker Apollo II ESI source used in the AmaZon mass spectrometer^[1]. With the ESI sprayer (1), spray chamber (2), spray shield (3), Waste line for solvents (4), temperature controlled dry gas heater (5), and metal-coated glass capillary (6).

2.1.2 ESI source of the Schlathölter group

The XMCD studies on the monometallic complex $[\text{Fe}(\text{btpa})]^{2+}$ (cf. chapter 7) were performed with the custom build ESI source kindly provided by the group of Thomas Schlathölter (Zernike Institute for Advanced Materials, University of Groningen, Netherlands)^[2-5]. This custom build ion source comprises a stainless steel spray needle, a transfer capillary, and a radio frequency (RF) ion funnel^[6]. The HamiltonTM gas-tight syringes and a syringe pump serve to constantly infuse the sample solution into the spray needle with a flow rate of $\sim 200 \mu\text{L/h}$. The spray needle is mounted on an x, y, z translation stage and allows an optimal position for the spray needle to maximize the ion signal intensity for the XMCD studies. This spray needle is kept at a constant voltage between 3-3.5 kV. After the ESI process, the ions are transferred into the vacuum by the transfer capillary. The transfer capillary is heated by applying a constant voltage between 10–30 V. This supports a desolvation process of the ions within the transfer capillary. After passing the transfer capillary, the ions enter a home built RF ion funnel containing 26 lenses with declining diameters to guide and focus ions onto the mass spectrometer's optical pathway. The ion funnel is operated with a frequency of $\sim 250 \text{ kHz}$ and an amplitude of $V_{\text{pp}} = 250\text{--}300 \text{ V}$. For better ion transfer into the mass spectrometer. In

addition, a constant DC gradient is overlaid to the RF field (120 V to 25 V), guiding the ions to the MS. After passing the ion funnel, the ions enter a hexapole ion guide of the “Ion Trap” mass spectrometer (cf. chapter 2.3.2) for further investigations.

2.1.3 ESI source of the Lau group

The XMCD studies on the complexes $[\text{Fe}_3(\text{OAc})_6(\text{py})_{0-3}]^+$ and $[\text{Mn}_3(\text{Hcht})_2(\text{Bipy})_4]^{3+}$ (cf. chapter 5 and 8) were performed with a custom built ESI source provided by the group of Tobias Lau (Helmholtz Zentrum für Materialien und Energie, Berlin) and designed by Martin Timm. This ion source is almost similar to the ion source in chapter 2.1.2. The significant difference in this ESI source is that the complete ESI setup is commercially bought (Varian 1200 API) and mounted on a 160 CF flange (cf. Fig. 2).

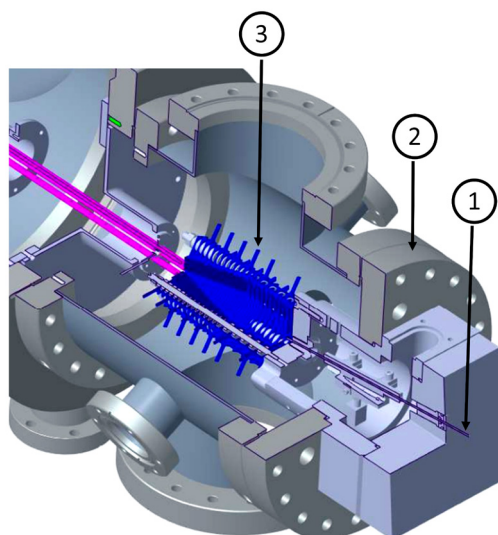


Fig. 2: Schematic overview of the custom built ESI ion source of the Lau group used in the Ion Trap. With the Varian ESI source (1), CF 160 flange (2), and the home built ion funnel (3).

The spray needle is kept at a constant voltage between 3-3.5 kV, and the transfer capillary is heated by a constant voltage between 10-30 V, leading to a temperature of 30-70 °C. The temperature leads to a better desolvation of the ions within the transfer capillary. After passing the transfer capillary, the ions enter a home built RF ion funnel containing 26 lenses with declining diameters to guide and focus ions onto the mass spectrometer's optical pathway. The ion funnel is operated with a frequency of ~250 kHz and an amplitude of $V_{pp} = 250-300$ V. For better ion transfer into the mass spectrometer. A constant DC gradient is overlaid to the RF field (120 V to 25 V), guiding the ions to the MS. After passing the ion

funnel, the ions enter a hexapole ion guide of the Ion Trap (cf. chapter 2.3.2) for further investigations.

2.1.4 Laser vaporization source (LVAP)

For the studies of transition metal (TM) clusters, a home built Laser vaporization (LVAP) ion source is used to create these clusters in different sizes at the GERTI instrument (cf. chapter 2.3.3). The LVAP cluster ion source was first described by Bondybey, English^[7, 8] and Smalley et al.^[9, 10]. Major parts of the current LVAP ion source are the piezoelectric valve^[11], the expansion block, and the expansion channel (cf. Fig. 3). The second harmonic of an Nd:YAG laser (surelight II, continuum) is focused onto a rotating metal foil, may vary in thickness between 0.1 and 0.5 mm, it pulses with a repetition rate of 10 Hz. A piezoelectric valve generates a sharp gas pulse synchronized to the laser pulse, an opening time between 10–80 μs , and a backing pressure between 10 and 20 bar. The gas pulse expands into the vacuum with a pressure of $\sim 5.0 \cdot 10^{-6}$ mbar. In vacuum, the ions cool down within a supersonic expansion, and the cluster formation starts by condensing the ions to the cluster. The maximum of the cluster distribution can be tuned by changing the opening time of the valve, the pulse delay, or changing the source voltage.

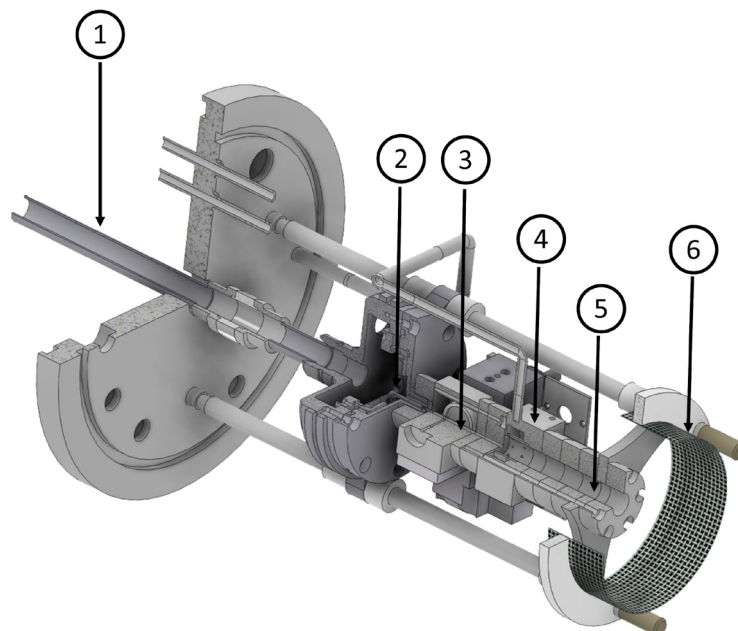


Fig. 3: Schematic overview of the Laser vaporization ion source with (1) gas inlet, (2) piezoelectric valve, (3) expansion block, (4) pick up unit, (5) expansion channel, and (6) mesh.

We modified a home built Laser vaporization source (LVAP) with a so-called “pick-up” block to enable the adsorption of small molecules to the clusters (cf. Fig. 4). The gas inlet is mounted directly after plasma formation to mix the adsorbed molecules and the resulting cluster before cluster condensation in vacuum (cf. Fig. 4). The carrier gas (He, Ar) takes this mixture of the adsorbate gas and metal ions into the expansion channel and condenses clusters via expansion cooling.

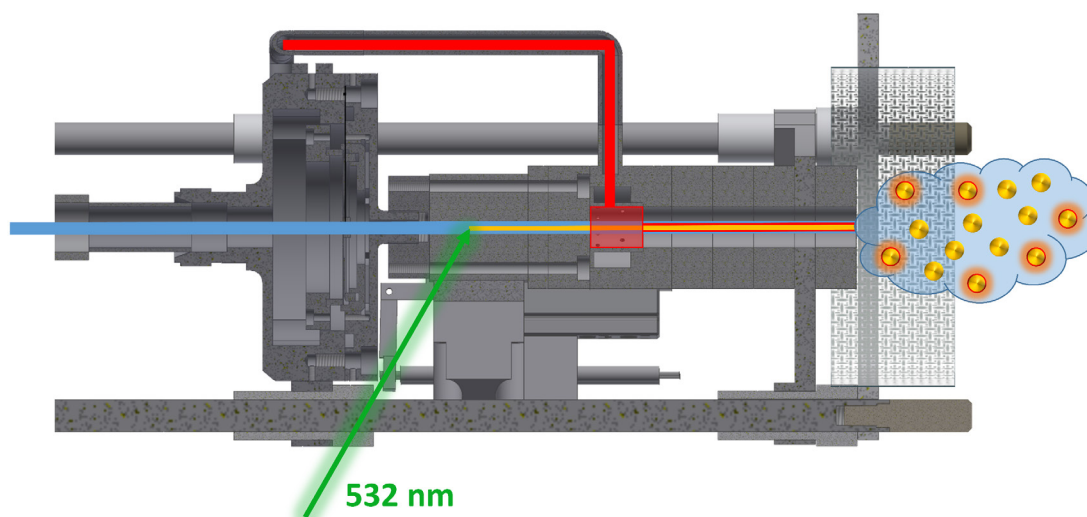


Fig. 4: Schematic aggregation of small molecules within the “pick-up” unit. Carrier gas in blue, molecules aggregated to the clusters in red and metal ions in orange after irradiation with a frequency doubled Nd:YAG ablation laser (green).

2.2 Mass Spectrometric Instrumentation

Mass spectrometry is a powerful method that allows the analysis of ions in gas phase^[12-14], and it characterizes these ions by their mass-to-charge (m/z) ratios. Various methods determine the m/z ratio of ions with electric and or magnetic fields^[15] and the separation of different ions by the Time of flight. Besides guiding and detecting the ions, they can be stored^[16] within ion optics (ion traps). The most common traps are linear multipoles and Paul traps^[17]. Both ion traps work with well-defined radio frequencies (RF) applied to the metal rods in linear multipoles or on hyperbolic electrodes in Paul traps. To generate a trapping potential^[18-20] for the ions of interest, the RF voltage alternate on the metal rods respective to the hyperbolic electrodes. The following chapters provide descriptions of the used mass spectrometer in this work.

2.2.1 AmaZon mass spectrometer (Speed, SL, ETD)

The commercial AmaZon (Speed, SL, ETD; bruker daltonics) mass spectrometer serves to conduct Collision Induced Dissociation (CID), InfraRed (Multiple) Photon Dissociation (IR(M)PD), and Ultra Violet Photon Dissociation (UVPD) studies^[21-28]. All three of these mass spectrometers are equipped with Apollo II Electrospray Ionization (ESI) ion sources (cf. chapter 2.1.1). This type of mass spectrometer is a four-staged differential pumped vacuum system that provides a pressure gradient when guiding ions into the ion trap (cf. Fig. 5).

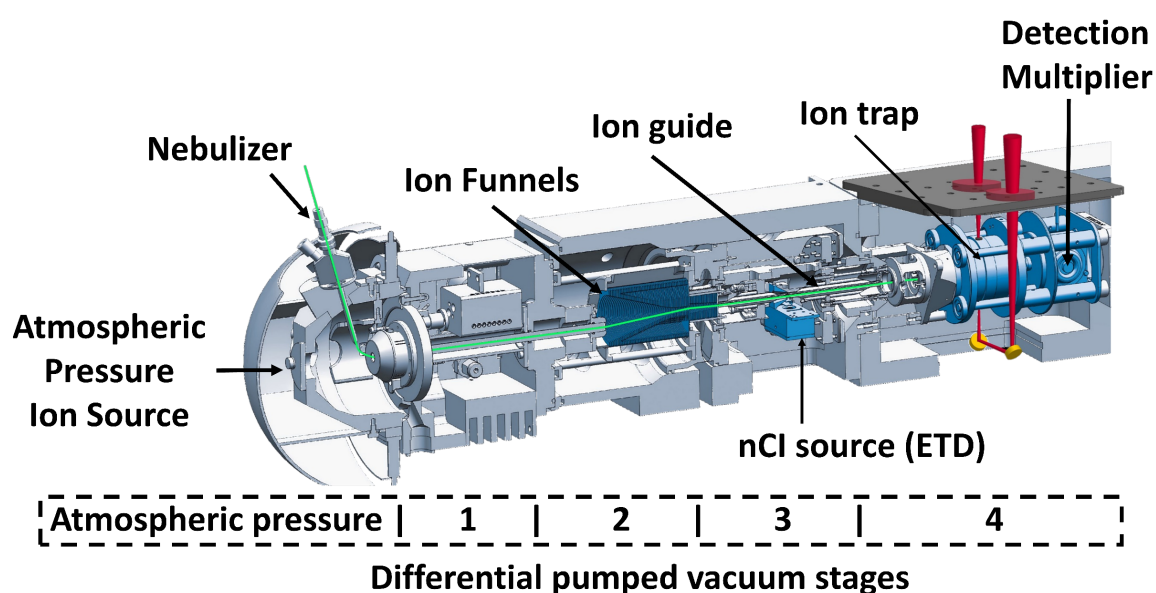


Fig. 5: Schematic overview of the Bruker AmaZon (Speed, SL, ETD) mass spectrometer^[1].

The ions created by the ESI process exit the transfer capillary into the first vacuum stage (~ 1 mbar). In this vacuum stage, there are two subsequent ion funnels arranged (cf. Fig. 6). Both ion funnels are fitted “off-axis” to the transfer capillary to avoid neutral molecules from the ESI process. The first ion funnel in this system comprises a wider entrance, as the second funnel provides a higher ion transport amount. A subsequent decreasing inner diameter in the ring electrodes leads to a focused ion beam. The ions pass a lense, separating the second funnel in a different vacuum stage to provide a pressure gradient. A radiofrequency (RF) voltage provides an electric field, which confines the ions into the field free area. An additional DC voltage applied to the ion funnel generates a voltage gradient between the first and the last ring electrode, resulting in a more efficient ion transfer combined with the pressure gradient.

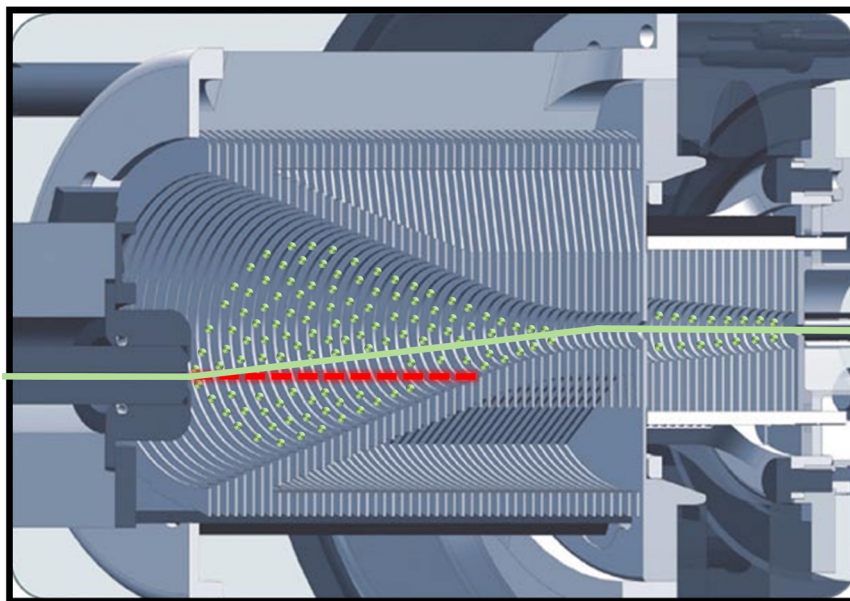


Fig. 6: Schematic overview of the double stacked ion funnel system in the Bruker AmaZon (Speed, SL, ETD) mass spectrometer.

After passing the ion funnels, the ions enter the third vacuum stage, consisting of two linear RF octupoles and the nCI source for ETD experiments. Then the ions enter the final vacuum chamber ($\sim 10^{-6}$ mbar). A Paul-type ion trap accumulates the ions in this chamber, allowing their m/z determination, isolation, and fragmentation.

The Paul trap is a three-dimensional quadrupole ion trap. It comprises a ring electrode and two end caps (cf. Fig. 7), forming a nearly hyperbolic inner profile. The ions enter and exit the trap through pinholes in the end caps. A high voltage RF potential (781 kHz) is applied to the ring electrode while the end caps are grounded. The accumulation of ions is possible by the resulting oscillating quadrupolar electric field. The mass range of the accumulated ions depends on the applied amplitude of the RF voltage. An auxiliary dipolar voltage is fed to either the exit cap or both end-caps for subsequent ion isolation and fragmentation. For effective ion trapping, it is necessary to slow down the ions in the Paul trap. Therefore, an integral derivative (PID) gas controller maintains a partial Helium buffer gas pressure of approximated 10^{-3} mbar in the ion trap. The collision with the Helium atoms leads to a deceleration of the ions and allows efficient storage of the ions. Typical accumulation times vary between 0.01 ms and 200 ms.

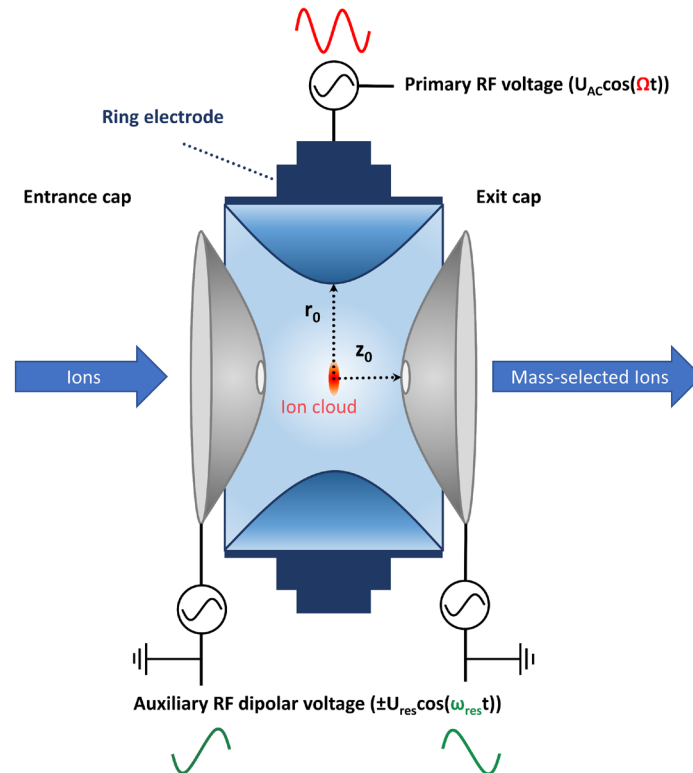


Fig. 7: Schematic cross-section of a Paul type ion trap in the AmaZon mass spectrometers^[29].

The oscillation of the ions inside the Paul trap depends on the radial and axial directions. This oscillation depends on the m/z ratios and the field parameters (e.g., voltage frequency, amplitude). The solution of the Mathieu equations leads to a two-dimensional stability diagram^[30]. This diagram shows stable orbits for ions inside the Paul trap (cf. Fig. 8). The orbit for ions is defined as stable if the oscillatory amplitudes in a radial direction (β_r) and the axial direction (β_z) point out a value between 0 and 1. All other orbits are unstable, and the ions can collide with the walls β_z and β_r are inversely proportional to the mass of the ions and directly proportional to the RF voltage. The axial direction (β_z) is the most important because this is the direction of the injection or ejection of the ion inside the trap. For the accumulation of the ions (RF-only mode), the diagram reveals a boundary of stabilities along with the line $\beta_z = 1$. This line determines the lowest m/z ratios in the RF field by given DC voltage, which leads to stable orbits. The range of m/z ratios stored simultaneously in the trap has a lower cut-off, determined by the applied RF amplitude on the ring electrode. In this theory, there is no limit to the mass range of storage ions. In practice, thermal reasons bring in an upper limit for the mass range. Usually, the limit is about 20-30 times the lower cut-off, meaning the applied RF field does not efficiently trap ions above this limit.

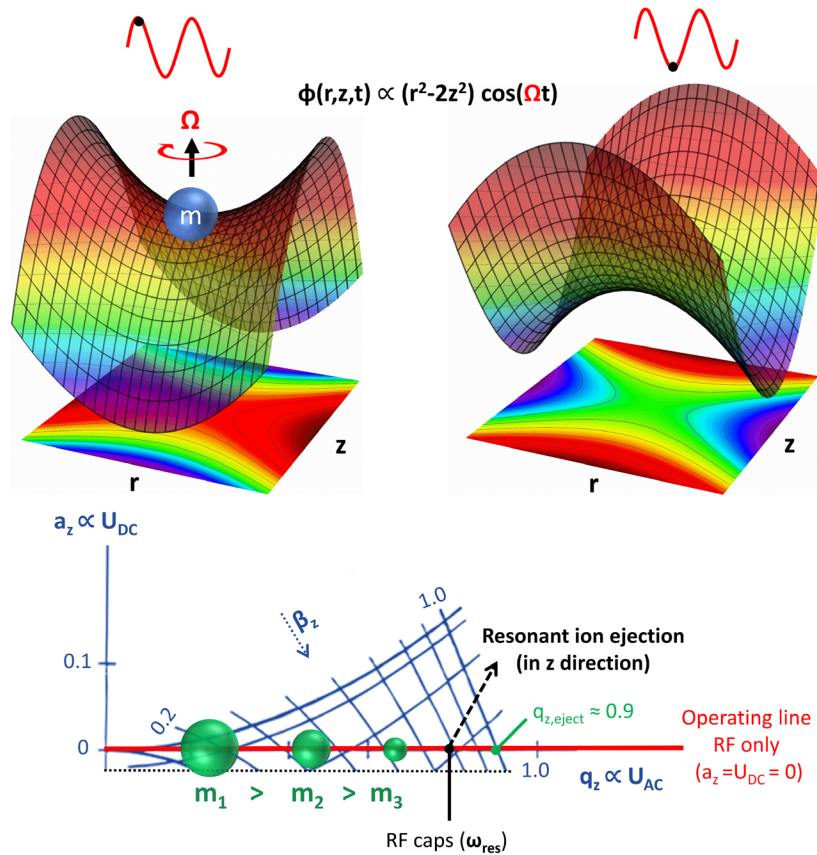


Fig. 8: Stability diagram for ions in a Paul trap. The parameter β_r describes oscillation in the radial direction, and the axial is represented by the parameter β_z . Stable orbits exhibit $0 \leq \beta_r, \beta_z \leq 1$ ^[30, 31].

Variation of the RF voltage in addition to the applied DC voltages a continuous ejection of the trapped ions under m/z controls. A Daly detector detects the ions. A scan of these ions leads to a mass spectrum, and the scan rate is around 32500 (m/z)/s in the ultra scan mode with a resolution of 0.3 FWHM. The isolation of ions with an m/z ratio leads to unstable orbits for all other ions with different m/z ratios.

For the AmaZon Speed and SL, several modifications allow IR(M)PD (SL) and UVPD (Speed) experiments. First, in both mass spectrometers, two pinholes are drilled in the Paul trap's ring electrode to create an optical path through the center of the ion trap (cf. Fig. 9). These holes have an outer diameter of 6 mm and decline to 2 mm to the inner side, resulting in a limitation of the loss of helium inside the trap. Also, Windows and mirrors have been installed to guide the laser beam in and outside the mass spectrometer. For the AmaZon SL, the instrument's software has been updated to synchronize the duty cycle of the mass spectrometer to the 10 Hz trigger signal of the pump laser. Further details on the modifications of the mass spectrometer are available in the doctoral thesis of Fabian S. Menges^[32].

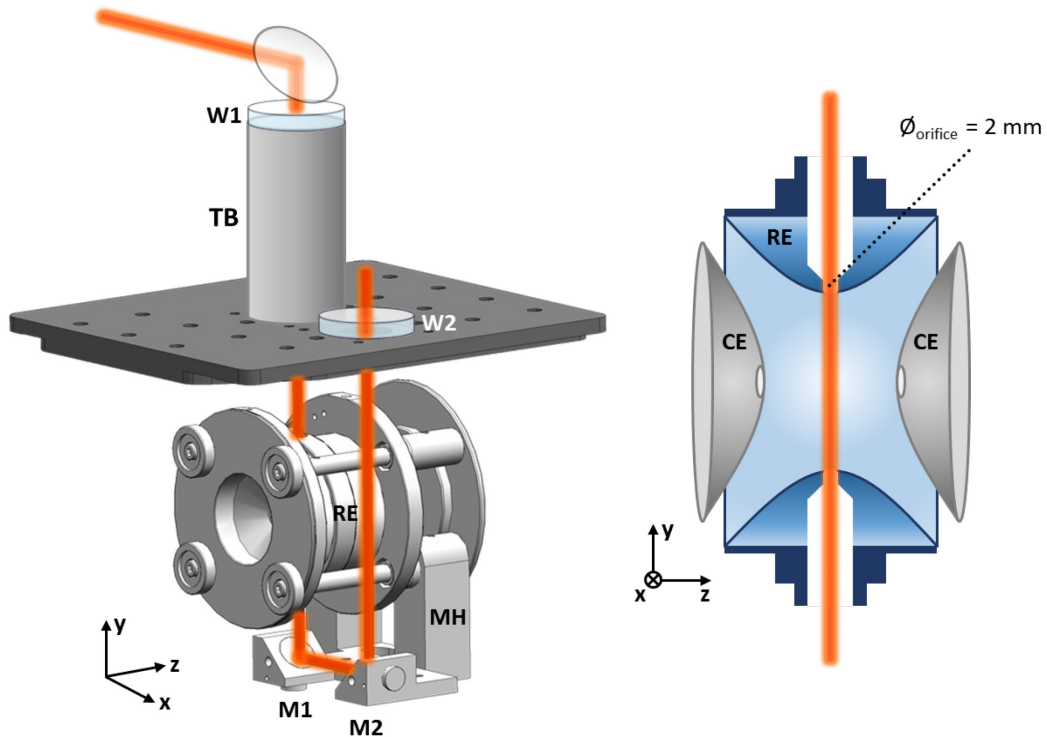


Fig. 9: Scheme of the modified ring electrode (RE). IR and UV/VIS laser beams pass the BaF2 windows (W1, W2) and are reflected by two mirrors (M1, M2)^[29].

2.2.2 Ion Trap mass spectrometer

The “Ion Trap” is a custom build mass spectrometer (cf. Fig. 10) at the UE52-PGM beamline at BESSY^[33-37] and serves for X-ray absorption (XAS) and X-ray magnetic circular dichroism studies of isolated transition metal clusters in gas phase. This instrument is built by the groups of Thomas Möller, Bernd von Issendorff, and Tobias Lau. The instrument is combined with the home build ESI ion source (chapter 2.1.2) by Tobias Lau's group.

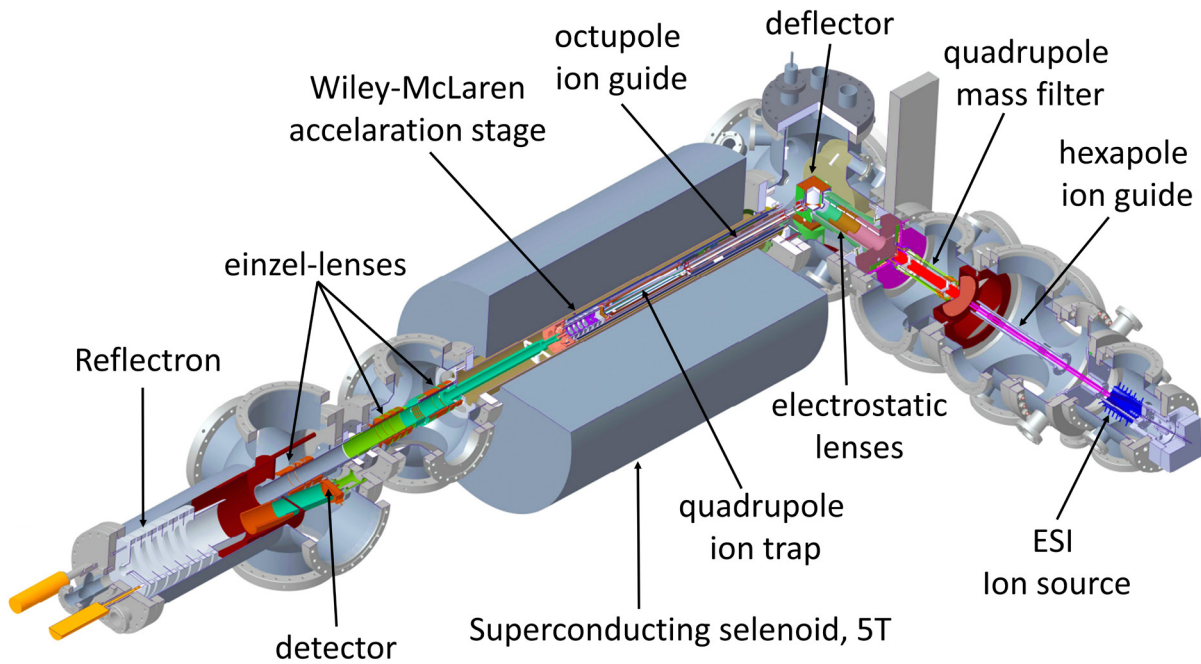


Fig. 10: Schematic overview of the Ion Trap instrument^[33-41] built by Thomas MÖLLER, Bernd von ISSENDORF, and Tobias LAU, operated by the group of Tobias LAU at the UE52 beamline at BESSY II. Akira Terasaki provided the 5 T superconducting magnet.

The ion of interest is mass-selected in a linear quadrupole mass filter (Extrel, 40 - 4000 amu) and transported through several electrostatic lenses into the quadrupole ion bender. It bends the ion beam by 90 ° onto the axis of a linear quadrupole ion trap (cf. Fig. 11) within the high field region (5 T) of a superconducting solenoid. The trap is operated at a frequency between 2 and 4 MHz (~500 V peak-to-peak voltage). The gained quadrupole field focuses the ions into the field-free region, which leads to a better overlap of the X-ray beam with the ions in the trap. Static DC voltages applied to the entrance and exit plates serve as axial ion trapping. Evaporative liquid He cooling cools down the ion trap to a temperature of 4 K. A constant He backing pressure of $1 \cdot 10^{-6}$ mbar within the vacuum chamber cools down the trapped ions by collisional cooling down to 4.5 K.

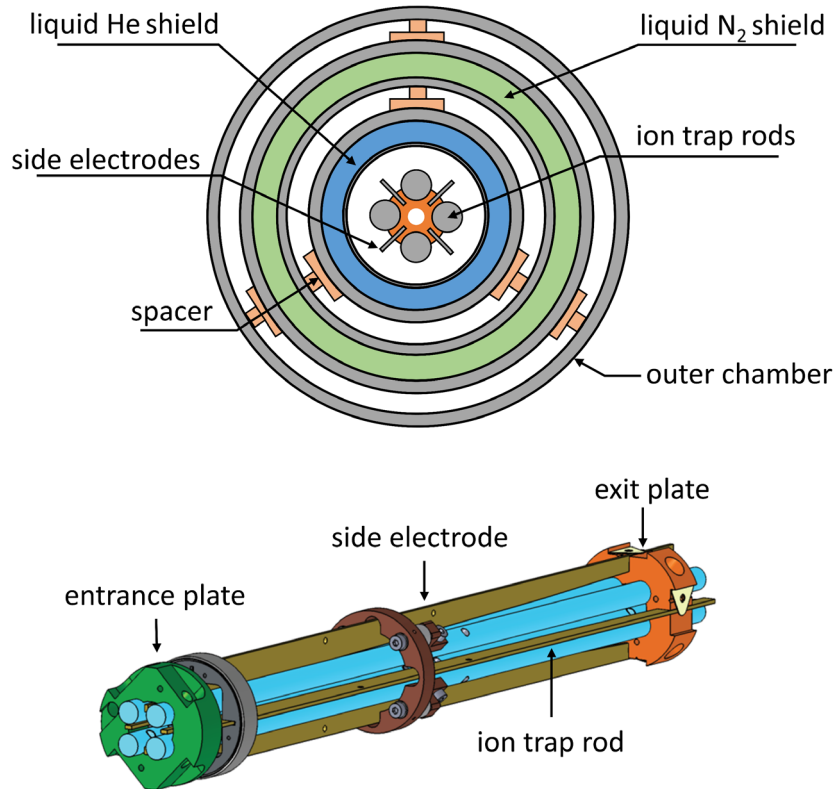


Fig. 11: Schematic drawing of the cryogenically cooled quadrupole of the Ion Trap mass spectrometer^[39]. It comprises four parallel rods ($d = 6\text{ mm}$, $L = 25\text{ cm}$) and two side electrodes, increasing trapping efficiency. The rods and side electrodes are made of non-magnetic Molybdenum since the quadrupole is located in the high field region of a superconducting solenoid.

The thermalized ions are slightly warmer than the applied temperature to the trap of $\sim 15\text{ K}$ ^[39] by cause of the RF heating. Cooling of the ions is necessary to reduce temperature-induced orientation and randomization of the magnetic moments in the investigated ions of interest. The ions are constantly injected into the ion trap and irradiated with the X-ray beam. The ions are ejected into the reflectron Time of flight mass spectrometer with a frequency of about 120 Hz to record mass spectra from the ion trap. For the XA spectra recorded by TIY spectroscopy, the ions are irradiated for 10 to 15 s at set photon energy. A GaAs-diode records the X-ray intensity from the undulator beamline used for photon flux normalization of the recorded spectra. Spectra on the Fe absorption edges were taken with an exit slit size of 200 μm and a respective resolution of 400 meV at 710 eV. Further instrumental details of the “Ion Trap” Trap are available in the doctoral thesis of Andreas. Langenberg^[39].

2.2.3 GERTI (General Electrospray Time of flight Instrument)

This instrument is a home built time of flight mass spectrometer. The instrument is a three-staged differential pumped system containing an ionization chamber, an acceleration chamber, and the Time of flight region (cf. Fig. 12). The most significant advantage in this setup is that the change of the ion sources can be done within several minutes up to one hour.

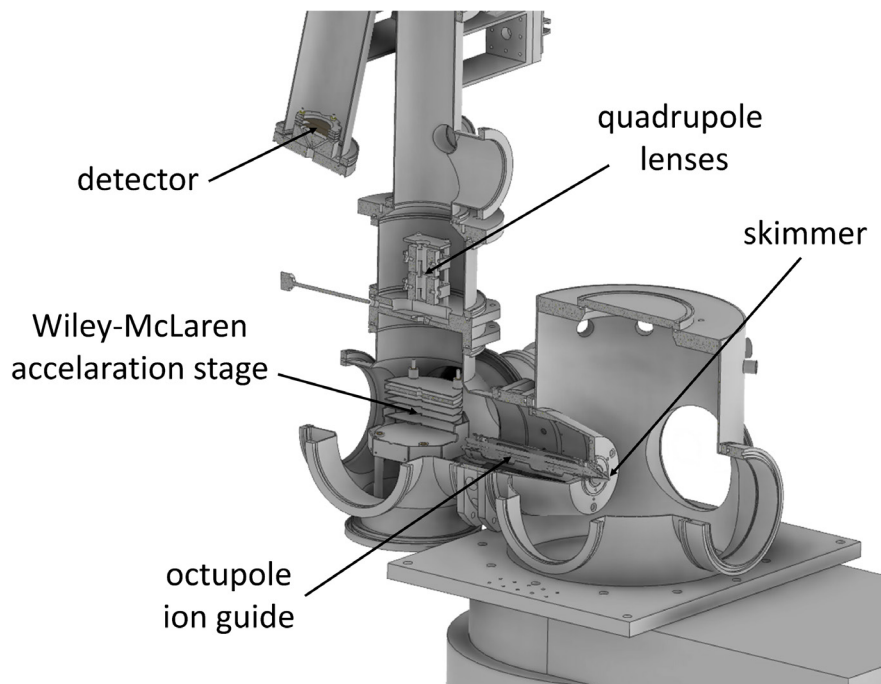


Fig. 12: Scheme of the GERTI instrument without an ion source implemented in the ion source chamber.

The ions of interest are created in different ion sources (e.g., chapter 2.1.4), adapted in the ion source chamber (cf. Fig. 12). The pressure in this chamber is $\sim 2.0 \cdot 10^{-5}$ mbar in operation mode. The ion source is on-axis to a skimmer, which separates neutrals and ions with the wrong polarity. Also, the skimmer separates the next vacuum stage from the source chamber. An octupole is installed after the skimmer and serves as an ion guide to transfer the ions to the acceleration chamber. A Wiley McLaren arrangement accelerates the ions into the time of flight region. In operating mode, an acceleration voltage between 3-5 kV is applied to the plates with a frequency of 10 Hz synchronized to the flashlamp trigger, which is the starting point for all delays in the experiment. The acceleration stage is a rebuild of the arrangement by T.P. Martin^[42]. The Time of flight area provides two stacks of multi-channel plates (MCP) in a chevron arrangement. Ions can be detected in a linear mode (LinTOF), or by applying voltages to the reflectron, the detection in the reflectron mode (ReTOF) is possible. The pressure in the time of flight region is $\sim 1.3 \cdot 10^{-7}$ mbar.

The Wiley McLaren arrangement consists of seven lenses with different voltages (cf. Fig. 13). In this arrangement, the lenses HV1 and HV2 get high voltage pulses at set time intervals with a 10 Hz trigger synchronized to the flash lamp trigger, starting the duty cycle for recording mass spectra. The HV1 plate suddenly deflects the ions orthogonal and eliminates neutrals in the ion beam by applying a high voltage. The HV2 lens slows down the faster ions and accelerates them with the same energy into the time of flight area. Following lenses, PL1–PL3 are grounded to provide a field-free region until they pass the PL4 lens with a high negative voltage to focus the ions for better collimation.

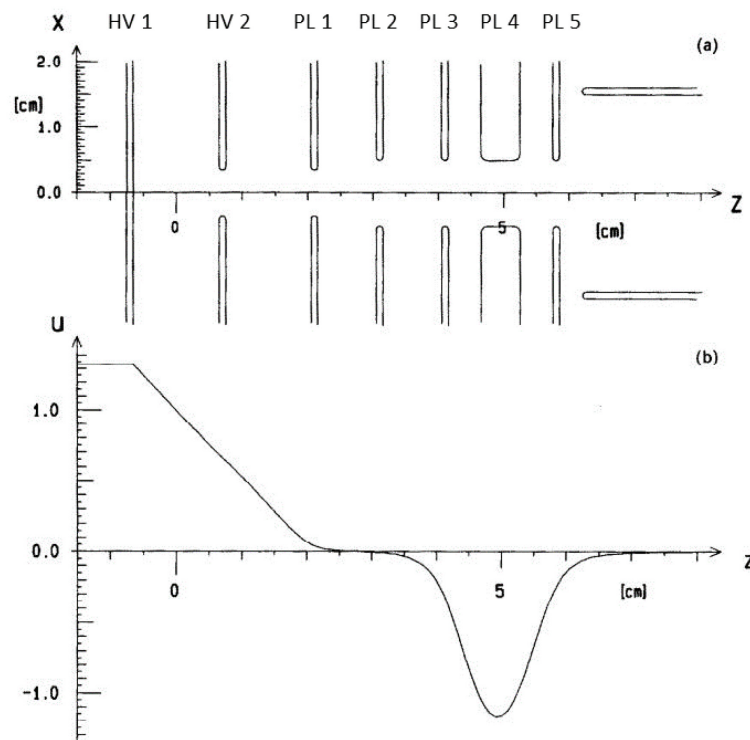


Fig. 13: Scheme of the voltage diagram for the Wiley McLaren arrangement to accelerate the ions into the Time of flight area^[42].

2.3 Light Sources

2.3.1 Optical Parametric Oscillator/Amplifier IR Laser system

Non-linear optical crystals can convert the wavelength of laser radiation with second-order non-linear optical interactions^[43]. This conversion leads to an approach to tune the frequency of laser radiation^[44]. However, due to low intrinsically low frequency conversion efficiency, these non-linear optical processes need very intensive and coherent light as pump sources^[45]. An optical parametrical oscillator^[46] (OPO) consists of a non-linear optical crystal and an

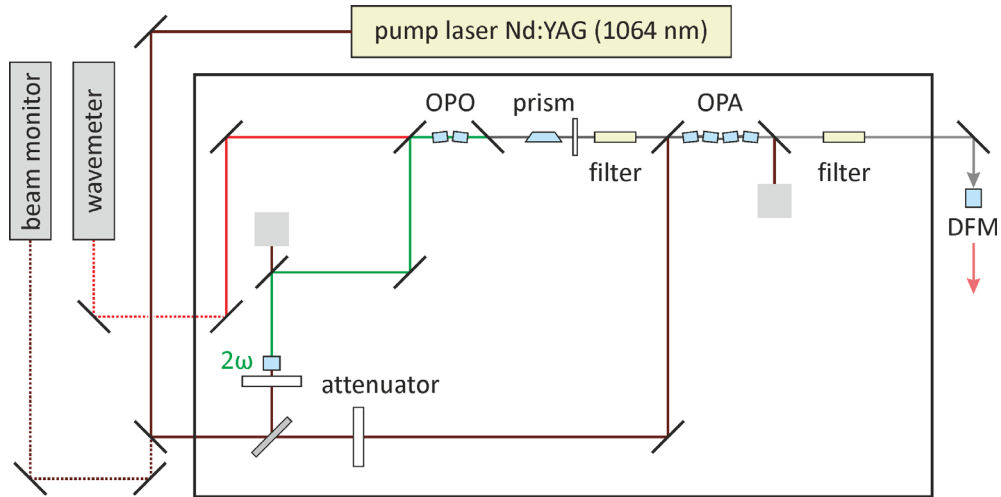


Fig. 15: Optical setup of the LaserVision broadband OPO/OPA laser system. Lines and arrows indicate the pathway of the incoming and outgoing laser beam.

A seeded Nd:YAG laser (Continuum-PL8000, 10 Hz, 540-560 mJ/pulse) serves as pump laser for laser radiation with well-defined pulses, operating with a wavelength of 1064 nm (9394 cm^{-1}) and a pulse length of 7 ns. The fundamental beam is guided to a beam splitter, and only one-third of the beam enters the OPO/OPA system. A beam splitter guides the fundamental beam to a potassium titanyl phosphate crystal for a second-harmonic generation^[45] (SHG). The SHG process combines two photons from the fundamental beam to one photon with a doubled frequency (532 nm , 18789 cm^{-1}). A $\lambda/2$ wave plate provides the variation in the laser intensity. A fundamental photon conversion into a frequency-doubled photon leads into two photons with different frequencies called signal 1 and idler 1. The signal photon has a higher frequency than the idler photon. The frequency of these photons can be changed by the incident angle variation between the beam and the KTP crystal surface. Due to the energy conservation, the sum of the signal and idler photon energy has to be identical to the photon energy of the frequency-doubled beam energy (cf. eq.1 and eq.2).

$$2\omega = 532 \text{ nm} = \nu_{\text{Signal 1}} + \nu_{\text{Idler 1}} \quad (1)$$

$$2\omega = 18789 \text{ cm}^{-1} = \tilde{\nu}_{\text{Signal 1}} + \tilde{\nu}_{\text{Idler 1}} \quad (2)$$

For the difference frequency mixture, a Silicon filter blocks signal 1, and only the idler 1 enters the OPA stage, comprising four potassium titanyl arsenal (KTA) crystals. In the OPA stage, the idler 1 beam overlaps with two-thirds of the fundamental beam. The fundamental beam splits into two frequency-doubled photons in the OPA process, signal 2 and idler 2. The idler 1 beam is amplified when the signal 2 photons generated in this process has the same frequency as

the idler 1 beam (cf. eq. 3-4). Thus, the frequency of idler 1 determines the frequency of the idler 2 photons. The intensity can be contracted by a $\lambda/2$ wave plate and a thin film polarizer.

$$\nu_{\text{Idler 1}} = \nu_{\text{Signal 2}} \quad (3)$$

$$1064 \text{ nm} = \nu_{\text{Signal 2}} + \nu_{\text{Idler 2}} \quad (4)$$

$$9394 \text{ cm}^{-1} = \tilde{\nu}_{\text{Signal 2}} + \tilde{\nu}_{\text{Idler 2}} \quad (5)$$

The generated signal 2 and idler 2 contain different linear polarizations due to their electric field vectors. To provide the beam for each case of experimental studies, a silicon filter aligned in a Brewster angle selectively separates the signal 2 (4700–7400 cm^{-1}) or idler 2 (2200–4700 cm^{-1}) beam. Another difference frequency mixing^[50] of signal 2 and idler 2 (cf. eq. 6) in a Silver Galium Diselenoid (AgGaSe_2) crystal generates a beam with a spectral range of 800 - 2200 cm^{-1} . Finally, a ZnSe filter separates the DFM beam from the remaining signal 2 and idler 2 beam.

$$\tilde{\nu}_{\text{DFM}} = \tilde{\nu}_{\text{Signal 2}} - \tilde{\nu}_{\text{Idler 2}} \quad (6)$$

With a given setup, the Laser provides a spectral resolution of $\sim 0.9 \text{ cm}^{-1}$. A delay generator (Stanford Research Systems DG645) is used for synchronization with the mass spectrometer. The calibrated wavelength outputs are monitored by a wavemeter (Bristol Instruments 821B-NIR). A Power meter with corresponding detector heads (Maestro, gentec-eo UP-19K-H5D0) records the laser power during scanning during the experiment. A beam profiler camera constantly monitors the beam profile of the pump laser (WinCamD, DataRAY Inc) to prevent hotspots in the laser beam to protect the mirror setup.

2.3.2 X-ray Synchrotron Radiation at BESSY II (UE52–PGM beamline)

The XA spectra presented in this work were recorded using the Ion Trap (cf. chapter 2.3.2) at BESSY II. The photons are generated within a soft X-ray undulator beamline UE52. Synchrotron radiation is generated by the acceleration of electrons to relativistic velocities in circular orbits. When they reach these velocities, they emit electromagnetic radiation. At BESSY II, the electrons are accelerated to 50 MeV and then injected into the storage ring, where the electron beam has a frequency of around 500 MHz^[38]. Alternating dipole, quadrupole, and sextupole magnets inside the storage ring focus and correct the electron beam pathway. The dipole magnets in the ring bend the electron beam and provide a circular path for the beam. This deflection of the electrons in the ring generates bremsstrahlung. Within the generation

of the bremsstrahlung, the electrons lose energy to compensate for this energy loss. RF cavities inside the storage ring reaccelerate the electrons up to 1.7 GeV^[38]. The obtained bremsstrahlung can be focused and monochromatized to perform X-ray studies.

In the straight pathways inside the storage ring are undulators located to provide high brilliant synchrotron radiation. The undulator is built of concatenated permanent magnets with alternating polarity (cf. Fig. 15). The electrons enter the magnet field to perform a sinusoidal motion with a specific wavelength. With this arrangement, the undulator generates photons with horizontal polarization (cf. Fig. 15 a). The change of the magnet pairs above and underneath about a half wavelength leads to a generation of circularly polarized photons (cf. Fig. 15 b). The variation of the gap in the undulator leads mainly to a change in the photons' wavelength.

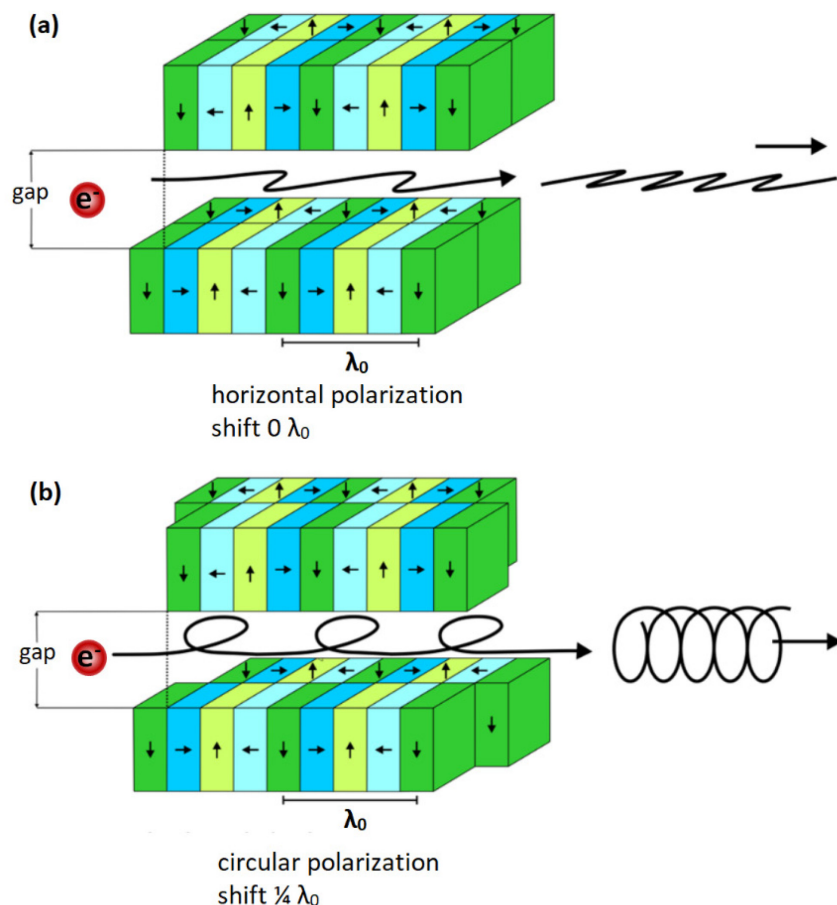


Fig. 16: Arrangement of the concatenated permanent magnets of an APPLE 2 (advanced planar polarized light emitter) undulator^[51-54]. **(a)** Magnet arrangement for horizontal photon polarization and **(b)** arrangement for circular photon polarization.

The UE52 beamline is equipped with an APPLE 2 (advanced planar polarized light emitter) undulator^[51-53, 55]. The undulator obtains four rows of permanent magnets with alternating polarization and can be shifted individually against each other. With this arrangement, the undulator can generate horizontally polarized photons and circularly polarized photons, depending on the magnet shift and gap. The beamline provides a soft X-ray beam with an energy range of 85 to 1600 eV. The spectral resolution is limited by the variation of the exit slit width of the plane-grating mirror (PGM) monochromator. The storage ring is operated in the Multibunch Topup mode. The electrons collide with residual gas inside the ring and constantly inject electrons into the storage ring to keep a constant ring current between 250–300 mA in top up mode.

Table 1: Technical specifications of the UE52-PGM beamline at BESSY II^[56].

energy range	85–1600 eV (soft X-ray regime)
resolving power at 400 eV	> 10000
polarization	variable
degree of polarization	90 %
photon flux (500 – 1000 eV)	> 10 ¹² photons / s
divergence	0.8 mrad x 0.2 mrad

2.3.3 Wyvern KMLaps system

The output of a Ti:Sa oscillator/CPA amplifier system is split into several branches for pump-probe experiments. In this work, the pump beam is not needed to record steady-state UVPD spectra. Instead, the beam enters the TOPAS-C system, and two sets of wavelength separators filter the required energy pulses from other beams with different wavelengths. The laser beam is focused onto the center of the ion cloud within the Paul trap. A beam shutter is synchronized with the mass spectrometer to allow radiation of the ions with a set frequency (10 Hz). The gained UVPD spectra (cf. chapter 5) were recorded with the wyvern setup (KMLaps). Further details can be found elsewhere^[21, 31, 57].

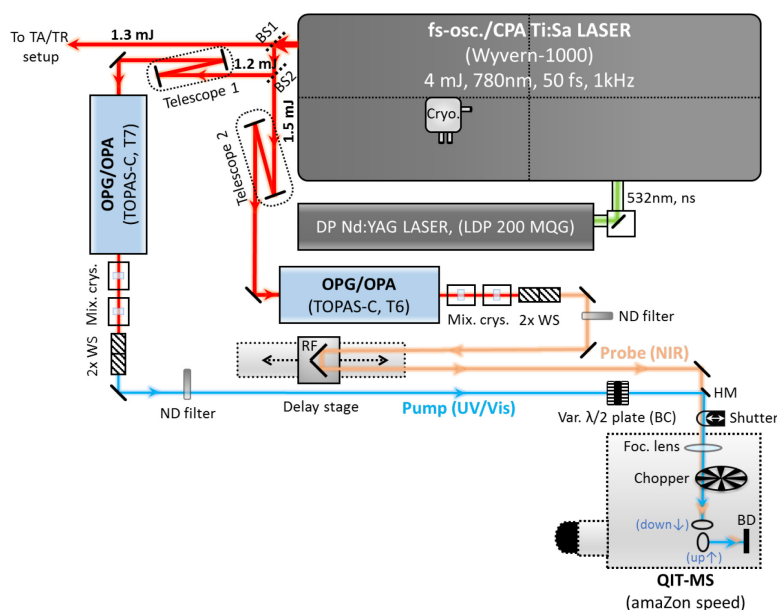


Fig. 17: Schematic setup for PD/tPD experiments, combining a tunable femtosecond pump/probe laser setup with a modified electrospray Paul-type ion trap mass spectrometer^[31].

2.4 References

- [1] B. Daltonics, AmaZon SL series user manual.
- [2] S. Bari, O. Gonzalez-Magaña, G. Reitsma, J. Werner, S. Schippers, R. Hoekstra, and T. Schlathölder, Photodissociation of protonated leucine-enkephalin in the VUV range of 8–40 eV, *J. Chem. Phys.*, 134, 024314, 2011.
- [3] D. Egorov, L. Schwob, M. Lalande, R. Hoekstra, and T. Schlathölder, Near edge X-ray absorption mass spectrometry of gas phase proteins: the influence of protein size, *Phys. Chem. Chem. Phys.*, 18, 26213-26223, 2016.
- [4] G. Reitsma, O. Gonzalez-Magaña, O. Versolato, M. Door, R. Hoekstra, E. Suraud, B. Fischer, N. Camus, M. Kremer, R. Moshhammer, and T. Schlathölder, Femtosecond laser induced ionization and dissociation of gas-phase protonated leucine enkephalin, *Int. J. Mass spectrom.*, 365-366, 365-371, 2014.
- [5] L. Schwob, M. Lalande, D. Egorov, J. Rangama, R. Hoekstra, V. Vizcaino, T. Schlathölder, and J.-C. Pouilly, Radical-driven processes within a peptidic sequence of type I collagen upon single-photon ionisation in the gas phase, *Phys. Chem. Chem. Phys.*, 19, 22895-22904, 2017.
- [6] R. R. Julian, S. R. Mabbett, and M. F. Jarrold, Ion funnels for the masses: Experiments and simulations with a simplified ion funnel, *J. Am. Soc. Mass. Spectrom.*, 16, 1708-1712, 2005.
- [7] C. Berg, T. Schindler, G. Niedner-Schatteburg, and V. E. Bondybey, Reactions of simple hydrocarbons with Nb+n: Chemisorption and physisorption on ionized niobium clusters, *The Journal of Chemical Physics*, 102, 4870-4884, 1995.
- [8] V. E. Bondybey, and J. H. English, Laser induced fluorescence of metal clusters produced by laser vaporization: Gas phase spectrum of Pb₂, *J. Chem. Phys.*, 74, 6978-6979, 1981.
- [9] T. G. Dietz, M. A. Duncan, D. E. Powers, and R. E. Smalley, Laser production of supersonic metal cluster beams, *The Journal of Chemical Physics*, 74, 6511-6512, 1981.
- [10] S. Maruyama, L. R. Anderson, and R. E. Smalley, Direct injection supersonic cluster beam source for FT-ICR studies of clusters, *Rev. Sci. Instrum.*, 61, 3686-3693, 1990.
- [11] D. Proch, and T. Trickl, A high-intensity multi-purpose piezoelectric pulsed molecular beam source, *Rev. Sci. Instrum.*, 60, 713-716, 1989.
- [12] H. Budzikiewicz, J.H. Gross: Mass Spectrometry. A Textbook, *Analytical and Bioanalytical Chemistry*, 381, 1319-1320, 2005.
- [13] E. d. Hoffmann, and V. Stroobant, "Mass Spectrometry: Principles and Applications."

- [14] F. W. McLafferty, Mass spectrometry across the sciences, *Proceedings of the National Academy of Sciences*, 105, 18088, 2008.
- [15] S. Maher, F. P. M. Jjunju, and S. Taylor, Colloquium: 100 years of mass spectrometry: Perspectives and future trends, *Rev. Mod. Phys.*, 87, 113-135, 2015.
- [16] R. G. Cooks, G. L. Glish, S. A. McLuckey, and R. E. Kaiser, Ion Trap Mass Spectrometry, *Chemical & Engineering News Archive*, 69, 26-41, 1991.
- [17] P. Wolfgang, and S. Helmut, Notizen: Ein neues Massenspektrometer ohne Magnetfeld, *ZS für Naturforschung A*, 8, 448-450, 1953.
- [18] F. M. Harris, Quadrupole storage mass spectrometry. Vol. 102 in chemical analysis: A series of monographs on analytical chemistry and its applications. Raymond E. March and Richard J. Hughes John Wiley and Sons, New York, 1989, pp. 471, *Rapid Commun. Mass Spectrom.*, 5, 58-58, 1991.
- [19] R. E. March, Quadrupole ion trap mass spectrometry: a view at the turn of the century, *Int. J. Mass spectrom.*, 200, 285-312, 2000.
- [20] G. Stafford, Ion trap mass spectrometry: a personal perspective, *J. Am. Soc. Mass. Spectrom.*, 13, 589-596, 2002.
- [21] D. Imanbaew, J. Lang, M. F. Gelin, S. Kaufhold, M. G. Pfeffer, S. Rau, and C. Riehn, Pump-Probe Fragmentation Action Spectroscopy: A Powerful Tool to Unravel Light-Induced Processes in Molecular Photocatalysts, *Angew. Chem. Int. Ed.*, 56, 5471-5474, 2017.
- [22] S. V. Kruppa, F. Böppler, C. Holzer, F. Dietrich, R. Diller, W. Klopper, and C. Riehn, Excited state vibrational coherence in a binuclear metal adduct: wave packet phase dependant molecular fragmentation under variation of ligand size, *EPJ Web Conf.*, 205, 2019.
- [23] S. V. Kruppa, F. Böppler, C. Holzer, W. Klopper, R. Diller, and C. Riehn, Vibrational Coherence Controls Molecular Fragmentation: Ultrafast Photodynamics of the [Ag₂Cl]⁺ Scaffold, *J. Phys. Chem. Lett.*, 9, 804-810, 2018.
- [24] S. V. Kruppa, Y. Nosenko, M.-O. Winghart, S. P. Walg, M. M. Kappes, and C. Riehn, Fragmentation pathways of dianionic [Pt₂(μ-P₂O₅H₂)₄+X,Y]²⁻ (X,Y=H, K, Ag) species in an ion trap induced by collisions and UV photoexcitation, *Int. J. Mass spectrom.*, 395, 7-19, 2016.
- [25] J. Lang, M. Cayir, S. P. Walg, P. Di Martino-Fumo, W. R. Thiel, and G. Niedner-Schatteburg, Intermetallic Competition in the Fragmentation of Trimetallic Au-Zn-Alkali Complexes, *Chemistry – A European Journal*, 22, 2345-2355, 2016.
- [26] J. Lang, D. V. Fries, and G. Niedner-Schatteburg, Characterization of Trinuclear Oxo Bridged Cobalt Complexes in Isolation, *Z. Phys. Chem.*, 232, 649-669, 2018.
- [27] J. Lang, M. Gaffga, F. Menges, and G. Niedner-Schatteburg, Two-color delay dependent IR probing of torsional isomerization in a [AgL₁L₂]⁺ complex, *Phys. Chem. Chem. Phys.*, 16, 17417-17421, 2014.
- [28] J. Lang, J. M. Hewer, J. Meyer, J. Schuchmann, C. van Wüllen, and G. Niedner-Schatteburg, Magnetostructural correlation in isolated trinuclear iron(iii) oxo acetate complexes, *Phys. Chem. Chem. Phys.*, 20, 16673-16685, 2018.
- [29] J. Martens, G. Berden, C. R. Gebhardt, and J. Oomens, Infrared ion spectroscopy in a modified quadrupole ion trap mass spectrometer at the FELIX free electron laser laboratory, *Rev. Sci. Instrum.*, 87, 103108, 2016.
- [30] N. W. Mclachlan, Theory and application of Mathieu functions, *Clarendon Press, Oxford*, 1947.
- [31] S.V.Kruppa, Photochemistry and Ultrafast Dynamics of Mass-selected Multinuclear Coinage Metal Complexes Studies by Photodissociation Ion Spectroscopy, 2020.
- [32] F. Menges, "Structure and Reactivity of Isolated Mononuclear and Oligonuclear Metal Complexes," 2013.
- [33] J. T. Lau, A. Achleitner, H. U. Ehrke, U. Langenbuch, M. Reif, and W. Wurth, Ultrahigh vacuum cluster deposition source for spectroscopy with synchrotron radiation, *Rev. Sci. Instrum.*, 76, 063902, 2005.
- [34] J. T. Lau, A. Föhlich, R. Nietubycè, M. Reif, and W. Wurth, Size-Dependent Magnetism of Deposited Small Iron Clusters Studied by X-Ray Magnetic Circular Dichroism, *Phys. Rev. L*, 89, 057201, 2002.
- [35] V. Zamudio-Bayer, K. Hirsch, A. Langenberg, A. Ławicki, A. Terasaki, B. v. Issendorff, and J. T. Lau, Electronic ground states of Fe²⁺ and Co²⁺ as determined by x-ray absorption and x-ray magnetic circular dichroism spectroscopy, *J. Chem. Phys.*, 143, 244318, 2015.
- [36] V. Zamudio-Bayer, L. Leppert, K. Hirsch, A. Langenberg, J. Rittmann, M. Kossick, M. Vogel, R. Richter, A. Terasaki, T. Möller, B. v. Issendorff, S. Kümmel, and J. T. Lau, Coordination-driven magnetic-to-nonmagnetic transition in manganese-doped silicon clusters, *Phys. Re.v B*, 88, 115425, 2013.
- [37] V. Zamudio-Bayer, R. Lindblad, C. Bülow, G. Leistner, A. Terasaki, B. V. Issendorff, and J. T. Lau, Electronic ground state of Ni²⁺, *J. Chem. Phys.*, 145, 2016.

- [38] C. Bülow, Magnetische Eigenschaften von Übergangsmetallkomplexen in der Gasphase, 22-23, 2018.
- [39] A. Langenberg, "Magnetische Momente freier, massenselektierter Eisen-, Cobalt- und Nickelcluster," Doctoral Thesis, Technische Universität Berlin, Fakultät II - Mathematik und Naturwissenschaften, Technische Universität Berlin, Berlin, 2013.
- [40] A. Langenberg, K. Hirsch, A. Ławicki, V. Zamudio-Bayer, M. Niemeyer, P. Chmiela, B. Langbehn, A. Terasaki, B. v. Issendorff, and J. T. Lau, Spin and orbital magnetic moments of size-selected iron, cobalt, and nickel clusters, *Phys. Rev. B*, 90, 184420, 2014.
- [41] M. Niemeyer, Untersuchung der magnetischen Eigenschaften kleiner Eisencluster mit zirkularem magnetischem Röntgendiffraktion, 2011.
- [42] T. Bergmann, and T. P. Martin, How to specify the ion optical system of a time-of-flight mass spectrometer, *IJMSI*, 131, 21-41, 1994.
- [43] J. A. Giordmaine, and R. C. Miller, Tunable Coherent Parametric Oscillation in LiNbO_3 at Optical Frequencies, *Phys. Rev. L*, 14, 973-976, 1965.
- [44] R. L. H. R.L. Byer, Parametric oscillation and mixing in: Shen: Y.R. (eds) Nonlinear Infrared Generation, *Top. Appl. Phys.*, 16, 1977.
- [45] P. A. Franken, A. E. Hill, C. W. Peters, and G. Weinreich, Generation of Optical Harmonics, *Phys. Rev. L*, 7, 118-119, 1961.
- [46] C. D. N. R.C Eckhardt, W.J. Kozlovsky, R.L. Byer, Optical parametric oscillator frequency tuning and control, *J. Opt. Soc. Am*, 646-667, 1991.
- [47] J. E. Midwinter, and J. Warner, The effects of phase matching method and of uniaxial crystal symmetry on the polar distribution of second-order non-linear optical polarization, *BJAP*, 16, 1135-1142, 1965.
- [48] C. M. D. Brida, G. Cirimi, M. Marangoni, S. De Silvestri, G. Cerullo, Generation of broadband mid-infrared pulses from an optical parametric amplifier, *Opt. Express*, 15, 15035-15040, 2007.
- [49] G. W. Baxter, M. A. Payne, B. D. W. Austin, C. A. Holloway, J. G. Haub, Y. He, A. P. Milce, J. F. Nibler, and B. J. Orr, Spectroscopic diagnostics of chemical processes: applications of tunable optical parametric oscillators, *Appl. Phys. B*, 71, 651-663, 2000.
- [50] M. Gerhards, High energy and narrow bandwidth mid IR nanosecond laser system, *OptCo*, 241, 493-497, 2004.
- [51] J. Bahrtdt, W. Frentrup, A. Gaupp, M. Scheer, W. Gudat, G. Ingold, and S. Sasaki, A quasi-periodic hybrid undulator at BESSY II, *Nuclear Instruments and Methods in Physics Research Section A: Accelerators, Spectrometers, Detectors and Associated Equipment*, 467-468, 130-133, 2001.
- [52] R. Kinjo, and T. Tanaka, Undulator configuration for helicity switching in in-vacuum undulators, *Physical Review Accelerators and Beams*, 23, 020705, 2020.
- [53] S. Sasaki, Analyses for a planar variably-polarizing undulator, *Nuclear Instruments and Methods in Physics Research Section A: Accelerators, Spectrometers, Detectors and Associated Equipment*, 347, 83-86, 1994.
- [54] H. Wende, Recent advances in x-ray absorption spectroscopy, *Rep. Prog. Phys.*, 67, 2105-2181, 2004.
- [55] J. Bahrtdt, W. Frentrup, A. Gaupp, M. Scheer, W. Gudat, G. Ingold, and S. Sasaki, Elliptically polarizing insertion devices at BESSY II, *Nuclear Instruments and Methods in Physics Research Section A: Accelerators, Spectrometers, Detectors and Associated Equipment*, 467-468, 21-29, 2001.
- [56] H. Zentrum, https://www.helmholtz-berlin.de/pubbin/igama_output?modus=einzel&sprache=en&gid=1927.
- [57] D. Imanbaew, "Time-resolved pump-probe action spectroscopy on isolated organic dyes and supramolecular photocatalysts," 2017.

3 Methods

3.1 Electrospray Ionization process

To transfer molecular ions from a solution into the gas phase^[1-3] with an amount of minimal fragmentation, electrospray ionization is the most common method to perform mass spectrometric investigations on transition metal complexes^[4] or biomolecules^[5, 6]. This kind of ion source has been continuously advanced^[7-9] to generate molecular ions with non covalent interactions^[10, 11] or scan reactive intermediates within a catalytic cycle^[12-14].

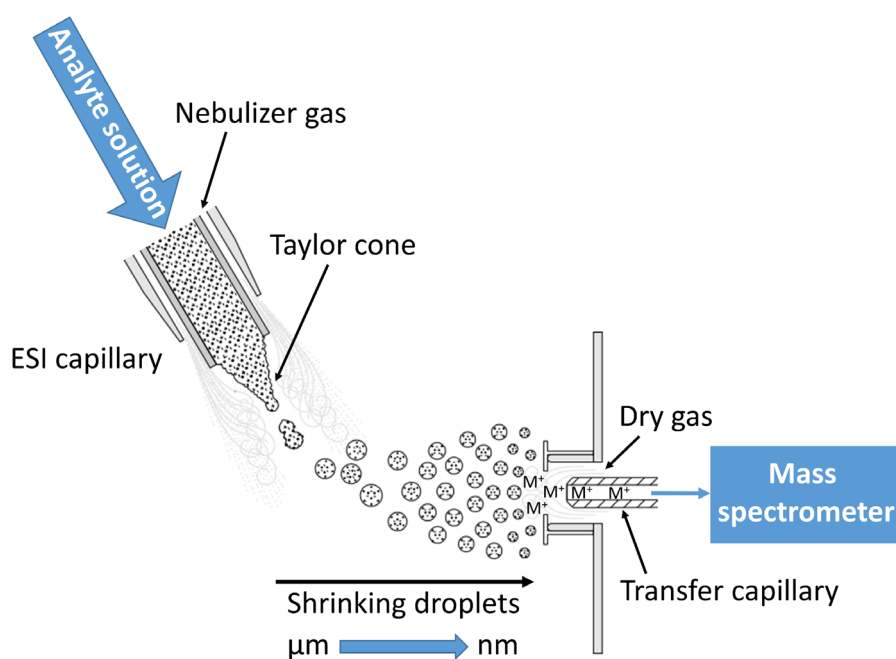


Fig. 1: Transfer of molecular ions from a solution into the gas phase by the Electrospray Ionization (ESI) process^[15-17].

The analyte solution is constantly infused into the ESI capillary (cf. Fig. 1). A strong electrostatic field is applied between the capillary and the orifice of the mass spectrometer generated by a power supply. This electrostatic field leads to a separation of cations and anions in the solution by electrophoresis. A so-called Taylor cone is formed at the exit of the capillary^[18, 19]. This cone releases charged droplets when the Coulomb repulsion between the ions in the solution overcomes the surface tension of the solvent. The released droplets shrink by thermal-induced desolvation. When the Rayleigh Limit^[20] is reached, a Coulomb explosion of these droplets starts. Repeating this process leads to completely desolvated ions in vacuum. Polar solvents with low boiling points suit the ESI process since they stabilize ions and facilitate desolvation.

The most common ESI models^[21] for the qualitative description of the desolvation mechanism are the charged residue model^[22, 23], the ion evaporation model^[24, 25], and the chain ejection model^[15, 26, 27].

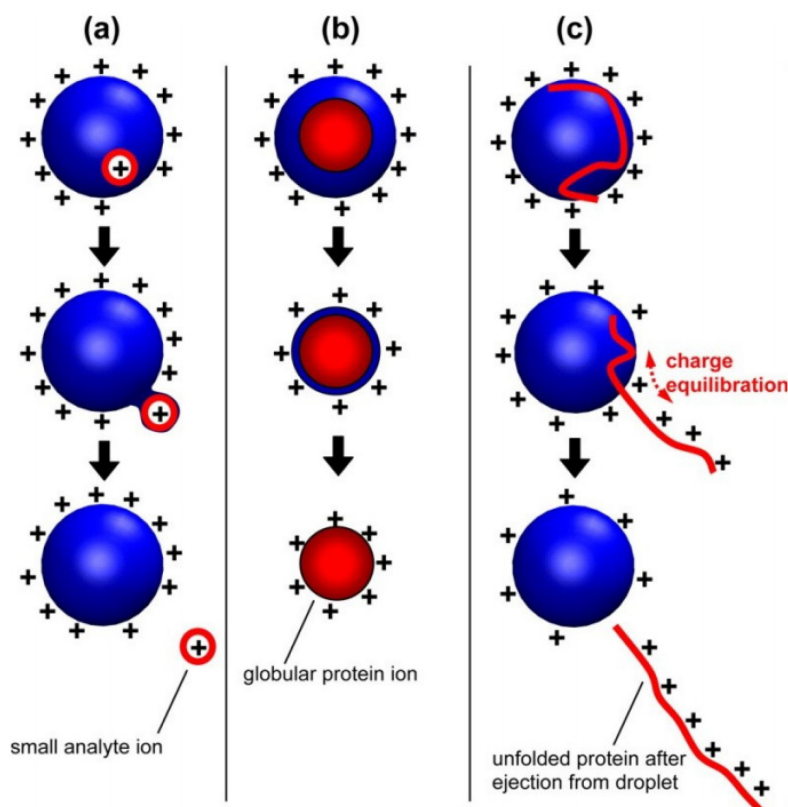


Fig. 2: Schematic description of the possible ESI models for transferring the ions into the vacuum^[15].

The ion evaporation model (cf. Fig. 2 (a)) assumes an amount of charged ions within one droplet. The ions on the surface are directly emitted by shrinking the droplet as a result of the smaller droplet's higher charge density. Otherwise, the charge residue model (cf. Fig. 2(b)) assumes just one ion in the droplet where the solvent successively shrinks until a desolvated ion is released into the vacuum. The chain ejection model (cf. Fig. 2(c)) tries to explain the transfer of protein within a droplet. In this model, non-polar groups in the protein are directed to the inside of the folded protein and interact with the solvent. The polar groups interact with the surface, and by shrinking the droplet, the protein is successively ejected into the vacuum.

3.2 Time of flight mass spectrometry (TOF-MS)

For the detection and separation of different ions, this technique uses the physical properties of the ions with distinct masses and the same kinetic energies, leading to varying velocities at a specific time for the ions^[28, 29]. The ion package is accelerated into the time of flight area with the same kinetic energy. In the field free Time of flight area, the ions separate because of their masses. Ions with higher masses gain lower velocities, and ions with lower masses get higher velocities. The kinetic energy corresponds to the potential energy of the electric field in the acceleration area.

$$\frac{1}{2} \cdot m \cdot v^2 = z \cdot e \cdot U \quad (1)$$

With m = mass of the ions, v = velocity of the ions, z = charge of the ions, U = applied acceleration voltage and e = elemental charge.

By solving the equation (1), we can acquire the time of flight velocity and also the mass-to-charge ratio for the ions:

$$v = \sqrt{\frac{2 \cdot z \cdot e \cdot U}{m}} \quad (2)$$

$$\frac{m}{z} = \frac{2 \cdot e \cdot U}{v^2} \quad (3)$$

A direct determination of the velocity is not possible in this method, but if the length of the time of flight area and the time of flight (TOF) is known, the velocity can be easily determined as:

$$v = 2 \cdot e \cdot U \cdot \left(\frac{TOF}{L}\right)^2 \quad (4)$$

The exact position of the ions in the acceleration stage is unknown. It leads to energy and location blurs, resulting in lower resolution of the mass peaks in the time of flight spectrum. The resolution of the mass peaks is defined as:

$$R = \frac{m}{\Delta m} \quad (5)$$

There, the resolution of the mass peaks is determined by the most negligible separable mass difference. This mass difference is correlated to the time of flight as:

$$\frac{1}{R} = \frac{\Delta m}{m} = \frac{2 \cdot \Delta t}{t_{tot}} \quad (6)$$

With eq. 6, the resolution of the mass peaks depends on the flight time. A longer time of flight leads to a better resolution^[30]. To generate longer time of flight areas, the ions are guided into a Reflectron (cf. Fig. 3) described by Mamyrin^[29].

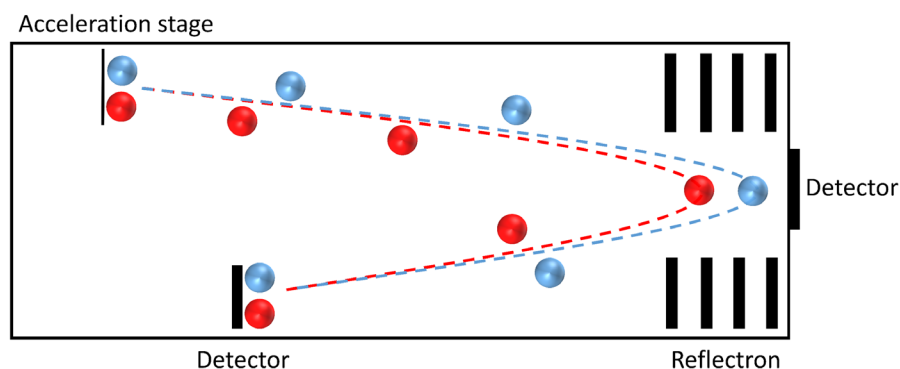


Fig. 3: Schematic description of the ions in the time of flight area within the Reflectron.

The ions with the same mass but different velocities enter the Reflectron and are deflected to the detector. The ions with higher velocity enter more profound in the Reflectron than the ions with lower velocities. Consequently, ions with higher velocity need to exit the Reflectron longer than those with lower velocity, resulting in ions with the same masses leaving the Reflectron simultaneously and enhancing the resolution.

3.3 Collision Induced Dissociation (CID)

The fragmentation of molecules via Collision Induced Dissociation (CID) with Helium atoms in the Paul trap leads to diffuse peaks with different m/z ratios in the mass spectrum^[31, 32]. With advancing technology of the mass spectrometers, CID experiments have grown to a standard tandem MS method^[33, 34] for the characterization of organic molecules^[35] and transition metal complexes^[36-41]. For the CID experiments within a Paul trap (cf. Fig. 4), additional DC voltages to trapping potentials accelerate the mass-selected ions in their trajectory. Increasing the DC voltage leads to higher kinetic energies of the ions and the number of collisions of the ions with the Helium buffer gas in the ion trap. Inelastic collisions with the Helium buffer gas transfer the additional kinetic energy of the ions into intramolecular degrees of freedom^[42]. The transferred energy accumulates in inner degrees of freedom until the dissociation threshold is exceeded and results in fragmentation of molecule^[43]. The masses of the

fragments and their fragmentation pathways can also yield information on the structure, stabilities, and bonding strengths of the precursor.

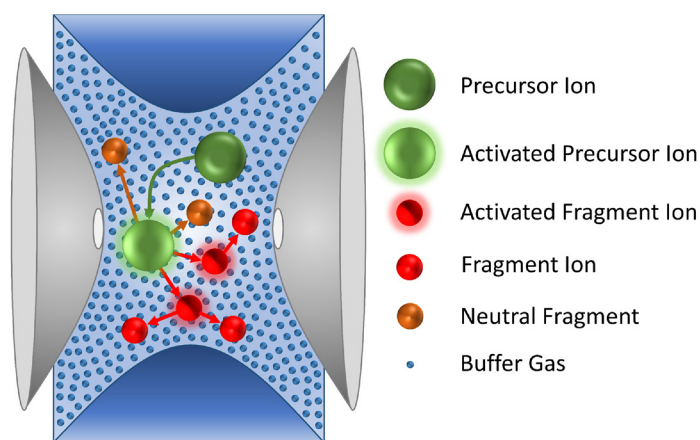


Fig. 4: Schematic CID process in the Paul trap. The precursor ions are activated by acceleration with an additional DC voltage and collide with the Paul trap's buffer gas. This leads to a fragmentation of the precursor into neutral, cationic, and anionic fragments, which decelerate by collisional cooling.

Another method for investigating the fragmentation pathways and their resulting stabilities of isolated ions is performed by continuously increasing the acceleration voltage while recording the precursor ion and their resulting fragment ions over a defined time. The acceleration voltage versus the relative intensity of the fragment ions is called CID appearance curve. The DC excitation amplitude determines the internal energy scale of the mass spectrometer in the laboratory frame (E_{LAB} in V). The relative abundance of the fragment ions can be calculated by eq. 7:

$$I_{tot}^{fr}(E_{lab}) = \left(\frac{\sum_i I_i^{fr}(E_{lab})}{\sum_i I_i^{fr}(E_{lab}) + \sum_i I_i^p(E_{lab})} \right) \quad (7)$$

where I_i^{fr} = intensity of the fragment ions and I_i^p = intensity of the parent ions. The amount of energy transfer by inelastic collisions depends on the mass of the ions (m_{ion}) and the mass (Helium, m_{He}) of the buffer gas. The excitation amplitude E_{lab} is corrected by the center of

$$E_{com} = \left(\frac{m_{He}}{m_{He} + m_{ion}} \right) \cdot E_{lab} \quad (8)$$

Current applications of CID techniques use RF excitation in the presence of multiple collisions, which result in a slow multi-collision heating operation mode^[44]. The resulting CID curves are fitted by sigmoidal functions using at least square criterion in eq. 9:

$$I_{fit}^{fr}(E_{com}) = \left(\frac{1}{1 + e^{(E_{COM}^{50} - E_{com}) B}} \right) \quad (9)$$

The resulting E_{COM}^{50} value represents the excitation amplitude at which the sigmoid function is at half maximum value (cf. Fig. 5). The parameter B in eq. 3 describes the rise of the sigmoid curve. The strong correlation between the excitation amplitude and the relative fragment intensities leads to a feasible assumption that the E_{COM}^{50} value can be associated with the relative stability of the ion, providing experimental access to activation energies^[45-47].

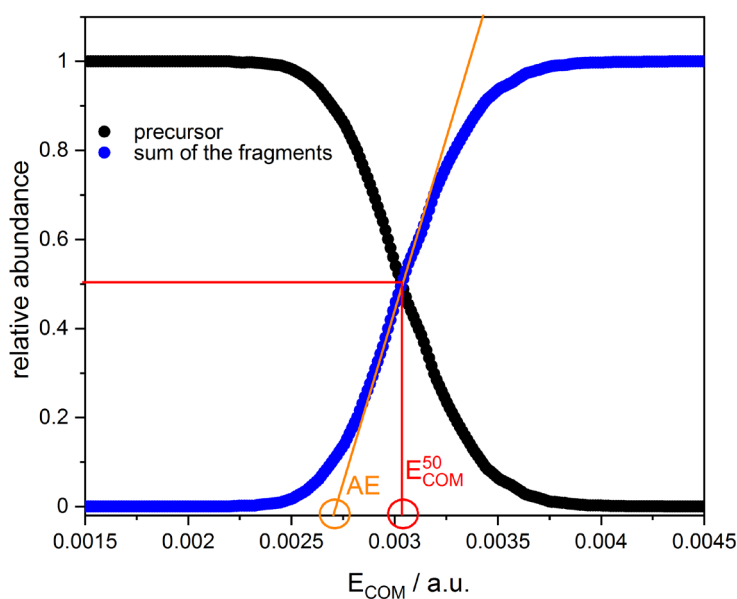


Fig. 5: CID breakdown curve with the associated appearance curve of $[\text{Fe}(\text{btpa})]^{2+}$, their corresponding appearance energies (AE) and E_{COM}^{50} values. The positions of the AE (orange) and E_{COM}^{50} (red) values are marked with circles.

The appearance energy (AE) values should deliver better results than the E_{COM}^{50} value because the AE value reduces the influence of kinetic effects on the derivation of the underlying intrinsic thermochemistry^[46, 48]. For simple bond cleavage, the rise of the fragment ions is mainly determined by the density of states in precursor ions, which is a size effect. Bigger ions should dissociate more slowly, which results in a flatter CID appearance curve and the E_{COM}^{50} value shifts to higher values. For the determination of the AE value, the extrapolation to the baseline lowers the effect of the slope on the energy value derived from E_{COM}^{50} ^[46]. The rise of the sigmoid fit is also an indicator of the transition state passed during the fragmentation process. The fragmentation can be performed by a kinetically controlled reaction or a thermodynamic reaction control. For the slope, this would mean that the kinetically controlled fragmentation leads to a steeper slope than in a thermodynamically controlled fragmentation.

A thermodynamically controlled fragmentation would lead to a tight transition and a more stable precursor. An activated complex with strict steric requirements is called a tight complex, whereas the transition state without such conditions is called a loose complex. The tight complex needs more energy to dissociate, leading to a flatter slope, while the loose complex is weakly bonded, resulting in steep slopes^[49, 50]. The CID experiments were performed with the AmaZon ETD (bruker daltonics) mass spectrometer (cf. chapter 6, 7, 8, and 9).

3.4 Electron Transfer Dissociation (ETD)

Hunt and coworkers developed this method to investigate large peptides in the gas phase^[51]. Otherwise, as in electron capture dissociation, which leads to a fragmentation of the ions, this technique allows attaching electrons to the ions without/almost no fragmentation^[52, 53]. This technique enables a deeper investigation of the fragmentation pathways, bonding strengths, and the stabilities of transition metal complexes. The radical anions were created with a chemical ionization (CI) source and guided to the Paul trap, where these radical anions can transfer the electron to the precursor ion (cf. Fig. 6).

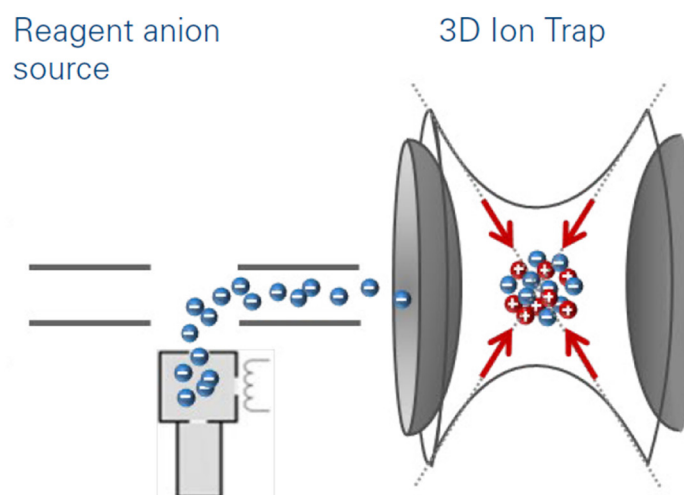


Fig. 6: Scheme of the ETD process in the AmaZon ETD mass spectrometer. The radical anions were led into the Paul trap and inelastic collisions with the precursor to attach the electron to the precursor^[17].

Two steps are necessary to generate the radical cations to perform the ETD process (cf. Fig. 7).

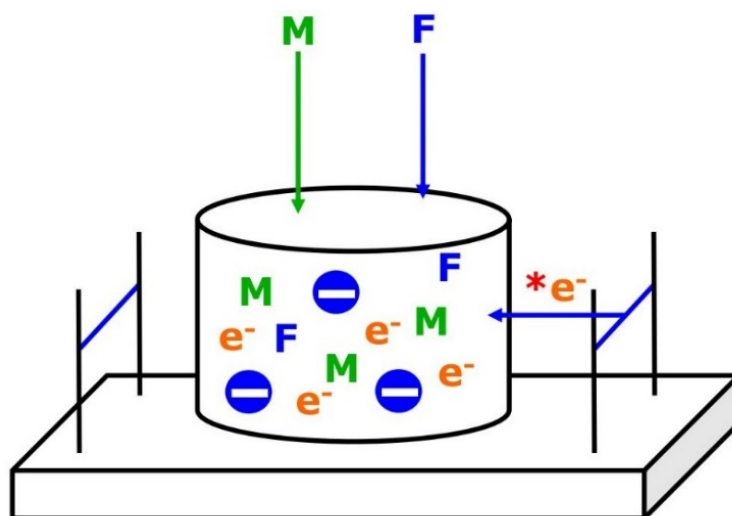
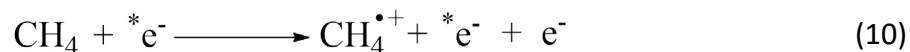
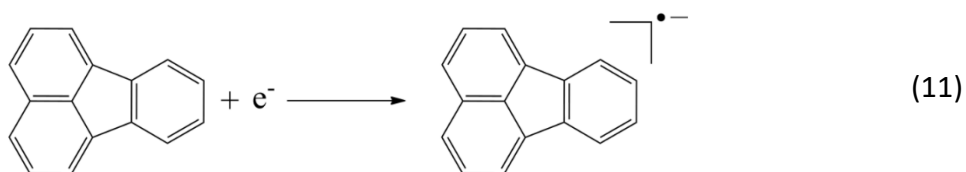


Fig. 7: Scheme of the ETD process in the AmaZon ETD mass spectrometer. The electrons were led into the NCI source and transformed into low-energy electrons by methane as a mediator (M). The radical anions (Fluoranthene (F^{-•})) were created by the attachment of the low-energy electron to the Fluoranthene (F)^[17].

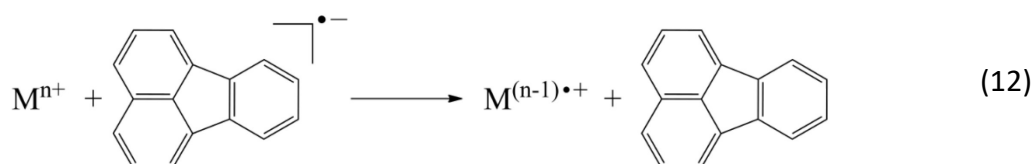
The first step is to generate low-energy electrons (< 1 eV) by the electron ionization (EI) of methane. Therefore, high-energy electrons (*e⁻) with a kinetic energy of 60-80 eV are injected into the methane (M) and perform Electron Impact (EI) ionization (cf. eq. 10) and thermalize by inelastic collisions with methane^[54].



In the second step, the low-energy electrons from the methane are attached to the Fluoranthene (F) and form a radical anion (cf. eq. 11). Many polyaromatic molecules were tested to capture the low-energy electrons^[55, 56], but Fluoranthene seems to work best with an efficiency of ~40%^[55]. Also, to capture and transport electrons, the molecule of choice should obtain a low ionization potential and a specific electron affinity to enhance the efficiency of the ETD process. Fluoranthene comprises both properties with an electron affinity of 0.76 eV^[57] and an ionization potential of 7.9 eV^[58]. For the formation of stable Fluoranthene radicals via electron capture of the low-energy electrons, the molecule exhibits the highest cross-section for electron capture (0.2 eV)^[59]. The high methane background pressure suppresses an Electron impact ionization of Fluoranthene because of its high ionization potential.



These radical anions can attach the electron to the precursor ion with a charge $n > 2$ and reduce the precursor ion to a radical cation with a charge of $(n-1)^+$ (cf. eq. 12).



The CID experiments with ETD reduced complexes were performed with the AmaZon ETD (bruker daltonics) mass spectrometer (cf. chapter 7, 8, and 9).

3.5 InfraRed (Multiple) Photon Dissociation (IR(M)PD)

Irradiation with IR light combined with electrospray ionization mass spectrometry (ESI-MS) allows investigation of the vibrational fingerprint of ions in gas phase void of any external effects or solvent influences (see chapter 6, 7, and 9). The vibrational fingerprint provides crucial information to understand the structure and reactivity of molecules and transition metal complexes^[60]. Unfortunately, the ion density in gas phase is very low ($<10^8 \text{ cm}^{-3}$) due to space charge limits. The optical density vanishes, so classical spectroscopic methods are not applicable, and they would achieve no detectable attenuation^[60].

Instead, InfraRed (Multiple) Photon Dissociation^[61] (IR(M)PD) is an “action spectroscopy”, which allows recording vibrational spectra of isolated ions in gas phase. Resonant absorption of single or multiple IR photons may lead to fragmentation of the isolated ion, which the mass spectrometer may detect. The strength of the fragment signal thus becomes an indirect indicator of the absorption strength. The Photon energy is in a range of 15-50 kJ/mol (800-4000 cm^{-1}), which is enough to boil off weakly bound messenger tags^[62, 63] or to break non covalent bonds as, e.g., hydrogen bonds^[64].

To overcome the dissociation threshold for stronger/covalent bondings, absorption of multiple photons is necessary in order to pump an enhanced amount of energy into the molecule^[65, 66].

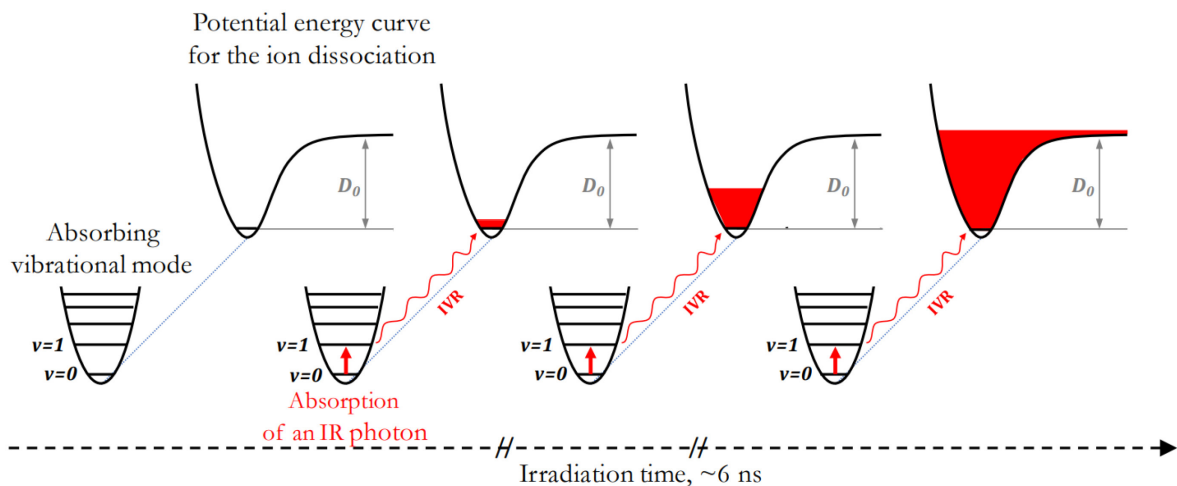


Fig. 8: General scheme of the non-coherent IR(M)PD processes^[67]: The isolated ion absorbs a resonant IR photon. The additional energy is redistributed within the ion by internal vibrational redistribution^[68] (IVR). This process repeats until the dissociation threshold of the ion is exceeded and starts fragmentation. The irradiation time is ~ 7 ns (a single IR laser pulse).

Resonant absorption of the IR photon results when the photon frequency resonates with a molecular energy transition (cf. Fig. 8). In the non-coherent IR(M)PD model, internal vibrational redistribution (IVR) rapidly scatters the additional energy into several molecular vibrational degrees of freedom. The IVR process also heats the molecular ions, allowing the original oscillation to absorb additional photons. This process repeats until the dissociation threshold is exceeded and the molecule begins fragmentation. In this process, the weakest bonding dissociates, even when it is not directly excited by the IR laser^[69]. The fragmentation yield ($Y(\nu)$) is defined by eq. 13.

$$Y(\nu) = \left(\frac{\sum_i I_i^{fr}(\nu)}{\sum_i I_i^{fr}(\nu) + \sum_i I_i^p(\nu)} \right) \quad (13)$$

where I_i^{fr} = intensity of the fragment ions and I_i^p = intensity of the parent ions. An experimental IR(M)PD spectrum arises from a plot of the fragmentation efficiency as a function of laser frequency (ν).

In comparison with quantum chemical calculations, IR(M)PD spectra help extract valuable structural information of isolated molecules void of external effects. However, the obtained band intensities may not correlate linearly with the laser intensity and the absorption energy of the oscillation mode because of the multiphoton processes in the experiment. Also,

inefficient IVR processes and high dissociation thresholds may lead to less or no fragmentation, which may result in undetected so called “dark” vibrational bands^[70, 71].

The IR(M)PD experiments were performed with the modified AmaZon SL (bruker daltonics) mass spectrometer (cf. chapter 6, 7, and 9).

3.6 Ultra Violet Photon Dissociation (UVPD)

To understand the electronic structure and reactivity of molecules and transition metal complexes, the UV/VIS absorption bands provide crucial information^[72]. Irradiation with UV/VIS light combined with electrospray ionization mass spectrometry (ESI-MS) allows investigation of the electronic transitions of ions in gas phase void of any external effects or solvent influences (see chapter 5). Electronic transitions are linked with vibrational excitation of the Franck Condon (FC) modes of the chromophore in the ions of interest (cf. Fig. 9). The electronic transition intensity depends on the moment, Franck Condon factors^[73], and resonant photon absorption^[74]. Resonant absorption of the UV/VIS photons leads to fragmentation if the photon energy is higher than the activation energy of the lowest fragmentation energy^[75, 76].

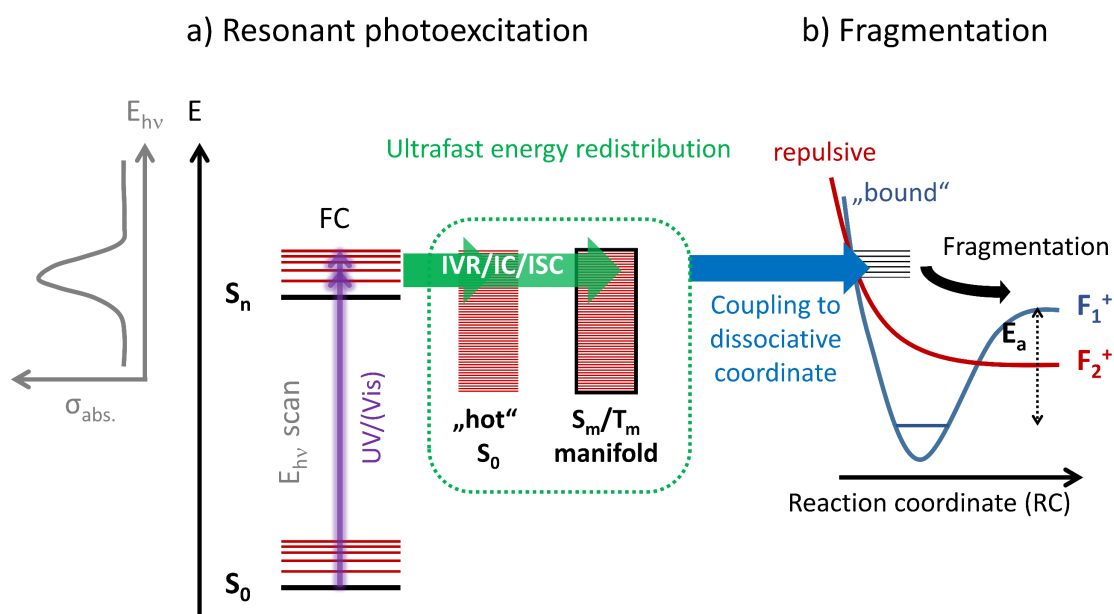


Fig. 9: Schematic representation of the UVPD process Ions in isolation absorbs a resonant UV/VIS photon from singlet ground state (S_0) into a higher excited singlet states (S_n , $n>1$)^[77].

The electronic states of the ions of interest determine the fragmentation pathways in the ions and directly affect the energy conversion (IVR, IC) respective redistribution processes (ISC)^[78]. The fragmentation yield ($Y(\nu)$) is defined similar to IR(M)PD (cf. eq. 13). For a more detailed explanation of the UVPD method, see elsewhere^[77, 79].

Steady-state UVPD spectra, in comparison with quantum chemical calculations, help extract valuable information of the electronic ground state of isolated molecules void of external effects. However, the gained absorption band intensities may not correlate linearly with the laser intensity because of the multiphoton processes in the experiment.

The steady-state UVPD experiments were performed with the modified AmaZon Speed (bruker daltonics) mass spectrometer (cf. chapter 5).

3.7 X-ray Absorption and X-ray Magnetic Circular Dichroism (XMCD)

3.7.1 X-ray absorption spectroscopy (XAS)

The absorption of X-ray photons usually leads to an excitation of a core-shell electron in an atom. The absorption can be resonant or non-resonant. In the resonant case, the electron is excited into an empty valence shell of the atom. In the non resonant case, the electron is excited into the continuum, leading to further excitation of the irradiated system. The resonant, either the non resonant case, leaves an empty core-shell in the atom, also called the core hole. This core hole can be filled by electrons, which are dropping from an energetically higher lying occupied state. The filling of the empty core holes leads to a release of energy, equal to the difference in the core hole energy and the higher filled state. The released energy leads either to emission as radiation (e.g., fluorescence) or further ejection of valence electrons (Auger electrons) into the continuum.

A resonant absorption from an initial core state $|i\rangle$ to an empty valence state $|f\rangle$ will be discussed in terms of a one-electron picture of a first-order process, meaning that the irradiation of a system with X-ray photons leads immediately to excitation from the core state $|i\rangle$ into the valence state $|f\rangle$ with no intermediate states $|n\rangle$ (cf. Fig. 10).

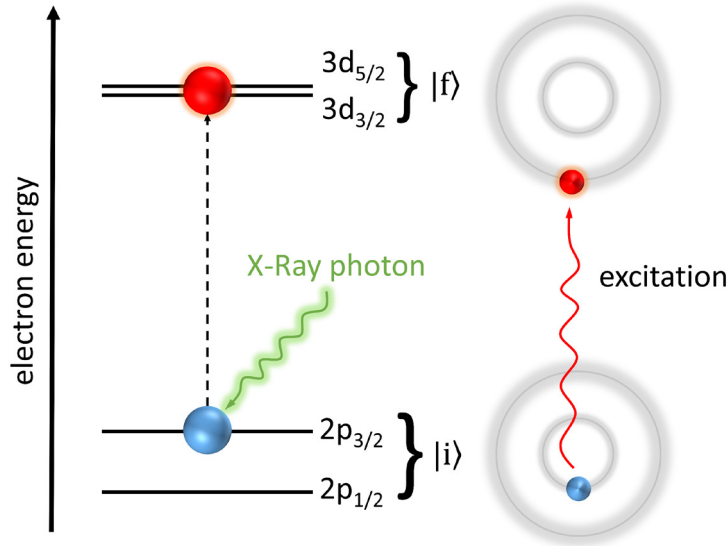


Fig. 10: Resonant $L_{2,3}$ edge absorption ($2p \rightarrow 3d$) in a one-electron picture. An electron is resonantly excited by the absorption of an X-ray photon. Their quantum numbers label their states and energy levels. The core state is the initial state $|i\rangle$ and the valence state into which the electron is excited is the final state $|f\rangle$.

The transition probability ($T_{i \rightarrow f}$) from a core state ($|i\rangle$) to a valence state ($|f\rangle$) can be described with Fermi's golden rule. For this description, only the first-order term as derived by Dirac^[80] is needed.

$$T_{i \rightarrow f} = \frac{2\pi}{\hbar} |\langle f | \hat{H}_{int} | i \rangle|^2 \delta(\varepsilon_i - \varepsilon_f) \rho(\varepsilon_f) \quad (15)$$

Where \hat{H}_{int} represents the Hamiltonian for the interaction between core state and valence state, $\varepsilon_{i,f}$ are the energies of the initial state ($|i\rangle$) and the final state ($|f\rangle$) and $\rho(\varepsilon_f)$ is the density of the possible valence states per energy unit. For the resonant case in X-ray absorption, the Hamiltonian is described as the product of the momentum operator (p) and a vector potential (A). with the quotient of the elementary charge (e) and the mass of the electron (m_e)^[81-84].

$$\hat{H}_{int} = \frac{e}{m_e} pA \quad (16)$$

By assuming a transition of one electron from the core state ($|i\rangle$) to the valence state ($|f\rangle$) the transition matrix element can be transformed into a one electron matrix element^[85].

$$M = |\langle e | \hat{H}_{int} | c \rangle| \approx |\langle f | \hat{H}_{int} | i \rangle| \quad (17)$$

In the one electron assumption, the wave function of the excited electron $|e\rangle$ and the bonded electron $|c\rangle$ can be exchanged with the initial state $|i\rangle$ and the final state $|f\rangle$. The intensity of

the X-ray absorption spectra mainly depends on the unoccupied density of states of the ion of interest due to a slight change in the energies of the one electron matrix element M . This leads to a more manageable equation than eq. 15.

$$T_{i \rightarrow f} = \frac{2\pi}{\hbar} |\langle \Psi_f | M | \Psi_i \rangle|^2 \rho(E_f) \quad (18)$$

$$I_{\text{XAS}} \approx M^2 \rho(E_f) \quad (19)$$

The Photon absorption in XA spectroscopy can be resonant or non resonant. As mentioned above, the core shell electron is excited into a valence shell in resonant photon absorption. In the non resonant photon absorption, the core shell electron is excited into the continuum above the ionization potential if the photon energy is sufficient. In both cases, the electron leaves the core shell and creates a “core hole”. This also points out that this kind of spectroscopy is element selective because of the different binding energies of the core electrons in the various elements. It is also possible to probe selective specific orbital momentum empty valence states with dipole selection rules by its corresponding core shell orbital (cf. Tab. 1).

Tab. 1: Dipole selection rules for the excitation of the core-shell electron into an empty valence shell in XA spectroscopy.

Δl	$l' - l$	± 1
Δm_l	$m'_l - m_l = q$	$0, \pm 1$
Δs	$s' - s$	0
Δm_s	$m'_s - m_s$	0

The localized empty density of atomic states is very sensitive to the hybridization and charge transfer and the symmetry of the molecular environment (e.g., crystal field)^[85]. This leads to a fine structure splitting and absorption spectra that reveal different transitions of $2p_{3/2}$ and the $2p_{1/2}$ core-shell electrons into the valence shell known as L_3 and L_2 edges (cf. Fig. 11).

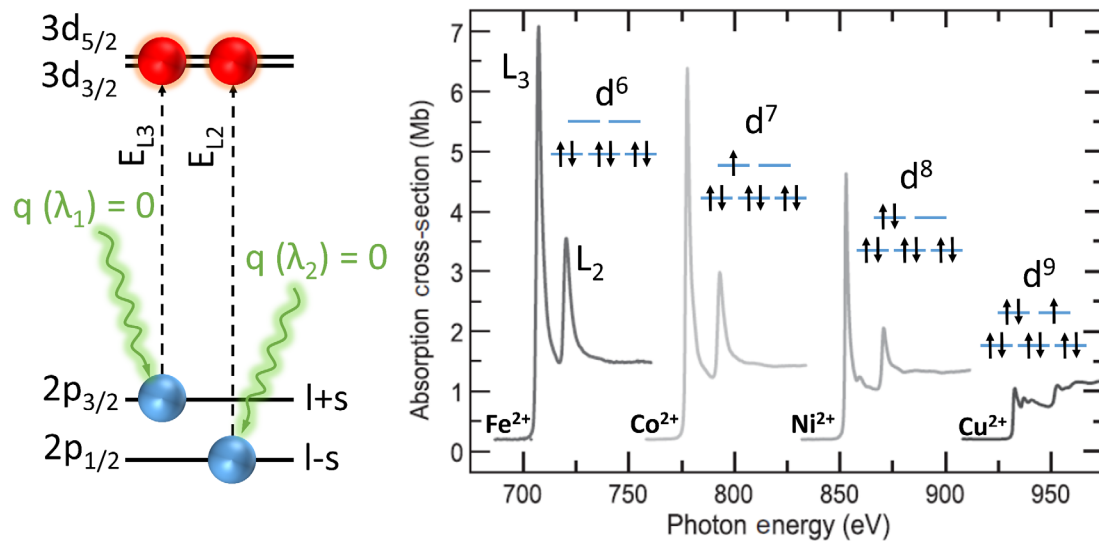


Fig. 11: Illustration of the intensity sum rule by absorption of linear polarized X-ray photons (left) and normalized L_{2,3} edge X-ray absorption spectra of the 3d metals iron, cobalt, nickel, and Copper (right). The absorption intensity drops with an increasing number of 3d electrons and a decreasing number of holes in the valence band.

The intensity in the spectra is mainly determined by the number of holes in the valence shell (n_H). More electrons lead to fewer holes in the valence shell, and therefore, the intensity of the XA spectra is reduced as a result of inefficient transitions from the core shell into the valence shell.

3.7.2 X-ray magnetic circular magnetism (XMCD)

The XMCD^[86-88] method can be seen as further development of the XAS method. Ions of interest are magnetized and measurement as a function of the photon energy and their corresponding polarization of the X-ray beam. Circularly polarized X-ray photons give access to orbital angular momentum and the spin of the empty valence states in the ions of interest. Therefore, the dipole selection rules are expanded with $\Delta m_l = +1, -1$ for positive (right hand side) and negative (left hand side) circular polarized X-ray absorption (cf. Fig. 12)

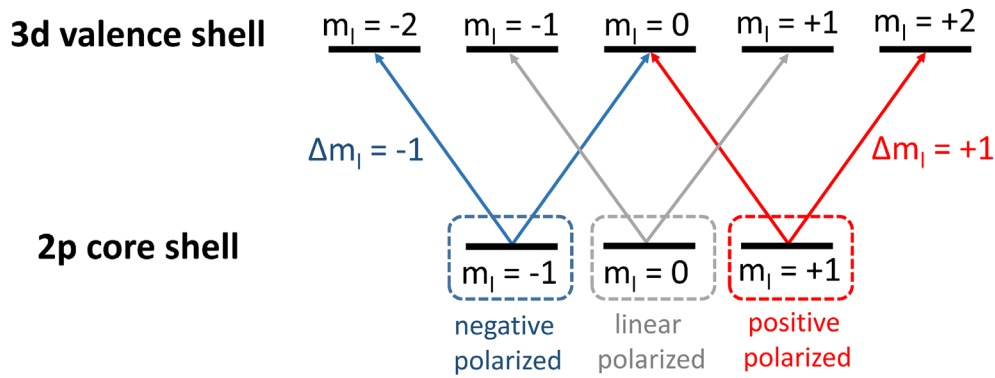


Fig. 12: Sensitivity of the XMCD effect of orbital magnetism from the core-shell into the valence shell.

The sensitivity of the spin polarization in XMCD is given by the Fano effect^[89], where photoelectrons excited by circularly polarized light are spin polarized. This enables the possibility of identifying characteristics in the “spin-up” and “spin-down” holes in the valence orbitals by evaluating the differences in the X-ray absorption intensities and allowing the determination of magnetic moments. A two-step model can explain the spin dependency in the X-ray absorption intensities (cf. Fig. 13):^[90]

1. An electron absorbs a circularly polarized X-ray photon in the spin-orbit split initial ground state $|i\rangle$. For $2p \rightarrow 3d$ transitions ($L_{2,3}$ absorption edges) like in transition metals, this corresponds to the $2p_{3/2}$ and the $2p_{1/2}$ levels. The spin-orbit orbit coupling of the ground state causes an angular momentum of the X-ray photons to be partially transferred to the exciting spin of the electron, resulting in spin polarization of the electron, and it is the opposite for the $2p_{3/2}$ (l+s) and $2p_{1/2}$ (l-s) levels. The quantization axis of the excited electron and the photon angular momentum are identical, parallel, or antiparallel to the propagation direction of the X-rays. The quantization axis of the excited electron and the photon angular momentum are similar, parallel, or antiparallel to the propagation direction of the X-rays.
2. Spin-polarized electrons are excited into an exchange split valence shell with an odd number of electrons. This leads to an uneven population of “spin-up” and “spin-down” electron holes. These holes serve as a detector for spin-polarized electron holes if the spin moment of the valence electrons are aligned to the photon angular momentum, which corresponds with the X-ray propagation direction, a maximum difference in the X-ray absorption (XMCD).

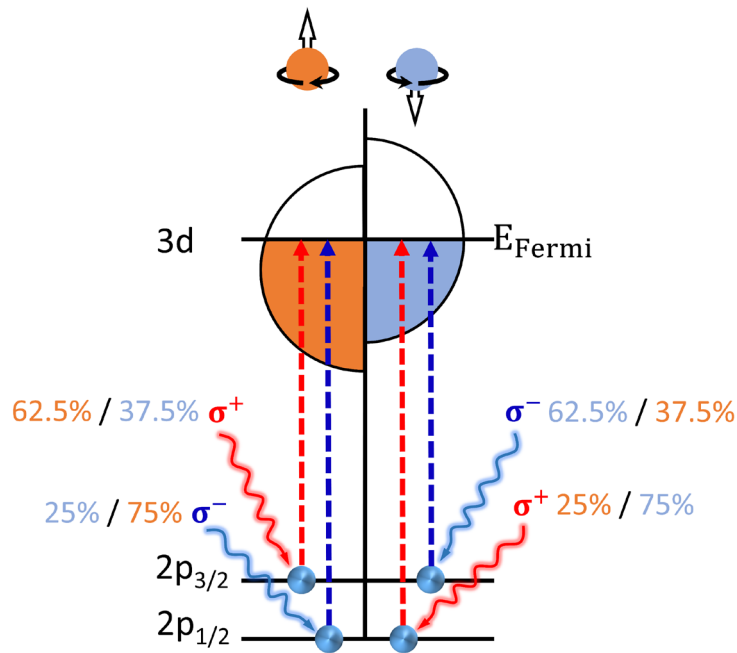


Fig. 13: Relative transition probabilities for “spin-up” (\uparrow) and “spin-down” (\downarrow) electrons from the spin-orbit split 2p levels ($2p_{3/2}$ and $2p_{1/2}$) upon excitation with circularly polarized photons for $q = +1$ (positive polarization σ^+) and $q = -1$ (negative polarization σ^-). Transition probabilities for the excitation of spin up or spin down electrons switch when the photon helicity is reversed. Positive ($q = +1$) circularly polarized light predominantly excites spin up electrons at the L_3 edge ($2p_{3/2} \rightarrow 3d$) and the L_2 edge ($2p_{1/2} \rightarrow 3d$), which mainly excites spin-down electrons. The situation is reversed for negative ($q = -1$) circularly polarized photons^[90-92].

Negatively polarized X-ray photons primarily excite “spin up” electrons in the $2p_{1/2}$ orbital and “spin down” electrons in the $2p_{3/2}$ orbital (cf. Fig. 13). The conservation of the angular momentum of the circularly polarized X-ray photon to the excited electron is transferred into the different terms of spin and orbital momentum degree of freedom. A magnetic valence shell can detect the transfer, resulting in different absorption intensities for the positive and negative circular polarized X-ray spectra (cf. Fig. 14).

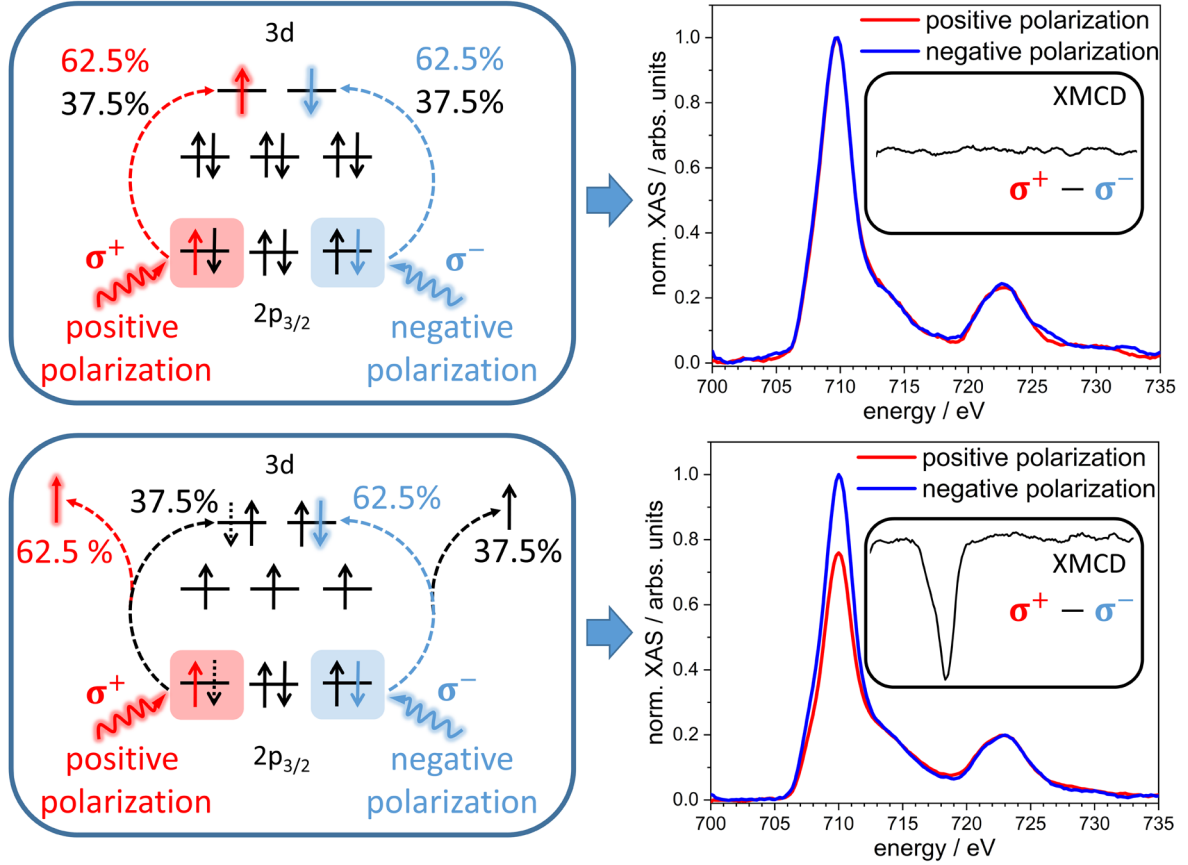


Fig. 14: Illustration of the transition probabilities from the $2p_{3/2}$ level with different circular polarized X-ray photons and their resulting XA spectra. The difference of the polarized dependent XA spectra obtains the derivation of the XMCD data.

Quantitative contributions of spin and orbital angular momenta to the XMCD effect were derived by Thole and Carra^[86, 88]. The resulting formulas are widely known as sum rules and give access to the quantitative expected spin $\langle S_z \rangle$ and orbital angular momentum $\langle L_z \rangle$ per 3d hole. When the number of the 3d hole (n_h) is known, the spin and orbital magnetic moments per metal atom can be calculated as:

$$m_S = -g_S \mu_B \frac{-\int_{L_3} (\sigma^+ - \sigma^-) d\omega - 2 \int_{L_2} (\sigma^+ - \sigma^-) d\omega}{\frac{2}{3} \int_{L_3+L_2} (\sigma^+ + \sigma^- + \sigma^0) d\omega} n_h - g_S \mu_B \frac{7}{2} \langle T_z \rangle \quad (20)$$

$$m_L = -g_L \mu_B \frac{4}{3} \frac{\int_{L_3+L_2} (\sigma^+ - \sigma^-) d\omega}{\int_{L_3+L_2} (\sigma^+ + \sigma^- + \sigma^0) d\omega} n_h \quad (21)$$

The integration of the sum rule can be achieved from the experimental XA spectra and their derivated XMCD data (cf. Fig. 15).

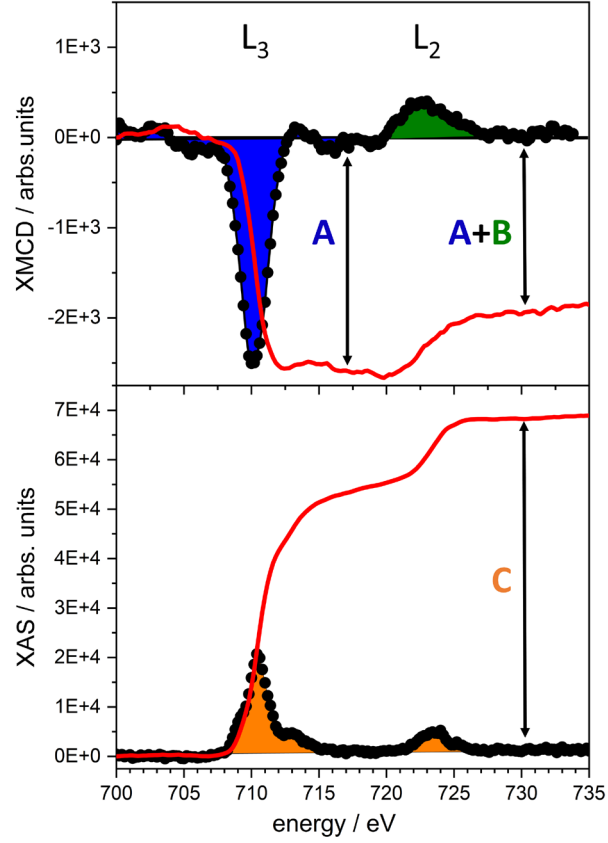


Fig. 15: Example of an XMCD spectrum and its integral over both $L_{3,2}$ absorption (top) and the integrated sum of both XA spectra for both photon helicities (bottom).

Therefore, sum rules for the spin and orbital magnetic moments per atom can be simplified with the abbreviations of the integrations as:

$$A = \int_{L_3} (\sigma^+ - \sigma^-) d\omega, \quad (21)$$

$$B = \int_{L_2} (\sigma^+ - \sigma^-) d\omega, \quad (22)$$

$$C = \frac{2}{3} \int_{L_3+L_2} (\sigma^+ + \sigma^- + \sigma^0) d\omega \text{ for } m_s, \quad C = \int_{L_3+L_2} (\sigma^+ + \sigma^- + \sigma^0) d\omega \text{ for } m_L \quad (23)$$

By summarizing the integrations to the factors A, B, and C, the simplified sum rules are defined as:

$$m_S = g_S \mu_B \frac{(A - 2B)}{C} n_h - g_S \mu_B \frac{7}{2} \langle T_z \rangle \quad (24)$$

$$m_L = -g_L \mu_B \frac{4A + B}{3C} n_h \quad (25)$$

The X-ray light direction and the magnetic field are aligned to the quantization axis (z). The magnetic dipole term $\langle T_z \rangle$ describes a foranistropy in the spin distribution and represents an expectation value of the spin magnetic dipole operator for the spin along the quantization axis^[87, 93]. The magnetic dipole term can alter up to 20 % when the spin distribution is asymmetric along the quantization axis. This phenomenon is called anisotropy^[93-95]. In angle averaged XMCD experiments, this term cancels out to zero, and the spin magnetic moment can be directly calculated from experimental data^[96, 97].

From the equations (20) and (21), the ratio of orbital to spin magnetic moment can be derived for a $2p \rightarrow 3d$ transition:

$$\frac{m_L}{m_S} \approx \frac{\mu_B \langle L_z \rangle}{2\mu_B \langle S_z \rangle} = \frac{2}{3} \frac{\int_{L_3+L_2} (\mu^+ - \mu^-) d\omega}{\int_{L_3} (\mu^+ - \mu^-) d\omega - 2 \int_{L_2} (\mu^+ - \mu^-) d\omega} = \frac{2}{3} \frac{A + B}{A - 2B} \quad (26)$$

The ratio $\langle L_z \rangle$ to $2\langle S_z \rangle + \langle T_z \rangle$ contributes to the magnetic dipole operator. This contribution can be ignored because, under the experimental conditions, these contributions are expected to be small in the investigated systems (cf. chapter 5, 7, and 8)^[98-100]. The m_L/m_S ratio can be determined with the normalization of the sum spectrum $\sigma^+ + \sigma^- + \sigma^0$, and even if an incomplete polarization of synchrotron radiation takes part and without the knowledge of the number of electron holes n_h in the valence shell. The determination of the m_L/m_S ratio is more precise than the determination of m_L or m_S .

For a $2p \rightarrow 3d$ transition ($c = 1, l = 2$; typical for first row transition metals), the integration limits from the spin-orbit split levels (j_+ and j_-) corresponds to the L_3 and L_2 absorption edges in the XA spectra. For rare earth compounds, usually, the $3d \rightarrow 4f$ ($M_{5,4}$ absorption edge) transitions are used to study the magnetism of such elements. The sum rules for the spin and orbital magnetic moments then contains prefactors as follows:

$$m_S^{(z)} = g_S \mu_B \frac{(A - bB)}{c \frac{3}{2} C} n_h - g_S \mu_B \frac{d}{c} \langle T_z \rangle \quad (27)$$

$$m_L^{(z)} = -g_L \mu_B \frac{A + B}{a \frac{3}{2} C} n_h \quad (28)$$

In general, if the orbital angular momentum of the initial state is l_i and of the final state is l_f , the sum rule related prefactors are summarized (cf. Tab. 2.).

Tab. 2: Sum rule related prefactors for different dipole transitions of the core into the valence shell^[101].

l_i	l_f	a	b	c	d
s: 0	p: 1	1	-	-	-
p: 1	d: 2	1/2	2	2/3	7/3
d: 2	f: 3	1/3	3/2	2/3	2

The spin sum rule deviation due to core-valence Coulomb interaction has not been quantified in the original derivation of the sum rule by Carra^[86]. The effect mainly depends on the atomic species and their corresponding configuration. A numerical investigation from the XMCD spin sum rule for selected 3d transition metal ions and trivalent 4f rare-earth ions by atomic calculations in order to determine the influence of this multipole electron-electron interaction was performed by Jo. et al. ^[102]. These contributions reach from about $\pm 7\%$ for Ni^{3+} to over $\pm 30\%$ for Mn^{3+} for the 3d transition metal ions and from less than $\pm 1\%$ for Er^{3+} to $\pm 230\%$ for Sm^{3+} for the rare-earth ions^[100].

The influence of the temperature and magnetic field on the magnetic properties

Magnetic dipole and the magnetic moments ($m_{s,l,j}$) of a sample are aligned to the quantization axis z (cf. Fig. 16), and these properties strongly depend on the applied temperature (T) and the external magnetic field (B). The quantization axis corresponds to the external magnetic field. A strong external magnetic field leads to a better alignment of the spins in a sample onto the quantization axis. A lower temperature leads to a higher probability of orientating spins by reducing thermal randomization.

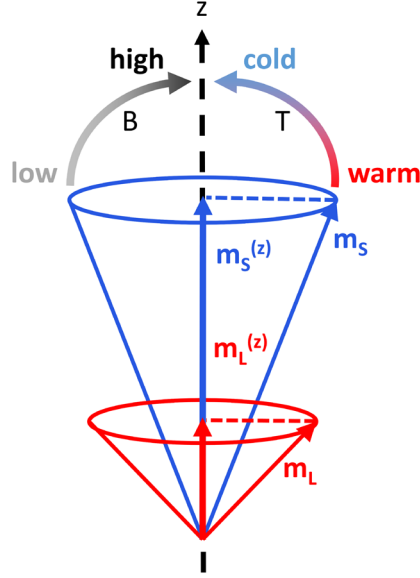


Fig. 12: Schematic description of the intrinsic spin (m_s) and orbital (m_L) magnetic moments and their projection (magnetizations) onto the quantization axis ($m_s^{(z)}$ and $m_L^{(z)}$) in dependency of the temperature (T) and the applied magnetic field (B).

For the description of the temperature and external applied magnetic dependency of the spin, orbital, and total magnetic moments per atom, Brillouin functions describe these phenomena:

$$m_S^{(z)} = g_S \mu_B S \left(\frac{2S+1}{2S} \coth \left(\frac{2S+1}{2S} \frac{\mu_B g_S S B}{k_B T} \right) - \frac{1}{2S} \coth \left(\frac{1}{2S} \frac{\mu_B g_S S B}{k_B T} \right) \right) \quad (29)$$

$$m_L^{(z)} = g_L \mu_B L \left(\frac{2L+1}{2L} \coth \left(\frac{2L+1}{2L} \frac{\mu_B g_L L B}{k_B T} \right) - \frac{1}{2L} \coth \left(\frac{1}{2L} \frac{\mu_B g_L L B}{k_B T} \right) \right) \quad (30)$$

$$m_J^{(z)} = g_J \mu_B J \left(\frac{2J+1}{2J} \coth \left(\frac{2J+1}{2J} \frac{\mu_B g_J J B}{k_B T} \right) - \frac{1}{2J} \coth \left(\frac{1}{2J} \frac{\mu_B g_J J B}{k_B T} \right) \right) \quad (31)$$

Where $m_{S/L/J}^{(z)}$ are the spin, orbital, and total magnetic moments projected onto the quantization axis. These functions consider the total spin (S), the total orbital momentum (L), and the total angular momentum ($J=L+S$). The Landé factors g_S , g_L and g_J are the quotient of a sample with the most significant measured magnetic moment and their expected magnetic moment and for this work set as $g_S = 2.0$ and $g_L = 1.0$. The Landé factor for g_J can be described as:

$$g_J = \frac{1}{2J} \left(\frac{g_L(j(j+1) + l(l+1) - s(s+1)) + g_S(j(j+1) + s(s+1) - l(l+1))}{j(j+1)} \right) \quad (32)$$

The Brillouin function allows scaling the experimental magnetizations at any applied magnetic field and temperature to a projection at 0 K and an infinite magnetic field. This projection equals their intrinsic total magnetic moments. Experimental magnetization can also be utilized to determine the temperature of the investigated system once the coupling between spin (S) and orbital (L) angular momentum to the total angular momentum (J) exceeds the individual coupling of S or L to the external magnetic field.

3.8 References

- [1] R. Colton, A. D'Agostino, and J. C. Traeger, Electrospray mass spectrometry applied to inorganic and organometallic chemistry, *Mass Spectrom. Rev.*, **14**, 79-106, 1995.
- [2] J. B. Fenn, Electrospray Wings for Molecular Elephants (Nobel Lecture), *Angew. Chem. Int. Ed.*, **42**, 3871-3894, 2003.
- [3] M. Wilm, Principles of Electrospray Ionization, *Molecular & Cellular Proteomics*, **10**, M111.009407, 2011.
- [4] V. Katta, S. K. Chowdhury, and B. T. Chait, Electrospray ionization: a new tool for the analysis of ionic transition-metal complexes, *J. Am. Chem. Soc.*, **112**, 5348-5349, 1990.
- [5] R. Aebersold, and D. R. Goodlett, Mass Spectrometry in Proteomics, *Chem. Rev.*, **101**, 269-296, 2001.
- [6] R. Lobiński, D. Schaumlöffel, and J. Szpunar, Mass spectrometry in bioinorganic analytical chemistry, *Mass Spectrom. Rev.*, **25**, 255-289, 2006.
- [7] G. T. T. Gibson, S. M. Mugo, and R. D. Oleschuk, Nanoelectrospray emitters: trends and perspective, *Mass Spectrom. Rev.*, **28**, 918-936, 2009.
- [8] K. L. Vikse, Z. Ahmadi, J. Luo, N. van der Wal, K. Daze, N. Taylor, and J. S. McIndoe, Pressurized sample infusion: An easily calibrated, low volume pumping system for ESI-MS analysis of reactions, *Int. J. Mass spectrom.*, **323-324**, 8-13, 2012.
- [9] K. Yamaguchi, Cold-spray ionization mass spectrometry: applications in structural coordination chemistry, *Mass spectrometry (Tokyo, Japan)*, **2**, S0012, 2013.
- [10] B. N. Pramanik, P. L. Bartner, U. A. Mirza, Y. H. Liu, and A. K. Ganguly, Electrospray ionization mass spectrometry for the study of non-covalent complexes: an emerging technology, *J. mass spectrom.*, **33**, 911-920, 1998.
- [11] S. J. Shields, O. Oyeyemi, F. C. Lightstone, and R. Balhorn, Mass spectrometry and non-covalent protein-ligand complexes: Confirmation of binding sites and changes in tertiary structure, *J. Am. Soc. Mass. Spectrom.*, **14**, 460-470, 2003.
- [12] D. Schröder, Applications of Electrospray Ionization Mass Spectrometry in Mechanistic Studies and Catalysis Research, *Acc. Chem. Res.*, **45**, 1521-1532, 2012.
- [13] K. L. Vikse, Z. Ahmadi, and J. Scott McIndoe, The application of electrospray ionization mass spectrometry to homogeneous catalysis, *Coord. Chem. Rev.*, **279**, 96-114, 2014.
- [14] K. L. Vikse, M. A. Henderson, A. G. Oliver, and J. S. McIndoe, Direct observation of key intermediates by negative-ion electrospray ionisation mass spectrometry in palladium-catalysed cross-coupling, *Chem. Com.*, **46**, 7412-7414, 2010.
- [15] L. Konermann, E. Ahadi, A. D. Rodriguez, and S. Vahidi, Unraveling the Mechanism of Electrospray Ionization, *Anal. Chem.*, **85**, 2-9, 2013.
- [16] Bruker, training document intro to electrospray ionization.
- [17] B. Daltonics, AmaZon ETD manual, 2015.
- [18] G. I. Taylor, Disintegration of water drops in an electric field, *Proceedings of the Royal Society of London. Series A. Mathematical and Physical Sciences*, **280**, 383-397, 1964.
- [19] M. S. Wilm, and M. Mann, Electrospray and Taylor-Cone theory, Dole's beam of macromolecules at last?, *JMSI*, **136**, 167-180, 1994.
- [20] L. Rayleigh, XX. On the equilibrium of liquid conducting masses charged with electricity, *The London, Edinburgh, and Dublin Philosophical Magazine and Journal of Science*, **14**, 184-186, 1882.
- [21] S. Crotti, R. Seraglia, and P. Traldi, Some Thoughts on Electrospray Ionization Mechanisms, *Eur. J. Mass Spectrom.*, **17**, 85-99, 2011.

- [22] M. Dole, L. L. Mack, R. L. Hines, R. C. Mobley, L. D. Ferguson, and M. B. Alice, Molecular Beams of Macroions, *J. Chem. Phys.*, 49, 2240-2249, 1968.
- [23] G. Schmelzeisen-Redeker, L. Bütfering, and F. W. Röllgen, Desolvation of ions and molecules in thermospray mass spectrometry, *IJMSI*, 90, 139-150, 1989.
- [24] J. V. Iribarne, and B. A. Thomson, On the evaporation of small ions from charged droplets, *J. Chem. Phys.*, 64, 2287-2294, 1976.
- [25] B. A. Thomson, and J. V. Iribarne, Field induced ion evaporation from liquid surfaces at atmospheric pressure, *J. Chem. Phys.*, 71, 4451-4463, 1979.
- [26] E. Ahadi, and L. Konermann, Modeling the Behavior of Coarse-Grained Polymer Chains in Charged Water Droplets: Implications for the Mechanism of Electrospray Ionization, *J. Phys. Chem. B*, 116, 104-112, 2012.
- [27] L. Konermann, A. D. Rodriguez, and J. Liu, On the Formation of Highly Charged Gaseous Ions from Unfolded Proteins by Electrospray Ionization, *Anal. Chem.*, 84, 6798-6804, 2012.
- [28] M. Guilhaus, Special feature: Tutorial. Principles and instrumentation in time-of-flight mass spectrometry. Physical and instrumental concepts, *J. Mass Spectrom.*, 30, 1519-1532, 1995.
- [29] B. A. Mamyryn, Time-of-flight mass spectrometry (concepts, achievements, and prospects), *Int. J. Mass spectrom.*, 206, 251-266, 2001.
- [30] C. G. Eisenhardt, Excited State Photoelectron Spectroscopy On Molecular Aggregates Containing Aromatic Molecules, 2000.
- [31] R. G. Cooks, Special feature: Historical. Collision-induced dissociation: Readings and commentary, *J. Mass Spectrom.*, 30, 1215-1221, 1995.
- [32] G. Hevesy, Francis William Aston. 1877-1945, *Obituary Notices of Fellows of the Royal Society*, 5, 635-650, 1948.
- [33] A. K. Shukla, and J. H. Futrell, Tandem mass spectrometry: dissociation of ions by collisional activation, *J. Mass Spectrom.*, 35, 1069-1090, 2000.
- [34] L. Sleno, and D. A. Volmer, Ion activation methods for tandem mass spectrometry, *J. Mass Spectrom.*, 39, 1091-1112, 2004.
- [35] F. W. McLafferty, R. Kornfeld, W. F. Haddon, K. Levsen, I. Sakai, P. F. Bente, S.-C. Tsai, and H. D. R. Schuddemage, Metastable ion characteristics. XXIV. Application of collisional activation spectra to the elucidation of organic ion structures, *J. Am. Chem. Soc.*, 95, 3886-3892, 1973.
- [36] M. Fabian, R. Christoph, and N.-S. Gereon, The Interaction of the Dipeptide Carnosine With Alkali Metal Ions Studied by Ion Trap Mass Spectrometry, *Z. Phys. Chem.*, 225, 595-609, 2011.
- [37] J. Lang, D. V. Fries, and G. Niedner-Schatteburg, Characterization of Trinuclear Oxo Bridged Cobalt Complexes in Isolation, *Z. Phys. Chem.*, 232, 649-669, 2018.
- [38] J. Lang, J. M. Hewer, J. Meyer, J. Schuchmann, C. van Wüllen, and G. Niedner-Schatteburg, Magnetostructural correlation in isolated trinuclear iron(III) oxo acetate complexes, *Phys. Chem. Chem. Phys.*, 20, 16673-16685, 2018.
- [39] J. Meyer, "Fragmentation and Infrared Spectroscopy of oxo-centered Homo- and Heterotrimetallic Carboxylate Bridged Transition Metal Complexes," 2018.
- [40] M. Gaffga, "Characterization of Mononuclear and Oligonuclear Transition Metal Complexes in Isolation," 2015.
- [41] J. Lang, J. Mohrbach, S. Dillinger, J. M. Hewer, and G. Niedner-Schatteburg, Vibrational blue shift of coordinated N₂ in [Fe₃O(OAc)₆(N₂)_n]⁺: "non-classical" dinitrogen complexes, *Chem. Com.*, 53, 420-423, 2017.
- [42] V. Gabelica, and E. D. Pauw, Internal energy and fragmentation of ions produced in electrospray sources, *Mass Spectrom. Rev.*, 24, 566-587, 2005.
- [43] K. Levsen, and H. Schwarz, Collisional Activation Mass Spectrometry—A New Probe for Determining the Structure of Ions in the Gas Phase, *Angew. Chem. Int. Ed.*, 15, 509-519, 1976.
- [44] S. A. McLuckey, and D. E. Goeringer, SPECIAL FEATURE: TUTORIAL Slow Heating Methods in Tandem Mass Spectrometry, *J. Mass Spectrom.*, 32, 461-474, 1997.
- [45] E.-L. Zins, C. Pepe, D. Rondeau, S. Rochut, N. Galland, and J.-C. Tabet, Theoretical and experimental study of tropylium formation from substituted benzylpyridinium species, *J. Mass Spectrom.*, 44, 12-17, 2009.
- [46] E.-L. Zins, C. Pepe, and D. Schröder, Energy-dependent dissociation of benzylpyridinium ions in an ion-trap mass spectrometer, *J. Mass Spectrom.*, 45, 1253-1260, 2010.
- [47] E.-L. Zins, D. Rondeau, P. Karoyan, C. Fosse, S. Rochut, and C. Pepe, Investigations of the fragmentation pathways of benzylpyridinium ions under ESI/MS conditions, *J. Mass Spectrom.*, 44, 1668-1675, 2009.

- [48] C. Lifshitz, Kinetic Shifts, *Eur. J. Mass Spectrom.*, 8, 85-98, 2002.
- [49] D. A. D. E.V. Anslyn, Modern Physical Organic Chemistry, 2006.
- [50] C. L. J. Laskin, Principles of Mass Spectrometry Applied to Biomolecules, 379-432, 2006.
- [51] J. J. C. D.F.Hunt, J.E.P.Syka, J.A.Marto, Electron transfer dissociation for biopolymer sequence mass spectrometric analysis, 2012.
- [52] D. Chhabil, Fundamentals of contemporary Mass spectrometry, 128, 2007.
- [53] G. Hart-Smith, A review of electron-capture and electron-transfer dissociation tandem mass spectrometry in polymer chemistry, *Anal. Chim. Acta*, 808, 44-55, 2014.
- [54] V. S. Ong, and R. A. Hites, Electron capture mass spectrometry of organic environmental contaminants, *Mass Spectrom. Rev.*, 13, 259-283, 1994.
- [55] M.-S. Kim, and A. Pandey, Electron transfer dissociation mass spectrometry in proteomics, *PROTEOMICS*, 12, 530-542, 2012.
- [56] J. E. P. Syka, J. J. Coon, M. J. Schroeder, J. Shabanowitz, and D. F. Hunt, Peptide and protein sequence analysis by electron transfer dissociation mass spectrometry, *Proc. Natl. Acad. Sci. U.S.A.*, 101, 9528, 2004.
- [57] S. J. Kregel, G. K. Thurston, and E. Garand, Photoelectron spectroscopy of anthracene and fluoranthene radical anions, *J. Chem. Phys.*, 148, 234306, 2018.
- [58] C. L. Y. Ling, Time-Dependent Mass Spectra and Breakdown Graphs. 19 Fluoranthene, *J. Phys. Chem.*, 99, 11074-11080, 1995.
- [59] W. F. Frey, R. N. Compton, W. T. Naff, and H. C. Schweinler, Electron impact studies of some cyclic hydrocarbons, *Int. J. Mass Spectrom. and Ion Physics*, 12, 19-32, 1973.
- [60] N. C. Polfer, Infrared multiple photon dissociation spectroscopy of trapped ions, *Chem. Soc. Rev.*, 40, 2211-2221, 2011.
- [61] J. Oomens, B. G. Sartakov, G. Meijer, and G. von Helden, Gas-phase infrared multiple photon dissociation spectroscopy of mass-selected molecular ions, *Int. J. Mass spectrom.*, 254, 1-19, 2006.
- [62] A. Masson, E. R. Williams, and T. R. Rizzo, Molecular hydrogen messengers can lead to structural infidelity: A cautionary tale of protonated glycine, *J. Chem. Phys.*, 143, 104313, 2015.
- [63] A. B. Wolk, C. M. Leavitt, E. Garand, and M. A. Johnson, Cryogenic Ion Chemistry and Spectroscopy, *Acc. Chem. Res.*, 47, 202-210, 2014.
- [64] G. Niedner-Schatteburg, Infrared Spectroscopy and Ab Initio Theory of Isolated H₅O₂⁺: From Buckets of Water to the Schrödinger Equation and Back, *Angew. Chem. Int. Ed.*, 47, 1008-1011, 2008.
- [65] E. R. Grant, P. A. Schulz, A. S. Sudbo, Y. R. Shen, and Y. T. Lee, Is Multiphoton Dissociation of Molecules a Statistical Thermal Process?, *Phys. Rev. Lett.*, 40, 115-118, 1978.
- [66] D. W. Lupo, and M. Quack, IR-laser photochemistry, *Chem. Rev.*, 87, 181-216, 1987.
- [67] J. Roithová, Characterization of reaction intermediates by ion spectroscopy, *Chem. Soc. Rev.*, 41, 547-559, 2012.
- [68] F. K. Y.M.E.Fung, O.A.Silivra, T.W.D. Chan, R.A.Zubarev, Facile Disulfide Bond Cleavage in Gaseous Peptide and Protein Cations by Ultraviolet Photodissociation at 157 nm, *Angew. Chem.*, 117, 6557-6561, 2005.
- [69] N. C. Polfer, and J. Oomens, Vibrational spectroscopy of bare and solvated ionic complexes of biological relevance, *Mass Spectrom. Rev.*, 28, 468-494, 2009.
- [70] D. Schröder, H. Schwarz, P. Milko, and J. Roithová, Dissociation Routes of Protonated Toluene Probed by Infrared Spectroscopy in the Gas Phase, *J. Phys. Chem. A*, 110, 8346-8353, 2006.
- [71] A. Simon, C. Joblin, N. Polfer, and J. Oomens, Infrared Spectroscopy of [XFeC₂₄H₁₂]⁺ (X = C₅H₅, C₅(CH₃)₅) Complexes in the Gas Phase: Experimental and Computational Studies of Astrophysical Interest, *J. Phys. Chem. A*, 112, 8551-8560, 2008.
- [72] H. M. M.Hesse, B.Zeeh, Spectroscopic Methods in Organic Chemistry, 2007.
- [73] S. E. Braslavsky, Glossary of terms used in photochemistry, 3rd edition (IUPAC Recommendations 2006), *Pure Appl. Chem.*, 79, 293-465, 2007.
- [74] T. V. Darnton, B. M. Hunter, M. G. Hill, S. Záliš, A. Vlček, and H. B. Gray, Reduced and Superreduced Diplatinum Complexes, *J. Am. Chem. Soc.*, 138, 5699-5705, 2016.
- [75] S. J. Blanksby, and G. B. Ellison, Bond Dissociation Energies of Organic Molecules, *Acc. Chem. Res.*, 36, 255-263, 2003.
- [76] J. S. Brodbelt, Photodissociation mass spectrometry: new tools for characterization of biological molecules, *Chem. Soc. Rev.*, 43, 2757-2783, 2014.
- [77] S. Kruppa, "Photochemistry and Ultrafast Dynamics of Mass-selected Multinuclear Coinage Metal Complexes Studied by Electronic Photodissociation Ion Spectroscopy in an Ion Trap," 2021.

- [78] H. Schmidbaur, and A. Schier, Auophilic interactions as a subject of current research: an up-date, *Chem. Soc. Rev.*, 41, 370-412, 2012.
- [79] D. Imanbaew, "Time-resolved pump-probe action spectroscopy on isolated organic dyes and supramolecular photocatalysts," 2017.
- [80] P. A. M. Dirac, and N. H. D. Bohr, The quantum theory of the emission and absorption of radiation, *Proceedings of the Royal Society of London. Series A, Containing Papers of a Mathematical and Physical Character*, 114, 243-265, 1927.
- [81] H. C. S. J. Stöhr, Magnetism, *Solid-State Sciences*, 5, 2006.
- [82] L. I. Schiff, Quantum Mechanics 3RD, *New York: McGraw-Hill*, 61-62, 1968.
- [83] G. S. F. Mandl, Quantum Field Theory, *John Wiley & Sons*, 2010.
- [84] D. M. J. Als-Nielsen, Elements of Modern X-Ray Physics, *John Wiley & Sons*, 2011.
- [85] F. d. Groot, Multiplet effects in X-ray spectroscopy, *Coord. Chem. Rev.*, 249, 31-63, 2005.
- [86] P. Carra, B. T. Thole, M. Altarelli, and X. Wang, X-ray circular dichroism and local magnetic fields, *Phys. Rev. Lett.*, 70, 694-697, 1993.
- [87] C. T. Chen, Y. U. Idzerda, H. J. Lin, N. V. Smith, G. Meigs, E. Chaban, G. H. Ho, E. Pellegrin, and F. Sette, Experimental Confirmation of the X-Ray Magnetic Circular Dichroism Sum Rules for Iron and Cobalt, *Phys. Rev. Lett.*, 75, 152-155, 1995.
- [88] B. T. Thole, P. Carra, F. Sette, and G. van der Laan, X-ray circular dichroism as a probe of orbital magnetization, *Phys. Rev. Lett.*, 68, 1943-1946, 1992.
- [89] U. Fano, Spin Orientation of Photoelectrons: Erratum and Addendum, *PhRv*, 184, 250-251, 1969.
- [90] M. Tombers, "Spin and orbital magnetic moments of isolated single molecule magnets and transition metal clusters," 2015.
- [91] J. Hewer, "Magnetic and Structural Characterization of Isolated Gaseous Ions by XMCD and IRMPD Spectroscopy," 2017.
- [92] J. Meyer, "Spin and orbital contributions to the magnetic moment of isolated transition metal clusters and complexes," 2014.
- [93] O. Šipr, J. Minár, and H. Ebert, On the importance of the magnetic dipole term T_z in analyzing X-ray magnetic circular dichroism spectra of clusters, *EPL (Europhysics Letters)*, 87, 67007, 2009.
- [94] J. Stöhr, and H. König, Determination of Spin- and Orbital-Moment Anisotropies in Transition Metals by Angle-Dependent X-Ray Magnetic Circular Dichroism, *Phys. Rev. Lett.*, 75, 3748-3751, 1995.
- [95] R. Wu, and A. J. Freeman, Limitation of the Magnetic-Circular-Dichroism Spin Sum Rule for Transition Metals and Importance of the Magnetic Dipole Term, *Phys. Rev. Lett.*, 73, 1994-1997, 1994.
- [96] M. Niemeyer, K. Hirsch, V. Zamudio-Bayer, A. Langenberg, M. Vogel, M. Kossick, C. Ebrecht, K. Egashira, A. Terasaki, T. Möller, B. v. Issendorff, and J. T. Lau, Spin Coupling and Orbital Angular Momentum Quenching in Free Iron Clusters, *Phys. Rev. Lett.*, 108, 057201, 2012.
- [97] S. Peredkov, A. Savci, S. Peters, M. Neeb, W. Eberhardt, H. Kampschulte, J. Meyer, M. Tombers, B. Hofferberth, F. Menges, and G. Niedner-Schatteburg, X-ray absorption spectroscopy of mass-selected transition metal clusters using a cyclotron ion trap: An experimental setup for measuring XMCD spectra of free clusters, *J. Electron. Spectrosc. Relat. Phenom.*, 184, 113-118, 2011.
- [98] J.T.Lau, Magnetische Eigenschaften Kleiner Masseneparieter Übergangsmetalcluster, 2002.
- [99] Y. Teramura, A. Tanaka, and T. Jo, Effect of Coulomb Interaction on the X-Ray Magnetic Circular Dichroism Spin Sum Rule in 3 d Transition Elements, *J. Phys. Soc. Jpn.*, 65, 1053-1055, 1996.
- [100] Y. Teramura, A. Tanaka, B. T. Thole, and T. Jo, Effect of Coulomb Interaction on the X-Ray Magnetic Circular Dichroism Spin Sum Rule in Rare Earths, *J. Phys. Soc. Jpn.*, 65, 3056-3059, 1996.
- [101] E. G. G. Schütz, H. Stoll, Handbook of Magnetism and Advanced Magnetic Materials, *John Wiley & Sons*, 2007.
- [102] T. Jo, The 3d-4f exchange interaction, X-ray second-order optical processes and the magnetic circular dichroism (MCD) spin sum rule in rare earths, *J. Electron. Spectrosc. Relat. Phenom.*, 86, 73-82, 1997.

4 Computational methods

4.1 Density Functional Theory

For interpreting the collected experimental data, it is imperative to obtain as much molecular information as possible. Thus, quantum chemical calculations are mandatory. A widely used approach for calculating molecular properties is the Density Functional Theory (DFT)^[1-3]. Thomas and Fermi formulated the basic idea of the DFT approach in the 1920s. All information to calculate the energy E of a molecule may be derived from the electron density $\rho(\vec{r})$ of the molecule of interest^[4, 5]. In the 1960s, Hohenberg and Kohn proved Thomas and Fermi's basic idea right, with the first Hohenberg-Kohn Theorem^[6]. The second Hohenberg-Kohn Theorem points out that the variational principle can compute electron densities accurately, and Kohn and Sham devised a simplified minimization of the energy (E) by variational principle^[7]. The total DFT energy can be described as a function of the total electron density map $\rho(\vec{r})$ reads:

$$E(\rho) = T_0(\rho) + \int \rho(\vec{r})(V_{\text{ext}}(\vec{r}) + \frac{1}{2}\varphi(\vec{r})) + E_{\text{XC}}(\rho) \, dr \quad (1)$$

$T_0(\rho)$ represents the kinetic energy functional of the molecule. $VE_{\text{ext}}(\vec{r})$ describes an external potential, e.g., an electron in a nuclear field. The Coulomb potential of the nuclei is represented by $\varphi(\vec{r})$, all other potential interactions and contributions, most often not known exactly, are summed up in $E_{\text{XC}}(\rho)$.

The electron density $\varphi(\vec{r})$ corresponds to the square of the normalized wave function of all electrons in the molecule. This so-called "Kohn-Sham" wave function is a single Slater determinant, which may be constructed from a set of orbitals $\Phi_i(r)$ with the lowest solution of the schrödinger equation (cf. eq. 2).

$$\left(-\frac{\hbar^2}{2m}\nabla^2 + V_{\text{eff}}(\vec{r}) \right) \Phi_i(r) = \varepsilon_i \Phi_i(r) \quad (2)$$

Where ε_i is the corresponding eigenvalue. The electron density of the complete molecule is defined as the squared sum of the Kohn-Sham orbitals (cf. eq. 3)

$$\rho(\vec{r}) = \sum_i^N |\Phi_i(r)|^2 \quad (3)$$

The terms $T_0(\rho)$ and $\int dr \rho(\vec{r})(V_{\text{eff}}(\vec{r}) + \frac{1}{2}\varphi(\vec{r}))$ in eq. 1 can be computed quite easily because these terms merely comprise one or two-electron integrals as opposed to wave function-

based Post Hartree Fock *ab initio* methods. However, it is More complicated is to compute the $E_{XC}(\rho)$ term. This term obtains all unknown factors, and the approximation of this term plays a dominant role in the definition of practical DFT schemes. As a first approximation to $E_{XC}(\rho)$ the local density (LSD) approach was developed^[7]:

$$E_{XC}(\rho) = \int \rho(\vec{r}) \varepsilon_{XC}(\rho_{\uparrow}(\vec{r}), \rho_{\downarrow}(\vec{r})) \, dr \quad (4)$$

where $\varepsilon_{XC}(\rho_{\uparrow}(\vec{r}), \rho_{\downarrow}(\vec{r}))$ describes the exchange correlation energy in a homogeneous electron gas. This term depends on the spin up ($\rho_{\uparrow}(\vec{r})$) and spin down ($\rho_{\downarrow}(\vec{r})$) electron densities. The LSD approach proves suitable for extended systems with largely constant electron densities, e.g., ideal metals. The more the electron density varies, the less precise the approximation is.

To circumvent this problem, e.g., when calculating small molecules properties, Hybrid functionals are used^[8, 9]. The exchange energy of these functionals mixes in exact exchange contributions via Hartree-Fock calculations (E_X^{HF})^[10] and utilizes correlation terms from DFT (E_{XC}^{DFT}). The adjustable parameter c^{HF} and c^{DFT} represents parametric prefactors, which are approximated empirically by adjusting the calculated results to carefully chosen best datasets:

$$E_{XC,hybrid} = c^{HF} E_X^{HF} + c^{DFT} E_{XC}^{DFT} \quad (5)$$

The advantages of this method have been established as a standard tool for quantum chemical calculations.

4.1.1 Geometry optimization

The Born-Oppenheimer approximation is used when calculating the total energies of molecular N nuclei arrangements^[11]. The obtained energies are functions of $3N-6$ nuclear coordinates, subtracting their three translational and rotational degrees of freedom. The result is a multidimensional potential energy hyper surface, lower dimensional cuts of which may be visualized (cf. Fig. 1). So called stationary points, where all first derivatives concerning the $3N-6$ degrees of freedom vanish, indicate a nuclei arrangement of either energetic minima (minima structures) or energetic saddle points (transition state structures). The second derivatives state the difference. An energetic minimum structure is reached if all of the second derivatives are positive. Instead, a transition state structure is characterized by a single

negative value. Iterative methods with energy gradient optimization usually perform geometry optimization in a largely automated fashion.

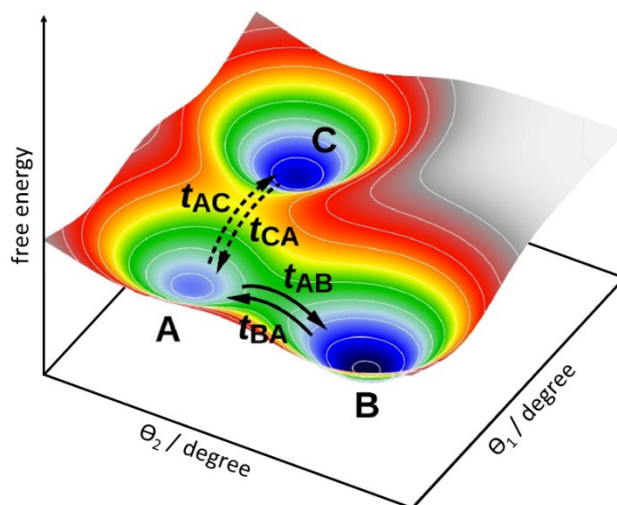


Fig. 1: Calculated potential energy surface with different minimum structures (A, B, C) and possible isomerization pathways along which locate the transition states (t_{AC} , t_{CA} , t_{AB} , t_{BA})^[12].

Minimum structures signify stable isomers of the molecule of interest. Once identified, they serve to compute molecular properties such as vibrational spectra to compare them with experimental gained Infrared spectra. Transition states, instead, are beneficial to identify and characterize a reaction mechanism of molecules. Electronically excited states UV/VIS spectra calculation compared with experimental UV/VIS spectra reveals information about the electronic ground state of the molecule.

4.1.2 Vibrational Frequencies

Once the molecular geometry optimization is performed, several properties of this structure can be obtained by further calculations. The second derivative of local stationary points of their potential energy surface is transformed to mass-weighted coordinates, and $3N$ eigenvectors/eigenvalues are determined. Calculating the $3N-6$ (angled molecules) and $3N-5$ (linear molecules), vibrational frequencies, rotational modes, and translational modes are sorted out. For minima structures, no negative frequencies, and their second derivatives are all positive. If this is not given and exactly one negative (imaginary) vibrational frequency is present, a transition state of the molecule is found. The negative frequency directly corresponds to a force constant associated with the motion along the reaction coordinate.

4.2 Non covalent Interactions (NCI)

For the non covalent interaction calculations, a single point calculation was performed, which obtain the wavefunctions of the molecule of interest. The first derivative of the reduced density gradient is needed for such calculations to get the wave functions of the DFT calculations^[13] (cf. eq. 6).

$$s = \frac{1}{(2(3\pi^2)^{\frac{1}{3}})^{\frac{1}{3}}} |\nabla\rho| \rho^{\frac{4}{3}} \quad (6)$$

The equation can be simplified by summarizing the first term to C_s because there are only constants present.

$$s = C_s |\nabla\rho| \rho^{\frac{4}{3}} \quad (7)$$

The first derivative density gradient is a fundamental quantity for homogenous electron distribution description [6, 14, 15]. In regions near the molecule, the gradient will be minimal for both regions of the covalent and the non covalent interactions. Therefore, the density will be zero in regions far from the molecule, and the reduced gradient obtains large positive values. An NCI plot can be achieved by plotting the first derivative reduced density gradient against the electron density (cf. Fig. 2).

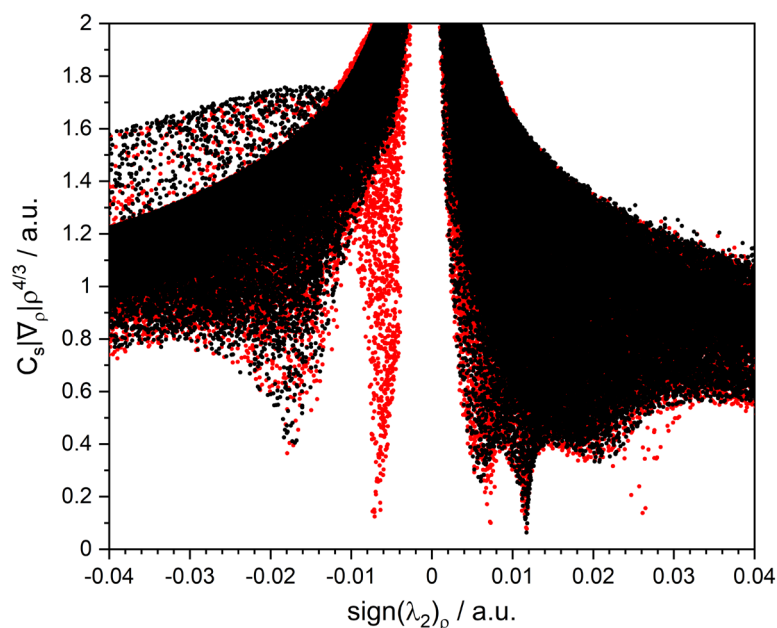


Fig. 2: Calculated two dimensional NCI plots of $[\text{Fe}_3\text{O}(\text{OAc})_6(\text{py})_n]^+$ ($n = 0$ (black), 1 (red)). The calculation was performed with Gaussian 09 at the B3LYP/cc-pVTZ (H, C, N, O) and ecp-10-mdf (Fe) level of theory.

These plots point out repulsive and attractive interactions. High positive sign values indicate covalent interactions, non covalent interactions become more repulsive. The area around $s = 0$ represents non covalent interactions near atoms in the molecule. Negative values and values around zero represent more attractive non covalent interactions in the molecule. Weak interactions such as van der Waals interactions are defined by low density regions. High density regions are characteristic for stronger interactions such as covalent bondings^[16]. At the point $s = 0$, the density reaches its maximum. In such plots the interactions are defined by one positive and two negative eigenvalues ($\lambda_1 < 0$, $\lambda_2 < 0$, $\lambda_3 > 0$). Covalent interactions are dominated by negative contributions and non covalent interactions by positive contributions^[17].

4.3 TD-DFT calculation

Time-dependent density functional theory (TD-DFT) has its foundation by the Runge-Gross-Theorem^[18]. The Theorem proved that all observables for an interacting many-body system, evolved from an initial state (Ψ_0), can be extracted from the density ($\rho(r, t)$) as in the Hohenberg Kohn-Theorem for static systems in DFT. The time-dependent effective core potential at a given time depends on all densities of previous times. Therefore, the Runge-Gross-Theorem is more involved in TD-DFT than static Hohenberg-Kohn theory. A detailed explanation of the approach can be found elsewhere^[19].

According to the equation, the time-dependent density can be obtained in the same approach as the static DFT (cf. eq. 8).

$$\rho(r, t) = \sum_i^N |\Phi_i(r, t)|^2 \quad (8)$$

With a set of N orthonormal $\Phi_i(r, t)$ orbitals, a time-dependent Kohn Sham equation can be derived.

$$\left(-\frac{\hbar^2}{2m} \nabla^2 + V_{\text{eff}}(r, t) \right) \Phi_i(r, t) = i \frac{\partial}{\partial t} \Phi_i(r, t) \quad (9)$$

Analog to static DFT, the potential in the ground state $V_{\text{eff}}(r, t)$ is split into three terms as in eq. (10).

$$V_{\text{eff}}[n; \Phi_0](r, t) = V_{\text{ext}}[n; \Psi_0](r, t) + \int \frac{n(r', t)}{|r - r'|} d^3 r' + V_{\text{XC}}[n; \Psi_0, \Phi_0](r, t) \quad (10)$$

The term $V_{ext}[n; \Psi_0](r, t)$ represents the external time-dependent field, $V_{XC}[n; \Psi_0, \Phi_0](r, t)$ is the exchange potential and $\int \frac{n(r', t)}{|r-r'|} d^3r'$ is the time-dependent Hartree potential. The exchange potential approximates the density and a function of the initial state and the Kohn-Sham initial state.

4.4 Broken symmetry

In Transition metal complexes with unpaired electrons (open-shell) intrinsic magnetic properties^[20] like spin-crossover^[21-23], spin frustration^[24-26] or single molecule magnetic^[27-31] behavior is possible. The magnetic interaction between multiple paramagnetic metal centers in a complex is usually referred as magnetic exchange coupling. The magnetic exchange coupling can be phenomenologically described by a model Hamiltonian such as the isotropic Heisenberg-Dirac –van Vleck (HDvV) Hamiltonian^[32] (cf. eq. 11)

$$\hat{H}_{HDvV} = - \sum_{i < j} J_{ij} \hat{S}_i \hat{S}_j \quad (11)$$

J_{ij} describes the coupling constants of the different metal centers i and j . \hat{S}_i and \hat{S}_j represents the total spin operator for the different metal centers i and j . A positive J value represents a ferromagnetic coupling (electron spin align parallel) and a negative J value, therefore, points out an antiferromagnetic coupling. The ferromagnetic coupling is not a problem for DFT calculations because the Kohn-Sham determinant is constructed that describes the whole oligonuclear system and the corresponding mononuclear species. An antiferromagnetic exchange coupling is not provided by basic DFT^[32, 33] because the antiferromagnetic coupling demands on several determinants, and these determinants are not provided in DFT. Broken symmetry^[34-37] approach is a valuable tool for calculating the antiferromagnetically coupled system. This approach permits to localize unpaired and anti-parallel spins separately on the metal center. The broken symmetry state (ψ_{BS}) is constructed from a single determinant wavefunction, which represents an antiferromagnetic exchange coupling for a “wrong” spin symmetry (cf. eq. 12)

$$\psi_{BS} = |\Phi_A(\alpha)\Phi_B(\beta)| \quad (12)$$

Assuming a structure with “spin up” electrons on one atom (A) and “spin down” electrons on another atom (B) would lead to positive (A) and negative (B) spin density in the system. For

qualitative description, this is wrong because proper singlet wave functions have no spin density at each point. The orbitals (Φ) in ψ_{BS} are optimized by applying the variational principle. The orbitals $\Phi_A(\alpha)$ and $\Phi_B(\beta)$ are orthogonal in their spin parts, but they are not orthogonally restricted to their space parts.

With more than one magnetic center (e.g., metal centers), it is challenging to find eigenfunctions of the HDvV Hamiltonian^[38, 39]. Therefore the Ising Hamiltonian (\hat{H}_{Ising}) is used to solve the problem for this case (cf. eq. 12). The total spin operators $\hat{\mathbf{S}}_i$ are substituted by the associated z-component $\hat{S}_{z,i}$:

$$\hat{H}_{Ising} = -2 \sum_{i < j} J_{ij} \hat{S}_{z,i} \hat{S}_{z,j} \quad (13)$$

The resulting eigenvalues of the Ising Hamiltonian and the HDvV Hamiltonian are not identical. Still, it is possible to extract the coupling constants (J_{ij}) from the differences in the energies from the broken symmetry configurations, assuming that all interaction in the system is additive^[40]. The coupling constants can be calculated by solving a linear system of equations based on the Ising operator.

4.5 XA Simulations

The calculation of X-ray spectra is complicated since the excitation of the core electron to a valence state is too laborious for metal centers with many electrons. Such core hole effects can be calculated with relativistic DFT. Still, $L_{2,3}$ edges cannot be calculated with one-electron integrals for transition metals, leading to an enormous computing effort. DFT calculations of the ground state have to be performed to solve charge transfer and multiplet effects on metal centers. Afterward, the resulting wave function is projected to the system of interest^[41-44]. For a faster quantitative interpretation of the XA spectra, a semi-empirical program called CTM4XAS^[45] interprets the experimentally obtained XA spectra better. The program can load batch files of cowan, where the two-electron integrals are described by Slater integrals^[46]. This program is freely available on the internet as the cowan batch files. More detailed information can be found elsewhere^[45].

In the present work, all geometry optimizations, frequency calculations, electronic excitation, and determination of the electronic ground state were performed using Gaussian 09^[47] program package. The used basis sets and functionals are individually labeled in the corresponding chapters.

Broken symmetry calculations were performed using the CANOSSA program^[48] as implemented in a local, customized TURBOMOLE 6.5^[49-51] program package. The CANOSSA program was provided by Prof. C. van Wüllen. The basis sets and the functionals of the calculations are labeled in the corresponding chapters in this work.

All calculations were performed on the computing clusters of the theoretical chemistry group of Prof. C. van Wüllen and the high performance computing Elwetritsch clusters at the TU Kaiserslautern.

4.6 References

- [1] I. N. Levine, *Quantum chemistry*, 5th ed. ed.: Upper Saddle River (N.J.) : Prentice-Hall, 2000.
- [2] R. G. Parr, and W. Yang, Density-Functional Theory of the Electronic Structure of Molecules, *Annu. Rev. Phys. Chem.*, 46, 701-728, 1995.
- [3] D. Sholl, and J. A. Steckel, "Density Functional Theory: A Practical Introduction."
- [4] E. Fermi, Eine statistische Methode zur Bestimmung einiger Eigenschaften des Atoms und ihre Anwendung auf die Theorie des periodischen Systems der Elemente, *ZS. f. Phys.*, 36, 73-79, 1928.
- [5] L. H. Thomas, The calculation of atomic fields, *MPCPS*, 23, 542-548, 2008.
- [6] P. Hohenberg, and W. Kohn, Inhomogeneous Electron Gas, *Phys. Rev.*, 136, B864-B871, 1964.
- [7] W. Kohn, and L. J. Sham, Self-Consistent Equations Including Exchange and Correlation Effects, *Phys. Rev.*, 140, A1133-A1138, 1965.
- [8] A. D. Becke, Density-functional thermochemistry. III. The role of exact exchange, *J. Chem. Phys.*, 98, 5648-5652, 1993.
- [9] A. D. Becke, A new mixing of Hartree-Fock and local density-functional theories, *J. Chem. Phys.*, 98, 1372-1377, 1993.
- [10] A. Szabó, and N. S. Ostlund, *Modern quantum chemistry : introduction to advanced electronic structure theory*: Mineola (N.Y.) : Dover publications, 1996.
- [11] M. Born, and R. Oppenheimer, Zur Quantentheorie der Molekeln, *AnP*, 389, 457-484, 1927.
- [12] F. Pietrucci, Strategies for the exploration of free energy landscapes: Unity in diversity and challenges ahead, *Rev. Phys.*, 2, 32-45, 2017.
- [13] E. R. Johnson, S. Keinan, P. Mori-Sánchez, J. Contreras-García, A. J. Cohen, and W. Yang, Revealing Noncovalent Interactions, *J. Am. Chem. Soc.*, 132, 6498-6506, 2010.
- [14] A. J. Cohen, P. Mori-Sánchez, and W. Yang, Insights into current limitations of density functional theory, *Science (New York, N.Y.)*, 321, 792-794, 2008.
- [15] D. Yarkony, "Modern electronic structure theory."
- [16] G. V. Gibbs, D. F. Cox, and K. M. Rosso, A Connection between Empirical Bond Strength and the Localization of the Electron Density at the Bond Critical Points of the SiO Bonds in Silicates, *J. Phys. Chem. A*, 108, 7643-7645, 2004.
- [17] R. F. W. Bader, and H. Essén, The characterization of atomic interactions, *The Journal of Chemical Physics*, 80, 1943-1960, 1984.
- [18] E. Runge, and E. K. U. Gross, Density-Functional Theory for Time-Dependent Systems, *Phys. Rev. Lett.*, 52, 997-1000, 1984.

- [19] N. T. M. M.A.L.Marques, F.M.S.Nogueira,E.K.U.Gross,A.Rubio, Fundamental of Time-dependent Density Functional Theory, 2012.
- [20] R. S. D.Gatteschi, J.Villain, Molecular Nanomagnets, 2011.
- [21] C. Brady, P. L. Callaghan, Z. Ciunik, C. G. Coates, A. Døssing, A. Hazell, J. J. McGarvey, S. Schenker, H. Toftlund, A. X. Trautwein, H. Winkler, and J. A. Wolny, Molecular Structure and Vibrational Spectra of Spin-Crossover Complexes in Solution and Colloidal Media: Resonance Raman and Time-Resolved Resonance Raman Studies, *Inorg. Chem.*, 43, 4289-4299, 2004.
- [22] H.-J. Krüger, Spin transition in octahedral metal complexes containing tetraazamacrocyclic ligands, *Coord. Chem. Rev.*, 253, 2450-2459, 2009.
- [23] S. Schenker, P. C. Stein, J. A. Wolny, C. Brady, J. J. McGarvey, H. Toftlund, and A. Hauser, Biphasic Behavior of the High-Spin \rightarrow Low-Spin Relaxation of [Fe(btpa)](PF₆)₂ in Solution (btpa = N,N,N',N'-Tetrakis(2-pyridylmethyl)-6,6'-bis(aminomethyl)-2,2'-bipyridine), *Inorg. Chem.*, 40, 134-139, 2001.
- [24] L. Johannes, V. F. Daniela, and N.-S. Gereon, Characterization of Trinuclear Oxo Bridged Cobalt Complexes in Isolation, *Z. Phys. Chem.*, 232, 649-669, 2018.
- [25] J. Lang, J. M. Hewer, J. Meyer, J. Schuchmann, C. van Wüllen, and G. Niedner-Schatteburg, Magnetostructural correlation in isolated trinuclear iron(III) oxo acetate complexes, *Phys. Chem. Chem. Phys.*, 20, 16673-16685, 2018.
- [26] J. Lang, J. Mohrbach, S. Dillinger, J. M. Hewer, and G. Niedner-Schatteburg, Vibrational blue shift of coordinated N₂ in [Fe₃O(OAc)₆(N₂)_n]⁺: "non-classical" dinitrogen complexes, *Chem. Comm.*, 53, 420-423, 2017.
- [27] J. Dreiser, K. S. Pedersen, A. Schnegg, K. Holldack, J. Nehr Korn, M. Sigrist, P. Tregenna-Piggott, H. Mutka, H. Weihe, V. S. Mironov, J. Bendix, and O. Waldmann, Three-Axis Anisotropic Exchange Coupling in the Single-Molecule Magnets NEt₄[MnIII₂(5-Brsalen)₂(MeOH)₂MII(CN)₆] (M=Ru, Os), *Chemistry – A European Journal*, 19, 3693-3701, 2013.
- [28] M. Hołyńska, D. Premužić, I.-R. Jeon, W. Wernsdorfer, R. Clérac, and S. Dehnen, [MnIII₆O₃Ln₂] Single-Molecule Magnets: Increasing the Energy Barrier Above 100 K, *Chemistry – A European Journal*, 17, 9605-9610, 2011.
- [29] K. Kim, A. Ford, V. Meenakshi, W. Teizer, H. Zhao, and K. R. Dunbar, Nanopatterning of Mn₁₂-acetate single-molecule magnet films, *J. Appl. Phys.*, 102, 094306, 2007.
- [30] J. A. A. J. Perenboom, J. S. Brooks, S. Hill, T. Hathaway, and N. S. Dalal, Relaxation of the magnetization of Mn_{12} acetate, *Phys. Rev. B*, 58, 330-338, 1998.
- [31] T. C. Stamatatos, D. Foguet-Albiol, C. C. Stoumpos, C. P. Raptopoulou, A. Terzis, W. Wernsdorfer, S. P. Perlepes, and G. Christou, New Mn₃ structural motifs in manganese single-molecule magnetism from the use of 2-pyridyloximate ligands, *Polyhedron*, 26, 2165-2168, 2007.
- [32] W. Heisenberg, Zur Theorie des Ferromagnetismus, *Z. Phys.*, 49, 619-636, 1928.
- [33] F. Neese, Prediction of molecular properties and molecular spectroscopy with density functional theory: From fundamental theory to exchange-coupling, *Coord. Chem. Rev.*, 253, 526-563, 2009.
- [34] R. Caballol, O. Castell, F. Illas, I. de P. R. Moreira, and J. P. Malrieu, Remarks on the Proper Use of the Broken Symmetry Approach to Magnetic Coupling, *J. Phys. Chem. A*, 101, 7860-7866, 1997.
- [35] F. Illas, I. P. R. Moreira, C. de Graaf, and V. Barone, Magnetic coupling in biradicals, binuclear complexes and wide-gap insulators: a survey of ab initio wave function and density functional theory approaches, *Theor. Chem. Acc.*, 104, 265-272, 2000.
- [36] L. Noodleman, Valence bond description of antiferromagnetic coupling in transition metal dimers, *J. Chem. Phys.*, 74, 5737-5743, 1981.
- [37] L. Noodleman, and J. G. Norman, The $\chi\alpha$ valence bond theory of weak electronic coupling. Application to the low-lying states of Mo₂Cl₈⁴⁻, *J. Chem. Phys.*, 70, 4903-4906, 1979.
- [38] E. Ising, Beitrag zur Theorie des Ferromagnetismus, *Z. Phys.*, 31, 253-258, 1925.
- [39] C. N. Yang, The Spontaneous Magnetization of a Two-Dimensional Ising Model, *Phys. Rev.*, 85, 808-816, 1952.
- [40] J. M. Ricart, R. Dovesi, C. Roetti, and V. R. Saunders, Electronic and magnetic structure of KNiF_3 perovskite, *Phys. Rev. B*, 52, 2381-2389, 1995.
- [41] A. Agui, T. Uozumi, M. Mizumaki, and T. Käämbre, Intermetallic charge transfer in FeTiO_3 probed by resonant inelastic soft x-ray scattering, *Phys. Rev. B*, 79, 092402, 2009.
- [42] H. Ikeno, F. M. F. de Groot, E. Stavitski, and I. Tanaka, Multiplet calculations of L_{2,3}-x-ray absorption near-edge structures for 3d transition-metal compounds, *J. Phys.: Condens. Matter*, 21, 104208, 2009.
- [43] P. Krüger, and C. R. Natoli, X-ray absorption spectra at the Ca $L_{2,3}$ edge calculated within multichannel multiple scattering theory, *Phys. Rev. B*, 70, 245120, 2004.

- [44] F. Strigari, T. Willers, Y. Muro, K. Yutani, T. Takabatake, Z. Hu, Y. Y. Chin, S. Agrestini, H. J. Lin, C. T. Chen, A. Tanaka, M. W. Haverkort, L. H. Tjeng, and A. Severing, Crystal-field ground state of the orthorhombic Kondo insulator $\text{CeRu}_2\text{Al}_{10}$, *Phys. Rev. B*, 86, 081105, 2012.
- [45] E. Stavitski, and F. M. F. de Groot, The CTM4XAS program for EELS and XAS spectral shape analysis of transition metal L edges, *Micron (Oxford, England : 1993)*, 41, 687-694, 2010.
- [46] R. D. Cowan, *The Theory of Atomic Structure and Spectra*: University of California Press, 1981.
- [47] M. J. Frisch, et. al, "Gaussian 16 Rev. C.01," 2016.
- [48] S. Schmitt, "Berechnung der Magnetischen Anisotropie mit Hilfe von ein- und zweikomponentigen dichtefunktionaltheoretischen Rechnungen: Weiterentwicklung vorhandener Methoden und Anwendung auf mehrkernige Übergangsmetallkomplexe," 2015.
- [49] R. Ahlrichs, M. Bär, M. Häser, H. Horn, and C. Kölmel, Electronic structure calculations on workstation computers: The program system turbomole, *Chem. Phys. Lett.*, 162, 165-169, 1989.
- [50] O. Treutler, and R. Ahlrichs, Efficient molecular numerical integration schemes, *J. Chem. Phys.*, 102, 346-354, 1995.
- [51] M. Von Arnim, and R. Ahlrichs, Performance of parallel TURBOMOLE for density functional calculations, *J. Comput. Chem.*, 19, 1746-1757, 1998.

5 Magnetic properties and their correlation to the electronics of isolated trinuclear 3d spin frustrated complexes

Michael Lembach^a, Johannes Lang^a, Maximilian Luczak^a, Yannick Mees^a, Roumany Israil^a, Vicente Zamudio-Bayer^b, Martin Timm^b, Christine Bülow^{b,c}, Bernd von Issendorff^c, Akira Terasaki^d, Christoph Riehn^a, Tobias Lau^{b,c} and Gereon Niedner-Schatteburg^a

*^aFachbereich Chemie and Forschungszentrum OPTIMAS,
Technische Universität Kaiserslautern,
67663 Kaiserslautern, Germany*

*^bHelmholtz-Zentrum für Materialien und Energie
BESSY II,
14109 Berlin, Germany*

*^cPhysikalisches Institut,
Universität Freiburg,
79104 Freiburg, Germany*

*^dDepartment of Chemistry,
Kyushu University,
Fukuoka, Japan*

5.1 Preamble

The following chapter is prepared as a manuscript for publication. I performed and managed the XMCD experiments, UVPD experiments, data evaluation, quantum chemical calculations, and XA simulations. I received experimental support from Maximilian Luczak, Yannick Mees, Vicente Zamudio-Bayer, Martin Timm, and Christine Bülow. Tobias Lau, Bernd von Issendorf and Akira Terasaki operate the Ion Trap experimental setup at the Helmholtz Zentrum BESSY II in Berlin. I received experimental support for the UVPD spectra to gain the UV light source in different spectral regions for the experiments by Roumany Israil. I wrote the chapter in form of a draft manuscript.

5.2 Abstract

This study elucidates molecular magnetism, and electronic structures of isolated trinuclear μ -oxo bridged iron complexes with the structural type $[\text{Fe}_3\text{O}(\text{OAc})_6(\text{py})_n]^+$ (OAc = acetate, py = pyridine, $n = 0, 1, 2, 3$). We present circularly polarized X-ray absorption (XA), Ultra Violet Photon Dissociation (UVPD) spectra, and DFT modeling. Combining these techniques reveals that the coordination of axial pyridine ligands to the complex disturbs the triangular geometry of the Fe_3O core, which otherwise exhibits a nearly equilateral triangular D_{3h} geometry. The coordination of one or two axial pyridine ligands leads to a lower C_{2v} symmetry of the triangular Fe_3O core geometry with a change in the ground state electronic structure and the magnetic exchange coupling. The coordination of a third pyridine ligand restores the equilateral triangular D_{3h} Fe_3O core geometry, as without pyridine coordination. The present results elucidate the stiffness of the Fe_3O core and respond to coordinative distortion, void of any other less controlled environmental interactions.

5.3 Introduction

The design and synthesis of paramagnetic transition metal (TM) complexes is an ongoing field of research, ultimately striving for technical applications. Magnetic exchange couplings of such complexes are governed by the spatial arrangement of the metallic center^[1-4]. The triangular arrangement leads to a so called spin frustrated electronic ground state^[5, 6]. Such spin frustrated systems are promising building blocks for molecular spintronics^[7-11] as models of nanomagnets^[12-15], as materials for quantum technology^[16-21], for data storage^[16, 22], as building blocks in metal-organic frameworks^[23-28], in metalloenzymes^[29] and also in catalytic applications^[27, 28, 30-32]. Spin frustrated complexes show remarkable magnetic properties due to the competing interactions of the spin orientation within such complexes^[3, 19, 33, 34]. The spin arrangement in spin frustrated complexes also induces a reduced magnetic ordering combined with an unusual electronic ground state as a result of their spin orientation (e. g., “spin up” and “spin down”)^[35-44].

Multiple researches conducted conceptual studies of μ -oxo bridged transition metal complexes with a spin frustrated ground state^[45-52] because of their magnetism. Surface deposition of μ -oxo bridged complexes leads to an antiferromagnetic exchange coupling^[53, 54].

The electronics and their resulting magnetism of complexes with the general structure $[\text{Fe}_3\text{O}(\text{OAc})_6(\text{py})_3]^+$ (OAc = acetate, py = pyridine)^[55-58] highly depend on the distortion of the M_3O core^[59] as a function of the axial ligand coordination, e.g., changing from an antiferromagnetic exchange coupling to a ferromagnetic exchange coupling of the high spin Fe^{3+} ions^[25]. Symmetrically coordinated $[\text{Fe}_3\text{O}(\text{OAc})_6(\text{H}_2\text{O})_3]\text{NO}_3$ ^[5] and the asymmetrically coordinated $[\text{Fe}_3\text{O}(\text{TIEO})_2(\text{O}_2\text{CPh})\text{Cl}_3]$ ^[5, 6] possess total spins of $S_T = 1/2$, and $S_T = 5/2$, respectively.

All of these experiments utilized condensed phase samples. It is argued that intermolecular effects such as crystal packing or solvation have little influence on the magnetic exchange couplings of this type of complexes. Gas phase investigations of isolated $[\text{Fe}_3\text{O}(\text{OAc})_6\text{L}_3]^+$ are desirable to verify these assumptions.

Model systems of interest are trinuclear transition metal complexes of the structural type $[\text{M}_3\text{O}(\text{O}_2\text{R})_6\text{L}_3]^+$ ($\text{M} = \text{Fe}$; $\text{L} =$ axial ligands)^[55-58] and establish their bonding distances of the neighbored metal centers by the oxo centered bridge^[60]. The three high spin Fe^{3+} ions coordinate around one O^{2-} center in a flat, almost equi triangular arrangement in these complexes. This arrangement builds the Fe_3O core in these complexes (cf. Fig. 1). Each Fe^{3+} center achieves a pseudooctahedral geometry through equatorial coordination with four bridging ligands (O_2CR) and axial coordination with another monodentate ligand (L). These complexes possess an antiferromagnetic exchange coupling between the high spin Fe^{3+} ions^[5, 6]. The long distances of more than 3 Å do not feature a direct Fe–Fe interaction. The electronic ground state presents a topological spin frustration. A pairwise antiferromagnetic coupling scheme of all three spins seems impossible^[61].

We have previously investigated $[\text{Fe}_3\text{O}(\text{OAc})_6(\text{L})_n]^+$ complexes ($\text{L} = \text{py}$ (pyridine), N_2 (Nitrogen); $n = 0, 1, 2, 3$) by IR(M)PD^[62, 63]. The coordination of molecular Nitrogen to the complex in cold conditions revealed a non-classical bonding situation between the iron atoms and the axial ligand, resulting in a blue shift of the N_2 stretching vibration^[63]. Pyridine coordination leads to a shift of the asymmetric CO stretching mode as a function of the pyridine coordination in different transition metal complexes^[62, 64]. *Abinitio* calculations via broken symmetry approach (BS) hint a change in their magnetic properties as a function of the amount of coordinated axial ligands^[62].

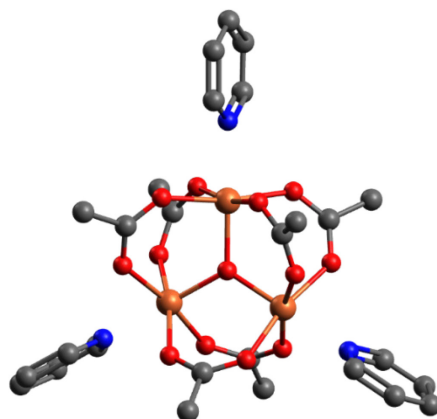


Fig. 1: Structure of the investigated trinuclear complexes $[\text{Fe}_3\text{O}(\text{OAc})_6(\text{py})_n]^+$ ($n = 0, 1, 2, 3$). The calculations were performed with Turbomole 6.5 at the unrestricted B3LYP/cc-pVTZ level of theory and a broken symmetry approach^[21]. Hydrogen atoms are omitted for clarity (C: grey, O: red, N: blue, Fe: orange).

Electrospray ionization^[65, 66] (ESI) enables routine mass spectrometric investigations of ionic complexes in vacuum. Innovative electronic structure investigation recently arose by the combination of Tandem-MS and irradiation of isolated ions with photons, thus enabling studies by X-ray magnetic circular dichroism^[67-71] (XMCD) or Ultra Violet Photon Dissociation^[72-77] (UVPD). Such schemes elucidate the electronic structure and the magnetic behavior. UVPD techniques enable the investigation of the electronic ground state for isolated complexes on a time scale from nanoseconds (ns) to femtoseconds (fs). For the element selective XMCD experiments, cold conditions (4 K) and an applied magnetic field (5 T) are necessary for the orientation of the unpaired spins in molecules with magnetic properties^[68-71]. This spectroscopic technique enables the investigation of the intrinsic magnetic properties of thin films^[78], deposited nanoparticles^[79], clusters^[69], or surfaces^[80, 81]. Applying the sum rule analysis^[67, 71, 82-84] allows for determining the spin, orbital, and total magnetic moments of the investigated complexes.

The main topic of this study is the characterization of the magnetic exchange coupling scheme and the determination of the electronics by XMCD and UVPD, with the corresponding influence on the exchange interactions in the Fe_3O core due to the coordination of pyridine to the complex.

We combine experimental XMCD and UVPD investigations of isolated $[\text{Fe}_3\text{O}(\text{OAc})_6(\text{py})_n]^+$ ($n = 0, 1, 2, 3$) with quantum chemical calculations by Density Functional Theory (DFT), Time-Dependent Density Functional Theory (TD-DFT), broken symmetry (BS) approach and X-ray absorption simulations with CTM4XAS^[85] and Cowan batch files. Our gas-phase approach excludes bulk or crystal packing effects. Also, it allows the isolation of the under coordinated molecular ions (e.g. $[\text{Fe}_3\text{O}(\text{OAc})_6]^+$), which would not be accessible in the condensed phase.

5.4 Experimental setup and methods

The sample iron(III) μ -oxo acetate perchlorate hydrate ($[\text{Fe}_3\text{O}(\text{OAc})_6(\text{H}_2\text{O})_3(\text{ClO}_4)]$; $\text{OAc} = \text{CH}_3\text{COO}_2^-$) was prepared in an acetonitrile/pyridine solution (10:1; $c \sim 1 \cdot 10^{-5}$ mol/L). Stepwise exchange of the water ligands forms the investigated cationic species with the structure $[\text{Fe}_3\text{O}(\text{OAc})_6(\text{py})_n]^+$ ($n = 0, 1, 2, 3$) during the ESI process^[62, 63].

We used the “Ion Trap” setup to record the presented polarization-dependent gas phase X-ray Absorption (XA) spectra. The Ion Trap is coupled to the UE52-PGM soft X-ray beamline at the BESSY II synchrotron facility of the Helmholtz Zentrum Berlin. The Ion Trap is a home built time of flight combined ion trap mass spectrometer to record Total Ion Yield (TIY) gas phase XA spectra^[68-71]. We used a custom-built electrospray ionization (ESI) source for ion creation for our experiments, kindly provided by the Lau (HZB) group. The ions of interest are transferred via an RF Hexapole into a linear quadrupole mass filter (Extrel, 40–4000 amu). After the mass selection, the selected ions are guided into a linear quadrupole ion trap located within the high field region (5 T) of a superconducting solenoid. The trap is operated at a frequency of 3.82 MHz. Evaporative liquid helium cools down the ion trap to a temperature of 4 K. A constant helium background pressure of $1 \cdot 10^{-6}$ mbar within the vacuum chamber thermalizes the trapped ions by collisional cooling. The ions are constantly injected into the ion trap instrument. The ions are ejected into the time of flight area with a repetition rate of 120 Hz to record mass spectra from the ion trap. For the XA spectra recorded by TIY spectroscopy, the ions are irradiated for 10 to 15 s at set photon energy. A GaAs-diode records the X-ray intensity from the undulator beamline used for photon flux normalization of the recorded spectra. Spectra on the Fe absorption edges were taken with an exit slit size of 200 μm and a respective resolution of 400 meV from 700 eV–735 eV.

XA spectra were recorded for negative and positive circularly polarized light in an alternating manner. The resulting XMCD spectra were analyzed in terms of sum rule analysis^[86]: The subtraction of the polarized dependent spectra leads to the corresponding XMCD spectrum and the sum spectrum, which is necessary to apply the sum rule analysis (cf. Fig. S1). The color-coded elements **A**, **B**, and **C** are extracted from the XMCD spectra integrals and the sum of polarization dependent XA spectra (**C**). We extract the projections ($m_S^{(z)}$ and $m_L^{(z)}$) of the intrinsic spin (m_S) and orbital (m_L) magnetic moments per iron atom onto the quantization axis by sum rule analysis. The quantization axis coincides with the magnetic field axis of the surrounding solenoid and the X-ray propagation direction. Under the given experimental conditions, a scaling of the molecule's total magnetic moment must be performed. Therefore, knowledge of the exact coupling of all containing magnetic centers is mandatory. This knowledge is not known to us. Therefore, we omit such a scaling and present magnetizations at the given experimental conditions ($B = 5 \text{ T}$, 4 K).

$$m_S^{(z)} = g_S \mu_B \frac{(A - bB)}{c \frac{3}{2} C} n_h - g_S \mu_B \frac{d}{c} \langle T_z \rangle \quad (1)$$

$$m_L^{(z)} = -g_L \mu_B \frac{A + B}{a \frac{3}{2} C} n_h \quad (2)$$

With n_h being the number of holes in the final state, g_S and g_L the Landé factors for the electron spin and orbital angular momentum ($g_S = 2.0$, $g_L = 1.0$), μ_B the Bohr magneton and a , b , c , and d are the sum rule related prefactors. We anticipate the containing Fe^{3+} ions to be in a $3d^5$ high spin state. Therefore, we assume the number of unoccupied valence orbitals n_h to be $n_h = 5$ for Fe^{3+} species, which is uncertain. Note that the ratio of m_L/m_S cancels this uncertainty. The sum rule related prefactors are $1/2$, 2 , $2/3$, and $7/3$ for investigations on the Fe $L_{3,2}$ absorption edges.

For the presented UVPD spectra, we used a quadrupole mass spectrometer (Amazon speed, bruker daltonics) with a modified Paul trap for UV laser irradiation experiments. The ions of interest are transferred into the gas phase by electrospray ionization. The sample solution was constantly infused into the ESI chamber by a syringe pump with a flow rate of $120 \mu\text{L/h}$. Nitrogen was used as a drying gas with a flow rate of 4 L/min at $180 \text{ }^\circ\text{C}$. The nebulizer pressure was set to 280 mbar (4 psi) for spraying the sample solution, and the spray needle was held at

4.5 kV. The Paul trap consists of a ring electrode and two end caps forming a nearly hyperbolic inner profile. Those end caps possess pinholes that allow them to enter or exit the ions in the trap. The ring electrode is powered with a high voltage RF (radio frequency) potential (781 kHz) while the end caps are grounded. Ions are accumulated in this resulting oscillating quadrupolar electric field generated from the three electrodes. An auxiliary dipolar voltage is fed to either the exit cap or both end caps for ion isolation and fragmentation. For providing a constant partial Helium buffer gas pressure of ca. 10^{-3} mbar inside the trap, a proportional integral derivative (PID) gas controller is used.

UV Laser system

The laser pulses were generated using a titanium sapphire (Ti: Sa) chirped-pulse cryogenic regenerative amplifier system (Wyvern 1000TM, KMLabs). The oscillator and amplifier stages were pumped by a diode-pumped solid state laser (Opus 532), and a frequency doubled Nd: YAG laser (LDP-200MQG, Lee Laser). For steady state, UV/VIS spectra from one of the TOPAS-C units were utilized in a spectral range of 250 nm to 600 nm. The spectra were achieved by setting the laser pulses according to wavelengths and measuring the parent ion's intensity and the sum of fragment ions. The fragment yield is defined as:

$$Y(\nu) = \left(\frac{\sum_i I_i^{fr}(\nu)}{\sum_i I_i^{fr}(\nu) + \sum_i I_i^p(\nu)} \right) \quad (3)$$

For normalization by its numeric wavelength value for the different photon energies at constant laser pulse fluence, a typical pulse intensity of $\sim 2 \mu\text{J}$ was set.

Absorption spectroscopy (solution)

Static absorption spectra were recorded with a PerkinElmer Lambda 35 spectrometer. For the sample preparation, acetonitrile (Uvasol grade) was used, and the complex $[\text{Fe}_3\text{O}(\text{OAc})_6(\text{H}_2\text{O})_3(\text{ClO}_4)]$ was dissolved ($c \sim 1 \cdot 10^{-6}$ mol/L) to record spectra without pyridine coordination. The complex was also dissolved in pyridine (Uvasol grade) to record the pyridine coordinated complexes. The Solution was convicted into a precision cuvette (light path 10 mm). The spectra were recorded in double beam operation to scan a wider spectroscopic area.

5.5 Computational methods

Published previous optimized structures of $[\text{Fe}_3\text{O}(\text{OAc})_6(\text{py})_n]^+$ ($n = 0, 1, 2, 3$)^[62] complexes serve as starting point for the calculation of the projected Density of States, weak interactions, and natural bond order analysis, by Density Functional Theory (DFT) using the B3LYP^[87, 88] functional and cc-pVTZ basis sets^[89] (C, H, N, O) in combination with ecp-10-mdf^[90] effective core potential (Fe) in a local installation of the Gaussian 09 program package^[91], as applied before in our previous study of $[\text{Fe}_3\text{O}(\text{OAc})_6(\text{L})_n]^+$ ($\text{L} = \text{N}_2, \text{py}; n = 1, 2, 3$)^[62, 63]. For the calculation of the UV spectra and further interpretation of the experimental spectra, we used the broken symmetry calculated geometries and performed TD-DFT calculations using UB3LYP^[87] with cc-pVTZ basis sets^[89] (C, H, N, O) and the ecp-10-mdf^[90] effective core potential (Fe) with the Gaussian 09 program package^[91]. The experimental XA spectra simulation was performed with cowan batch files using the Mathematica plugin CTM4XAS^[85].

5.6 Results and Discussion

5.6.1 Results I: X-ray magnetic circular dichroism

The cations with the structure $[\text{Fe}_3\text{O}(\text{OAc})_6(\text{py})_n]^+$ ($n = 0, 1, 2, 3$) were created within an electrospray process in a solution of acetonitrile/pyridine (10:1). According to a typical isotopic iron pattern, the mass spectra reveal four isotropic peaks at $m/z = 538, 617, 696,$ and 774 (cf. Fig. S2)^[62]. Isolating these complexes and optimizing their fragment yield with tunable X-ray exposure yielded polarized dependent XAS and XMCD data (cf. Fig. 2).

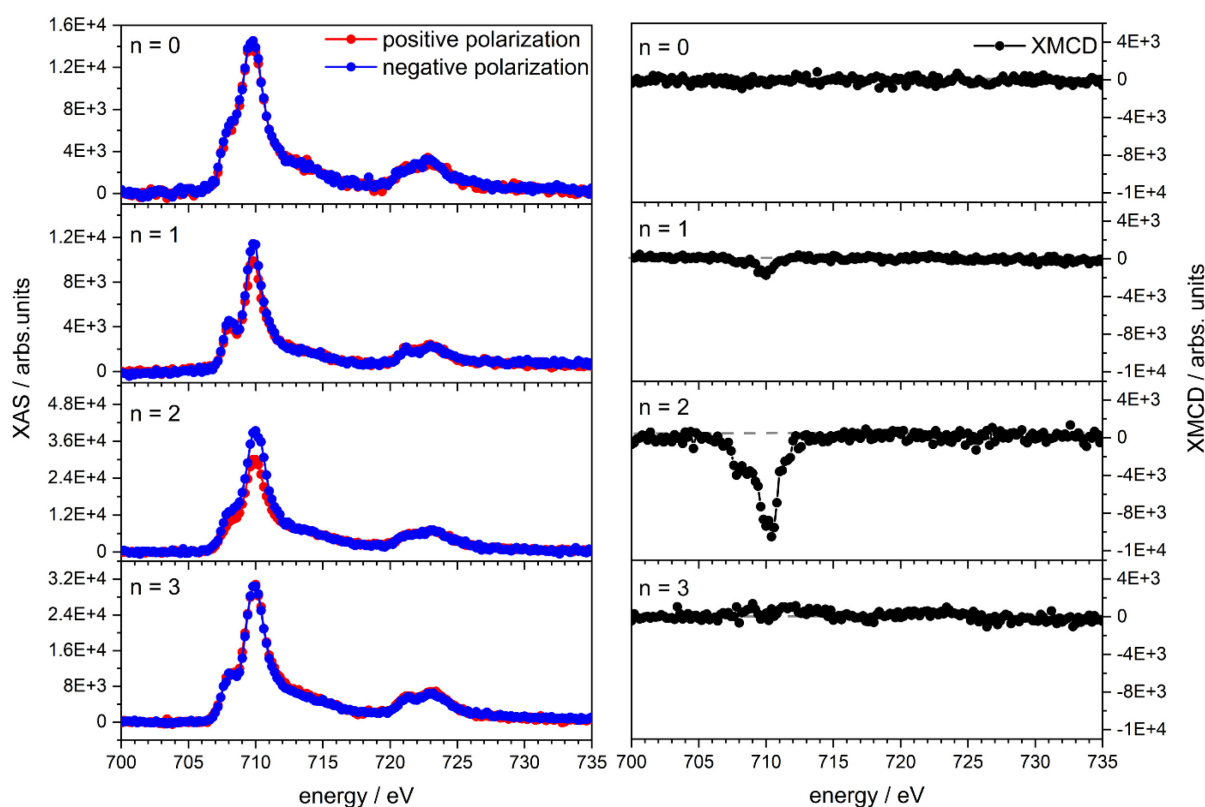


Fig. 2: Recorded XAS (left) and evaluated XMCD data (right) of $[\text{Fe}_3\text{O}(\text{OAc})_6(\text{py})_n]^+$ ($n = 0, 1, 2, 3$). The XMCD data are derived from the difference between the negative polarized XAS and the positive polarized XAS.

We observe no dichroic effect for the bare complex ($n = 0$). Stepwise coordination of pyridine ($n = 1, 2$) leads to an increasing dichroic effect in the XAS and concomitant the XMCD signal. The dichroic effect vanishes with the third coordination ($n = 3$), and the recorded data resemble those of the bare complex. There is no dichroic effect observed on the L_2 edge. The XMCD spectra better visualize the increasing dichroic effect as a function of the coordinating axial ligand resulting in higher spin and orbital magnetic moments. We deduce the intrinsic magnetic moments per iron atom for each complex (cf. Tab. 1). Then, with estimated

uncertainties of $\pm 5\%$, considering a transition from a 2p core state to a 3d valence state for the iron atoms in this complex series. The most common problem is that the states are not always completely separated, which might lead to inaccuracies in determining magnetic moments^[92]. Teramura et al. have introduced correction factors for the spin sum rule based on calculations on an atomic model, taking into account the Coulomb interaction in the $L_{3,2}$ absorption edges and the expectation value for the magnetic dipole operator not accessible in our XMCD experiments^[93-98]. Experimental magnetizations were corrected with the suggestions of Teramura.

Tab. 1: Experimental magnetic values projected on the z-axis for m_S , m_L , m_J and m_L/m_S for $[\text{Fe}_3\text{O}(\text{OAc})_6(\text{py})_n]^+$ ($n = 0, 1, 2, 3$) with the correction of 4.5 %^[97, 98] and a statistic uncertainty of 5 %^[92].

	exp.				corrected			
	n = 0	n = 1	n = 2	n = 3	n = 0	n = 1	n = 2	n = 3
$m_S^{(z)}$	0.00(0)	0.09(05)	0.97(5)	0.00(0)	0.00(0)	0.08(04)	0.93(5)	0.00(0)
$m_L^{(z)}$	0.00(0)	0.26(1)	0.43(2)	0.00(0)	0.00(0)	0.25(1)	0.41(2)	0.00(0)
$m_J^{(z)}$	0.00(0)	0.35(2)	1.40(7)	0.00(0)	0.00(0)	0.33(1)	1.33(6)	0.00(0)
$m_L^{(z)}/m_S^{(z)}$	0.00(0)	0.37(1)	0.44(2)	0.00(0)	0.00(0)	0.35(1)	0.42(2)	0.00(0)

The magnetic moments of the bare complex and the complex with three pyridines (cf. Tab. 1, cf. Fig. S6) are in both complexes zero because no dichroic effect is observed. With the coordination of one pyridine to the complex, a small dichroic effect is monitored and increases with further pyridine coordination until the third pyridine coordinates to the complex. The complexes with symmetric geometric properties hint an antiferromagnetic exchange coupling as described^[5, 6]. The asymmetric ones feature a ferromagnetic exchange coupling scheme considering the change from a D_{3h} to a C_{2v} symmetry.

5.6.2 Discussion I: X-ray magnetic circular dichroism

The experimental magnetic moments reveal no spin and orbital magnetic moments for the symmetric complexes in this complex series, indicating a change from an antiferromagnetic to a ferromagnetic exchange coupling as a function of the pyridine coordination. By calculating the total spin magnetic moments, we observe small different iron atom values (cf. Tab. 2) from the expected values of a Fe^{3+} ion in a high spin ground state.

Tab. 2: Experimental total Spin ground state for $[\text{Fe}_3\text{O}(\text{OAc})_6(\text{py})_n]^+$ ($n = 0, 1, 2, 3$) with statistic uncertainties of 5 % in comparison with calculated total Spin ground states. The calculations were performed at the B3LYP/cc-pVTZ (H, C, N, O) and ecp-10-mdf (Fe) level of theory with a high spin state for each Fe center in a UUD ($n = 0, 1, 3$) and DUU ($n = 2$) broken symmetry configuration corresponding to the minimum structure^[62].

	$S_{\text{T, exp}}$	$S_{\text{T, calc}}$
$n = 0$	0.00(0)	0.50
$n = 1$	1.27(6)	1.50
$n = 2$	2.91(14)	2.50
$n = 3$	0.00(0)	0.50

The experimental total spins of this series of complexes are in good agreement with the calculated spin ground states^[62]. For symmetric complexes, the total spin ground state is reduced due to the antiferromagnetic exchange coupling of the Fe^{3+} ions. The coordination of one pyridine leads to a reduced spin state of 1.5 instead of 2.5 as in a pure Fe^{3+} ion. Because the total spin is higher than for a completely antiferromagnetic coupled complex but lower than a completely ferromagnetic coupled one, we assume that the distortion of the Fe_3O core leads to a suspension of the antiferromagnetic coupling between two Fe atoms in the complex. The coordination of two pyridine leads to a higher experimental spin ground state than the calculated one. Therefore, we assume a complete breakdown of the antiferromagnetic coupling to favor a ferromagnetic exchange coupling as a result of the higher distortion in the Fe_3O core. The coordination of three pyridine leads to the recovery of the D_{3h} symmetry in the complex, resulting in an antiferromagnetic exchange coupling.

Determination of the geometrical properties

A change of the magnetic exchange coupling must occur either from the change in their electronic ground state or its geometry. The spectra show the characteristic spectral shape of a Fe^{3+} ion^[99]. The splitting of the Absorption edge is given by the crystal field splitting into the t_{2g} and e_g levels^[100]. Therefore, we extracted the crystal field splittings (CF) of each molecular cation by subtracting the L_3 preedge from the L_3 main absorption edge (cf. Tab. 3, cf. Fig. S7). The crystal field splittings increase as a function of pyridine coordination until the third pyridine coordination takes part (cf. Tab. 3).

The coordination of three pyridine reduces slightly due to the recovery of the symmetry resulting in the same structural motif as in the bare complex. A more extensive Fe₃O core gives the higher crystal field splitting in the complex with three pyridines than without pyridine coordination.

Tab. 3: Experimental crystal field splittings of [Fe₃O(OAc)₆(py)_n]⁺ (n = 0, 1, 2, 3) from the experimental XA spectra with uncertainties of 10 %.

	L ₃ edge/eV	L ₃ preedge/eV	ΔL ₃ /eV
n = 0	709.88	708.00	1.88(19)
n = 1	709.83	708.00	1.82(18)
n = 2	709.81	708.00	1.81(17)
n = 3	709.86	708.00	1.86(19)

The shift of the L₃-edge is marginal but significant for the electronic and structural influence on the absorption edge. In Literature, those shifts are declared as a change of the oxidation state of the metal^[99-102] or a change in the crystal field^[101-104]. A change in the Oxidation state would lead to a shift of 1-3 eV^[105, 106]. The low energy shift points out an exclusion of the change in the oxidation state. The change in the crystal field must induce the shift as function of the pyridine coordination. Every Fe³⁺ atom has a quasi-octahedral coordination shell in the bare complex and provides a free coordination spot. With the coordination of one pyridine, one iron atom is fully octahedral surrounded, leading at one hand to a change of the crystal field splitting and on the other hand to a change in its spin ground state from 1/2 to 3/2. The coordination of two pyridines to the complex reveals the highest crystal field splitting. Two pyridine coordinates to the iron atoms result in two completely octahedral coordinated Fe atoms, whose spin ground state shifts from 3/2 to 5/2. With three coordinated pyridines, all iron centers are in octahedral coordination, and the spin ground state changes back to 1/2.

Besides the crystal field splitting change in this series of complexes resulting from the pyridine coordination, a determination of the exciting p orbitals seems necessary because a change in the crystal field splitting might lead to different energy levels in the Fe atom itself. Therefore, we calculated the projected Density of State (pDOS) spectra to determine each transition in these complexes (cf. Fig. 3).

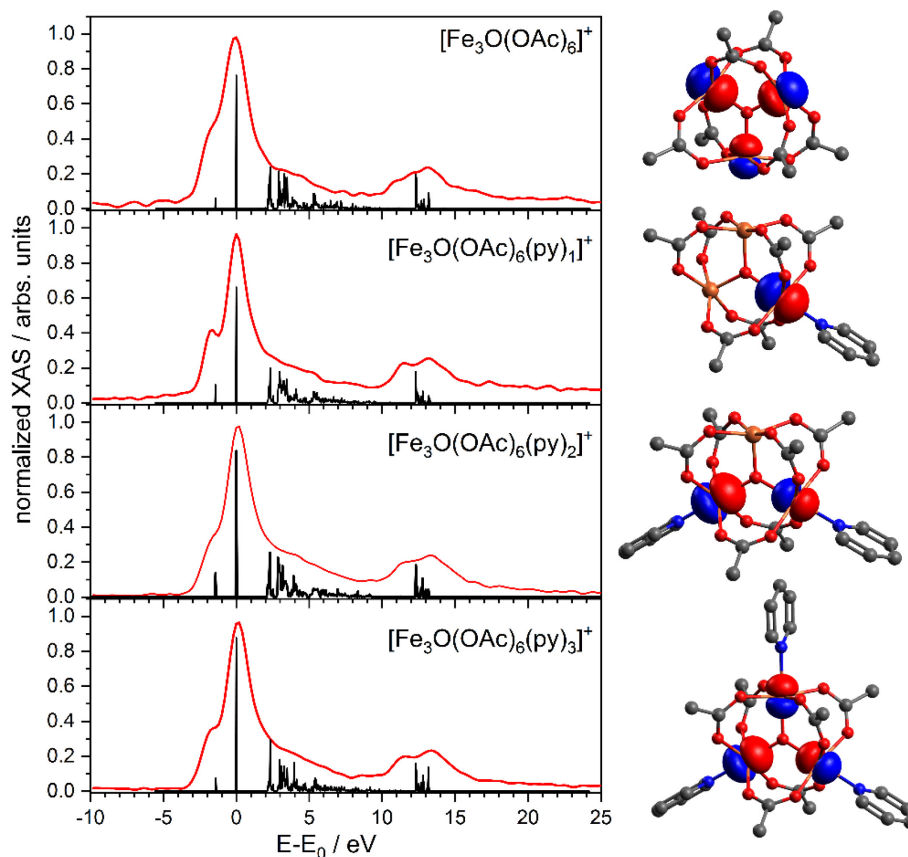


Fig. 3: Calculated pDOS (black) spectra for $[\text{Fe}_3\text{O}(\text{OAc})_6(\text{py})_n]^+$ ($n = 0, 1, 2, 3$) in comparison with the experimental positive polarized XA spectra (red), and their corresponding calculated molecular orbital plots. The calculations were performed with Gaussian 09 at the B3LYP/cc-pVTZ (H, C, N, O) and ecp-10-mdf (Fe) level of theory. Hydrogen is omitted for clarity.

The calculated pDOS spectra show an excellent agreement with the experimental XA spectra. Two lines are monitored in the pDOS spectra, which are also present in the L_3 absorption edge. The core orbital plots show that the axial ligand coordination significantly influences the magnetic properties in this complex series. All Fe^{3+} atoms are involved in the X-ray absorption at the L_3 absorption edge in the bare complex. The coordination of one pyridine leads to an X-ray absorption of only one Fe atom with axial coordination. With further coordination, the amount of absorbed Fe atoms in the X-ray absorption rises as a pyridine coordination function (cf. Fig. 3), indicating that the axial ligand coordination directly affects the crystal field splittings, resulting in different magnetic properties of this complex. The other bands in the XA are so close that a determination of these bands is impossible with the given spectral resolution. On the L_2 -edge, the resolution is also not given, but two bands fit the experimental spectra in every isomere. The X-ray absorption of the Fe^{3+} atom highly depends on the coordination of the axial ligands.

Therefore, we extracted the calculated orbital energies of the core-shell orbitals and compared them with the broken symmetry calculated spin densities^[62] of these complexes (cf. Fig. 4). The core shell orbital energies are similar for all Fe³⁺ atoms in the bare complex, resulting in an antiferromagnetic exchange coupling. By coordinating one pyridine, the orbital energy rises for the axial coordinated Fe³⁺ atom. It represents the primary L₃ absorption edge in the XAS, resulting in a weak ferromagnetic exchange coupling, while the other two uncoordinated Fe³⁺ ions remain in an antiferromagnetic exchange coupling. Coordination of two pyridines leads to slightly higher core shell orbital energies combined with spin densities, getting “spin up” electrons representing the primary X-ray absorption, resulting in a strong ferromagnetic exchange coupling. Restoring the symmetry by coordinating three pyridine leads to similar core shell orbitals energies slightly higher than in the bare complex due to the pyridine coordination, resulting in the antiferromagnetic exchange coupling.

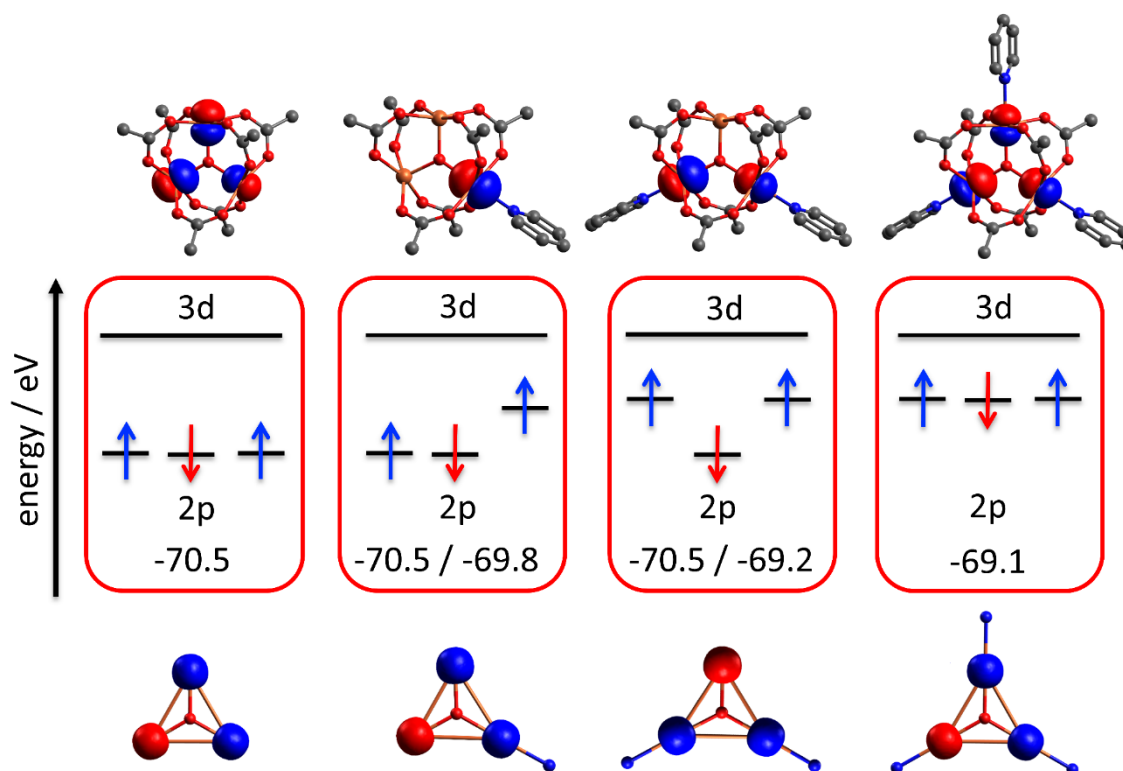


Fig. 4: Calculated core-shell orbitals, their corresponding orbital energies, and their spin densities (red: Spin down, blue: Spin up) for $[\text{Fe}_3\text{O}(\text{OAc})_6(\text{py})_n]^+$ ($n = 0, 1, 2, 3$). The calculations were performed with Gaussian 09 at the B3LYP/cc-pVTZ (H, C, N, O) and ecp-10-mdf (Fe) level of theory. Hydrogen and ligand are omitted for clarity.

Influence of geometrical changes to the magnetic properties

The axial ligand coordination leads to a distortion of the Fe₃O core in the complex, as described in earlier IR(M)PD investigations combined with calculated Natural bond order analysis (cf. Fig. S8)^[62, 63]. A change in the electronic ground state must occur from the geometrical changes in this series of complexes. The correlation of geometrical properties reveals a strong dependency between the total magnetic moment per Fe atom and the corresponding Fe-O-Fe-py_n angle (cf. Fig. 5). With the angle change in these complexes, the Fe-Fe distances enlarge, but no strong correlation to the magnetic moment is monitored. The magnetic moments per iron atom increases for the asymmetric isomers by elongation of the Fe-Fe distances. Still, for the symmetric complexes, the Fe-Fe distances vary with similar magnetic moments. The averaged bonding distances between the Fe³⁺ atoms are 3.28 Å for the bare complex and 3.36 Å for the isomer with three coordinated pyridines. Still, an antiferromagnetic exchange coupling is observed in both isomers, which does not feature a dependency of the Fe-Fe distances to magnetic properties. For the asymmetric complexes with one or two coordinated pyridines, the Fe-Fe averaged bonding distance is 3.31 Å and 3.34 Å. These bonding distances are shorter than in the complex with three coordinated pyridines, but both isomers feature a ferromagnetic exchange coupling. Therefore, we can exclude a correlation between the Fe-Fe bonding situation and the different exchange coupling. The different bonding distances between the Fe³⁺ ions and the central Oxygen atoms show no correlation to the magnetic moment in this series of complexes. Therefore, we exclude a geometrical influence of the Fe-O bonding distance.

Stepwise coordination of pyridine leads to stronger ferromagnetic exchange coupling as a function of the Fe-O-Fe angle. The angle increases with further pyridine coordination until the third pyridine coordinates to the complex and restores the Fe₃O core with similar angles. Angle dependent magnetism is also observed by other groups^[15, 103, 107]. By coordinating one pyridine to the complex, the coordinated Fe³⁺ atom does not couple with the other metal atoms in the complex, but the antiferromagnetic coupling between the uncoordinated iron atoms remains. There is only a weak antiferromagnetic coupling with the second pyridine coordination. Both coordinated Fe³⁺ atoms with the same spin orientation cannot establish an antiferromagnetic exchange coupling as a result of the strong distortion in the Fe₃O triangle and different core shell orbital energies.

The third pyridine coordination leads to an antiferromagnetic exchange coupling due to similar angles and core shell orbital energies in the Fe₃O triangle.

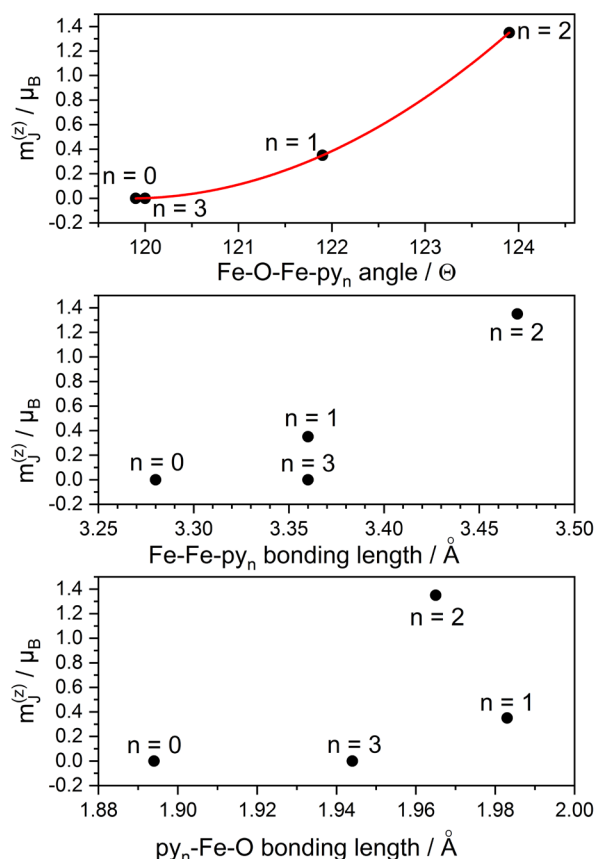


Fig. 5: Total magnetic moment per Fe³⁺ atom of [Fe₃O(OAc)₆(py)_n]⁺ (n = 0, 1, 2, 3) with their associated Fe-O-Fe-py_n angle (top), Fe-Fe distance of the coordinated Fe atoms (middle), and bonding length of the central Oxygen to the coordinated Fe center (bottom).

The angle change directly affects the d-orbitals of the metal centers in this series of complexes (cf. Fig. 6). In the bare complex, no overlap of the d_{x²-y²} between the Fe³⁺ atoms with a “spin up” configuration is observed. By coordinating one pyridine to the complex, the angle leads to an overlap of the orbitals for all Fe atoms, resulting in a small ferromagnetic exchange coupling. The coordination of a second pyridine leads to a wider angle and a strong overlap of the d_{x²-y²} orbitals for the Fe atoms with “spin up” configuration. The remaining Fe atom with a “spin down” configuration acts as a free atom. Because both “spin up” iron centers do not generate an antiferromagnetic exchange coupling, this results in ferromagnetic exchange coupling. The “spin down” iron center is not involved in the exchange coupling, resulting in a strong ferromagnetic exchange coupling. With the coordination of the third pyridine, the angles in the complex are equal and point out a similar d_{x²-y²} orbital distribution as in the bare

complex, resulting in an antiferromagnetic exchange coupling. For the other 3d orbitals, such behavior is not observed (cf. Fig. S9).

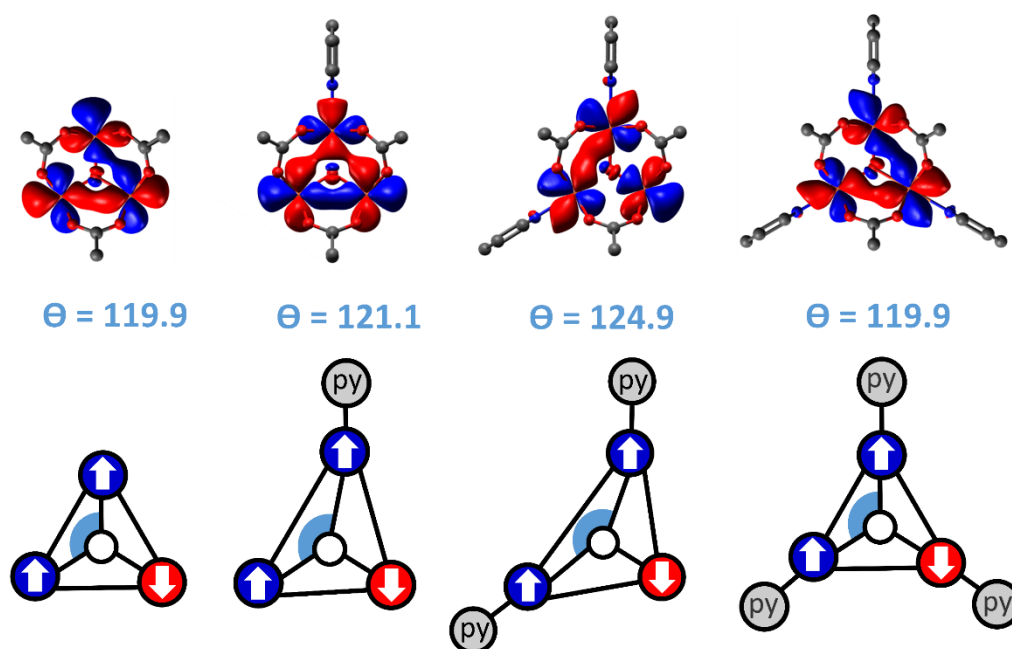


Fig. 6: Calculated $d_{x^2-y^2}$ Natural Atomic orbitals (NAOs) of $[\text{Fe}_3\text{O}(\text{OAc})_6(\text{py})_n]^+$ ($n = 0, 1, 2, 3$) with their associated Fe-O-Fe-py $_n$ angles. The calculations were performed with Gaussian 09 at the B3LYP/cc-pVTZ (H, C, N, O) and ecp-10-mdf (Fe) level of theory. Ligand is omitted for clarity.

As mentioned before, the primary X-ray absorption highly depends on the amount of coordinated pyridine and their corresponding core-shell orbitals. Therefore, we extracted the spin-orbit coupling constant from the core shell to the valence shell by subtracting the L_3 absorption edge from the L_2 absorption edge (cf. Tab. 4). We observe an increasing trend for the spin-orbit couplings with further coordination of pyridine to the complex. The third coordination of an axial ligand leads to a slight decrease in the value.

Tab. 4: Experimental spin-orbit coupling constant from the core-shell to the valence shell for $[\text{Fe}_3\text{O}(\text{OAc})_6(\text{py})_n]^+$ ($n = 0, 1, 2, 3$) from the experimental XA spectra with uncertainties of 5 %.

	L_2 edge/eV	L_3 edge/eV	SOC/eV
n = 0	723.00	709.88	13.12(7)
n = 1	723.00	709.83	13.17(7)
n = 2	723.00	709.81	13.19(7)
n = 3	723.00	709.86	13.14(7)

A correlation of these values with geometrical properties also reveals a strong correlation with the Fe-O-Fe-py_n angles rather than the bonding distances in this complex series (cf. Fig. S10). We assume that the change of the angle combined with the change in the core shell orbital energies, the spin-orbit coupling from the core to the valence shell must increase until coordination of two pyridine takes part. A wider angle leads to a more significant distance of the different Fe³⁺ atoms in this complex. Higher orbital energies lead to a collapse of the antiferromagnetic exchange coupling resulting in higher spin-orbit couplings for the asymmetric complexes. The third coordination of pyridine leads to almost similar angles but higher core-shell energies, and therefore a higher spin-orbit coupling is examined.

Branching ratio analysis and differential orbital covalency

Because of the strong core-valence interaction described above, we analyzed with the spin-orbit sum rule.^[108-110] This method yields very accurate values for the spin-orbit interactions per hole. For p → d transitions, the branching ratio is defined as:

$$BR = \frac{I(L_3)}{I(L_3) + I(L_2)} \quad (4)$$

Where I are the intensities of the absorption edges, the sum rule^[108-111] gives the relation for the spin-orbit interactions per hole.

$$SOC = n_{j_2} - \frac{l+1}{l} n_{j_1} \quad (5)$$

n_{j1} and n_{j2} represent the occupation number per hole, where j₁ = l – 0.5 and j₂ = l + 0.5. Thus, at least the branching ratio without a spin-orbit interaction can be derived with:

$$B = B_0 - \frac{c}{2c+1} \frac{SOC}{n_h} \quad (6)$$

B₀ is the branching ratio without spin-orbit interactions, $\frac{c}{2c+1}$ is a statistical value, and for d⁵, it is $\frac{2}{5}$ and n_h represents the holes in the valence shell^[112].

Tab. 5: Branching ratio values with spin-orbit interaction (BR), terms of occupation numbers (n_{j1} , n_{j2}), spin-orbit expectation (SOC), branching ratio without spin-orbit interaction (B_0), and the difference of the branching ratios (ΔB) with expected uncertainties of 5 % for the presented spin-orbit expectations.

	BR	statistical value	n_{j1}	n_{j2}	SOC	B_0	ΔB
n = 0	0.81	0.60	-0.50	0.50	0.00(0)	0.81	0.00
n = 1	0.82	0.60	-0.24	0.76	-3.92(19)	0.35	0.47
n = 2	0.85	0.60	-0.07	0.93	-3.16(15)	0.46	0.38
n = 3	0.82	0.60	-0.50	0.50	0.00(0)	0.82	0.00

The branching ratio rises from 0.81 to 0.85, increasing pyridine coordination until the second pyridine coordinates to the complex. Afterward, it decreases to 0.82 with the third pyridine coordination because of the shift of the L_3 edge as described above. Interesting are the expected spin-orbit interaction per hole. There is no spin-orbit interaction for the symmetric isomers observed due to the antiferromagnetic exchange coupling. The coordination of one pyridine leads to spin-orbit coupling of -3.92 and second pyridine coordination to a value of -3.16. We observe slightly higher values when comparing the absolute spin-orbit coupling with the spin-orbit couplings for a free Fe^{3+} atom (SOC = 2.5). We also observe marginally higher values than for a free Fe^{3+} ion. These variations may occur from the orbital moments in a free Fe^{3+} ion. The orbital momentum should be zero by assuming $l = 0.5$. The experimental values presented in this work are not precisely 0.5. This leads to aberrations in the spin-orbit couplings because the total orbital momentum is not zero in the experimental values. The coordination of two pyridines results in a spin-orbit coupling of 2.53 considering the uncertainties, which is in good agreement with the SOC of a free Fe^{3+} ion. Therefore, we assume that a range of uncertainties is higher than expected.

We performed Differential Orbital Covalency (DOC) analysis to determine the metal d character in this complex series ^[100, 113-115] with experimental data and observe almost similar DOC values (88.7 %, 89.3 %) for the symmetrical complexes. The asymmetric isomers show significant changes in the metal d character as a function of the pyridine coordination (cf. Tab. 6). The coordination of one pyridine leads to a decrease (86 %) of the metal d character, and the second coordination leads to an enhancement of the metal d character

(91 %). Pyridine coordination changes the crystal field splittings, resulting in different p orbital energies, as discussed before. Therefore, we assume that a coordination of the axial ligand leads to more or less p covalent mixing in the other isomers. Coordination of one pyridine reduces the metal d character because the coordination distorts the Fe₃O core towards the pyridine ligand. The coordinated Fe atom is more embedded in the ligand system resulting in a lower metal d character. Second ligand coordination enlarges the triangle towards the axial ligands, and the third Fe atom acts more like a free atom, resulting in an increased metal d character. A reduced number of 3d holes per Fe³⁺ atom also hints an antiferromagnetic exchange coupling in this complex series. The coordination of one pyridine leads to a reduced number of 3d holes per Fe³⁺ atom, indicating a stronger antiferromagnetic exchange coupling between the uncoordinated Fe³⁺ ions. This induces a small ferromagnetic exchange coupling, as observed. The coordination of two pyridines leads to the highest number of 3d holes per Fe³⁺ atom and predominates a ferromagnetic exchange coupling in this isomer. For the symmetric complexes, the number of holes is similar.

Tab. 6: Approximated metal d character with differential orbital covalency approach for the complexes with the general structure [Fe₃O(OAc)₆(py)_n]⁺ (n = 0, 1, 2, 3) with expected uncertainties of 5 % for the presented number of 3d holes.

	Oxidation state	Number of 3d holes (exp.)	DOC
n = 0	3	2.67(13)	89.3
n = 1	3	2.58(13)	86.0
n = 2	3	2.73(14)	91.0
n = 3	3	2.67(13)	88.7

The differential orbital covalency analysis reveals changes of the metal d character by coordinating pyridine to the complex. Therefore we calculated Electron Localized Field^[116] (ELF) plots and observed weakened bonding situations of the central Oxygen atom by coordination of pyridine in these series of complexes (cf. Fig. 7).

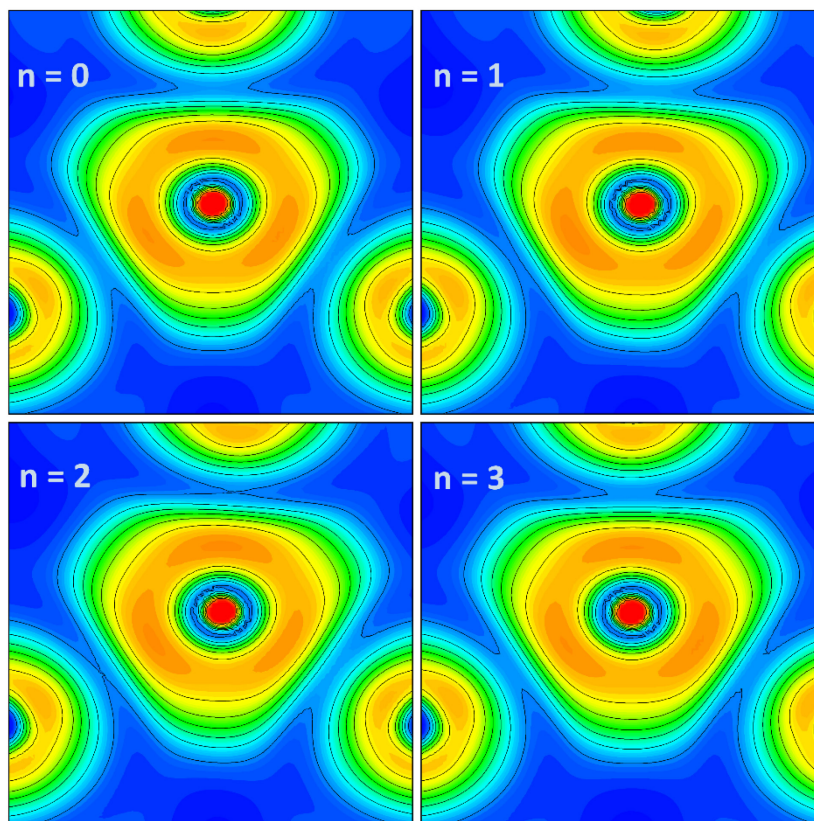


Fig. 7: Calculated electron localized field for $[\text{Fe}_3\text{O}(\text{OAc})_6(\text{py})_n]^+$ ($n = 0, 1, 2, 3$) of the central Oxygen atom. The calculations were performed with Gaussian 09 at the B3LYP/cc-pVTZ (H, C, N, O) and ecp-10-mdf (Fe) level of theory.

Electron localized field plots reveal almost similar bonding strengths for the symmetric complexes. The significant difference between both isomers is a weakened bonding strength because of the more significant Fe_3O core. The coordinated Fe^{3+} atoms obtain weakened bonding strengths in the other isomers, assuming that the pyridine coordinated iron atoms behave more like free ions than the bare iron atoms. Also, the not coordinated iron atom bondings reveal a more vital bonding situation to the central Oxygen atoms, resulting in different metal d characters and a reduced number of 3d holes as observed. Covalent bondings between the Fe^{3+} atoms and pyridine seem not to be present in these complexes. Therefore we calculated the differential overlap region indicator (DORI) and non covalent interactions (NCI) for these complexes. Both plots reveal strong non covalent interactions between the pyridine rings to the Oxygen of the acetate ligand in these complexes, resulting in a more strengthened bonding situation due to a non-classical bonding situation (cf. Fig. S11)^[63].

5.6.3 Results II: Ultra Violet Photon Dissociation

We recorded mass spectra for every 3 nm with the sample to obtain the UVPD spectra (cf. Fig. S13). We observe a series of isotopic peaks at $m/z = 538, 617, 695,$ and 775 matching with the simulated isotopic patterns of $[\text{Fe}_3\text{O}(\text{OAc})_6(\text{py})_n]^+$. Gas phase reactions for the bare complex are monitored due to free coordination spheres at the iron centers. A peak at 622 m/z develops in the absence of pyridine coordination and appears to coordinate molecular oxygen, water, and hydrogen peroxide. The hydrogen peroxide may occur from light-induced conversion from gas phase reactions within the ion trap. The experimental UVPD spectra of $[\text{Fe}_3\text{O}(\text{OAc})_6(\text{py})_n]^+$ ($n = 0, 1, 2, 3$) reveal at first sight one strong absorption band at around 320 nm (cf. Fig. 7). We observe weak shoulders in the area around 400 - 500 nm (cf. Fig. S14). The spectra look quite similar as expected. The only change in the spectra is the increasing coordination of pyridine to the complex. We also recorded UV/VIS spectra in the condensed phase compared to the gas phase spectra and observed a strong blue shift for each isomer in the gas phase.

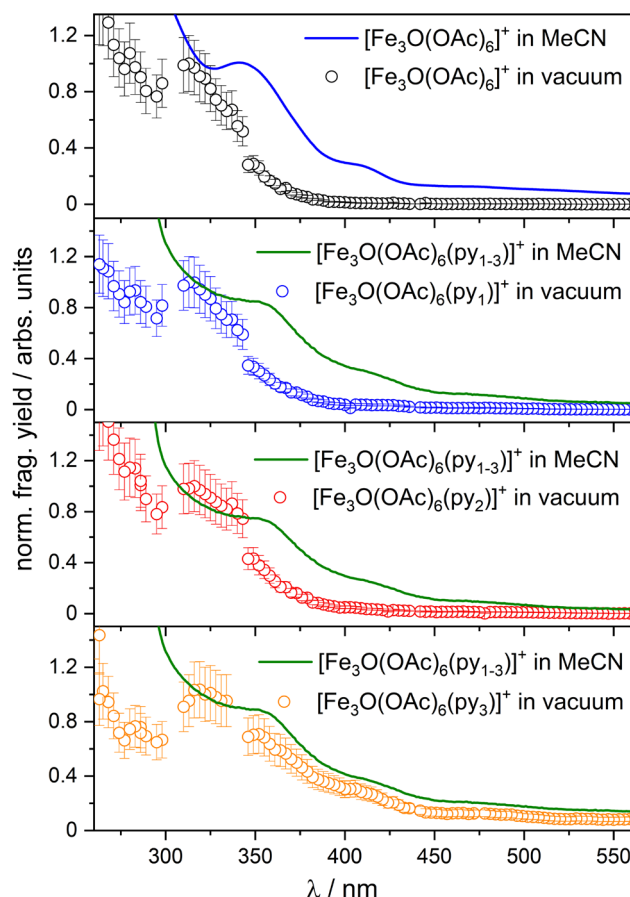


Fig. 8: UVPD spectra of $[\text{Fe}_3\text{O}(\text{OAc})_6(\text{py})_n]^+$ ($n = 0, 1, 2, 3$) in comparison of the UV/VIS spectra in condensed phase. With uncertainties of 20 %.

The UVPD spectra in this series of complexes reveal a significant blue shift in all spectra compared to the UV/VIS spectra in the condensed phase, assuming that solvation processes lead to the observed shift in energy, but the spectral shape is almost similar. A closer look at the spectra reveals a redshift from the bare complex with further pyridine coordination to the complex (cf. Tab. 7) at around 300 nm and a blue shift at around 400 nm. This is given by the distortion of the Fe₃O core with pyridine coordination, as discussed earlier^[62, 63].

Tab. 7: Absorption energies and their corresponding energetic shifts of [Fe₃O(OAc)₆(py_n)]⁺ (n = 0, 1, 2, 3).

n	λ/nm	Δλ	λ/nm	Δλ
0	310	0	485	0
1	313	3	476	-9
2	321	11	474	-11
3	312	2	481	-4

These energetic shifts are minimal, but we did not expect high energy shifts compared to the slight distortion of the Fe₃O core.

5.6.4 Discussion II: Ultra Violet Photon Dissociation

The experimental UVPD spectra of this series of complexes do not show significant changes in their absorptions. Nevertheless, the slight shifts observed in the UVPD spectra hint an almost similar trend as the XA spectra. Therefore, we performed TD-DFT modeling to determine the ground states in the different isomers (cf. Fig. S15). The calculations reveal that the transitions in these complexes are HOMO-LUMO transitions at 300 nm. The very weak absorption bands around 470 nm represent spin forbidden metal to ligand charge transfer (MLCT) bands (cf. Fig. S15).

As shown in the XA results, non covalent interactions have minor effects on the complex. Therefore, we compared the molecular orbitals of the pyridine bonding situation with the non covalent interactions and observed a non-classical bonding situation between the iron center and the pyridine ligand (cf. Fig. 9). Molecular orbitals of the Nitrogen in the pyridine points directly to the d orbital of the iron center, which establishes the coordination of pyridine to the complex. The orbitals from the hydrogen atoms in the pyridine ring directly point between two Oxygen atoms of the bridging ligand and form an attractive interaction between the

ligands. NCI plots reveal strong, engaging interactions of the axial ligand and the bridging ligand.

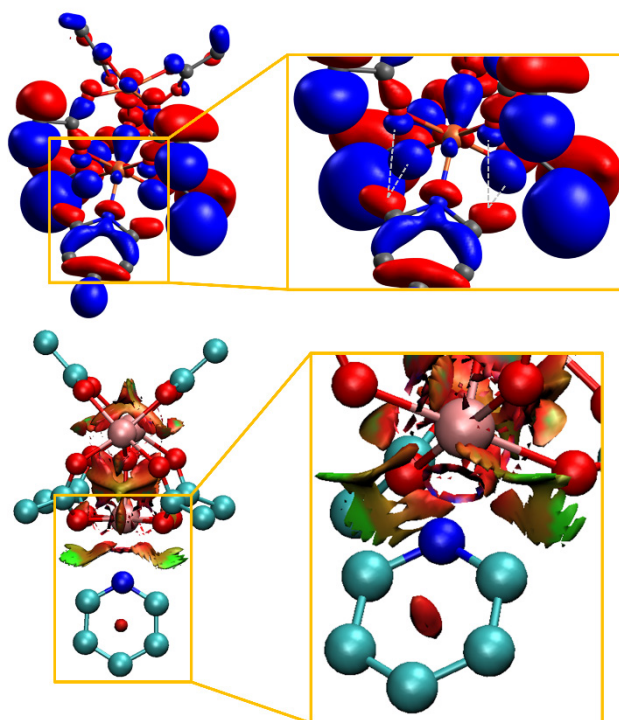


Fig. 9: Calculated orbitals and non covalent interactions^[116] of $[\text{Fe}_3\text{O}(\text{OAc})_6(\text{py}_1)]^+$. The calculations were performed with Gaussian 09 at the B3LYP/cc-pVTZ (H, C, N, O) and ecp-10-mdf (Fe) level of theory. Hydrogen is omitted for clarity.

We assume that the coordination of pyridine does not lead to a simple distortion of the Fe_3O core. Because of non-covalent interactions, the coordination causes a little shift in the bridging ligand position, resulting in distinct crystal field splittings, different orbital energies, and modest variations in the UVPD spectra, as observed.

Influence of geometrical changes to the absorption bands

The XA spectra show that the experimental shift mainly occurs by geometrical changes in the Fe_3O core. Therefore, we compared the relative energy shifts of the UVPD spectra with the isomers calculated geometrical properties (cf. Fig. 10). The change of the py-Fe bonding length does not show any trend and excludes a correlation of the bonding length to the shifts in the UVPD spectra. A change of the Fe-O-Fe-py_n angle reveals a strong dependency on the energy shift until the coordination of the second pyridine takes part. Coordination of three pyridines results in identical angles in the Fe_3O core as the bare complex but in a higher shift in the absorption energy.

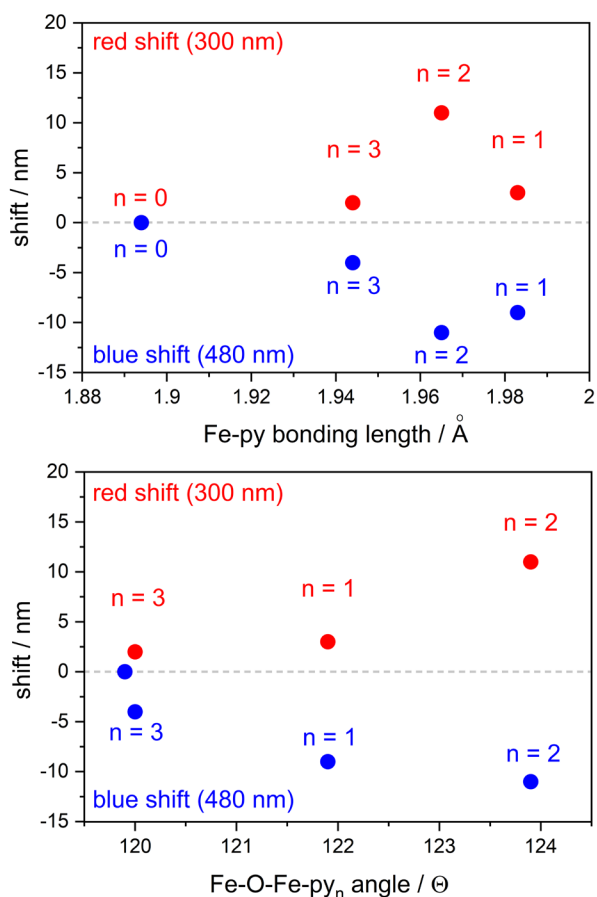


Fig. 10: Experimental blue and redshifts corresponding to their calculated bonding lengths and angles of $[\text{Fe}_3\text{O}(\text{OAc})_6(\text{py}_n)]^+$ ($n = 0, 1, 2, 3$). The calculations were performed with Gaussian 09 at the B3LYP/cc-pVTZ (H, C, N, O) and ecp-10-mdf (Fe) level of theory.

The HOMO-LUMO gaps can explain the higher shift in absorption energy (cf. Fig. S17) of the different isomers. Calculated HOMO-LUMO gaps for the complex with three coordinated pyridines have higher energy than the bare complex but the same angles in the Fe_3O core. More energy for absorption is needed, and this results in higher shifts in the UVPD spectrum. Also, the trend is like the relative energy shift trend compared to the angles of these complexes.

5.6.5 Discussion III: Opto- magnetic correlation

Notice that the UVPD spectra reveal the same trend observed in the XA spectra (cf. Fig. S19). This hints strong evidence that the different spectroscopic approaches lead to an entire picture describing the electronic ground state with magnetic and optical properties of these complexes. For better visualization, comparing the first derivation of the L_3 edge in the XA spectra with the UVPD spectra (cf. Fig. S18) in the area of 300 nm reveals the same trend for

both spectroscopic approaches. We observe a shift to higher energies in both spectroscopic methods until coordinating the second pyridine to the complex. Following that, the third coordination of pyridine results in a shift to lower energy. We consider that both spectroscopic approaches are steady state experiments, and therefore the spin ground state in this series of complexes is the same for both types of investigations.

The inverse trend for the weak MLCT transitions (Fig. S19) occurs from weak electron transfer from the metal center into the ligands. The experimental crystal field splittings from the XA spectra and the absorption energies from the UVPD spectra within a Tanabe-Sugano diagram for a $3d^5$ high spin atom can correlate with both methods. As a result, these values must be normalized using the Racah parameter B ($B = 917 \text{ cm}^{-1}$)^[104]. The correlation in a Tanabe-Sugano diagram shows that crystal field splitting results in a shift in energy in the UV/VIS spectra and vice versa. This corresponds extremely well to our experimental findings (cf. Tab. 8).

Tab. 8: Normalized crystal field splittings (ΔL_3 , cf. Tab. 3), absorption energies, and their corresponding energies from the Tanabe-Sugano diagram of $[\text{Fe}_3\text{O}(\text{OAc})_6(\text{py})_n]^+$ ($n = 0, 1, 2, 3$) with uncertainties of 10 %. The TD-DFT calculations were performed with Gaussian 09 at the uB3LYP/cc-pVTZ (H, C, N, O) level of theory.

	ΔL_3		Tanabe Sugano		λ_{exp}		λ_{calc}
	$\Delta L_3/\text{eV}$	$\Delta L_3/B$	E/B	E/(nm)	E/B	E/(nm)	E/(nm)
n = 0	1.88(19)	16.54	22.61	482	22.48	485	486
n = 1	1.83(18)	16.10	23.30	468	22.91	476	468
n = 2	1.81(17)	15.93	23.37	462	23.01	474	466
n = 3	1.86(19)	16.35	22.82	477	22.67	481	475

We are also able to determine an excitation from a 6A_1 ground state to a ${}^2T_{2g}$ state. The crystal field splitting decrease with pyridine coordination from the bare complex until the second pyridine coordination occurs because of the change from pseudo octahedral coordination to a real octahedral one and the corresponding minor Jahn Teller distortion in the pyridine coordinated iron center. The crystal field splitting for the complex with two pyridines coordinated slightly differ from the other ones but including uncertainties of 10% the approximated absorption energy is within the range of the uncertainties. Therefore, a crystal

field splitting of 1.82 eV would result in a normalized crystal field of 16.00 and this value would fit to the experimental and calculated UV/VIS absorption energies. By coordination with three axial ligands, there is no Jahn Teller distortion. All Fe^{3+} centers are in the same coordination sphere, leading to the same electronic structure as in the case without coordination of the axial ligand. The crucial difference between the bare and fully coordinated complex is that the Fe_3O core in the bare complex is smaller than in the complex with three coordinated axial ligands. The approximated energies from the Tanabe-Sugano diagram match the experimental XA and UVPD data.

The Correlation between the normalized UVPD absorptions (E/B) and the approximated absorption energies from the Tanabe-Sugano diagram points out a linear dependency with further coordination of pyridine to the complex (cf. Fig. 11 b)) until the third pyridine coordinates to the complex. This demonstrates that the measured absorption energies in this sequence of spin frustrated systems accord well with the estimated transitions. The correlation of the total magnetic moment per iron atom with the absorption energies of the UVPD spectra reveals a nonlinear trend (cf. Fig. 11 a)). A distortion of the Fe_3O core increases ferromagnetic exchange coupling, leading in a blue shift for the weak and spin prohibited MLCT transitions due to a change in orbital energies as a function of the pyridine coordination. Because the orbital energies are somewhat higher than in the bare complex, the coordination of three pyridines results in a reduced blue shift with an antiferromagnetic exchange coupling. Also, the determined crystal field splitting is slightly lower than in the bare complex, resulting in a lower shift of the absorption energy. For better visualization, the correlation of the normalized absorption energies (E/B) with the total magnetic moments per Fe^{3+} atom points out a similar behavior as the correlation with the not normalized approximated absorption energies (cf. Fig. 11a)) by reaching an almost entirely ferromagnetic coupled complex (cf. Fig. 11c)). This demonstrates that the spin arrangement in the Fe_3O core is vulnerable to axial ligand coordination and the subsequent core distortion. As discussed earlier, the different crystal field splittings change the exchange coupling scheme by changing the orbital energies. In XMCD spectroscopy, the Fe^{3+} iron centers absorption edge highly depends on pyridine coordination in these complexes. Previous research has shown that coordination influences the orbital energy for the transition from the core shell to the valence state.

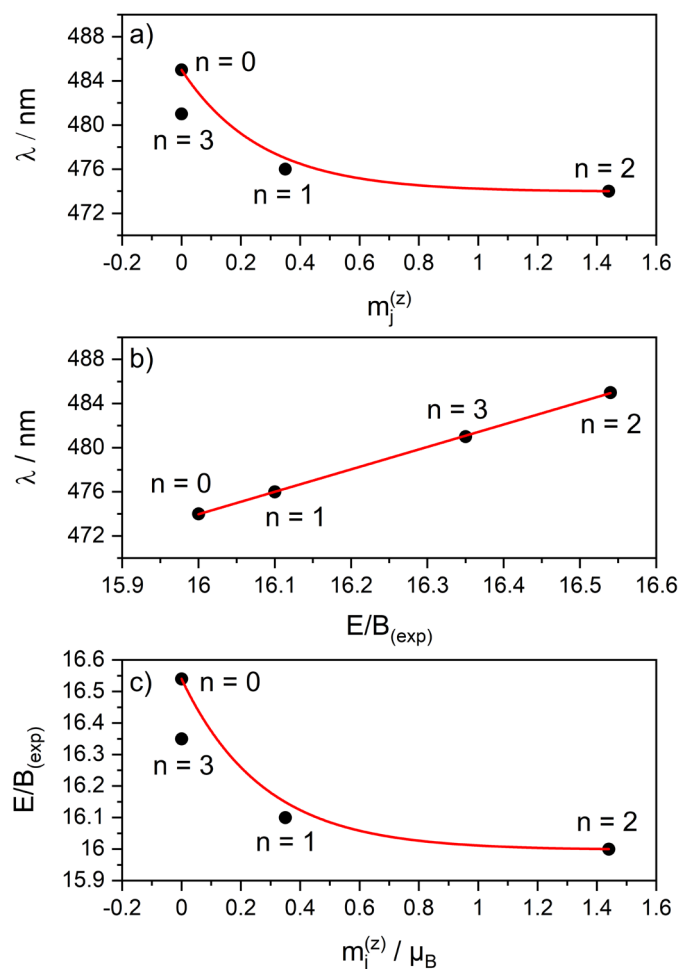


Fig. 11: Dependency of the total magnetic moments per Fe^{3+} atom, absorption energies, and the normalized absorption energies of $[\text{Fe}_3\text{O}(\text{OAc})_6(\text{py})_n]^+$ ($n = 0, 1, 2, 3$) in isolation.

The orbital energies of the core shell orbitals reveal a strong dependency on the different Fe- O-Fe-py_n angles in the isomers (cf. Fig. 12 a)). That proves that the angle change changes the core shell energies, resulting in a switch from an antiferromagnetic exchange coupling to a ferromagnetic exchange coupling. The fully coordinated complex angles are the same as the bare complex but have higher core shell orbital energies. The antiferromagnetic exchange is given by cause of the symmetry in the complex but at a higher energy level. In all iron atoms, the core shell energy is the same as in the bare complex. In asymmetric complexes, the core shell energy of the coordinated iron atoms differs from the uncoordinated iron atoms. The calculated total coupling constants from the XA experiments also increase with the orbital energies from the core shell, pointing out that the angle change affects these core shell energies, leading to the observed magnetic behavior in this series of complexes (cf. Fig. 12 b)).

The total coupling constants in this series of complexes are closely related to the Fe-O-Fe-py_n angles, implying that changing the angle immediately leads to a change in the coupling scheme in these complexes (cf. Fig. 12 c)). By comparing the bare complex and the fully coordinated complex with the same angles, no magnetic moment is observed due to the symmetry in both complexes.

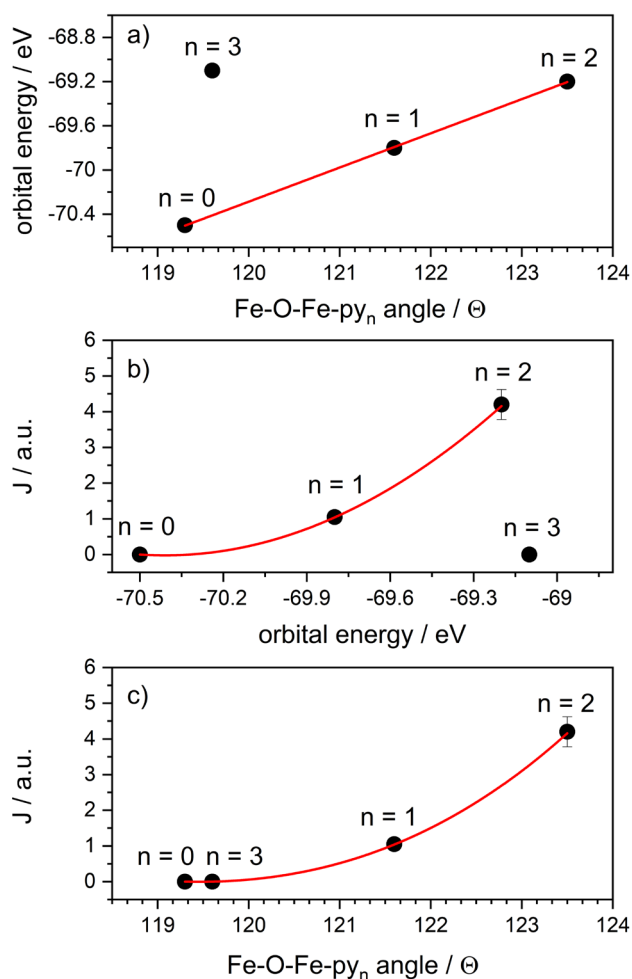


Fig. 12: Different correlations of $[\text{Fe}_3\text{O}(\text{OAc})_6(\text{py})_n]^+$ (n = 0, 1, 2, 3) for the determination of the caused magnetism. With a) orbital energies of the transition from the $2p_{3/2}$ into the 3d orbital via Density of states calculation and their associated Fe-O-Fe-py_n dihedral angles, b) the total magnetic moments and the orbital energies, and c) total magnetic moment and the dihedral Fe-O-Fe-py_n angle. The calculations were performed at the B3LYP-Gaussian/cc-pVTZ (H, C, N, O) and ecp-10-mdf (Fe) level of theory with five unpaired electrons on each Fe center and a UUD (n = 0, 1, 3) or DUU (n = 2) broken symmetry configuration corresponding to the minimum structures^[62].

The absorption maxima of the UVPD spectra in this series of complexes strongly correlate with the absorption edges of the XA spectra (cf. Fig. S20). UVPD spectra follow a linear trend in the area of around 300 nm. We consider that magnetism, electronics, and the angle-dependent shift of crystal field splittings are all tightly interconnected. The spin forbidden absorption bands in the UVPD spectra correlated with the XA absorption edges increase. In comparison with the above discussed dependency, the explanation is almost the same. However, due to small metal to ligand charge transfers (MLCT) and the pyridines non-classical bonding state to the metal center, there is another impact in these absorption bands that cannot be ignored.

Relative energy shifts in the UVPD spectra compared to the total magnetic moment per iron atom also reveal an almost linear correlation (cf. Fig. 13). The higher the shift, the higher the magnetic value. The explanation follows the same as discussed before. Variations in angles cause changes in crystal field splittings, which vary the orbital core shell energies, resulting in various absorption maxima and magnetism.

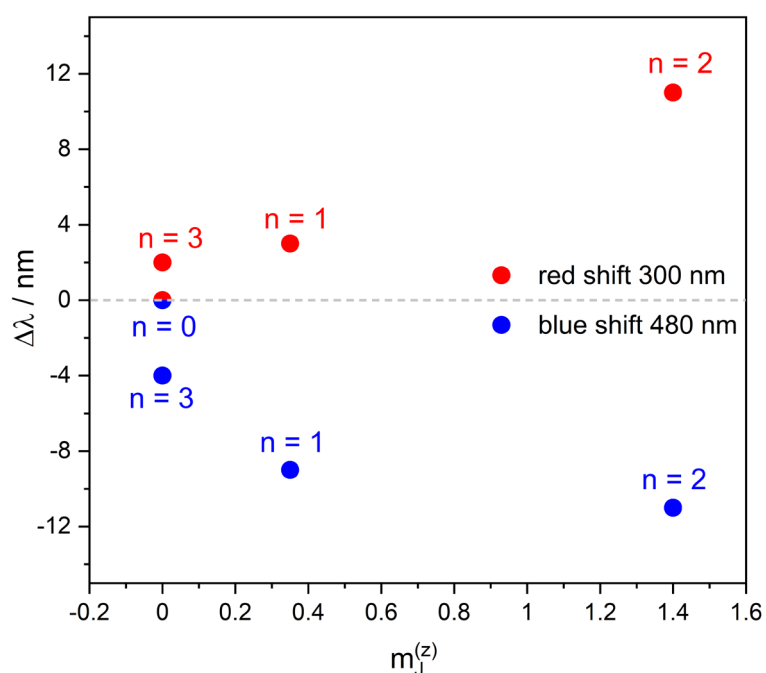


Fig. 13: Experimental red- and blue shifts from the UVPD spectra with the experimental magnetic moments per atom of $[\text{Fe}_3\text{O}(\text{OAc})_6(\text{py})_n]^+$ ($n = 0, 1, 2, 3$) in isolation.

A deeper examination of the experimental alterations in the UVPD and XA spectra from our analyses of these compounds reveals a nearly same pattern (cf. Fig. S20). We monitor an increase in the absorption energies in both spectroscopic approaches until the second pyridine

coordinates the complex. Further coordination results in a declining trend in this complex series. On the one hand, the distortion causes a change in the crystal field splitting and a change in the core-shell energies, as previously described, and on the other hand, it causes a tiny shift in the excitation from the HOMO orbitals into the LUMO orbitals.

As discussed earlier, the shift in the absorption energies mainly occurs by changing the Fe-O-Fe-py_n angle (cf. Fig. S21), pointing out the chain reaction in the magnetism and the electronics of the distortion in the Fe₃O core because of the change of the angle. Because the Fe₃O core is symmetric, the symmetric complexes produce equivalent absorption shifts in both spectroscopic techniques, resulting in similar core shell energies and HOMO-LUMO excitations. Pyridine coordination causes a shift in the crystal field splitting, resulting in differing core shell energies. Both spectroscopic approaches reveal a strong dependency between the core shell energies and the absorption energies (cf. Fig. S23). The shifts increase with higher core shell energies until the coordination of two pyridine takes part. By further coordination to the complex, the core shell energy decreases slightly as the absorption energy. The higher shift and core shell energy appear from the pyridine coordination, leading to an enlarged Fe₃O core with a symmetric motif. A correlation with the total magnetic moments and their corresponding shifts in the spectra indicates an almost linear trend from the bare complex to the complex with two coordinated pyridines (cf. Fig. S23). This indicates that the exchange coupling of the iron atoms has a direct effect on the spectral pattern in both spectroscopic techniques in all types of spectroscopic research. The highest shift arises with the coordination of two pyridines to the complex, with the strongest distortion, the highest total magnetic moments, and the highest crystal field splitting of all these complexes. For the complex with three coordinated pyridine ligands, the shift is higher in all spectra. Still, the total magnetic moment is the same as in the bare complex because of the restored symmetry and results in a restoration of the antiferromagnetic exchange coupling at a higher level of orbital energies caused by the coordination of pyridine to the system.

Influence to the correlation by changing the axial or the bridging ligands

The correlation in this series of complexes highly depends on the distortion of the Fe₃O core. This hints that the coordination of the axial ligand mainly causes the observed effects in this system. DFT calculations with the exchange of the axial ligands serve to prove the influence of the ligand on the complex. Therefore, we compare the bonding lengths of the central Oxygen atoms to the Fe³⁺ ions by coordination with the axial ligand (cf. Tab. S1).

The exchange of smaller to larger ligands results in nearly identical bonding lengths for all estimated ligands. We did not anticipate a change in the magnetic characteristics or electronic ground state in these complexes, suggesting that the axial ligand causes the observed effects but does not increase or lessen them due to its size. Besides the geometrical changes, there also could be changes in the electronics by non-classical bonding situations. Non covalent interactions^[116] (NCI) with different axial ligands reveal more attractive non covalent interactions from nitrogen to pyridine (cf. Fig. S24). These interactions gain more repulsive by larger ligands for the Fe-L_{het} bonding. The Hydrogen of DMF and pyridine immediately points towards and between two Oxygen atoms of the bridging ligands, enhancing non covalent interactions and leading in a shift in UVPD absorption bands due to orbital energies, e.g., HOMO-LUMO orbitals. The total magnetic moments should not be affected because the orbital energies should be higher in every case of coordination than in the bare complex. Also, the symmetric complexes should obtain an antiferromagnetic coupling scheme because the orbital energies are the same for every Fe³⁺ in the investigated isomers. An exchange of the bridging ligand in these complexes leads to minor or no changes in the bonding lengths and their corresponding angles (cf. Tab. S2). With similar bonding distances and angles, we did not expect a change in the magnetic properties. A change in the spectral shape of the UVPD spectra cannot be excluded due to additional chromophores like benzoic acid. Switching the bridging ligands to dicarboxylic acids predicts a loss of one dicarboxylic acid in the complex, resulting in significant distortions in the Fe₃O core in every isomer where the central Oxygen atom is out of plane.

Influence to the correlation by changing the central Oxygen atom

The last possible influence on the geometrical, electronic, and magnetic behavior could arise from the central Oxygen atom in the Fe_3O core of the complex. We also performed DFT calculations for the exchange of the central Oxygen atom with carbon and Sulfur. Nitrogen and phosphorus as central atoms would change from an uneven multiplicity to an even multiplicity. Electron localized field plots explain the effect by changing the central atom from Oxygen to other atoms (cf. Fig. S25). For the bare complex, a symmetrical electron density of the Oxygen atom occurs. Also, all bonding strengths are equal for the Fe-O bonding distances. Changing the central Oxygen atom to a carbon atom leads to a more diffuse electron density with stronger bondings. Sulfur as a central atom leads to an almost similar pattern with stronger bonding distances as in the Fe_3O analoga. These estimated geometries should produce an antiferromagnetic exchange coupling, greater or weaker in this complicated series, implying that the central atom in the Fe_3M ($\text{M} = \text{Oxygen, Carbon, Sulfur}$) has a considerable impact on the antiferromagnetic coupling. The absorption bands in the UVPD spectra should have a minor influence on their shifts since the electronic ground state should be unaffected. The carbon and Sulfur analoga show the same angles and bonding distances as the investigated species. The bonding strength of the complex weakens with one pyridine coordinated to it, resulting in increased antiferromagnetic coupling. By exchanging the Oxygen atom to a carbon atom reveals almost similar behavior, the ferromagnetic coupling could be established. Still, it should be weaker than the investigated complex because of the higher bonding strength in this complex. In the Sulfur analoga, the Sulfur is out of plane, assuming there must be a ferromagnetic exchange coupling. For the UVPD absorption bands, we carry an almost similar behavior for Oxygen and carbon. In the Sulfur analoga, the absorption band should be significantly shifted.

For two coordinated pyridine to the complexes, a more substantial ferromagnetic coupling scheme is observed. A change to carbon would not favor a ferromagnetic coupling. The stronger electron overlap between carbon and the iron center and Sulfur analoga does not hint a ferromagnetic exchange coupling. In UVPD, we assume the same trend by changing the Oxygen to carbon or Sulfur. The complexes with three pyridines coordinated to the complex, the Fe_3O core reveals an antiferromagnetic exchange coupling. Carbon as a central atom should also obtain an antiferromagnetic exchange coupling as a result of stronger bondings

and high symmetry. For the Sulfur analoga, a ferromagnetic coupling should be present because of its strong distortion and the out of plane position of the central Sulfur atom.

The magnetic behavior is very sensitive to the central atom in the complex. With Oxygen as a central atom, we observe a change of the antiferromagnetic exchange coupling to a ferromagnetic one as a function of the pyridine coordination until the recovery of the symmetry is given. Changing the central atom to carbon leads in every case to complexes with antiferromagnetic exchange coupling because of the diffuse electron density in the carbon atom. A change from Oxygen to Sulfur must lead to a way different magnetic behavior. In the bare complex, we assume an antiferromagnetic coupling with the coordination of one or three axial ligands. The complexes become distorted so that the iron center does not feature a strong overlap to the Sulfur atom because the Sulfur is out of plane.

The complex becomes more symmetrical with the coordination of two axial ligands, and an antiferromagnetic coupling scheme should be established.

5.7 Conclusions

In the presented work, we investigate the intrinsic spin and orbital magnetic moments of isolated spin frustrated systems of the type $[\text{Fe}_3\text{O}(\text{OAc})_6(\text{py})_n]^+$. Element selectivity of the used XMCD technique allows the separation of the total magnetic moments. The distortion of the Fe_3O core dominates the total magnetic moment as a function of stepwise pyridine coordination. The recorded XMCD spectra analysis allows separating these unique contributions into their spin and orbital magnetic moments. The recorded XA spectra and the corresponding XMCD spectra of these complexes reveal a change from an antiferromagnetic exchange coupling for the symmetric complexes and a ferromagnetic exchange coupling by coordinating pyridine to the complex. Experimental total Spin values slightly differ from the total spin of earlier broken symmetry calculations. By assuming uncertainties of 5 % in the experimental data, these values agree with the calculations.

By coordinating pyridine, we observe a change in the crystal field splittings in this series of complexes. The crystal field splittings rise with further coordination of the axial ligand, and with the third coordination, a slight decrease is observed. Electronic ground state determination reveals that pyridine coordination changes the exciting core shell energies. The

energy rises with further coordination because of different spin states resulting in antiferromagnetic exchange coupling for symmetric complexes and a ferromagnetic exchange coupling for asymmetric complexes.

The Fe-O-Fe-py_n angles shift significantly, causing major variations in the magnetic characteristics of this series of complexes, which directly influences the crystal field splittings and the related core shell orbitals.

Branching ratio analysis indicates that an antiferromagnetic exchange coupling is present in every isomer, but with rising coordination, until two pyridines coordinate to the complex, ferromagnetic exchange coupling predominates.

UVPD investigations reveal a slight shift in their absorption spectra because of the pyridine coordination in this complex series. In combination with TD-DFT calculations, different HOMO-LUMO transitions for these complexes can be determined. Distinct orbital energies emerge from pyridine coordination, leading in different HOMO-LUMO transitions in the UVPD spectra. These energy shifts follow the same trend as for the energy shift in the XA spectra.

We found an Opto structural correlation within the Tanabe-Sugano diagram. We able to determine an excitation from a ⁶A₁ ground state to a ²T_{2g} excited state for weak MLCT transitions. Also, the observed shifts of the UVPD spectra directly correlate with the experimental total magnetic moments per atom from the XMCD studies.

The XMCD and UVPD spectra show the same trend for almost every isomer. The correlation strongly depends on the coordination of pyridine. Coordination causes the angles of the Fe₃O core to alter, leading in distinct core-shell orbitals, crystal field splittings, orbital energies, energetic changes in the UVPD spectra, and coupling schemes. We do not observe any correlation between the bonding distances and the shifts in the experimental spectra. All absorption bands belong to HOMO LUMO transitions in these series of complexes. With the change of the angles in these complexes, the energies of the LUMO orbitals change and result in small shifts as a result of the raising HOMO–LUMO gaps.

Changing the axial and/or bridging ligands reveals that the size of the bridging ligand does not affect the properties of these series of complexes. The change of the axial ligand points out that the non covalent attraction becomes higher as a function of the ligand size from nitrogen

to pyridine. A change of the central atom in the Fe₃M core (M = O, C, S) significantly influences this complex series. The change of the central atom should lead to different coupling schemes, as observed. The out-of-plane situation in the calculated Sulfur complexes has to lead to various exchange coupling schemes. ELF plots also point out that the coupling scheme's change and their corresponding orbital energies highly depend on an interplay of the central atom and the axial ligands. This spin frustrated system shows a correlation between two different gas phase investigations only in this unique situation.

In summary, we have shown that gas-phase XMCD experiments combined with UVPD investigations add valuable additional insight into the fascinating magnetic properties of spin frustrated systems.

5.8 Acknowledgment

The German research foundation DFG supported this work within the transregional collaborative research center SFB/TRR 88 "Cooperative effects in homo and heterometallic complexes" (3MET) and by the state research center OPTIMAS.

5.9 References

- [1] J. M. Baik, Y. Shon, S. J. Lee, Y. H. Jeong, T. W. Kang, and J.-L. Lee, Electronic Structure and Magnetism in Transition Metals Doped 8-Hydroxy-Quinoline Aluminum, *J. Am. Chem. Soc.*, **130**, 13522-13523, 2008.
- [2] W. A. Hoffert, A. K. Rappé, and M. P. Shores, Topological and Electronic Influences on Magnetic Exchange Coupling in Fe(III) Ethynylbenzene Dendritic Building Blocks, *J. Am. Chem. Soc.*, **133**, 20823-20836, 2011.
- [3] T. C. Stamatatos, D. Foguet-Albiol, S.-C. Lee, C. C. Stoumpos, C. P. Raptopoulou, A. Terzis, W. Wernsdorfer, S. O. Hill, S. P. Perlepes, and G. Christou, "Switching On" the Properties of Single-Molecule Magnetism in Triangular Manganese(III) Complexes, *J. Am. Chem. Soc.*, **129**, 9484-9499, 2007.
- [4] Y. Wang, Z. Zhou, T. Wen, Y. Zhou, N. Li, F. Han, Y. Xiao, P. Chow, J. Sun, M. Pravica, A. L. Cornelius, W. Yang, and Y. Zhao, Pressure-Driven Cooperative Spin-Crossover, Large-Volume Collapse, and Semiconductor-to-Metal Transition in Manganese(II) Honeycomb Lattices, *J. Am. Chem. Soc.*, **138**, 15751-15757, 2016.
- [5] G. Filoti, J. Bartolome, D. P. E. Dickson, C. Rillo, I. Prisecaru, T. Jovmir, V. Kuncser, and C. Turta, Intermediate frustration in [Fe₃O(CH₃COO)₆(H₂O)₃] NO₃ · 4(H₂O) trinuclear cluster, *J. Magn. Magn. Mater.*, **196-197**, 561-563, 1999.
- [6] A. N. Georgopoulou, Y. Sanakis, and A. K. Boudalis, Magnetic relaxation in basic iron(III) carboxylate [Fe₃O(O₂CPh)₆(H₂O)₃]ClO₄·py, *Dalt. Trans.*, **40**, 6371-6374, 2011.
- [7] S. D. Bader, and S. S. P. Parkin, Spintronics, *An. Rev. Cond. Matter Physics*, **1**, 71-88, 2010.
- [8] V. Baltz, A. Manchon, M. Tsoi, T. Moriyama, T. Ono, and Y. Tserkovnyak, Antiferromagnetic spintronics, *RvMP*, **90**, 015005, 2018.
- [9] C. Chakravarty, B. Mandal, and P. Sarker, Bis(dithioline)-Based Metal–Organic Frameworks with Superior Electronic and Magnetic Properties: Spin Frustration to Spintronics and Gas Sensing, *J. Phys. Chem. C*, **120**, 28307-28319, 2016.

- [10] J. M. Crabtree, and A. Soncini, Toroidal quantum states in molecular spin-frustrated triangular nanomagnets with weak spin-orbit coupling: Applications to molecular spintronics, *Phys. Rev. B*, 98, 094417, 2018.
- [11] S. V. Rao, J. M. Ashtree, and A. Soncini, Toroidal moment in a family of spin-frustrated heterometallic triangular nanomagnets without spin-orbit coupling: Applications in a molecular spintronics device, *Physica B: Condensed Matter*, 592, 412237, 2020.
- [12] S. Bi, C. Liu, and H. Hu, Theoretical Study on Magnetostructural Correlation in Unsymmetrical Oxamidocopper(II) Complexes, *J. Phys. Chem. B*, 106, 10786-10792, 2002.
- [13] T. Cauchy, E. Ruiz, and S. Alvarez, Magnetostructural Correlations in Polynuclear Complexes: The Fe₄ Butterflies, *J. Am. Chem. Soc.*, 128, 15722-15727, 2006.
- [14] D. Gatteschi, and R. Sessoli, Quantum Tunneling of Magnetization and Related Phenomena in Molecular Materials, *Angew. Chem. Int. Ed.*, 42, 268-297, 2003.
- [15] S. M. Gorun, and S. J. Lippard, Magnetostructural correlations in magnetically coupled (μ-oxo)diiron(III) complexes, *Inorg. Chem.*, 30, 1625-1630, 1991.
- [16] G. Aromí, D. Aguilà, P. Gamez, F. Luis, and O. Roubeau, Design of magnetic coordination complexes for quantum computing, *Chem. Soc. Rev.*, 41, 537-546, 2012.
- [17] J. Ferrando-Soria, Samantha A. Magee, A. Chiesa, S. Carretta, P. Santini, Iñigo J. Vitorica-Yrezabal, F. Tuna, George F. S. Whitehead, S. Sproules, Kyle M. Lancaster, A.-L. Barra, Grigore A. Timco, Eric J. L. McInnes, and Richard E. P. Winpenny, Switchable Interaction in Molecular Double Qubits, *Chem*, 1, 727-752, 2016.
- [18] M. N. Leuenberger, and D. Loss, Quantum computing in molecular magnets, *Natur*, 410, 789-793, 2001.
- [19] T. N. Nguyen, W. Wernsdorfer, M. Shiddiq, K. A. Abboud, S. Hill, and G. Christou, Supramolecular aggregates of single-molecule magnets: exchange-biased quantum tunneling of magnetization in a rectangular [Mn₃]₄ tetramer, *Chemical Science*, 7, 1156-1173, 2016.
- [20] M. Trif, F. Troiani, D. Stepanenko, and D. Loss, Spin-Electric Coupling in Molecular Magnets, *Phys. Rev. Lett.*, 101, 217201, 2008.
- [21] J. P. S. Walsh, S. B. Meadows, A. Ghirri, F. Moro, M. Jennings, W. F. Smith, D. M. Graham, T. Kihara, H. Nojiri, I. J. Vitorica-Yrezabal, G. A. Timco, D. Collison, E. J. L. McInnes, and R. E. P. Winpenny, Electronic Structure of a Mixed-Metal Fluoride-Centered Triangle Complex: A Potential Qubit Component, *Inorg. Chem.*, 54, 12019-12026, 2015.
- [22] R. W. volume editor, and G. A. with contributions by, *Single-molecule magnets and related phenomena*: Berlin ; New York : Springer, 2006.
- [23] G. Férey, M. Latroche, C. Serre, F. Millange, T. Loiseau, and A. Percheron-Guégan, Hydrogen adsorption in the nanoporous metal-benzenedicarboxylate M(OH)(O₂C-C₆H₄-CO₂) (M = Al³⁺, Cr³⁺), MIL-53, *Chem. Commun.*, 2976-2977, 2003.
- [24] G. Férey, C. Mellot-Draznieks, C. Serre, F. Millange, J. Dutour, S. Surblé, and I. Margiolaki, A Chromium Terephthalate-Based Solid with Unusually Large Pore Volumes and Surface Area, *Sci*, 309, 2040, 2005.
- [25] G. Férey, C. Serre, C. Mellot-Draznieks, F. Millange, S. Surblé, J. Dutour, and I. Margiolaki, A Hybrid Solid with Giant Pores Prepared by a Combination of Targeted Chemistry, Simulation, and Powder Diffraction, *Angew. Chem. Int. Ed.*, 43, 6296-6301, 2004.
- [26] J. S. Seo, D. Whang, H. Lee, S. I. Jun, J. Oh, Y. J. Jeon, and K. Kim, A homochiral metal-organic porous material for enantioselective separation and catalysis, *Natur*, 404, 982-986, 2000.
- [27] S. Uchida, M. Hashimoto, and N. Mizuno, A Breathing Ionic Crystal Displaying Selective Binding of Small Alcohols and Nitriles: K₃[Cr₃O(OOCH)₆(H₂O)₃][α-SiW₁₂O₄₀]-16 H₂O, *Angew. Chem. Int. Ed.*, 41, 2814-2817, 2002.
- [28] S. Uchida, and N. Mizuno, Unique Guest-Inclusion Properties of a Breathing Ionic Crystal of K₃[Cr₃O(OOCH)₆(H₂O)₃][α-SiW₁₂O₄₀]-16 H₂O, *Chemistry – A European Journal*, 9, 5850-5857, 2003.
- [29] Y.-W. Lin, Rational design of metalloenzymes: From single to multiple active sites, *Coord. Chem. Rev.*, 336, 1-27, 2017.
- [30] J.-L. Chen, L.-Y. Zhang, L.-X. Shi, H.-Y. Ye, and Z.-N. Chen, Syntheses, characterization and redox properties of di- and poly-phosphine linked oligomeric complexes of oxo-centered triruthenium clusters, *Inorg. Chim. Acta*, 359, 1531-1540, 2006.
- [31] M. Lu, T. Chen, M. Wang, G. Jiang, T. Lu, G. Jiang, and J. Du, A new μ₃-oxo-centered tri-nuclear carboxyl bridged iron (III) complex with thio-methyl groups in the periphery: Structural, spectroscopic and electrochemical studies, *J. Mol. Struct.*, 1060, 131-137, 2014.

5. Magnetic properties and their correlation to the electronics of isolated trinuclear 3d spin frustrated complexes

- [32] S. T. Wilson, R. F. Bondurant, T. J. Meyer, and D. J. Salmon, OXIDATION STATE PROPERTIES OF DELOCALIZED, LIGAND-BRIDGED METAL COMPLEXES. (RU₃O(CH₃CO₂)₆L₃)N⁺ AND THE PYRAZINE-BRIDGED, CLUSTER-CLUSTER DIMER, (RU₃O(CH₃CO₂)₆(PY)₂)₂PYZM⁺, 1975.
- [33] A. Dikhtiarenko, S. Khainakov, J. R. García, and J. Gimeno, Research paper, *Inorg. Chim. Acta*, 454, 107-116, 2017.
- [34] H.-Y. Ye, F.-R. Dai, L.-Y. Zhang, and Z.-N. Chen, Low-Valence Triruthenium Compounds via Substitution of a Bridging Acetate in the Parent Ru₃O(OAc)₆ Cluster Core by 2,2'-Azobispyridine (abpy) or 2,2'-Azobis(5-chloropyrimidine) (abcp), *Inorg. Chem.*, 46, 6129-6135, 2007.
- [35] M. I. Belinsky, Spin-Frustrated Trinuclear Cu(II) Clusters with Mixing of 2(S = 1/2) and S = 3/2 States by Antisymmetric Exchange. 1. Dzialoshinsky-Moriya Exchange Contribution to Zero-Field Splitting of the S = 3/2 State, *Inorg. Chem.*, 47, 3521-3531, 2008.
- [36] B. Cage, F. A. Cotton, N. S. Dalal, E. A. Hillard, B. Rakvin, and C. M. Ramsey, Observation of Symmetry Lowering and Electron Localization in the Doublet-States of a Spin-Frustrated Equilateral Triangular Lattice: Cu₃(O₂C₁₆H₂₃)₁·1.2C₆H₁₂, *J. Am. Chem. Soc.*, 125, 5270-5271, 2003.
- [37] S. Carretta, P. Santini, G. Amoretti, F. Troiani, and M. Affronte, Spin triangles as optimal units for molecule-based quantum gates, *PhRvB*, 76, 024408, 2007.
- [38] K.-Y. Choi, Y. H. Matsuda, H. Nojiri, U. Kortz, F. Hussain, A. C. Stowe, C. Ramsey, and N. S. Dalal, Observation of a Half Step Magnetization in the Cu₃-Type Triangular Spin Ring, *Phys. Rev. Lett.*, 96, 107202, 2006.
- [39] O. Kahn, Competing spin interactions and degenerate frustration for discrete molecular species, *Chem. Phys. Lett.*, 265, 109-114, 1997.
- [40] S. Khanra, B. Biswas, C. Golze, B. Büchner, V. Kataev, T. Weyhermüller, and P. Chaudhuri, A spin-frustrated star-shaped heterotetranuclear CrIIIMnII₃ species and its magnetic and HF-EPR measurements, *Dalt. Trans.*, 481-487, 2007.
- [41] S. Nakatsuji, Y. Nambu, H. Tonomura, O. Sakai, S. Jonas, C. Broholm, H. Tsunetsugu, Y. Qiu, and Y. Maeno, Spin Disorder on a Triangular Lattice, *Sci*, 309, 1697, 2005.
- [42] M. Prinz, K. Kuepper, C. Taubitz, M. Raekers, S. Khanra, B. Biswas, T. Weyhermüller, M. Uhlarz, J. Wosnitza, J. Schnack, A. V. Postnikov, C. Schröder, S. J. George, M. Neumann, and P. Chaudhuri, A Star-Shaped Heteronuclear CrIIIMnII₃ Species and Its Precise Electronic and Magnetic Structure: Spin Frustration Studied by X-Ray Spectroscopic, Magnetic, and Theoretical Methods, *Inorg. Chem.*, 49, 2093-2102, 2010.
- [43] T. Yamase, H. Abe, E. Ishikawa, H. Nojiri, and Y. Ohshima, Structure and Magnetism of [n-BuNH₃]₁₂[Cu₄(GeW₉O₃₄)₂·14H₂O] Sandwiching a Rhomblike Cu₄⁸⁺ Tetragon through α-Keggin Linkage, *Inorg. Chem.*, 48, 138-148, 2009.
- [44] J. Yoon, and E. I. Solomon, Electronic structures of exchange coupled trigonal trimeric Cu(II) complexes: Spin frustration, antisymmetric exchange, pseudo-A terms, and their relation to O₂ activation in the multicopper oxidases, *Coord. Chem. Rev.*, 251, 379-400, 2007.
- [45] P. Alborés, C. Plenck, and E. Rentschler, Tailoring the Exchange Interaction in Covalently Linked Basic Carboxylate Clusters through Bridging Ligand Selection, *Inorg. Chem.*, 51, 8373-8384, 2012.
- [46] D. Alexandropoulos, A. Mowson, M. Pilkington, V. Bekiari, G. Christou, and T. Stamatatos, Emissive molecular nanomagnets: Introducing optical properties in triangular oximate {MnIII₃} SMMs from the deliberate replacement of simple carboxylate ligands with their fluorescent analogues, *Dalt. Trans.*, 43, 2013.
- [47] A. Boudalis, K., J. Robert, and P. Turek, First Demonstration of Magnetoelectric Coupling in a Polynuclear Molecular Nanomagnet: Single-Crystal EPR Studies of [Fe₃O(O₂CPh)₆(py)₃]ClO₄·py under Static Electric Fields, 24, 14896-14900, 2018.
- [48] A. K. Boudalis, Y. Sanakis, F. Dahan, M. Hendrich, and J.-P. Tuchagues, An Octanuclear Complex Containing the {Fe₃O}⁷⁺ Metal Core: Structural, Magnetic, Mössbauer, and Electron Paramagnetic Resonance Studies, *Inorg. Chem.*, 45, 443-453, 2006.
- [49] E. Ruiz, J. Cano, S. Alvarez, and P. Alemany, Broken symmetry approach to calculation of exchange coupling constants for homobinuclear and heterobinuclear transition metal complexes, *J. Comput. Chem.*, 20, 1391-1400, 1999.
- [50] Y. Sanakis, A. K. Boudalis, and J.-P. Tuchagues, J-strain and antisymmetric exchange in a polynuclear compound containing the {Fe₃O}⁷⁺ core, *Comptes Rendus Chimie*, 10, 116-124, 2007.
- [51] A. Vlachos, V. Psycharis, C. P. Raptopoulou, N. Lalioti, Y. Sanakis, G. Diamantopoulos, M. Fardis, M. Karayanni, G. Papavassiliou, and A. Terzis, A nearly symmetric trinuclear chromium(III) oxo carboxylate

- assembly: preparation, molecular and crystal structure, and magnetic properties of $[\text{Cr}_3\text{O}(\text{O}_2\text{CPh})_6(\text{MeOH})_3](\text{NO}_3)\cdot 2\text{MeOH}$, *Inorg. Chim. Acta*, 357, 3162-3172, 2004.
- [52] M. P. Yutkin, M. S. Zavakhina, A. V. Virovets, D. N. Dybtsev, V. P. Fedin, T. Kusamoto, and H. Nishihara, Synthesis, structure and magnetic behavior of new 1D metal-organic coordination polymer with Fe_3O core, *Inorg. Chim. Acta*, 365, 513-516, 2011.
- [53] M. Eshel, and A. Bino, Polynuclear chromium(III) carboxylates. 3. Cyclic and cubane type hexachromium acetates, *Inorg. Chim. Acta*, 329, 45-50, 2002.
- [54] M. Eshel, A. Bino, I. Felner, D. C. Johnston, M. Luban, and L. L. Miller, Polynuclear Chromium(III) Carboxylates. 1. Synthesis, Structure, and Magnetic Properties of an Octanuclear Complex with a Ring Structure, *Inorg. Chem.*, 39, 1376-1380, 2000.
- [55] V. Amani, N. Safari, and H. R. Khavasi, Solution and solid state characterization of oxo-centered trinuclear iron(III) acetate complexes $[\text{Fe}_3(\mu_3\text{-O})(\mu\text{-OAc})_6(\text{L})_3]^+$, *Spectrochimica Acta Part A: Molecular and Biomolecular Spectroscopy*, 85, 17-24, 2012.
- [56] R. D. Cannon, U. A. Jayasooriya, R. Wu, S. K. arapKoske, J. A. Stride, O. F. Nielsen, R. P. White, G. J. Kearley, and D. Summerfield, Spin Frustration in High-Spin Triiron(III) Complexes: An Inelastic Neutron Scattering Study, *J. Am. Chem. Soc.*, 116, 11869-11874, 1994.
- [57] F. E. Sowrey, C. Tilford, S. Wocadlo, C. E. Anson, A. K. Powell, S. M. Bennington, W. Montfrooij, U. A. Jayasooriya, and R. D. Cannon, Spin frustration and concealed asymmetry: structure and magnetic spectrum of $[\text{Fe}_3\text{O}(\text{O}_2\text{CPh})_6(\text{py})_3]\text{ClO}_4\cdot \text{py}$, *J. Chem. Soc., Dalton Trans.*, 862-866, 2001.
- [58] R. Wu, M. Poyraz, F. E. Sowrey, C. E. Anson, S. Wocadlo, A. K. Powell, U. A. Jayasooriya, R. D. Cannon, T. Nakamoto, M. Katada, and H. Sano, Electron Localization and Delocalization in Mixed-Valence Transition Metal Clusters: Structural and Spectroscopic Studies of Oxo-Centered Trinuclear Complexes $[\text{Fe}_3\text{O}(\text{OOCMe}_3)_6(\text{py})_3]^+/\text{O}$ and $[\text{Mn}_3\text{O}(\text{OOCMe}_3)_6(\text{py})_3]^+/\text{O}$, *Inorg. Chem.*, 37, 1913-1921, 1998.
- [59] D. N. Hendrickson, "SPIN FRUSTRATION IN POLYNUCLEAR COMPLEXES," *Research Frontiers in Magnetochemistry*, pp. 87-108: WORLD SCIENTIFIC, 1993.
- [60] R. Werner, S. Ostrovsky, K. Griesar, and W. Haase, Magnetostructural correlations in exchange coupled phenoxo-, alkoxo-, and hydroxo-bridged dinuclear iron(III) compounds, *Inorg. Chim. Acta*, 326, 78-88, 2001.
- [61] C. T. Dziobkowski, J. T. Wroblewski, and D. B. Brown, *Magnetic properties and moessbauer spectra of several iron (3) dicarboxylic acid complexes*, 1980.
- [62] J. Lang, J. M. Hewer, J. Meyer, J. Schuchmann, C. van Wüllen, and G. Niedner-Schatteburg, Magnetostructural correlation in isolated trinuclear iron(III) oxo acetate complexes, *Phys. Chem. Chem. Phys.*, 20, 16673-16685, 2018.
- [63] J. Lang, J. Mohrbach, S. Dillinger, J. M. Hewer, and G. Niedner-Schatteburg, Vibrational blue shift of coordinated N_2 in $[\text{Fe}_3\text{O}(\text{OAc})_6(\text{N}_2)_n]^+$: "non-classical" dinitrogen complexes, *Chem. Comm.*, 53, 420-423, 2017.
- [64] J. Lang, D. V. Fries, and G. Niedner-Schatteburg, Characterization of Trinuclear Oxo Bridged Cobalt Complexes in Isolation, *Z. Phys. Chem.*, 232, 649-669, 2018.
- [65] R. Colton, A. D'Agostino, and J. C. Traeger, Electrospray mass spectrometry applied to inorganic and organometallic chemistry, *Mass Spectrom. Rev.*, 14, 79-106, 1995.
- [66] J. B. Fenn, Electrospray Wings for Molecular Elephants (Nobel Lecture), *Angew. Chem. Int. Ed.*, 42, 3871-3894, 2003.
- [67] A. Langenberg, K. Hirsch, A. Ławicki, V. Zamudio-Bayer, M. Niemeyer, P. Chmiela, B. Langbehn, A. Terasaki, B. v. Issendorff, and J. T. Lau, Spin and orbital magnetic moments of size-selected iron, cobalt, and nickel clusters, *PhRvB*, 90, 184420, 2014.
- [68] J. T. Lau, A. Achleitner, H. U. Ehrke, U. Langenbuch, M. Reif, and W. Wurth, Ultrahigh vacuum cluster deposition source for spectroscopy with synchrotron radiation, *Rev. Sci. Instrum.*, 76, 063902, 2005.
- [69] J. T. Lau, A. Föhlich, R. Nietubyc, M. Reif, and W. Wurth, Size-Dependent Magnetism of Deposited Small Iron Clusters Studied by X-Ray Magnetic Circular Dichroism, *Phys. Rev. L*, 89, 057201, 2002.
- [70] V. Zamudio-Bayer, K. Hirsch, A. Langenberg, A. Ławicki, A. Terasaki, B. v. Issendorff, and J. T. Lau, Electronic ground states of Fe^{2+} and Co^{2+} as determined by x-ray absorption and x-ray magnetic circular dichroism spectroscopy, *J. Chem. Phys.*, 143, 244318, 2015.
- [71] V. Zamudio-Bayer, R. Lindblad, C. Bülow, G. Leistner, A. Terasaki, B. V. Issendorff, and J. T. Lau, Electronic ground state of Ni^{2+} , *J. Chem. Phys.*, 145, 2016.

5. Magnetic properties and their correlation to the electronics of isolated trinuclear 3d spin frustrated complexes

- [72] J.-F. Greisch, A. Ballester-Caudet, S. V. Kruppa, Z. Lei, Q.-M. Wang, C. Riehn, and F. Remacle, Gas-Phase Photoluminescence and Photodissociation of Silver-Capped Hexagold Clusters, *J. Phys. Chem. A*, 122, 5799-5810, 2018.
- [73] D. Imanbaew, Y. Nosenko, K. Chevalier, F. Rupp, C. Kerner, F. Breher, W. R. Thiel, R. Diller, and C. Riehn, "Excited-state dynamics of catalytically active transition metal complexes studied by transient photofragmentation in gas phase and transient absorption in solution," *OSA Technical Digest (online)*. p. 08.Tue.P2.28.
- [74] D. Imanbaew, Y. Nosenko, C. Kerner, K. Chevalier, F. Rupp, C. Riehn, W. R. Thiel, and R. Diller, Excited-state dynamics of a ruthenium(II) catalyst studied by transient photofragmentation in gas phase and transient absorption in solution, *Chem. Phys.*, 442, 53-61, 2014.
- [75] S. V. Kruppa, F. Bappler, C. Holzer, W. Klopper, R. Diller, and C. Riehn, Vibrational Coherence Controls Molecular Fragmentation: Ultrafast Photodynamics of the [Ag₂Cl]⁺ Scaffold, *J. Phys. Chem. Lett.*, 9, 804-810, 2018.
- [76] S. V. Kruppa, F. Bappler, W. Klopper, S. P. Walg, W. R. Thiel, R. Diller, and C. Riehn, Ultrafast excited-state relaxation of a binuclear Ag(I) phosphine complex in gas phase and solution, *Phys. Chem. Chem. Phys.*, 19, 22785-22800, 2017.
- [77] S. V. Kruppa, Y. Nosenko, M.-O. Winghart, S. P. Walg, M. M. Kappes, and C. Riehn, Fragmentation pathways of dianionic [Pt₂(μ-P₂O₅H₂)₄+X,Y]²⁻ (X,Y=H, K, Ag) species in an ion trap induced by collisions and UV photoexcitation, *Int. J. Mass spectrom.*, 395, 7-19, 2016.
- [78] S. Bornemann, O. Šipr, S. Mankovsky, S. Polesya, J. B. Staunton, W. Wurth, H. Ebert, and J. Minar, Trends in the magnetic properties of Fe, Co, and Ni clusters and monolayers on Ir(111), Pt(111), and Au(111), *Phys. Rev. B*, 86, 104436, 2012.
- [79] J. Bansmann, A. Kleibert, M. Getzlaff, A. F. Rodriguez, F. Nolting, C. Boeglin, and K.-H. Meiwes-Broer, Magnetism of 3d transition metal nanoparticles on surfaces probed with synchrotron radiation – from ensembles towards individual objects, *physica status solidi (b)*, 247, 1152-1160, 2010.
- [80] K. Baberschke, The magnetism of nickel monolayers, *Appl. Phys. A*, 62, 417-427, 1996.
- [81] M. Tischer, O. Hjortstam, D. Arvanitis, J. Hunter Dunn, F. May, K. Baberschke, J. Trygg, J. M. Wills, B. Johansson, and O. Eriksson, Enhancement of Orbital Magnetism at Surfaces: Co on Cu(100), *Phys. Rev. Lett.*, 75, 1602-1605, 1995.
- [82] J. Meyer, M. Tombers, C. van Wullen, G. Niedner-Schatteburg, S. Peredkov, W. Eberhardt, M. Neeb, S. Palutke, M. Martins, and W. Wurth, The spin and orbital contributions to the total magnetic moments of free Fe, Co, and Ni clusters, *J. of Chem. Phys.*, 143, 104302, 2015.
- [83] M. Niemeyer, K. Hirsch, V. Zamudio-Bayer, A. Langenberg, M. Vogel, M. Kossick, C. Ebrecht, K. Egashira, A. Terasaki, T. Moller, B. v. Issendorff, and J. T. Lau, Spin Coupling and Orbital Angular Momentum Quenching in Free Iron Clusters, *Phys. Rev. Lett.*, 108, 057201, 2012.
- [84] S. Peredkov, A. Savci, S. Peters, M. Neeb, W. Eberhardt, H. Kampschulte, J. Meyer, M. Tombers, B. Hofferberth, F. Menges, and G. Niedner-Schatteburg, X-ray absorption spectroscopy of mass-selected transition metal clusters using a cyclotron ion trap: An experimental setup for measuring XMCD spectra of free clusters, *J. Electron. Spectrosc. Relat. Phenom.*, 184, 113-118, 2011.
- [85] E. Stavitski, and F. M. F. de Groot, The CTM4XAS program for EELS and XAS spectral shape analysis of transition metal L edges, *Micron (Oxford, England : 1993)*, 41, 687-694, 2010.
- [86] P. Carra, B. T. Thole, M. Altarelli, and X. Wang, X-ray circular dichroism and local magnetic fields, *Phys. Rev. Lett.*, 70, 694-697, 1993.
- [87] A. D. Becke, Density-functional thermochemistry. III. The role of exact exchange, *J. Chem. Phys.*, 98, 5648-5652, 1993.
- [88] B. Miehlich, A. Savin, H. Stoll, and H. Preuss, Results obtained with the correlation energy density functionals of Becke and Lee, Yang and Parr, *Chem. Phys. Lett.*, 157, 200-206, 1989.
- [89] T. H. Dunning, Gaussian basis sets for use in correlated molecular calculations. I. The atoms boron through neon and hydrogen, *J. Chem. Phys.*, 90, 1007-1023, 1989.
- [90] M. Dolg, H. Stoll, H. Preuss, and R. M. Pitzer, Relativistic and correlation effects for element 105 (hahnium, Ha): a comparative study of M and MO (M = Nb, Ta, Ha) using energy-adjusted ab initio pseudopotentials, *J. Phys. Chem.*, 97, 5852-5859, 1993.
- [91] M. J. Frisch et. al, "Gaussian 16 Rev. C.01," 2016.
- [92] C. Piamonteze, P. Miedema, and F. M. F. de Groot, Accuracy of the spin sum rule in XMCD for the transition-metal L edges from manganese to copper, *Phys. Rev. B*, 80, 184410, 2009.

- [93] F. Bondino, C. Cepek, N. Tagmatarchis, M. Prato, H. Shinohara, and A. Goldoni, Element-Specific Probe of the Magnetic and Electronic Properties of Dy Incar-Fullerenes, *J. Phys. Chem. B*, 110, 7289-7295, 2006.
- [94] T. Jo, The 3d–4f exchange interaction, X-ray second-order optical processes and the magnetic circular dichroism (MCD) spin sum rule in rare earths, *J. Electron. Spectrosc. Relat. Phenom.*, 86, 73-82, 1997.
- [95] S. Qiao, A. Kimura, H. Adachi, K. Iori, K. Miyamoto, T. Xie, H. Namatame, M. Taniguchi, A. Tanaka, T. Muro, S. Imada, and S. Suga, Direct evidence of ferromagnetism without net magnetization observed by x-ray magnetic circular dichroism, *Phys. Rev. B*, 70, 134418, 2004.
- [96] S. Qiao, A. Kimura, H. Adachi, K. Iori, K. Miyamoto, T. Xie, H. Namatame, M. Taniguchi, A. Tanaka, T. Muro, S. Imada, and S. Suga, Temperature dependence of spin and orbital magnetic moments of Sm 4f electrons in (Sm, Gd)Al₂, *J. Electron. Spectrosc. Relat. Phenom.*, 144-147, 749-752, 2005.
- [97] Y. Teramura, A. Tanaka, and T. Jo, Effect of Coulomb Interaction on the X-Ray Magnetic Circular Dichroism Spin Sum Rule in 3 d Transition Elements, *J. Phys. Soc. Jpn.*, 65, 1053-1055, 1996.
- [98] Y. Teramura, A. Tanaka, B. T. Thole, and T. Jo, Effect of Coulomb Interaction on the X-Ray Magnetic Circular Dichroism Spin Sum Rule in Rare Earths, *J. Phys. Soc. Jpn.*, 65, 3056-3059, 1996.
- [99] J. Everett, E. Céspedes, L. R. Shelford, C. Exley, J. F. Collingwood, J. Dobson, G. van der Laan, C. A. Jenkins, E. Arenholz, and N. D. Telling, Ferrous iron formation following the co-aggregation of ferric iron and the Alzheimer's disease peptide β -amyloid (1–42), *J. Royal Soc. Interface*, 11, 20140165, 2014.
- [100] R. K. Hocking, S. DeBeer George, K. N. Raymond, K. O. Hodgson, B. Hedman, and E. I. Solomon, Fe L-edge X-ray absorption spectroscopy determination of differential orbital covalency of siderophore model compounds: electronic structure contributions to high stability constants, *J. Am. Chem. Soc.*, 132, 4006-4015, 2010.
- [101] J. K. Kowalska, A. W. Hahn, A. Albers, C. E. Schiewer, R. Bjornsson, F. A. Lima, F. Meyer, and S. DeBeer, X-ray Absorption and Emission Spectroscopic Studies of [L₂Fe₂S₂]_n Model Complexes: Implications for the Experimental Evaluation of Redox States in Iron–Sulfur Clusters, *Inorg. Chem.*, 55, 4485-4497, 2016.
- [102] J. K. Kowalska, B. Nayyar, J. A. Rees, C. E. Schiewer, S. C. Lee, J. A. Kovacs, F. Meyer, T. Weyhermüller, E. Otero, and S. DeBeer, Iron L_{2,3}-Edge X-ray Absorption and X-ray Magnetic Circular Dichroism Studies of Molecular Iron Complexes with Relevance to the FeMoco and FeVco Active Sites of Nitrogenase, *Inorg. Chem.*, 56, 8147-8158, 2017.
- [103] O. Kahn, and B. Briat, Exchange interaction in polynuclear complexes. Part 1.—Principles, model and application to the binuclear complexes of chromium(III), *J. Chem. Soc., Faraday Transactions 2: Molecular and Chemical Physics*, 72, 268-281, 1976.
- [104] G. B. Kaufman, Inorganic chemistry: principles of structure and reactivity, 4th ed. (Huheey, James E.; Keiter, Ellen A.; Keiter, Richard L.), *J. Chem. Educ.*, 70, A279, 1993.
- [105] W. Gu, H. Wang, and K. Wang, Nickel L-edge and K-edge X-ray absorption spectroscopy of non-innocent Ni[S₂C₂(CF₃)₂]_{2n} series (n = –2, –1, 0): direct probe of nickel fractional oxidation state changes, *DTr*, 43, 6406-6413, 2014.
- [106] G. S. Henderson, F. M. F. De Groot, and B. J. A. Moulton, X-ray absorption near-edge structure (XANES) spectroscopy, *Reviews in Mineralogy and Geochemistry*, 78, 75 - null, 2014.
- [107] P. J. Hay, J. C. Thibeault, and R. Hoffmann, Orbital interactions in metal dimer complexes, *J. Am. Chem. Soc.*, 97, 4884-4899, 1975.
- [108] B. T. Thole, and G. van der Laan, Branching ratio in x-ray absorption spectroscopy, *Phys. Rev. B*, 38, 3158-3171, 1988.
- [109] G. van der Laan, K. T. Moore, J. G. Tobin, B. W. Chung, M. A. Wall, and A. J. Schwartz, Applicability of the Spin-Orbit Sum Rule for the Actinide 5f₅ States, *Phys. Rev. Lett.*, 93, 097401, 2004.
- [110] G. van der Laan, and B. T. Thole, Strong magnetic x-ray dichroism in 2p absorption spectra of 3d transition-metal ions, *Phys. Rev. B*, 43, 13401-13411, 1991.
- [111] R. Ahlrichs, M. Bär, M. Häser, H. Horn, and C. Kölmel, Electronic structure calculations on workstation computers: The program system turbomole, *Chem. Phys. Lett.*, 162, 165-169, 1989.
- [112] M. Barysz, and Y. Ishikawa, *Relativistic Methods for Chemists*: Springer Netherlands, 2010.
- [113] M. L. Baker, M. W. Mara, J. J. Yan, K. O. Hodgson, B. Hedman, and E. I. Solomon, K- and L-edge X-ray absorption spectroscopy (XAS) and resonant inelastic X-ray scattering (RIXS) determination of differential orbital covalency (DOC) of transition metal sites, *Coord. Chem. Rev.*, 345, 182-208, 2017.
- [114] D. Drevon, M. Görlin, P. Chernev, L. Xi, H. Dau, and K. M. Lange, Uncovering The Role of Oxygen in Ni-Fe(OxHy) Electrocatalysts using In situ Soft X-ray Absorption Spectroscopy during the Oxygen Evolution Reaction, *Scientific Reports*, 9, 1532, 2019.

5. Magnetic properties and their correlation to the electronics of isolated trinuclear 3d spin frustrated complexes

- [115] R. K. Hocking, E. C. Wasinger, Y.-L. Yan, F. M. F. deGroot, F. A. Walker, K. O. Hodgson, B. Hedman, and E. I. Solomon, Fe L-Edge X-ray Absorption Spectroscopy of Low-Spin Heme Relative to Non-heme Fe Complexes: Delocalization of Fe d-Electrons into the Porphyrin Ligand, *J. Am. Chem. Soc.*, 129, 113-125, 2007.
- [116] R. F. W. Bader, A quantum theory of molecular structure and its applications, *Chem. Rev.*, 91, 893-928, 1991.

5.10 Supplementary material

Magnetic properties and their correlation of the electronic ground states of isolated trinuclear 3d spin frustrated complexes

Michael Lembach^a, Johannes Lang, Maximilian Luczak^a, Yannick Mees^a, Roumany Israil^a, Vicente Zamudio-Bayer^{b,c}, Martin Timm^b, Christine Bülow^{b,c}, Bernd von Issendorff^c, Akira Terasaki^d, Christoph Riehn^a, Tobias Lau^{b,c} and Gereon Niedner-Schatteburg^a

(a) Fachbereich Chemie and Forschungszentrum OPTIMAS, Kaiserslautern, Germany

(b) Institut für Methoden und Instrumentierung der Forschung mit Synchrotronstrahlung, Helmholtz-Zentrum Berlin für Materialien und Energie, Berlin, Germany

(c) Physikalisches Institut, Universität Freiburg, Germany

(d) Department of Chemistry, Kyushu University, Fukuoka, Japan

Content

Fig. S1: (a) Example of an XMCD spectrum and its integral over both $L_{3,2}$ absorption (b) Integrated sum of both XA spectra for both photon helicities in the case of $[\text{Fe}_3\text{O}(\text{OAc})_6(\text{py})_2]^+$.

Fig. S2: Mass spectra of $[\text{Fe}_3\text{O}(\text{OAc})_6(\text{py})_n]^+$ ($n = 0, 1, 2, 3$) with stepwise coordinated pyridine 538 m/z ($n = 0$), 616 m/z ($n = 1$), 694 m/z ($n = 2$) and 775 m/z ($n = 3$).

Fig. S3: Carbon K-edge of $[\text{Fe}_3\text{O}(\text{OAc})_6(\text{py})_n]^+$ ($n = 2$) to verify that the selected mass is the complex of interest.

Fig. S4: Experimental polarized depended XA Spectra (top), sum XA spectra with integral (middle) and XMCD spectra with integral (Bottom) for $[\text{Fe}_3\text{O}(\text{OAc})_6(\text{py})_n]^+$ ($n = 0, 1, 2, 3$) at 4 K.

Fig. S5: Sum of positive and negative XA spectra (black) of $[\text{Fe}_3\text{O}(\text{OAc})_6(\text{py})_n]^+$ ($n = 0, 1, 2, 3$) at 4 K. The shaded areas represent the two-step functions subtracted after normalization, approximating the direct 2p photo ionization and $2p \rightarrow nd$ ($n > 3$) contributions.

Fig.S6: Spin magnetic moments (blue), orbital magnetic moments (red), total magnetic moments (orange), and the spin-orbital ratio (green) per atom of $[\text{Fe}_3\text{O}(\text{OAc})_6(\text{py})_n]^+$ ($n = 0, 1, 2, 3$) with given spectra from the sum rule analysis and uncertainties of 20 %.

Fig. S7: Normalized negative polarized XA spectra of $[\text{Fe}_3\text{O}(\text{OAc})_6(\text{py})_n]^+$ ($n = 0, 1, 2, 3$) in blue with gauss folded (broadening 0.2) simulated XA spectra of a Fe^{3+} atom in a octahedral ($0 \text{ Dq} = 1.88$ ($n = 0$), 1.82 ($n = 1$), 1.81 ($n = 2$) and 1.86 ($n = 3$) eV) coordination (black dotted) and stick spectra (black) by CTM4XAS and Cowan batch file.

Fig. S8: Atom distances ($\text{Fe}-\text{O}_{\text{central}}$ and $\text{Fe}-\text{Fe}$ distances, all in Å) of the Fe_3O -core in $[\text{Fe}_3\text{O}(\text{OAc})_6(\text{py})_n]^+$ ($n = 0, 1, 2, 3$). The calculations were performed at the B3LYP-Gaussian/cc-pVTZ (H, C, N, O) and ecp-10-mdf (Fe) level of theory with five unpaired electrons on each Fe center and a UUD ($n = 0, 1, 3$) or DUU ($n = 2$) broken symmetry configuration corresponding to the minimum structures. The Ligand is omitted for clarity.

Fig. S9: Calculated Natural Atomic orbitals (NAOs) of $[\text{Fe}_3\text{O}(\text{OAc})_6(\text{py})_n]^+$ ($n = 0, 1, 2, 3$) with their associated $\text{Fe}-\text{O}-\text{Fe}-\text{py}_n$ angles. The calculations were performed with Gaussian 09 at the B3LYP/cc-pVTZ (H, C, N, O) and ecp-10-mdf (Fe) level of theory. Hydrogen and ligand are omitted for clarity.

Fig. S10: Spin orbit coupling of the core hole for $[\text{Fe}_3\text{O}(\text{OAc})_6(\text{py})_n]^+$ ($n = 0, 1, 2, 3$) with their associated $\text{Fe}-\text{O}-\text{Fe}-\text{py}_n$ angle (top) and bonding length of the coordinated Fe center (bottom).

Fig. S11: Electron localized field (ELF), differential overlap region interaction (DORI), and non-covalent interactions (NCI) in $[\text{Fe}_3\text{O}(\text{OAc})_6(\text{py})_n]^+$ ($n = 0, 1, 2, 3$) The calculations were performed at the B3LYP/cc-pVTZ (H, C, N, O) and ecp-10-mdf (Fe) level of theory with five unpaired electrons on the Fe.

Fig. S12: Approximated metal d character with differential orbital covalency approach for the complexes with the general structure $[\text{Fe}_3\text{O}(\text{OAc})_6(\text{py})_n]^+$ $n = 0$ (red circle), $n = 1$ (orange triangle), $n = 2$ (blue hexagon), $n = 3$ (green square)) with a derivation of 100 % metal d character slope of known values from a Fe film and $\text{Fe}(\text{pha})_3$.

Fig. S13: Photon dissociation mass spectra of $[\text{Fe}_3\text{O}(\text{OAc})_6(\text{py})_n]^+$ ($n = 0, 1, 2, 3$) with their associated fragmentation channels. From top to bottom with increasing coordination of pyridine.

Fig. S14: UVPD spectra of $[\text{Fe}_3\text{O}(\text{OAc})_6(\text{py}_n)]^+$ ($n = 0, 1, 2, 3$) with their corresponding minimum structure. The calculations were performed with Gaussian 09 at the B3LYP/cc-pVTZ (H, C, N, O) and ecp-10-mdf (Fe) level of theory. H atoms are omitted for clarity.

Fig. S15: UVPD spectra of $[\text{Fe}_3\text{O}(\text{OAc})_6(\text{py}_n)]^+$ ($n = 0, 1, 2, 3$) in around 470 nm in comparison with calculated UV/VIS spectra. The calculations were performed with Gaussian 09 at the B3LYP/ cc-pVTZ (H, C, N, O) and ecp-10-mdf (Fe) level of theory.

Fig. S16: Calculated orbital energies of the different transitions at around 470 nm (black) and around 300 nm (blue) of $[\text{Fe}_3\text{O}(\text{OAc})_6(\text{py}_n)]^+$ ($n = 0, 1, 2, 3$). The calculations were performed with Gaussian 09 at the B3LYP/cc-pVTZ (H, C, N, O) and ecp-10-mdf (Fe) level of theory.

Fig. S17: Calculated HOMO-LUMO gaps of $[\text{Fe}_3\text{O}(\text{OAc})_6(\text{py}_n)]^+$ ($n = 0, 1, 2, 3$) corresponding to their associated Fe-O-Fe- py_n angles. The calculations were performed with Gaussian 09 at the B3LYP/cc-pVTZ (H, C, N, O) and ecp-10-mdf (Fe) level of theory.

Fig. S18: Derivated XA spectra of the L_3 edge (top) and UVPD spectra (bottom) of $[\text{Fe}_3\text{O}(\text{OAc})_6(\text{py})_n]^+$ ($n = 0, 1, 2, 3$) in isolation.

Fig. S19: Absorption maxima of the L_3 edge from the experimental XA spectra and their associated absorption maxima from the UVPD spectra of $[\text{Fe}_3\text{O}(\text{OAc})_6(\text{py})_n]^+$ ($n = 0, 1, 2, 3$) in isolation.

Fig. S20: Experimental energy shifts from the UVPD and XA spectra of $[\text{Fe}_3\text{O}(\text{OAc})_6(\text{py})_n]^+$ ($n = 0, 1, 2, 3$) in isolation.

Fig. S21: Experimental energy shifts from the UVPD and XA spectra of $[\text{Fe}_3\text{O}(\text{OAc})_6(\text{py})_n]^+$ ($n = 0, 1, 2, 3$) in isolation in comparison with the calculated Fe-O-Fe-py angle. The calculations were performed at the B3LYP-Gaussian/cc-pVTZ (H, C, N, O) and ecp-10-mdf (Fe) level of theory with five unpaired electrons on each Fe center.

Fig. S22: Experimental energy shifts from the UVPD, IR(M)PD, and XA spectra of $[\text{Fe}_3\text{O}(\text{OAc})_6(\text{py})_n]^+$ ($n = 0, 1, 2, 3$) in isolation in comparison with the calculated orbital energies for the transition in the XA spectra. The calculations were performed at the B3LYP-Gaussian/cc-pVTZ (H, C, N, O) and ecp-10-mdf (Fe) level of theory with five unpaired electrons on each Fe center.

Fig. S23: Experimental energy shifts from the UVPD, IR(M)PD, and XA spectra of $[\text{Fe}_3\text{O}(\text{OAc})_6(\text{py})_n]^+$ ($n = 0, 1, 2, 3$) in isolation in comparison with the experimental $m_j^{(z)}$. The calculations were performed at the B3LYP-Gaussian/cc-pVTZ (H, C, N, O) and ecp-10-mdf (Fe) level of theory with five unpaired electrons on each Fe center.

Tab. S1: Calculated bonding lengths and angles for $[\text{Fe}_3\text{O}(\text{OAc})_6(\text{L})_n]^+$ ($n = 0, 1, 2, 3$; L = Nitrogen, Dimethylformamide (DMF), pyridine). The calculations were performed at the B3LYP/cc-pVTZ (H, C, N, O) and ecp-10-mdf (Fe) level of theory with a high spin state for each Fe corresponding to the minimum structure.

Fig. S24: Non covalent interactions of $[\text{Fe}_3\text{O}(\text{OAc})_6(\text{L})_1]^+$ (L = Nitrogen, Dimethylformamide, pyridine). Calculations were performed at the B3LYP/cc-pVTZ (H, C, N, O) and ecp-10-mdf (Fe) level of theory with five unpaired electrons on each Fe center.

Tab. S2: Calculated bonding lengths and angles for $[\text{Fe}_3\text{O}(\text{L})_6(\text{py})_n]^+$ ($n = 0, 1, 2, 3$; L = acetate, propionic acid, benzoic acid). The calculations were performed at the B3LYP/cc-pVTZ (H, C, N, O) and ecp-10-mdf (Fe) level of theory with a high spin state for each Fe corresponding to the minimum structure.

Fig. S25: Electron localized field plots of $[\text{Fe}_3\text{M}(\text{OAc})_6(\text{py})_n]^+$ ($n = 0, 1, 2, 3$; M = O, C, S). Calculations were performed at the B3LYP-Gaussian/cc-pVTZ (H, C, N, O) and ecp-10-mdf (Fe) level of theory with five unpaired electrons on each Fe center.

Fig. S26: Tanabe Sugano diagram of a Fe^{3+} octahedral system with high spin configuration and the CF splittings from the XAS spectra with the transition of the UV/VIS spectra of $[\text{Fe}_3\text{O}(\text{OAc})_6(\text{py})_n]^+$ ($n = 0, 1, 2, 3$) in isolation.

Fig. S27: Density overlap region indicator plots of $[\text{Fe}_3\text{O}(\text{OAc})_6(\text{L})_1]^+$ (L = Nitrogen, Dimethylformamide, pyridine). Calculations were performed at the B3LYP-Gaussian/cc-pVTZ (H, C, N, O) and ecp-10-mdf (Fe) level of theory with five unpaired electrons on each Fe center.

Tab. S3: Atom coordinates for $[\text{Fe}_3\text{O}(\text{OAc})_6(\text{py})_n]^+$ ($n = 0$). The calculation was performed at the B3LYP/cc-pVTZ (H, C, N, O) and ecp-10-mdf (Fe) level of theory with a high spin state for each Fe center.

Tab. S4: Atom coordinates for $[\text{Fe}_3\text{O}(\text{OAc})_6(\text{py})_n]^+$ ($n = 1$). The calculation was performed at the B3LYP/cc-pVTZ (H, C, N, O) and ecp-10-mdf (Fe) level of theory with a high spin state for each Fe center.

Tab. S5: Atom coordinates for $[\text{Fe}_3\text{O}(\text{OAc})_6(\text{py})_n]^+$ ($n = 2$). The calculation was performed at the B3LYP/cc-pVTZ (H, C, N, O) and ecp-10-mdf (Fe) level of theory with a high spin state for each Fe center.

Tab. S6: Atom coordinates for $[\text{Fe}_3\text{O}(\text{OAc})_6(\text{py})_n]^+$ ($n = 3$). The calculation was performed at the B3LYP/cc-pVTZ (H, C, N, O) and ecp-10-mdf (Fe) level of theory with a high spin state for each Fe center.

Fig. S28: calculated HOMO-, LUMO energies and their resulted HOMO-LUMO gap for $[\text{Fe}_3\text{O}(\text{OAc})_6(\text{py})_n]^+$ ($n = 0, 1, 2, 3$). The calculations were performed at the B3LYP/cc-pVTZ (H, C, N, O) and ecp-10-mdf (Fe) level of theory with a high spin state for each Fe center.

Fig. S29: Calculated alpha spin orbital for the d orbitals in $[\text{Fe}_3\text{O}(\text{OAc})_6(\text{py})_n]^+$ ($n = 0, 1, 2, 3$). The calculations were performed with Gaussian 09 at the B3LYP/cc-pVTZ (H, C, N, O) and ecp-10-mdf (Fe) level of theory.

Fig. S30: Integrated intensities of the experimental XMCD spectra and their corresponding derivated 3d holes for $[\text{Fe}_3\text{O}(\text{OAc})_6(\text{py})_n]^+$ ($n = 0, 1, 2, 3$).

Fig. S31: Calculated susceptibilities for $[\text{Fe}_3\text{O}(\text{OAc})_6(\text{py})_n]^+$ ($n = 0, 1, 2, 3$) with their corresponding transition orbital energies (top), Fe-O-Fe-py angle (middle), and their total spin magnetic moments (bottom).

Fig. S32: Calculated HOMO, LUMO energies, and the HOMO-LUMO gap of $[\text{Fe}_3\text{O}(\text{OAc})_6(\text{py})_n]^+$ ($n = 0, 1, 2, 3$). The calculations were performed with Gaussian 09 at the B3LYP/cc-pVTZ (H, C, N, O) and ecp-10-mdf (Fe) level of theory.

Fig. S33: Calculated electron localized field for $[\text{Fe}_3\text{O}(\text{OAc})_6(\text{py})_n]^+$ ($n = 0, 1, 2, 3$) of the central oxygen atom. The calculations were performed with Gaussian 09 at the B3LYP/cc-pVTZ (H, C, N, O) and ecp-10-mdf (Fe) level of theory.

Fig. S34: Maxima of the different absorption bands and calculated HOMO-LUMO gaps of $[\text{Fe}_3\text{O}(\text{OAc})_6(\text{py}_n)]^+$ ($n = 0, 1, 2, 3$). The calculations were performed with Gaussian 09 at the B3LYP/cc-pVTZ (H, C, N, O) and ecp-mdf (Fe) level of theory.

Fig. S35: Single fragment evaluation of the Ultra Violet Photon Dissociation mass spectra of $[\text{Fe}_3\text{O}(\text{OAc})_6(\text{py}_n)]^+$ ($n = 0, 1, 2, 3$) in the region of 240 nm–580 nm with a constant laser power of 2 μJ / pulse.

Fig. S36: Derivated XA spectra of the L_3 edge (top) and UV/VIS spectra (middle) and IR(M)PD spectra(bottom) of $[\text{Fe}_3\text{O}(\text{OAc})_6(\text{py}_n)]^+$ ($n = 0, 1, 2, 3$) in isolation.

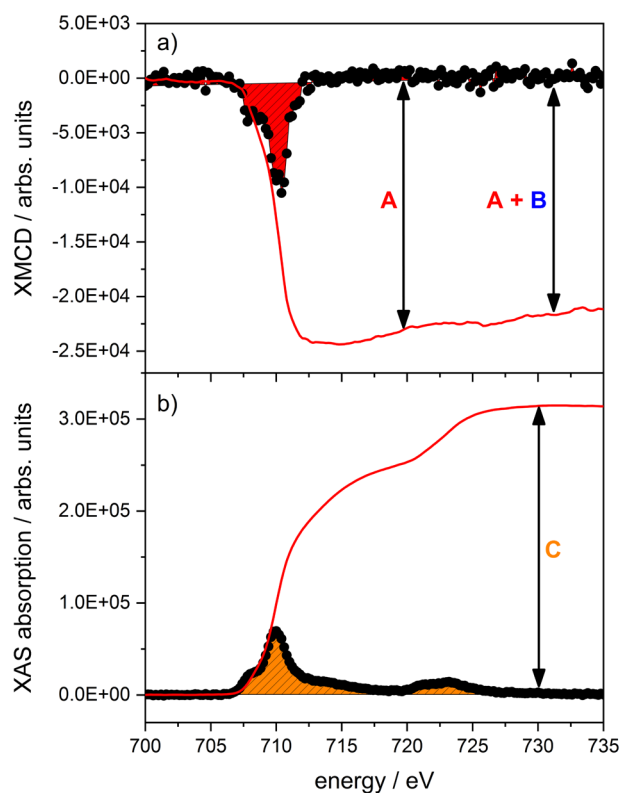


Fig. S1: (a) Example of an XMCD spectrum and its integral over both $L_{3,2}$ absorption (b) Integrated sum of both XA spectra for both photon helicities in the case of $[\text{Fe}_3\text{O}(\text{OAc})_6(\text{py})_2]^+$.

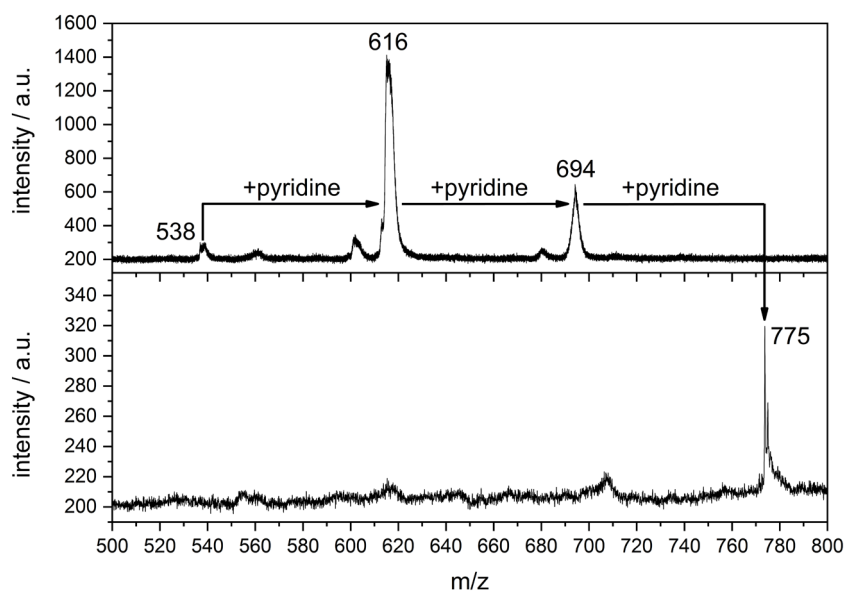


Fig. S2: Mass spectra of $[\text{Fe}_3\text{O}(\text{OAc})_6(\text{py})_n]^+$ ($n = 0, 1, 2, 3$) with stepwise coordinated pyridine 538 m/z ($n = 0$), 616 m/z ($n = 1$), 694 m/z ($n = 2$) and 775 m/z ($n = 3$).

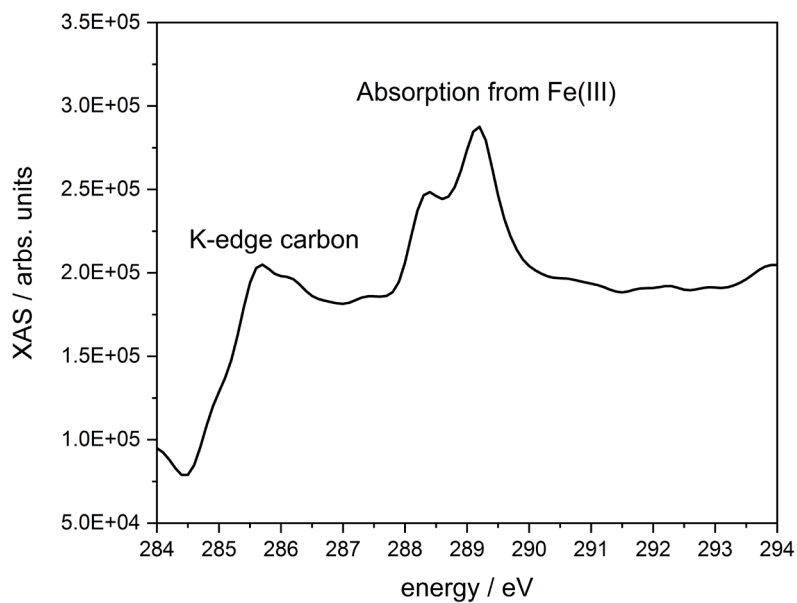


Fig. S3: Carbon K-edge of $[\text{Fe}_3\text{O}(\text{OAc})_6(\text{py})_n]^+$ ($n = 2$) to verify that the selected mass is the complex of interest.

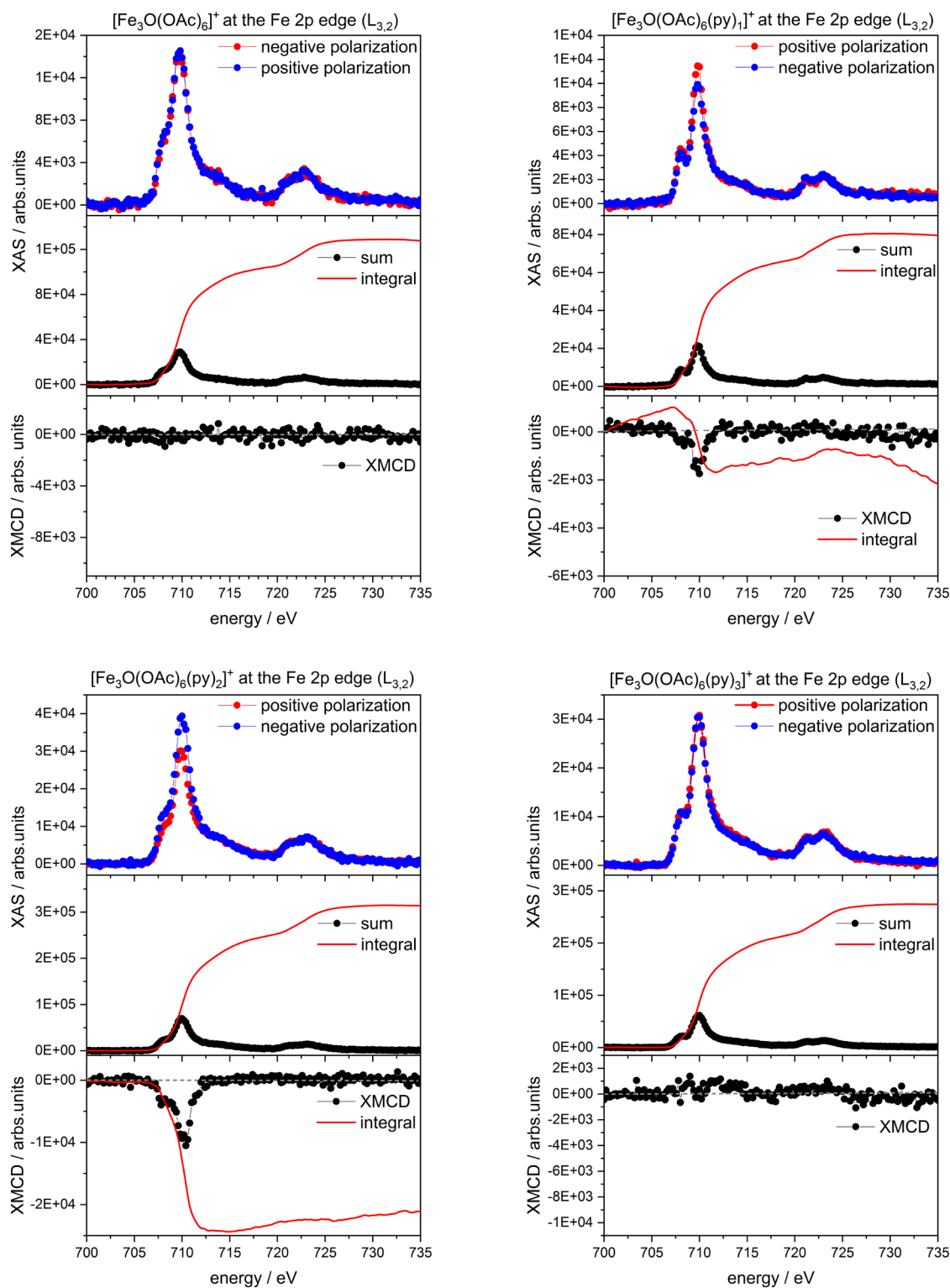


Fig. S4: Experimental polarized depended XA Spectra (top), sum XA spectra with integral (middle) and XMCD spectra with integral (Bottom) for $[\text{Fe}_3\text{O}(\text{OAc})_6(\text{py})_n]^+$ ($n = 0, 1, 2, 3$) at 4 K.

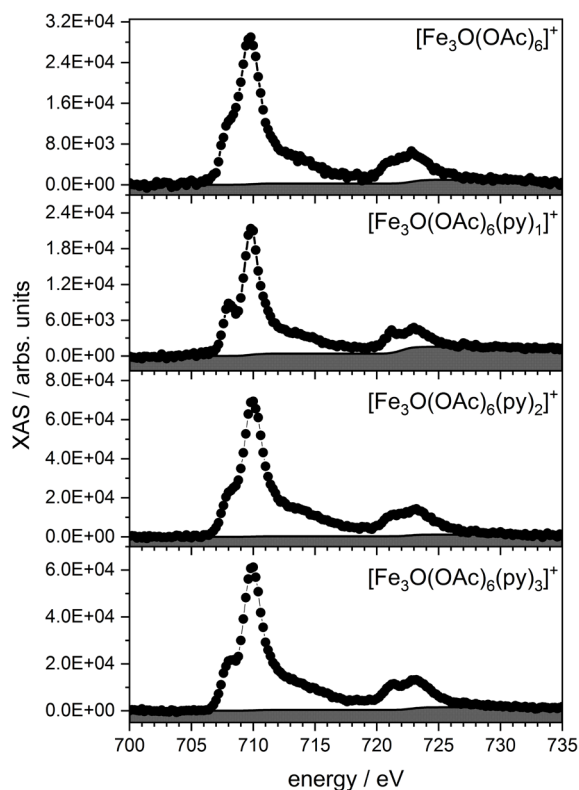


Fig. S5: Sum of positive and negative XA spectra (black) of $[\text{Fe}_3\text{O}(\text{OAc})_6(\text{py})_n]^+$ ($n = 0, 1, 2, 3$) at 4 K. The shaded areas represent the two-step functions subtracted after normalization, approximating the direct 2p photoionization and $2p \rightarrow nd$ ($n > 3$) contributions.

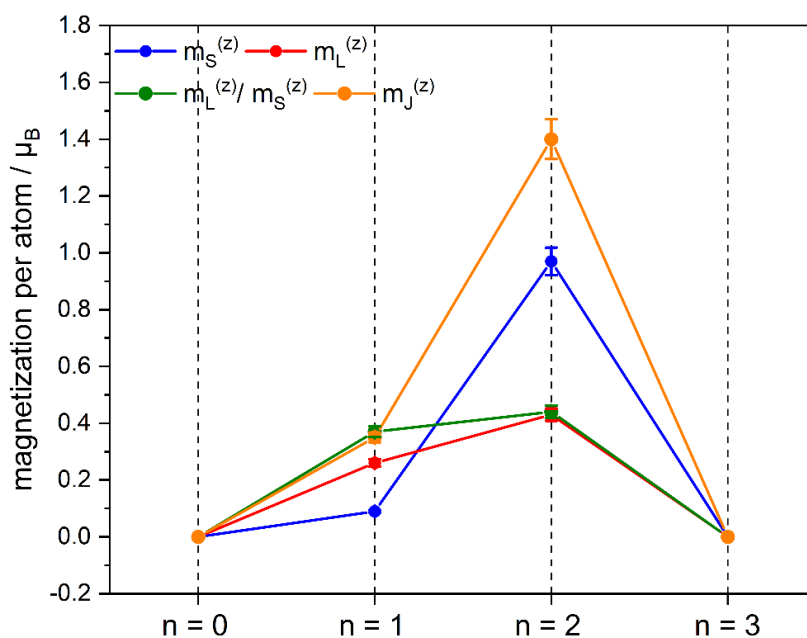


Fig. S6: Spin magnetic moments (blue), orbital magnetic moments (red), total magnetic moments (orange), and the spin-orbital ratio (green) per atom of $[\text{Fe}_3\text{O}(\text{OAc})_6(\text{py})_n]^+$ ($n = 0, 1, 2, 3$) with given spectra from the sum rule analysis and uncertainties of 5 %.

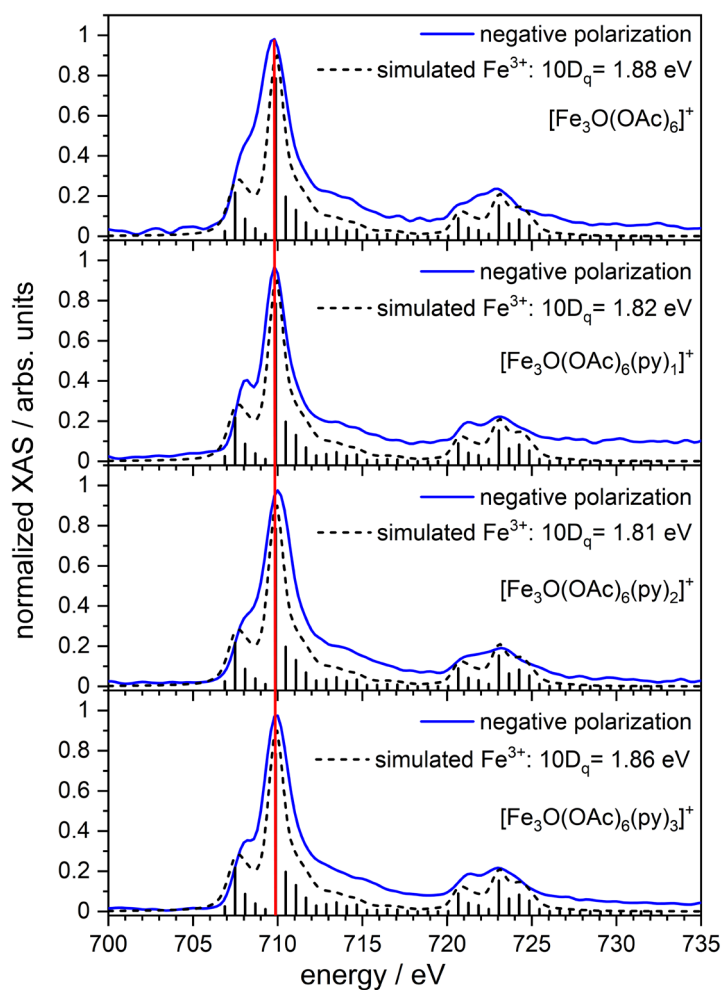


Fig. S7: Normalized negative polarized XA spectra of $[\text{Fe}_3\text{O}(\text{OAc})_6(\text{py})_n]^+$ ($n = 0, 1, 2, 3$) in blue with gauss folded (broadening 0.2) simulated XA spectra of a Fe^{3+} atom in a octahedral ($10 Dq = 1.88$ ($n=0$), 1.82 ($n=1$), 1.81 ($n=2$) and 1.86 ($n=3$) eV) coordination (black dotted) and stick spectra (black) by CTM4XAS and Cowan batch file.

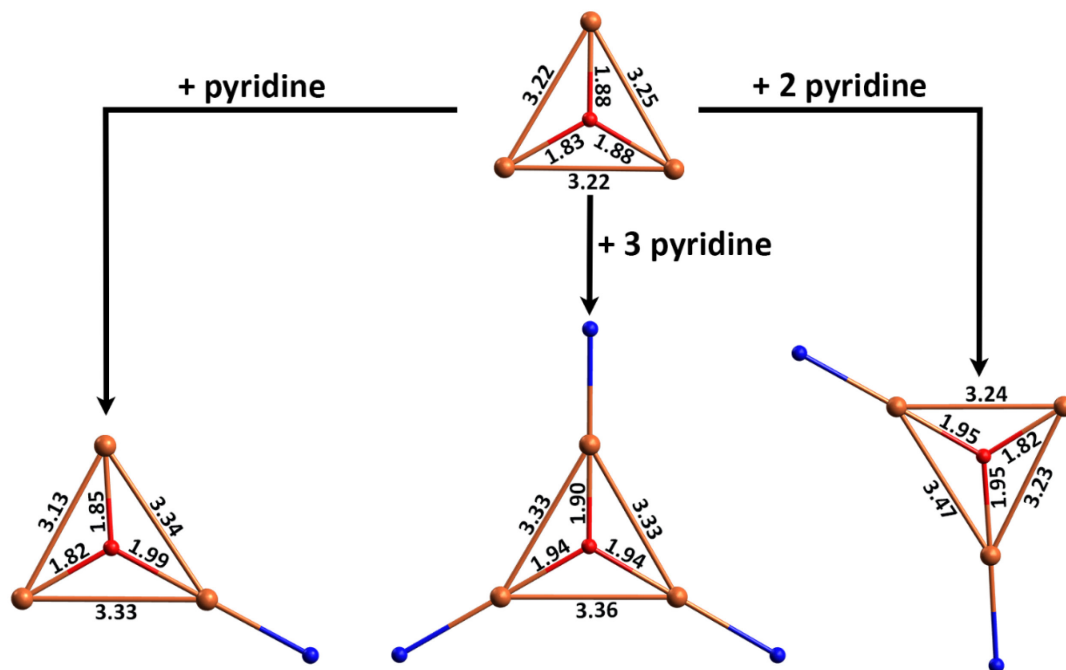


Fig. S8: Atom distances Fe–O_{central} and Fe–Fe distances, all in Å of the Fe₃O-core in [Fe₃O(OAc)₆(py)_n]⁺ (n = 0, 1, 2, 3). The calculations were performed at the B3LYP-Gaussian/cc-pVTZ (H, C, N, O) and ecp-10-mdf (Fe) level of theory with five unpaired electrons on each Fe center and a UUD (n = 0, 1, 3) or DUU (n = 2) broken symmetry configuration corresponding to the minimum structures. The Ligand is omitted for clarity.

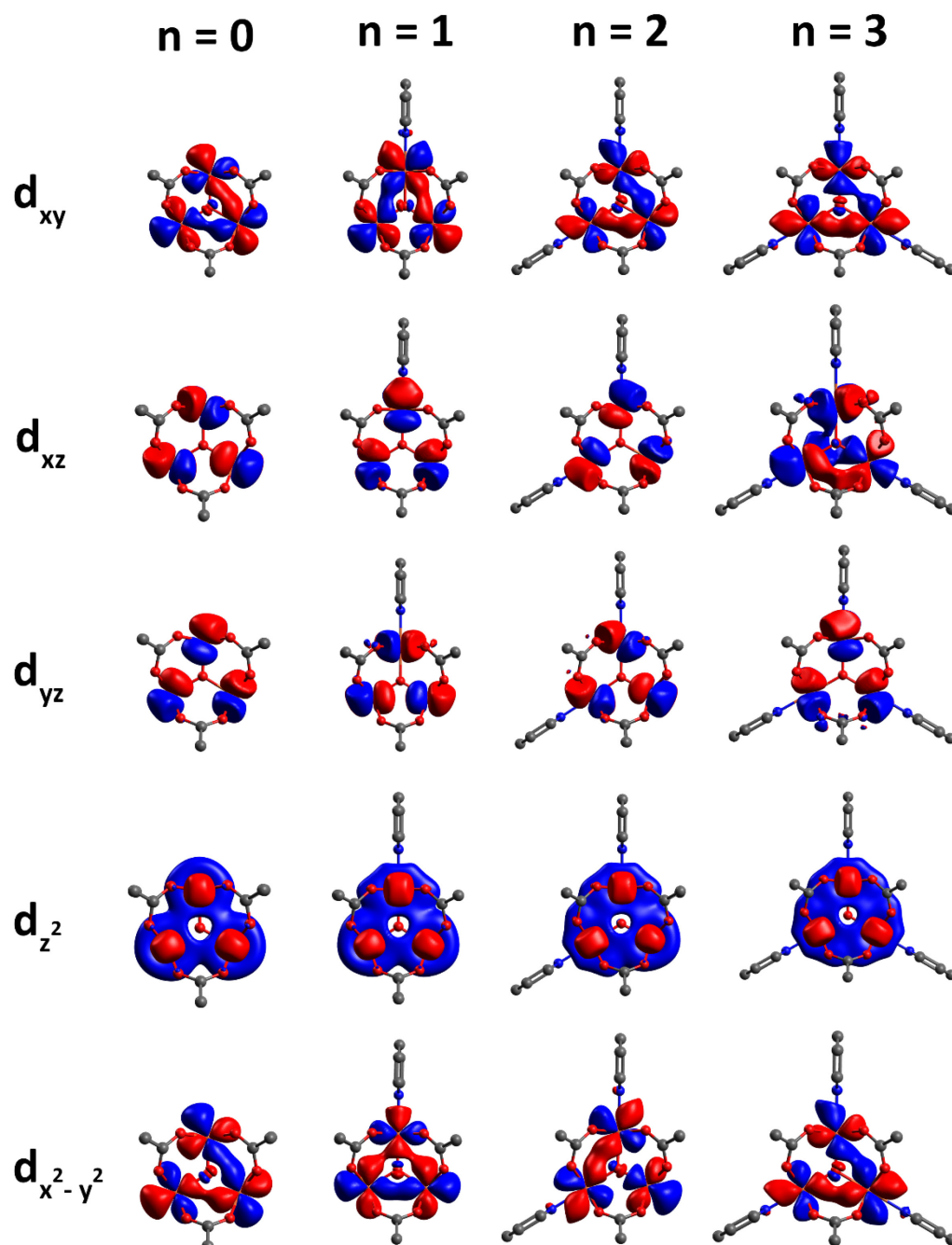


Fig. S9: Calculated Natural Atomic orbitals (NAOs) of $[\text{Fe}_3\text{O}(\text{OAc})_6(\text{py})_n]^+$ ($n = 0, 1, 2, 3$) with their associated Fe-O-Fe- py_n angles. The calculations were performed with Gaussian 09 at the B3LYP/cc-pVTZ (H, C, N, O) and ecp-10-mdf (Fe) level of theory. Hydrogen and ligand are omitted for clarity.

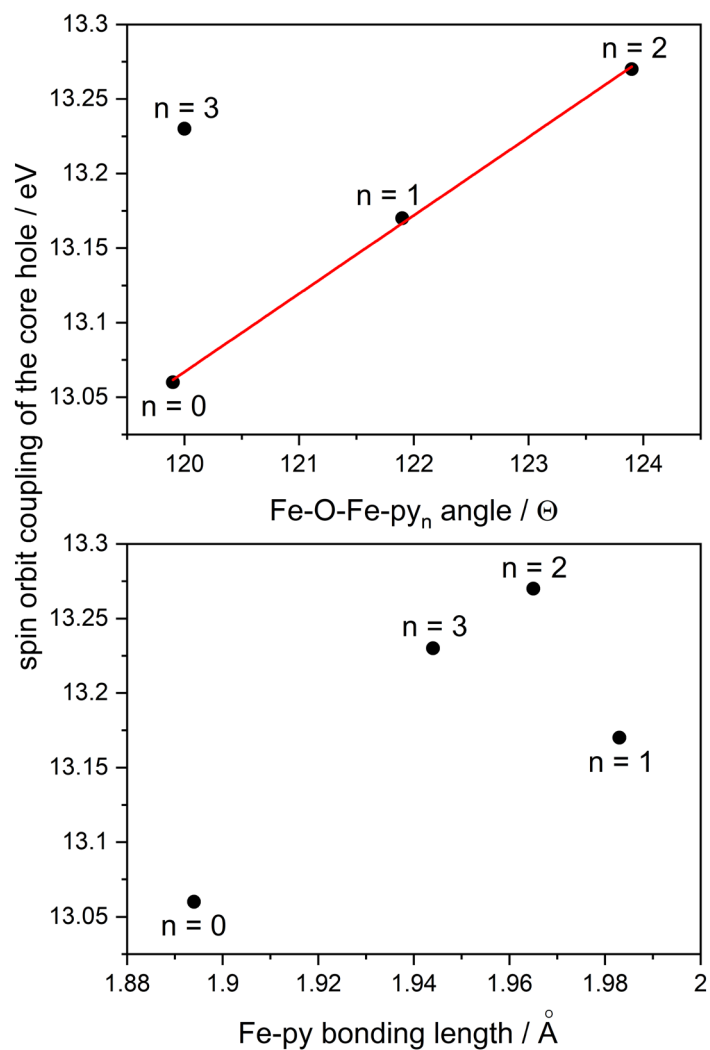


Fig. S10: Spin orbit coupling of the core hole for $[\text{Fe}_3\text{O}(\text{OAc})_6(\text{py})_n]^+$ ($n = 0, 1, 2, 3$) with their associated Fe-O-Fe-py_n angle (top) and bonding length of the coordinated Fe center (bottom).

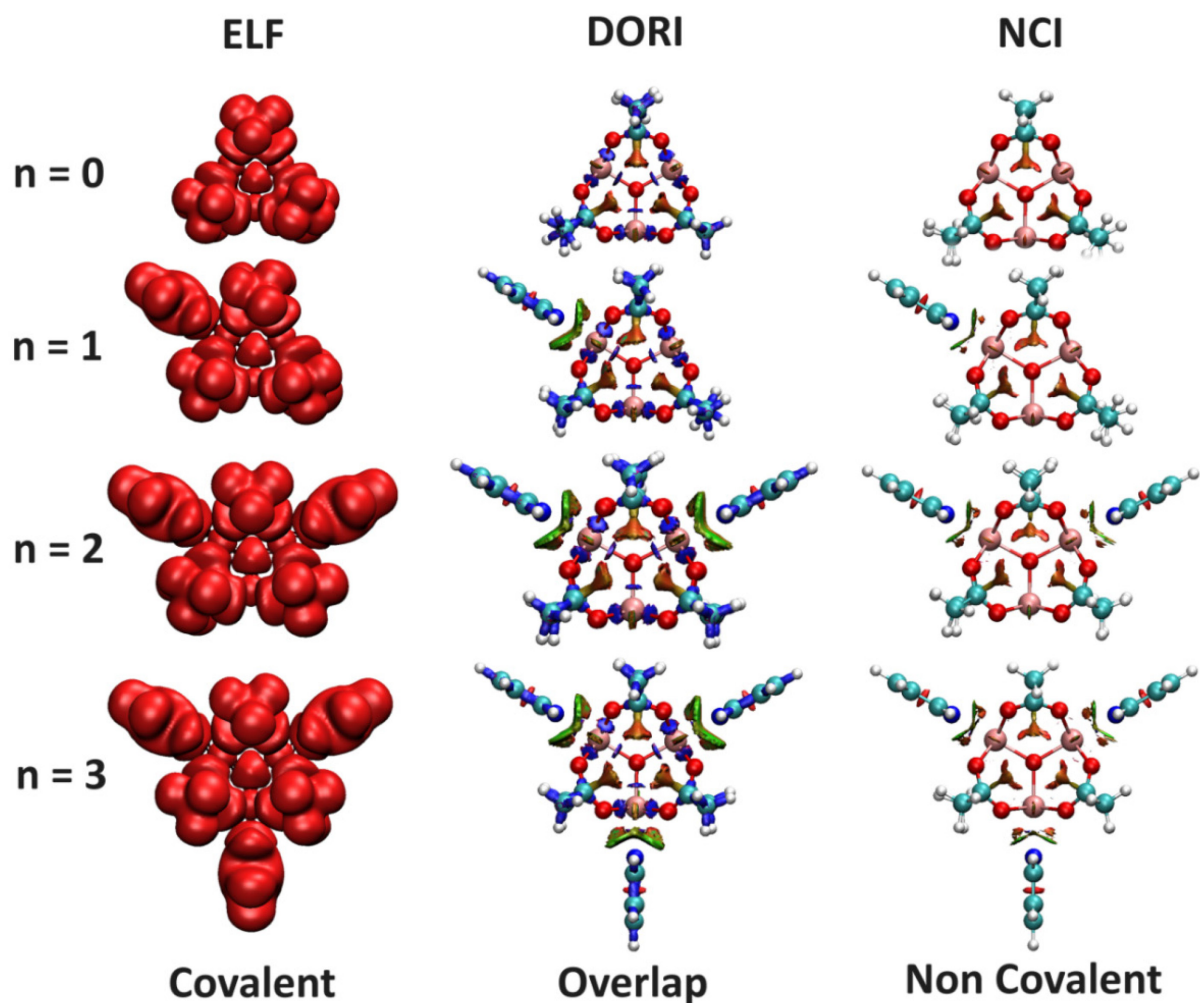


Fig. S11: Electron localized field (ELF), differential overlap region interaction (DORI), and Non covalent interactions (NCI) in $[\text{Fe}_3\text{O}(\text{OAc})_6(\text{py})_n]^+$ ($n = 0, 1, 2, 3$) The calculations were performed at the B3LYP/cc-pVTZ (H, C, N, O) and ecp-10-mdf (Fe) level of theory with five unpaired electrons on the Fe.

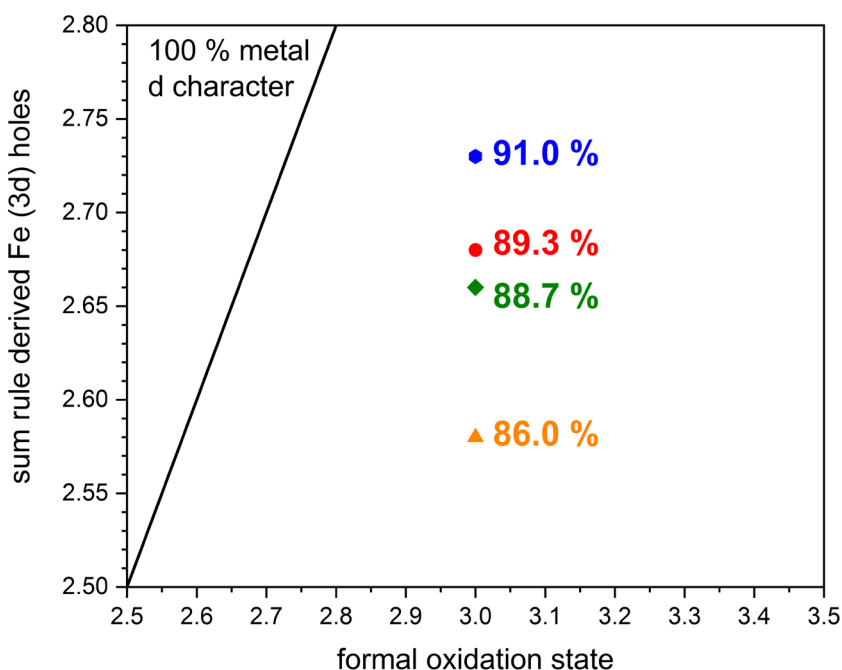


Fig. S12: Approximated metal d character with differential orbital covalency approach for the complexes with the general structure $[\text{Fe}_3\text{O}(\text{OAc})_6(\text{py})_n]^+$ ($n = 0$ (red circle), $n = 1$ (orange triangle), $n = 2$ (blue hexagon), $n = 3$ (green square)) with a derivation of 100 % metal d character slope of known values from a Fe film and $\text{Fe}(\text{pha})_3$.

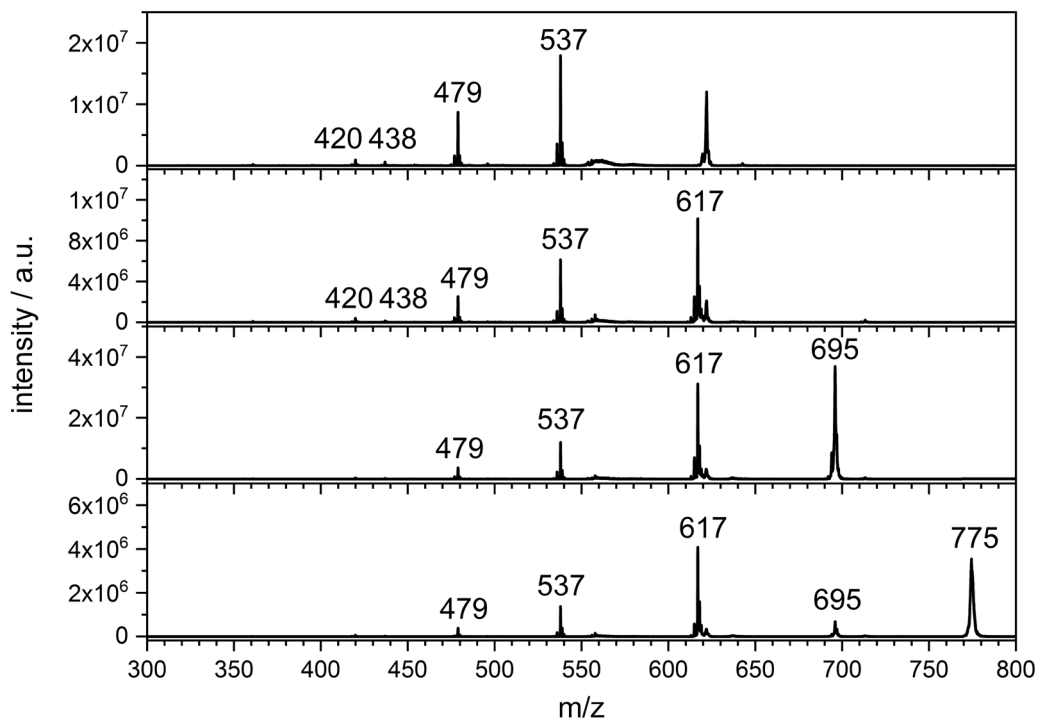


Fig. S13: Photon dissociation mass spectra of $[\text{Fe}_3\text{O}(\text{OAc})_6(\text{py})_n]^+$ ($n = 0, 1, 2, 3$) with their associated fragmentation channels. From top to bottom with increasing coordination of pyridine.

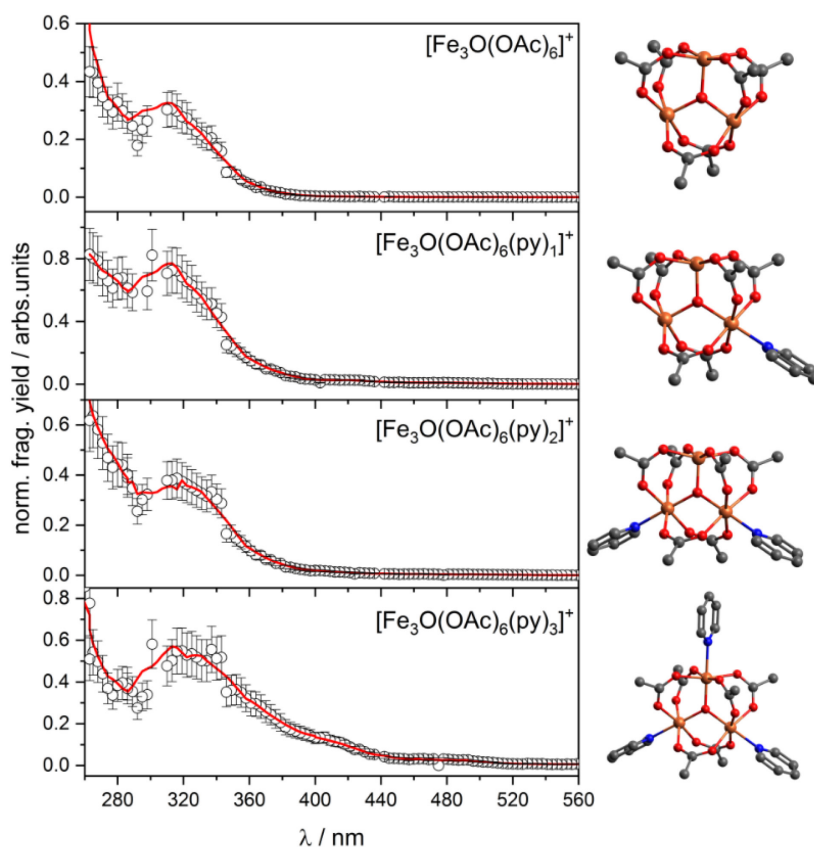


Fig. S14: UVPD spectra of $[\text{Fe}_3\text{O}(\text{OAc})_6(\text{py})_n]^+$ ($n = 0, 1, 2, 3$) with their corresponding minimum structure. The calculations were performed with Gaussian 09 at the B3LYP/cc-pVTZ (H, C, N, O) and ecp-10-mdf (Fe) level of theory. Hydrogen atoms are omitted for clarity.

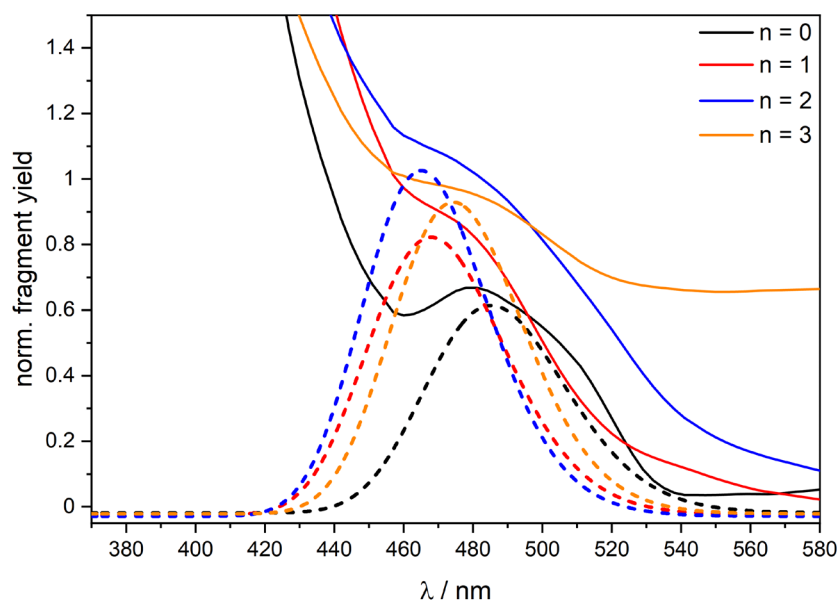


Fig. S15: UVPD spectra of $[\text{Fe}_3\text{O}(\text{OAc})_6(\text{py})_n]^+$ ($n = 0, 1, 2, 3$) in around 470 nm in comparison with calculated UV/VIS spectra. The calculations were performed with Gaussian 09 at the B3LYP/cc-pVTZ (H, C, N, O) and ecp-10-mdf (Fe) level of theory.

5. Magnetic properties and their correlation to the electronics of isolated trinuclear 3d spin frustrated complexes

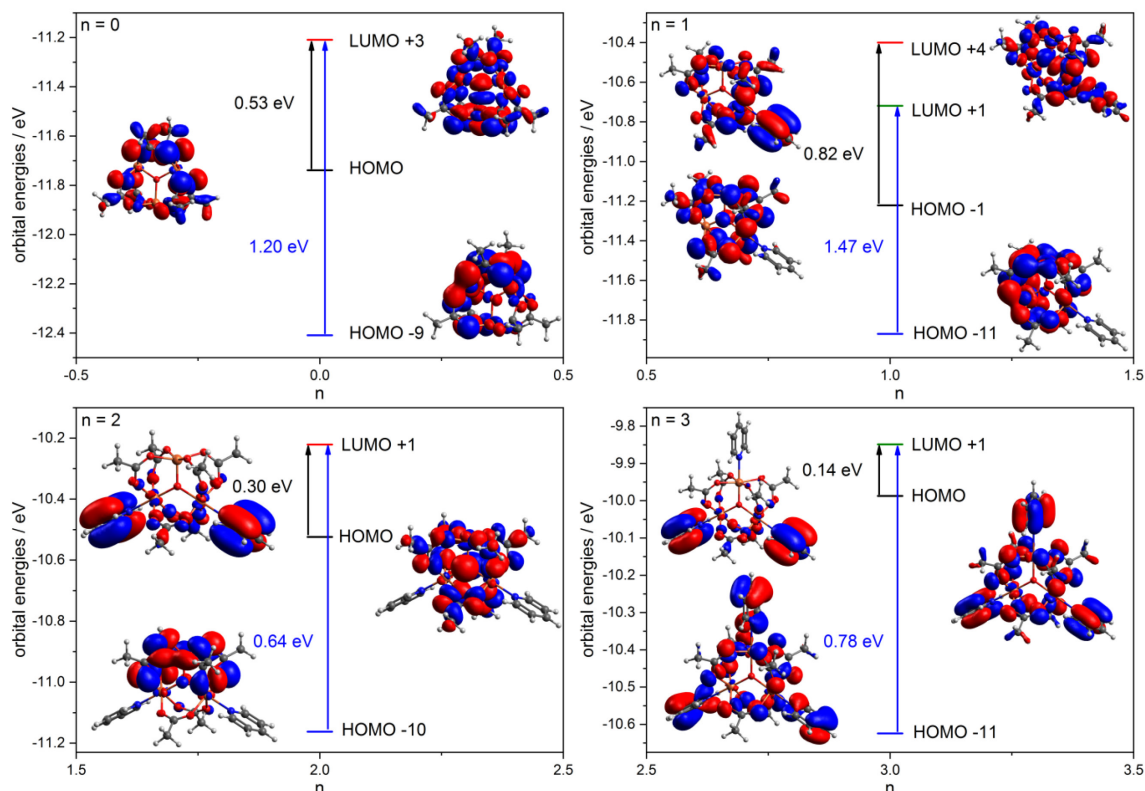


Fig. S16: Calculated orbital energies of the different transitions at around 470 nm (black) and around 300 nm (blue) of $[\text{Fe}_3\text{O}(\text{OAc})_6(\text{py}_n)]^+$ ($n = 0, 1, 2, 3$). The calculations were performed with Gaussian 09 at the B3LYP/cc-pVTZ (H, C, N, O) and ecp-10-mdf (Fe) level of theory.

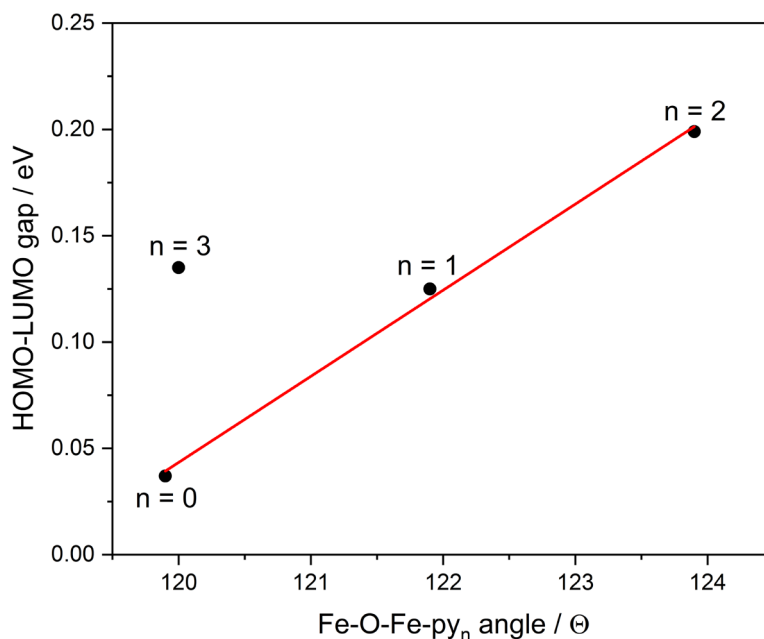


Fig. S17: Calculated HOMO-LUMO gaps of $[\text{Fe}_3\text{O}(\text{OAc})_6(\text{py}_n)]^+$ ($n = 0, 1, 2, 3$) corresponding to their associated Fe-O-Fe- py_n angles. The calculations were performed with Gaussian 09 at the B3LYP/cc-pVTZ (H, C, N, O) and ecp-10-mdf (Fe) level of theory.

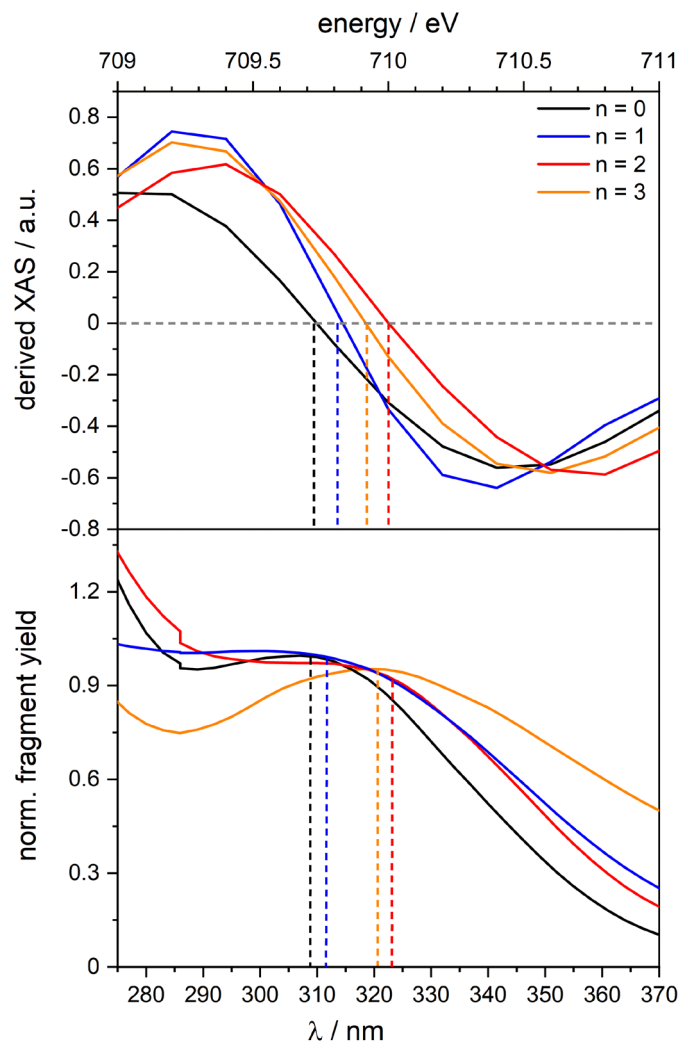


Fig. S18: Derivated XA spectra of the L_3 edge (top) and UVPD spectra (bottom) of $[\text{Fe}_3\text{O}(\text{OAc})_6(\text{py})_n]^+$ ($n = 0, 1, 2, 3$) in isolation.

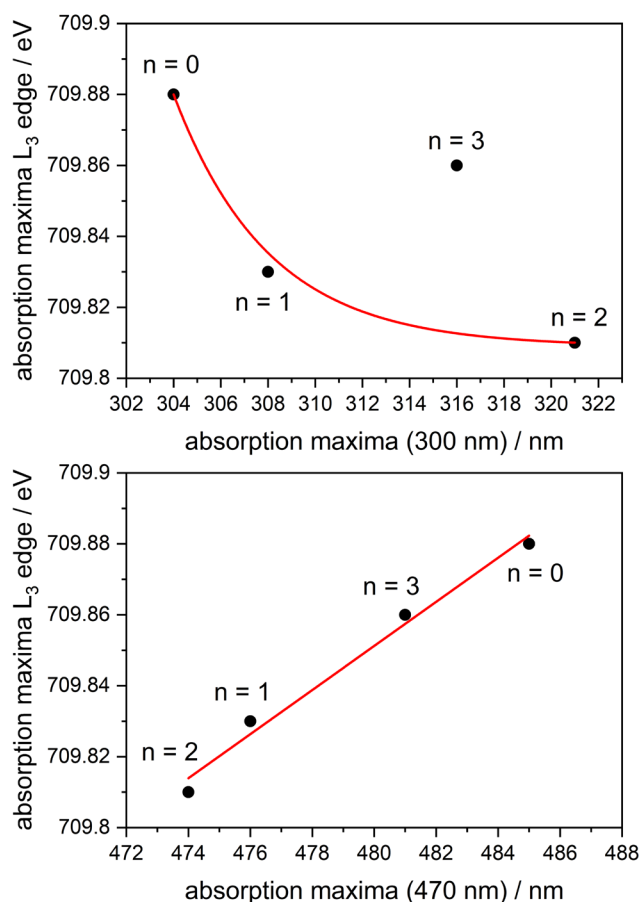


Fig. S19: Absorption maxima of the L₃ edge from the experimental XA spectra and their associated absorption maxima from the UVPD spectra of $[\text{Fe}_3\text{O}(\text{OAc})_6(\text{py})_n]^+$ ($n = 0, 1, 2, 3$) in isolation.

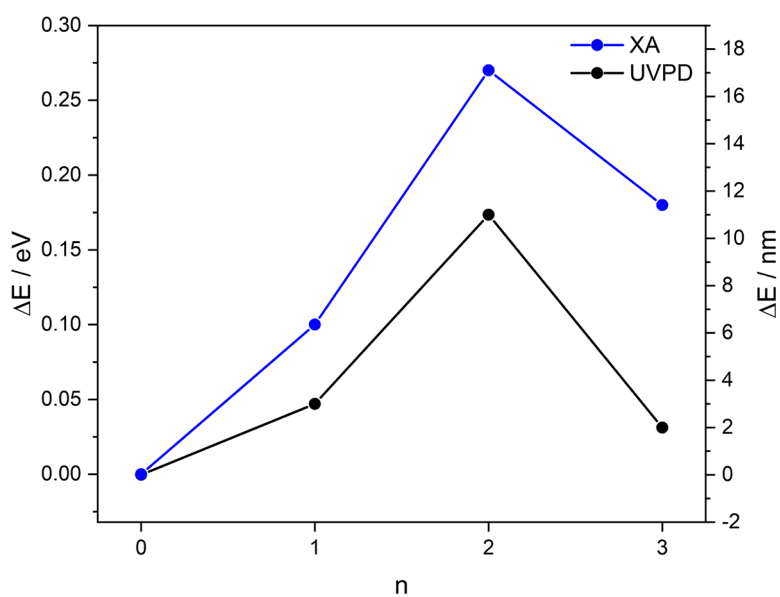


Fig. S20: Experimental energy shifts from the UVPD (300 nm) and XA (709 eV) spectra of $[\text{Fe}_3\text{O}(\text{OAc})_6(\text{py})_n]^+$ ($n = 0, 1, 2, 3$) in isolation.

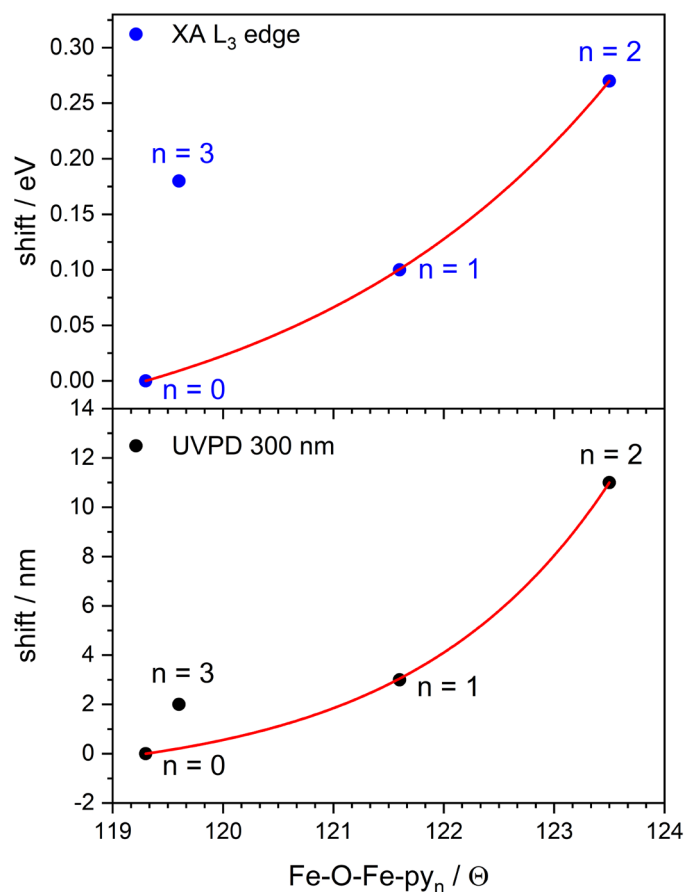


Fig. S21: Experimental energy shifts from the UVPD and XA spectra of $[\text{Fe}_3\text{O}(\text{OAc})_6(\text{py})_n]^+$ ($n = 0, 1, 2, 3$) in isolation in comparison with the calculated Fe-O-Fe-py angle. The calculations were performed at the B3LYP-Gaussian/cc-pVTZ (H, C, N, O) and ecp-10-mdf (Fe) level of theory with five unpaired electrons on each Fe center.

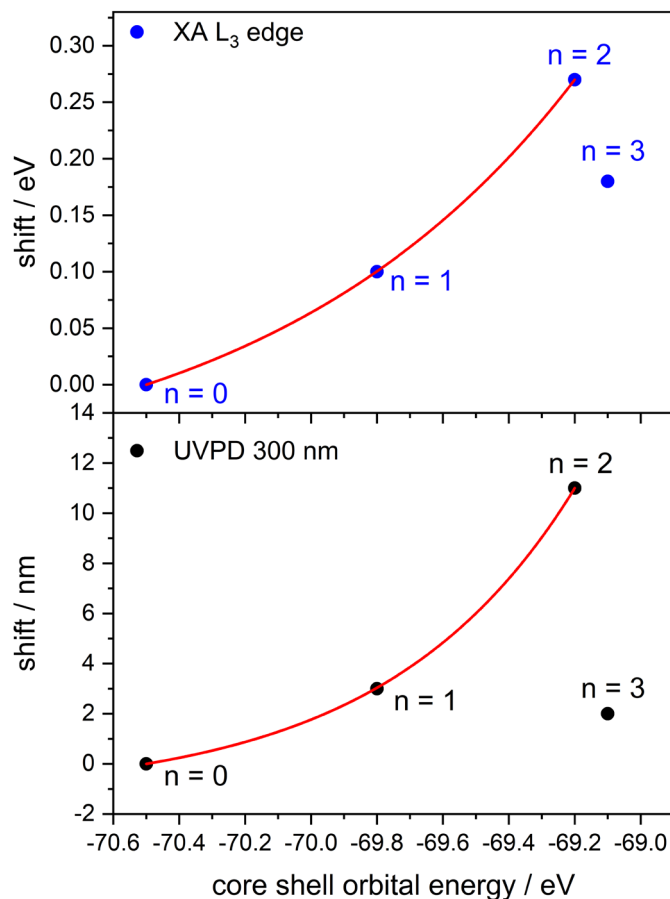


Fig. S22: Experimental energy shifts from the UVPD, IR(M)PD, and XA spectra of $[\text{Fe}_3\text{O}(\text{OAc})_6(\text{py})_n]^+$ ($n = 0, 1, 2, 3$) in isolation in comparison with the calculated orbital energies for the transition in the XA spectra. The calculations were performed at the B3LYP-Gaussian/cc-pVTZ (H, C, N, O) and ecp-10-mdf (Fe) level of theory with five unpaired electrons on each Fe center.

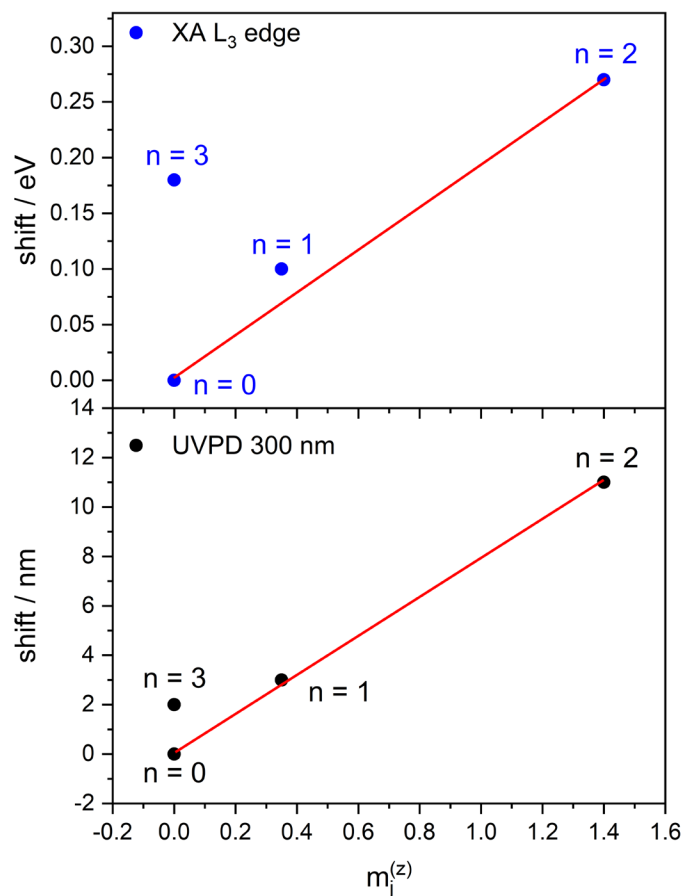


Fig. S23: Experimental energy shifts from the UVPD and XA spectra of $[\text{Fe}_3\text{O}(\text{OAc})_6(\text{py})_n]^+$ ($n = 0, 1, 2, 3$) in isolation in comparison with the experimental gained $m_j^{(z)}$. The calculations were performed at the B3LYP-Gaussian/cc-pVTZ (H, C, N, O) and ecp-10-mdf (Fe) level of theory with five unpaired electrons on each Fe center.

Tab. S1: Calculated bonding lengths and angles for $[\text{Fe}_3\text{O}(\text{OAc})_6(\text{L})_n]^+$ ($n = 0, 1, 2, 3$; L = Nitrogen, Dimethylformamide (DMF), pyridine). The calculations were performed at the B3LYP/cc-pVTZ (H, C, N, O) and ecp-10-mdf (Fe) level of theory with a high spin state for each Fe corresponding to the minimum structure.

	n	Fe-O distance/Å			Fe-O-Fe-L _n /°		
		Fe ₁	Fe ₂	Fe ₃	Fe ₁	Fe ₂	Fe ₃
N₂	0	1.89	1.89	1.89	119.9	120.0	120.1
	1	1.87	1.91	1.88	120.6	120.9	118.5
	2	1.88	1.91	1.91	121.4	119.2	119.3
	3	1.90	1.91	1.91	119.9	120.0	120.1
DMF	0	1.89	1.88	1.89	119.9	120.0	120.1
	1	1.87	1.98	1.87	121.8	121.9	116.3
	2	1.85	1.96	1.96	123.9	118.1	118.0
	3	1.94	1.94	1.94	120.3	119.7	120.0
pyridine	0	1.89	1.88	1.89	119.9	120.0	120.1
	1	1.87	1.98	1.87	121.7	121.9	116.4
	2	1.85	1.97	1.96	123.9	118.0	118.1
	3	1.94	1.95	1.94	119.9	120.1	120.0

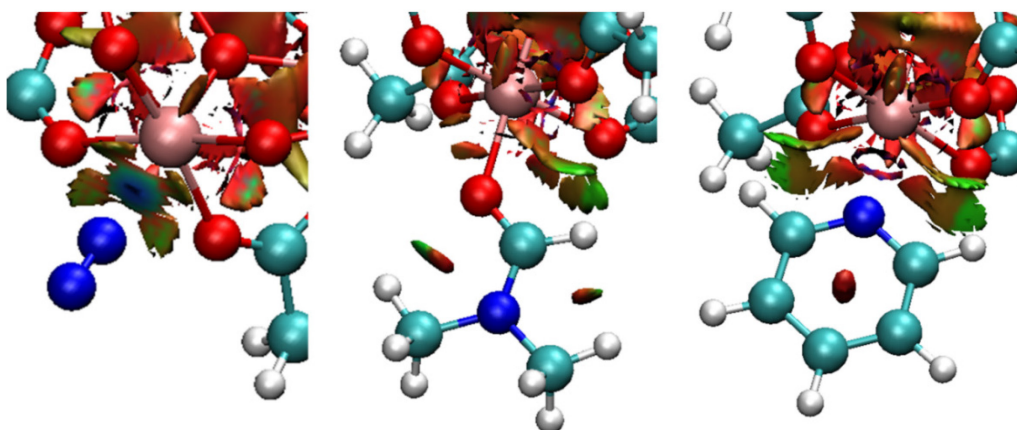


Fig. S24: Non covalent interactions of $[\text{Fe}_3\text{O}(\text{OAc})_6(\text{L})_1]^+$ (L = Nitrogen, Dimethylformamide, pyridine). Calculations were performed at the B3LYP/cc-pVTZ (H, C, N, O) and ecp-10-mdf (Fe) level of theory with five unpaired electrons on each Fe center.

Tab. S2: Calculated bonding lengths and angles for $[\text{Fe}_3\text{O}(\text{L})_6(\text{py})_n]^+$ ($n = 0, 1, 2, 3$; L = acetate, propionic acid, benzoic acid). The calculations were performed at the B3LYP/cc-pVTZ (H, C, N, O) and ecp-10-mdf (Fe) level of theory with a high spin state for each Fe corresponding to the minimum structure.

	n	Fe-O distance/Å			Fe-O-Fe-L _n /θ		
		Fe ₁	Fe ₂	Fe ₃	Fe ₁	Fe ₂	Fe ₃
Acetate	0	1.89	1.89	1.89	119.9	120.0	120.1
	1	1.87	1.98	1.87	121.9	121.7	116.4
	2	1.97	1.96	1.85	123.9	118.8	118.0
	3	1.94	1.94	1.95	119.9	120.0	120.1
Propionic acid	0	1.89	1.88	1.89	120.0	120.0	120.0
	1	1.86	1.99	1.86	121.7	121.8	116.4
	2	1.97	1.96	1.84	124.0	118.1	117.9
	3	1.94	1.95	1.94	119.9	120.0	120.1
Benzoic acid	0	1.89	1.88	1.89	119.9	120.1	120.0
	1	1.85	1.97	1.85	122.1	121.9	117.9
	2	1.95	1.95	1.85	124.9	117.8	117.8
	3	1.94	1.95	1.94	119.9	120.1	120.0

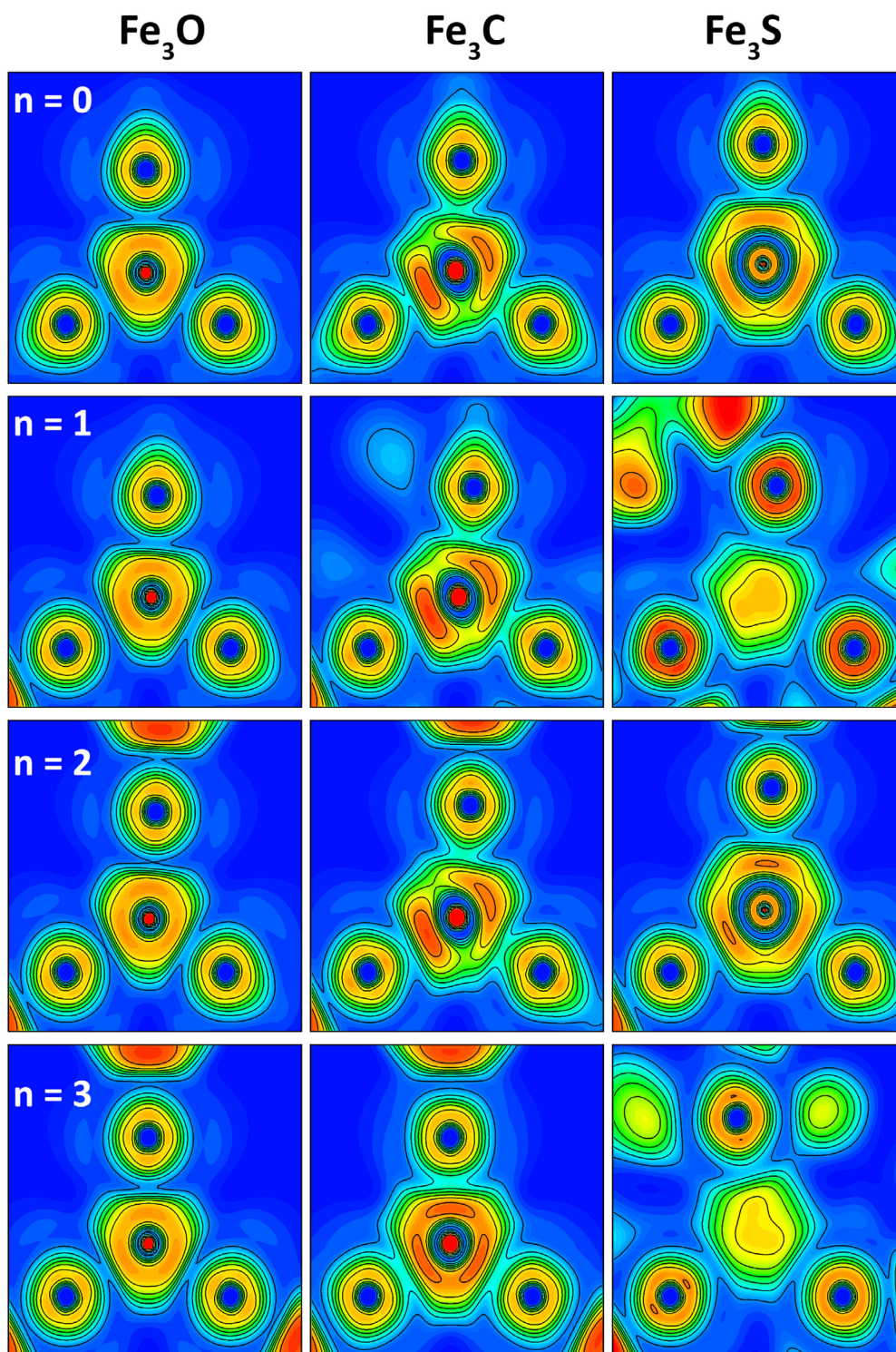


Fig. S25: Electron localized field plots of $[\text{Fe}_3\text{M}(\text{OAc})_6(\text{py})_n]^+$ ($n = 0, 1, 2, 3$; $M = \text{O}, \text{C}, \text{S}$). Calculations were performed at the B3LYP-Gaussian/cc-pVTZ (H, C, N, O) and ecp-10-mdf (Fe) level of theory with five unpaired electrons on each Fe center.

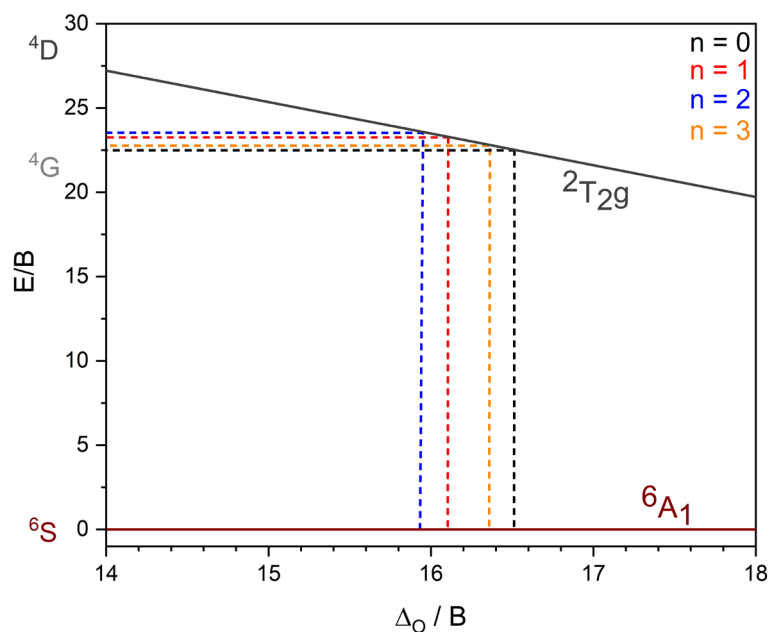


Fig. S26: Tanabe Sugano diagram of a Fe³⁺ octahedral system with high spin configuration and the CF splittings from the XAS spectra with the transition of the UV/VIS spectra of [Fe₃O(OAc)₆(py)_n]⁺ (n = 0, 1, 2, 3) in isolation.

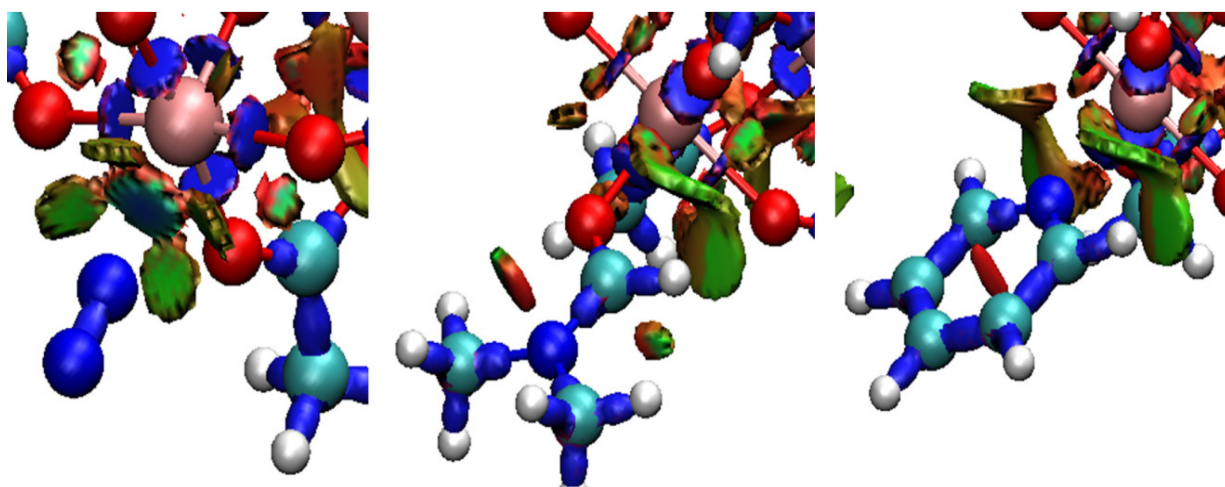


Fig. S27: Density overlap region indicator plots of [Fe₃O(OAc)₆(L)₁]⁺ (L = Nitrogen, Dimethylformamide, pyridine). Calculations were performed at the B3LYP-Gaussian/cc-pVTZ (H, C, N, O) and ecp-10-mdf (Fe) level of theory with five unpaired electrons on each Fe center.

Tab. S3: Atom coordinates for $[\text{Fe}_3\text{O}(\text{OAc})_6(\text{py})_n]^+$ ($n = 0$). The calculation was performed at the B3LYP/cc-pVTZ (H, C, N, O) and ecp-10-mdf (Fe) level of theory with a high spin state for each Fe center.

atom	X	y	z
C	-2.67857	-0.32278	-1.82940
C	-3.75142	-0.45748	-2.87246
H	-3.80581	0.44859	-3.48880
H	-4.71762	-0.57639	-2.35269
H	-3.58296	-1.35169	-3.48556
C	-2.67558	-0.33428	1.82272
C	-3.69092	-0.45701	2.92351
H	-3.15394	-0.42333	3.88684
H	-4.21118	-1.42124	2.86037
H	-4.39609	0.38288	2.89457
C	1.06924	2.48107	-1.82654
C	1.47706	3.42638	-2.92081
H	0.86369	4.33553	-2.89457
H	1.30605	2.92241	-3.88735
H	2.54657	3.66095	-2.84651
C	1.04342	2.48798	1.82525
C	1.44294	3.43107	2.92459
H	1.24005	2.93491	3.88902
H	0.84442	4.34960	2.88121
H	2.51722	3.64870	2.87359
C	1.62053	-2.15698	-1.82736
C	2.23250	-2.97394	-2.92971
H	1.84841	-2.59074	-3.89048
H	1.92805	-4.02482	-2.84150
H	3.32451	-2.87086	-2.92851
C	1.62954	-2.15377	1.82654
C	2.26712	-2.97866	2.90852
H	2.25093	-2.39645	3.84459
H	3.32204	-3.16372	2.66039
H	1.72597	-3.92028	3.05547
Fe	-1.13899	1.51491	-0.00821
Fe	-0.73781	-1.74260	-0.00159
Fe	1.88011	0.22970	0.00275
O	-0.00020	0.00122	-0.00161
O	-2.39154	0.84818	-1.41305
O	-2.12240	-1.38658	-1.39999
O	-2.40042	0.83169	1.38679
O	-2.11983	-1.40184	1.40029
O	-0.13054	2.53912	-1.39917
O	1.93686	1.64937	-1.39990
O	-0.15662	2.54128	1.39653

5. Magnetic properties and their correlation to the electronics of isolated trinuclear 3d spin frustrated complexes

O	1.91630	1.66337	1.39668
O	0.46914	-2.50062	-1.39817
O	2.26720	-1.14706	-1.39613
O	0.47788	-2.49476	1.40206
O	2.27274	-1.13665	1.40119

Tab. S4: Atom coordinates for $[\text{Fe}_3\text{O}(\text{OAc})_6(\text{py})_n]^+$ ($n = 1$). The calculation was performed at the B3LYP/cc-pVTZ (H, C, N, O) and ecp-10-mdf (Fe) level of theory with a high spin state for each Fe center.

atom	x	y	z
C	-0.54412	2.36224	-1.82026
C	-1.00188	3.24662	-2.94694
H	-0.56814	2.86937	-3.87542
H	-0.63418	4.25967	-2.80216
H	-2.08385	3.23540	-3.03646
C	-0.54773	2.30411	1.89459
C	-1.00434	3.17884	3.02915
H	-0.37390	2.98392	3.89776
H	-2.04259	2.98789	3.28031
H	-0.86365	4.22492	2.76072
C	3.44126	0.03146	-1.80386
C	4.53801	0.04838	-2.82903
H	4.49254	0.95710	-3.42276
H	4.48867	-0.83638	-3.45743
H	5.49453	0.03680	-2.30149
C	3.42492	-0.03159	1.81135
C	4.45570	-0.06128	2.90307
H	3.95150	-0.29128	3.84395
H	4.95000	0.90069	2.99616
H	5.17555	-0.85491	2.71653
C	-0.54961	-2.29338	-1.90543
C	-1.00355	-3.14267	-3.06006
H	-0.49151	-2.79937	-3.96106
H	-2.07579	-3.06135	-3.20842
H	-0.71271	-4.17821	-2.89691
C	-0.54231	-2.37395	1.81052
C	-1.00035	-3.26964	2.92808
H	-0.60196	-2.87608	3.86566
H	-0.60123	-4.27208	2.79555
H	-2.08424	-3.28792	2.99249
C	-4.13851	0.06043	-1.15060
H	-3.54475	0.11053	-2.05076
C	-5.52177	0.06067	-1.19155
H	-6.02954	0.11001	-2.14344
C	-6.22793	-0.00328	0.00239
H	-7.30920	-0.00494	0.00151

5. Magnetic properties and their correlation to the electronics of isolated trinuclear 3d spin frustrated complexes

C	-5.52342	-0.06507	1.19742
H	-6.03262	-0.11575	2.14848
C	-4.14010	-0.06174	1.15863
H	-3.54784	-0.11002	2.05992
N	-3.46024	-0.00017	0.00450
Fe	1.65370	1.58980	0.02537
Fe	-1.31439	-0.00115	0.00362
Fe	1.65099	-1.58662	-0.03545
O	0.66825	0.00174	-0.00062
O	0.62222	2.56234	-1.36774
O	-1.33389	1.46492	-1.40704
O	0.60903	2.53029	1.42772
O	-1.32650	1.39808	1.48185
O	3.02450	1.14418	-1.36443
O	3.00432	-1.09503	-1.42205
O	3.00424	1.09708	1.41846
O	3.01340	-1.14276	1.36241
O	-1.33176	-1.39721	-1.47676
O	0.60869	-2.52155	-1.44450
O	-1.32908	-1.46638	1.41383
O	0.62073	-2.57328	1.34998

Tab. S5: Atom coordinates for $[\text{Fe}_3\text{O}(\text{OAc})_6(\text{py})_n]^+$ ($n = 2$). The calculation was performed at the B3LYP/cc-pVTZ (H, C, N, O) and ecp-10-mdf (Fe) level of theory with a high spin state for each Fe center.

atom	x	y	z
C	-2.28472	2.02734	-1.84716
C	-3.13994	2.57660	-2.95738
H	-2.52729	2.67494	-3.85476
H	-3.48409	3.57525	-2.69346
H	-3.98335	1.92537	-3.16340
C	-2.28968	2.01409	1.85536
C	-3.13912	2.54251	2.97994
H	-2.65692	2.28034	3.92411
H	-4.12472	2.08513	2.96484
H	-3.21117	3.62524	2.92770
C	2.29531	2.03418	-1.83453
C	3.15703	2.57045	-2.94612
H	3.16628	3.65638	-2.93431
H	2.73371	2.24058	-3.89718
H	4.16591	2.17222	-2.87292
C	2.27000	2.02169	1.86463
C	3.11527	2.54244	2.99602
H	2.67147	2.20825	3.93623
H	3.13141	3.62844	2.99416

5. Magnetic properties and their correlation to the electronics of isolated trinuclear 3d spin frustrated complexes

H	4.12255	2.13803	2.93808
C	0.00002	-1.99009	-1.92016
C	0.00198	-2.90241	-3.11971
H	0.03493	-2.28385	-4.01918
H	-0.90526	-3.49932	-3.15090
H	0.88311	-3.53847	-3.11594
C	0.00500	-2.02023	1.89682
C	0.01233	-2.96099	3.07434
H	0.12285	-2.36893	3.98523
H	0.85926	-3.63986	3.01330
H	-0.92059	-3.51392	3.13419
C	-4.24245	-1.72642	-1.16129
H	-3.72794	-1.42247	-2.06018
C	-5.45676	-2.38986	-1.20816
H	-5.90821	-2.61508	-2.16319
C	-6.06922	-2.75154	-0.01583
H	-7.01799	-3.27033	-0.02038
C	-5.44321	-2.43538	1.18238
H	-5.88387	-2.69698	2.13315
C	-4.22923	-1.77047	1.14712
H	-3.70392	-1.50247	2.05121
C	4.24418	-1.72417	-1.16060
H	3.72991	-1.42277	-2.06048
C	5.45759	-2.38940	-1.20548
H	5.90855	-2.61846	-2.15983
C	6.06982	-2.74791	-0.01215
H	7.01796	-3.26786	-0.01516
C	5.44459	-2.42709	1.18520
H	5.88531	-2.68604	2.13668
C	4.23142	-1.76078	1.14811
H	3.70638	-1.48914	2.05129
N	-3.63929	-1.42269	-0.00430
N	3.64169	-1.41599	-0.00432
Fe	-0.00394	2.40425	0.00378
Fe	-1.73202	-0.37099	0.00249
Fe	1.73381	-0.36526	-0.00036
O	-0.00209	0.55512	0.00264
O	-1.37131	2.78190	-1.40197
O	-2.51514	0.85492	-1.43557
O	-1.39773	2.78041	1.38985
O	-2.50094	0.83131	1.46094
O	1.39552	2.79421	-1.37496
O	2.50745	0.85009	-1.44354
O	1.36706	2.78302	1.41248
O	2.49737	0.84816	1.45131
O	-1.12246	-1.62936	-1.4657

5. Magnetic properties and their correlation to the electronics of isolated trinuclear 3d spin frustrated complexes

O	1.12129	-1.63207	-1.46137
O	-1.11795	-1.65490	1.44833
O	1.12560	-1.64618	1.44876

Tab. S6: Atom coordinates for $[\text{Fe}_3\text{O}(\text{OAc})_6(\text{py})_n]^+$ ($n = 3$). The calculation was performed at the B3LYP/cc-pVTZ (H, C, N, O) and ecp-10-mdf (Fe) level of theory with a high spin state for each Fe center.

atom	X	Y	z
C	-1.94125	1.80533	1.90242
C	-2.63903	2.44469	3.07685
H	-2.27607	1.97066	3.99121
H	-3.71197	2.28019	3.01833
H	-2.41441	3.50621	3.12866
C	-1.94512	1.79762	-1.90618
C	-2.63829	2.45374	-3.07400
H	-2.09617	2.19584	-3.98599
H	-2.61227	3.53583	-2.96882
H	-3.66139	2.10147	-3.16673
C	-0.59014	-2.58153	1.90758
C	-0.80182	-3.50614	3.08028
H	-1.76136	-4.01068	2.99553
H	-0.82108	-2.90647	3.99255
H	0.00627	-4.22768	3.15659
C	-0.58349	-2.58736	-1.90182
C	-0.80377	-3.51042	-3.07408
H	-0.85159	-2.90737	-3.98303
H	-1.75328	-4.03068	-2.97195
H	0.01376	-4.21884	-3.16988
C	2.53217	0.78085	1.90401
C	3.43908	1.05683	3.07698
H	2.91423	0.77310	3.99153
H	3.68682	2.11275	3.13513
H	4.34054	0.45268	3.00998
C	2.53065	0.78345	-1.90827
C	3.43958	1.05652	-3.08049
H	2.91700	0.76832	-3.99492
H	4.34258	0.45527	-3.00929
H	3.68488	2.11285	-3.14240
C	-4.63474	-1.41699	1.14981
H	-4.07179	-1.23240	2.05196
C	-5.95854	-1.82303	1.18986
H	-6.44887	-1.96109	2.14243
C	-6.62803	-2.04447	-0.00601
H	-7.66180	-2.36192	-0.00760
C	-5.94620	-1.85102	-1.19967

5. Magnetic properties and their correlation to the electronics of isolated trinuclear 3d spin frustrated complexes

H	-6.42636	-2.01140	-2.15393
C	-4.62287	-1.44371	-1.15503
H	-4.05066	-1.27981	-2.05533
C	1.07069	4.72087	1.15335
H	0.93377	4.14118	2.05335
C	1.37777	6.07090	1.19886
H	1.48614	6.56473	2.15346
C	1.54000	6.76145	0.00562
H	1.78032	7.81584	0.00808
C	1.38812	6.07403	-1.19079
H	1.50498	6.57044	-2.14304
C	1.08063	4.72386	-1.15160
H	0.95293	4.14647	-2.05447
C	3.54507	-3.29940	1.15460
H	3.10191	-2.90383	2.05569
C	4.56085	-4.24030	1.19787
H	4.92548	-4.59303	2.15156
C	5.08974	-4.71030	0.00364
H	5.88340	-5.44490	0.00435
C	4.58162	-4.22035	-1.19159
H	4.96267	-4.55729	-2.14457
C	3.56498	-3.28025	-1.15030
H	3.13728	-2.86930	-2.05197
N	-3.97833	-1.23022	-0.00159
N	0.92487	4.05853	-0.00064
N	3.05531	-2.82752	0.00167
Fe	-1.85914	-0.57660	0.00169
Fe	0.43151	1.89443	-0.00293
Fe	1.42637	-1.31926	0.00000
O	-0.00108	-0.00004	0.00015
O	-2.43622	0.73738	1.44587
O	-0.89951	2.36744	1.46528
O	-2.42543	0.71505	-1.47138
O	-0.91505	2.36932	-1.45169
O	-1.60060	-1.96401	1.46987
O	0.58155	-2.47109	1.45228
O	-1.59363	-1.98273	-1.44564
O	0.59388	-2.46520	-1.46475
O	1.85117	1.74204	1.45160
O	2.50024	-0.40195	1.46365
O	1.83819	1.74271	-1.46925
O	2.50877	-0.39449	-1.45497

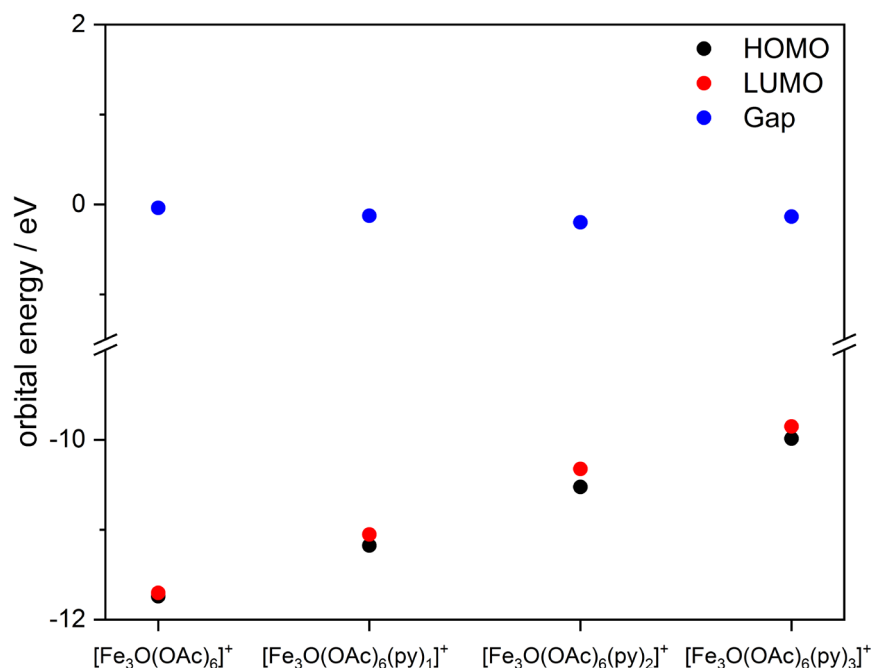


Fig. S28: calculated HOMO-, LUMO energies and their resulted HOMO-LUMO gap for $[\text{Fe}_3\text{O}(\text{OAc})_6(\text{py})_n]^+$ ($n = 0, 1, 2, 3$). The calculations were performed at the B3LYP/cc-pVTZ (H, C, N, O) and ecp-10-mdf (Fe) level of theory with a high spin state for each Fe center.

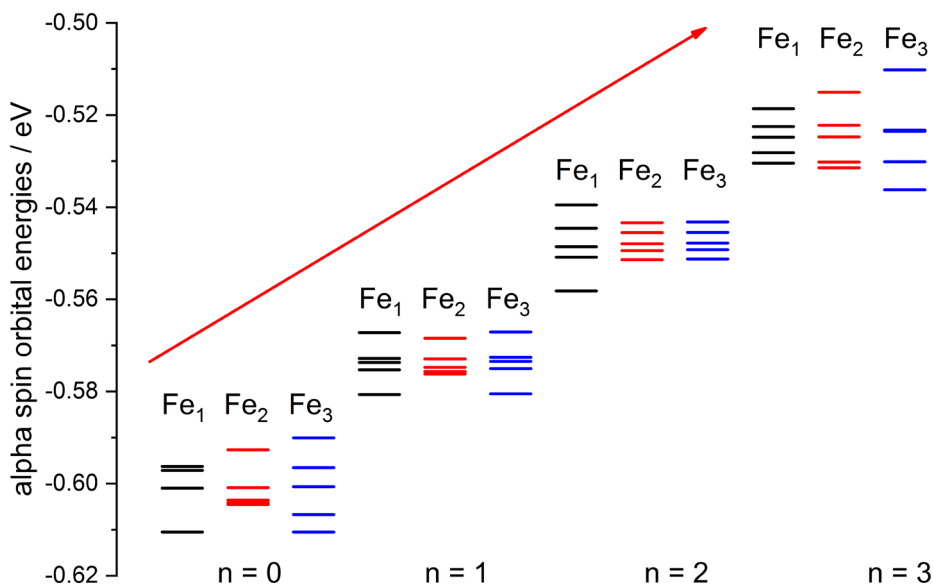


Fig. S29: Calculated alpha spin orbital for the d orbitals in $[\text{Fe}_3\text{O}(\text{OAc})_6(\text{py})_n]^+$ ($n = 0, 1, 2, 3$). The calculations were performed with Gaussian 09 at the B3LYP/cc-pVTZ (H, C, N, O) and ecp-10-mdf (Fe) level of theory.

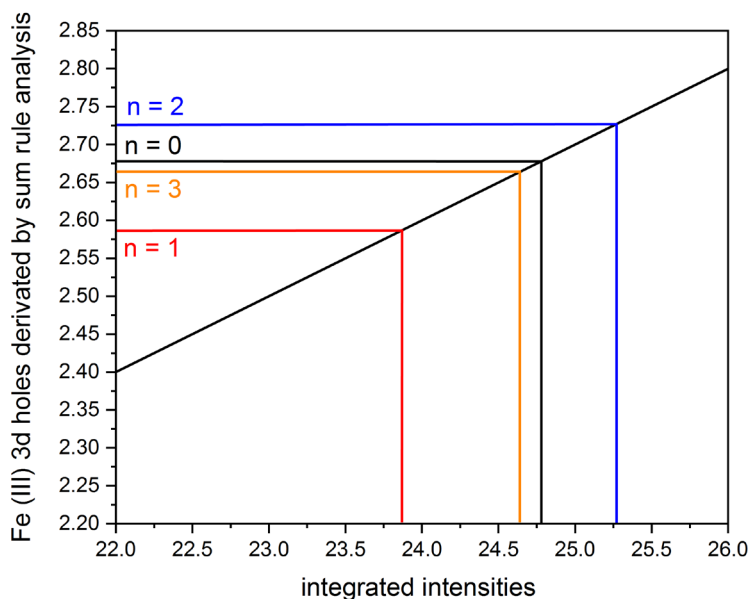


Fig. S30: Integrated intensities of the experimental XMCD spectra and their corresponding derived 3d holes for $[\text{Fe}_3\text{O}(\text{OAc})_6(\text{py})_n]^+$ ($n = 0, 1, 2, 3$).

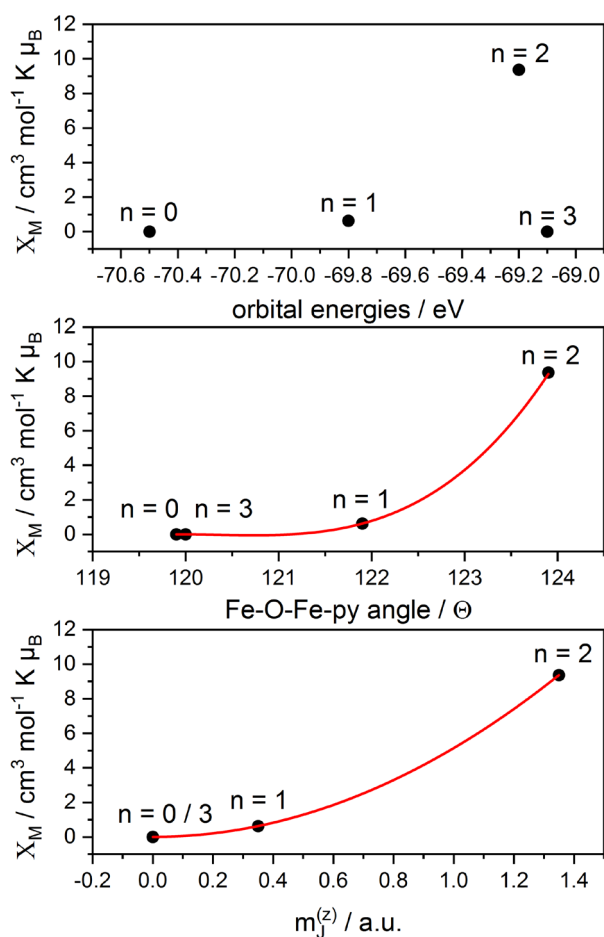


Fig. S31: Calculated susceptibilities for $[\text{Fe}_3\text{O}(\text{OAc})_6(\text{py})_n]^+$ ($n = 0, 1, 2, 3$) with their corresponding transition orbital energies (top), Fe-O-Fe-py angle (middle), and their total spin magnetic moments (bottom).

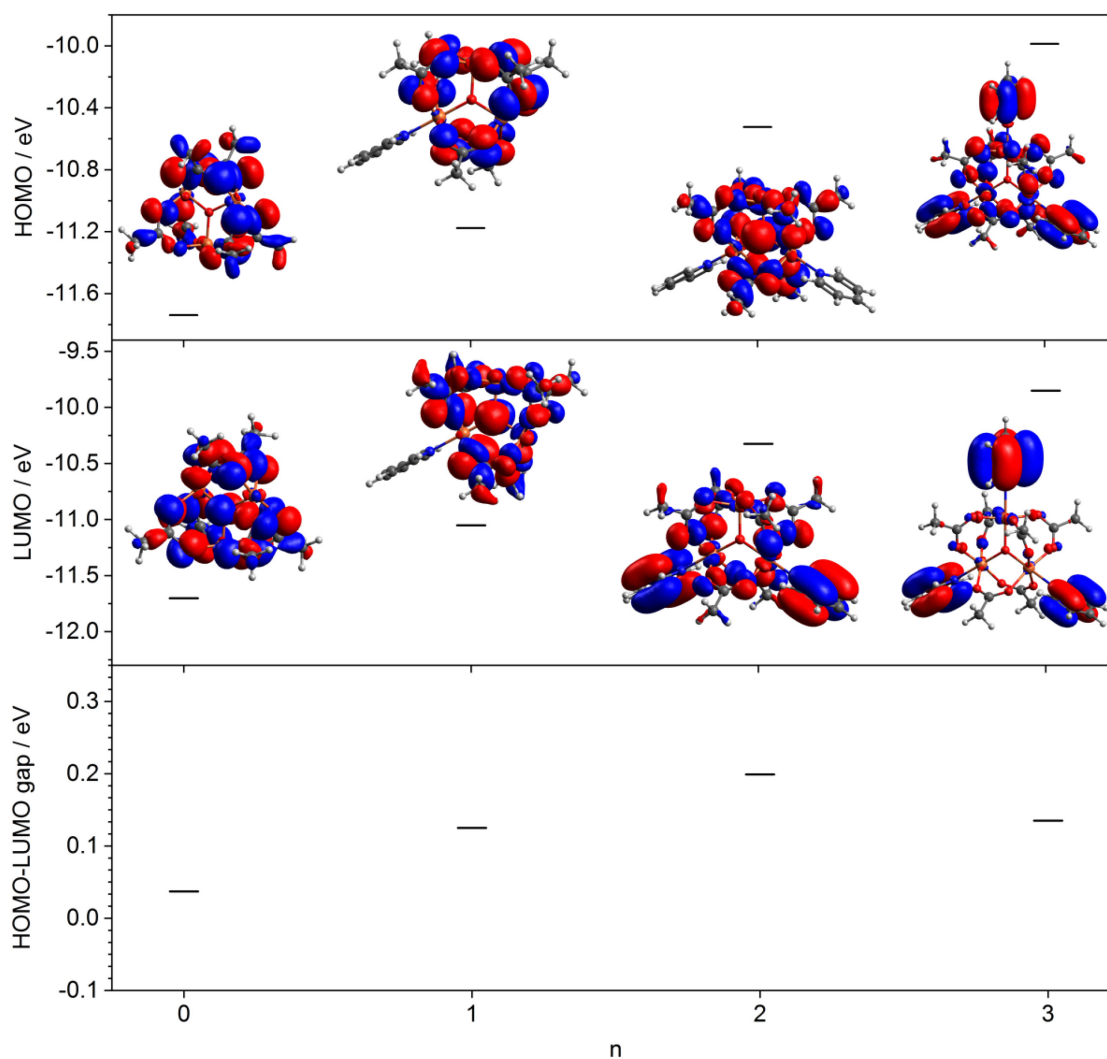


Fig. S32: Calculated HOMO, LUMO energies, and the HOMO-LUMO gap of $[\text{Fe}_3\text{O}(\text{OAc})_6(\text{py}_n)]^+$ ($n = 0, 1, 2, 3$). The calculations were performed with Gaussian 09 at the B3LYP/cc-pVTZ (H, C, N, O) and ecp-10-mdf (Fe) level of theory.

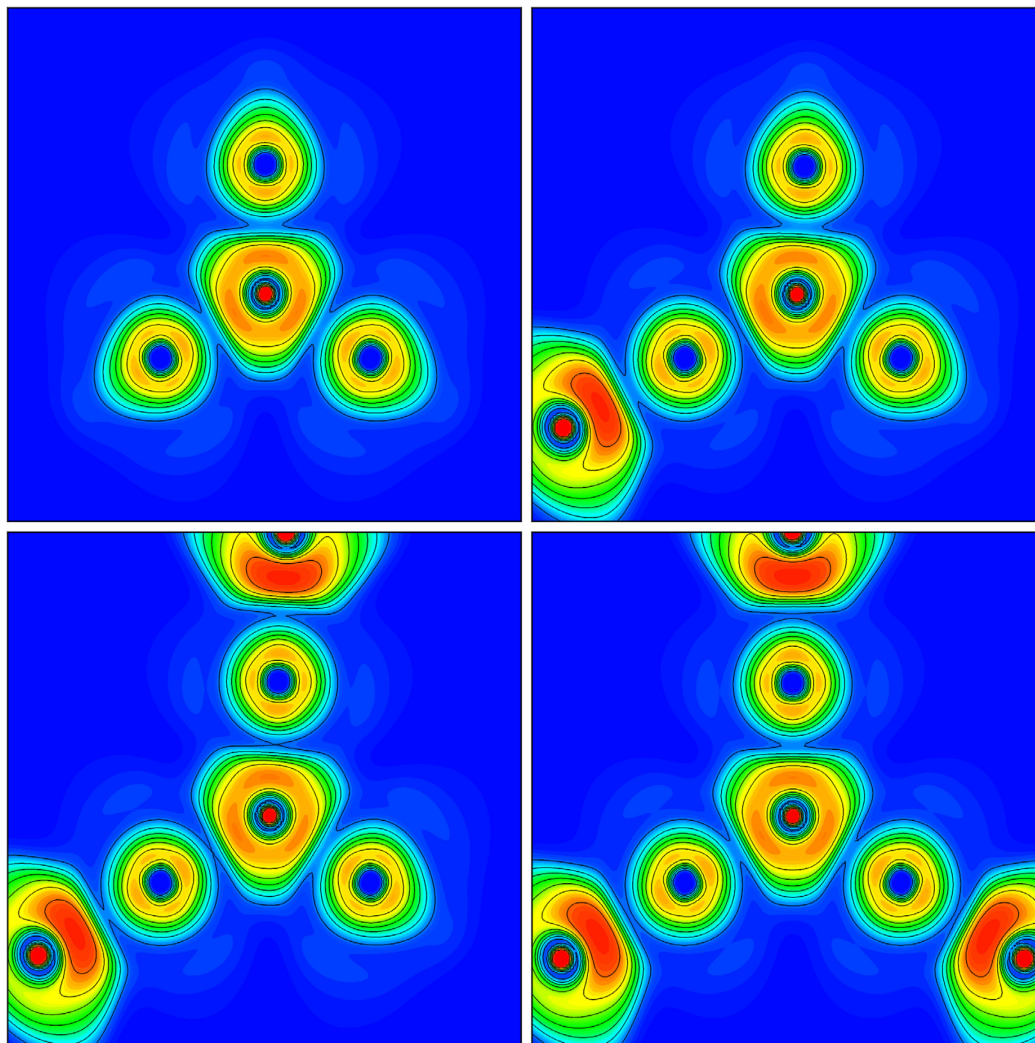


Fig. S33: Calculated electron localized field for $[\text{Fe}_3\text{O}(\text{OAc})_6(\text{py})_n]^+$ ($n = 0, 1, 2, 3$) of the central oxygen atom. The calculations were performed with Gaussian 09 at the B3LYP/cc-pVTZ (H, C, N, O) and ecp-10-mdf (Fe) level of theory.

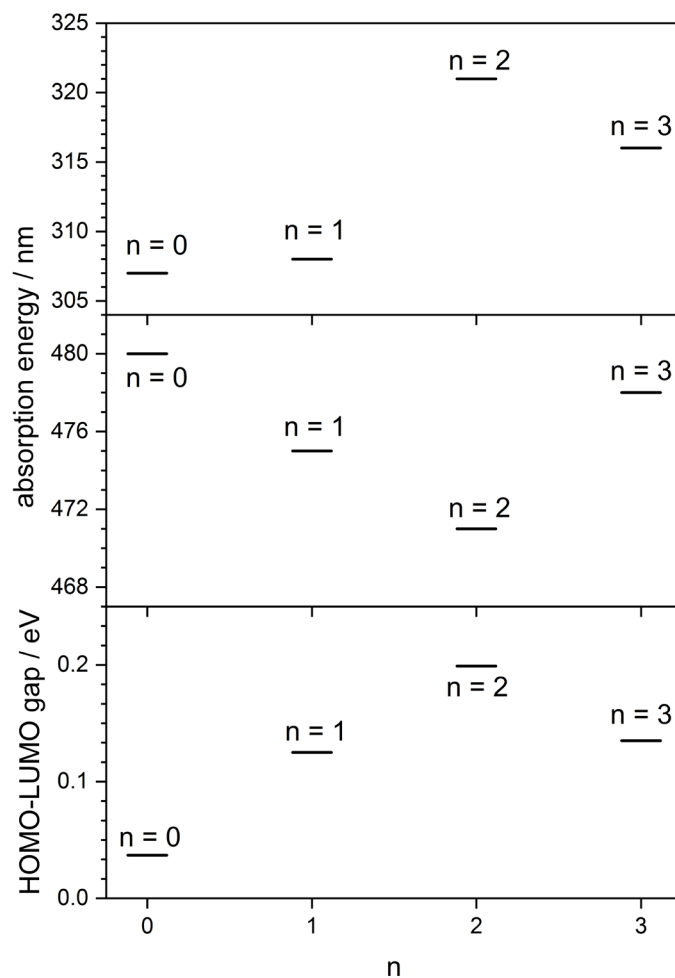


Fig. S34: Maxima of the different absorption bands and calculated HOMO-LUMO gaps of $[\text{Fe}_3\text{O}(\text{OAc})_6(\text{py}_n)]^+$ ($n = 0, 1, 2, 3$). The calculations were performed with Gaussian 09 at the B3LYP/cc-pVTZ (H, C, N, O) and ecp-10-mdf (Fe) level of theory.

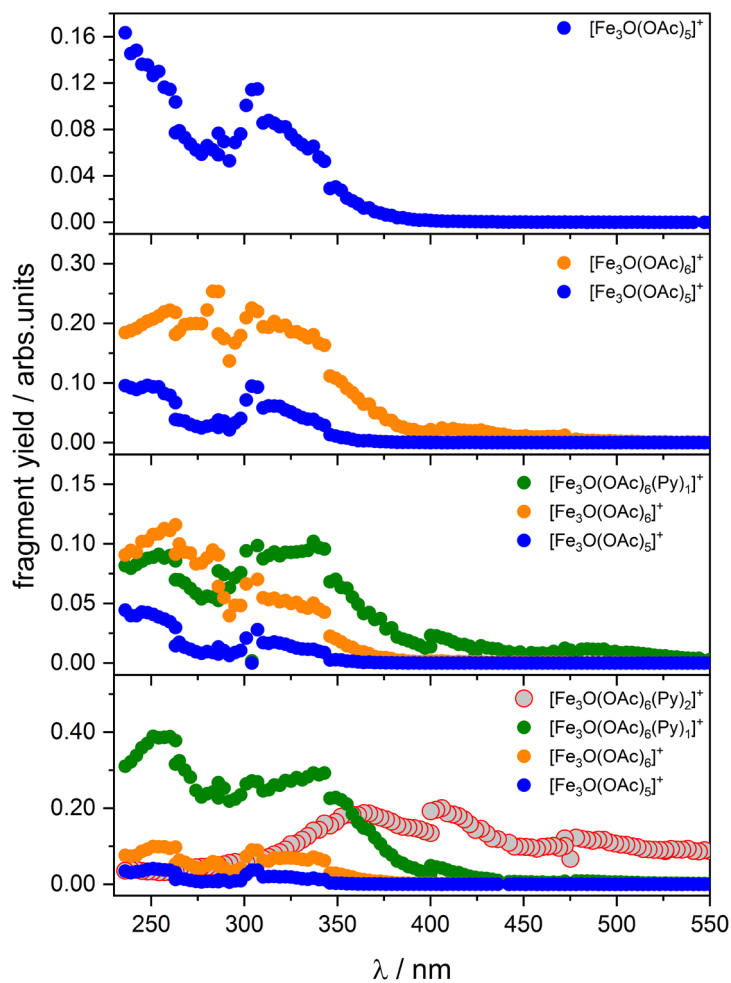


Fig. S35: Single fragment evaluation of the Ultra Violet Photon Dissociation mass spectra of $[\text{Fe}_3\text{O}(\text{OAc})_6(\text{py}_n)]^+$ ($n = 0, 1, 2, 3$) in the region of 240 nm–580 nm with a constant laser power of 2 μJ / pulse.

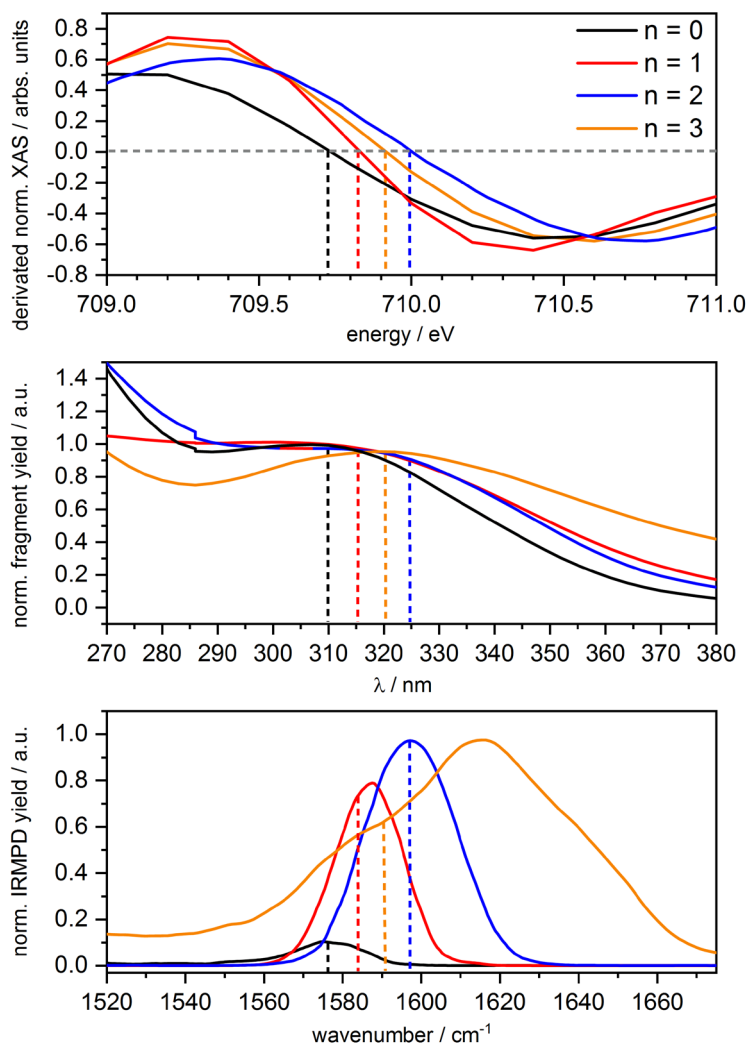


Fig. S36: Derivated XA spectra of the L_3 edge (top) and UV/VIS spectra (middle) and IR(M)PD spectra^[46] (bottom) of $[\text{Fe}_3\text{O}(\text{OAc})_6(\text{py})_n]^+$ ($n = 0, 1, 2, 3$) in isolation.

Correction of the spin sum rules by Takeo Jo et al.

The S_z sum rule for the $L_{2,3}$ edge in **3d transition metal** systems is expressed as:

$$X_I = X_E.$$

The relative integrated magnetic circular dichroism (MCD) intensity is defined as

$$X_E = \frac{\int_{L_3} (\mu_+(\omega) - \mu_-(\omega)) d\omega - 2 \int_{L_2} (\mu_+(\omega) - \mu_-(\omega)) d\omega}{\int_{L_3+L_2} (\mu_+(\omega) + \mu_0(\omega) + \mu_-(\omega)) d\omega}$$

And the expectation value is given by

$$X_E = \frac{2}{3(10-n)} \langle S_z \rangle + \frac{7}{3(10-n)} \langle T_z \rangle.$$

The absorption spectra with positive and negative light helicity are given by $\mu_{\pm}(\omega)$, with linearly polarized light by $\mu_0(\omega)$ along the z direction. L_3 and L_2 denote the integrated region with respect to ω , the number of 3d electrons is given by n.

6 IR(M)PD studies of isolated spin frustrated trimetallic μ -oxo bridged 4d complexes

Michael Lembach, Florian Breitschaft and Gereon Niedner-Schatteburg

*Fachbereich Chemie and Forschungszentrum OPTIMAS,
Technische Universität Kaiserslautern,
67663 Kaiserslautern, Germany*

6.1 Preamble

The following chapter is prepared as manuscript for publication. I managed and performed the IR(M)PD experiments, data evaluation for the IR(M)PD and CID experiments, quantum chemical calculations, and XA simulations. In addition, I received experimental support from Florian Breitschaft for the sample preparation and to record the CID breakdown curves. I wrote the chapter in form of a draft manuscript.

6.2 Abstract

This study elucidates the molecular structure and their calculated magnetism of isolated trinuclear μ -oxo bridged Ruthenium complexes of the structural type $[\text{Ru}_3\text{O}(\text{OAc})_6(\text{py})_n]^+$ (OAc = acetate, py = pyridine, $n = 0, 1, 2, 3$). We present InfraRed (Multiple) Photon Dissociation (IR(M)PD) spectra combined with quantum chemical calculations and their theoretical calculated coupling exchange constants via Broken Symmetry (BS) approach. They indicate that the coordination of axial pyridine ligands to the $[\text{Ru}_3\text{O}(\text{OAc})_6]^+$ subunit disturbs the triangular geometry of the Ru_3O core. $[\text{Ru}_3\text{O}(\text{OAc})_6]^+$ exhibits a nearly equilateral triangular core geometry. The coordination of one or two axial ligands leads to a distortion of the triangular Ru_3O core geometries. The coordination of three pyridine ligands does not result in an equilateral triangular Ru_3O core geometry as in the case of $[\text{Fe}_3\text{O}(\text{OAc})_6(\text{py})_n]^+$. The presented results help gain further insight into the molecular structure of trinuclear μ -oxo bridged Ruthenium complexes, void of any external effects such as crystal packing or solvation.

6.3 Introduction

Transition Metal (TM) complexes provide a highly fascinating field of research due to their broad properties in many technical^[1-4], medical^[5-9], and industrial^[10-12] applications. In recent decades, molecular magnetism research has grown in importance for the efficient modeling of nanomagnets^[13-16], storage devices^[17], and quantum computing^[18-21]. Much effort has been spent in the design and modeling for paramagnetic transition metal complexes such as spin-crossover^[13-18] (SCO) complexes, single molecule magnets^[19-22] (SMM), or spin frustrated systems^[9, 23-26]. Spin frustrated complexes are one of the most promising candidates for the design of molecular spintronics^[16, 27-34], as a model system in metalloenzymes^[35], catalysis^[35-40], and in metal organic frameworks^[38, 39, 41-43]. Because the resultant spin arrangement leads to opposing interactions of their orientation, such complexes exhibit distinct magnetic properties^[19, 37, 49, 50]. These competing interactions reduce magnetic ordering with an unusual electronic ground state^[44-53]. Spin frustrated systems with the general structure $[\text{M}_3\text{O}(\text{O}_2\text{R})_6\text{L}_3]^+$ (L = axial ligands)^[54-57] serve as model systems due to their extraordinary spin orientation.

The electronic ground state of spin frustrated complexes with the structure $[M_3O(O_2R)_6L_3]^+$ are extremely sensitive to the geometric distortion of the M_3O core induced by the axial ligands^[58].

Many groups have previously studied such complexes, revealing a total spin (S_T) of 1/2 in symmetric $[Fe_3O(OAc)_6(H_2O)_3]NO_3$ ^[66] and asymmetric $[Fe_3O(TlEO)_2(O_2CPh)Cl_3]$ ^[66,67] complexes with a S_T of 5/2 in asymmetric complexes. The complex with the structure $[Mn_3(OAc)_6(py)_3]$ (py = pyridine) reveals a paramagnetic susceptibility and a decreasing magnetic moment per Mn atom by increasing the temperature^[59]. A distortion of the Mn_3O leads to a single molecule magnetic behavior with ferromagnetic coupled Mn ions^[60]. The μ -oxo bridged Ruthenium complexes with the structure $[Ru_3(OAc)_6(H_2O)_3] \cdot 2 \cdot H_2O$ ^[61] and $[Ru_3(OAc)_6(py)_3](PF_6)$ ^[62] reveal a mixed valence state for the different Ruthenium ions, e.g., $Ru^{2+, 3+, 3+}$. Changing one axial coordinated from pyridine to methanol, the oxidation states change to $Ru^{3+, 3+, 3+}$ ^[62].

Previous experiments have been performed in the condensed or solid phase. It seems that external effects such as crystal packing or solvation have major importance to the electronics of these complexes. Gas phase investigations of isolated $[M_3O(O_2CR)_6L_3]^+$ are essential to exclude external effects.

The Ru_3O core leads to a pairwise coupling due to the oxo bridge in these compounds^[63]. In this complex, the three Ru ions coordinate around one O^{2-} center in a flat, almost equal triangular arrangement. This arrangement builds the Ru_3O core in these complexes (cf. Fig. 1). Without coordinating the axial ligand, these complexes obtain pseudo octahedral coordination through their equatorial coordination of four bridging ligands. Such complexes usually possess an antiferromagnetic coupling scheme for iron^[28, 64]. However, long M-M distances ($> 3 \text{ \AA}$) do not indicate a direct interaction between the metals, leading to spin frustrated systems because a pairwise antiferromagnetic coupling of all metal ions within the M_3O core seems impossible^[65].

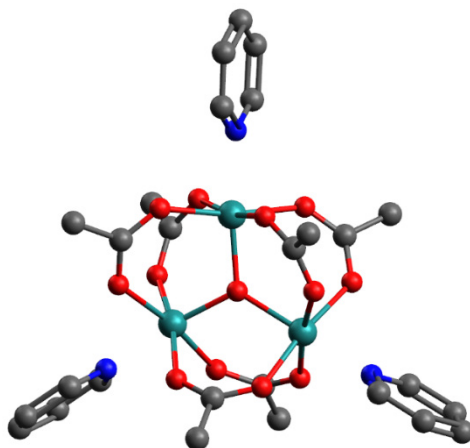


Fig. 1: Structure of the investigated trinuclear complexes with the structure $[\text{Ru}_3\text{O}(\text{OAc})_6(\text{py})_n]^+$ ($n = 0, 1, 2, 3$). The calculations were performed with Turbomole 6.5 at the unrestricted B3LYP/cc-pVTZ level of theory and a broken symmetry approach. Hydrogen atoms are omitted for clarity (C: grey, O: red, N: blue, Ru: green).

Electrospray ionization^[66, 67] gives access to mass spectrometric investigations of complexes in isolation and their geometrical structure by irradiation with IR photons. In addition, Tandem MS-based methods have helped investigate complexes void from external effects, e.g., packing and solvation effects.

We previously conducted IR(M)PD experiments on $[\text{Fe}_3(\text{OAc})_6(\text{L})_{0-3}]^+$ ($\text{L} = \text{N}_2, \text{pyridine}$)^[74, 75] and discovered a non-classical bonding scenario, resulting in a blue shift of the asymmetric CO stretching modes in the IR(M)PD spectra for the N_2 coordinated species. With the coordination of pyridine, we could establish a magneto structural correlation via IR(M)PD and DFT calculations. By stepwise coordination of pyridine to the complex, our XMCD investigations of $[\text{Fe}_3(\text{OAc})_6(\text{py})_{0-3}]^+$ indicated a switch in the coupling scheme from antiferromagnetic to ferromagnetic exchange coupling. In addition, IR(M)PD studies on heterometallic -oxo (Fe, Cr) complexes were carried out^[76]. Changing the metal from a ferromagnetic ion to a diamagnetic atom, e.g., from Fe^{3+} to Co^{3+} instead, does feature a redshift of the asymmetric CO stretching mode^[68].

Stepwise coordination of the axial pyridine ligands ($n = 1-3$) induces significant geometrical distortions of the M_3O core. The primary goal of this research is to characterize the geometric structural motif and its related change in electronic structure in the ground state using IR(M)PD. All prior measurements were carried out using 3d metals, and we switched from a

high spin 3d transition metal to a low spin 4d transition metal with just one unpaired spin on each metal center. Furthermore, our gas phase technique enables the separation of under coordinated molecular ions (e.g., $[\text{Fe}_3\text{O}(\text{OAc})_6]^+$) that would not be accessible in the condensed phase.

We combine experimental IR(M)PD investigations of isolated $[\text{Ru}_3\text{O}(\text{OAc})_6(\text{py})_n]^+$ ($n = 0, 1, 2, 3$) with quantum chemical calculations by broken symmetry approach, Density Functional Theory (DFT), Time Dependent Density Functional Theory (TD-DFT) and XA simulations with CTM4XAS^[69] in combination with Cowan batch files.

6.4 Experimental setup and methods

6.4.1 Collision Induced Dissociation

ESI MS and CID measurements were performed with a quadrupole mass spectrometer (amazon ETD, Bruker daltonics), obtaining a Paul trap. The ions of interest are transferred into gas phase by electrospray ionization. The sample solution of $[\text{Ru}_3\text{O}(\text{OAc})_6(\text{py})_n]^+$ ($n = 0, 1, 2, 3$) in pyridine/acetonitrile (1:10; $c \sim 1 \cdot 10^{-6}$ mol/L) was constantly infused into the ESI chamber by a syringe pump with a flow rate of 180 $\mu\text{L}/\text{h}$. Nitrogen was used as a drying gas with a flow rate of 12 L/min at 180 °C. The nebulizer pressure was set to 280 mbar (4 psi) for spraying the sample solution, and the spray needle was held at 4.5 kV. The Paul trap consists of a ring electrode and two end caps forming a nearly hyperbolic inner profile. The end caps possess pinholes that allow to enter or exit the ions in the trap. The ring electrode is powered with a high voltage RF (radio frequency) potential (781 kHz) while the end caps are grounded. The ions are accumulated in this resulting oscillating quadrupolar electric field generated from the three electrodes. An auxiliary dipolar voltage is fed to either the exit cap or both end caps for ion isolation and fragmentation. For providing a constant partial Helium buffer gas pressure of ca. 10^{-3} mbar inside the trap, a proportional integral derivative (PID) gas controller is used.

CID breakdown curves were recorded by stepwise variation of the excitation amplitudes (Amp_{exp}) from 0.5 V–3.0 V while monitoring the extend of fragmentation and relative abundances of fragments for the isolated complex of interest. The excitation amplitudes determine the internal scale of the mass spectrometer E_{lab} in V. Relative abundances were calculated according to

$$I_{tot}^{fr}(E_{lab}) = \left(\frac{\sum_i I_i^{fr}(E_{lab})}{\sum_i I_i^{fr}(E_{lab}) + \sum_i I_i^p(E_{lab})} \right) \quad (1)$$

where I_i^{fr} = intensity of the fragment ions and I_i^p = intensity of the parent ions. Center of mass transferred fragmentation amplitudes (E_{com}) were calculated from internal amplitudes by:

$$E_{com} = \left(\frac{m_{He}}{m_{He} + m_{ion}} \right) \cdot E_{lab} \quad (2)$$

where m_{ion} stands for the isotopically averaged mass of the molecular ion. Note that the current application of the CID technique by RF excitation in the presence of multiple collisions results in a so called "slow multi collision heating" mode of operation.

Fragmentation amplitude dependent CID spectra were modeled and fitted by sigmoidal functions of the type

$$I_{fit}^{fr}(E_{com}) = \left(\frac{1}{1 + e^{(E_{com}^{50} - E_{com}) B}} \right) \quad (3)$$

Using a least-squares criterion. The E_{com}^{50} fit parameter is the amplitude at which the sigmoid function is at half maximum value, whereas B describes the rise of the sigmoid curve. Due to the correlation of fragmentation amplitude and appearance energy, it is feasible to assume that the appearance curves can be associated with the isolated complexes' relative stability.

6.4.2 InfraRed (Multiple) Photon Dissociation (IR(M)PD)

InfraRed (Multiple) Photon Dissociation (IR(M)PD) experiments were performed using a modified Paul-type quadrupole ion trap mass spectrometer (Amazon SL, Bruker Daltonics) at room temperature. The ions of interest are transferred into gas phase by electrospray ionization. The sample solution of $[Ru_3O(OAc)_6(py)_n]^+$ ($n = 0, 1, 2, 3$) in pyridine/acetonitrile (1:10) as a solvent with a concentration of $\sim 1 \cdot 10^{-6}$ mol/L was constantly infused into the ESI chamber by a syringe pump with a flow rate of 180 μ L/h. Nitrogen was used as a drying gas with a flow rate of 12 L/min at 180 °C. The nebulizer pressure was set to 280 mbar (4 psi) for spraying the sample solution, and the spray needle was held at 4.5 kV. The Paul trap consists of a ring electrode and two end caps forming a nearly hyperbolic inner profile. The end caps possess pinholes that allow to enter or exit the ions in the trap. The ring electrode is powered with a high voltage RF (radio frequency) potential (781 kHz) while the end caps are grounded.

The ions are accumulated in this resulting oscillating quadrupolar electric field generated from the three electrodes. An auxiliary dipolar voltage is fed to either the exit cap or both end caps for ion isolation and fragmentation. For providing a constant partial Helium buffer gas pressure of ca. 10^{-3} mbar inside the trap, a proportional integral derivative (PID) gas controller is used.

Laser system

The laser pulses were generated using a KTP/KTA optical parametric oscillator/amplifier (OPO/OPA, LaserVision) system. A pulsed 10 Hz injection seeded Nd³⁺ Yag laser (PL 8000, Continuum) pumps the system and serves as source for tunable IR radiation. The difference frequency (DF) between the OPA signal and idler waves is generated within an AgGaSe₂ crystal, applied for the range between 1000 cm⁻¹ and 2000 cm⁻¹. The IR beam is guided into the ion trap by a 90° off axis parabolic silver mirror with a focal length of 15 cm. After passing the Paul-trap, the IR beam was guided to a power meter (Maestro, Gentech) to monitor the laser power. IR(M)PD spectra are obtained by plotting the fragment yield as a function of the laser frequency (ν). The fragment yield is defined as:

$$Y(\nu) = \left(\frac{\sum_i I_i^{fr}(\nu)}{\sum_i I_i^{fr}(\nu) + \sum_i I_i^p(\nu)} \right) \quad (4)$$

Calibration of the IR frequency is done by a wavemeter (821B-NIR, Bristol instruments). The resulting power curves are recorded parallel to the IR(M)PD experiments by digitizing the analog output of the laser power meter through an ADC input of the Amazon SL mass spectrometer. No normalization of the recorded spectra was done because there is an intrinsically nonlinear power dependence of the IR(M)PD fragmentation efficiencies.

6.5 Computational methods

Minimum structures of previously calculated $[\text{Fe}_3\text{O}(\text{OAc})_6(\text{py})_n]^+$ ($n = 0, 1, 2, 3$) complexes served as starting point^[70]. For the multiplicity dependent determination of the minimum structure, linear absorption spectra, and weak interactions, we performed Density Functional Theory (DFT) calculations with B3LYP^[71, 72] functional and cc-PVTZ^[73] basis sets in combination with ecp-28-mdf^[74] effective core potential (Ru) in Gaussian 09 program package^[75]. For the broken symmetry^[76, 77] approach, we utilized Density Functional Theory (DFT) using the B3LYP_Gaussian^[71, 72] functional and cc-pVTZ basis sets^[73] (C, H, N, O) in combination with the ecp-28-mdf^[74] effective core potential (Ru) as implemented in a local, customized installation of the TURBOMOLE 7.0 program package^[78-80]. We studied the antiferromagnetic couplings between the three Ruthenium centers in the complex with our custom CANOSSA program. This program makes it possible to localize anti-parallel, unpaired spins separately on the system's metal centers. A broken symmetry state is constructed from a single determinant wave function that reflects the antiferromagnetic coupling. The orbitals in the broken symmetry states are optimized by applying the variational principle.

6.6 Results and Discussion

6.6.1 Collision Induced Dissociation (CID)

With the above described sample solution, we recorded the mass spectra via electrospray process. The ions of interest were stored within a Paul trap and we monitored a series of isotopic peaks at $m/z = 674, 753, 832, \text{ and } 912$ matching with the simulated isotopic patterns of $[\text{Ru}_3\text{O}(\text{OAc})_6(\text{py})_n]^+$ ($n = 0, 1, 2, 3$). In solution, the axial H_2O ligands of the precursor ion $[\text{Ru}_3\text{O}(\text{OAc})_6(\text{H}_2\text{O})_3]^+$ exchange with the stronger binding pyridine ligand^[68, 70, 81] (py, $\text{C}_5\text{H}_5\text{N}$). However, the fully-coordinated mass peak intensity is significantly higher than in the under-coordinated isomers, indicating that $[\text{Ru}_3\text{O}(\text{OAc})_6(\text{py})_3]^+$ is the most stable complex in the solution. Furthermore, we do not observe the bare complex and the complex with one pyridine coordinated without isolation. Also, water attachment to the unsaturated coordinated Ruthenium centers for the under coordinated complexes is observed (cf. Fig. S1).

CID of isolated $[\text{Ru}_3\text{O}(\text{OAc})_6(\text{py})_n]^+$ ($n = 0, 1, 2, 3$) reveal fragment mass peaks by the loss of the axial pyridine ligands. These are the main fragmentation channels in the complexes with pyridine coordination. With higher excitation amplitudes, the loss of neutral acetate radicals (OAc^*) appears, indicating an intense bonding situation in these complexes, as previously observed^[68, 70, 81, 82].

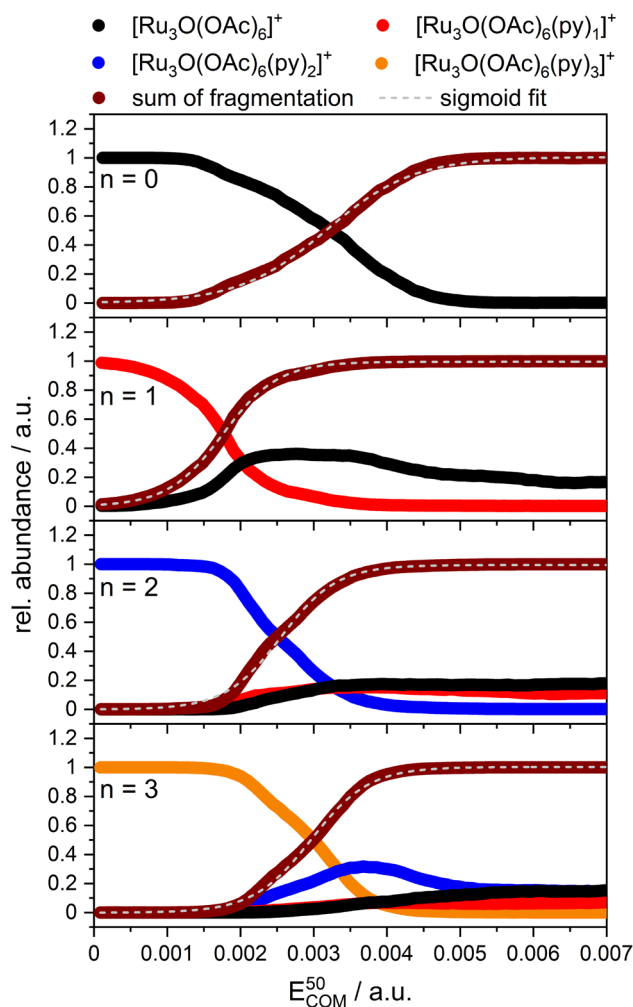


Fig. 2: CID breakdown curves of $[\text{Ru}_3\text{O}(\text{OAc})_6(\text{py})_n]^+$ ($n = 0, 1, 2, 3$), appearance curves of the associated fragments, and sigmoid fits.

We investigate the relative stabilities of $[\text{Ru}_3\text{O}(\text{OAc})_6(\text{py})_n]^+$ ($n = 0, 1, 2, 3$) by recording so-called CID breakdown curves of these complexes and their corresponding appearance curves of the associated fragments (cf. Fig. 2). In the case of $[\text{Ru}_3\text{O}(\text{OAc})_6(\text{py})_3]^+$ (cf. Fig. 2; $n = 3$; red circles), the elimination of one pyridine represents the primary fragmentation channel as recorded by the fragment peak $[\text{Ru}_3\text{O}(\text{OAc})_6(\text{py})_2]^+$. The fragmentation starts within an E_{COM} value of 0.002 a.u.

As the CID amplitude increases, the fragment $[\text{Ru}_3\text{O}(\text{OAc})_6(\text{py})_2]^+$ decreases with the loss of the second and third pyridine. With a CID amplitude of 0.00176 a.u., the fragmentation channel of the loss of three pyridines appears, recorded as $[\text{Ru}_3\text{O}(\text{OAc})_6]^+$. We assume that the elimination of the second and third pyridine occurs contemporaneously from the $[\text{Ru}_3\text{O}(\text{OAc})_6(\text{py})_3]^+$ complex and also from the $[\text{Ru}_3\text{O}(\text{OAc})_6(\text{py})_2]^+$ fragment by rising the CID amplitude. With a CID amplitude of $E_{\text{COM}} 0.00317$ a.u. we observe the elimination of three acetates (OAc^*) ligands for the complex $[\text{Ru}_3\text{O}(\text{OAc})_6]^+$. The loss of three acetate ligands belongs to the fragmentation of the complex $[\text{Ru}_3\text{O}(\text{OAc})_6]^+$ and not of a pyridine coordinated complex.

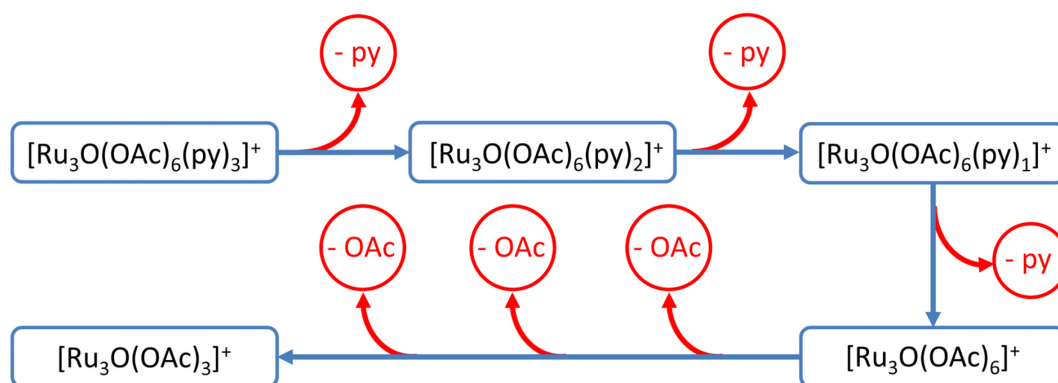


Fig. 3: Fragmentation pathways of $[\text{Ru}_3\text{O}(\text{OAc})_6(\text{py})_n]^+$ ($n = 0, 1, 2, 3$) by varying the excitation amplitude in the CID experiments.

With the CID breakdown curves, we are able to determine the relative gas phase stability of the complexes $[\text{Ru}_3\text{O}(\text{OAc})_6(\text{py})_n]^+$ ($n = 1, 2, 3$) by fitting the appearance curve with a sigmoid fit. The E_{COM}^{50} values reveal an increasing trend from $n = 1$ to $n = 3$ (cf. fig. 4). This is the complete opposite behavior in their stabilities as in our earlier research of $[\text{Fe}_3\text{O}(\text{OAc})_6(\text{py})_n]^+$ ($n = 1, 2, 3$)^[70]. The gas phase stability rises from 1.76 a.u. for $n = 0$ to 2.96 for $n = 3$.

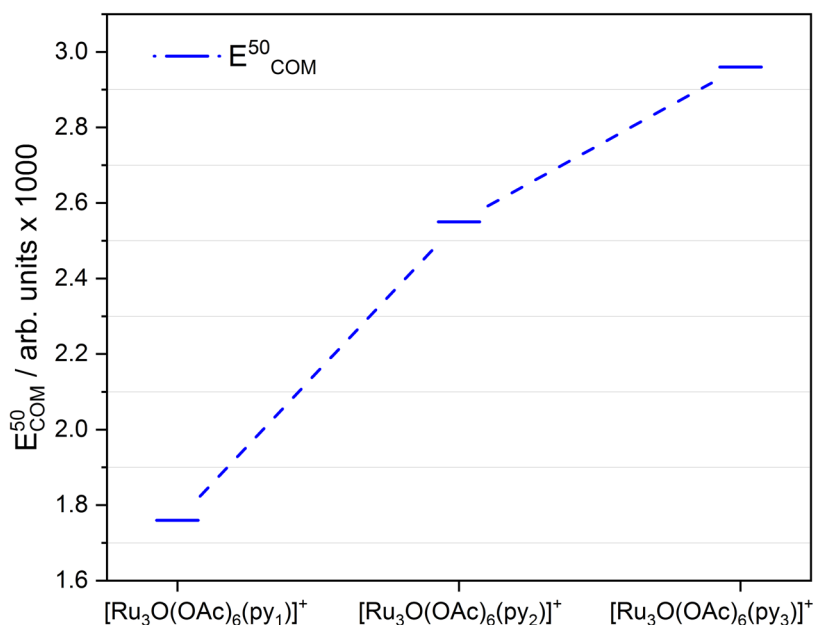


Fig. 4: Determined gas phase stabilities (E_{COM}^{50}) values of $[Ru_3O(OAc)_6(py)_n]^+$ ($n = 1, 2, 3$).

We presume that this trend is provided by transitioning from a 3d high spin metal to a 4d low spin metal. The orbitals in the 4d metal reach further into the environment, and the unsaturated species are more unstable. We also observe gas phase reactions with water when the complex is not saturated. Furthermore, the coordination of pyridine leads to a significant change in the stability of the complex, indicating an influence on the structural geometry.

6.6.2 InfraRed (Multiple) Photon Dissociation (IR(M)PD)

We recorded IR(M)PD spectra of $[Ru_3O(OAc)_6(py)_n]^+$ ($n = 0, 1, 2, 3$) (cf. Fig. 5) in comparison with calculated linear absorption spectra for each complex. DFT calculations reveal a minimum structure of a complex with three Ru^{3+} atoms in a low spin configuration and one unpaired electron on each Ru^{3+} atom. The broken symmetry calculated spin densities reveal localized spin densities on the Ruthenium center as in earlier studies of $[Fe_3O(OAc)_6(py)_n]^+$ ($n = 0, 1, 2, 3$)^[70]. The isosurfaces are not spherical as in the iron analogs. Different behavior of the magnetic moments in these series of complexes could be occurring. The spin density changes from a d_z orbital like density to a d_{xy} orbital like one by coordinating pyridine to the complex. We assume a change in the electron occupancy by coordination of pyridine to the complex. The spectra show the emergence of two or more vibrational modes due to stepwise coordination of pyridine, indicating that the geometry is strongly dependent on the number of detected vibrational modes in these complexes.

Furthermore, these bands did not disappear with three pyridines coordinated to the complex, suggesting that the D_{3h} symmetry does not fully restore in this case as in the earlier investigations of J. Lang^[68, 70] and J. Meyer^[82].

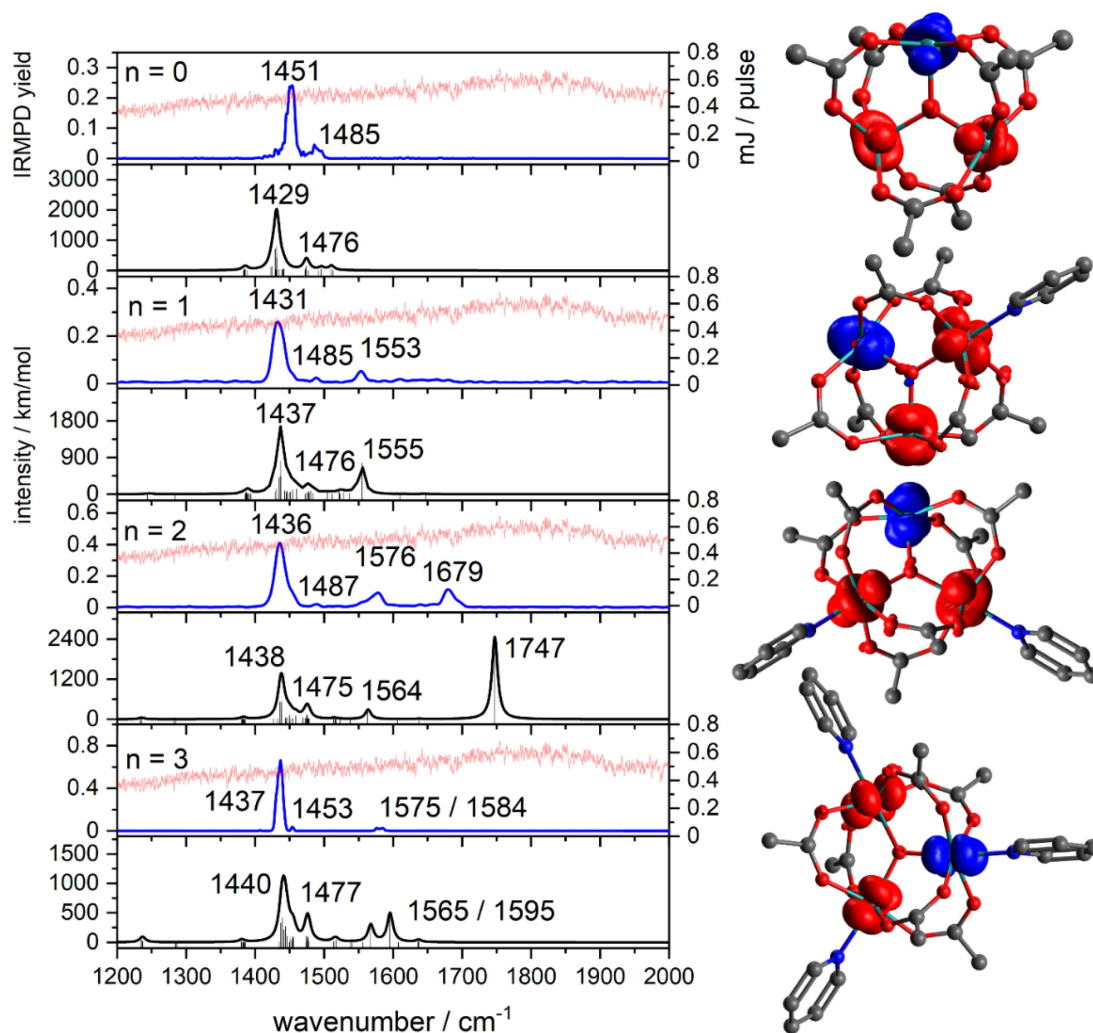


Fig. 5: IR(M)PD spectra (blue) in comparison with quantum chemistry calculation of $[Ru_3O(OAc)_6(py)_n]^+$ ($n = 0, 1, 2, 3$) (black). The broken symmetry minimum structure calculations were performed with Turbomole 7.0 at the B3LYP_Gaussian/cc-pVTZ (H, C, N, O) and ecp-28-mdf (Ru) level of theory in UDU configuration for $n = 0, 3$ and DUU configuration for $n = 1, 2$. Spin density isosurfaces indicate unpaired alpha (U, red) and beta (D, blue) spin density. Calculation of the Linear absorption spectra was performed with Gaussian 09 at the B3LYP/cc-pVTZ (H, C, N, O) and ecp-28-mdf (Ru) level of theory. The frequencies are scaled at 0.996, and stick spectra were convoluted with Gaussian curves (FWHM = $10 cm^{-1}$). Hydrogen is omitted for clarity.

IR(M)PD and DFT spectra of $[\text{Ru}_3\text{O}(\text{OAc})_6]^+$

The experimental IR(M)PD spectra of $[\text{Ru}_3\text{O}(\text{OAc})_6]^+$ obtains two bands. The predicted $\nu_s(\text{COO})_{\text{OAc}}$ and $\delta(\text{CH}_3)_{\text{OAc}}$ absorption bands at 1429 cm^{-1} and 1476 cm^{-1} find reasonable correspondence in the recorded IR(M)PD bands at 1451 cm^{-1} . The band at 1485 cm^{-1} is in good agreement with the predicted $\delta(\text{CH}_3)_{\text{OAc}}$ absorption band at 1476 cm^{-1} . The complex is in a D_{3h} symmetry, and all CO stretching modes degenerate to one band. We do not observe the predicted band at 1384 cm^{-1} . Weak absorption in conjunction with a high fragmentation threshold for OAc^* elimination seems to hamper IR(M)PD detection in these cases.

IR(M)PD and DFT spectra of $[\text{Ru}_3\text{O}(\text{OAc})_6(\text{py})_1]^+$

The DFT calculation predict three bands at 1437 cm^{-1} for $\nu_s(\text{COO})_{\text{OAc}}$, 1476 cm^{-1} for $\delta(\text{CH}_3)_{\text{OAc}}$ and 1555 cm^{-1} for $\nu_{\text{as}}(\text{COO})_{\text{OAc}}$. Predicted CO stretching modes are delocalized over the four bridging acetate groups, neighbouring the pyridine ligand. This is in good agreement with the experimental IR(M)PD spectra for the bands at 1431 cm^{-1} for $\nu_s(\text{COO})_{\text{OAc}}$, 1485 cm^{-1} for $\delta(\text{CH}_3)_{\text{OAc}}$, and 1553 cm^{-1} for $\nu_{\text{as}}(\text{COO})_{\text{OAc}}$. The distortion of the Ru_3O core leads to a cancellation of the degeneration to a C_{2v} symmetry. Within the distortion, there is an appearance of the asymmetric CO stretching mode. There is a strong coupling between the symmetric CO stretching modes and the pyridine and a weaker coupling for the asymmetric CO stretching modes in this complex.

IR(M)PD and DFT spectra of $[\text{Ru}_3\text{O}(\text{OAc})_6(\text{py})_2]^+$

DFT calculation reveal four bands at 1436 cm^{-1} for $\nu_s(\text{COO})_{\text{OAc}}$, 1475 cm^{-1} for $\delta(\text{CH}_3)_{\text{OAc}}$, 1564 cm^{-1} for $\nu_{\text{as}}(\text{COO})_{\text{OAc}}$ and 1747 cm^{-1} for $\nu_{\text{as}}(\text{COO})_{\text{OAc}}$. In this case, the distortion of the complex is bigger than in the complex with one coordinated pyridine, leading to a more blue shifted asymmetric CO stretching mode. Furthermore, the distortion of the complex is that high that two pairs of asymmetric CO stretching modes appear. The band at 1436 cm^{-1} belongs to the six folded degenerated symmetric CO stretching mode. The first asymmetric CO stretching mode consists of two pairs of the acetate ligand between the pyridine coordinated Ru^{3+} atom and the free Ru^{3+} atom. The other acetate ligands between the pyridine coordinated Ru^{3+} atoms show a small vibrational mode at this band. The pyridine appears to reduce the

vibrational modes at these ligands. The second asymmetric stretching mode belongs to the six-fold degenerated CO vibration of all acetate ligands.

IR(M)PD and DFT spectra of $[\text{Ru}_3\text{O}(\text{OAc})_6(\text{py})_3]^+$

The calculated energies corresponding to the minimum structure of different multiplicities reveal a possibility of a mixed valence state in this complex (cf. Tab. S1). Several groups^[61, 62, 83-89] observed in their investigations that the complex has a mixed valence state with a composition of $\text{Ru}^{3+, 2+, 2+}$. The energies are well separated for all isomers. For the fully-coordinated complex, it is still uncertain whether all Ruthenium ions are in an oxidation state +3 or in a mixed valence state. Therefore, the calculated linear absorption spectra should have small changes with the change of the multiplicity (cf. Tab. S1, cf. Fig. S2). The IR(M)PD spectra reveal one sharp band at 1437 cm^{-1} , a minor vibrational bending mode from the methyl groups, and a tiny band at 1575 cm^{-1} . A deeper examination of the tiny band reveals a modest splitting of 9 cm^{-1} , which is expected by the DFT calculation for a compound containing three Ru^{3+} ions. The symmetric CO stretching mode at 1437 cm^{-1} is in good agreement with the expected vibration mode from the DFT calculation. The $\delta(\text{CH}_3)_{\text{OAc}}$ mode does not match the predicted one and is redshifted with 34 cm^{-1} . Different coupling of the acetate vibrational modes causes the asymmetric CO stretching mode to divide. The vibrational mode at 1575 cm^{-1} is a result of the coupling of the six folded degraded vibrational modes of acetates. The other band at 1584 cm^{-1} belongs to the four folded degenerated acetate vibration modes. The asymmetric CO stretching modes are very small. This suggests that the symmetry is nearly a D_{3h} symmetry, but not exactly as for $[\text{Ru}_3\text{O}(\text{OAc})_6]^+$. In comparison with the DFT calculations, we can exclude a mixed valence state in this complex because the asymmetric CO stretching mode seems to split as in the calculation for the quartet state. A doublet state does not provide such splittings.

Influence of pyridine coordination on the IR(M)PD spectra

As proven before, axial ligands modulate the shape, frequency, and intensity of the CH_3 bending modes and the CO stretching modes^[68, 70, 81]. The $\delta(\text{CH}_3)$ frequencies are almost the same until the second pyridine coordination takes part. With the third coordination, the $\delta(\text{CH}_3)$ is red shifted by 33 cm^{-1} .

The symmetric CO stretching modes are also blue shifted by 23 cm^{-1} , 20 cm^{-1} , 17 cm^{-1} for the coordinated complexes. The calculated linear absorption spectra show no shift for the symmetric CO stretching mode. Therefore, the bare complex does not obtain an asymmetric CO stretching mode neither calculations predict this stretching mode. The high symmetry of the complex leads to degenerated CO stretching modes. Coordination of one pyridine causes a distortion of the Ru_3O core owing to elongation of the Ru-O bonding, culminating in the development of an asymmetric CO stretching mode due to degeneration loss. With the second pyridine coordination, the Ru_3O core becomes more distorted than with one coordinated pyridine. The distortion leads to two pairs of pairwise degenerated asymmetric CO stretching modes. These asymmetric CO stretching modes are mostly shielded from the other acetate ligands, which do not feature a vibrational coupling in this complex. The coordination of three pyridines restores the D_{3h} symmetry, and the asymmetric CO stretching almost vanish. We discover a small vibrational mode, implying that the symmetry in the Ru_3O core has not been completely restored. The blueshift of the asymmetric CO stretching modes is common with the predicted blueshift from DFT calculations (cf. Fig. 6). The calculated blue shifts are overestimated but reveal the same trend as the experimental blue shifts from the IR(M)PD experiments. The bare complex shows no asymmetric CO stretching modes, neither in the calculations nor the experimental spectrum. Therefore, the first appearance of the asymmetric CO stretching mode in the complex with one coordinated pyridine serves as a starting point for interpreting the observed blue shifts. The coordination of pyridine leads to a distortion of the Ru_3O core, resulting in the repeal of the degeneration of the CO stretching modes.

Further coordination of pyridine results in two distinct degraded asymmetric stretching modes in these complexes. The coordination of three axial ligands should lead to a restoration of the symmetry. Still, the blue shift of the asymmetric CO stretching mode points out that the symmetry in this complex is not restored as in $[\text{Fe}_3\text{O}(\text{OAc})_6(\text{py})_n]^+$ ($n = 0, 1, 2, 3$)^[70].

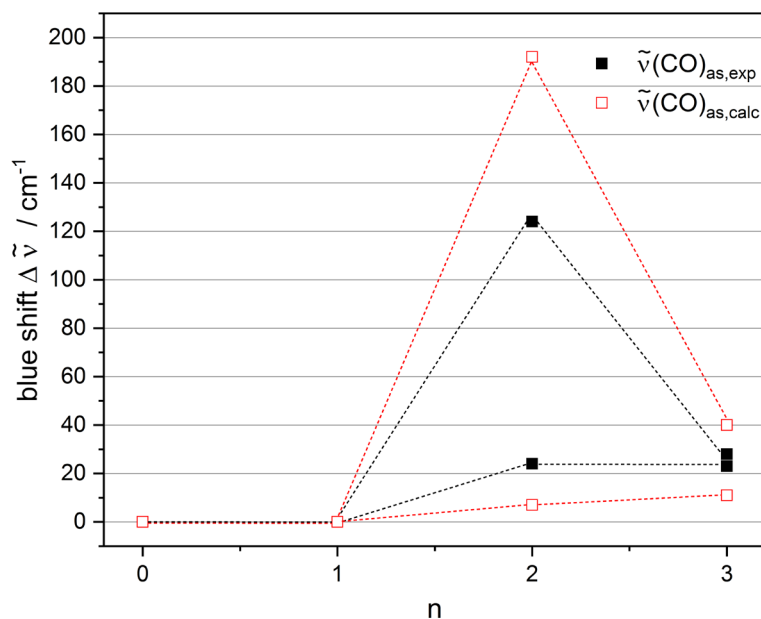


Fig. 6: Blueshift of the experimental IR(M)PD spectra and calculated linear absorption spectra of $[\text{Ru}_3\text{O}(\text{OAc})_6(\text{py})_n]^+$ ($n = 0, 1, 2, 3$). The calculations were performed with Gaussian 09 at the B3LYP/cc-pVTZ (H, C, N, O) and ecp-28-mdf (Ru) level of theory.

To determine the structural distortion in this series of complexes and their resulting influence on the axial ligand, we performed Natural Bond Order (NBO) calculations. The calculations seem to confirm our assumption (cf. Fig. S4). Without coordination of pyridine, all Ru-O bonding lengths in the complex are almost equal. Just one Ru-O bonding is elongated by 0.002 Å. With the coordination of one or two pyridines to the complex, the Ru-O-py bondings are elongated by 0.108 Å for one coordinated pyridine and 0.065 Å for two coordinated pyridines. The coordination of one or two pyridines results in longer free Ru-O bonding lengths. The Ru-O coordination with the third pyridine is almost equal to the bare complex, except one Ru-O bonding is slightly longer with a distance of 2.008 Å. This substantiates our assumption that the complex is not in a D_{3h} symmetry as in the bare complex. In comparison with our early published paper of $[\text{Fe}_3\text{O}(\text{OAc})_6(\text{py})_n]^{+}$ ^[70].

The blue shift of these complexes clearly shows the distortion of the Ru_3O core by coordinating pyridine to the complex (cf. Fig. S4). The complex is in a D_{3h} symmetry without pyridine coordination, resulting in degenerated CO stretching modes, and we do not observe asymmetric CO stretching modes. With further coordination of pyridine, the symmetry reduces from D_{3h} to a C_{2v} symmetry resulting in the repeal of the degeneration, and the asymmetric CO stretching becomes more present.

The intensity of the asymmetric CO stretching mode decreases with the third pyridine coordination due to the almost symmetrical Ru_3O core, which is not in ideal D_{3h} symmetry.

Electron Localization Field plots (ELF)^[90] reveal strong covalent bondings from the Ru ions to the central O^{2-} core for the bare complex (cf. Fig. 7). All three Ruthenium ions have the same bonding situation due to their symmetry. Due to the more diffuse 4d orbitals in the Ruthenium core, we detect a stronger bonding condition in the Ruthenium complex than in the Fe^{3+} analogon. The coordination of one pyridine to the complex leads to a stronger py-M bonding in Ruthenium than in the iron complex. Also, the Ru-O bonding is slightly weaker for the Ruthenium complex, resulting in a suspension of the D_{3h} symmetry. Therefore, more vibrational bands in the IR(M)PD spectrum are observed. Coordination of two pyridines causes a greater deformation of the M_3O core in both complexes. Due to the more extensive variations in electron density of the Ruthenium centers than the iron centers, two pyridine coordinations result in separate weakening Ru-O bondings for the Ruthenium complex, resulting in two different asymmetric CO stretching modes.

With the coordination of three pyridines to the complex, the Ru_3O core is almost symmetric again. Still, the ELF plots point out slightly different electronic densities for the bare and fully-coordinated complex. This also shows that the coordination of three pyridines does not entirely restore D_{3h} symmetry. The symmetry is entirely restored in our previous experiments with $[\text{Fe}_3\text{O}(\text{OAc})_6(\text{py})_n]^+$ ($n = 0, 1, 2, 3$)^[74, 75] due to the spherical electron density in the Fe^{3+} ions, which is not present in the Ru^{3+} ions. The axial coordinated pyridine ligands reveal more covalent bondings in the Ruthenium complexes than in the iron complexes. Stepwise pyridine coordination to the complex results in decreased bonding strengths in both complexes. Still, in the Ruthenium complexes, the covalent bonding situation is stronger than in the iron analoga. As with iron complexes, the coordination of the axial ligand results in more minor non covalent interactions. In the iron complexes, we observe the strongest covalent bonding with one pyridine coordinated to the complex, and then the significant interaction of the pyridine is non covalent. In the Ruthenium complexes the axial pyridine is always more covalent bonded to the complex.

Further coordination of pyridine does not change the bonding strength towards the axial ligand. We observe weakened Ru-O bonding strength as in the Fe analog complexes, but the main difference is that these bondings are more vital in every isomer for the Ruthenium

complex. With three coordinated pyridines to the complex, we observe similar behavior as in the bare complex for both metal centers. The main difference in both cases must be that the iron complex does not influence the ligands as the Ruthenium complex. The IR(M)PD spectra are more affected than in the earlier investigated IR(M)PD experiments with the iron complexes^[70].

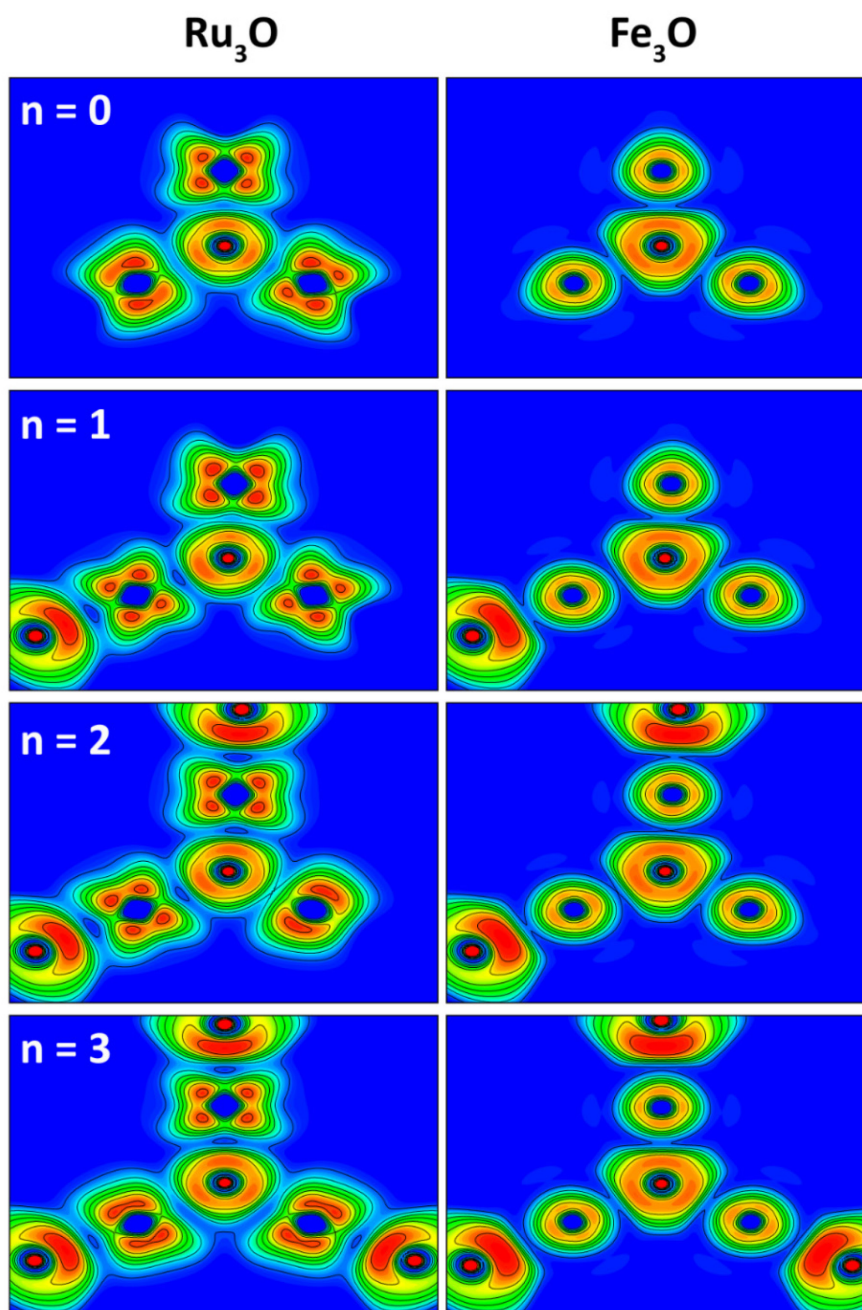


Fig. 7: Calculated ELF plots of $[\text{M}_3\text{O}(\text{OAc})_6(\text{py})_n]^+$ ($\text{M} = \text{Ru}, \text{Fe}; n = 0, 1, 2, 3$). The calculations were performed at the B3LYP/cc-pVTZ (H, C, N, O) and ecp-(28, 10)-mdf (Ru, Fe) level of theory one unpaired electron on each Ru center and five unpaired electrons on each Fe center.

The isosurfaces of Electron Localization Field (ELF), Density Overlap Region Indicator (DORI), and Non covalent Interaction (NCI) demonstrate a significant non covalent interaction through coordination of pyridine to the complex (cf. Fig. S5). As discussed before, the covalent bonding situation of the pyridine to the Ruthenium leads to weakened Ru-O bonding strengths. Strong van der Waals interactions between pyridine and the complex are shown by non covalent interactions. For all pyridine coordinated systems, the non covalent interactions are between pyridine H atoms in ortho position of the heteroatom and the acetate oxygen of the bridging ligands. This non covalent interaction becomes more prominent with further coordination with strong repulsion in the complex. The non-classical bonding situation of the axial pyridine ligand to the complex leads to the blue shift of the asymmetric CO stretching mode. The distances for pyridine coordination are between 2.102 Å and 2.139 Å for the complex with one pyridine coordination to the fully-coordinated complex. DORI plots show that the complex is stabilized by progressive coordination of pyridine. The pyridine ligands establish solid non covalent interactions. Still, the Ru-O bonding is very strong, and the non covalent interactions do not destabilize the complex; instead, they favor their stabilities to the coordinated complexes. The mass spectra and CID experiments show that every complex except the fully-coordinated complex offers gas phase reactions with water or water directly coordinated.

The distortion of the Ru_3O core gives the appearance of asymmetric CO stretching modes. Still, the influence of the vibrational modes may occur from the Ru-O bonding distance change or the change in Ru-O-Ru-py_n angles. The observed blue shift in these complexes demonstrates that the angle change has a substantial impact on the experimental IR(M)PD spectra (cf. Fig. 8 a)) when compared to their geometrical attributes. The bare complex does not show an asymmetric CO stretching mode. Therefore, we used the complex with one pyridine coordination as a reference for the observed blue shift. The coordination of pyridine leads to a broader Ru-O-Ru angle than in the bare complex. The wider the angle, the more significant the observed blue shift in this series of complexes. Due to the reduced remarkably symmetry, two pyridine coordination produces the largest angles in the complex, as well as the most severe vibrational changes and asymmetric CO stretching modes. The third coordination of pyridine does not lead to the same angles as the bare complex. Therefore, we observe a minor asymmetric CO stretching mode splitting into two pairs of different degenerated asymmetric CO stretching modes.

On the one hand, this indicates that no restoration of the D_{3h} symmetry takes part. On the other hand, the extreme sensitivity of the Ru_3O core corresponding to the IR(M)PD spectrum changes as a function of pyridine coordination. We do not observe a similar correlation with the Ru-O bonding length. The complex with one coordinated pyridine obtains the longest Ru-O bonding distance but a minor blue shift. The coordination of two pyridines shortens the Ru-O bonding, but the observed shifts are higher than with one coordination. Three pyridines coordinated to the complex shorten the Ru-O bondings almost to similar bonding distances as the bare complex but reveal small asymmetric CO stretching modes and point out the exclusion of the restoration in the symmetry.

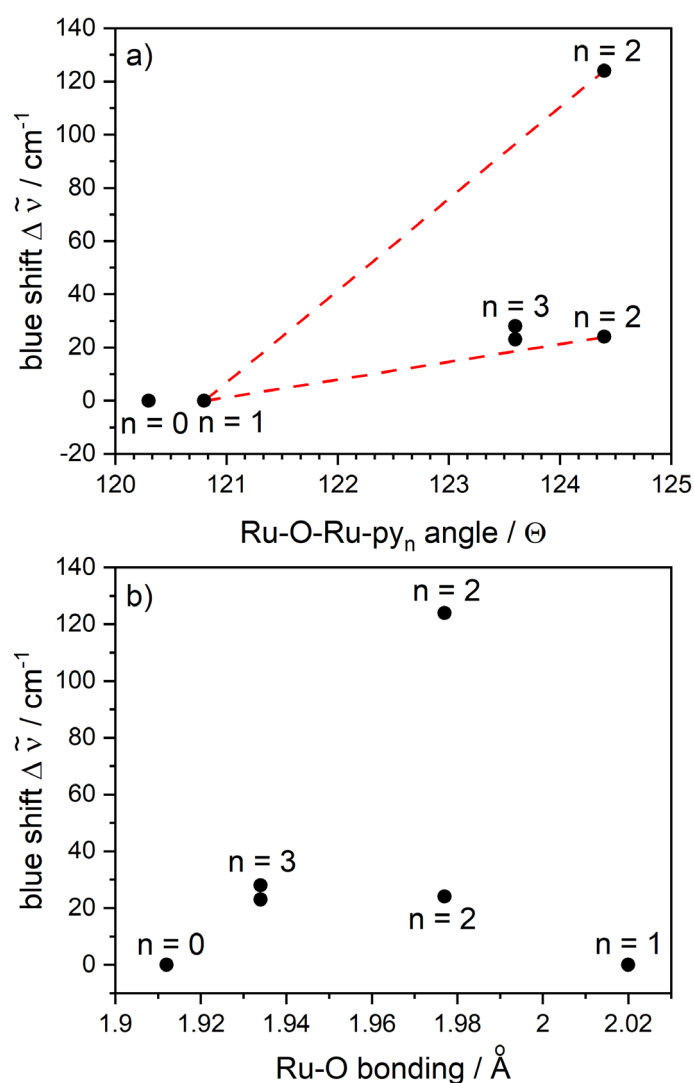


Fig. 8: Blueshift of the experimental IR(M)PD spectra in correlation of their corresponding calculated a) Ru-O-Ru- py_n angles and b) Ru-O bonding distances of $[Ru_3O(OAc)_6(py)_n]^+$ ($n = 0, 1, 2, 3$). The calculations were performed with Gaussian 09 at the B3LYP/cc-pVTZ (H, C, N, O) and ecp-28-mdf (Ru) level of theory.

Influence of the different Metal centers in this series of complexes

Earlier investigations on such μ -oxo bridged complexes have shown the influence of the axial ligand on the M_3O core ($M = Fe, Co$)^[68, 70, 81]. The experiments were performed with 3d high spin or 3d low spin metal centers. The first investigations with a 4d low spin metal center point out slightly different results in this work. The Ruthenium complex is the first complex, where two other asymmetric CO stretching modes are observed (cf. Tab. 1, cf. Fig. S6).

Tab. 1: Vibrational modes of the symmetric and asymmetric CO stretching modes in $[M_3O(OAc)_6(py)_n]^+$ ($M = Ru, Fe$ ^[70], Co ^[68]; $n = 0, 1, 2, 3$).

	Sym. CO stretching mode/cm ⁻¹			Asym. CO stretching mode/cm ⁻¹			
	Ru	Fe	Co	Ru	Ru	Fe	Co
n = 0	1453	1445	1419	0	0	1575	1516
n = 1	1432	1445	1429	1554	0	1587	1579
n = 2	1436	1446	1437	1577	1679	1597	1609
n = 3	1436	1455	1441	1575	1584	1615	1618

For the iron species, we observed almost similar vibrational absorption energies for the symmetric CO stretching modes. An increasing blue shift is observed in the Cobalt species with no unpaired electrons in a low spin state. We observe a redshift for the Ruthenium complex by changing from a 3d to a 4d low spin metal. The asymmetric CO stretching modes reveal an increasing blue shift for the Cobalt and iron complex. An increasing blue shift appears for Ruthenium, and the third pyridine coordination leads to a slight redshift. We assume that the complex feature interesting properties as long the metal centers obtain unpaired electrons. A larger Fe_3O core gives the shift to higher wavenumbers in the symmetric complexes with a slightly different force constant, resulting in another dipole moment in these complexes. DFT calculations with broken symmetry approach also predict a change in the exchange coupling scheme from the symmetric complexes to asymmetric complexes^[70]. Earlier X-ray magnetic circular dichroism (XMCD) studies (cf. chapter 5) confirm the predicted calculations in this complex series. Changing the metal from iron to Ruthenium reduces the number of unpaired electrons from five to one electron per metal center. Also, the 4d orbitals are more diffuse than the 3d orbitals, leading to a more substantial covalent bonding situation of the axial ligand to the metal center. The stronger covalent bonding situation distorts the Ru_3O core, resulting in small asymmetric CO stretching modes as observed. In the 3d metal complexes,

the 3d orbitals are more contracted, and the axial ligands have shorter bonding lengths than in the 4d complex. This results in non degenerated asymmetric stretching modes, resulting in two bands.

6.6.3 Spin magnetic determination via Broken symmetry

Broken symmetry calculations investigate their magnetic properties and resulting spin states for the exchange coupling determination in this series of complexes. We computed eight potential spin isomers for each complex, which were reduced to four isomers due to symmetry and exclusion by relative energy instabilities. For the bare complex, we found similar energies for the antiferromagnetically coupled complexes as for the ferromagnetically coupled complex (cf. Fig. 9). We observe a stabilization with a DUU configuration by 9 kJ/mol with the coordination of one pyridine to the complex. The second pyridine coordination increases the stability of the DUU structure by 27 kJ/mol. Three coordinated pyridines to the complex lead to two possible isomers, DUU and UDU, with the same energy. Earlier investigations of $[\text{Fe}_3\text{O}(\text{OAc})_6(\text{py})_n]^+$ showed an antiferromagnetic exchange coupling for the symmetric complexes^[70]. Other groups also found different spin states for symmetric μ -oxo complexes than for asymmetric complexes^[64, 91]. We assume that in this case also an antiferromagnetic exchange coupling for the bare complex is favored. Because of the high symmetry, the energy difference between a spin up and a spin down electronic is insufficient to identify a preferred structure. For the other isomer, it is clear that a “spin down” electron in these complexes is more favored. The symmetry of the vertical axis helps explain the two potential spin isomers in the isomer with three pyridines. Applying the rotating mirror axis on the DUU configuration leads to the UDU configuration. Therefore we assume that the complex obtains a DUU configuration as the other pyridine coordinated complexes. The spin isomer calculation demonstrates that three pyridine coordination does not result in values that are equivalent to the bare complex. This demonstrates that the energetics and spin configuration are heavily influenced by the quantity of pyridine coordinated to the complex and the resultant distortion.

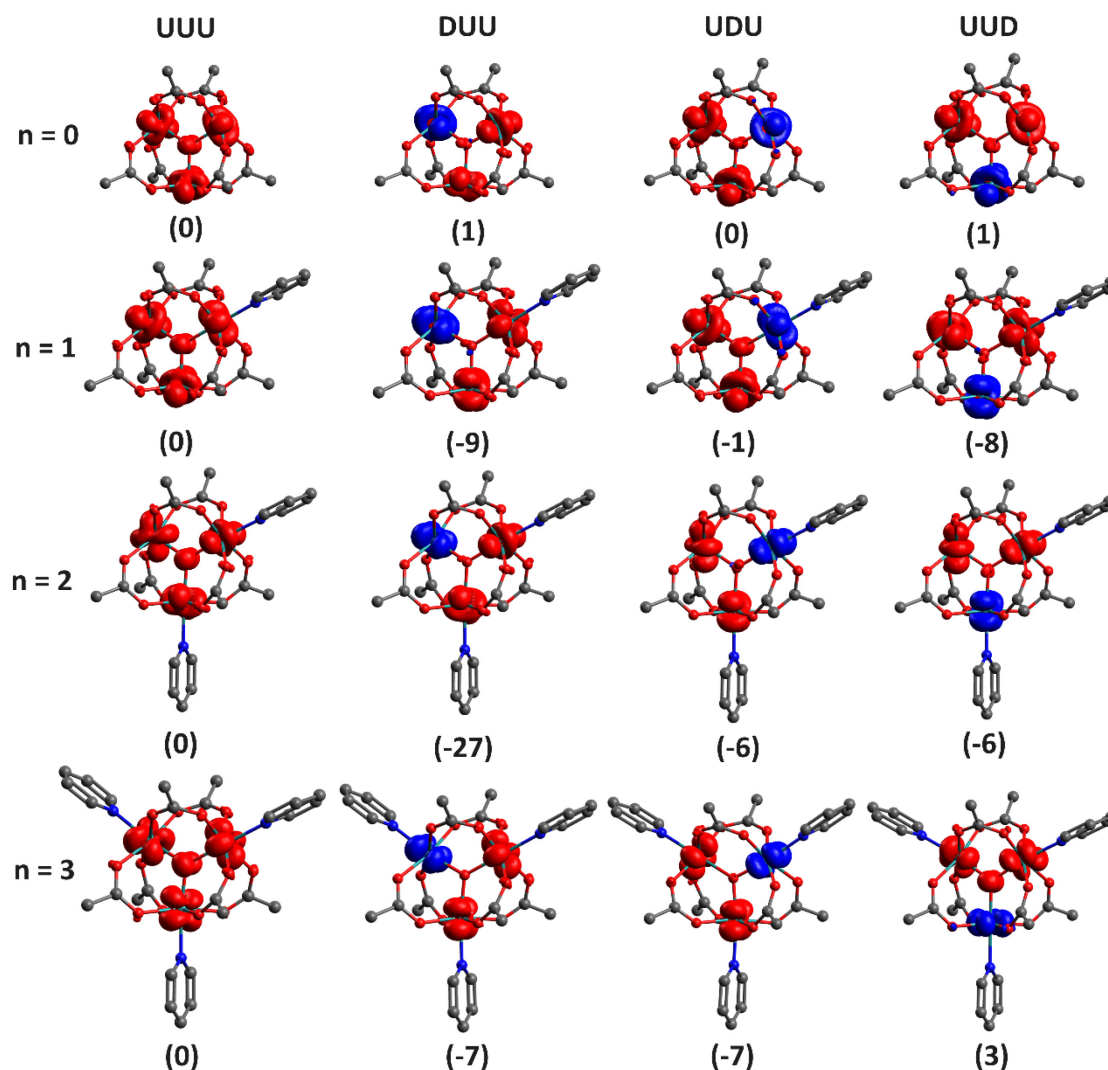


Fig. 9: Spin density iso surfaces (Iso = 0.01) of $[\text{Ru}_3\text{O}(\text{OAc})_6(\text{py})_n]^+$ ($n = 0, 1, 2, 3$) in the one ferromagnetic and the three broken symmetry configurations. red and blue surfaces indicate alpha and beta spin, respectively. The relative energies in paratheses are given in kJ/mol. The calculations were performed at the B3LYP_Gaussian/cc-pVTZ (H, C, N, O) and Stuttgart 1997 ECP (Ru) level of theory.

With the broken symmetry calculated energies from these structures, it is possible to calculate the different coupling constants of the metal centers in the complex. A positive value represents a ferromagnetic coupling scheme, and a negative value represents antiferromagnetic coupling schemes. These complex series calculated coupling constants reveal that each Ruthenium center is antiferromagnetically coupled for the bare complex (cf. Tab. 2). A modest ferromagnetic exchange coupling between one Ru ion and two antiferromagnetic linked Ruthenium centers results from the coordination of one pyridine. The ferromagnetic exchange coupling is that weak that an overall antiferromagnetic exchange coupling is expected.

The coordination of two pyridines predicts an antiferromagnetic exchange coupling for all Ruthenium atoms. Additional pyridine coordination to the complex results in an antiferromagnetic exchange coupling between all Ruthenium centers. These coupling constants reveal slightly different results than in earlier studies of $[\text{Fe}_3\text{O}(\text{OAc})_6(\text{py})_n]^+$, where the asymmetric complexes show a ferromagnetic exchange coupling and the symmetric ones an antiferromagnetic exchange coupling. The Ruthenium complex reveals an antiferromagnetic exchange coupling for every isomer. The total coupling constants show a decreasing trend as a function of the distortion in the Ru_3O core. The fully coordinated complex reveals a slightly lower total coupling constant than the bare complex. However, it is not as low as the complex with two coordinated pyridines, indicating that it is almost symmetrical but not precisely.

Tab. 2: Calculated coupling constants of each pair in the Ru_3O core and their total coupling constants of $[\text{Ru}_3\text{O}(\text{OAc})_6(\text{py})_n]^+$ ($n = 0, 1, 2, 3$).

n	J_{12}/cm^{-1}	J_{13}/cm^{-1}	J_{23}/cm^{-1}	$J_{\text{total}}/\text{cm}^{-1}$	J/J^*
0	-9.29	-11.98	-14.53	-35.80	0.73
1	-34.88	-33.03	0.76	-67.15	0.46
2	-34.34	-36.94	-39.53	-110.82	0.90
3	-46.57	0.00	0.00	-46.58	0.00

For the determination of the spin states of $[\text{Ru}_3\text{O}(\text{OAc})_6(\text{py})_n]^+$ ($n = 0, 1, 2, 3$), we used the formula which is already established by Lang et al. ^[70]. Therefore we determine an HDvV Hamiltonian as follows^[92]:

$$\hat{S}_T = \hat{S}_A + \hat{S}_{\text{Ru}1} \quad (5)$$

$$\hat{S}_A = \hat{S}_{\text{Ru}2} + \hat{S}_{\text{Ru}3} \quad (6)$$

$$\hat{H}_{\text{HDvV}} = -2J(\hat{S}_T^2 - \hat{S}_A^2) - J^*(\hat{S}_A^2) \quad (7)$$

The Hamiltonian yields 27 eigenstates with four degenerated ground states. Furthermore, two of the four ground states yield the same spin states due to symmetry. Thus, the total spin (S_T) of these ground states can be 5/2 (UUU), 1/2 (UDU), and 1/2 (UUD). Determining the partial spin ground state and the total spin ground state reveals a constant partial spin ground state for all isomers and a decreasing spin ground state by coordinating pyridine to complex. After the first coordination, no changes in the total spin ground state are observed (cf. Tab. 3).

Tab. 3: Calculated partial and total spin groundstates of $[\text{Ru}_3\text{O}(\text{OAc})_6(\text{py})_n]^+$ ($n = 0, 1, 2, 3$) by the hamiltonian in eq. 7

n	$S_T = S_A + S_1$	$S_A = S_2 + S_3$
0	3/2	1
1	1/2	1
2	1/2	1
3	1/2	1

The calculations do not change their magnetic properties by changing the exchange coupling in this complex series. Still, in experimental, it is not possible to measure the strength of an antiferromagnetic exchange coupling.

Theoretical determination of the crystal field splitting and UV correlation

Earlier investigations on $[\text{Fe}_3\text{O}(\text{OAc})_6(\text{py})_n]^+$ (cf. chapter 5) have shown slightly different crystal field splittings by stepwise coordination of pyridine to the complex via X-ray magnetic circular dichroism (XMCD). Unfortunately, the energy for the Ruthenium $L_{3,2}$ edge is too high for X-ray measurements on the $L_{3,2}$ edge. The theoretical crystal field splitting determination can be achieved by normalizing the UV/VIS absorption energy in the Tanabe Sugano diagram. We performed TD-DFT calculations of these complexes and observed several bands in the absorption spectra. To determine the crystal field splitting, we used the calculated MLCT transitions in the area of 320–500 nm (cf. Fig. S13).

In the calculated UV/VIS spectra, all transitions are HOMO-LUMO transitions. The main difference in the spectra is the shifts due to transitions from different HOMO orbitals into different LUMO orbitals depending on the amount of pyridine coordination to complex (cf. Fig. S14). For complexes containing one or two coordinated pyridines, the corresponding orbitals of the axial ligands are implicated in the UV/VIS absorption, resulting in modest redshifts of the absorption bands. The electron density of the HOMO orbital in the bare complex is delocalized over the whole complex. With the axial ligand coordination, the electron density is more located onto two of three Ruthenium centers and their neighboring acetate ligands. The excitation of the MLCT transition in the bare complex starts from a HOMO-2 orbital, and the coordination of pyridine leads to excitation from the HOMO orbital. Thus, the energy gap between the HOMO and LUMO is getting smaller, resulting in the energy

shift observed in the calculated UV/VIS spectra. With the averaged Racah parameter $B^{[93]}$ of a Ru^{3+} atom, the predicted absorption bands in the UV spectra and the Tanabe Sugano diagram (cf. Tab. 4, cf. Fig. S15)) are possible to approximate the crystal field splittings in these series of complexes. However, the crystal field splittings have to be renormalized by the Racah parameter B for further interpretation. The calculated absorption spectra show the strongest redshift for the complex with one coordinated pyridine after the first coordination. Further coordination leads to a higher blue shift of the absorption band.

Tab. 4: Calculated absorption energies for the MLCT transitions of $[Ru_3O(OAc)_6(Py)_n]^+$ ($n = 0, 1, 2, 3$). The calculations were performed at the TD-DFT UB3LYP/cc-pVTZ (H, C, N, O) and ecp-28-mdf (Ru) level of theory one unpaired electron on each Ru center.

n	E/nm	E/cm ⁻¹	E/B	CF/B	CF/cm ⁻¹	CF/eV
0	399	25094	35.90	9.30	6501	0.81
1	414	24150	34.55	10.10	7060	0.88
2	408	24513	35.07	9.80	6850	0.86
3	396	25230	36.13	9.00	6291	0.79

The approximated crystal field splittings changes with the amount of pyridine coordination in this series of complexes. The coordination of one pyridine leads to the highest crystal field splittings in the complex. Further coordination leads to lower crystal field splittings by stepwise elongating the Ru-O bondings to almost similar lengths. The three pyridine coordination results in nearly identical crystal field splittings to the bare complex, but the minor divergence suggests that the complex is not in D_{3h} symmetry. With these crystal field splittings we performed XAS simulations^[69] of $[Ru_3O(OAc)_6(py)_n]^+$ ($n = 0, 1, 2, 3$). The spectra look similar, and no bigger changes in the spectral pattern are observed (cf. Fig. S16). A closer look at the simulated XA spectra reveals a small shift at the L_3 edge (cf. Fig. 10). This implies that pyridine coordination only results in minor ligand induced effects. In comparison with the calculated UV/VIS spectra, we observe an almost similar trend for all the complexes as observed in the studies of $[Fe_3O(OAc)_6(py)_n]^+$ ($n = 0, 1, 2, 3$). There is an increasing shift monitored for both simulations by coordination of one pyridine to the complex. We assume same behavior as in $[Fe_3O(OAc)_6(py)_n]^+$ ($n = 0, 1$). With the second and third coordination of pyridine to the complex, the absorption energies decrease. In the case of $[Fe_3O(OAc)_6(py)_n]^+$

($n = 0, 1, 2, 3$), we observe an increase of the absorption energies from bare complex to a complex with two coordinated pyridines and afterward a decrease of the energy with three coordinated pyridines. We observe the highest shift with one coordinated pyridine with Ruthenium, and afterward, the energies decrease.

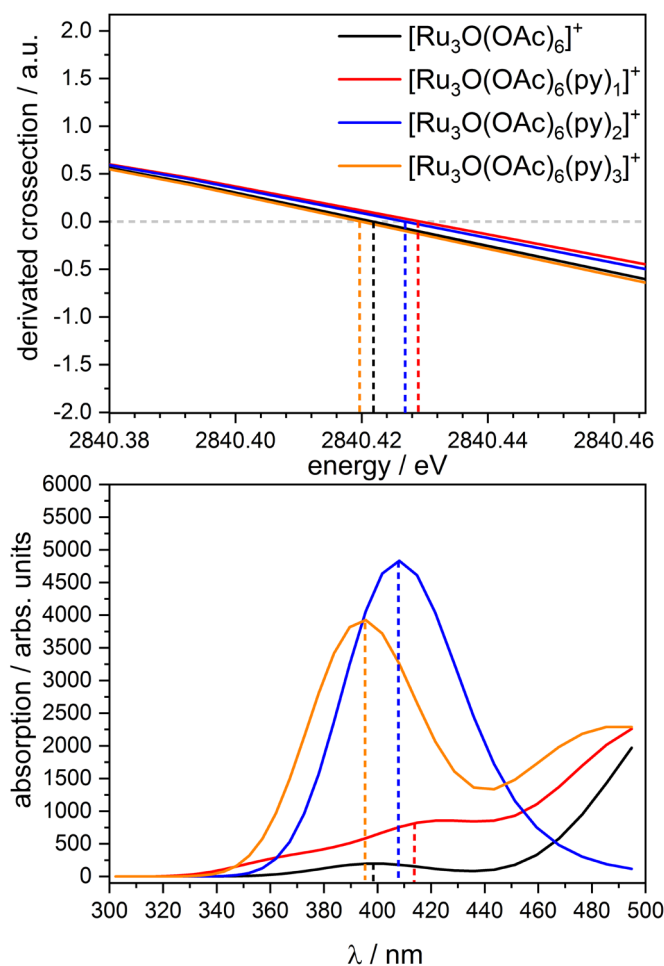


Fig. 10: First derivation of the simulated XA spectra with CTM4XAS^[69] and Batch files by Cowan (top). Calculated UV/VIS spectra of $[\text{Ru}_3\text{O}(\text{OAc})_6(\text{py})_n]^+$ ($n = 0, 1, 2, 3$) (bottom). The calculations were performed at the B3LYP-Gaussian/cc-pVTZ (H, C, N, O) and ecp-28-mdf (Ru) level of theory one unpaired electron on each Ru center.

A similar pattern is observed for the XAS simulations for the UV/VIS spectra simulations, indicating that the absorption energy is closely related to the corresponding crystal field splittings. Thus, a higher crystal field splitting leads to a higher shift in the absorption energies in both simulated spectra. As a result, the energy shift in these complexes is largely dependent on crystal field splitting, which can only be affected by complex deformation with axial ligand coordination.

6.7 Conclusion

We successfully measured IR(M)PD spectra of isolated $[\text{Ru}_3\text{O}(\text{OAc})_6(\text{py})_n]^+$ ($n = 0, 1, 2, 3$) and compared them to DFT predicted linear absorption spectra, which correlate well with the actual spectra. We can determine a strong influence from the axial pyridine ligand to the Ru_3O core. The coordination of pyridine causes a deformation of the Ru_3O core, resulting in the formation of one or more asymmetric stretching modes. With the third coordination of pyridine, the complex does not restore its symmetry as in the case of $[\text{Fe}_3\text{O}(\text{OAc})_6(\text{py})_n]^+$ ($n = 0, 1, 2, 3$). Calculated ELF plots and non covalent interactions reveal a strong covalent bonding situation and high non covalent interactions in this series of complexes, leading to a stabilization of the complex.

Previous research with other metals in this family of complexes has revealed one asymmetric CO stretching mode in complexes generating 3d metals. With Ruthenium as metal center, the asymmetric CO stretching mode appearance becomes present by the first coordination of pyridine to the complex. In these complexes, the more diffuse 4d orbitals have a better overlap for axial coordination and prevent the degradation of the asymmetric CO stretching modes. The calculated IR spectra in the fingerprint areas reveal that pyridine coordination leads to a C_{2v} symmetry. The coordination of three pyridines also points out that the D_{3h} symmetry is not entirely restored.

Broken symmetry calculations reveal a stabilization of the antiferromagnetic exchange coupling scheme as a pyridine coordination function. The different spin isomers' energies are equal for the bare complex, but the calculated coupling constants reveal an antiferromagnetic exchange coupling. The coordination of pyridine leads to a weaker antiferromagnetic exchange coupling. The total coupling constants point out that these complexes do not change their antiferromagnetic exchange coupling to a ferromagnetic one.

Calculated UV/VIS spectra reveal a shift in their absorption as a function of the pyridine coordination. All transitions belong to HOMO–LUMO transitions. With the absorption energies of the MLCT transitions, the determination of the crystal field splitting by the Tanabe Sugano diagram is possible. The simulated XA spectra show the same trend in their energy

shift as the UV/VIS spectra by changing the crystal field energy due to the complex's distortion by coordinating the axial ligand.

In summary, we have shown that gas phase IR(M)PD experiments combined with DFT calculations and Broken symmetry approach add valuable additional insight into the fascinating geometrical, optical and magnetic properties of spin frustrated systems.

6.8 Acknowledgment

The German research foundation DFG supported this work within the transregional collaborative research center SFB/TRR 88 "Cooperative effects in homo and heterometallic complexes" (3MET) and by the state research center OPTIMAS.

6.9 References

- [1] C. D. Falk, and J. J. Mooney, "Three-Way Conversion Catalysts: Effect of Closed-Loop Feed-Back Control and Other Parameters on Catalyst Efficiency," 1980.
- [2] J. Kalinowski, V. Fattori, M. Cocchi, and J. Williams, Light-emitting devices based on organometallic platinum complexes as emitters, *Coord. Chem. Rev.*, 255, 2401-2425, 2011.
- [3] B. Ozdemir, and V. Barone, Thickness dependence of solar cell efficiency in transition metal dichalcogenides MX₂ (M: Mo, W; X: S, Se, Te), *Sol. Energy Mater. Sol. Cells*, 212, 110557, 2020.
- [4] H. Yersin, A. F. Rausch, R. Czerwieniec, T. Hofbeck, and T. Fischer, The triplet state of organo-transition metal compounds. Triplet harvesting and singlet harvesting for efficient OLEDs, *Coord. Chem. Rev.*, 255, 2622-2652, 2011.
- [5] M. Frezza, S. Hindo, D. Chen, A. Davenport, S. Schmitt, D. Tomco, and Q. P. Dou, Novel metals and metal complexes as platforms for cancer therapy, *Current pharmaceutical design*, 16, 1813-1825, 2010.
- [6] U. Ndagi, N. Mhlongo, and M. E. Soliman, Metal complexes in cancer therapy - an update from drug design perspective, *Drug design, development and therapy*, 11, 599-616, 2017.
- [7] A. T. Odularu, P. A. Ajibade, J. Z. Mbese, and O. O. Oyediji, Developments in Platinum-Group Metals as Dual Antibacterial and Anticancer Agents, *Journal of Chemistry*, 2019, 5459461, 2019.
- [8] R. Wai-Yin Sun, D.-L. Ma, E. L.-M. Wong, and C.-M. Che, Some uses of transition metal complexes as anti-cancer and anti-HIV agents, *Dalt. Trans.*, 4884-4892, 2007.
- [9] P. Zhang, and P. J. Sadler, Redox-Active Metal Complexes for Anticancer Therapy, *Eur. J. Inorg. Chem.*, 2017, 1541-1548, 2017.
- [10] H. Kumobayashi, Industrial application of asymmetric reactions catalyzed by BINAP-metal complexes, *Recl. Trav. Chim. Pays-Bas*, 115, 201-210, 1996.
- [11] K. Matyjaszewski, Atom Transfer Radical Polymerization (ATRP): Current Status and Future Perspectives, *Macromolecules*, 45, 4015-4039, 2012.
- [12] K. Schröder, D. Konkolewicz, R. Poli, and K. Matyjaszewski, Formation and Possible Reactions of Organometallic Intermediates with Active Copper(I) Catalysts in ATRP, *Organometallics*, 31, 7994-7999, 2012.
- [13] Y. Garcia, P. J. van Koningsbruggen, E. Codjovi, R. Lapouyade, O. Kahn, and L. Rabardel, Non-classical FeII spin-crossover behaviour leading to an unprecedented extremely large apparent thermal hysteresis of 270 K: application for displays, *J. Mater. Chem.*, 7, 857-858, 1997.
- [14] P. Gütllich, Y. Garcia, and H. A. Goodwin, Spin crossover phenomena in Fe(I) complexes, *Chem. Soc. Rev.*, 29, 419-427, 2000.
- [15] P. Gütllich, H. A. Goodwin, and Y. Garcia, *Spin Crossover in Transition Metal Compounds I*: Springer, 2004.
- [16] H.-J. Krüger, Spin transition in octahedral metal complexes containing tetraazamacrocyclic ligands, *Coord. Chem. Rev.*, 253, 2450-2459, 2009.

- [17] V. Niel, J. M. Martínez-Agudo, M. C. Muñoz, A. B. Gaspar, and J. A. Real, Cooperative Spin Crossover Behavior in Cyanide-Bridged Fe(II)–M(II) Bimetallic 3D Hofmann-like Networks (M = Ni, Pd, and Pt), *Inorg. Chem.*, 40, 3838-3839, 2001.
- [18] M. Schmitz, M. Seibel, H. Kelm, S. Demeshko, F. Meyer, and H.-J. Krüger, How Does a Coordinated Radical Ligand Affect the Spin Crossover Properties in an Octahedral Iron(II) Complex?, *Angew. Chem. Int. Ed.*, 53, 5988-5992, 2014.
- [19] J. M. Clemente-Juan, E. Coronado, A. Forment-Aliaga, A. Gaita-Ariño, C. Giménez-Saiz, F. M. Romero, W. Wernsdorfer, R. Biagi, and V. Corradini, Electronic and Magnetic Study of Polycationic Mn₁₂ Single-Molecule Magnets with a Ground Spin State $S = 11$, *Inorg. Chem.*, 49, 386-396, 2010.
- [20] J. Dreiser, K. S. Pedersen, A. Schnegg, K. Holldack, J. Nehr Korn, M. Sigrist, P. Tregenna-Piggott, H. Mutka, H. Weihe, V. S. Mironov, J. Bendix, and O. Waldmann, Three-Axis Anisotropic Exchange Coupling in the Single-Molecule Magnets $\text{NEt}_4[\text{MnIII}_2(5\text{-Brsalen})_2(\text{MeOH})_2\text{MIII}(\text{CN})_6]$ (M=Ru, Os), *Chemistry – A European Journal*, 19, 3693-3701, 2013.
- [21] T. Lis, Preparation, structure, and magnetic properties of a dodecanuclear mixed-valence manganese carboxylate, *AcCrB*, 36, 2042-2046, 1980.
- [22] A. V. Paliy, S. M. Ostrovsky, S. I. Klokishner, B. S. Tsukerblat, C. P. Berlinguette, K. R. Dunbar, and J. R. Galán-Mascarós, Role of the Orbitally Degenerate Mn(III) Ions in the Single-Molecule Magnet Behavior of the Cyanide Cluster $\{[\text{MnII}(\text{tmphen})_2]_3[\text{MnIII}(\text{CN})_6]_2\}$ (tmphen = 3,4,7,8-tetramethyl-1,10-phenanthroline), *J. Am. Chem. Soc.*, 126, 16860-16867, 2004.
- [23] B. Kintzel, M. Böhme, J. Liu, A. Burkhardt, J. Mrozek, A. Buchholz, A. Ardavan, and W. Plass, Molecular electronic spin qubits from a spin-frustrated trinuclear copper complex, *Chem. Commun.*, 54, 12934-12937, 2018.
- [24] D. MasPOCH, D. Ruiz-Molina, K. WurSt, C. Rovira, and J. Veciana, A very bulky carboxylic perchlorotriphenylmethyl radical as a novel ligand for transition metal complexes. A new spin frustrated metal system, *Chem. Commun.*, 2958-2959, 2002.
- [25] R. Shaw, R. H. Laye, L. F. Jones, D. M. Low, C. Talbot-Eeckelaers, Q. Wei, C. J. Milios, S. Teat, M. Helliwell, J. Raftery, M. Evangelisti, M. Affronte, D. Collison, E. K. Brechin, and E. J. L. McInnes, 1,2,3-Triazolate-Bridged Tetradecametallic Transition Metal Clusters $[\text{M}_{14}(\text{L})_6\text{O}_6(\text{OMe})_{18}\text{X}_6]$ (M = FeIII, CrIII and VIII/IV) and Related Compounds: Ground-State Spins Ranging from $S = 0$ to $S = 25$ and Spin-Enhanced Magnetocaloric Effect, *Inorg. Chem.*, 46, 4968-4978, 2007.
- [26] W.-X. Zhang, W. Xue, J.-B. Lin, Y.-Z. Zheng, and X.-M. Chen, 3D geometrically frustrated magnets assembled by transition metal ion and 1,2,3-triazole-4,5-dicarboxylate as triangular nodes, *Cryst. Eng. Comm.*, 10, 1770-1776, 2008.
- [27] T. Cauchy, E. Ruiz, and S. Alvarez, Magnetostructural Correlations in Polynuclear Complexes: The Fe₄ Butterflies, *J. Am. Chem. Soc.*, 128, 15722-15727, 2006.
- [28] D. Gatteschi, and R. Sessoli, Quantum Tunneling of Magnetization and Related Phenomena in Molecular Materials, *Angew. Chem. Int. Ed.*, 42, 268-297, 2003.
- [29] S. M. Gorun, and S. J. Lippard, Magnetostructural correlations in magnetically coupled (μ -oxo)diiron(III) complexes, *Inorg. Chem.*, 30, 1625-1630, 1991.
- [30] J.-F. Létard, P. Guionneau, and L. Goux-Capes, "Towards Spin Crossover Applications," *Spin Crossover in Transition Metal Compounds III*, P. Gütllich and H. A. Goodwin, eds., pp. 221-249, Berlin, Heidelberg: Springer Berlin Heidelberg, 2004.
- [31] M. N. Leuenberger, and D. Loss, Quantum computing in molecular magnets, *Natur*, 410, 789-793, 2001.
- [32] T. N. Nguyen, W. Wernsdorfer, M. Shiddiq, K. A. Abboud, S. Hill, and G. Christou, Supramolecular aggregates of single-molecule magnets: exchange-biased quantum tunneling of magnetization in a rectangular $[\text{Mn}_3]_4$ tetramer, *Chemical Science*, 7, 1156-1173, 2016.
- [33] O. Kahn, and J. Launay, MOLECULAR BISTABILITY. AN OVERVIEW, *Chemtronics*, 3, 140-151, 1988.
- [34] J. P. S. Walsh, S. B. Meadows, A. Ghirri, F. Moro, M. Jennings, W. F. Smith, D. M. Graham, T. Kihara, H. Nojiri, I. J. Vitorica-Yrezabal, G. A. Timco, D. Collison, E. J. L. McInnes, and R. E. P. Winpenny, Electronic Structure of a Mixed-Metal Fluoride-Centered Triangle Complex: A Potential Qubit Component, *Inorg. Chem.*, 54, 12019-12026, 2015.
- [35] Y.-W. Lin, Rational design of metalloenzymes: From single to multiple active sites, *Coord. Chem. Rev.*, 336, 1-27, 2017.
- [36] J.-L. Chen, L.-Y. Zhang, L.-X. Shi, H.-Y. Ye, and Z.-N. Chen, Syntheses, characterization and redox properties of di- and poly-phosphine linked oligomeric complexes of oxo-centered triruthenium clusters, *Inorg. Chim. Acta*, 359, 1531-1540, 2006.

- [37] M. Lu, T. Chen, M. Wang, G. Jiang, T. Lu, G. Jiang, and J. Du, A new μ_3 -oxo-centered tri-nuclear carboxyl bridged iron (III) complex with thio-methyl groups in the periphery: Structural, spectroscopic and electrochemical studies, *J. Mol. Struct.*, 1060, 131–137, 2014.
- [38] S. Uchida, M. Hashimoto, and N. Mizuno, A Breathing Ionic Crystal Displaying Selective Binding of Small Alcohols and Nitriles: $K_3[Cr_3O(OOCH)_6(H_2O)_3][\alpha\text{-SiW}_{12}O_{40}] \cdot 16 H_2O$, *Angew. Chem. Int. Ed.*, 41, 2814–2817, 2002.
- [39] S. Uchida, and N. Mizuno, Unique Guest-Inclusion Properties of a Breathing Ionic Crystal of $K_3[Cr_3O(OOCH)_6(H_2O)_3][\alpha\text{-SiW}_{12}O_{40}] \cdot 16 H_2O$, *Chemistry – A European Journal*, 9, 5850–5857, 2003.
- [40] S. T. Wilson, R. F. Bondurant, T. J. Meyer, and D. J. Salmon, OXIDATION STATE PROPERTIES OF DELOCALIZED, LIGAND-BRIDGED METAL COMPLEXES. $(Ru_3O(CH_3CO_2)_6L_3)N^+$ AND THE PYRAZINE-BRIDGED, CLUSTER-CLUSTER DIMER, $(Ru_3O(CH_3CO_2)_6(PY)_2)2PYZM^+$, 1975.
- [41] G. Férey, C. Mellot-Draznieks, C. Serre, F. Millange, J. Dutour, S. Surblé, and I. Margiolaki, A Chromium Terephthalate-Based Solid with Unusually Large Pore Volumes and Surface Area, *Sci*, 309, 2040, 2005.
- [42] G. Férey, C. Serre, C. Mellot-Draznieks, F. Millange, S. Surblé, J. Dutour, and I. Margiolaki, A Hybrid Solid with Giant Pores Prepared by a Combination of Targeted Chemistry, Simulation, and Powder Diffraction, *Angew. Chem. Int. Ed.*, 43, 6296–6301, 2004.
- [43] J. S. Seo, D. Whang, H. Lee, S. I. Jun, J. Oh, Y. J. Jeon, and K. Kim, A homochiral metal–organic porous material for enantioselective separation and catalysis, *Natur*, 404, 982–986, 2000.
- [44] M. I. Belinsky, Spin-Frustrated Trinuclear Cu(II) Clusters with Mixing of $2(S = 1/2)$ and $S = 3/2$ States by Antisymmetric Exchange. 1. Dzialoshinsky–Moriya Exchange Contribution to Zero-Field Splitting of the $S = 3/2$ State, *Inorg. Chem.*, 47, 3521–3531, 2008.
- [45] B. Cage, F. A. Cotton, N. S. Dalal, E. A. Hillard, B. Rakvin, and C. M. Ramsey, Observation of Symmetry Lowering and Electron Localization in the Doublet-States of a Spin-Frustrated Equilateral Triangular Lattice: $Cu_3(O_2C_6H_4)_3 \cdot 1.2C_6H_{12}$, *J. Am. Chem. Soc.*, 125, 5270–5271, 2003.
- [46] S. Carretta, P. Santini, G. Amoretti, F. Troiani, and M. Affronte, Spin triangles as optimal units for molecule-based quantum gates, *PhRvB*, 76, 024408, 2007.
- [47] K.-Y. Choi, Y. H. Matsuda, H. Nojiri, U. Kortz, F. Hussain, A. C. Stowe, C. Ramsey, and N. S. Dalal, Observation of a Half Step Magnetization in the $\{\{\mathit{Cu}\}_3\}$ -Type Triangular Spin Ring, *Phys. Rev. Lett.*, 96, 107202, 2006.
- [48] O. Kahn, Competing spin interactions and degenerate frustration for discrete molecular species, *Chem. Phys. Lett.*, 265, 109–114, 1997.
- [49] S. Khanra, B. Biswas, C. Golze, B. Büchner, V. Kataev, T. Weyhermüller, and P. Chaudhuri, A spin-frustrated star-shaped heterotetranuclear $CrIII MnII_3$ species and its magnetic and HF-EPR measurements, *DTr*, 481–487, 2007.
- [50] S. Nakatsuji, Y. Nambu, H. Tonomura, O. Sakai, S. Jonas, C. Broholm, H. Tsunetsugu, Y. Qiu, and Y. Maeno, Spin Disorder on a Triangular Lattice, *Sci*, 309, 1697, 2005.
- [51] M. Prinz, K. Kuepper, C. Taubitz, M. Raekers, S. Khanra, B. Biswas, T. Weyhermüller, M. Uhlarz, J. Wosnitza, J. Schnack, A. V. Postnikov, C. Schröder, S. J. George, M. Neumann, and P. Chaudhuri, A Star-Shaped Heteronuclear $CrIII MnII_3$ Species and Its Precise Electronic and Magnetic Structure: Spin Frustration Studied by X-Ray Spectroscopic, Magnetic, and Theoretical Methods, *Inorg. Chem.*, 49, 2093–2102, 2010.
- [52] T. Yamase, H. Abe, E. Ishikawa, H. Nojiri, and Y. Ohshima, Structure and Magnetism of $[n\text{-BuNH}_3]_{12}[Cu_4(GeW_9O_{34})_2] \cdot 14H_2O$ Sandwiching a Rhomblike Cu_4^{4+} Tetragon through α -Keggin Linkage, *Inorg. Chem.*, 48, 138–148, 2009.
- [53] J. Yoon, and E. I. Solomon, Electronic structures of exchange coupled trigonal trimeric Cu(II) complexes: Spin frustration, antisymmetric exchange, pseudo-A terms, and their relation to O_2 activation in the multicopper oxidases, *Coord. Chem. Rev.*, 251, 379–400, 2007.
- [54] V. Amani, N. Safari, and H. R. Khavasi, Solution and solid state characterization of oxo-centered trinuclear iron(III) acetate complexes $[Fe_3(\mu_3\text{-O})(\mu\text{-OAc})_6(L)_3]^+$, *Spectrochimica Acta Part A: Molecular and Biomolecular Spectroscopy*, 85, 17–24, 2012.
- [55] R. D. Cannon, U. A. Jayasooriya, R. Wu, S. K. arapKoske, J. A. Stride, O. F. Nielsen, R. P. White, G. J. Kearley, and D. Summerfield, Spin Frustration in High-Spin Triiron(III) Complexes: An Inelastic Neutron Scattering Study, *J. Am. Chem. Soc.*, 116, 11869–11874, 1994.
- [56] F. E. Sowrey, C. Tilford, S. Wocadlo, C. E. Anson, A. K. Powell, S. M. Bennington, W. Montfrooij, U. A. Jayasooriya, and R. D. Cannon, Spin frustration and concealed asymmetry: structure and magnetic spectrum of $[Fe_3O(O_2CPh)_6(py)_3]ClO_4 \cdot py$, *J. Chem. Soc., Dalton Trans.*, 862–866, 2001.

- [57] R. Wu, M. Poyraz, F. E. Sowrey, C. E. Anson, S. Wocadlo, A. K. Powell, U. A. Jayasooriya, R. D. Cannon, T. Nakamoto, M. Katada, and H. Sano, Electron Localization and Delocalization in Mixed-Valence Transition Metal Clusters: Structural and Spectroscopic Studies of Oxo-Centered Trinuclear Complexes $[\text{Fe}_3\text{O}(\text{OCCMe}_3)_6(\text{py})_3]^{+}/0$ and $[\text{Mn}_3\text{O}(\text{OCCMe}_3)_6(\text{py})_3]^{+}/0$, *Inorg. Chem.*, 37, 1913-1921, 1998.
- [58] D. N. Hendrickson, "SPIN FRUSTRATION IN POLYNUCLEAR COMPLEXES," *Research Frontiers in Magnetochemistry*, pp. 87-108: WORLD SCIENTIFIC, 1993.
- [59] J. B. Vincent, H. R. Chang, K. Folting, J. C. Huffman, G. Christou, and D. N. Hendrickson, Preparation and physical properties of trinuclear oxo-centered manganese complexes of general formulation $[\text{Mn}_3\text{O}(\text{O}_2\text{CR})_6\text{L}_3]^{0,+}$ (R = methyl or phenyl; L = a neutral donor group) and the crystal structures of $[\text{Mn}_3\text{O}(\text{O}_2\text{CMe})_6(\text{pyr})_3](\text{pyr})$ and $[\text{Mn}_3\text{O}(\text{O}_2\text{CPh})_6(\text{pyr})_2(\text{H}_2\text{O})] \cdot 0.5\text{MeCN}$, *J. Am. Chem. Soc.*, 109, 5703-5711, 1987.
- [60] T. C. Stamatatos, D. Foguet-Albiol, C. C. Stoumpos, C. P. Raptopoulou, A. Terzis, W. Wernsdorfer, S. P. Perlepes, and G. Christou, Initial Example of a Triangular Single-Molecule Magnet from Ligand-Induced Structural Distortion of a $[\text{Mn}^{\text{III}}_3\text{O}]^{7+}$ Complex, *J. Am. Chem. Soc.*, 127, 15380-15381, 2005.
- [61] A. Dikhtiarenko, S. Khainakov, J. R. García, and J. Gimeno, Research paper, *Inorg. Chim. Acta*, 454, 107-116, 2017.
- [62] H.-Y. Ye, F.-R. Dai, L.-Y. Zhang, and Z.-N. Chen, Low-Valence Triruthenium Compounds via Substitution of a Bridging Acetate in the Parent $\text{Ru}_3\text{O}(\text{OAc})_6$ Cluster Core by 2,2'-Azobispyridine (abpy) or 2,2'-Azobis(5-chloropyrimidine) (abcp), *Inorg. Chem.*, 46, 6129-6135, 2007.
- [63] R. Werner, S. Ostrovsky, K. Griesar, and W. Haase, Magnetostructural correlations in exchange coupled phenoxo-, alkoxo-, and hydroxo-bridged dinuclear iron(III) compounds, *Inorg. Chim. Acta*, 326, 78-88, 2001.
- [64] G. Filoti, J. Bartolome, D. P. E. Dickson, C. Rillo, I. Prisecaru, T. Jovmir, V. Kuncser, and C. Turta, Intermediate frustration in $[\text{Fe}_3\text{O}(\text{CH}_3\text{COO})_6(\text{H}_2\text{O})_3] \text{NO}_3 \cdot 4(\text{H}_2\text{O})$ trinuclear cluster, *J. Magn. Magn. Mater.*, 196-197, 561-563, 1999.
- [65] C. T. Dziobkowski, J. T. Wroblewski, and D. B. Brown, *Magnetic properties and moessbauer spectra of several iron (3) dicarboxylic acid complexes*, 1980.
- [66] R. Colton, A. D'Agostino, and J. C. Traeger, Electrospray mass spectrometry applied to inorganic and organometallic chemistry, *Mass Spectrom. Rev.*, 14, 79-106, 1995.
- [67] J. B. Fenn, Electrospray Wings for Molecular Elephants (Nobel Lecture), *Angew. Chem. Int. Ed.*, 42, 3871-3894, 2003.
- [68] J. Lang, D. V. Fries, and G. Niedner-Schatteburg, Characterization of Trinuclear Oxo Bridged Cobalt Complexes in Isolation, *Z. Phys. Chem.*, 232, 649-669, 2018.
- [69] E. Stavitski, and F. M. F. de Groot, The CTM4XAS program for EELS and XAS spectral shape analysis of transition metal L edges, *Micron*, 41, 687-694, 2010.
- [70] J. Lang, J. M. Hewer, J. Meyer, J. Schuchmann, C. van Wüllen, and G. Niedner-Schatteburg, Magnetostructural correlation in isolated trinuclear iron(III) oxo acetate complexes, *Phys. Chem. Chem. Phys.*, 20, 16673-16685, 2018.
- [71] A. D. Becke, Density-functional thermochemistry. III. The role of exact exchange, *J. Chem. Phys.*, 98, 5648-5652, 1993.
- [72] B. Miehlich, A. Savin, H. Stoll, and H. Preuss, Results obtained with the correlation energy density functionals of Becke and Lee, Yang and Parr, *Chem. Phys. Lett.*, 157, 200-206, 1989.
- [73] T. H. Dunning, Gaussian basis sets for use in correlated molecular calculations. I. The atoms boron through neon and hydrogen, *J. Chem. Phys.*, 90, 1007-1023, 1989.
- [74] M. Dolg, H. Stoll, H. Preuss, and R. M. Pitzer, Relativistic and correlation effects for element 105 (hahnium, Ha): a comparative study of M and MO (M = Nb, Ta, Ha) using energy-adjusted ab initio pseudopotentials, *J. Phys. Chem.*, 97, 5852-5859, 1993.
- [75] M. J. Frisch et. al, "Gaussian 16 Rev. C.01," 2016.
- [76] F. Illas, I. P. R. Moreira, C. de Graaf, and V. Barone, Magnetic coupling in biradicals, binuclear complexes and wide-gap insulators: a survey of ab initio wave function and density functional theory approaches, *Theor. Chem. Acc.*, 104, 265-272, 2000.
- [77] E. M. V. Kessler, S. Schmitt, and C. van Wüllen, Broken symmetry approach to density functional calculation of zero field splittings including anisotropic exchange interactions, *J. Chem. Phys.*, 139, 184110, 2013.
- [78] R. Ahlrichs, M. Bär, M. Häser, H. Horn, and C. Kölmel, Electronic structure calculations on workstation computers: The program system turbomole, *Chem. Phys. Lett.*, 162, 165-169, 1989.

- [79] B. T. Thole, and G. van der Laan, Branching ratio in x-ray absorption spectroscopy, *Phys. Rev. B*, 38, 3158-3171, 1988.
- [80] M. Von Arnim, and R. Ahlrichs, Performance of parallel TURBOMOLE for density functional calculations, *J. Comput. Chem.*, 19, 1746-1757, 1998.
- [81] J. Lang, J. Mohrbach, S. Dillinger, J. M. Hewer, and G. Niedner-Schatteburg, Vibrational blue shift of coordinated N2 in $[\text{Fe}_3\text{O}(\text{OAc})_6(\text{N}_2)_n]^+$: "non-classical" dinitrogen complexes, *Chem. Comm.*, 53, 420-423, 2017.
- [82] J. Meyer, "Fragmentation and Infrared Spectroscopy of oxo-centered Homo- and Heterotrimetallic Carboxylate Bridged Transition Metal Complexes," 2018.
- [83] M. Abe, Y. Sasaki, Y. Yamada, K. Tsukahara, S. Yano, T. Yamaguchi, M. Tominaga, I. Taniguchi, and T. Ito, Oxo-Centered Mixed-Ligand Triruthenium Complexes Having Redox-Active N-Methyl-4,4'-bipyridinium Ions (mbpy+). Reversible Multistep Electrochemical Properties of $[\text{Ru}^{\text{III}}_2\text{Ru}^{\text{II}}(\mu_3\text{-O})(\mu\text{-CH}_3\text{CO}_2)_6(\text{mbpy}^+)_2(\text{CO})]^{2+}$ and $[\text{Ru}^{\text{III}}_3(\mu_3\text{-O})(\mu\text{-CH}_3\text{CO}_2)_6(\text{mbpy}^+)_2(\text{L})]^{3+}$ (L = H₂O and N-Heterocyclic Ligands), *Inorg. Chem.*, 35, 6724-6734, 1996.
- [84] M. Abe, Y. Sasaki, T. Yamaguchi, and T. Ito, X-Ray Structure, Ligand Substitution, and Other Properties of Trinuclear Ruthenium Complex, $[\text{Ru}_3(\mu_3\text{-O})(\mu\text{-C}_6\text{H}_5\text{COO})_6(\text{py})_3](\text{PF}_6)$ (py = pyridine), and X-Ray Structure of Dinuclear Ruthenium Complex, $[\text{Ru}_2(\mu\text{-C}_6\text{H}_5\text{COO})_4\text{Cl}]$, *Bull. Chem. Soc. Jpn.*, 65, 1585-1590, 1992.
- [85] M. Abe, A. Sato, T. Inomata, T. Kondo, K. Uosaki, and Y. Sasaki, Characterization of novel redox-active triruthenium(III) complexes with a disulfide alkyl ligand. Anion-dependent redox behaviour of monolayer assemblies on gold, *J. Chem. Soc., Dalton Trans.*, 2693-2702, 2000.
- [86] J. A. Baumann, D. J. Salmon, S. T. Wilson, T. J. Meyer, and W. E. Hatfield, Electronic structure and redox properties of the clusters $[\text{Ru}_3\text{O}(\text{CH}_3\text{CO}_2)_6\text{L}_3]^{n+}$, *Inorg. Chem.*, 17, 3342-3350, 1978.
- [87] T. Ito, T. Hamaguchi, H. Nagino, T. Yamaguchi, J. Washington, and C. P. Kubiak, Effects of Rapid Intramolecular Electron Transfer on Vibrational Spectra, *Sci*, 277, 660, 1997.
- [88] M. B. Moreira, C. F. N. Da Silva, R. B. P. Pesci, V. M. Deflon, and S. Nikolaou, Revisiting oxo-centered carbonyl-triruthenium clusters: investigating CO photorelease and some spectroscopic and electrochemical correlations, *Dalt. Trans.*, 45, 16799-16809, 2016.
- [89] S. Nikolaou, and H. E. Toma, Synthesis, spectroscopy and electrochemistry of a μ -oxo-triruthenium cluster containing a bridged bis(2,2'-bipyridyl)ruthenium(II) moiety, *Polyhedron*, 20, 253-259, 2001.
- [90] R. F. W. Bader, A quantum theory of molecular structure and its applications, *Chem. Rev.*, 91, 893-928, 1991.
- [91] A. N. Georgopoulou, Y. Sanakis, and A. K. Boudalis, Magnetic relaxation in basic iron(III) carboxylate $[\text{Fe}_3\text{O}(\text{O}_2\text{CPh})_6(\text{H}_2\text{O})_3]\text{ClO}_4\cdot\text{py}$, *DTr*, 40, 6371-6374, 2011.
- [92] C. J. O'Connor, *Research Frontiers in Magnetochemistry*: World Scientific, 1993.
- [93] M. Ogryzek, A. Chylewska, A. Króllicka, R. Banasiuk, K. Turecka, D. Lesiak, D. Nidzworski, and M. Makowski, Coordination chemistry of pyrazine derivatives analogues of PZA: design, synthesis, characterization and biological activity, *RSC Advances*, 6, 52009-52025, 2016.

6.10 Supplementary material

IR(M)PD studies of isolated spin frustrated trimetallic μ -oxo bridged 4d complexes

Michael Lembach, Florian Breitschaft and Gereon Niedner-Schatteburg

Fachbereich Chemie and Forschungszentrum OPTIMAS, Kaiserslautern, Germany

Content

Fig. S1: Cationic mass spectrum of a $[\text{Ru}_3\text{O}(\text{OAc})_6(\text{H}_2\text{O})_3]\text{ClO}_4$ acetonitrile/pyridine = 1/10 solution using the Paul type ion trap.

Tab.1: Calculated energies relative to the minimum structure of $[\text{Ru}_3\text{O}(\text{OAc})_6(\text{py})_n]^+$ ($n = 0, 1, 2, 3$) with different multiplicities. The calculations were performed with Gaussian 09 at the unrestricted B3LYP/cc-pVTZ level of theory and ecp-28-mdf (Ru) level of theory.

Fig. S2: IR(M)PD spectra in comparison with calculated linear absorption spectra of $[\text{Ru}_3\text{O}(\text{OAc})_6(\text{py})_3]^+$ ($M = 2, 4$). The calculations were performed with Gaussian 09 at the B3LYP/cc-pVTZ (H, C, N, O) and ecp-28-mdf (Ru) level of theory.

Fig. S3: Powercurve during the IR(M)PD experiments of $[\text{Ru}_3\text{O}(\text{OAc})_6(\text{py})_n]^+$ ($n = 0, 1, 2, 3$) in area of $1200\text{--}2000\text{ cm}^{-1}$.

Fig. S4: Atom distances ($\text{Ru}\text{--}\text{O}_{\text{central}}$ and Ru-Ru distances, all in \AA of the Ru_3O -core in $[\text{Ru}_3\text{O}(\text{OAc})_6(\text{py})_n]^+$ ($n = 0, 1, 2, 3$). The calculations were performed at the B3LYP/cc-pVTZ (H, C, N, O) and ecp-28-mdf (Ru) level of theory with one unpaired electron on each Ru center corresponding to the minimum structures. The ligand is omitted for clarity.

Fig. S5: Calculated Electron Localized Field (ELF), Density Overlap Region Indicator (DORI) and Non covalent Interactions (NCI) of $[\text{Ru}_3\text{O}(\text{OAc})_6(\text{py})_n]^+$ ($n = 0, 1, 2, 3$). The calculations were performed at the B3LYP/cc-pVTZ (H, C, N, O) and ecp-28-mdf (Ru) level of theory one unpaired electron on each Ru center.

Fig. S6: Experimental gas phase stabilities of $[\text{M}_3\text{O}(\text{OAc})_6(\text{py})_{1-3}]^+$ ($M = \text{Co}^{3+}, \text{Fe}^{3+}, \text{Ru}^{3+}$). J. Lang measured the Co^{3+} and Fe^{3+} complexes.

Fig. S7: Energetic shifts of the experimental IR(M)PD spectra of $[M_3O(OAc)_6(py)_n]^+$ ($M = Ru, Co, Fe; n = 0, 1, 2, 3$).

Fig. S8: Vibrational modes of the symmetric CO stretching modes from the experimental gained IR(M)PD spectra of $[M_3O(OAc)_6(Py)_n]^+$ ($n = 0, 1, 2, 3; M = Co^{3+}, Fe^{3+}, Ru^{3+}$) with their corresponding $M-O_{\text{central}}-M-py_n$ angle. The Co^{3+} and Fe^{3+} complexes were measured and calculated by J. Lang.

Fig. S9: Vibrational modes of the asymmetric CO stretching modes from the experimental gained IR(M)PD spectra of $[M_3O(OAc)_6(py)_n]^+$ ($n = 0, 1, 2, 3; M = Co^{3+}, Fe^{3+}, Ru^{3+}$) with their corresponding $M-O_{\text{central}}-M-py_n$ angle. The Co^{3+} and Fe^{3+} complexes were measured and calculated by J. Lang.

Fig. S10: Experimental IR(M)PD spectra of $[M_3O(OAc)_6(py)_n]^+$ ($n = 0, 1, 2, 3; M = Co^{3+}, Fe^{3+}, Ru^{3+}$). J. Lang measured the Co^{3+} and Fe^{3+} complexes.

Fig. S11: Calculated linear absorption spectra of $[Ru_3O(OAc)_6(py)_n]^+$ ($n = 0, 1, 2, 3$) in the region of 100 cm^{-1} to 1000 cm^{-1} . The calculations were performed with Gaussian 09 at the B3LYP/cc-pVTZ (H, C, N, O) and ecp-28-mdf (Ru) level of theory.

Fig. S12: Calculated linear absorption spectra of $[Ru_3O(OAc)_6(py)_n]^+$ ($n = 0, 1, 2, 3$) in the region of 250 cm^{-1} to 500 cm^{-1} . The calculations were performed with Gaussian 09 at the B3LYP/cc-pVTZ (H, C, N, O) and ecp-28-mdf (Ru) level of theory.

Fig. S13: Calculated UV/VIS spectra of $[Ru_3O(OAc)_6(py)_n]^+$ ($n = 0, 1, 2, 3$). The calculations were performed at the B3LYP-Gaussian/cc-pVTZ (H, C, N, O) and ecp-28-mdf (Ru) level of theory one unpaired electron on each Ru center.

Fig. S14: Calculated HOMO–LUMO transitions of $[Ru_3O(OAc)_6(py)_n]^+$ ($n = 0, 1, 2, 3$). The calculations were performed at the TD-DFT UB3LYP/cc-pVTZ (H, C, N, O) and ecp-28-mdf (Ru) level of theory one unpaired electron on each Ru center.

Fig. S15: Tanabe Sugano diagram of a d^5 LS transition metal with the normalized absorption energies of $[\text{Ru}_3\text{O}(\text{OAc})_6(\text{py})_n]^+$ ($n = 0, 1, 2, 3$) for the approximation of the crystal field splitting. The calculations were performed at the TD-DFT UB3LYP/cc-pVTZ (H, C, N, O) and ecp-28-mdf (Ru) level of theory one unpaired electron on each Ru center.

Fig. S16: Simulated XA spectra of $[\text{Ru}_3\text{O}(\text{OAc})_6(\text{py})_n]^+$ ($n = 0, 1, 2, 3$) with the approximated crystal field splittings from the Tanabe Sugano diagram. The simulations were performed by CTM4XAS with Cowan Batch files.

Tab. S2: Atom coordinates for $[\text{Ru}_3\text{O}(\text{OAc})_6(\text{py})_n]^+$ ($n = 0$). The calculation was performed at the B3LYP/cc-pVTZ (H, C, N, O) and ecp-28-mdf (Ru) level of theory with a high spin state for each Ru center.

Tab. S3: Atom coordinates for $[\text{Ru}_3\text{O}(\text{OAc})_6(\text{py})_n]^+$ ($n = 1$). The calculation was performed at the B3LYP/cc-pVTZ (H, C, N, O) and ecp-28-mdf (Ru) level of theory with a high spin state for each Ru center.

Tab. S4: Atom coordinates for $[\text{Ru}_3\text{O}(\text{OAc})_6(\text{py})_n]^+$ ($n = 2$). The calculation was performed at the B3LYP/cc-pVTZ (H, C, N, O) and ecp-28-mdf (Ru) level of theory with a high spin state for each Ru center.

Tab. S5: Atom coordinates for $[\text{Ru}_3\text{O}(\text{OAc})_6(\text{py})_n]^+$ ($n = 3$). The calculation was performed at the B3LYP/cc-pVTZ (H, C, N, O) and ecp-28-mdf (Ru) level of theory with a high spin state for each Ru center.

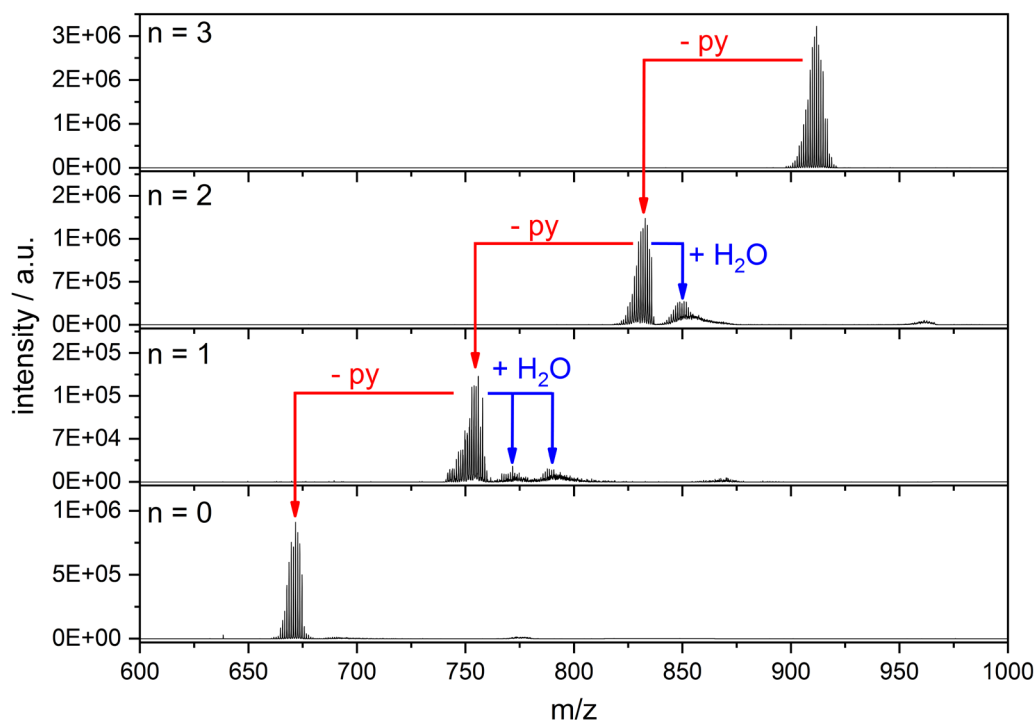


Fig. 1: Cationic mass spectrum of a $[\text{Ru}_3\text{O}(\text{OAc})_6(\text{H}_2\text{O})_3]\text{ClO}_4$ acetone/pyridine = 1/10 solution using the Paul type ion trap.

Tab.1: Calculated energies relative to the minimum structure of $[\text{Ru}_3\text{O}(\text{OAc})_6(\text{py})_n]^+$ ($n = 0, 1, 2, 3$) with different multiplicities. The calculations were performed with Gaussian 09 at the unrestricted B3LYP/cc-pVTZ level of theory and ecp-28-mdf (Ru) level of theory.

n	M = 2	M = 4
	$\Delta E/\text{kJ/mol}$	$\Delta E/\text{kJ/mol}$
0	106	0
1	40	0
2	44	0
3	1	0

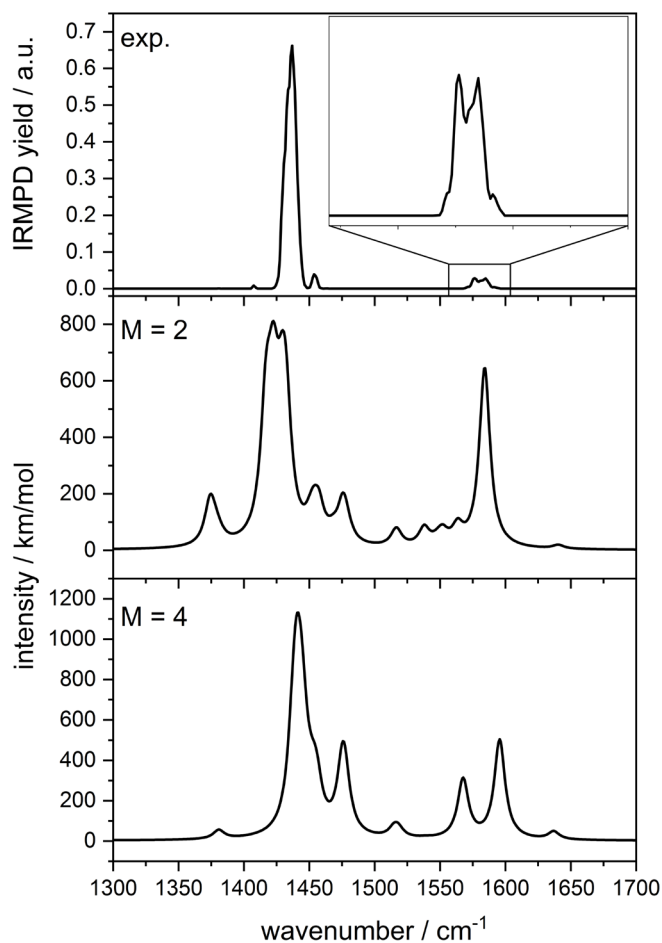


Fig. S2: IR(M)PD spectra in comparison with calculated linear absorption spectra of $[\text{Ru}_3\text{O}(\text{OAc})_6(\text{py})_3]^+$ ($M = 2, 4$). The calculations were performed with Gaussian 09 at the B3LYP/ cc-pVTZ (H, C, N, O) and ecp-28-mdf (Ru) level of theory.

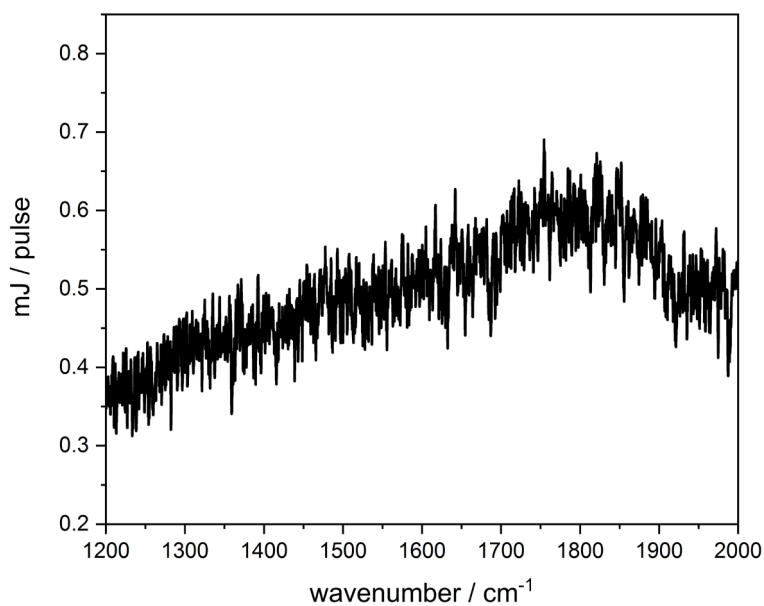


Fig. S3: Powercurve during the IR(M)PD experiments of $[\text{Ru}_3\text{O}(\text{OAc})_6(\text{py})_n]^+$ ($n = 0, 1, 2, 3$) in area of 1200–2000 cm^{-1} .

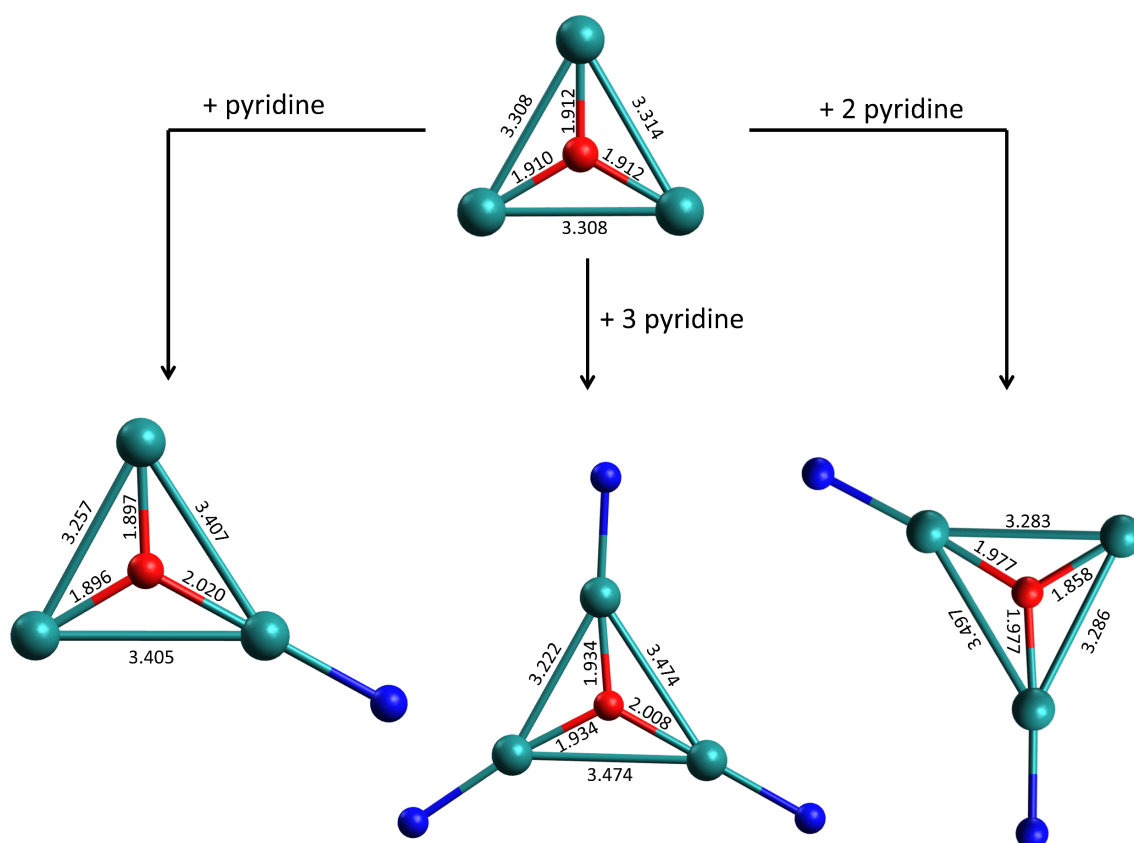


Fig. S4: Atom distances (Ru–O_{central} and Ru–Ru distances, all in Å) of the Ru₃O-core in [Ru₃O(OAc)₆(py)_n]⁺ (n = 0, 1, 2, 3). The calculations were performed at the B3LYP/cc-pVTZ (H, C, N, O) and ecp-28-mdf (Ru) level of theory with one unpaired electron on each Ru center corresponding to the minimum structures.^[21] The ligand is omitted for clarity.

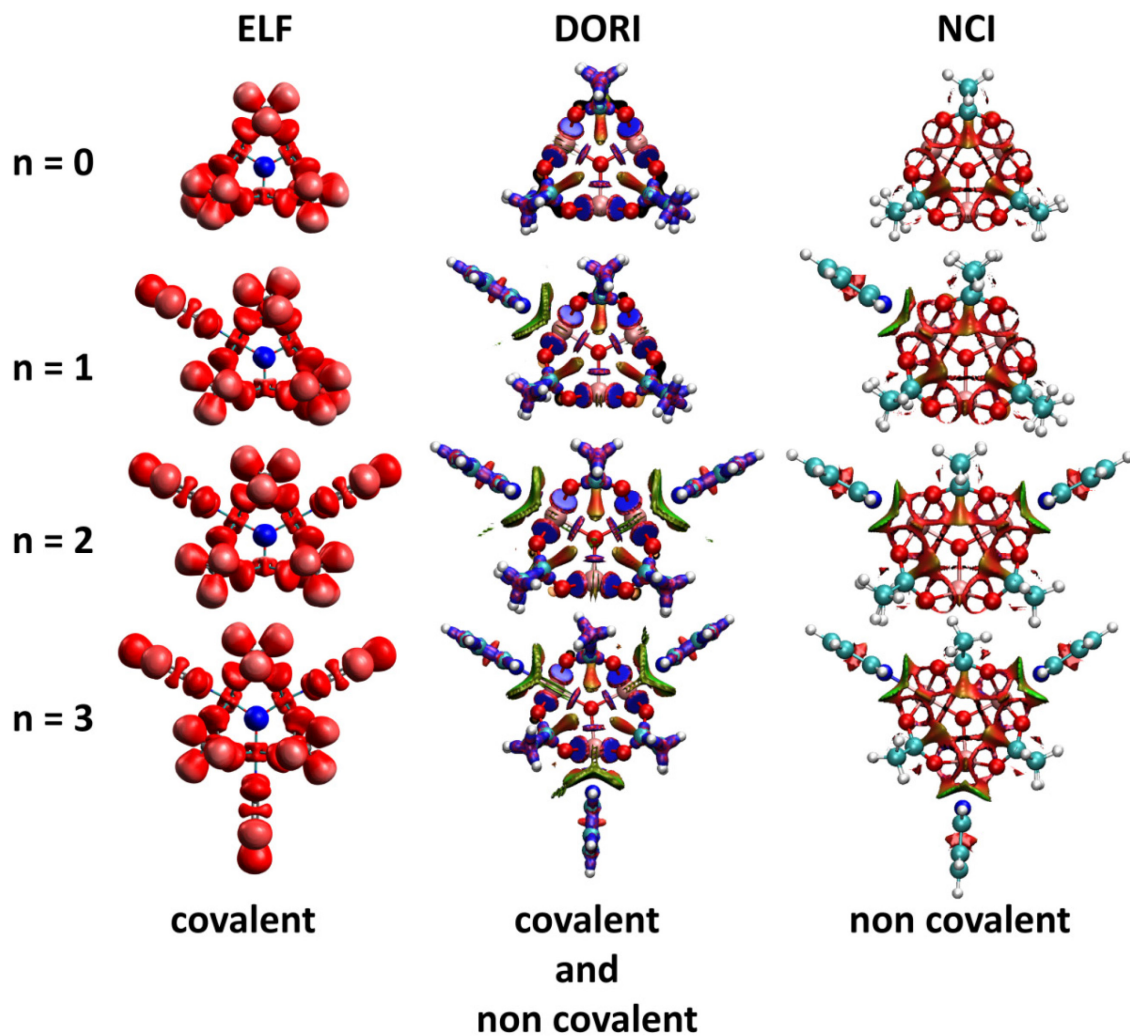


Fig. S5: Calculated Electron Localized Field (ELF), Density Overlap Region Indicator (DORI) and Non covalent Interactions (NCI) of $[\text{Ru}_3\text{O}(\text{OAc})_6(\text{py})_n]^+$ ($n=0, 1, 2, 3$). The calculations were performed at the B3LYP/cc-pVTZ (H, C, N, O) and ecp-28-mdf (Ru) level of theory one unpaired electron on each Ru center.

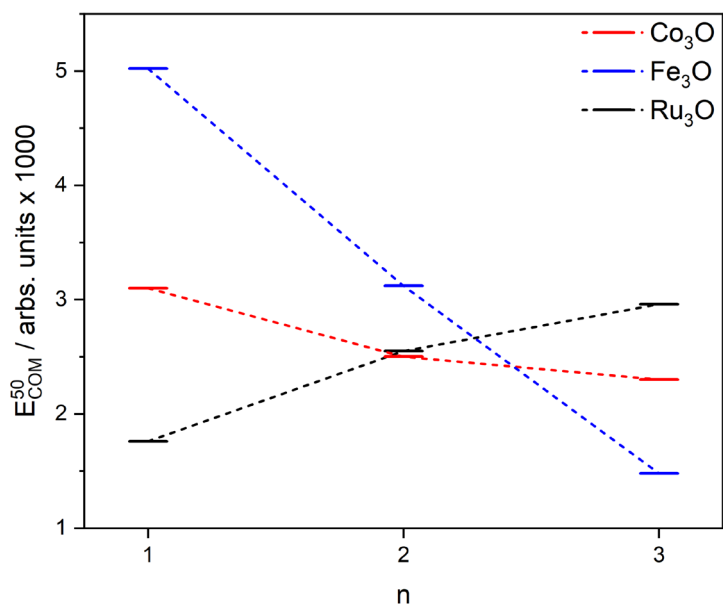


Fig. S6: Experimental gas phase stabilities of $[M_3O(OAc)_6(py)_{1-3}]^+$ ($n = 0, 1, 2, 3$; $M = Co^{3+}, Fe^{3+}, Ru^{3+}$). J. Lang measured the Co^{3+} and Fe^{3+} complexes.

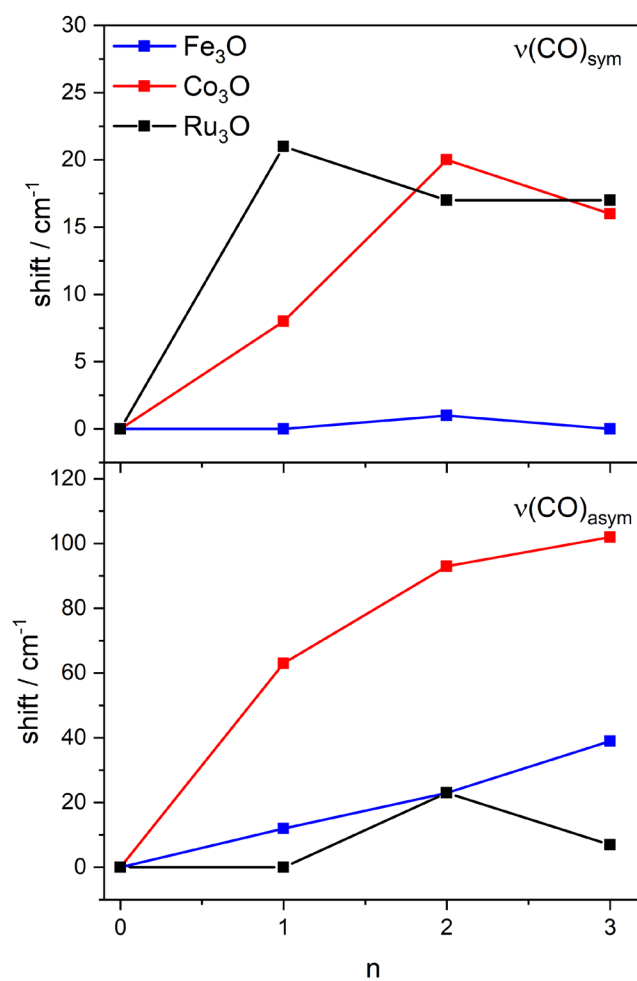


Fig. S7: Energetic shifts of the experimental IR(M)PD spectra of $[M_3O(OAc)_6(py)_n]^+$ ($M = Ru, Co, Fe$; $n = 0, 1, 2, 3$).

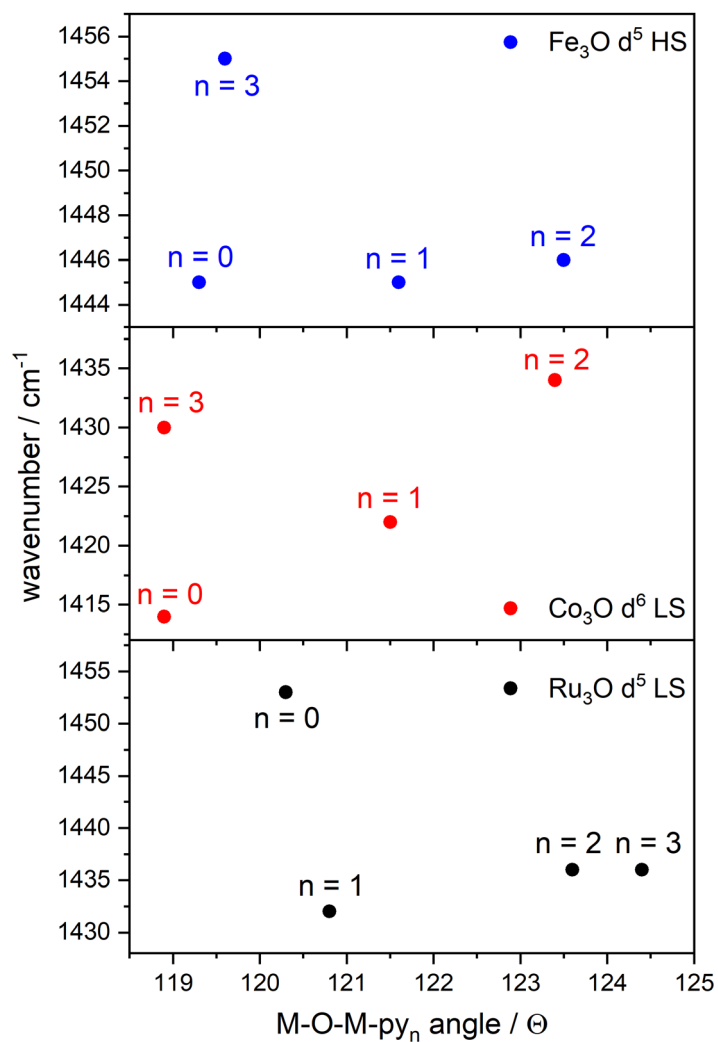


Fig. S8: Vibrational modes of the symmetric CO stretching modes from the experimental gained IR(M)PD spectra of $[\text{M}_3\text{O}(\text{OAc})_6(\text{py})_n]^+$ ($n = 0, 1, 2, 3$; $\text{M} = \text{Co}^{3+}, \text{Fe}^{3+}, \text{Ru}^{3+}$) with their corresponding $\text{M}-\text{O}_{\text{central}}-\text{M}-\text{py}_n$ angle. The Co^{3+} and Fe^{3+} complexes were measured and calculated by J. Lang.

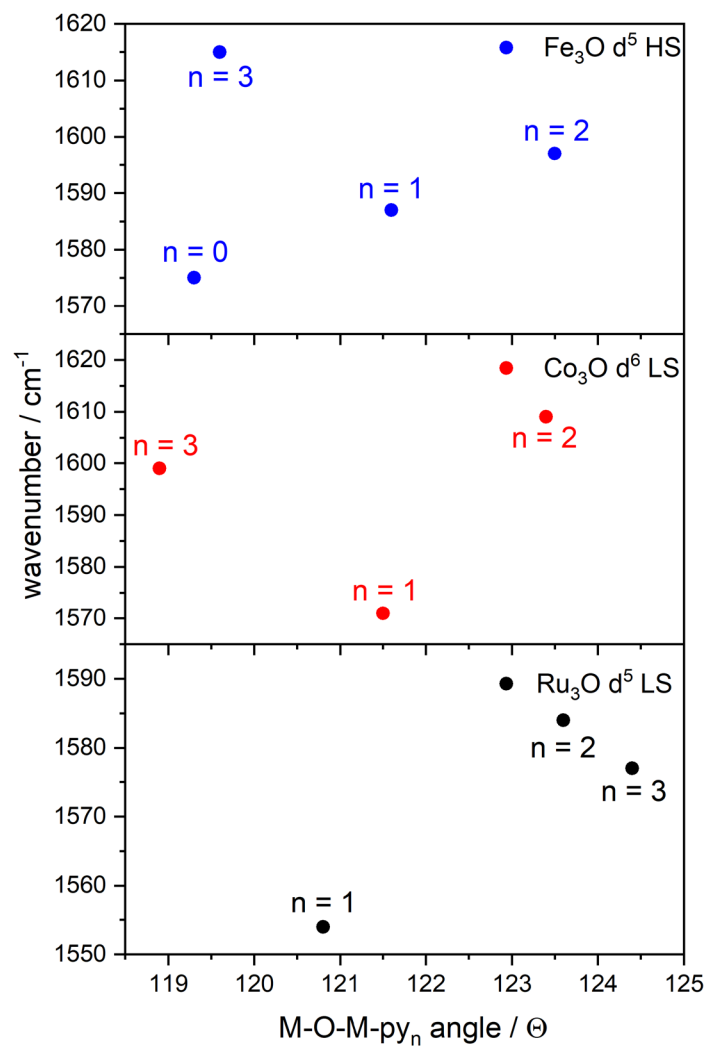


Fig. S9: Vibrational modes of the asymmetric CO stretching modes from the experimental gained IR(M)PD spectra of $[M_3O(OAc)_6(py)_n]^+$ ($n = 0, 1, 2, 3$; $M = Co^{3+}, Fe^{3+}, Ru^{3+}$) with their corresponding M-O_{central}-M-py_n angle. The Co^{3+} and Fe^{3+} complexes were measured and calculated by J. Lang.

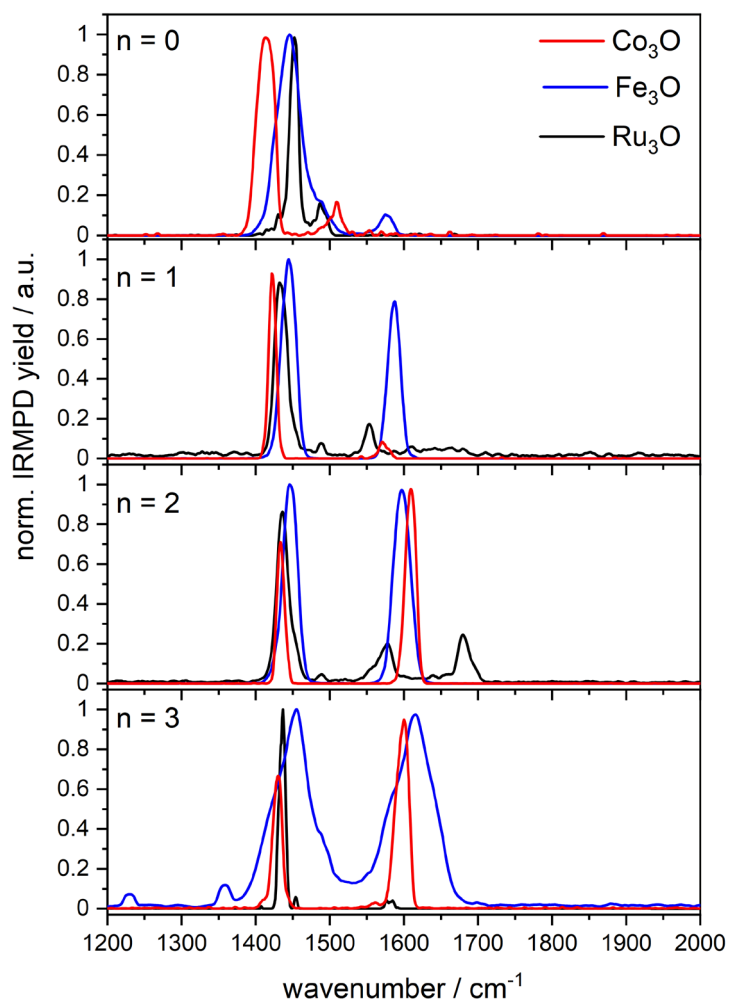


Fig. S10: Experimental IR(M)PD spectra of $[M_3O(OAc)_6(py)_n]^+$ ($n = 0, 1, 2, 3$; $M = Co^{3+}, Fe^{3+}, Ru^{3+}$). J. Lang measured the Co^{3+} and Fe^{3+} complexes.

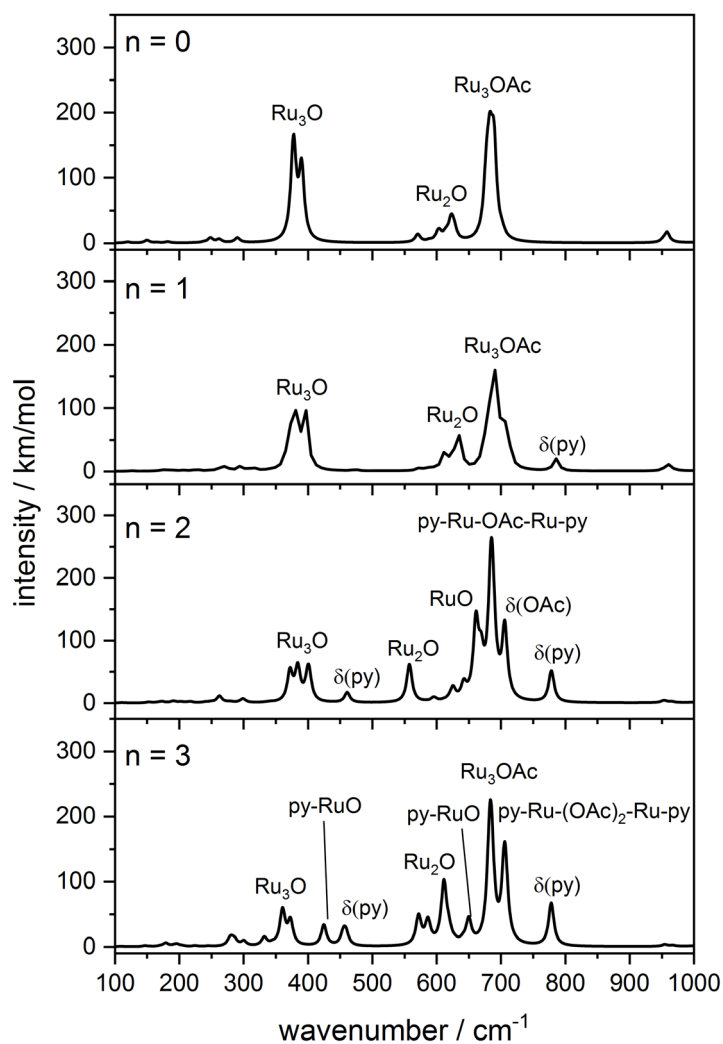


Fig. S11: Calculated linear absorption spectra of $[\text{Ru}_3\text{O}(\text{OAc})_6(\text{py})_n]^+$ ($n = 0, 1, 2, 3$) in the region of 100 cm^{-1} to 1000 cm^{-1} . The calculations were performed with Gaussian 09 at the B3LYP/cc-pVTZ (H, C, N, O) and ecp-28-mdf (Ru) level of theory.

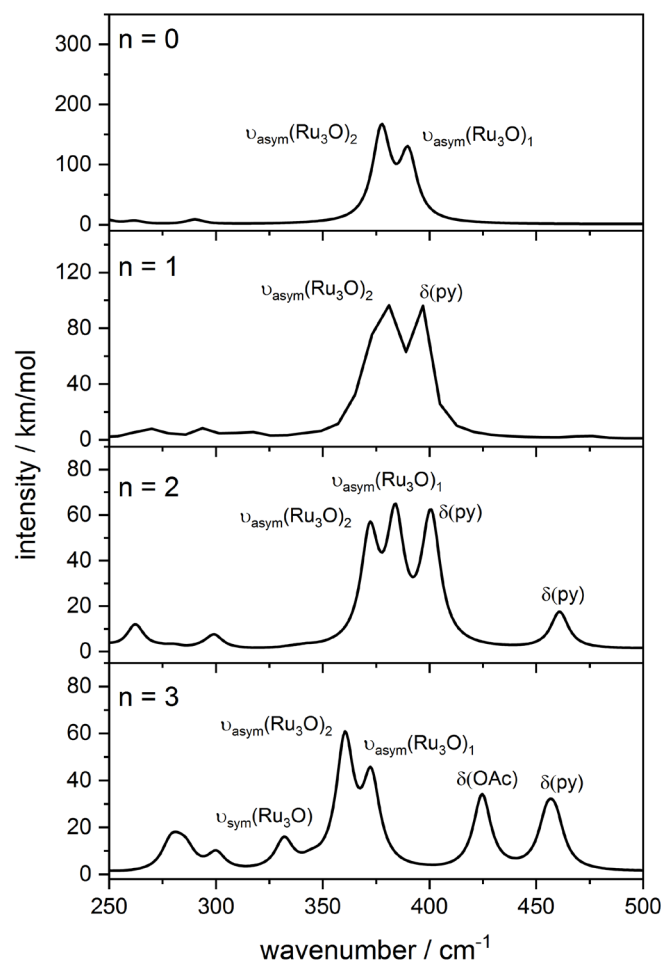


Fig. S12: Calculated linear absorption spectra of $[\text{Ru}_3\text{O}(\text{OAc})_6(\text{py})_n]^+$ ($n = 0, 1, 2, 3$) in the region of 250 cm^{-1} to 500 cm^{-1} . The calculations were performed with Gaussian 09 at the B3LYP/ cc-pVTZ (H, C, N, O) and ecp-28-mdf (Ru) level of theory.

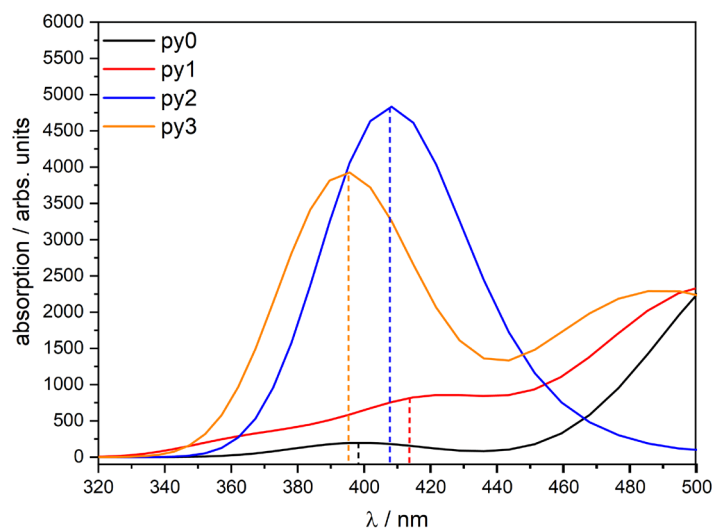


Fig. S13: Calculated UV/VIS spectra of $[\text{Ru}_3\text{O}(\text{OAc})_6(\text{py})_n]^+$ ($n = 0, 1, 2, 3$). The calculations were performed at the TD-DFT UB3LYP/cc-pVTZ (H, C, N, O) and ecp-28-mdf (Ru) level of theory one unpaired electron on each Ru center.

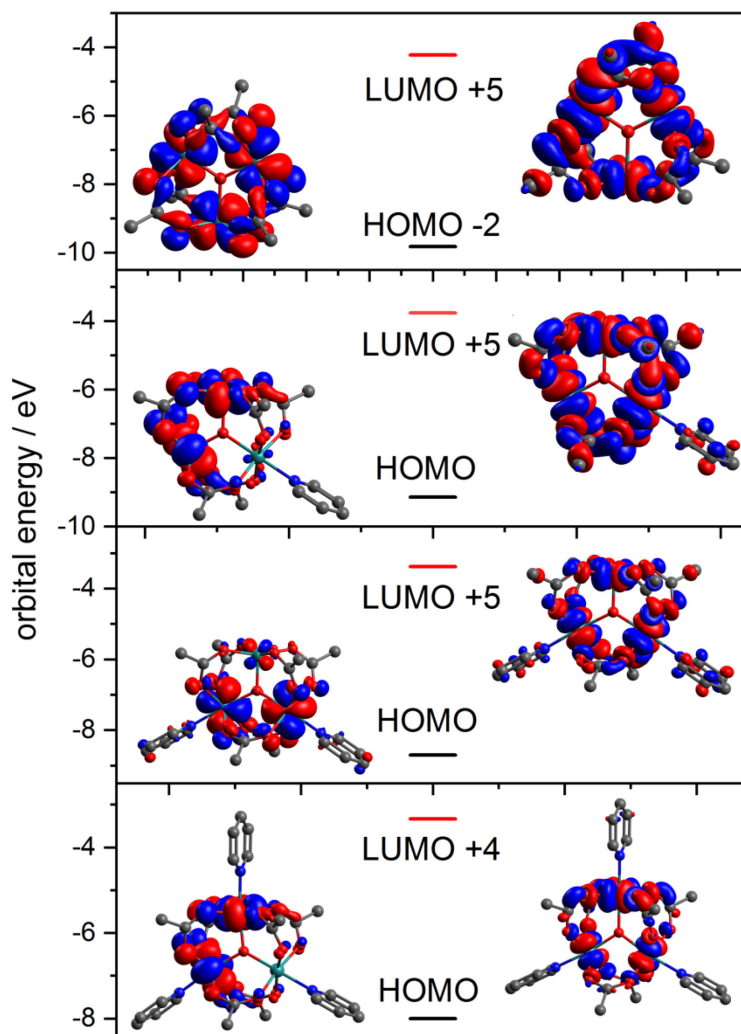


Fig. S14: Calculated HOMO–LUMO transitions of $[\text{Ru}_3\text{O}(\text{OAc})_6(\text{py})_n]^+$ ($n = 0, 1, 2, 3$). The calculations were performed at the TD-DFT UB3LYP/cc-pVTZ (H, C, N, O) and ecp-28-mdf (Ru) level of theory one unpaired electron on each Ru center.

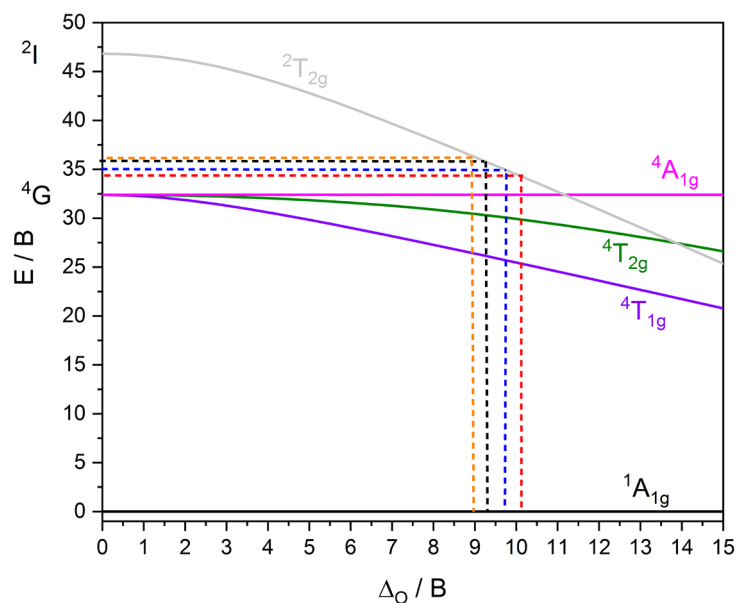


Fig. S15: Tanabe Sugano diagram of a d^5 LS transition metal with the normalized absorption energies of $[\text{Ru}_3\text{O}(\text{OAc})_6(\text{py})_n]^+$ ($n = 0, 1, 2, 3$) for the approximation of the crystal field splitting. The calculations were performed at the TD-DFT UB3LYP/cc-pVTZ (H, C, N, O) and ecp-28-mdf (Ru) level of theory one unpaired electron on each Ru center.

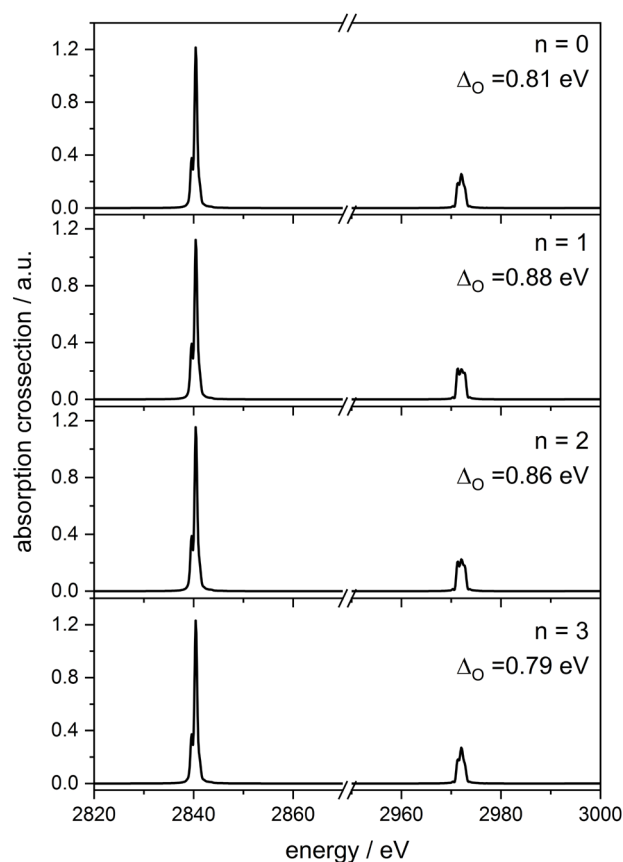


Fig. S16: Simulated XA spectra of $[\text{Ru}_3\text{O}(\text{OAc})_6(\text{py})_n]^+$ ($n = 0, 1, 2, 3$) with the approximated crystal field splittings from the Tanabe Sugano diagram. The simulations were performed by CTM4XAS with Cowan Batch files.

Tab. S2: Atom coordinates for $[\text{Ru}_3\text{O}(\text{OAc})_6(\text{py})_n]^+$ ($n = 0$). The calculation was performed at the B3LYP/cc-pVTZ (H, C, N, O) and ecp-28-mdf (Ru) level of theory with a high spin state for each Ru center.

atom	x	Y	z
C	-2.63497	0.00749	-1.88098
C	-3.61529	0.00936	-3.01723
H	-3.50635	0.91198	-3.61174
H	-4.62482	-0.00527	-2.60138
H	-3.48923	-0.88013	-3.62826
C	-2.69659	0.00728	1.85775
C	-3.71390	0.00979	2.96041
H	-3.18517	-0.00062	3.91594
H	-4.33346	-0.88111	2.90761
H	-4.31877	0.91114	2.91775
C	1.32328	2.27581	-1.88907
C	1.78733	3.07156	-3.07348
H	1.32121	4.05279	-3.07849
H	1.48431	2.54555	-3.98129
H	2.87055	3.15393	-3.07516
C	1.35902	2.33594	1.85777
C	1.87274	3.21556	2.95909
H	1.62042	2.75232	3.91535
H	1.39739	4.19152	2.91918
H	2.95406	3.30345	2.90133
C	1.31027	-2.28267	-1.88957
C	1.77003	-3.08065	-3.07417
H	1.47176	-2.55172	-3.98185
H	1.29710	-4.05860	-3.08054
H	2.85266	-3.17055	-3.07472
C	1.34672	-2.34373	1.85729
C	1.85570	-3.22661	2.95821
H	1.60554	-2.76268	3.91470
H	2.93657	-3.31996	2.90061
H	1.37542	-4.20012	2.91759
Ru	-0.94749	1.65950	0.01829
Ru	-0.95656	-1.65400	0.01838
Ru	1.91107	-0.00529	0.01750
O	0.00117	0.00020	-0.00806
O	-2.26619	1.12940	-1.42276
O	-2.27374	-1.11627	-1.42102
O	-2.28846	1.13320	1.43980
O	-2.29323	-1.12096	1.44120
O	0.17284	2.53152	-1.42418
O	2.11250	1.40154	-1.42327
O	0.17974	2.55087	1.44268

O	2.12781	1.41856	1.43869
O	0.15783	-2.53110	-1.42574
O	2.10492	-1.41394	-1.42258
O	0.16665	-2.55273	1.44142
O	2.12011	-1.42974	1.43925

Tab. S3: Atom coordinates for $[\text{Ru}_3\text{O}(\text{OAc})_6(\text{py})_n]^+$ ($n = 1$). The calculation was performed at the B3LYP/cc-pVTZ (H, C, N, O) and ecp-28-mdf (Ru) level of theory with a high spin state for each Ru center.

atom	x	y	z
C	-0.72138	2.30726	-1.87483
C	-1.20666	3.16782	-3.00895
H	-1.12015	2.59975	-3.93725
H	-0.60359	4.06652	-3.09397
H	-2.25574	3.41749	-2.86896
C	-0.65283	2.26582	1.91836
C	-1.07812	3.07445	3.11293
H	-1.22154	2.40629	3.96282
H	-2.03551	3.55187	2.90884
H	-0.33092	3.82185	3.35885
C	3.35177	-0.00138	-1.87336
C	4.44029	-0.00411	-2.90717
H	4.42010	0.91471	-3.48597
H	4.34959	-0.87450	-3.55141
H	5.40167	-0.06467	-2.39265
C	3.31553	0.00150	1.85269
C	4.26469	0.00137	3.01653
H	3.67983	-0.00917	3.93853
H	4.87365	0.90104	3.01120
H	4.88640	-0.88951	3.00003
C	-0.72271	-2.30946	-1.87030
C	-1.20841	-3.17109	-3.00344
H	-1.11839	-2.60518	-3.93274
H	-2.25845	-3.41752	-2.86502
H	-0.60761	-4.07159	-3.08559
C	-0.65313	-2.26021	1.92201
C	-1.08767	-3.08632	3.10122
H	-1.49876	-2.43874	3.87393
H	-0.25760	-3.66478	3.49368
H	-1.88272	-3.76291	2.78507
C	-4.16753	0.00074	-1.16400
H	-3.56784	0.00023	-2.05945
C	-5.55060	0.00072	-1.21345
H	-6.04760	0.00014	-2.17239
C	-6.26977	0.00147	-0.02658
H	-7.35080	0.00146	-0.03648

C	-5.57254	0.00223	1.17356
H	-6.08670	0.00281	2.12337
C	-4.18912	0.00222	1.14824
H	-3.60672	0.00284	2.05569
N	-3.49600	0.00147	-0.00182
Ru	1.59686	1.62841	-0.03325
Ru	-1.39421	0.00143	0.01942
Ru	1.59708	-1.62827	-0.03170
O	0.62594	0.00099	0.01477
O	0.45365	2.51447	-1.45866
O	-1.52739	1.42637	-1.44347
O	0.49197	2.48804	1.43864
O	-1.49461	1.42849	1.46814
O	2.93034	1.12372	-1.47039
O	2.92851	-1.12645	-1.47069
O	2.94445	1.12289	1.39804
O	2.94602	-1.12034	1.39717
O	-1.52817	-1.42797	-1.43961
O	0.45243	-2.51697	-1.45416
O	-1.49354	-1.42109	1.47296
O	0.49194	-2.48289	1.44289

Tab. S4: Atom coordinates for $[\text{Ru}_3\text{O}(\text{OAc})_6(\text{py})_n]^+$ ($n = 2$). The calculation was performed at the B3LYP/cc-pVTZ (H, C, N, O) and ecp-28-mdf (Ru) level of theory with a high spin state for each Ru center.

atom	x	Y	z
C	-2.34460	1.92109	-1.86819
C	-3.20078	2.49856	-2.96265
H	-2.62692	2.50816	-3.89043
H	-3.45518	3.53043	-2.72803
H	-4.10016	1.90722	-3.10198
C	-2.34905	1.92337	1.86281
C	-3.20036	2.48879	2.96704
H	-2.76761	2.19112	3.92420
H	-4.20918	2.08899	2.91123
H	-3.21094	3.57424	2.92379
C	2.34862	1.92236	-1.86685
C	3.20204	2.48493	-2.97096
H	3.14975	3.56962	-2.98187
H	2.82511	2.11169	-3.92518
H	4.22986	2.14826	-2.86139
C	2.34021	1.92071	1.87253
C	3.19057	2.47857	2.98156
H	2.80938	2.10298	3.93319
H	3.13853	3.56330	2.99631

H	4.21854	2.14185	2.87461
C	-0.00177	-1.99743	-1.94038
C	-0.00011	-2.87134	-3.16847
H	0.02277	-2.23146	-4.05300
H	-0.90248	-3.47512	-3.20915
H	0.88389	-3.50315	-3.18529
C	0.00139	-1.99761	1.93950
C	0.00483	-2.87243	3.16695
H	0.08465	-2.23581	4.05045
H	0.86350	-3.53888	3.15530
H	-0.91858	-3.44026	3.23583
C	-4.12811	-1.86934	-1.15572
H	-3.62146	-1.56366	-2.05678
C	-5.31178	-2.58561	-1.19393
H	-5.74372	-2.84780	-2.14858
C	-5.91928	-2.95100	-0.00085
H	-6.84438	-3.51048	-0.00110
C	-5.31424	-2.58257	1.19256
H	-5.74821	-2.84225	2.14698
C	-4.13043	-1.86650	1.15500
H	-3.62586	-1.55824	2.05636
C	4.12766	-1.86783	-1.15566
H	3.61968	-1.56480	-2.05698
C	5.31294	-2.58149	-1.19304
H	5.74483	-2.84480	-2.14743
C	5.92220	-2.94259	0.00050
H	6.84865	-3.49986	0.00085
C	5.31731	-2.57273	1.19356
H	5.75268	-2.82905	2.14827
C	4.13186	-1.85938	1.15529
H	3.62710	-1.54981	2.05618
N	-3.54442	-1.51422	-0.00022
N	3.54422	-1.51122	-0.00040
Ru	0.00099	2.36695	-0.00096
Ru	-1.74900	-0.41479	0.00049
Ru	1.74794	-0.41306	-0.00119
O	-0.00092	0.50873	-0.00026
O	-1.38203	2.64054	-1.46734
O	-2.62977	0.76521	-1.44499
O	-1.40156	2.65134	1.44276
O	-2.62118	0.75833	1.45609
O	1.40178	2.65019	-1.44649
O	2.62110	0.75765	-1.45853
O	1.38176	2.64187	1.46771
O	2.62740	0.76585	1.44607
O	-1.13348	-1.66462	-1.48148

O	1.12938	-1.67186	-1.47473
O	-1.12981	-1.67386	1.47340
O	1.13306	-1.66290	1.48117

Tab. S5: Atom coordinates for $[\text{Ru}_3\text{O}(\text{OAc})_6(\text{py})_n]^+$ ($n = 3$). The calculation was performed at the B3LYP/cc-pVTZ (H, C, N, O) and ecp-28-mdf (Ru) level of theory with a high spin state for each Fe center.

atom	x	Y	z
C	-2.77904	-0.00137	1.89479
C	-3.78562	-0.00341	3.01721
H	-3.24953	-0.04128	3.96747
H	-4.42373	-0.88099	2.95447
H	-4.38173	0.90479	2.99800
C	-2.77922	-0.00190	-1.89464
C	-3.78620	-0.00046	-3.01671
H	-3.25099	0.05219	-3.96676
H	-4.43311	0.87011	-2.94577
H	-4.37317	-0.91465	-3.00545
C	1.29834	-2.21330	1.93870
C	1.76105	-3.02043	3.12595
H	0.98421	-3.70061	3.46012
H	2.03424	-2.34542	3.93716
H	2.65556	-3.58115	2.85623
C	1.29860	-2.21300	-1.93900
C	1.76034	-3.01864	-3.12763
H	2.01220	-2.34263	-3.94506
H	0.99017	-3.71198	-3.45004
H	2.66709	-3.56347	-2.86689
C	1.29614	2.21464	1.93891
C	1.75662	3.02028	3.12803
H	2.00012	2.34431	3.94809
H	0.98862	3.71835	3.44539
H	2.66785	3.55929	2.87109
C	1.29585	2.21495	-1.93866
C	1.75722	3.02190	-3.12655
H	2.01929	2.34665	-3.94132
H	2.65799	3.57473	-2.86171
H	0.98332	3.70861	-3.45414
C	-2.30839	-4.13373	1.15497
H	-2.04427	-3.60121	2.05438
C	-2.93145	-5.36915	1.19369

H	-3.16187	-5.82022	2.14776
C	-3.24829	-6.00225	-0.00023
H	-3.73457	-6.96800	-0.00024
C	-2.92997	-5.36987	-1.19414
H	-3.15919	-5.82152	-2.14821
C	-2.30696	-4.13442	-1.15539
H	-2.04167	-3.60246	-2.05479
C	-2.31167	4.13181	1.15536
H	-2.04582	3.60014	2.05477
C	-2.93595	5.36661	1.19411
H	-3.16564	5.81804	2.14818
C	-3.25495	5.99864	0.00019
H	-3.74222	6.96389	0.00020
C	-2.93749	5.36585	-1.19373
H	-3.16840	5.81666	-2.14779
C	-2.31315	4.13108	-1.15499
H	-2.04851	3.59881	-2.05440
C	4.83213	0.00228	1.15448
H	4.23983	0.00165	2.05529
C	6.21587	0.00292	1.19316
H	6.72144	0.00280	2.14773
C	6.92467	0.00371	0.00001
H	8.00585	0.00422	0.00002
C	6.21589	0.00384	-1.19315
H	6.72147	0.00446	-2.14772
C	4.83214	0.00317	-1.15449
H	4.23985	0.00325	-2.05531
N	-1.99902	-3.52498	-0.00020
N	-2.00310	3.52268	0.00018
N	4.14845	0.00238	-0.00001
Ru	-1.04243	-1.61136	-0.00014
Ru	-1.04422	1.61016	0.00012
Ru	2.03508	0.00122	-0.00002
O	0.02712	0.00006	-0.00001
O	-2.38436	-1.12641	1.47833
O	-2.38475	1.12417	1.47951
O	-2.38363	-1.12700	-1.47944
O	-2.38562	1.12357	-1.47830
O	0.12967	-2.39825	1.52621
O	2.16430	-1.41364	1.45301
O	0.13040	-2.39883	-1.52558

6. IR(M)PD studies of isolated spin frustrated trimetallic μ -oxo bridged 4d complexes

O	2.16432	-1.41268	-1.45399
O	0.12773	2.39916	1.52547
O	2.16276	1.41531	1.45391
O	0.12698	2.39857	-1.52615
O	2.16274	1.41628	-1.45300

7 Opto-magnetic correlation of a mass-selected monometallic spin-crossover iron complex

Michael Lembach^a, Matthias Klein^a, Joachim Hewer^a, Julius Wolny^b, Vicente Zamudio-Bayer^c, Martin Timm^c, Christine Bülow^{c,d}, Tobias Lau^c, Volker Schünemann^b, Bernd von Issendorff^d, Akira Terasaki^e and Gereon Niedner-Schatteburg^a

^a*Fachbereich Chemie and Forschungszentrum OPTIMAS,
Technische Universität Kaiserslautern,
67663 Kaiserslautern, Germany*

^b*Fachbereich Biophysik,
Technische Universität Kaiserslautern,
67663 Kaiserslautern, Germany*

^c*Helmholtz-Zentrum für Materialien und Energie
BESSY II,
14109 Berlin, Germany*

^d*Physikalisches Institut,
Universität Freiburg,
79104 Freiburg, Germany*

^e*Department of Chemistry,
Kyushu University,
Fukuoka, Japan*

7.1 Preamble

The following chapter is prepared as manuscript for publication. I managed and performed the XMCD, IR(M)PD, CID, UV/VIS experiments, data evaluation, quantum chemical calculations, and XA simulations. I received experimental support from Matthias Klein, Joachim Hewer, Vicente Zamudio-Bayer, Martin Timm, and Christine Bülow to record the presented XA spectra. Tobias Lau, Bernd von Issendorf and Akira Terasaki operate the Ion Trap experimental setup at the Helmholtz Zentrum BESSY II in Berlin. Julius Wolny synthesized the samples in the group of Volker Schünemann and provided calculated minimum structures of the presented complexes. I wrote the chapter in form of a draft manuscript.

7.2 Abstract

This study elucidates the existence of different isomers of an isolated monometallic spin-crossover complex with the structure $[\text{Fe}(\text{btpa})]^{2+}$ (btpa = *N, N, N', N'*-Tetrakis(2-pyridylmethyl)-6,6'-bis(aminomethyl)-2,2'-bipyridine). We present the X-ray magnetic circular dichroism (XMCD) and InfraRed (Multiple) Photon Dissociation (IR(M)PD) spectroscopic studies of an isolated octahedral iron(II) spin-crossover complex. The combination of temperature dependent XMCD spectroscopy and sum rule analysis allows the temperature dependent determination of magnetic moments of transition metal complexes. Our investigations show that the determination of a spin-crossover process in the gas phase is demanding. The results suggest an actual transition from low spin (LS) to high spin (HS) configuration upon increasing the ion temperature. The presented IR(M)PD spectrum compared with Collision Induced Dissociation (CID) and quantum chemical calculations of the complex hint different isomers in its spin state and geometry. The correlation of the X-ray absorption (XA) spectroscopic studies with UV/VIS studies in condensed phase allows a precise determination of the electronic structure and its geometric properties. The presented results help gain a fundamental insight into the molecular structure of spin-crossover iron complexes, void of any external effects, such as crystal packing or solvation.

7.3 Introduction

Paramagnetic Transition Metal (TM) complexes have emerged as a high interest research area in the last decades because of their magnetic^[1-5], optical^[6-9], or catalytic^[10-14] properties and potential applications encompassing molecular electronic devices^[15-17], quantum computing^[18-23], or nanomagnets^[24-26]. Therefore, much effort has been spent on their molecular design in order to tailor and enhance magnetic properties. TM complexes with single molecule magnetic behavior^[27-34] (SMM), spin-crossover^[15, 35-39] (SCO) processes, or a spin frustrated^[40-44] ground state seem to be promising candidates for the investigation of the magnetic properties for technical applications. Here, the focus is on SCO complexes which have the property to change their redistribution of the electrons in the d valence orbitals upon external stimuli, resulting in a change from a low spin (LS) to a high spin (HS). This redistribution can be achieved by changing the temperature, the pressure, or photon

irradiation^[37, 39, 45-49]. Octahedral Fe(II) spin-crossover complexes are reported by many groups^[15, 35, 36, 38, 39, 46, 50].

In these cases, the $^1A_{1g}$ low spin ground state with a $(t_{2g})^6$ electron configuration can be thermally excited into a $^5T_{2g}$ high spin state with a $(t_{2g})^4(e_g)^2$ electron configuration^[15]. The transition can result in extended bond lengths originating from the σ -antibonding e_g orbitals occupation in the high spin state^[15, 51, 52]. The transition temperature depends on different parameters as external effects, crystal packing, or solvation. Dissolving a spin-crossover complex in suitable solvents can decimate the transition temperature^[53].

Temperature dependent investigations of $[Fe(ptz)_6](BF_4)_2$ reveal an increasing effective magnetic moment with rising temperature^[36]. Studies of the complex with the structure $[Fe(H_2B(pz)_2)_2L]$ point out an increasing susceptibility at higher temperatures^[54]. The complex with the structure $[Fe(L-N_4Me_2)(NCS)_2]$ also reveals strong increasing hysteresis by increasing the temperature and also an elongation of the bonding length from the metal center to the ligand by the transition from an LS complex to an HS complex^[15].

Earlier studies on the given complex $[Fe(btpa)](PF_6)_2$ show that altering the temperature causes a change in the electronic ground state, indicating a thermally driven spin-crossover process^[55, 56].

All investigations show spin-crossover behavior in these complexes, which are similar to the reported complex. Unfortunately, all these experiments were performed in solid state or condensed phase. Therefore, external effects such as packing effects or solvation cannot be excluded and may affect the actual spin-crossover process. To exclude these effects, gas phase investigations seem to be necessary.

The presented complex, synthesized and kindly provided by Julius Wolny, serves as a model system in order to determine the spin-crossover process in complexes containing a Fe^{2+} ion. The complex acquires a Fe^{2+} ion surrounded by an eight dentate ligand *N, N, N', N'*-Tetrakis(2-pyridylmethyl)-6,6'-bis(aminomethyl)-2,2'-bipyridine (btpa), which build an octahedrally coordinated dication. Two hexafluorophosphate anions serve as counterions in this complex (cf. Fig. 1).

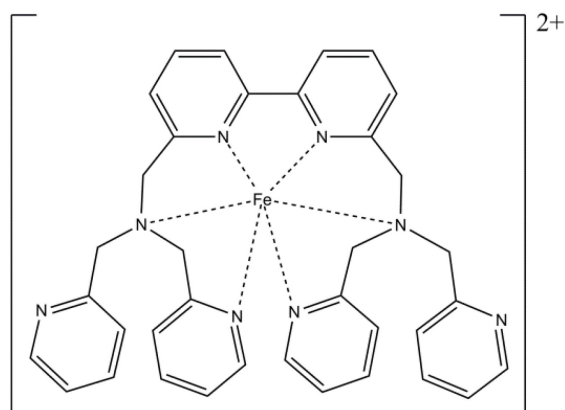


Fig. 1: General structure of the spin-crossover complex [Fe(btpa)]²⁺.

Electrospray ionization^[55, 56] (ESI) enables mass spectrometric investigations of ionic complexes in vacuum and their electronic structure by irradiation with X-ray photons or IR photons. Tandem-MS-based methods like X-ray magnetic circular dichroism (XMCD) have helped to elucidate electronic structures^[57-62] and InfraRed (Multiple) Photon Dissociation (IR(M)PD) for the determination of the geometrical structure^[63-69]. XMCD techniques were instrumental under cryogenic conditions^[61, 70-72] and applied magnetic fields. The IR(M)PD experiments were performed at room temperature. Combining XMCD spectroscopy and sum rule analysis allows for a temperature dependent determination of magnetic moments of transition metal ions or transition metal complexes^[61, 71-74]. The primary topics in this study are the characterization of the magnetic moments per iron atom at different temperatures, the geometrical determination, and the determination of the electronic ground state of the complex.

We combine experimental XMCD and IR(M)PD investigations of isolated [Fe(btpa)]²⁺ (btpa = N, N, N', N'-Tetrakis(2-pyridylmethyl)-6,6'-bis(aminomethyl)-2,2'-bipyridine)^[57, 75] in combination with quantum chemical calculations by Density Functional Theory (DFT), XA simulations and UV/VIS spectra to gain a better insight of the magnetic properties and electronics in spin-crossover complexes.

7.4 Experimental setup and methods

X-ray magnetic circular dichroism (XMCD)

For the presented polarized dependent gas phase X-ray Absorption (XA) spectra, we used the “Ion Trap” coupled to the UE52-PGM soft X-ray beamline at the BESSY II synchrotron facility of the Helmholtz Zentrum Berlin^[58-62, 73]. The Ion Trap is a home built time of flight combined ion trap mass spectrometer to record Total Ion Yield (TIY) XA spectra^[58-62].

For our experiments, we used a custom built electrospray ionization (ESI) source for ion creation, kindly provided by the Schlathölter group (Zernike Institute for Advanced Materials, University of Groningen, Netherlands) group.

[Fe(btpa)](PF₆)₂ was prepared in an acetonitrile solution ($c \sim 1 \cdot 10^{-5}$ mol/L). The investigated species forms a doubly charged cation by losing two hexafluorophosphate anions.

Ions are transferred via an RF Hexapole into a linear quadrupole mass filter (Extrel, 40 - 4000 amu). After the mass selection, the selected ions are guided into a linear quadrupole ion trap within the high field region (5 T) of a superconducting solenoid. The trap is operated at a frequency of 3.82 MHz. Evaporative liquid helium cools down the ion trap to 4 K, 10 K, and 20 K. A constant helium background pressure of $1 \cdot 10^{-6}$ mbar thermalizes the trapped ions by collisional cooling. A continuous infusion of the ions into the ion trap serves for a stable ion signal. The ions are ejected into the time of flight area with a repetition rate of 120 Hz to record the mass spectra. For the XA spectra recorded by TIY spectroscopy, the ions are irradiated for 10 to 15s at set photon energy. Therefore, we recorded mass spectra as a function of the X-ray energy, with the quantization axis projected to the z-axis. A GaAs-diode records the X-ray intensity from the undulator beamline used for photon flux normalization of the recorded spectra. Spectra on the Fe absorption edges were taken with an exit slit size of 200 μm , a respective resolution of 400 meV from 700 eV to 735 eV for the L₃ and L₂ absorption edges.

XA spectra are recorded with positive and negative polarization in an alternating manner. The subtraction of the polarized dependent spectra leads to the corresponding XMCD spectrum and the addition to the sum spectrum, which is necessary to apply the sum rule analysis (cf. Fig. S1). The color-coded elements **A**, **B**, and **C**, are extracted from the XMCD spectra's integrals and the sum of polarization-dependent XA spectra (**C**). We extract the projections ($m_S^{(z)}$ and $m_L^{(z)}$) of the intrinsic spin (m_S) and orbital (m_L) magnetic moments per atom onto the quantization axis by sum rule analysis. The quantization axis coincides with the magnetic field axis of the surrounding solenoid and the X-ray propagation direction. Under the given experimental conditions, a scaling of the total magnetic moment must be performed. Therefore, knowledge of all exact contributing coupling of the magnetic centers is needed, which is presently unknown. Therefore, such scaling is omitted, and present magnetizations at the given experimental conditions ($B = 5 \text{ T}$; $T = 4 \text{ K}, 10 \text{ K}, 20 \text{ K}$) are given. The resulting XMCD spectra were analyzed with sum analysis^[76].

$$m_S^{(z)} = g_S \mu_B \frac{(\mathbf{A} - b\mathbf{B})}{c \frac{3}{2} \mathbf{C}} n_h - g_S \mu_B \frac{d}{c} \langle T_z \rangle \quad (1)$$

$$m_L^{(z)} = -g_L \mu_B \frac{\mathbf{A} + \mathbf{B}}{a \frac{3}{2} \mathbf{C}} n_h \quad (2)$$

We anticipated the containing Fe^{2+} ions to be in a $3d^6$ high spin state and chose the number of unoccupied valence orbitals n_h to be $n_h = 5$ for species. With n_h being the number of holes per iron atom in the final state, g_S and g_L the Landé factors for the electron spin and orbital angular momentum ($g_S = 2.0$, $g_L = 1.0$), μ_B the Bohr magneton and a , b , c , and d are the sum rule related prefactors. The sum rule related prefactors are $1/2$, 2 , $2/3$, and $7/3$ for investigations on the Fe $L_{3,2}$ absorption edges.

Collision Induced Dissociation

For ESI mass spectrometric and Collision Induced Dissociation (CID) measurements, we used a quadrupole mass spectrometer (amazon ETD, Bruker daltonics) with a three-dimensional Paul trap. A sample solution of $[\text{Fe}(\text{btpa})](\text{PF}_6)_2$ ^[57, 75] in acetonitrile ($c \sim 1 \cdot 10^{-6} \text{ mol/L}$) was constantly infused into the spray chamber by a syringe pump with a flow rate of $180 \mu\text{L/h}$. The losing two hexafluorophosphate anions formed the investigated cationic species during the ESI process Nitrogen was used as a drying gas with a flow rate of 9 L/min at $200 \text{ }^\circ\text{C}$.

The nebulizer pressure was set to 280 mbar (4psi) for spraying the sample solution, and the spray needle was kept at 4.5 kV. The Paul trap comprises a ring electrode and two end caps forming a nearly hyperbolic inner profile. The end caps possess pinholes that allow them to enter or exit the ions in the trap. The ring electrode is powered with a high voltage RF (radio frequency) potential (781 kHz) while the end caps are grounded. The ions are accumulated in this resulting oscillating quadrupolar electric field generated from the three electrodes. An auxiliary dipolar voltage is fed to either the exit cap or both end caps for ion isolation and fragmentation. A proportional integral derivative (PID) gas controller set a constant partial Helium buffer gas pressure to 10^{-3} mbar inside the trap by a proportional integral derivative (PID) gas controller.

CID breakdown curves were recorded by stepwise variation of the excitation amplitudes (Amp_{exp}) from 0.0 V–2.0 V while monitoring the extend of fragmentation and relative abundances of fragments for the isolated complex of interest. The excitation amplitudes determine the internal scale of the mass spectrometer E_{lab} in V. Relative abundances were calculated according to

$$I_{tot}^{fr}(E_{lab}) = \left(\frac{\sum_i I_i^{fr}(E_{lab})}{\sum_i I_i^{fr}(E_{lab}) + \sum_i I_i^p(E_{lab})} \right) \quad (3)$$

where I_i^{fr} = intensity of the fragment ion and I_i^p = intensity of the parent ions. Center of mass transferred fragmentation energies (E_{com}) were calculated from internal energies by:

$$E_{com} = \left(\frac{m_{He}}{m_{He} + m_{ion}} \right) \cdot E_{lab} \quad (4)$$

where m_{ion} stands for the isotopically averaged mass of the molecular ion. Note that the current application of the CID technique by RF excitation in the presence of multiple collisions result in a so called “slow multi-collision heating” mode of operation^[77].

Fragmentation amplitude dependent CID spectra were modeled and fitted by sigmoidal functions of the type

$$I_{fit}^{fr}(E_{com}) = \left(\frac{1}{1 + e^{(E_{com}^{50} - E_{com}) B}} \right) \quad (3)$$

Using a least-squares criterion. The E_{com}^{50} fit parameter is the amplitude at which the sigmoid function is at half maximum value, whereas B describes the rise of the sigmoid curve. As a result of the correlation between fragmentation amplitude and appearance energy, it is

feasible to assume that the appearance curves can be associated with the isolated complexes' relative stability [78-80].

For the experiments, via Electron Transfer Dissociation (ETD), we admitted methane in the ETD cell as a mediator to create low energy electrons. Inside the ETD cell, methane is oxidized to a methane radical cation ($\text{CH}_4^{*\cdot} + 2e^-$) via electron impact ionization. The collision of the methane radical cation with the Fluoranthene ($\text{C}_{16}\text{H}_{10}$) leads to an electron capture of the low-energy electrons by the Fluoranthene. Afterward, the Fluoranthene radical anion ($\text{C}_{16}\text{H}_{10}^-$) is guided into the Paul trap, and collisions with the complex of interest lead to an anion-cation electron transfer reaction resulting in a reduction of the complex.

InfraRed (Multiple) Photon Dissociation (IR(M)PD)

ESI mass spectrometric and InfraRed (Multiple) Photon Dissociation (IR(M)PD) measurements, we used a quadrupole mass spectrometer (amazon SL, Bruker daltonics) with a three-dimensional Paul trap and followed the scheme as discussed for the CID experiments. The significant difference is a modified Paul trap, where the IR photons can irradiate the ions resulting in fragmentation of the ions. The IR(M)PD spectra are acquired as a function of the fragments by resonant irradiation with IR photons.

Laser system

The laser pulses were generated using a KTP/KTA optical parametric oscillator/amplifier (OPO/OPA, LaserVision) system. A pulsed 10 Hz injection seeded Nd^{3+} Yag laser (PL 8000, Continuum) pumps the system and serves as source for tunable IR radiation. The difference frequency (DF) between the OPA signal and idler waves is generated within an AgGaSe_2 crystal, applied for the range between 1000 cm^{-1} and 2000 cm^{-1} . The IR beam is guided into the ion trap by a 90° off axis parabolic silver mirror with a focal length of 15 cm. After passing the Paul-trap, the IR beam was guided to a power meter (Maestro, Gentech) to monitor the laser power. IR(M)PD spectra are obtained by plotting the fragment yield as a function of the laser frequency (ν). The fragment yield is defined as:

$$Y(\nu) = \left(\frac{\sum_i I_i^{fr}(\nu)}{\sum_i I_i^{fr}(\nu) + \sum_i I_i^p(\nu)} \right) \quad (4)$$

Calibration of the IR frequency is done by a wavemeter (821B-NIR, Bristol instruments). The resulting power curves are recorded parallel to the IR(M)PD experiments by digitizing the analog output of the laser power meter through an ADC input of the Amazon SL mass spectrometer. No normalization of the recorded spectra was done because there is an intrinsically nonlinear power dependence of the IR(M)PD fragmentation efficiencies.

UV/VIS absorption spectroscopy (solution)

Static absorption spectra were recorded with a PerkinElmer Lambda 35 spectrometer. For the sample preparation, acetonitrile (Uvasol grade) was used, and the complex $[\text{Fe}(\text{btpa})](\text{PF}_6)_2$ was dissolved ($c \sim 1 \times 10^{-6}$ mol/L). The Solution was convicted into a precision cuvette (light path 10 mm). The spectra were recorded in double beam operation to scan a wider spectroscopic area.

7.5 Computational methods

For calculating the optimized minimum energy structures and linear absorption spectra, Wolny provided the geometry optimized structures. Minimum structures were calculated for different multiplicities with density functional theory (DFT) using B3LYP^[81, 82] functional and cc-pVTZ basis sets^[83-86] (C, H, N) in combination with Stuttgart ecp effective core potential (Fe) with Gaussian 09 program package^[87]. Three minimum structures, one octahedral low spin in a singlet state, and two high spin complexes with a multiplicity of 5 were found for $[\text{Fe}(\text{btpa})]^{2+}$. For relativistic 0th ZORA calculations, we used the orca program package^[88] to gain the electronic behavior of the spin-crossover complex. The XA simulations were performed with a Mathematica-based program package CTM4XAS^[89] with batch files from Cowan, attaining orca calculated parameters for XA spectra to perform the simulations.

7.6 Results and Discussion

7.6.1 Results I: X-ray magnetic circular dichroism (XMCD)

The cations with the structure $[\text{Fe}(\text{btpa})]^{2+}$ were created within the electrospray process and mass-selected at the mass of 317 m/z . We obtained polarization dependent XA spectra and their related XMCD spectra at different ion trap temperatures ($T = 4.5$ K, 15 K, and 25 K) after selecting the ions of interest and optimizing the fragmentation with X-ray irradiation (cf. Fig. 2).

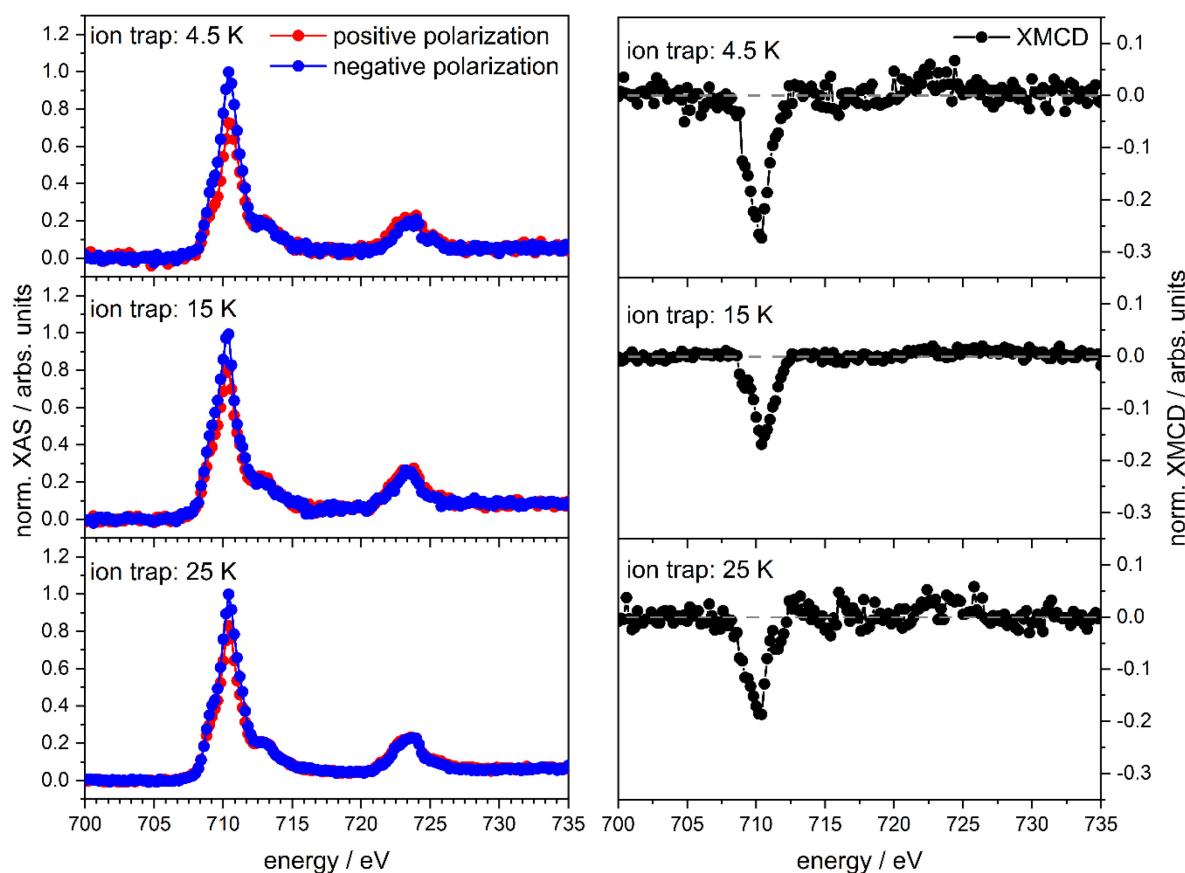


Fig. 2: polarized dependent XA spectra of $[\text{Fe}(\text{btpa})]^{2+}$ (left) and their corresponding XMCD spectra (right) at different ion trap temperatures.

The temperature dependent XA spectra and corresponding XMCD spectra show a decreasing trend from 4.5 K to 15 K ion trap temperature. The dichroic effect is nearly unchanged when the ion trap temperature is raised from 15 K to 25 K. (cf. Fig. 2). Applying the sum rule analysis for the projected spin and orbital magnetic moments per iron atom reveal slightly different values for the ion trap temperatures at 4.5 K and 15 K. By increasing the ion trap temperature to 25 K, we observe small changes in the magnetic values (cf. Tab. 1, cf. Fig. S4). For the

reported magnetic values derived from the sum rule analysis, we estimate a 5% uncertainty. We consider a transition from the 2p core to a 3d valence state in the Fe iron. The valence states are not always entirely separated, resulting in mistakes in the magnetic moments computed by the sum rules, notably for the spin sum rule analysis^[90]. Teramura et al. have introduced correction factors for the sum rule analysis based on atomic model systems. They entail Coulomb interactions at the L_{2,3} absorption edges as well as the expectation value for the magnetic dipole operator, which is not accessible in our XMCD experiments^[90-94]. The suggested procedure of Teramura corrects the presented magnetizations in this work.

Tab. 1: Experimental magnetic values projected on the z-axis for m_S , m_L , m_J , and m_L/m_S for $[\text{Fe}(\text{btpa})]^{2+}$ at given temperatures and with the correction of 4.5%^[90, 91].

	exp.			corrected		
	4.5 K	15 K	25 K	4.5 K	15 K	25 K
$m_S^{(z)}$	1.03(5)	0.67(3)	0.60(3)	0.98(5)	0.64(3)	0.64(3)
$m_L^{(z)}$	0.39(2)	0.21(1)	0.20(1)	0.39(2)	0.21(1)	0.20(1)
$m_J^{(z)}$	1.42(7)	0.88(4)	0.80(4)	1.37(2)	0.85(1)	0.84(1)
$m_L^{(z)}/m_S^{(z)}$	0.39(2)	0.33(2)	0.31(2)	0.39(2)	0.33(2)	0.31(2)

The spin and orbital magnetic moments reveal reduced values by increasing the temperature. The spin magnetic values are lower at all ion trap temperatures, indicating a combination of low spin (LS) and high spin (HS) configurations. A pure LS complex should not lead to a dichroic effect due to paired electrons in the 3d orbitals.

Approximation of the spin isomer composition by the ion temperature

Using previous investigations of the ion temperatures within the ion trap^[74, 95], we can approximate an spin isomer composition for the complex at different temperatures. Langenberg assumed a constant temperature offset of $7 \text{ K} \pm 3 \text{ K}$ of the ions in the ion trap. The offset can be explained by inefficient collisional cooling of the ions with the helium buffer gas in the trap. Also, collisions between the ions themselves cannot be excluded. The other effect of warming up ions in the trap could occur from the RF heating^[92]. Approximation of the isomer composition is feasible by correlating the magnetic values from the sum rule analysis onto the Brillouin function, which fits the ions assumed temperature (cf. Fig. S5 and Fig. S6).

We observe slightly warmer ions, excluding the orbital magnetic moments at a given temperature (cf. Fig. S5). The approximation of the total magnetic moments onto the Brillouin function leads to significantly warmer ions than the applied ion trap temperature (cf. Fig. S6), and are in good agreement with Langenberg's results^[93]. The other way around approximates the spin isomer composition by fitting the Brillouin function to the magnetic values (cf. Tab. 2).

Tab. 2: Adjusted ion trap temperatures, obtained S , L , J from the Brillouin functions at given temperatures, S , L , J values from a Fe(II) HS ground state, and approximated spin isomer composition.

T/K	S_{Brill}	L_{Brill}	J_{Brill}	$S_{\text{Fe(II)}}$	$L_{\text{Fe(II)}}$	$J_{\text{Fe(II)}}$	$S_{\text{Brill}}/S_{\text{Fe(II)}}$	$L_{\text{Brill}}/L_{\text{Fe(II)}}$	$J_{\text{Brill}}/J_{\text{Fe(II)}}$
4.5	1.1	1.1	2.2	2	2	4	55	55	55
15	1.3	1.3	2.6	2	2	4	65	65	65
25	1.6	1.6	3.2	2	2	4	80	80	80

The approximated isomer composition between HS and LS isomers indicates that a mixture of both spin isomers is present in every applied ion trap temperature. Also, the quantity of the HS complex rises with increasing ion trap temperature. Therefore, we assume an almost equal amount of both spin isomers at 4.5 K and 80% of the HS complex at 25 K.

Determination of the crystal field splitting of the complex

The determination of crystal field splitting contributes to a better understanding of the actual spin-crossover mechanism at various temperatures. The transition from an LS spin complex to an HS spin complex causes elongated bondings^[15, 51, 52], which causes the associated crystal field splittings to shift from the LS configuration to the HS configuration. The spectroscopic pattern obtains the crystal field splittings at a set temperature. The XA spectra have a characteristic spectroscopic pattern, as described by Everett^[94]. The separation between the primary L_3 absorption edge and the little shoulder is described as splitting and representing the e_g and t_{2g} orbitals, resulting in complicated crystal field splitting (cf. Tab. 3)^[98]. The separation between the primary L_3 absorption edge and the little shoulder is described as splitting and representing the e_g and t_{2g} orbitals, resulting in complicated crystal field splitting (cf. Tab. 3)^[98].

Tab. 3: Determined crystal field splittings of $[\text{Fe}(\text{btpa})]^{2+}$ from the experimental XA spectra at given temperatures

T/K	E_{L_3}/eV	$E_{L_3 \text{ after}}/\text{eV}$	$\Delta E_{L_3}/\text{eV}$
4.5	710.40	713.00	2.60(1)
15	710.20	713.00	2.80(1)
25	710.40	713.00	2.60(1)

The energy differences show identical values for a constant ion trap temperature of 4.5 K and 25 K, and a slightly higher value for a constant ion trap temperature of 15 K, suggesting a change in the geometry by raising the temperature. The elongation of the bonding length might lead to a change in the crystal field splitting. At 4.5 K and 25 K, similar crystal field splittings are monitored, implying another HS isomer with the same crystal field splittings as the LS spin isomer. At 15 K, the HS composition is higher than at lower temperatures, resulting in an HS isomer with seven-fold coordination and a distinct crystal field splitting. The higher the temperature, the more entropic the effects become, allowing the pyridine rings in the ligand to freely rotate. This would result in the same crystal field splitting as for an ion trap temperature of 4.5 K, as a seven-folded HS complex would be converted to an octahedral HS complex.

XA simulations^[89] combined with the experimental crystal field splittings are in good agreement (cf. Fig. S7). A change in the oxidation state of the iron atom can be ruled out since it would result in a change in the netto charge of the complex, and the L_3 edge would move to higher energies for a Fe^{3+} ion at about 1-3 eV, which is not found in the experimental spectra^[97]. The 0.2 eV shift in the experimental spectra indicates a change in structural characteristics, which results in a distinct crystal field splitting^[97-102]. To further illustrate the ligand-induced change in the complex, the initial derivation of the XAS highlights the minor shift in their absorption energies on the L_3 edge (cf. Fig. S8). The XA spectrum at 15 K shifts to smaller energies than the XA spectra for 4.5 K and 25 K. As a result, at this temperature, a different structure must be present, leading to the idea that, in addition to the mixing of LS and HS complexes, various geometrical isomers are present, when compared to the calculated minimum structures for the octahedral LS, HS spin, and a heptagonal coordinated HS complex. The octahedral HS complex reveals a relative destabilization of 9 kJ/mol to the other structures. Therefore, we consider that the octahedral LS complexes are present at 4.5 K and

25 K, and a heptagonal HS complex is more present at 15 K. We assume that the mixture at 4.5 K is more given by the octahedral LS and HS complexes because the rotation of the free pyridine rings from the ligand are frozen in their position. At 15 K, the energy is enough to rotate the pyridine rings slightly and establish a weak bonded heptagonal coordinated complex. The rotation of the pyridine rings is no longer frozen at 25 K, resulting in an octahedral coordinated HS complex. Also, the bonding lengths of all these isomers are almost similar. There is a slight elongation of both HS isomers in their bonding lengths (cf. Fig. S9). The heptagonal coordinated HS complex has longer bonding distances in the z-direction, leading to higher Jahn Teller distortion resulting in different crystal field splitting than in the octahedrally coordinated complexes.

Theoretical calculations of the electronics in the complex

We performed projected Density of States (pDOS) calculations to identify the core-shell orbitals for the transfer of core-shell electrons into valence orbitals (cf. Fig. 3). Calculated pDOS spectra reveal a good agreement with the experimental XA spectra. For a set ion trap temperature of 4.5 K, a mixture of both octahedral complexes fits very well to the experimental XA spectrum. In the area around 13-15 eV, we observe a shoulder in the XA spectra, also given in the octahedral complexes. In the area between 0 and 5 eV, small wiggles in the XA spectra are in good agreement with the calculated pDOS spectra for the octahedral complexes. The estimated pDOS spectra for the heptagonal coordinated HS complex and octahedrally coordinated complex are similarly quite comparable to the observed XA spectrum at a fixed ion trap temperature. We observe a broader distribution in the pDOS spectrum of the heptagonal coordinated complex in the area around 0 eV. The experimental XA spectrum at 15 K ion trap temperature shows a slightly broader L_3 edge than the other spectra, suggesting a heptagonal coordinated complex. The spectral pattern of the XA spectra implies a mixture of both octahedral coordinated LS and HS complexes. We observe a decreasing shoulder at around 15 eV with higher temperature and assume that this feature belongs to the octahedral LS complex, which is also predicted in the pDOS spectrum of the LS complex. At all temperatures, a tiny shoulder at roughly -1 eV on the main L_3 edge is seen, indicating a combination of all three isomers. Still, we consider that in cold conditions, the rotational modes of pyridine are frozen. Almost no heptagonal coordination can be

established, and at the highest temperature, these rotational modes are that active that, on average, an octahedral coordinated HS complex is observed.

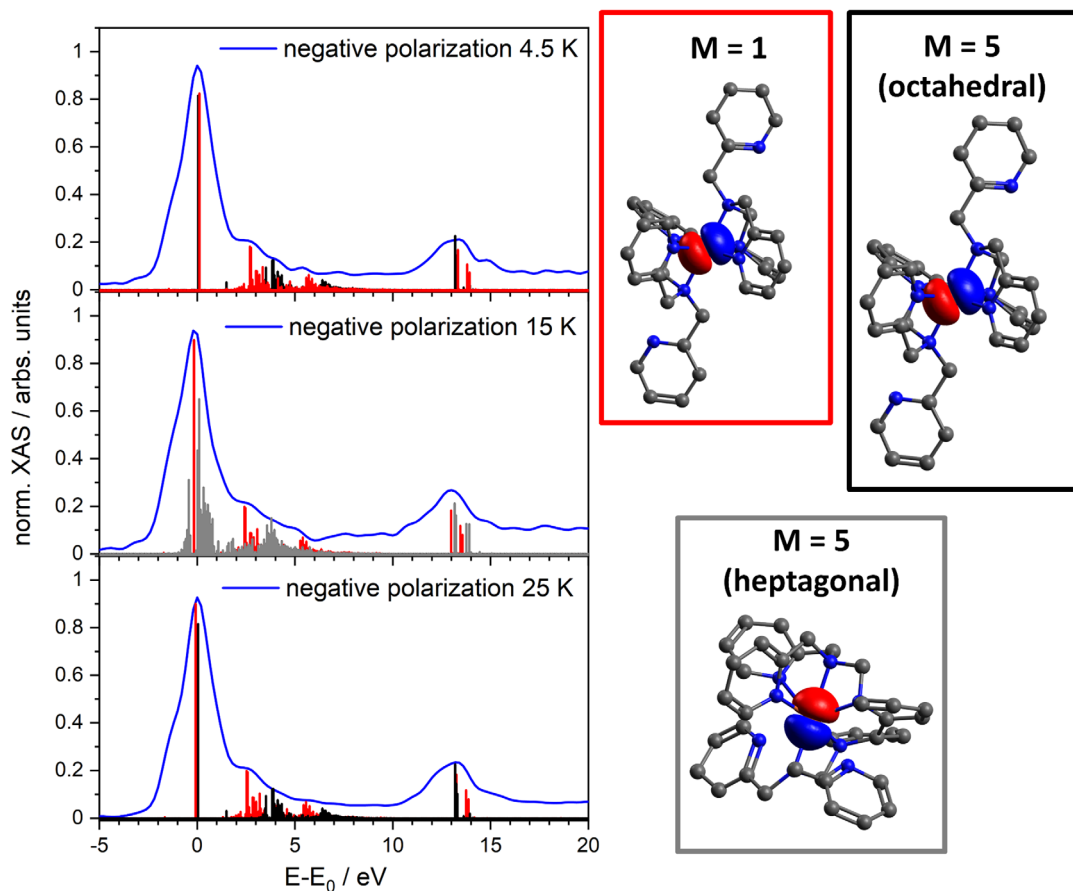


Fig. 3: Calculated pDOS spectra for $[\text{Fe}(\text{btpa})]^{2+}$ ($M = 1$ (red), $M = 5$ (black) and $M = 5$ heptagonal coordinated (grey)) in comparison of the experimental positive polarized XA spectra (blue) and their corresponding core-shell orbitals. The calculations were performed with Gaussian 09 at the B3LYP/cc-pVTZ (H, C, N, O) and Stuttgart ecp effective core potential (Fe) level of theory.

Branching ratio analysis and differential orbital covalency

We assumed strong core valence interactions for the spin-orbit sum rules^[95-97] as described above. This method yields very accurate values for spin-orbit interactions per hole. The branching ratio for such $p \rightarrow d$ transitions are defined as:

$$BR = \frac{I(L_3)}{I(L_3) + I(L_2)} \quad (5)$$

Where I are the intensities of the transition metal absorption edges, the sum rule^[95-98] gives the relation for the spin-orbit interactions per hole:

$$SOC = n_{j_2} - \frac{l+1}{l} n_{j_1} \quad (6)$$

n_{j_1} and n_{j_2} represent the occupation number per hole, where $j_1 = l - 0.5$ and $j_2 = l + 0.5$. At least the branching ratio without a spin-orbit interaction can be derived with:

$$B = B_0 - \frac{c}{2c+1} \frac{SOC}{n_h} \quad (7)$$

B_0 is the branching ratio without spin-orbit interactions $\frac{c}{2c+1}$ is a statistical value, and for d^5 , it is $\frac{2}{5}$ and n_h represent the holes in the valence shell. In the following table are all values shown^[99].

Tab. 4: Obtained branching ratio values with spin-orbit interaction (BR), terms of occupation numbers (n_{j_1} , n_{j_2}), spin-orbit expectation (SOC), branching ratio without spin-orbit interaction (B_0), and the difference of the branching ratios (ΔB) with expected uncertainties of 5 % for the presented spin-orbit expectations.

T/K	BR	statistical value	n_{j_1}	n_{j_2}	SOC	B_0	ΔB
4.5	0.80	0.60	-0.11	0.89	-3.28(16)	0.41	0.39
15	0.76	0.60	-0.29	0.71	-4.38(21)	0.24	0.53
25	0.80	0.60	-0.30	0.70	-4.50(23)	0.26	0.54

The calculated branching ratios are 0.76 and 0.80 and slightly lower than the typical values between 0.81-0.85^[100]. Here, the branching ratio for the ion trap temperature of 15 K differs somewhat from the other temperatures. The broadened absorption edge gives this at 15 K, inducing a lower intensity of the experimental spectra. From 4 K to 25 K, the resultant spin-orbit expectations show a declining trend. This also suggests that when temperatures rise, the quantity of an HS isomer increases as a result of an increase in unpaired electrons in the iron core caused by a spin-crossover event. The diminishing spin-orbit predictions are explained by the electrical distribution of the transition metal center. The ligand's strong impact should have an effect on the spin-orbit coupling. As a result, we computed electron localized field plots^[107] for all three isomers of this complex (cf. Fig. 4).

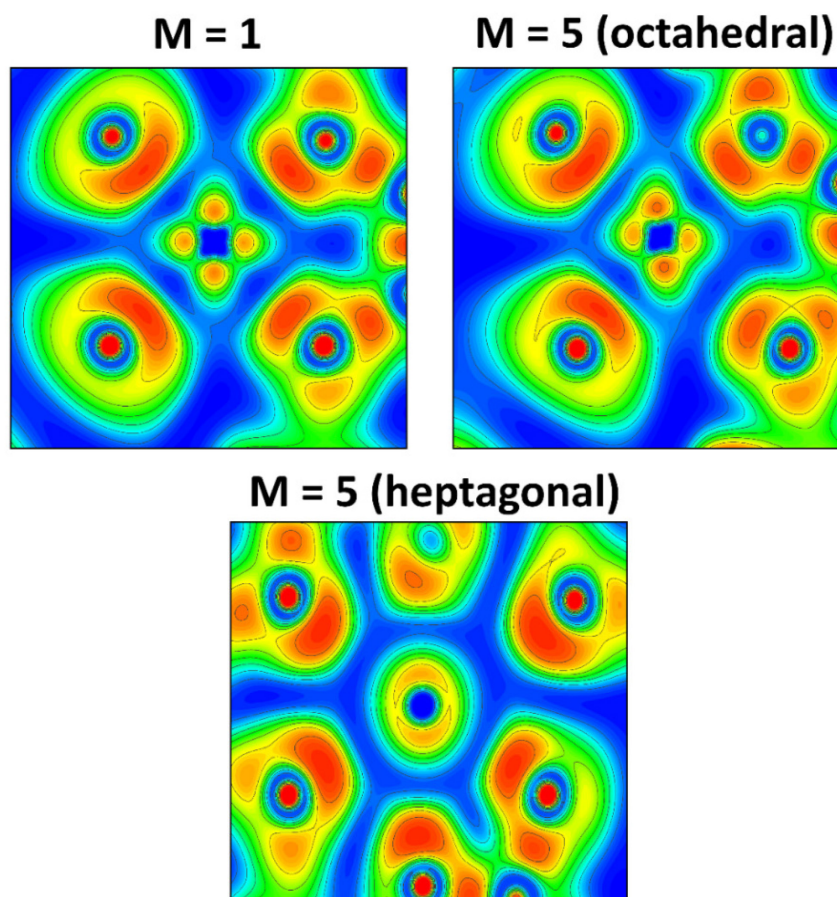


Fig. 4: Calculated ELF plots for $[\text{Fe}(\text{btpa})]^{2+}$ ($M = 1$ (octahedral), 5 (octahedral), 5 (heptagonal)). The calculation was performed at the B3LYP/cc-pVTZ (H, C, N, O) and Stuttgart ecp effective core potential (Fe) level of theory with a low spin and high spin state for the Fe center.

These graphs show that the electron distributions of the octahedrally coordinated complexes are almost identical, whereas the heptagonal coordinated complex has a more spherical distribution. This agrees well with the experimental data for a set ion trap temperature of 15 K. A more spherical electron distribution results in more free ion-like behavior than octahedrally coordinated complexes, resulting in a distinct crystal field splitting and somewhat different SOC. The octahedrally coordinated complexes reveal a more square like electron distribution, and therefore the crystal field splitting must change, resulting in various SOC for the complex. Furthermore, because the iron core is in an HS configuration, the spin and orbital magnetic values do not fluctuate significantly between 15 K and 25 K, but the expected combination of these complexes lowers the measured results.

The Differential Orbital Covalency (DOC) technique approximates the metal d character at a given temperature by determining the ligand impact on the metal ion. DOC analysis

demonstrates that the metal d character increases with increasing temperature (cf. Fig. S11)^[98, 109]. At an ion trap temperature of 4.5 K, we observe the lowest metal d character. As previously stated, a shift in a high spin configuration causes elongated bondings in the complex, resulting in weaker covalent interactions between the ligand and the metal center and the metal center acts more like a free ion. Therefore, the LS complex population is favored in colder conditions, and shorter bonding distances lead to stronger covalent interactions resulting in lower metal d character. For a set ion trap temperature of 15 K, we observe the highest metal d character. The spherical electron distribution of the heptagonal coordinated complex leads to the supposition that the metal center is less impacted than in octahedral coordination, which corresponds very well with the DOC analysis, and shows the maximum metal d character at 15 K. This supports the thesis that the temperature at 25 K is enough that the rotational modes for the free pyridine rings are active and in average, an octahedral coordinated HS complex is observed. With the XMCD technique, we cannot determine MLCT transitions from the spectral pattern, and therefore, we cannot exclude such transitions. Earlier investigations point out that MLCT transitions appear in UV/VIS investigations^[57, 75]. Such effects also can reduce the metal d character of transition metal complexes.

7.6.2 Results II: Collision Induced Dissociation (CID) and InfraRed (Multiple) Photon Dissociation (IR(M)PD)

Collision Induced Dissociation (CID)

With the above described sample solution, we recorded the mass spectra via electrospray process. The ions of interest were stored within a Paul trap. We observe one isotopic peak at $m/z = 317$ for $[\text{Fe}(\text{btpa})]^{2+}$ matching the simulated isotopic pattern. Also, the mass differences are half of the actual masses, and this points out that the complexes studied in this case are dicationic ones (cf. Fig. S12). We performed Collision Induced Dissociation (CID) breakdown curves for the complex and Electron Transfer Dissociation breakdown curves of the reduced complex (cf. Fig. 5).

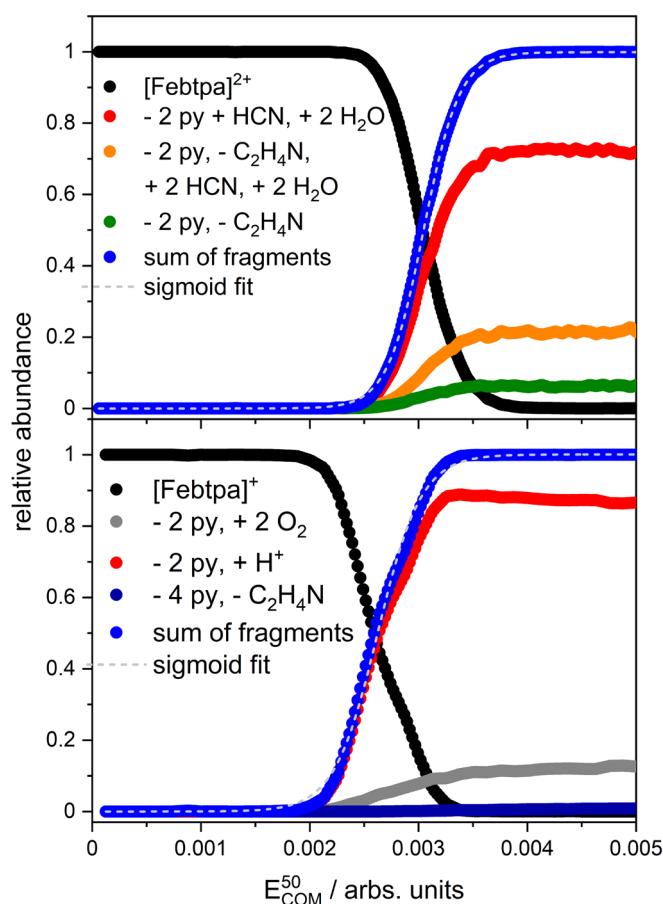


Fig. 5: CID (top) and ETD (bottom) breakdown curves of $[Fe(btppa)]^{2+}$ with their corresponding appearance curves of the associated fragments.

CID breakdown curves of isolated $[Fe(btppa)]^{2+}$ reveal as main fragment the loss of both free rotating pyridine rings in the ligand and the addition of water and hydrogen cyanide. With increasing excitation amplitudes, we monitor the loss of water, hydrogen cyanide, and two methylene groups. In the same quantity, a loss of the whole arm from the ligand, e.g. $(\text{pyridine})_2(\text{NC}_2\text{H}_4)$, is seen in this complex. The addition of water occurs because a little quantity of water is present in the ion trap and attaches to the complex. Also, the addition of hydrogen cyanide occurs from the solvent of the sample preparation for the electrospray process. The fragmentation begins with an E_{COM} value of 0.0025 arbs. units and progresses with rising CID amplitude by losing two methylene groups and two pyridine rings. At the same fragmentation amplitude, losing the complete ligand arm takes part. When a complex is reduced from a dicationic to a monocationic state using Electron Transfer Dissociation in conjunction with CID studies, the fragmentation paths and related gas phase stabilities vary significantly (cf. Fig. 5). For $[Fe(btppa)]^{+}$, we do not observe water and hydrogen cyanide addition to the complex.

Instead, we observe an addition of molecular oxygen. Losing two pyridine rings and adding two protons or molecular hydrogen represents the main fragmentation channel in this complex.

As discussed above, there is a possibility that different isomers are present as a mixture of LS and HS complexes. Therefore, we used a 1:1 solution of $[\text{Fe}(\text{btpa})]^+$ and $\text{M}(\text{OAc})_2$ ($\text{M} = \text{Mn}, \text{Cu}, \text{Zn}, \text{Pd}$) with a concentration of $\sim 10^{-4}$ mol/L as a starting point for the evidence of a heptagonal coordinated complex in this solution. Only in this geometry may the $\text{M}(\text{OAc})_2$ molecules coordinate with two pyridine ligands of the complex, resulting in the second metal center with octahedral coordination. We observe a coordination for every metal acetate to the complex, which hints the heptagonal coordinated HS complex. The recorded CID breakdown curves reveal an almost similar fragmentation pattern of these complexes (cf. Fig. S13). The main fragmentation channel in this series of complexes is the loss of one acetate or acetic acid ligand. Also, we observe an exchange from the Fe^{2+} ion with Copper and Palladium by using these metal acetates. All complexes have the general structure of $[\text{M}_1(\text{btpa})\text{M}_2(\text{OAc})_2]^{2+}$ ($\text{M}_1 = \text{Fe}, \text{Cu}, \text{Pd}$; $\text{M}_2 = \text{Mn}, \text{Cu}, \text{Zn}, \text{Pd}$). The free pyridine rings in this geometry act as tweezers for the coordination of the metal acetates. The pyridine rings are oriented in opposing orientations in octahedral geometry, therefore metal acetate coordination would not result in octahedral coordination of the metal in the metal acetate.

To determine the stabilities of the different isomers, we performed calculations of weak interactions in this series of complexes. We performed Electron Localized Field (ELF), Different Overlap Region Interaction (DORI), and Non covalent Interaction (NCI) calculations^[99] (cf. Fig. S14). The ELF plots reveal the covalent bonding situation in these complex geometries and do not feature any unusual bonding situation. The NCI plots instead represent weak interactions, e.g., van der Waals interactions. We observe strong non covalent interactions for the heptagonal coordinated HS complex, explaining its stability for the heptagonal coordination. The octahedrally coordinated complex reveals strong van der Waals interactions, almost similar to the octahedral LS complex. The DORI plots point out a sensitive interplay between the covalent and non covalent interactions, meaning the better this interplay, the more stabilized these complexes are.

InfraRed (Multiple) Photon Dissociation (IR(M)PD)

The recorded IR(M)PD spectra reveal several vibrational modes in the area around 1500-1700 cm^{-1} (cf. Fig. 6). In comparison to the calculated IR spectra, the experimental IR(M)PD spectrum contains features from more than one isomer. The most prominent bands at around 1600 cm^{-1} in combination with the calculations features all three isomers. The heptagonal coordinated complex exhibits a slight energy shift to higher energies. Both octahedrally coordinated complexes show almost similar vibrational modes at around 1600 cm^{-1} but a minor splitting at the band at around 1610 cm^{-1} . We assume that all three isomers are present in the recorded spectrum at room temperature.

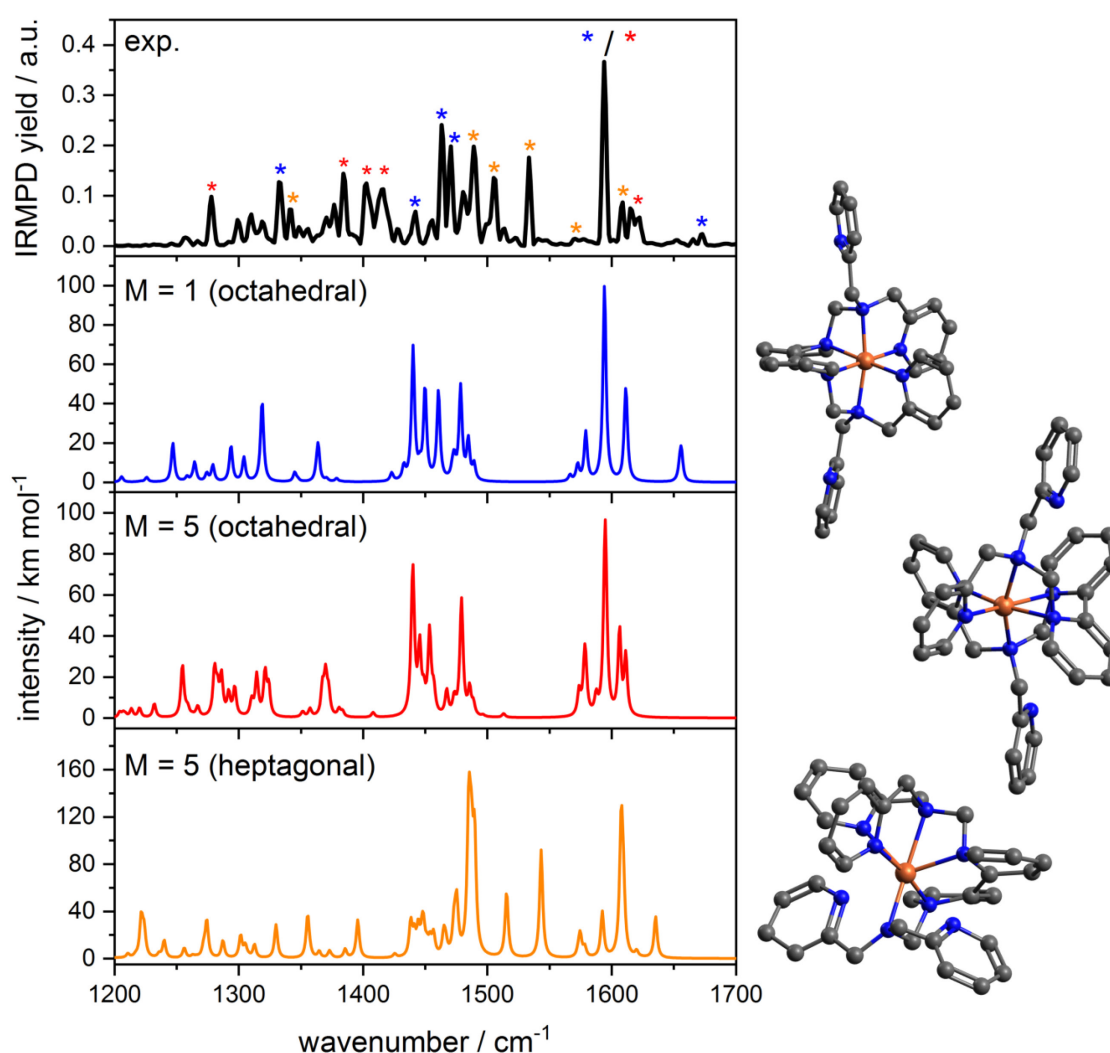


Fig. 6: IR(M)PD spectra (black) in comparison with quantum chemistry calculation of $[\text{Fe}(\text{btpa})]^{2+}$. The calculations were performed with Gaussian 09 at the B3LYP/cc-pVTZ (H, C, N, O) and Stuttgart ecp effective core potential (Fe) level of theory. The calculated spectra are scaled with a factor of 0.977.

IR(M)PD and DFT spectra of [Fe(btpa)]²⁺ for M = 1 in octahedral coordination

The experimental IR(M)PD spectrum compared to the linear absorption spectrum of the octahedral LS complex reveals the presence of this complex in the LS/HS mixture (cf. Fig. S15). At 1673 cm⁻¹, we monitor a small vibrational band that belongs to the C-C stretching modes combined with the bending modes from the hydrogen atoms of the bipyrimidyl ring in this complex. This vibrational mode is only predicted with the octahedral LS complex and is not observed in any of the other calculated isomers. The vibrational mode at 1593 cm⁻¹ belongs to the symmetric stretching modes of the free pyridine rings. The bending modes of the methylene groups are represented by the vibrational band at 1461 cm⁻¹. At 1450 cm⁻¹, there is a combination band from the bending mode of the methylene groups to the metal center, as well as the bending modes of the coordinated pyridine rings. A combination mode of the bending mode from the methylene groups and the free pyridine in ligand appears at 1440 cm⁻¹. The vibrational mode at 1319 cm⁻¹ could be associated with the LS spin complex. It occurs from a combination of the bending modes of the accessible and coordinated bending modes of the pyridine rings in the ligand. The calculated spectrum may be distorted due to high anharmonicity, which is not taken into account in the calculations.

IR(M)PD and DFT spectra of [Fe(btpa)]²⁺ for M = 5 in octahedral coordination

The comparison of the experimental IR(M)PD spectrum to the calculated IR spectrum of the octahedral coordinated HS complex reveals features unique to the octahedral coordinated HS complex (cf. Fig. S16). The doubly splitted band 1622/1616 cm⁻¹ belongs to the symmetric stretching modes of the coordinated pyridine rings to the metal center. The band 1594 cm⁻¹ belongs to the symmetric stretching mode of the free pyridine. The bands at 1415 cm⁻¹ and 1401 cm⁻¹, as in the low spin complex, are combination bands of the bending modes of the methylene groups and the coordinated pyridine bending modes. The bending modes of the methylene groups combined with the bending modes of the free pyridine ring give rise to the vibrational band at 1384 cm⁻¹. The band at 1278 cm⁻¹ is a combination mode of methylene's asymmetric bending modes and coordinated pyridine bending modes.

IR(M)PD and DFT spectra of [Fe(btpa)]²⁺ for M = 5 in heptagonal coordination

The change in the geometry has to lead to a significant change in the vibrational modes. As a result, the seven folded HS isomers are more easily observed than the octahedral HS complex. We can partially attribute the experimental spectra to a seven-folded HS complex by comparing the experimental spectrum with DFT calculations (cf. Fig. S17). At 1607 cm⁻¹, the vibrational modes represent the symmetric stretching modes of two coordinated pyridine rings in this complex. The band at 1533 cm⁻¹ belongs to the bipyrimidylring's symmetric C-C stretching modes, while the band at 1505 cm⁻¹ belongs to the asymmetric C-C stretching modes. The broad band at 1489 cm⁻¹ is a combination band of the bending mode of one methylene group, the bending mode of one coordinated pyridine, and an asymmetric stretching mode of one part of the bipyrimidylring.

In gas phase, the experimental IR(M)PD spectrum appears to represent all three assumed isomers. We observe a distinct vibrational mode for each isomer. Interpreting the area beneath 1500 cm⁻¹ cannot be precisely determined because of the high anharmonicity in the vibrational combination bands of the complex. The vibrational modes at 1533 cm⁻¹ and 1505 cm⁻¹ determine the heptagonal coordinated complex. The calculated vibrational spectra of the octahedral LS and heptagonal HS coordinated complexes predict two bands at 1656 cm⁻¹ for the LS complex and one at 1635 cm⁻¹ for the heptagonal coordinated HS complex. We assign the experimental band at 1672 cm⁻¹ to the LS complex by cause of more negligible aberration than the HS complex. Because of minor differences in geometry, we did not have as many hints to determine the octahedral coordinated HS complex as we did for the heptagonal coordinated complex. The predicted band at 1605 cm⁻¹ with a minor splitting at 1611 cm⁻¹ is the most significant hint from the octahedral coordinated HS complex. The IR(M)PD spectra at 1616 cm⁻¹ and 1622 cm⁻¹ show a similar pattern, which we attribute to the octahedrally coordinated complex. Furthermore, the calculated spectra do not predict an LS complex vibrational mode at 1672 cm⁻¹. The blue shift in the experimental IR(M)PD spectra of the various spin and geometrical isomers follows the same trend as the calculated shifts (cf. Fig. S18). Considering an almost identical structure motif, no shift is assumed for the spin isomers in octahedral coordination. The pyridine iron bonding becomes more stable when the geometry is changed to a heptagonal coordinated system. As a result, more energy is required to establish a vibrational mode that occurs in a higher blue shifted band, as seen in the other isomers.

Theoretical determination for the isomerization of the different isomers

There are two possibilities for the formation of the heptagonal coordinated structure (cf. Fig. 7). One possibility is to switch from an octahedral LS complex to an octahedral high spin complex, resulting in bipyrimidylring distortion and longer bonding distances. The elongation of bonding distances may result in the formation of a new coordination point, and heptagonal coordination is established by rotating the free pyridine rings towards the metal center. Another possibility is that the spin-crossover occurs via a direct transition from the octahedral LS complex to the heptagonal coordinated HS complex by rotating the pyridine rings towards the iron center.

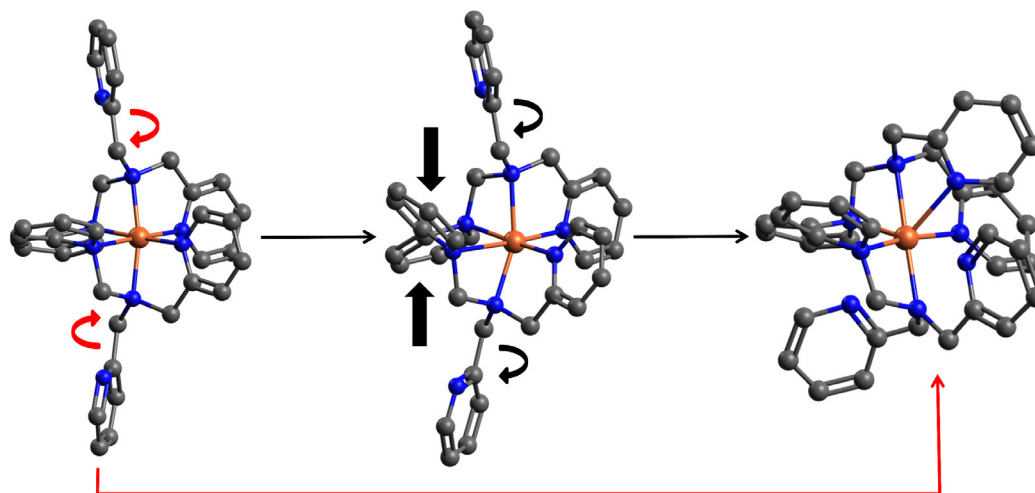


Fig. 7: Possible pathways for the isomerization from the low spin to the high spin and geometrical change in the complex with the structure $[\text{Fe}(\text{btpa})]^{2+}$.

The calculated minimum structures reveal nearly identical relative energies associated with the minimum structure (cf. Tab. S1). According to the calculations, the octahedral LS and the heptagonal coordinated HS complex are the preferred minimum structures. The octahedral HS complex has a slightly higher energy of 9 kJ/mol. As a result, excluding this isomer is impossible because, on the other hand, the relative energy of the complex is close to the minimum structures and the experimental IR(M)PD spectra hints at features of the octahedral HS complex. We performed transition state calculations to determine the isomerization between the octahedral complex and the heptagonal coordinated complex. We calculated the free Gibbs energies, as well as the corresponding entropies and enthalpies, for each isomer (cf. Tab. 5, cf. Fig. S20).

Tab. 5: Calculated free Gibbs energies, free enthalpies, and entropies for different isomers of $[\text{Fe}(\text{btpa})]^{2+}$. The calculations were performed with Gaussian 09 at the B3LYP/cc-pVTZ (H, C, N, O) and Stuttgart ecp effective core potential (Fe) level of theory.

M	$\Delta G/\text{kJ/mol}$	$\Delta H/\text{kJ/mol}$	$\Delta S/\text{J/mol K}$	$\Delta\Delta G/\text{kJ/mol}$
1 (octahedral)	45.04	43.08	-0.01	0.00
5 (octahedral)	128.97	127.67	0.00	73.80
5 (heptagonal)	0.00	0.00	0.00	-50.60
TS (M1-M5)	344.93	344.36	0.00	299.88

The free Gibbs energy differences indicate a reaction coordinate from the octahedral LS complex to the heptagonal coordinated HS complex. For the determination of the possible pathway, we set the relative energy for the LS complex zero. Because of the relative energy of 300 kJ/mol, we rule out the direct isomerization pathway from the octahedrally coordinated complex to the heptagonal coordinated complex. The energy barrier required to perform a geometrical change and a spin configuration change simultaneously for a direct isomerization is far too high. As a result, an octahedral coordinated HS complex must be present in order to perform the geometrical change to a heptagonal coordinated complex. The octahedral HS complex has a destabilization of 9 kJ/mol than the other two isomers. We assume that the isomerization from an octahedral complex to a heptagonal coordinated complex occurs in two steps. The first step is the change from an LS state to an HS state in same geometry by thermal effects and in the second step the pyridine rings rotate towards the metal center to establish an additional coordination to iron center.

7.6.3 Results III: UV/VIS and XMCD correlation

The magnetism in spin-crossover complexes depends extremely on the occupation in the d orbitals of the metal center. As a result, investigations of the electronic ground state in such complexes appear necessary in order to better visualize the spin-crossover process. MLCT transitions of such complexes appear to be good predictors of spin-crossover processes^[55, 56, 108, 110, 111]. Several bands are visible in the UV/VIS data, but the MLCT transitions at 516 and 560 nm are the most interesting. Wolny et al. assumed that the 560 nm absorption band belonged to the heptagonal coordinated HS complex^[55, 56].

They also considering a change in intensity by increasing the temperature, implying a change in spin states. These bands are very weak, indicating that these MLCT transitions are spin forbidden.

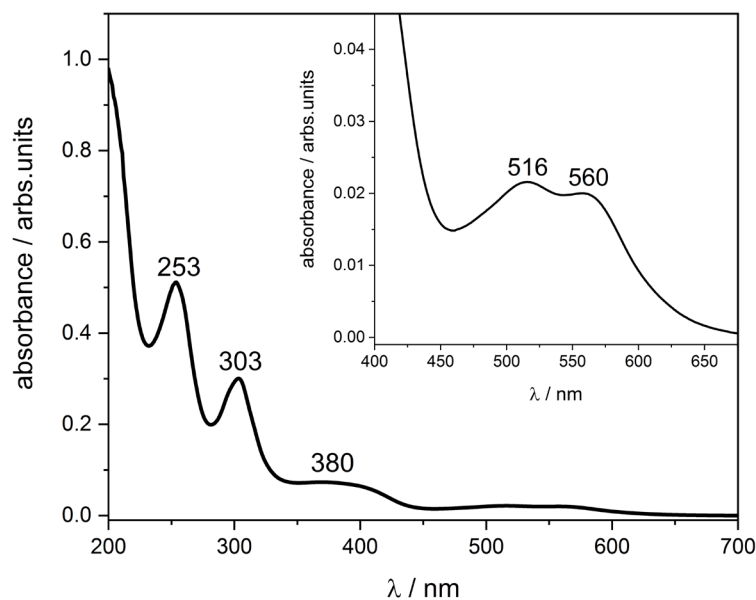


Fig. 8: Normalized UV/VIS spectra of $[\text{Fe}(\text{btpa})]^{2+}$ ($c \sim 1 \cdot 10^{-6}$ mol/L) solved in acetonitrile at 298 K.

In combination with the XA spectra, we gain better visualization of the properties of the complex. A correlation between the various approaches is also possible. The first derivation of the XA spectra reveals an energy shift for a set ion trap temperature of 15 K. Comparing the derived XA spectra with the UV/VIS spectrum, we observe two different Absorption maxima in both spectra (cf. Fig. S21). Knowing that the complex has two different geometrical isomers, we assume that one absorption band in the UV/VIS spectrum belongs to one isomer with octahedral coordination and one to the complex with heptagonal coordination.

As previously stated, the XA spectra exhibit different crystal field splittings at 15 K ion trap temperature than the other XA spectra with the same ion trap temperature. The Tanabe Sugano diagram for a d6 HS metal with a normalization of the experimental crystal field splitting and the absorption energies of the UV/VIS spectrum by the Racah parameter B for a Fe^{2+} ion^[112] can be used to perform the correlation between the XA spectra and the UV/VIS spectrum (cf. Fig. S22).

The approximation in the Tanabe Sugano diagram leads to excitation from a $^1A_{1g}$ ground state to a $^1T_{1g}$ excited state for each crystal field splitting of the complex by given temperature. The approximated UV/VIS absorption energies vary slightly from the experimental ones (cf. Tab. 6).

Tab. 6: Normalized excitation energies, excitation energies from the Tanabe Sugano diagram, and normalized excitation energies, excitation energies from the experimental UV/VIS spectrum of $[\text{Fe}(\text{btpa})]^{2+}$.

	E/B(TS)	E/cm ⁻¹ (TS)	E/nm(TS)	E/B(exp)	E/cm ⁻¹ (exp)	E/nm(exp)
octahedral	17.90	18168	550	17.59	17857	560
heptagonal	19.60	19894	502	19.09	19380	516

The approximated absorption energies to corresponding crystal field energies from the Tanabe-Sugano diagram fit the experimental UV/VIS spectrum well. This highlights the presence of two distinct geometrical isomers in all spectroscopic approaches. We are unable to determine whether an octahedral coordinated LS or HS complex is present. Therefore, we performed TD-DFT calculations of the complex to obtain the linear absorption spectrum of the different isomers. In comparison to the experimental UV/VIS spectrum, both absorption bands at 400-700 nm belong to two different HS complexes (cf. Fig. S11). The octahedral coordinated HS complex predicts an absorption band at 516 nm, while the heptagonal coordinated complex predicts a band at 560 nm and the LS complex does not feature an absorption band in this area. Because of the reduced magnetic values and IR(M)PD spectrum vibrational modes, the LS complex must be present. Because there are no unpaired electrons in the spin configuration, the LS complex exhibits no absorption in this region, resulting in the complex MLCT transitions.

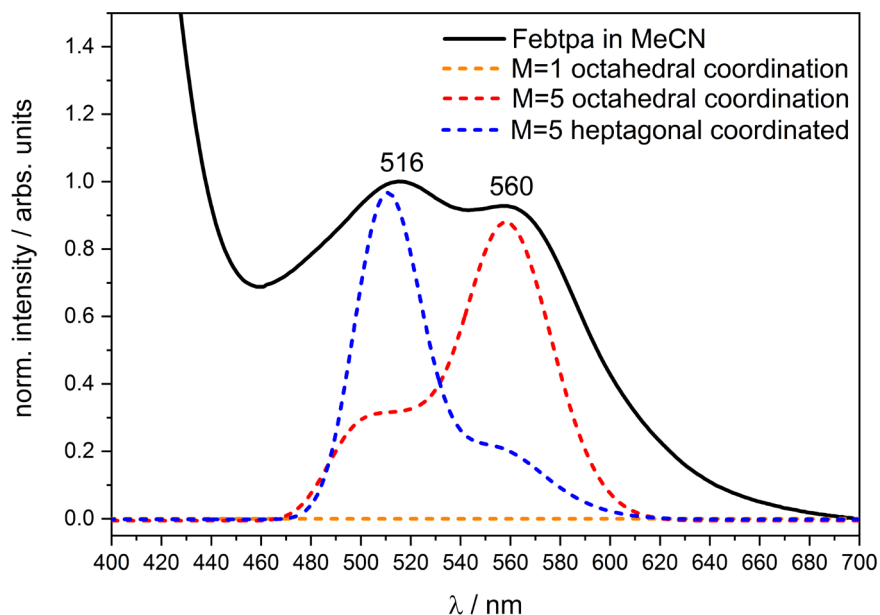


Fig. 9: UV/VIS spectrum of $[\text{Fe}(\text{btpa})]^{2+}$ ($T = 298 \text{ K}$) in comparison with TD-DFT calculated UV/VIS spectra of $[\text{Fe}(\text{btpa})]^{2+}$ with different multiplicities and geometrical structures. The calculations were performed with Gaussian 09 at the unrestricted B3LYP/cc-pVTZ level of theory.

Because they are spin forbidden, the absorption band in this region is very weak, but this transition occurs from a HOMO to a LUMO orbital in both isomers (cf. Fig. S23). The HOMO LUMO gap is higher in the octahedrally coordinated complex (-2.4 eV) than in the heptagonal coordinated complex (-1.3 eV). The weaker MLCT transitions are primarily responsible for the shift to higher energies in the heptagonal coordinated complex. The electron density is more localized onto the metal center in the heptagonal coordinated complex than in the octahedrally coordinated complex, resulting in higher energy to perform such transitions. The orbital energies of the d orbitals in the various isomers show a decrease from an octahedral complex to a heptagonal coordinated complex (cf. Fig. S24). The energies of the d_{yz} orbitals decrease as the multiplicity changes, resulting in an intense mixing of the orbitals and a better overlap of the metal to the ligand. The LS complex reveals a slightly higher gap between the e_g and t_{2g} orbitals than the corresponding HS complex and the reorganization of the complex leads to a higher stabilization in the energies. The energies between the e_g and t_{2g} orbitals are lower in the heptagonal coordinated complex than in the octahedral complex, indicating that the d orbital contraction in the seven folded complex results in a more straightforward spin-crossover process.

With the different spectroscopic approaches, we are able to determine the magnetic behavior, structural and electronic properties of the complex. We also observe the same shifts in all spectroscopic approaches (cf. Fig. S25). The highest shift in the energy occurs in the heptagonal coordinated complex. The shift in the XA spectra also causes a shift in the IR(M)PD and UV/VIS spectra. The change in geometry causes a change in the electronic ground state, resulting in different vibrational modes with a higher possibility of a spin-crossover process. Because the magnetic moments did not change from 15 K to 25 K in the ion trap, the spin-crossover process occurs between 4.5 K and 15 K. Only a change in the geometry can occur at higher temperatures.

7.7 Conclusions

We present the intrinsic spin and orbital magnetic moments of the spin-crossover with the structure $[\text{Fe}(\text{btpa})]^{2+}$. The recorded spectra on the Fe $L_{3,2}$ absorption edges show decreasing dichroic effects by switching from LS to HS. At all temperatures, the experimental spin and orbital magnetic moments show a mixture of LS and HS. We could approximate the relation between LS and HS at every temperature.

The approximation of the ion temperature by fitting to a Brillouin function reveals significantly warmer ions than the applied ion trap temperature. Also, an approximation of the isomer composition points out a mixture at every temperature with decreasing LS amount by increasing the ion trap temperature.

The determination of crystal field splittings suggests two distinct geometries for the complex in different spin states. The calculated projected density states spectra for the different isomers show good agreement with the experimental XA spectra, indicating that a mixture of these different isomers must be present.

Compared with electron localized field plots, Branching ratio analysis brought a deeper insight into the spin-crossover complex. We observe a decreasing trend for the spin-orbit expectations. The ELF plots point out an almost similar distortion of the electron density for the Fe^{2+} ion in octahedral coordination and a nearly spherical electron distribution for the heptagonal coordinated system. The highest metal d character appears at a temperature of 15 K, according to differential orbital covalency analysis. Compared to the ELF plots, this only

occurs when a heptagonal coordinated complex is present, where the Fe^{2+} ion acts more like a free ion than in the octahedrally coordinated complexes.

Collision Induced Dissociation breakdown curves reveal characteristic fragmentation channels for $[\text{Fe}(\text{btpa})]^{2+}$. The reduction of the complex via ETD reveals different fragmentation patterns and completely different additions to the complex. ELF, DORI, and NCI plots show strong non covalent interactions, which explain the high stability of the complex. The heptagonal coordinated complex also has the highest non-covalent interactions. The addition of different metal acetates is only possible to $[\text{Fe}(\text{btpa})]^{2+}$. The first hint is that the complex has an isomer in heptagonal coordination because the acetates' transition metals prefer an octahedral configuration. The addition of Copper acetate and palladium acetate leads to an exchange of the iron center with the corresponding metal. Furthermore, the fragmentation channels are nearly identical, differing only by one hydrogen atom. The obtained gas phase stabilities are lowered for the complexes with the structure $[\text{Fe}(\text{btpa})\text{M}(\text{OAc})_2]^{2+}$ as for the bare complex. The gas phase stabilities for these complexes that reveal a metal exchange are slightly higher than the other metal acetate complexes but lower than the bare complex.

The IR(M)PD spectrum of $[\text{Fe}(\text{btpa})]^{2+}$ compared to quantum chemical calculations reveals that three different isomers are present in the gas phase. The most crucial area between 1500 cm^{-1} and 1700 cm^{-1} gives the best hint for two octahedral LS/HS complexes and one heptagonal coordinated HS complex. The spectra also reveal vibrational modes for free rotating pyridine ligands as well as different vibrational bands for coordinated pyridine rings that only appear in heptagonal coordination. The calculation for the LS complex predicts a band at 1673 cm^{-1} , which also appears in the experimental IR(M)PD spectrum.

The possible pathway from an LS configuration to the heptagonal coordinated HS complex is rearranged from the octahedral coordinated LS complex over an octahedral HS complex to the heptagonal coordinated HS complex. We can exclude the direct conversation because the transition state with a change in the spin configuration and the geometry would lead to an energy barrier of 300 kJ/mol .

The correlation between XA and UV/VIS spectra reveals the same trending in the absorption spectra shift. The obtained crystal field splittings have a direct correlation with the absorption energies of the UV/VIS spectrum, and these values are normalized with the Racah parameter B. The UV/VIS spectrum reveals two spin forbidden MLCT transitions belonging to two different HS isomers in different geometries. These transitions belong to HOMO-LUMO+1 transitions in every isomer but with varying gaps of energy. The orbital energies of the d-orbitals reveal an intense mixing for these orbitals in various geometries and spin states.

The energy shifts for all the different spectroscopic approaches reveal the same trends for the complex. The highest shift occurs with the heptagonal coordinated complex in all spectroscopic investigations. The shift in the XA spectra is given by the change of the crystal field splittings, leading to a higher shift in the vibrational modes due to the structure's change, which changes the electronic energies.

In summary, we have shown that gas phase XMCD, IR(M)PD, and UV/VIS investigations add valuable additional insight into the fascinating molecular properties of molecular switches called “spin-crossover” complexes.

7.8 Acknowledgment

The German research foundation DFG supported this work within the transregional collaborative research center SFB/TRR 88 “Cooperative effects in homo and heterometallic complexes” (3MET) and by the state research center OPTIMAS.

7.9 References

- [1] A. Earnshaw, P. C. Hewlett, E. A. King, and L. F. Larkworthy, Transition metal–Schiff's base complexes. Part III. The magnetic properties of some oxygen-carrying cobalt(II) complexes, *Journal of the Chemical Society A: Inorganic, Physical, Theoretical*, 241-246, 1968.
- [2] O. Kahn, Dinuclear Complexes with Predictable Magnetic Properties, *Angew. Chem. Int. Ed.*, 24, 834-850, 1985.
- [3] J. Owen, and J. H. M. Thornley, Covalent bonding and magnetic properties of transition metal ions, *Rep. Prog. Phys.*, 29, 675-728, 1966.
- [4] Y. Yang, L. Xu, G. Gao, F. Li, Y. Qiu, X. Qu, and H. Liu, Transition-Metal (MnII and CoII) Complexes with the Heteropolymolybdate Fragment [AsVMo9O33]7-: Crystal Structures, Electrochemical and Magnetic Properties, *Eur. J. Inorg. Chem.*, 2007, 2500-2505, 2007.
- [5] W. Zhang, S. Bruda, C. P. Landee, J. L. Parent, and M. M. Turnbull, Structures and magnetic properties of transition metal complexes of 1,3,5-benzenetricarboxylic acid, *Inorg. Chim. Acta*, 342, 193-201, 2003.
- [6] S. Di Bella, Second-order nonlinear optical properties of transition metal complexes, *Chem. Soc. Rev.*, 30, 355-366, 2001.

- [7] V. Guerschais, L. Ordonneau, and H. Le Bozec, Recent developments in the field of metal complexes containing photochromic ligands: Modulation of linear and nonlinear optical properties, *Coord. Chem. Rev.*, 254, 2533-2545, 2010.
- [8] O. Maury, L. Viau, K. Sénéchal, B. Corre, J.-P. Guégan, T. Renouard, I. Ledoux, J. Zyss, and H. Le Bozec, Synthesis, Linear, and Quadratic-Nonlinear Optical Properties of Octupolar D3 and D2d Bipyridyl Metal Complexes, *Chemistry – A European Journal*, 10, 4454-4466, 2004.
- [9] J. L. Reddinger, and J. R. Reynolds, Tunable Redox and Optical Properties Using Transition Metal-Complexed Polythiophenes, *Macromolecules*, 30, 673-675, 1997.
- [10] H. Brunner, T. Zwack, M. Zabel, W. Beck, and A. Böhm, Optically Active Transition Metal Complexes. 130.1 Synthesis, Crystal Structures, and Catalytic Properties of Chiral-at-Metal (η^6 -Arene)ruthenium(II) and (η^6 -Arene)osmium(II) Half-Sandwich Complexes. Crystallization of Pure Diastereomers versus Diastereomer Mixtures in a 1:1 Ratio, *Organometallics*, 22, 1741-1750, 2003.
- [11] A. Hayashi, M. Okazaki, F. Ozawa, and R. Tanaka, Synthesis, Structures, and Catalytic Properties of Late-Transition-Metal 2,6-Bis(2-phosphaethenyl)pyridine Complexes, *Organometallics*, 26, 5246-5249, 2007.
- [12] C. Jin, W. Fan, Y. Jia, B. Fan, J. Ma, and R. Li, Encapsulation of transition metal tetrahydro-Schiff base complexes in zeolite Y and their catalytic properties for the oxidation of cycloalkanes, *J. Mol. Catal. A: Chem.*, 249, 23-30, 2006.
- [13] W. Orellana, Catalytic Properties of Transition Metal–N4 Moieties in Graphene for the Oxygen Reduction Reaction: Evidence of Spin-Dependent Mechanisms, *J. Phys. Chem. C*, 117, 9812-9818, 2013.
- [14] C. Xu, Y. Feng, L.-R. Wang, W.-P. Ma, Y.-M. He, and Q.-H. Fan, Development of Quinoline-Derived Chiral Diaminocarbene Ligands and Their Transition Metal Complexes: Synthesis, Structural Characterization, and Catalytic Properties, *Organometallics*, 39, 1945-1960, 2020.
- [15] H.-J. Krüger, Spin transition in octahedral metal complexes containing tetraazamacrocyclic ligands, *Coord. Chem. Rev.*, 253, 2450-2459, 2009.
- [16] J.-F. Létard, P. Guionneau, and L. Goux-Capes, "Towards Spin Crossover Applications," *Spin Crossover in Transition Metal Compounds III*, P. Gülich and H. A. Goodwin, eds., pp. 221-249, Berlin, Heidelberg: Springer Berlin Heidelberg, 2004.
- [17] O. Kahn, and J. Launay, MOLECULAR BISTABILITY. AN OVERVIEW, *Chemtronics*, 3, 140-151, 1988.
- [18] G. Aromí, D. Aguilà, P. Gamez, F. Luis, and O. Roubeau, Design of magnetic coordination complexes for quantum computing, *Chem. Soc. Rev.*, 41, 537-546, 2012.
- [19] J. Ferrando-Soria, Samantha A. Magee, A. Chiesa, S. Carretta, P. Santini, Iñigo J. Vitorica-Yrezabal, F. Tuna, George F. S. Whitehead, S. Sproules, Kyle M. Lancaster, A.-L. Barra, Grigore A. Timco, Eric J. L. McInnes, and Richard E. P. Winpenny, Switchable Interaction in Molecular Double Qubits, *Chem*, 1, 727-752, 2016.
- [20] M. N. Leuenberger, and D. Loss, Quantum computing in molecular magnets, *Natur*, 410, 789-793, 2001.
- [21] T. N. Nguyen, W. Wernsdorfer, M. Shiddiq, K. A. Abboud, S. Hill, and G. Christou, Supramolecular aggregates of single-molecule magnets: exchange-biased quantum tunneling of magnetization in a rectangular [Mn₃]₄ tetramer, *Chemical Science*, 7, 1156-1173, 2016.
- [22] M. Trif, F. Troiani, D. Stepanenko, and D. Loss, Spin-Electric Coupling in Molecular Magnets, *Phys. Rev. Lett.*, 101, 217201, 2008.
- [23] J. P. S. Walsh, S. B. Meadows, A. Ghirri, F. Moro, M. Jennings, W. F. Smith, D. M. Graham, T. Kihara, H. Nojiri, I. J. Vitorica-Yrezabal, G. A. Timco, D. Collison, E. J. L. McInnes, and R. E. P. Winpenny, Electronic Structure of a Mixed-Metal Fluoride-Centered Triangle Complex: A Potential Qubit Component, *Inorg. Chem.*, 54, 12019-12026, 2015.
- [24] T. Cauchy, E. Ruiz, and S. Alvarez, Magnetostructural Correlations in Polynuclear Complexes: The Fe₄ Butterflies, *J. Am. Chem. Soc.*, 128, 15722-15727, 2006.
- [25] D. Gatteschi, and R. Sessoli, Quantum Tunneling of Magnetization and Related Phenomena in Molecular Materials, *Angew. Chem. Int. Ed.*, 42, 268-297, 2003.
- [26] S. M. Gorun, and S. J. Lippard, Magnetostructural correlations in magnetically coupled (μ -oxo)diiron(III) complexes, *Inorg. Chem.*, 30, 1625-1630, 1991.
- [27] J. M. Clemente-Juan, E. Coronado, A. Forment-Aliaga, A. Gaita-Ariño, C. Giménez-Saiz, F. M. Romero, W. Wernsdorfer, R. Biagi, and V. Corradini, Electronic and Magnetic Study of Polycationic Mn₁₂ Single-Molecule Magnets with a Ground Spin State S = 11, *Inorg. Chem.*, 49, 386-396, 2010.
- [28] A. Dey, S. Das, V. Mereacre, A. K. Powell, and V. Chandrasekhar, Butterfly-shaped, heterometallic, hexanuclear, [FeII₂LnIII₄] (LnIII = GdIII, TbIII, DyIII and HoIII) Complexes: Syntheses, structure and magnetism, *Inorg. Chim. Acta*, 486, 458-467, 2019.

- [29] J. Dreiser, K. S. Pedersen, A. Schnegg, K. Holldack, J. Nehr Korn, M. Sigrist, P. Tregenna-Piggott, H. Mutka, H. Weihe, V. S. Mironov, J. Bendix, and O. Waldmann, Three-Axis Anisotropic Exchange Coupling in the Single-Molecule Magnets $\text{NEt}_4[\text{MnIII}_2(5\text{-Brsalen})_2(\text{MeOH})_2\text{MIII}(\text{CN})_6]$ ($\text{M}=\text{Ru}, \text{Os}$), *Chemistry – A European Journal*, 19, 3693-3701, 2013.
- [30] P. Hahn, S. Ullmann, J. Klose, Y. Peng, A. K. Powell, and B. Kersting, Dinuclear Tb and Dy complexes supported by hybrid Schiff-base/calixarene ligands: synthesis, structures and magnetic properties, *Dalt. Trans.*, 2020.
- [31] T. Lis, Preparation, structure, and magnetic properties of a dodecanuclear mixed-valence manganese carboxylate, *AcCrB*, 36, 2042-2046, 1980.
- [32] J.-W. Lu, Y.-H. Huang, S.-I. Lo, and H.-H. Wei, New μ -oxo-bridged tetranuclear Cu(II) complex with Schiff-base ligand: Synthesis, crystal structure and magnetic properties, *Inorg. Chem. Commun.*, 10, 1210-1213, 2007.
- [33] R. Modak, Y. Sikdar, A. E. Thuijs, G. Christou, and S. Goswami, CoII_4 , CoII_7 , and a Series of $\text{CoII}_2\text{LnIII}$ ($\text{LnIII} = \text{NdIII}, \text{SmIII}, \text{GdIII}, \text{TbIII}, \text{DyIII}$) Coordination Clusters: Search for Single Molecule Magnets, *Inorg. Chem.*, 55, 10192-10202, 2016.
- [34] A. V. Pali, S. M. Ostrovsky, S. I. Klokishner, B. S. Tsukerblat, C. P. Berlinguette, K. R. Dunbar, and J. R. Galán-Mascarós, Role of the Orbitally Degenerate Mn(III) Ions in the Single-Molecule Magnet Behavior of the Cyanide Cluster $\{[\text{MnII}(\text{tmphen})_2]_3[\text{MnIII}(\text{CN})_6]_2\}$ ($\text{tmphen} = 3,4,7,8\text{-tetramethyl-1,10-phenanthroline}$), *J. Am. Chem. Soc.*, 126, 16860-16867, 2004.
- [35] Y. Garcia, P. J. van Koningsbruggen, E. Codjovi, R. Lapouyade, O. Kahn, and L. Rabardel, Non-classical FeII spin-crossover behaviour leading to an unprecedented extremely large apparent thermal hysteresis of 270 K: application for displays, *J. Mater. Chem.*, 7, 857-858, 1997.
- [36] P. Gütllich, Y. Garcia, and H. A. Goodwin, Spin crossover phenomena in Fe(I) complexes, *Chem. Soc. Rev.*, 29, 419-427, 2000.
- [37] P. Gütllich, H. A. Goodwin, and Y. Garcia, *Spin Crossover in Transition Metal Compounds I*: Springer, 2004.
- [38] V. Niel, J. M. Martínez-Agudo, M. C. Muñoz, A. B. Gaspar, and J. A. Real, Cooperative Spin Crossover Behavior in Cyanide-Bridged Fe(II)–M(II) Bimetallic 3D Hofmann-like Networks ($\text{M} = \text{Ni}, \text{Pd}, \text{and Pt}$), *Inorg. Chem.*, 40, 3838-3839, 2001.
- [39] M. Schmitz, M. Seibel, H. Kelm, S. Demeshko, F. Meyer, and H.-J. Krüger, How Does a Coordinated Radical Ligand Affect the Spin Crossover Properties in an Octahedral Iron(II) Complex?, *Angew. Chem. Int. Ed.*, 53, 5988-5992, 2014.
- [40] B. Kintzel, M. Böhme, J. Liu, A. Burkhardt, J. Mrozek, A. Buchholz, A. Ardavan, and W. Plass, Molecular electronic spin qubits from a spin-frustrated trinuclear copper complex, *Chem. Commun.*, 54, 12934-12937, 2018.
- [41] D. Maspoch, D. Ruiz-Molina, K. Wurst, C. Rovira, and J. Veciana, A very bulky carboxylic perchlorotriphenylmethyl radical as a novel ligand for transition metal complexes. A new spin frustrated metal system, *Chem. Commun.*, 2958-2959, 2002.
- [42] R. Shaw, R. H. Laye, L. F. Jones, D. M. Low, C. Talbot-Eckelaers, Q. Wei, C. J. Milios, S. Teat, M. Helliwell, J. Raftery, M. Evangelisti, M. Affronte, D. Collison, E. K. Brechin, and E. J. L. McInnes, 1,2,3-Triazolate-Bridged Tetradecametallic Transition Metal Clusters $[\text{M}_{14}(\text{L})_6\text{O}_6(\text{OMe})_{18}\text{X}_6]$ ($\text{M} = \text{FeIII}, \text{CrIII}$ and VIII/IV) and Related Compounds: Ground-State Spins Ranging from $S = 0$ to $S = 25$ and Spin-Enhanced Magnetocaloric Effect, *Inorg. Chem.*, 46, 4968-4978, 2007.
- [43] P. Zhang, and P. J. Sadler, Redox-Active Metal Complexes for Anticancer Therapy, *Eur. J. Inorg. Chem.*, 2017, 1541-1548, 2017.
- [44] W.-X. Zhang, W. Xue, J.-B. Lin, Y.-Z. Zheng, and X.-M. Chen, 3D geometrically frustrated magnets assembled by transition metal ion and 1,2,3-triazole-4,5-dicarboxylate as triangular nodes, *Cryst. Eng. Comm*, 10, 1770-1776, 2008.
- [45] S. Bonhommeau, G. Molnár, A. Galet, A. Zwick, J.-A. Real, J. J. McGarvey, and A. Bousseksou, One Shot Laser Pulse Induced Reversible Spin Transition in the Spin-Crossover Complex $[\text{Fe}(\text{C}_4\text{H}_4\text{N}_2)\{\text{Pt}(\text{CN})_4\}]$ at Room Temperature, *Angew. Chem. Int. Ed.*, 44, 4069-4073, 2005.
- [46] P. Gütllich, A. Hauser, and H. Spiering, Thermal and Optical Switching of Iron(II) Complexes, *Angew. Chem. Int. Ed.*, 33, 2024-2054, 1994.
- [47] A. Hauser, "Light-Induced Spin Crossover and the High-Spin \rightarrow Low-Spin Relaxation," *Spin Crossover in Transition Metal Compounds II*, P. Gütllich and H. A. Goodwin, eds., pp. 155-198, Berlin, Heidelberg: Springer Berlin Heidelberg, 2004.
- [48] A. Hauser, Spin-Crossover Materials. Properties and Applications. Edited by Malcolm A. Halcrow, *Angew. Chem. Int. Ed.*, 52, 10419-10419, 2013.

- [49] Y. Ogawa, S. Koshihara, K. Koshino, T. Ogawa, C. Urano, and H. Takagi, Dynamical Aspects of the Photoinduced Phase Transition in Spin-Crossover Complexes, *Phys. Rev. Lett.*, **84**, 3181-3184, 2000.
- [50] J.-F. Létard, Photomagnetism of iron(ii) spin crossover complexes—the T(LIESST) approach, *J. Mater. Chem.*, **16**, 2550-2559, 2006.
- [51] E. Collet, and P. Guionneau, Structural analysis of spin-crossover materials: From molecules to materials, *Comptes Rendus Chimie*, **21**, 1133-1151, 2018.
- [52] W. Phonsri, P. Harding, K. S. Murray, B. Moubaraki, and D. J. Harding, Spin crossover in mixed ligand iron(iii) complexes, *New J. Chem.*, **41**, 13747-13753, 2017.
- [53] M. Schmitz, "Spincrossover-Prozesse und π -Radikalliganden," 2016.
- [54] M. Mörtel, A. Witt, F. W. Heinemann, S. Bochmann, J. Bachmann, and M. M. Khusniyarov, Synthesis, Characterization, and Properties of Iron(II) Spin-Crossover Molecular Photoswitches Functioning at Room Temperature, *Inorg. Chem.*, **56**, 13174-13186, 2017.
- [55] R. Colton, A. D'Agostino, and J. C. Traeger, Electrospray mass spectrometry applied to inorganic and organometallic chemistry, *Mass Spectrom. Rev.*, **14**, 79-106, 1995.
- [56] J. B. Fenn, Electrospray Wings for Molecular Elephants (Nobel Lecture), *Angew. Chem. Int. Ed.*, **42**, 3871-3894, 2003.
- [57] C. Brady, P. L. Callaghan, Z. Ciunik, C. G. Coates, A. Døssing, A. Hazell, J. J. McGarvey, S. Schenker, H. Toftlund, A. X. Trautwein, H. Winkler, and J. A. Wolny, Molecular Structure and Vibrational Spectra of Spin-Crossover Complexes in Solution and Colloidal Media: Resonance Raman and Time-Resolved Resonance Raman Studies, *Inorg. Chem.*, **43**, 4289-4299, 2004.
- [58] J. T. Lau, A. Achleitner, H. U. Ehrke, U. Langenbuch, M. Reif, and W. Wurth, Ultrahigh vacuum cluster deposition source for spectroscopy with synchrotron radiation, *Rev. Sci. Instrum.*, **76**, 063902, 2005.
- [59] J. T. Lau, A. Föhlich, R. Nietubyċ, M. Reif, and W. Wurth, Size-Dependent Magnetism of Deposited Small Iron Clusters Studied by X-Ray Magnetic Circular Dichroism, *PhRvL*, **89**, 057201, 2002.
- [60] V. Zamudio-Bayer, K. Hirsch, A. Langenberg, A. ławicki, A. Terasaki, B. v. Issendorff, and J. T. Lau, Electronic ground states of Fe²⁺ and Co²⁺ as determined by x-ray absorption and x-ray magnetic circular dichroism spectroscopy, *J. Chem. Phys.*, **143**, 244318, 2015.
- [61] V. Zamudio-Bayer, L. Leppert, K. Hirsch, A. Langenberg, J. Rittmann, M. Kossick, M. Vogel, R. Richter, A. Terasaki, T. Möller, B. v. Issendorff, S. Kümmel, and J. T. Lau, Coordination-driven magnetic-to-nonmagnetic transition in manganese-doped silicon clusters, *Phys. Rev. B*, **88**, 115425, 2013.
- [62] V. Zamudio-Bayer, R. Lindblad, C. Bülow, G. Leistner, A. Terasaki, B. V. Issendorff, and J. T. Lau, Electronic ground state of Ni²⁺, *J. Chem. Phys.*, **145**, 2016.
- [63] M. Gaffga, I. Munstein, P. Müller, J. Lang, W. R. Thiel, and G. Niedner-Schatteburg, Multistate-Mediated Rearrangements and FeCl₂ Elimination in Dinuclear FePd Complexes, *J. Phys. Chem. A*, **119**, 12587-12598, 2015.
- [64] J. Lang, M. Cayir, S. P. Walg, P. Di Martino-Fumo, W. R. Thiel, and G. Niedner-Schatteburg, Intermetallic Competition in the Fragmentation of Trimetallic Au–Zn–Alkali Complexes, *Chemistry – A European Journal*, **22**, 2345-2355, 2016.
- [65] J. Lang, D. V. Fries, and G. Niedner-Schatteburg, Characterization of Trinuclear Oxo Bridged Cobalt Complexes in Isolation, *Z. Phys. Chem.*, **232**, 649-669, 2018.
- [66] J. Lang, M. Gaffga, F. Menges, and G. Niedner-Schatteburg, Two-color delay dependent IR probing of torsional isomerization in a [AgL₁L₂]⁺ complex, *Phys. Chem. Chem. Phys.*, **16**, 17417-17421, 2014.
- [67] J. Lang, J. M. Hewer, J. Meyer, J. Schuchmann, C. van Wüllen, and G. Niedner-Schatteburg, Magnetostructural correlation in isolated trinuclear iron(iii) oxo acetate complexes, *Phys. Chem. Chem. Phys.*, **20**, 16673-16685, 2018.
- [68] J. Lang, J. Mohrbach, S. Dillinger, J. M. Hewer, and G. Niedner-Schatteburg, Vibrational blue shift of coordinated N₂ in [Fe₃O(OAc)₆(N₂)_n]⁺: "non-classical" dinitrogen complexes, *Chem. Comm.*, **53**, 420-423, 2017.
- [69] J. Meyer, "Fragmentation and Infrared Spectroscopy of oxo-centered Homo- and Heterotrimetallic Carboxylate Bridged Transition Metal Complexes," 2018.
- [70] K. Hirsch, J. T. Lau, P. Klar, A. Langenberg, J. Probst, J. Rittmann, M. Vogel, V. Zamudio-Bayer, T. Möller, and B. von Issendorff, X-ray spectroscopy on size-selected clusters in an ion trap: from the molecular limit to bulk properties, *J. Phys. B: Atomic, Molecular and Optical Physics*, **42**, 154029, 2009.
- [71] J. Meyer, M. Tombers, C. van Wüllen, G. Niedner-Schatteburg, S. Peredkov, W. Eberhardt, M. Neeb, S. Palutke, M. Martins, and W. Wurth, The spin and orbital contributions to the total magnetic moments of free Fe, Co, and Ni clusters, *J. Chem. Phys.*, **143**, 104302, 2015.

- [72] M. Niemeyer, K. Hirsch, V. Zamudio-Bayer, A. Langenberg, M. Vogel, M. Kossick, C. Ebrecht, K. Egashira, A. Terasaki, T. Möller, B. v. Issendorff, and J. T. Lau, Spin Coupling and Orbital Angular Momentum Quenching in Free Iron Clusters, *Phys. Rev. Lett.*, 108, 057201, 2012.
- [73] A. Langenberg, K. Hirsch, A. Ławicki, V. Zamudio-Bayer, M. Niemeyer, P. Chmiela, B. Langbehn, A. Terasaki, B. v. Issendorff, and J. T. Lau, Spin and orbital magnetic moments of size-selected iron, cobalt, and nickel clusters, *Phys. Rev. B*, 90, 184420, 2014.
- [74] S. Peredkov, A. Savci, S. Peters, M. Neeb, W. Eberhardt, H. Kampschulte, J. Meyer, M. Tombers, B. Hofferberth, F. Menges, and G. Niedner-Schatteburg, X-ray absorption spectroscopy of mass-selected transition metal clusters using a cyclotron ion trap: An experimental setup for measuring XMCD spectra of free clusters, *J. Electron. Spectrosc. Relat. Phenom.*, 184, 113-118, 2011.
- [75] S. Schenker, P. C. Stein, J. A. Wolny, C. Brady, J. J. McGarvey, H. Toftlund, and A. Hauser, Biphasic Behavior of the High-Spin \rightarrow Low-Spin Relaxation of [Fe(btpa)](PF₆)₂ in Solution (btpa = N,N,N',N'-Tetrakis(2-pyridylmethyl)-6,6'-bis(aminomethyl)-2,2'-bipyridine), *Inorg. Chem.*, 40, 134-139, 2001.
- [76] P. Carra, B. T. Thole, M. Altarelli, and X. Wang, X-ray circular dichroism and local magnetic fields, *Phys. Rev. Lett.*, 70, 694-697, 1993.
- [77] S. A. McLuckey, and D. E. Goeringer, SPECIAL FEATURE: TUTORIAL Slow Heating Methods in Tandem Mass Spectrometry, *J. Mass Spectrom.*, 32, 461-474, 1997.
- [78] E.-L. Zins, C. Pepe, D. Rondeau, S. Rochut, N. Galland, and J.-C. Tabet, Theoretical and experimental study of tropylium formation from substituted benzylpyridinium species, *J. Mass Spectrom.*, 44, 12-17, 2009.
- [79] E.-L. Zins, C. Pepe, and D. Schröder, Energy-dependent dissociation of benzylpyridinium ions in an ion-trap mass spectrometer, *J. Mass Spectrom.*, 45, 1253-1260, 2010.
- [80] E.-L. Zins, D. Rondeau, P. Karoyan, C. Fosse, S. Rochut, and C. Pepe, Investigations of the fragmentation pathways of benzylpyridinium ions under ESI/MS conditions, *J. Mass Spectrom.*, 44, 1668-1675, 2009.
- [81] A. D. Becke, Density-functional thermochemistry. III. The role of exact exchange, *J. Chem. Phys.*, 98, 5648-5652, 1993.
- [82] B. Miehlich, A. Savin, H. Stoll, and H. Preuss, Results obtained with the correlation energy density functionals of Becke and Lee, Yang and Parr, *Chem. Phys. Lett.*, 157, 200-206, 1989.
- [83] E. R. Davidson, Comment on "Comment on Dunning's correlation-consistent basis sets", *Chem. Phys. Lett.*, 260, 514-518, 1996.
- [84] T. H. Dunning, Gaussian basis sets for use in correlated molecular calculations. I. The atoms boron through neon and hydrogen, *J. Chem. Phys.*, 90, 1007-1023, 1989.
- [85] R. A. Kendall, T. H. Dunning, and R. J. Harrison, Electron affinities of the first-row atoms revisited. Systematic basis sets and wave functions, *J. Chem. Phys.*, 96, 6796-6806, 1992.
- [86] D. E. Woon, and T. H. Dunning, Gaussian basis sets for use in correlated molecular calculations. III. The atoms aluminum through argon, *J. Chem. Phys.*, 98, 1358-1371, 1993.
- [87] M. J. Frisch et. al, "Gaussian 16 Rev. C.01," 2016.
- [88] F. Neese, Software update: the ORCA program system, version 4.0, *WIREs Computational Molecular Science*, 8, e1327, 2018.
- [89] E. Stavitski, and F. M. F. de Groot, The CTM4XAS program for EELS and XAS spectral shape analysis of transition metal L edges, *Micron (Oxford, England : 1993)*, 41, 687-694, 2010.
- [90] Y. Teramura, A. Tanaka, and T. Jo, Effect of Coulomb Interaction on the X-Ray Magnetic Circular Dichroism Spin Sum Rule in 3 d Transition Elements, *J. Phys. Soc. Jpn.*, 65, 1053-1055, 1996.
- [91] Y. Teramura, A. Tanaka, B. T. Thole, and T. Jo, Effect of Coulomb Interaction on the X-Ray Magnetic Circular Dichroism Spin Sum Rule in Rare Earths, *J. Phys. Soc. Jpn.*, 65, 3056-3059, 1996.
- [92] O. Asvany, and S. Schlemmer, Numerical simulations of kinetic ion temperature in a cryogenic linear multipole trap, *Int. J. Mass spectrom.*, 279, 147-155, 2009.
- [93] A. Langenberg, "Magnetische Momente freier, massenselektierter Eisen-, Cobalt- und Nickelcluster," Doctoral Thesis, Technische Universität Berlin, Fakultät II - Mathematik und Naturwissenschaften, Technische Universität Berlin, Berlin, 2013.
- [94] J. Everett, E. Céspedes, L. R. Shelford, C. Exley, J. F. Collingwood, J. Dobson, G. van der Laan, C. A. Jenkins, E. Arenholz, and N. D. Telling, Ferrous iron formation following the co-aggregation of ferric iron and the Alzheimer's disease peptide β -amyloid (1-42), *J. Royal Soc. Interface*, 11, 20140165, 2014.
- [95] B. T. Thole, and G. van der Laan, Branching ratio in x-ray absorption spectroscopy, *PhRvB*, 38, 3158-3171, 1988.
- [96] G. van der Laan, K. T. Moore, J. G. Tobin, B. W. Chung, M. A. Wall, and A. J. Schwartz, Applicability of the Spin-Orbit Sum Rule for the Actinide 5f States, *Phys. Rev. Lett.*, 93, 097401, 2004.

- [97] G. van der Laan, and B. T. Thole, Strong magnetic x-ray dichroism in 2p absorption spectra of 3d transition-metal ions, *Phys. Rev. B*, 43, 13401-13411, 1991.
- [98] R. Ahlrichs, M. Bär, M. Häser, H. Horn, and C. Kölmel, Electronic structure calculations on workstation computers: The program system turbomole, *Chem. Phys. Lett.*, 162, 165-169, 1989.
- [99] R. F. W. Bader, A quantum theory of molecular structure and its applications, *Chem. Rev.*, 91, 893-928, 1991.
- [100] H. Naggert, A. Bannwarth, S. Chemnitz, T. von Hofe, E. Quandt, and F. Tuczek, First observation of light-induced spin change in vacuum deposited thin films of iron spin crossover complexes, *Dalt. Trans.*, 40, 6364-6366, 2011.

7.10 Supplementary material

Opto-magnetic correlation of a mass-selected monometallic spin-crossover iron complex

Michael Lembach^a, Matthias Klein^a, Joachim Hewer^a, Julius Wolny^b, Vicente Zamudio-Bayer^c, Martin Timm^c, Christine Bülow^{c,d}, Tobias Lau^c, Volker Schünemann^b, Bernd von Issendorff^d, Akira Terasaki^e and Gereon Niedner-Schatteburg^a

(a) Fachbereich Chemie and Forschungszentrum OPTIMAS, Kaiserslautern, Germany

(b) Fachbereich Biophysik, Technische Universität Kaiserslautern, Kaiserslautern, Germany

(c) Institut für Methoden und Instrumentierung der Forschung mit Synchrotronstrahlung, Helmholtz-Zentrum Berlin für Materialien und Energie, Berlin, Germany

(d) Physikalisches Institut, Universität Freiburg, Germany

(e) Department of Chemistry, Kyushu University, Fukuoka, Japan

Content

Fig. S1: Example of a XMCD spectrum and its integral over both $L_{3,2}$ absorption edges for the $[\text{Fe}(\text{btpa})]^{2+}$ (top). Integrated sum of both XA spectra for both photon helicities for the $[\text{Fe}(\text{btpa})]^{2+}$ (bottom).

Fig. S2: Experimental polarized depended XA Spectra (top), sum XA spectra with integral (middle) and XMCD spectra with integral (Bottom) for $[\text{Fe}(\text{btpa})]^{2+}$ ($T = 4.5 \text{ K}, 15 \text{ K}, 25 \text{ K}$).

Fig. S3: Sum of positive and negative XA spectra (black) of $[\text{Fe}(\text{btpa})]^{2+}$ ($T = 4.5 \text{ K}, 15 \text{ K}, 25 \text{ K}$). The shaded areas represent the two-step functions subtracted after normalization, approximating the direct $2p$ photon ionization and $2p \rightarrow nd$ ($n > 3$) contributions.

Fig.S4: Spin magnetic moments (blue), orbital magnetic moments (red), total magnetic moments (orange), and the spin-orbital ratio (green) per atom of $[\text{Fe}(\text{btpa})]^{2+}$ with given spectra from the sum rule analysis and error bars of 5 %.

Fig. S5: Determination of the isomer composition of $[\text{Fe}(\text{btpa})]^{2+}$ with given ion trap temperatures onto the experimental $m_s^{(z)}$ values.

Fig. S6: Determination of the isomer composition of $[\text{Fe}(\text{btpa})]^{2+}$ with given ion trap temperatures onto the experimental gained $m_j^{(z)}$ values.

Fig. S7: Normalized negative polarized XA spectra of $[\text{Fe}(\text{btpa})]^{2+}$ at different temperatures in blue with gauss folded (broadening 0.2) simulated XA spectra of a Fe^{2+} atom in an octahedral ($10 Dq = 2.60$ (T = 4.5 K), 2.80 (T = 15 K), 2.60 (T = 25 K) eV) coordination (black dotted) and stick spectra (black) by CTM4XAS and Cowan batch file.

Fig. S8: First derivation of the negative polarized XA spectra of $[\text{Fe}(\text{btpa})]^{2+}$ (T = 4.5 K (red), T = 15 K (blue) and T = 25 K (black)).

Fig. S9: Atom distances in Å of the Fe-N in $[\text{Fe}(\text{btpa})]^{2+}$ for the multiplicities M = 1, M = 5 (octahedral), and M = 5 (heptagonal). The calculations were performed at the B3LYP/cc-pVTZ (H, C, N, O) and Stuttgart ecp effective core potential (Fe) level of theory with six unpaired electrons on the Fe center for M= 5 and no unpaired electron for M = 1 corresponding to the minimum structures.

Fig. S10: Approximated metal d character with differential orbital covalency approach for $[\text{Fe}(\text{btpa})]^{2+}$ (T = 4.5 K (blue), T = 15 K (orange), T = 25 K (red), with a derivation of 100 % metal d character slope of known values from a Fe film and $\text{Fe}(\text{tacn})_2$.

Fig. S11: Mass spectra of a $[\text{Fe}(\text{btpa})]^{2+}$ in acetonitrile solution using the Paul type ion trap mass spectrometer.

Fig. S12: CID breakdown curves of $[\text{Fe}(\text{btpa})\text{M}(\text{OAc})_2]^{2+}$ (M = Mn, Cu, Zn, Pd) and their corresponding appearance curves of the associated fragments.

Fig. S13: Electron localized field (ELF), differential overlap region interaction (DORI) and Non covalent interactions (NCI) in $[\text{Fe}(\text{btpa})]^{2+}$ for the multiplicities M = 1 and M = 5 in octahedral coordination and also M = 5 in heptagonal coordination. The calculations were performed at the B3LYP/cc-pVTZ (H, C, N, O) and Stuttgart ecp effective core potential (Fe) level of theory with six unpaired electrons on the Fe center for M= 5 and no unpaired electron for M = 1 corresponding to the minimum structures.

Fig. S14: IR(M)PD spectra (black) in comparison with quantum chemistry calculation (blue) of $[\text{Fe}(\text{btpa})]^{2+}$ in octahedral low spin coordination. The calculations were performed with Gaussian 09 at the B3LYP/cc-pVTZ (H, C, N, O) and Stuttgart ecp effective core potential (Fe) level of theory. The calculated spectrum is scaled with a factor of 0.977.

Fig. S15: IR(M)PD spectra (black) in comparison with quantum chemistry calculation (red) of $[\text{Fe}(\text{btpa})]^{2+}$ in octahedral high spin coordination. The calculations were performed with Gaussian 09 at the B3LYP/cc-pVTZ (H, C, N, O) and Stuttgart ecp effective core potential (Fe) level of theory. The calculated spectrum is scaled with a factor of 0.977.

Fig. S16: IR(M)PD spectra (black) in comparison with quantum chemistry calculation (orange) of $[\text{Fe}(\text{btpa})]^{2+}$ in heptagonal high spin coordination. The calculations were performed with Gaussian 09 at the B3LYP/cc-pVTZ (H, C, N, O) and Stuttgart ecp effective core potential (Fe) level of theory. The calculated spectrum is scaled with a factor of 0.977.

Fig. S17: Blueshift of the free pyridine in the complex with the structure $[\text{Fe}(\text{btpa})]^{2+}$ (red) in comparison with quantum chemistry calculation (black). The calculations were performed with Gaussian 09 at the B3LYP/cc-pVTZ (H, C, N, O) and Stuttgart ecp effective core potential (Fe) level of theory.

Fig. S18: IR(M)PD spectra (black) in comparison with quantum chemistry calculation of $[\text{Fe}(\text{btpa})]^{2+}$ in different geometries and spin states. The calculations were performed with Gaussian 09 at the B3LYP/cc-pVTZ (H, C, N, O) and Stuttgart ecp effective core potential (Fe) level of theory. The calculated spectrum is scaled with a factor of 0.977.

Fig. S19: Calculated relative Gibbs energies of $[\text{Fe}(\text{btpa})]^{2+}$ in different spin and structural geometries. The calculations were performed with Gaussian 09 at the B3LYP/cc-pVTZ (H, C, N, O) and Stuttgart ecp effective core potential (Fe) level of theory.

Fig. S20: Normalized, derivated negative polarized XA spectra of $[\text{Fe}(\text{btpa})]^{2+}$ at different temperatures (4.5 K, 15 K, 25 K, top) in comparison with the UV/ Vis spectra at 298 K (bottom).

Tab. S1: Calculated energies relative to their minimum structures of $[\text{Fe}(\text{btpa})]^{2+}$. The calculations were performed with Gaussian 09 at the B3LYP/cc-pVTZ (H, C, N, O) and Stuttgart ecp effective core potential (Fe) level of theory.

Fig. S21: Tanabe Sugano diagram of a d^6 electronic configuration compared with the experimental values for Δ_0 and the absorption energies of $[\text{Fe}(\text{btpa})]^{2+}$ at different temperatures.

Fig. S22: Calculated HOMO-LUMO transitions of $[\text{Fe}(\text{btpa})]^{2+}$ in different geometries with the five unpaired electrons. The calculations were performed with Gaussian 09 at the unrestricted B3LYP/cc-pVTZ level of theory.

Fig. S23: Orbital energies and occupation of the metal center in different multiplicities and geometrical structures of $[\text{Fe}(\text{btpa})]^{2+}$. The calculations were performed with Gaussian 09 at the unrestricted B3LYP/cc-pVTZ level of theory.

Fig. S24: Energetic shifts in different spectroscopic approaches compared to each other for $[\text{Fe}(\text{btpa})]^{2+}$.

Tab. S2: atom coordinates for $[\text{Fe}(\text{btpa})]^{2+}$ ($M = 1$). The calculation was performed at the B3LYP/cc-pVTZ (H, C, N, O) and Stuttgart ecp effective core potential (Fe) level of theory with a high spin state for the Fe center.

Tab. S3: atom coordinates for $[\text{Fe}(\text{btpa})]^{2+}$ ($M = 5$). The calculation was performed at the B3LYP/cc-pVTZ (H, C, N, O) and Stuttgart ecp effective core potential (Fe) level of theory with a high spin state for the Fe center.

Tab. S4: atom coordinates for $[\text{Fe}(\text{btpa})]^{2+}$ ($M = 5$ (seven coordinated)). The calculation was performed at the B3LYP/cc-pVTZ (H, C, N, O) and Stuttgart ecp effective core potential (Fe) level of theory with a high spin state for the Fe center.

Tab. S5: Calculated anisotropy barrier of $[\text{Fe}(\text{btpa})]^{2+}$ ($M = 1, 5, 5$ (seven coordinated)) in quasi seven coordinated surrounding. The calculations were performed at the B3LYP/cc-pVTZ (H, C, N, O, Fe) with relativistic Douglas, Kroll, Hess 4th order.

Fig. S25: Energy shifts of the free and coordinated pyridine in the complex with the structure $[\text{Fe}(\text{btpa})]^{2+}$ (red) in comparison with quantum chemistry calculation (black). The calculations were performed with Gaussian 09 at the B3LYP/ cc-pVTZ (H, C, N, O) and Stuttgart ecp effective core potential (Fe) level of theory.

Fig. S26: Calculated orbital energies and spin occupation of the orbitals of $[\text{Fe}(\text{btpa})]^{2+}$ with $M = 1, 5$ in octahedral coordination and $M = 5$ in quasi seven coordination. The calculations were performed at the B3LYP/cc-pVTZ (H, C, N, O) and Stuttgart ecp effective core potential (Fe) level of theory with a high spin state for the Fe center.

Fig. S27: Calculated Spin densities of $[\text{Fe}(\text{btpa})]^{2+}$ for the multiplicities $M = 1$, $M = 5$ (octahedral), and $M = 5$ (heptagonal). The calculations were performed at the B3LYP-Gaussian/cc-pVTZ (H, C, N, O) and Stuttgart ecp effective core potential (Fe) level of theory with six unpaired electrons on the Fe center for $M = 5$ (octahedral), $M = 5$ (heptagonal) and no unpaired electron for $M = 1$ corresponding to the minimum structures.

Fig. S28: Calculated susceptibility of $[\text{Fe}(\text{btpa})]^{2+}$ with obtained magnetic moments from the XA spectra and their corresponding ion trap temperature, which was set.

Fig. S29: Calculated susceptibility of $[\text{Fe}(\text{btpa})]^{2+}$ with obtained magnetic moments from the XA spectra and their approximated ion temperature, derived by fitting the Brillouin function.

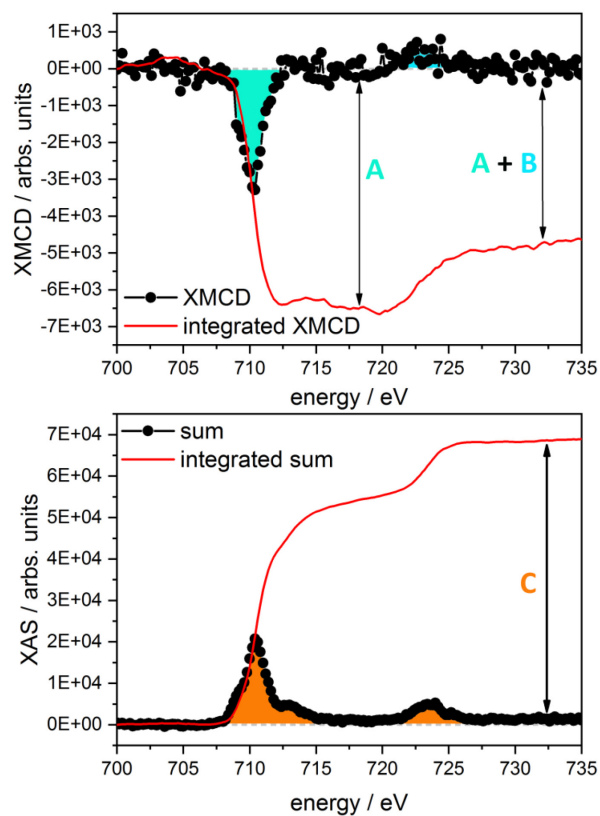


Fig. S1: Example of a XMCD spectrum and its integral over both $L_{3,2}$ absorption edges for the $[\text{Fe}(\text{btpa})]^{2+}$ (top). Integrated sum of both XA spectra for both photon helicities for the $[\text{Fe}(\text{btpa})]^{2+}$ (bottom).

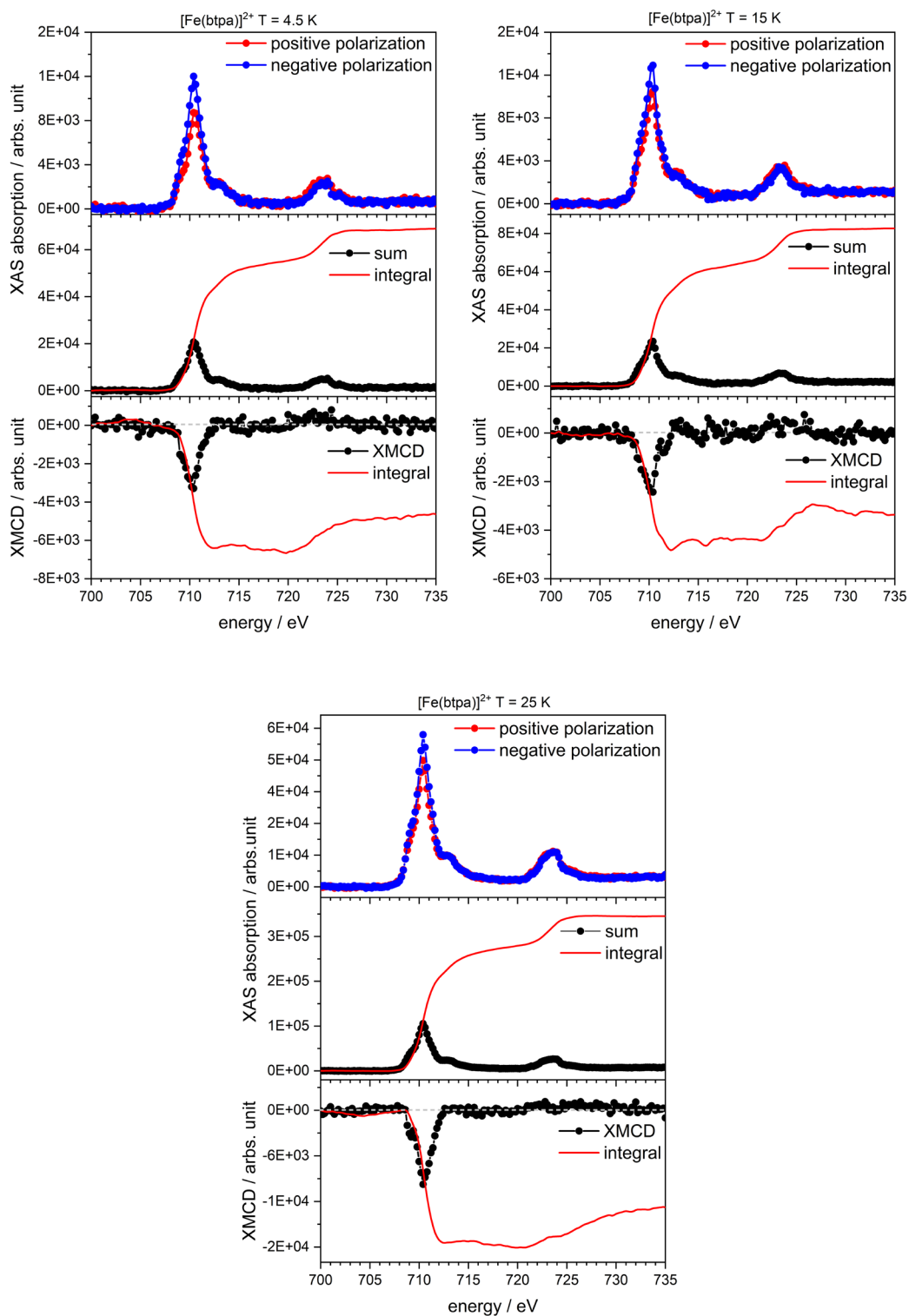


Fig. S2: Experimental polarized depended XA Spectra (top), sum XA spectra with integral (middle) and XMCD spectra with integral (Bottom) for $[\text{Fe}(\text{btpa})]^{2+}$ ($T = 4.5 \text{ K}, 15 \text{ K}, 25 \text{ K}$).

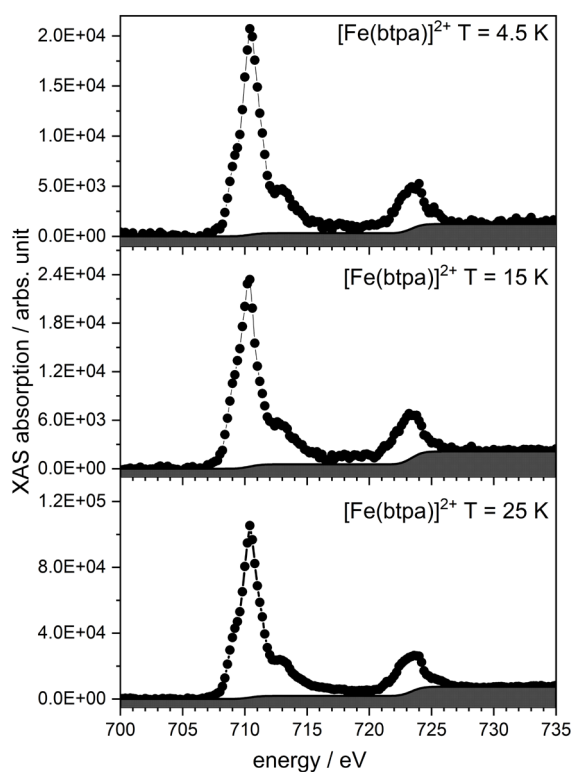


Fig. S3: Sum of positive and negative XA spectra (black) of $[\text{Fe}(\text{btpa})]^{2+}$ ($T = 4.5 \text{ K}, 15 \text{ K}, 25 \text{ K}$). The shaded areas represent the two-step functions subtracted after normalization, approximating the direct 2p photon ionization and 2p \rightarrow nd ($n > 3$) contributions.

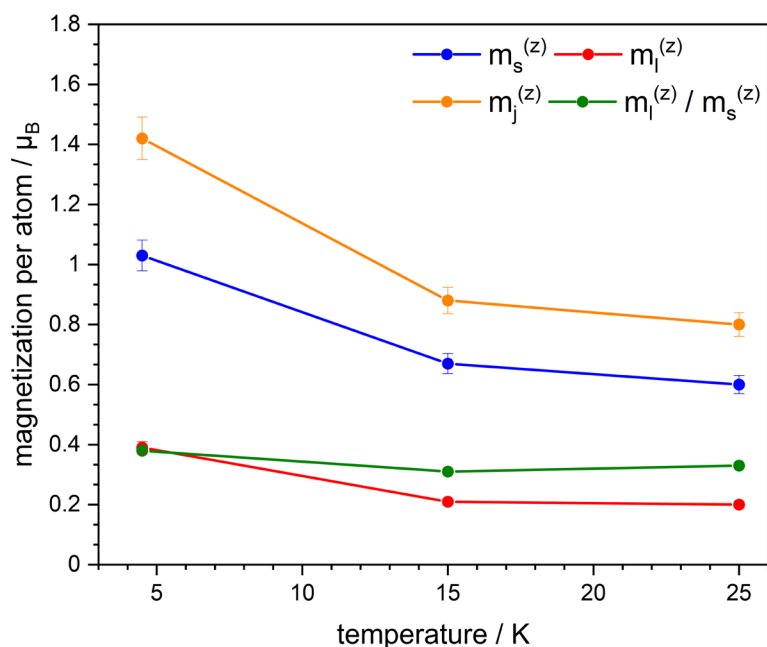


Fig.S4: Spin magnetic moments (blue), orbital magnetic moments (red), total magnetic moments (orange) and the spin-orbital ratio (green) per atom of $[\text{Fe}(\text{btpa})]^{2+}$ with given spectra from the sum rule analysis and uncertainties of 5 %.

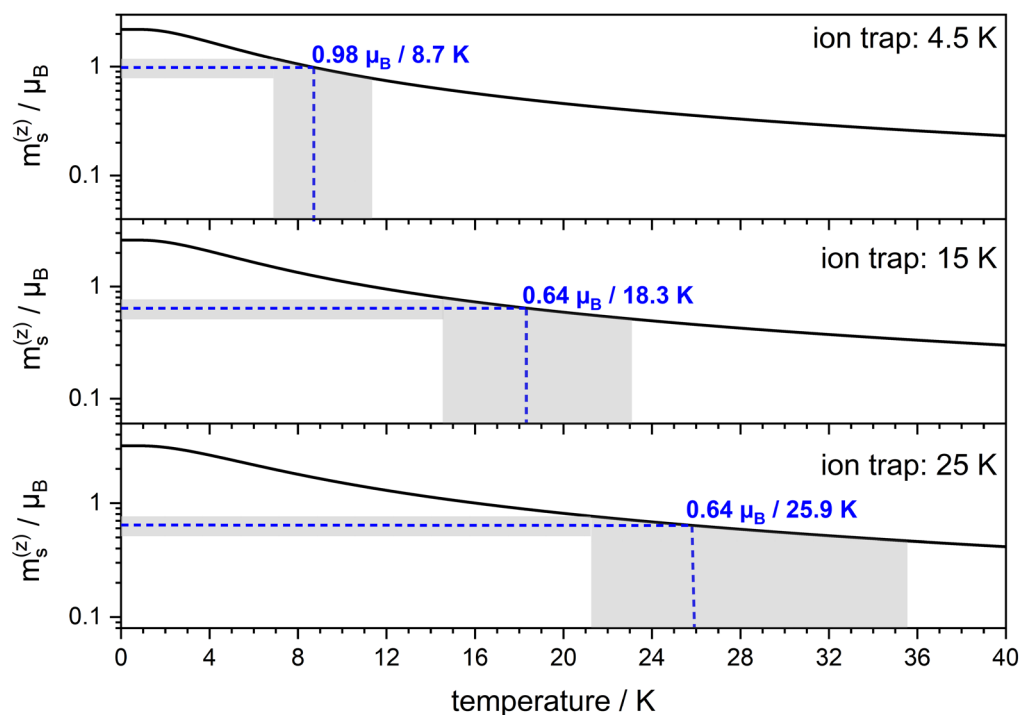


Fig. S5: Determination of the isomer composition of $[\text{Fe}(\text{btpa})]^{2+}$ with given ion trap temperatures onto the experimental gained $m_s^{(z)}$ values.

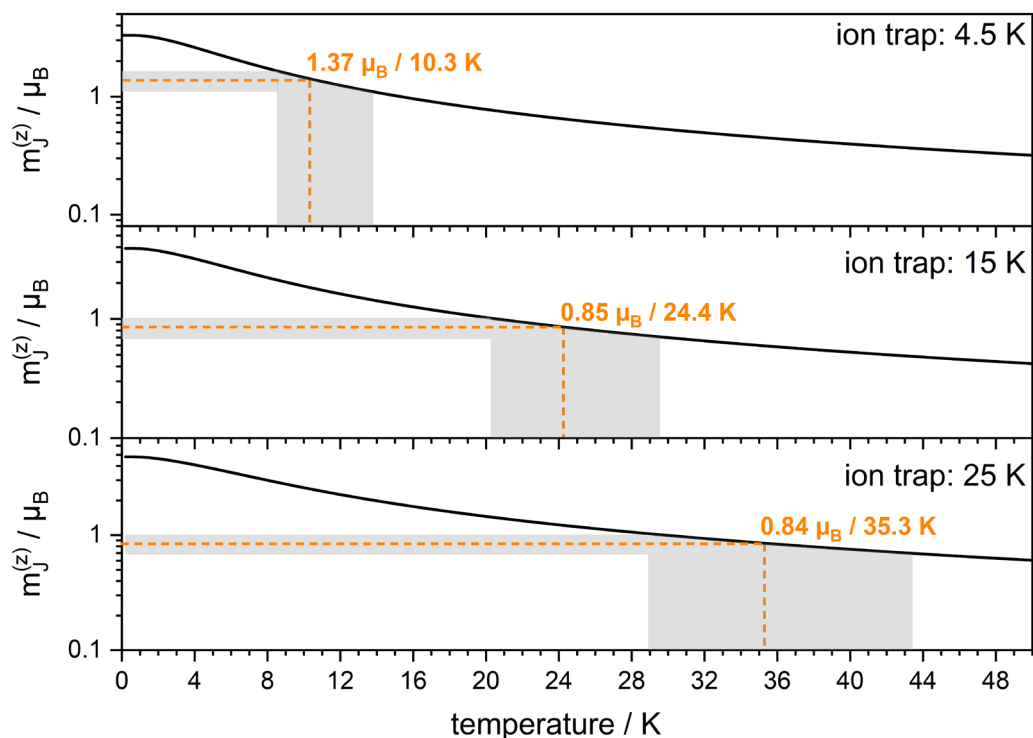


Fig. S6: Determination of the isomer composition of $[\text{Fe}(\text{btpa})]^{2+}$ with given ion trap temperatures onto the experimental $m_j^{(z)}$ values.

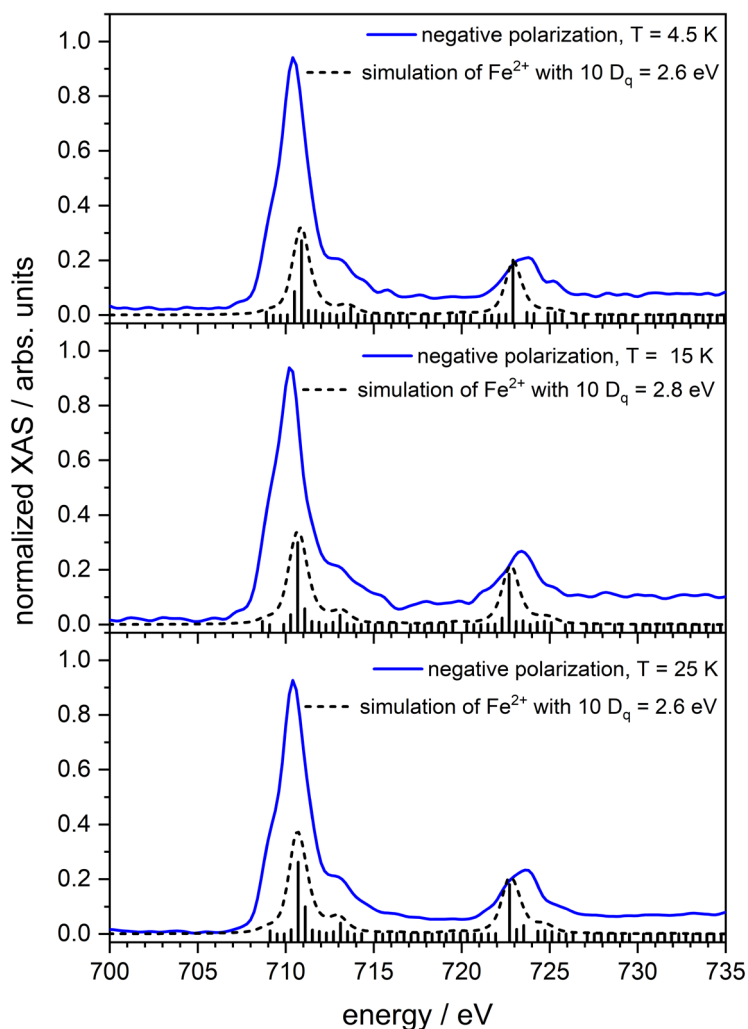


Fig. S7: Normalized negative polarized XA spectra of $[\text{Fe}(\text{btpa})]^{2+}$ at different temperatures in blue with gauss folded (broadening 0.2) simulated XA spectra of a Fe^{2+} atom in a octahedral ($10 D_q = 2.60$ ($T = 4.5$ K), 2.80 ($T = 15$ K), 2.60 ($T = 25$ K) eV) coordination (black dotted) and stick spectra (black) by CTM4XAS and Cowan batch file.

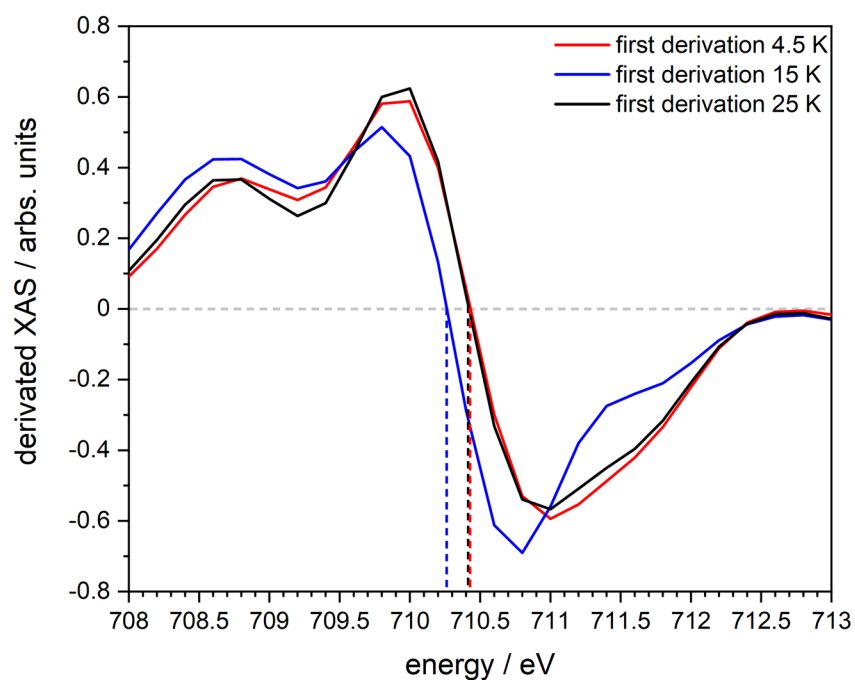


Fig. S8: First derivation of the negative polarized XA spectra of $[\text{Fe}(\text{btpa})]^{2+}$ ($T = 4.5 \text{ K}$ (red), $T = 15 \text{ K}$ (blue) and $T = 25 \text{ K}$ (black)).

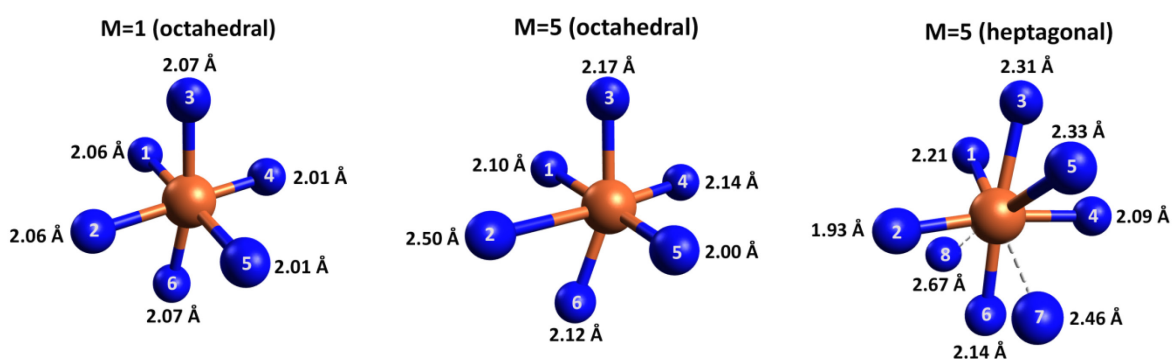


Fig. S9: Atom distances in Å of the Fe-N in $[\text{Fe}(\text{btpa})]^{2+}$ for the multiplicities $M = 1$, $M = 5$ (octahedral) and $M = 5$ (heptagonal). The calculations were performed at the B3LYP/cc-pVTZ (H, C, N, O) and Stuttgart ecp effective core potential (Fe) level of theory with six unpaired electrons on the Fe center for $M = 5$ and no unpaired electron for $M = 1$ corresponding to the minimum structures.

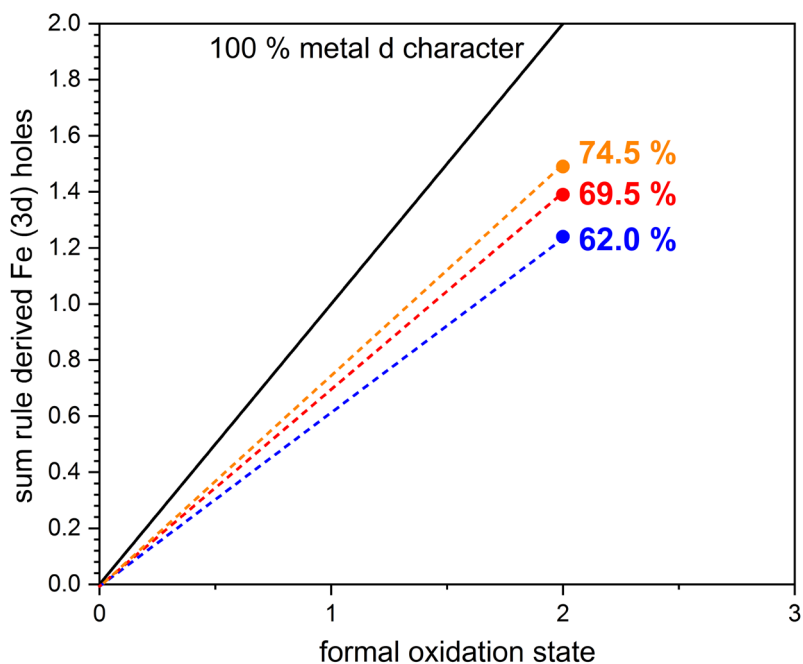


Fig. S10: Approximated metal d character with differential orbital covalency approach for $[\text{Fe}(\text{btpa})]^{2+}$ ($T = 4.5 \text{ K}$ (blue), $T = 15 \text{ K}$ (orange), $T = 25 \text{ K}$ (red), with a derivation of 100 % metal d character slope of known values from a Fe film and $\text{Fe}(\text{tacn})_2$.

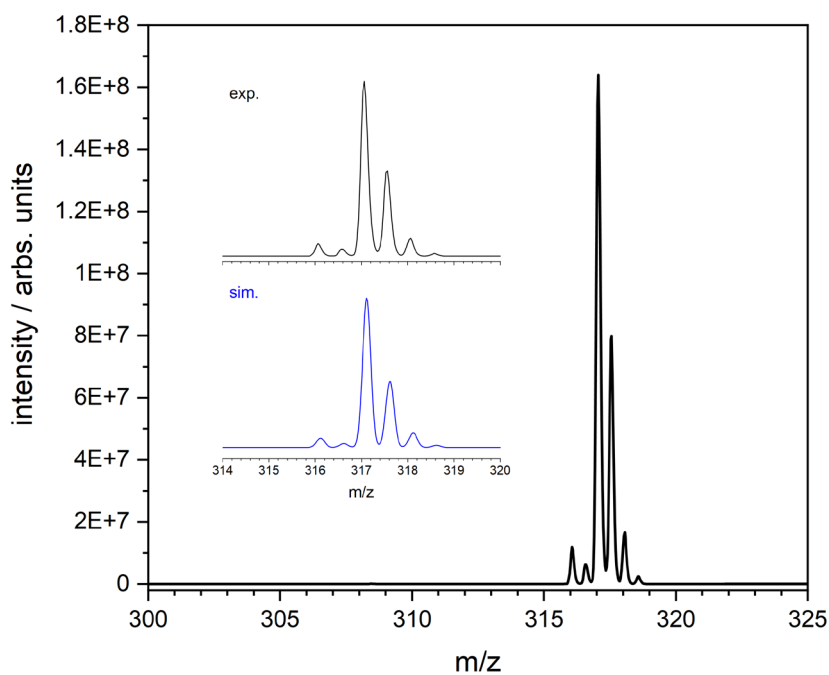


Fig. S11: Mass spectra of a $[\text{Fe}(\text{btpa})]^{2+}$ in acetonitrile solution using the Paul type ion trap mass spectrometer.

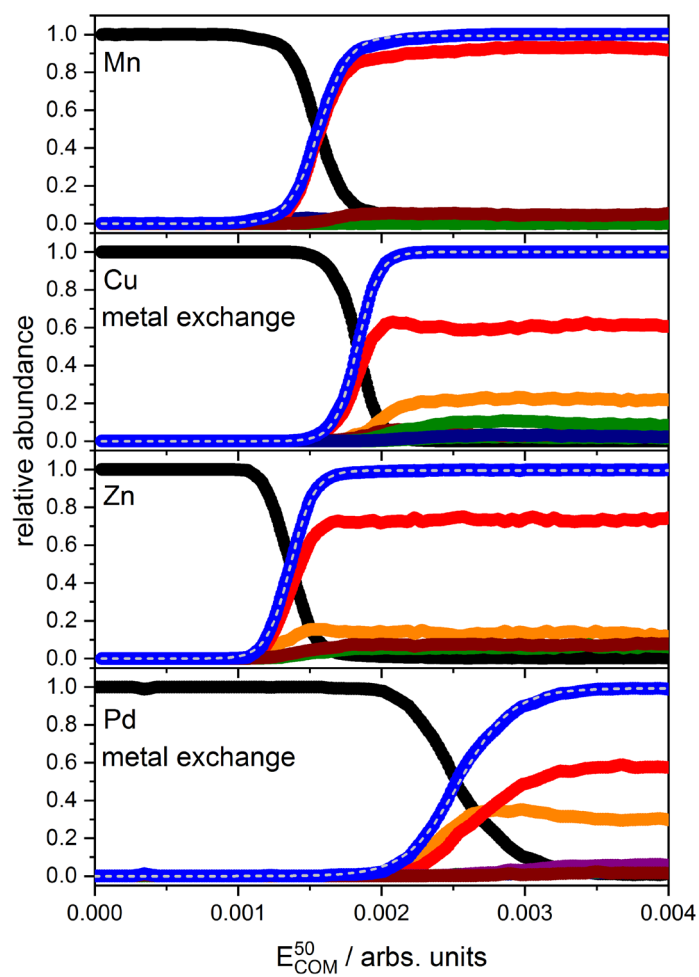


Fig. S12: CID breakdown curves of $[\text{Fe}(\text{btpa})\text{M}(\text{OAc})_2]^{2+}$ ($\text{M} = \text{Mn}, \text{Cu}, \text{Zn}, \text{Pd}$) and their corresponding appearance curves of the associated fragments.

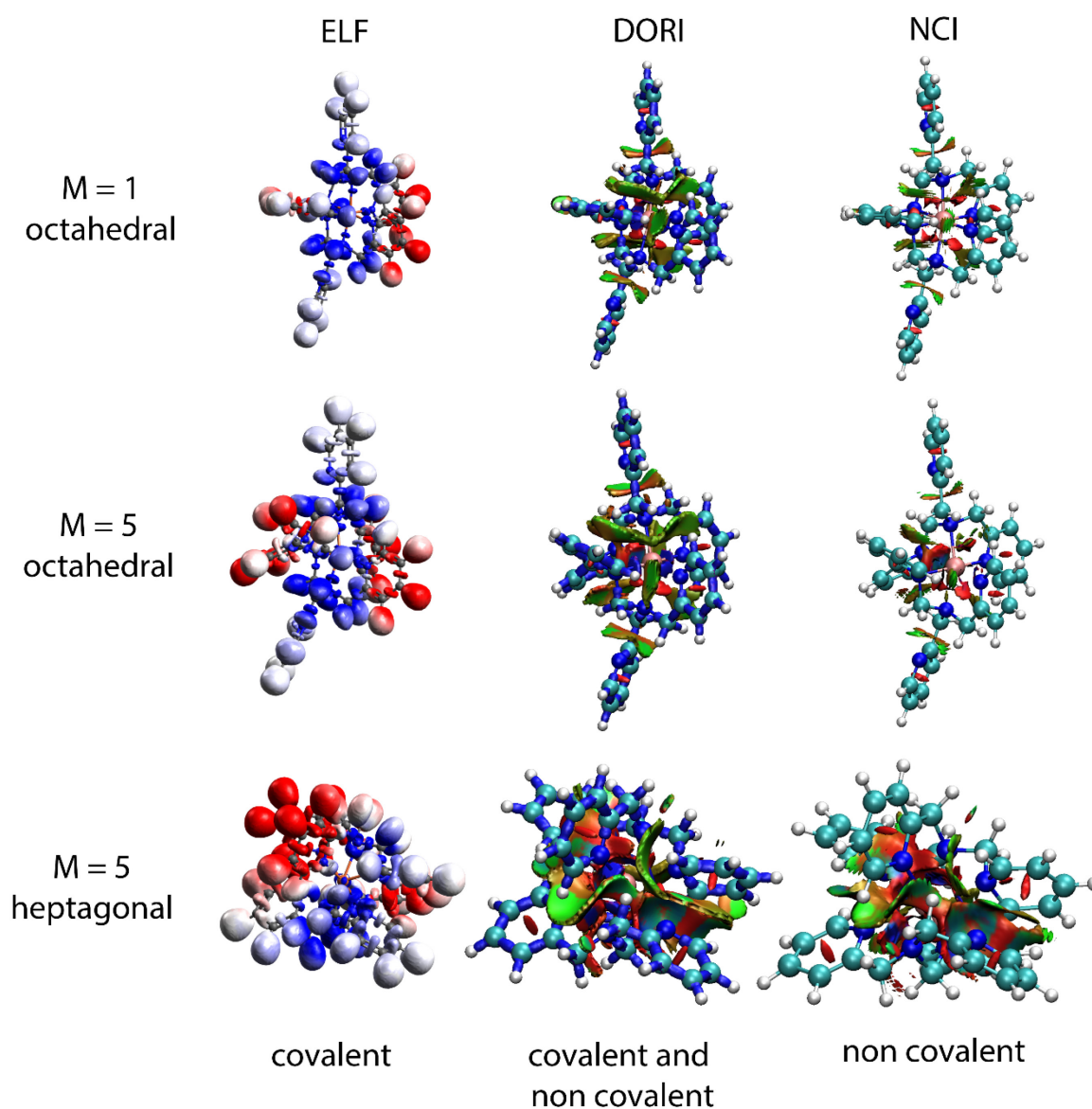


Fig. S13: Electron localized field (ELF), differential overlap region interaction (DORI) and Non covalent interactions (NCI) in $[\text{Fe}(\text{btpa})]^{2+}$ for the multiplicities $M=1$ and $M=5$ in octahedral coordination and also $M = 5$ in heptagonal coordination. The calculations were performed at the B3LYP/cc-pVTZ (H, C, N, O) and Stuttgart ecp effective core potential (Fe) level of theory with six unpaired electrons on the Fe center for $M = 5$ and no unpaired electron for $M=1$ corresponding to the minimum structures.

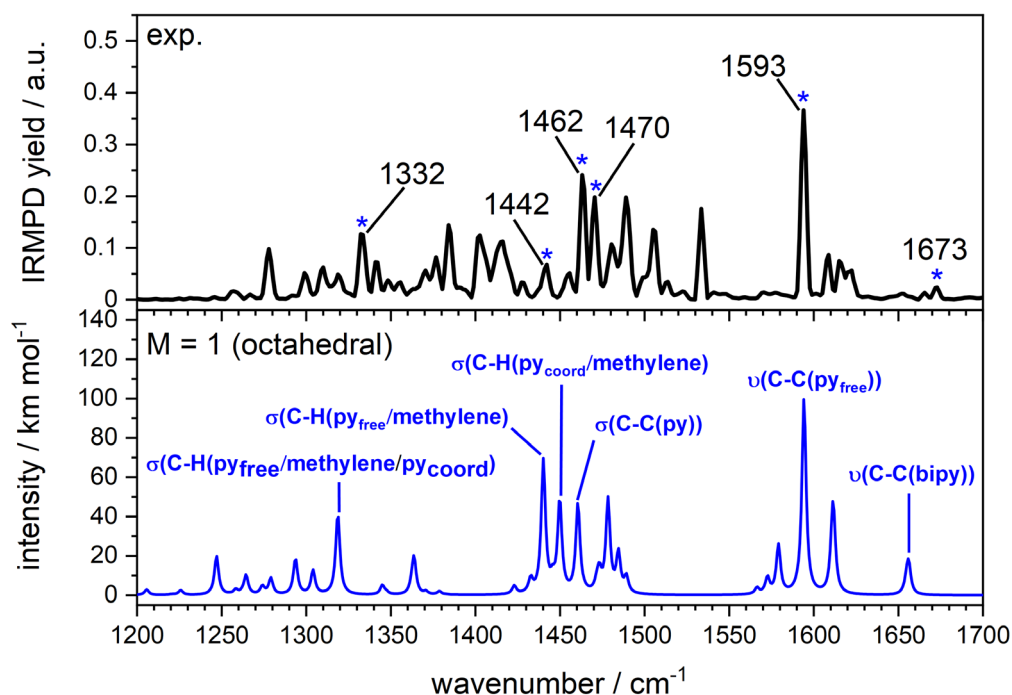


Fig. S14: IR(M)PD spectra (black) in comparison with quantum chemistry calculation (blue) of $[\text{Fe}(\text{btpa})]^{2+}$ in octahedral low spin coordination. The calculations were performed with Gaussian 09 at the B3LYP/cc-pVTZ (H, C, N, O) and Stuttgart ecp effective core potential (Fe) level of theory. The calculated spectrum is scaled with a factor of 0.977.

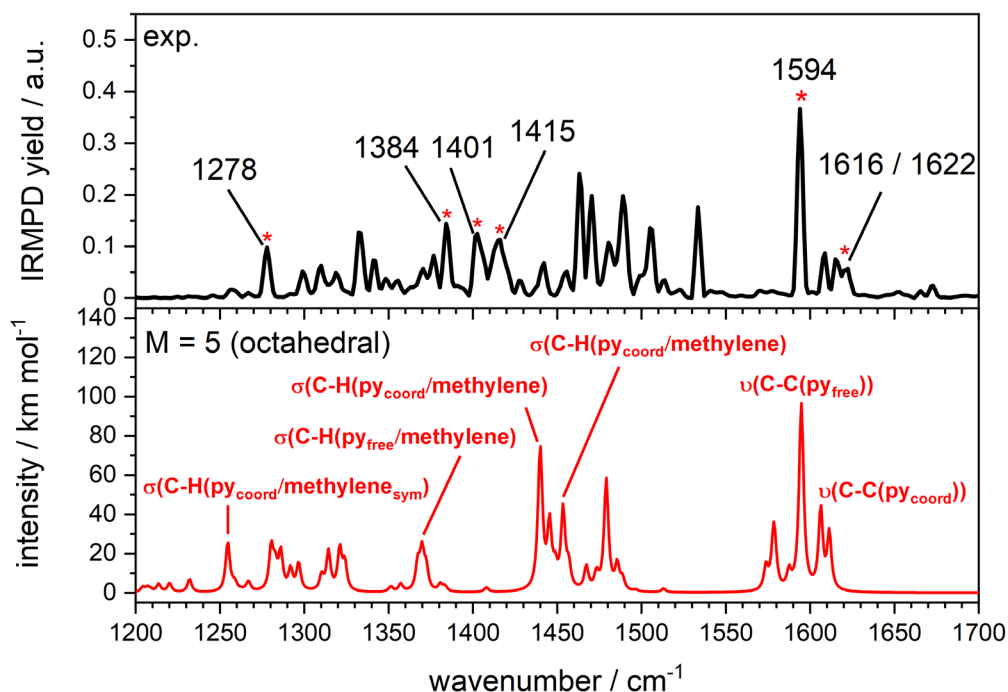


Fig. S15: IR(M)PD spectra (black) in comparison with quantum chemistry calculation (red) of $[\text{Fe}(\text{btpa})]^{2+}$ in octahedral high spin coordination. The calculations were performed with Gaussian 09 at the B3LYP/cc-pVTZ (H, C, N, O) and Stuttgart ecp effective core potential (Fe) level of theory. The calculated spectrum is scaled with a factor of 0.977.

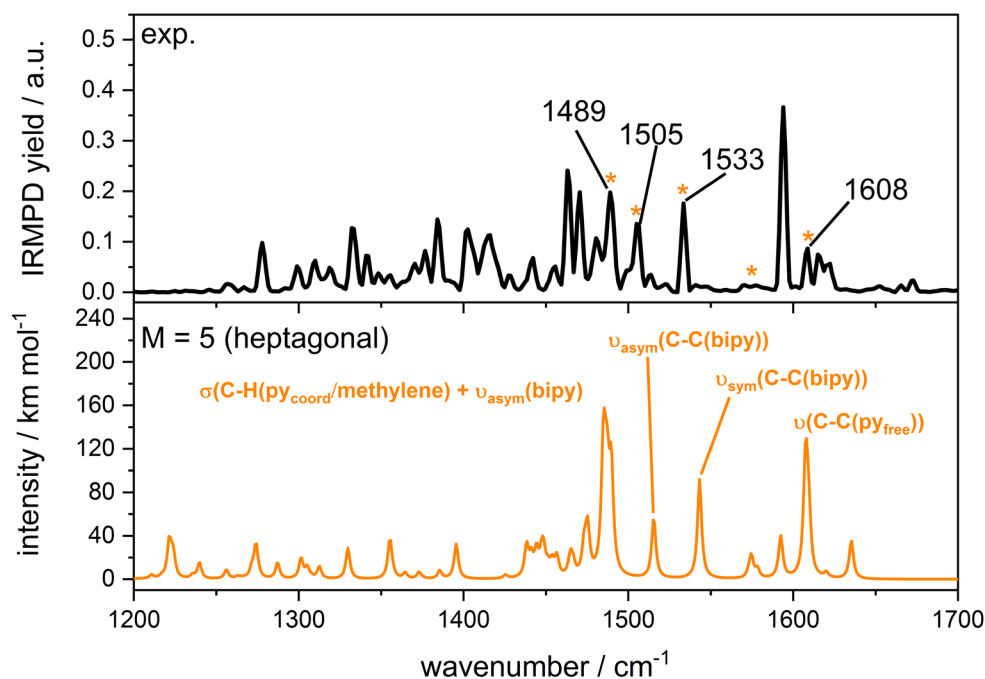


Fig. S16: IR(M)PD spectra (black) in comparison with quantum chemistry calculation (orange) of $[\text{Fe}(\text{btpa})]^{2+}$ in heptagonal high spin coordination. The calculations were performed with Gaussian 09 at the B3LYP/cc-pVTZ (H, C, N, O) and Stuttgart ecp effective core potential (Fe) level of theory. The calculated spectrum is scaled with a factor of 0.977.

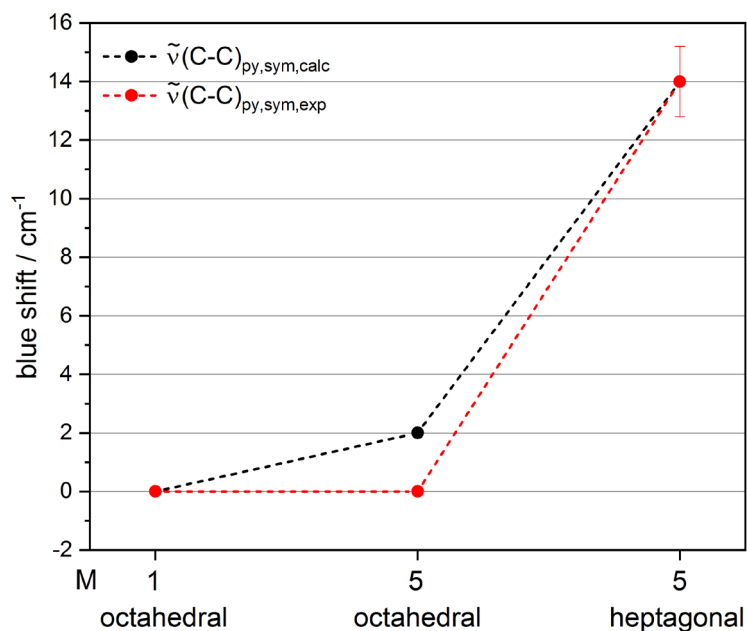


Fig. S17: Blue shift of the free pyridine in the complex with the structure $[\text{Fe}(\text{btpa})]^{2+}$ (red) in comparison with quantum chemistry calculation (black). The calculations were performed with Gaussian 09 at the B3LYP/cc-pVTZ (H, C, N, O) and Stuttgart ecp effective core potential (Fe) level of theory.

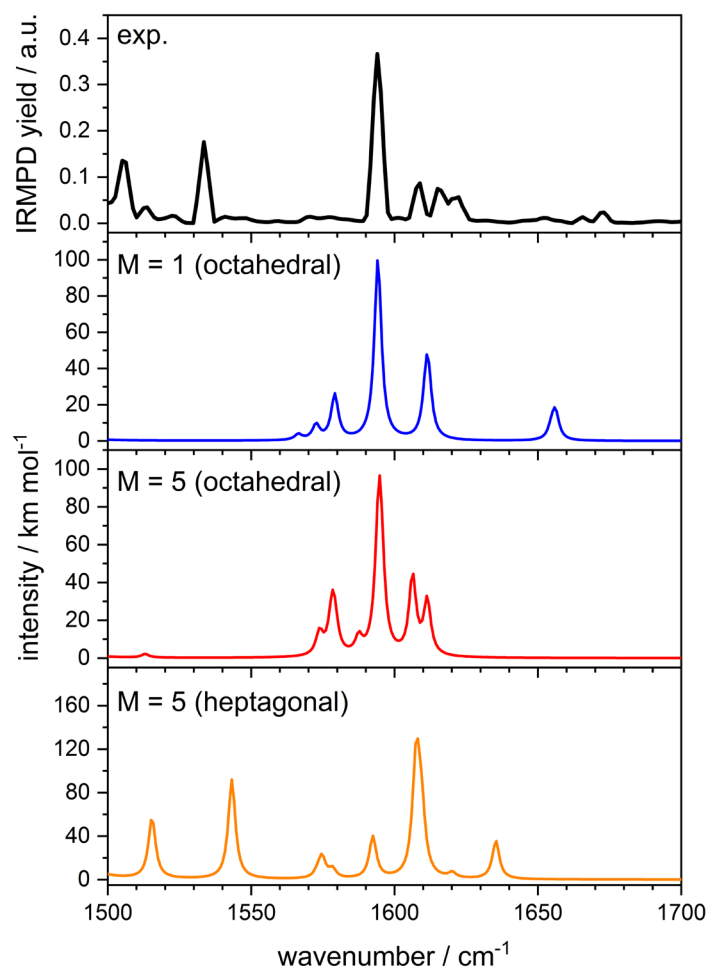


Fig. S18: IR(M)PD spectra (black) in comparison with quantum chemistry calculation of $[\text{Fe}(\text{btpa})]^{2+}$ in different geometries and spin states. The calculations were performed with Gaussian 09 at the B3LYP/cc-pVTZ (H, C, N, O) and Stuttgart ecp effective core potential (Fe) level of theory. The calculated spectrum is scaled with a factor of 0.977.

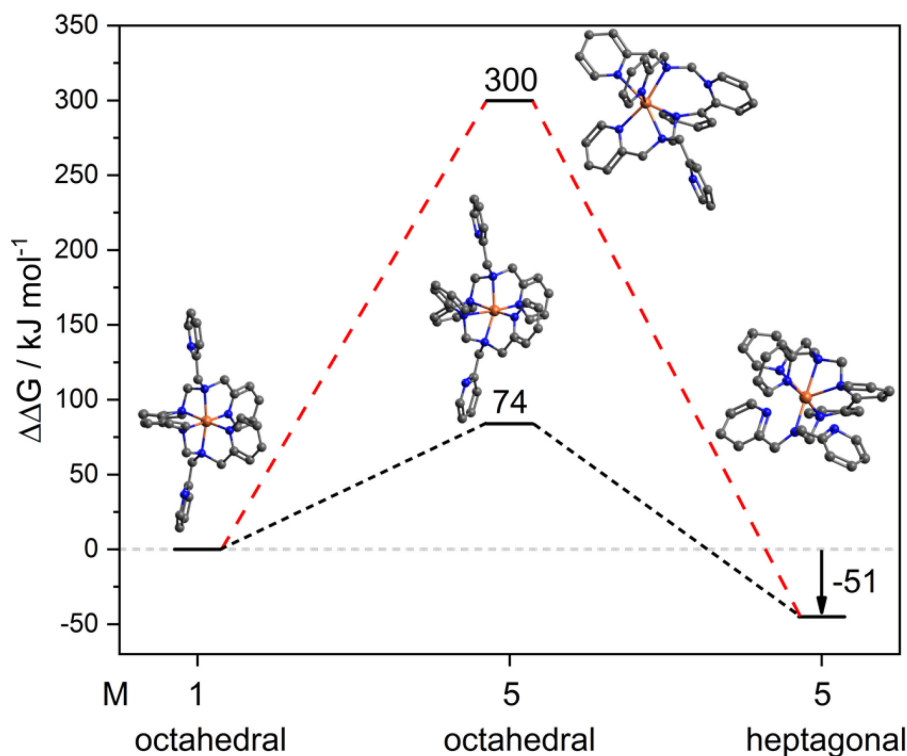


Fig. S19: Calculated relative Gibbs energies of $[\text{Fe}(\text{btpa})]^{2+}$ in different spin and structural geometries. The calculations were performed with Gaussian 09 at the B3LYP/cc-pVTZ (H, C, N, O) and Stuttgart ecp effective core potential (Fe) level of theory.

Tab. S1: Calculated energies relative to their minimum structures of $[\text{Fe}(\text{btpa})]^{2+}$. The calculations were performed with Gaussian 09 at the B3LYP/cc-pVTZ (H, C, N, O) and Stuttgart ecp effective core potential (Fe) level of theory.

	SCF/Hartree	$\Delta\text{SCF}/\text{Hartree}$	$\Delta E/\text{kJ/mol}$
M = 1 (oct)	-1955.698	0.000	0
M = 5 (oct)	-1955.695	0.003	9
M = 1 (hept)	-1955.191	0.048	126
M = 5 (hept)	-1955.239	0.000	0

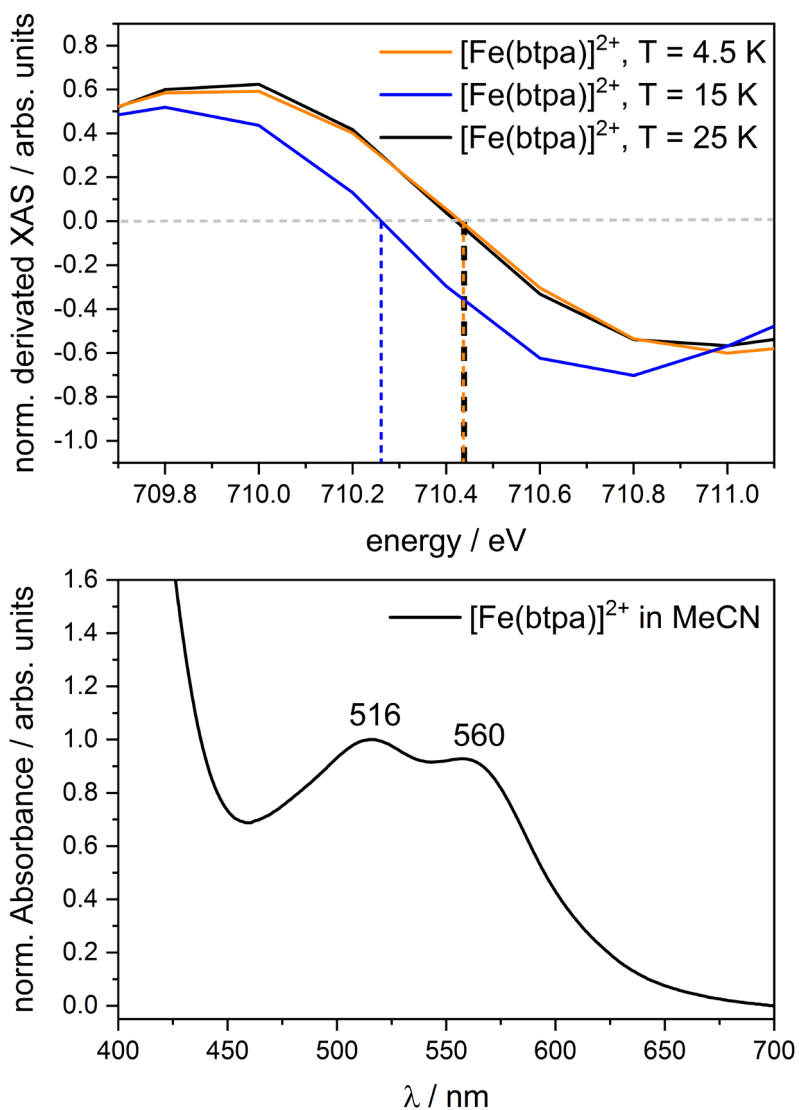


Fig. S20: Normalized, derivated negative polarized XA spectra of $[\text{Fe}(\text{btpa})]^{2+}$ at different temperatures (4.5 K, 15 K, 25 K, top) in comparison with the UV/ Vis spectra at 298 K (bottom).

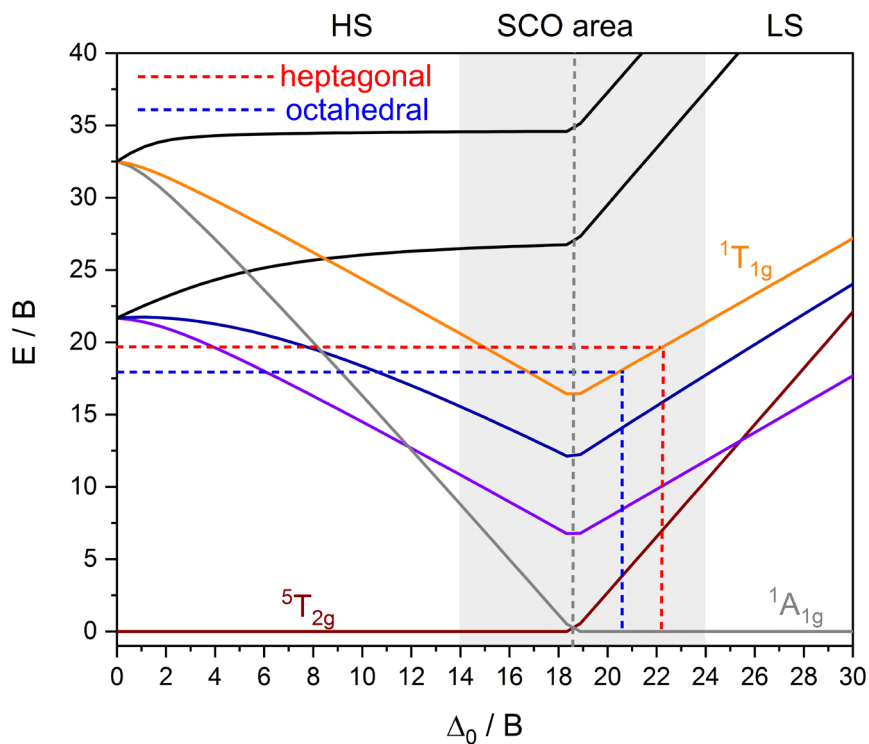


Fig. S21: Tanabe Sugano diagram of a d^6 electronic configuration compared with the experimental values for Δ_0 and the absorption energies of $[\text{Fe}(\text{btpa})]^{2+}$ at different temperatures.

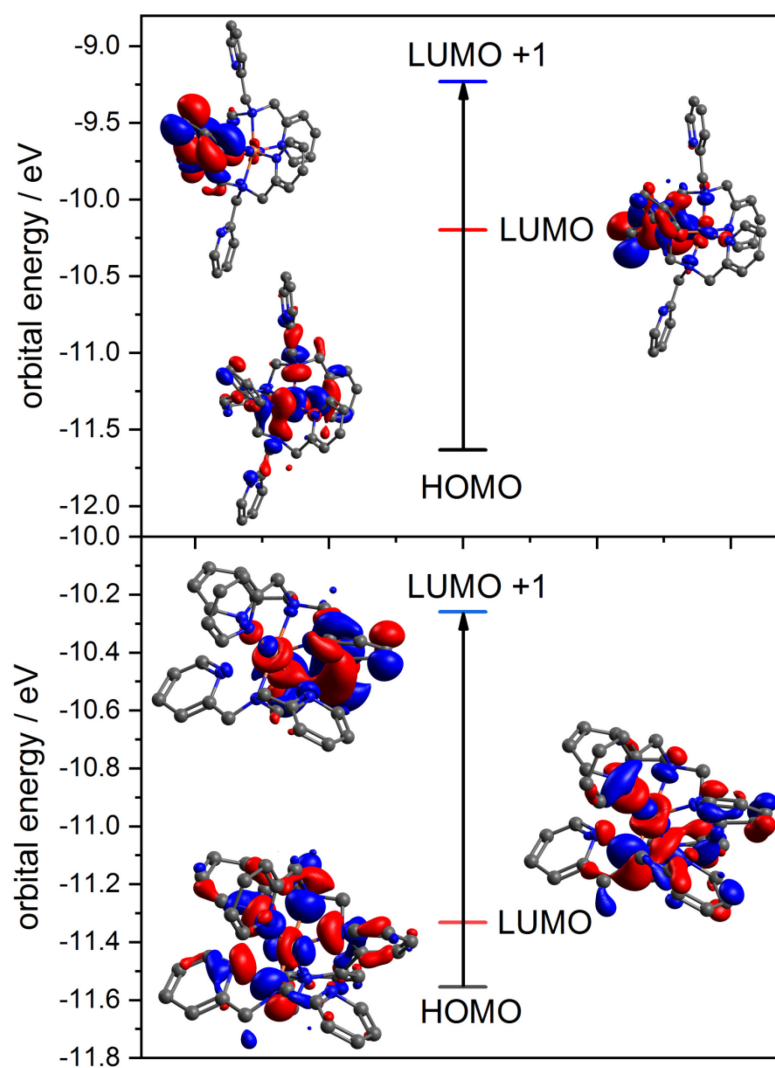


Fig. S22: Calculated HOMO-LUMO transitions of $[\text{Fe}(\text{btpa})]^{2+}$ in different geometries with the five unpaired electrons. The calculations were performed with Gaussian 09 at the unrestricted B3LYP/cc-pVTZ level of theory.

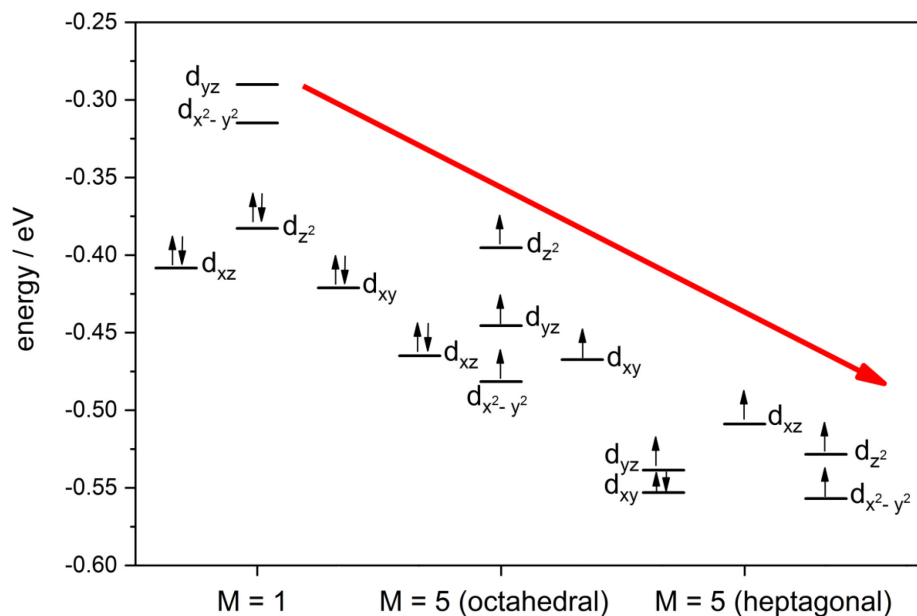


Fig. S23: Orbital energies and occupation of the metal center in different multiplicities and geometrical structures of $[\text{Fe}(\text{btpa})]^{2+}$. The calculations were performed with Gaussian 09 at the unrestricted B3LYP/cc-pVTZ level of theory.

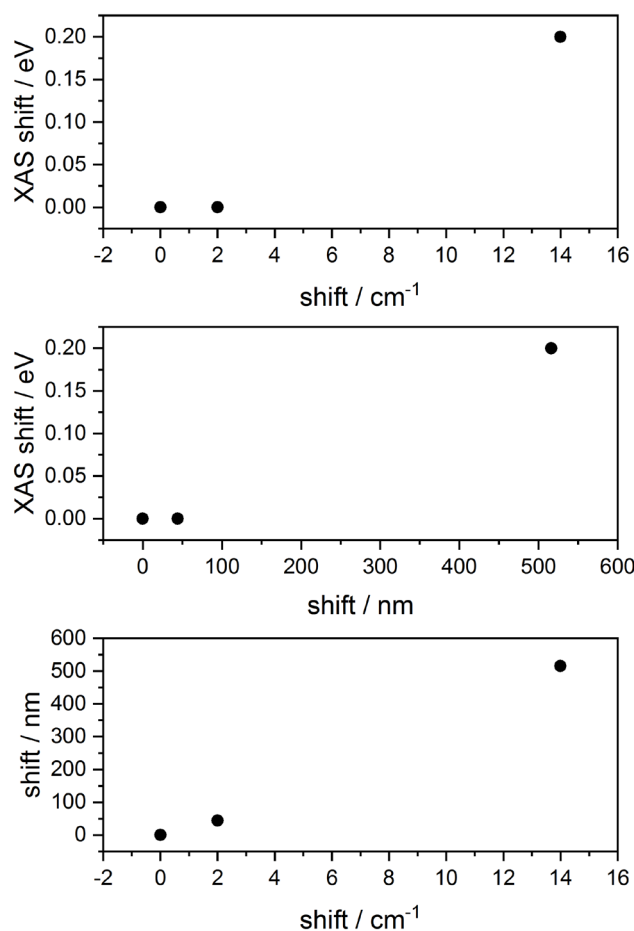


Fig. S24: Energetic shifts in different spectroscopic approaches compared to each other for $[\text{Fe}(\text{btpa})]^{2+}$.

Tab. S2: Atom coordinates for $[\text{Fe}(\text{btpa})]^{2+}$ ($M = 1$). The calculation was performed at the B3LYP/cc-pVTZ (H, C, N, O) and Stuttgart ecp effective core potential (Fe) level of theory with a high spin state for the Fe center.

atom	x	y	z
C	0.06206	-3.59489	-1.51628
C	0.32693	-3.46792	-2.83228
C	0.21764	-1.06245	-2.69196
N	-0.30425	-1.15046	-1.34646
C	-0.04463	-2.42818	-0.68008
H	-0.00588	-4.57318	-1.06609
C	0.04448	-2.42826	0.67988
N	0.30411	-1.15062	1.34641
C	-0.06223	-3.59505	1.51596
C	-0.32717	-3.46821	2.83196
C	-0.50612	-2.15277	3.40454
C	-0.21787	-1.06273	2.69189
H	0.00577	-4.5733	1.06568
H	-0.45038	-4.34115	3.4558
H	-0.87041	-2.04712	4.4161
H	-0.2892	-0.05935	3.07663
C	-1.79089	-0.84392	-1.3497
N	-2.03293	0.17426	-0.30383
H	-2.06075	-0.46407	-2.32911
H	-2.35576	-1.74901	-1.16926
C	-2.88152	-0.33066	0.80666
C	-4.35331	-0.50382	0.4823
H	-2.7642	0.34041	1.65454
H	-2.46114	-1.286	1.11695
C	-5.30866	-0.39852	1.48701
C	-6.63987	-0.63523	1.167
C	-6.96652	-0.95793	-0.14277
C	-5.94478	-1.0254	-1.08162
N	-4.66222	-0.80554	-0.7813
H	-5.0212	-0.14266	2.49817
H	-7.4069	-0.56453	1.92564
H	-7.98875	-1.14793	-0.43586
H	-6.16023	-1.26445	-2.11549
C	-2.55565	1.44125	-0.86895
C	-1.49422	2.16037	-1.65159
H	-3.43769	1.26074	-1.48281
H	-2.87603	2.07131	-0.03875
C	-1.81765	3.14581	-2.57479
C	-0.80214	3.81786	-3.23727
C	0.51586	3.47235	-2.96199
C	0.75944	2.47033	-2.04205

7. Opto-magnetic correlation of a mass-selected monometallic spin-crossover iron complex

N	-0.21801	1.81829	-1.39127
H	-2.85544	3.37891	-2.76713
H	-1.03237	4.59099	-3.95662
H	1.34168	3.96442	-3.45405
H	1.76755	2.16498	-1.81426
C	1.79074	-0.84411	1.34979
N	2.03288	0.174	0.30388
H	2.06047	-0.46417	2.3292
H	2.35566	-1.74921	1.16951
C	4.3532	-0.50411	-0.48239
C	2.55577	1.44093	0.86899
C	5.30851	-0.39846	-1.4871
C	6.63976	-0.63506	-1.16716
C	6.96647	-0.95799	0.14254
C	5.94476	-1.02581	1.08139
N	4.66216	-0.80607	0.78114
H	5.02099	-0.14245	-2.4982
H	7.40677	-0.56409	-1.9258
H	7.98874	-1.14789	0.43557
H	6.16026	-1.26507	2.1152
C	0.50584	-2.15241	-3.40474
H	0.45013	-4.34079	-3.45621
H	0.28897	-0.05903	-3.07661
H	0.87006	-2.04666	-4.41631
C	2.88137	-0.33105	-0.80664
H	2.461	-1.28645	-1.11674
H	2.76394	0.3399	-1.6546
C	1.49445	2.16007	1.65175
H	3.43785	1.26033	1.48276
H	2.87611	2.07098	0.03877
C	1.818	3.14532	2.57511
C	0.80258	3.81736	3.23775
C	-0.51546	3.47205	2.96243
C	-0.75917	2.47021	2.04231
N	0.21819	1.81817	1.3914
H	2.85583	3.37827	2.76748
H	1.03291	4.59032	3.95723
H	-1.34122	3.96412	3.45458
H	-1.76732	2.16505	1.81445
Fe	0.00002	0.38383	0.00002

Tab. S3: Atom coordinates for $[\text{Fe}(\text{btpa})]^{2+}$ ($M = 5$). The calculation was performed at the B3LYP/cc-pVTZ (H, C, N, O) and Stuttgart ecp effective core potential (Fe) level of theory with a high spin state for the Fe center.

Atom	x	y	z
C	-0.88758	-2.10783	2.84874
C	-1.29015	-1.28903	3.9226
C	-0.24338	0.5802	2.8271
N	0.257	-0.23109	1.75635
C	-0.1574	-1.63012	1.80298
H	-1.18157	-3.14776	2.81889
C	0.21034	-2.41845	0.62282
N	-0.356	-1.9546	-0.61403
C	1.09624	-3.45878	0.63445
C	1.50522	-4.09821	-0.549
C	1.01366	-3.5935	-1.77122
C	0.12197	-2.56966	-1.79746
H	1.51166	-3.75851	1.5869
H	2.18648	-4.93316	-0.52131
H	1.33759	-4.01767	-2.71096
H	-0.2883	-2.17186	-2.71285
C	1.7672	-0.06286	1.58936
N	2.04819	0.44404	0.23763
H	2.11379	0.62657	2.35087
H	2.23856	-1.0207	1.76053
C	2.87429	-0.48194	-0.57553
C	4.31671	-0.64076	-0.12982
H	2.84263	-0.14194	-1.60844
H	2.38241	-1.45151	-0.5616
C	5.25617	-1.17419	-1.00661
C	6.55545	-1.36128	-0.55571
C	6.87009	-1.00454	0.74948
C	5.86776	-0.47248	1.54843
N	4.61268	-0.2932	1.12361
H	4.97827	-1.43958	-2.01808
H	7.30944	-1.77384	-1.21164
H	7.86921	-1.13055	1.14034
H	6.07418	-0.17618	2.56918
C	2.59283	1.82216	0.24142
C	1.54808	2.86905	0.54203
H	3.42918	1.90021	0.93523
H	2.9984	2.01859	-0.75238
C	1.91173	4.13895	0.97409
C	0.92669	5.09622	1.16769
C	-0.40034	4.75802	0.92377
C	-0.68353	3.47125	0.50523

7. Opto-magnetic correlation of a mass-selected monometallic spin-crossover iron complex

N	0.26621	2.54161	0.3244
H	2.95255	4.37028	1.15289
H	1.18823	6.09006	1.50305
H	-1.19748	5.47423	1.05737
H	-1.69911	3.15892	0.30447
C	-1.81195	-1.65602	-0.60206
N	-2.06712	-0.19432	-0.43326
H	-2.24391	-2.00531	-1.53276
H	-2.28806	-2.2024	0.20165
C	-4.41686	-0.2456	0.54917
C	-2.57737	0.43837	-1.677
C	-5.39482	0.44524	1.25657
C	-6.71797	0.04215	1.12834
C	-7.01444	-1.02706	0.29415
C	-5.97149	-1.64675	-0.38221
N	-4.69589	-1.26938	-0.26021
H	-5.13083	1.27683	1.89634
H	-7.50234	0.5564	1.66613
H	-8.02967	-1.37227	0.16345
H	-6.16284	-2.47825	-1.04885
C	-0.97215	0.07632	3.85795
H	-1.84306	-1.69754	4.75348
H	0.04397	1.6161	2.76652
H	-1.29309	0.75442	4.63606
C	-2.95363	0.11579	0.72063
H	-2.55051	-0.40756	1.58387
H	-2.85514	1.18029	0.93158
C	-1.47436	0.67702	-2.66283
H	-3.38833	-0.14526	-2.10879
H	-2.9963	1.40837	-1.40061
C	-1.70098	0.76001	-4.02804
C	-0.65056	1.09523	-4.87199
C	0.59961	1.34294	-4.3195
C	0.75375	1.22398	-2.95048
N	-0.25344	0.88493	-2.13248
H	-2.6906	0.57253	-4.41969
H	-0.80626	1.16733	-5.93919
H	1.44245	1.62094	-4.93464
H	1.70533	1.40785	-2.4791
Fe	-0.07506	0.48819	-0.18451

Tab. S4: Atom coordinates for $[\text{Fe}(\text{btpa})]^{2+}$ ($M = 5$ (seven coordinated)). The calculation was performed at the B3LYP/cc-pVTZ (H, C, N, O) and Stuttgart ecp effective core potential (Fe) level of theory with a high spin state for the Fe center.

Atom	x	y	z
C	3.79368	2.14984	0.48796
C	4.31448	2.29043	0.74339
C	-2.33748	-1.24416	1.7797
N	-1.6364	-1.42262	0.53332
C	-2.47799	-1.45536	-0.60509
H	-4.36881	-2.45295	-1.35507
C	-1.93241	-0.81299	-1.86519
N	-0.80112	0.13531	-1.78192
C	-2.29129	-1.48044	-3.13355
C	-1.42528	-1.47318	-4.13614
C	-0.14025	-0.78913	-3.97483
C	0.13445	-0.06274	-2.8738
H	-3.19675	-2.06905	-3.22766
H	-1.64003	-2.02561	-5.04635
H	0.60048	-0.87197	-4.76429
H	1.08824	0.42525	-2.85364
C	-0.98691	-2.7098	0.53137
N	0.37495	-2.32722	0.32692
H	-1.2078	-3.32644	1.43475
H	-1.30839	-3.41577	-0.28378
C	1.05029	-2.88457	-0.85728
C	2.28354	-2.17696	-0.80091
H	0.49467	-2.61904	-1.77847
H	1.17204	-3.98878	-0.77331
C	3.50804	-2.859	-0.91339
C	4.66355	-2.27182	-0.42775
C	4.56597	-1.07385	0.25498
C	3.3222	-0.44943	0.38421
N	2.16911	-0.93637	-0.25534
H	3.55104	-3.86501	-1.31179
H	5.61587	-2.78133	-0.50132
H	5.4455	-0.63073	0.70544
H	3.30671	0.46691	0.94826
C	1.09327	-2.54863	1.64582
C	1.23713	-1.26494	2.43187
H	0.61579	-3.31381	2.29749
H	2.10671	-2.98449	1.52201
C	1.75098	-1.31637	3.6755
C	2.02335	-0.06218	4.44438
C	1.95521	1.20466	3.65733
C	1.4505	1.20652	2.41979

7. Opto-magnetic correlation of a mass-selected monometallic spin-crossover iron complex

N	0.95534	-0.003	1.80784
H	1.99136	-2.2717	4.13192
H	2.49901	-0.08777	5.44598
H	2.31538	2.13004	4.09567
H	1.42638	2.1425	1.89074
C	-0.97055	1.63956	-1.54892
N	-0.40681	2.01753	-0.08629
H	-0.40993	2.19299	-2.34168
H	-1.99113	2.02451	-1.75049
C	-2.31203	1.9792	1.03138
C	0.24086	3.30676	-0.25205
C	-3.31145	2.85483	1.46798
C	-4.57639	2.70574	0.97114
C	-4.78678	1.71778	0.03228
C	-3.72912	0.8612	-0.34071
N	-2.42608	0.95444	0.21953
H	-3.08384	3.66374	2.15466
H	-5.36375	3.38793	1.26421
H	-5.75571	1.63361	-0.44099
H	-4.00147	0.21605	-1.1477
C	-3.59449	-1.72351	1.91994
H	-5.29758	-2.73308	0.87008
H	-1.82085	-0.82732	2.63725
H	-4.09063	-1.67866	2.88371
C	-1.0606	2.13733	1.27912
H	-0.88817	1.26615	1.92
H	-0.8372	3.00922	1.93624
C	1.48742	2.94006	-0.68854
H	-0.32672	3.96411	-0.95254
H	0.43346	3.9176	0.66176
C	2.35303	3.9147	-1.035
C	3.72175	3.59724	-1.46708
C	3.89011	2.1782	-1.83828
C	2.9958	1.24377	-1.46491
N	1.77028	1.53116	-0.67761
H	2.05101	4.96088	-0.99028
H	4.35823	4.39222	-1.90985
H	4.73599	1.90089	-2.45824
H	3.19156	0.26742	-1.88909
Fe	0.01834	-0.07662	-0.05314

Tab. S5: Calculated anisotropy barrier of $[\text{Fe}(\text{btpa})]^{2+}$ ($M = 1, 5, 5$ (seven coordinated)) in quasi seven coordinated surrounding. The calculations were performed at the B3LYP/cc-pVTZ (H, C, N, O, Fe) with relativistic Douglas, Kroll, Hess 4th order.

multiplicity	anisotropy barrier/kJ/mol
1	45.01
5	46.66
5 (seven coordinated)	36.71

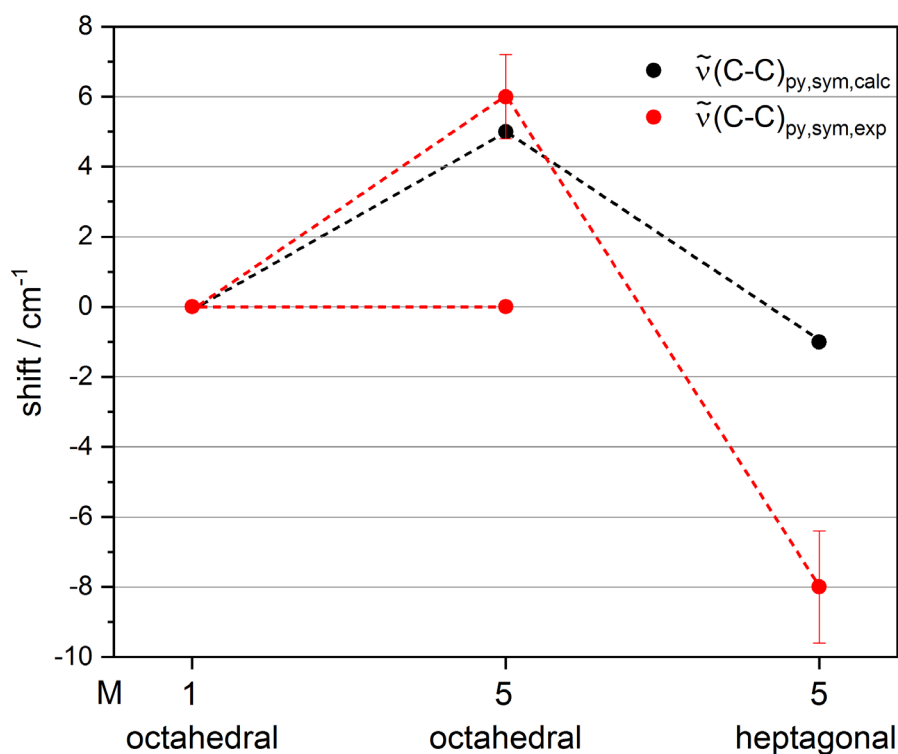


Fig. S25: Energy shifts of the free and coordinated pyridine in the complex with the structure $[\text{Fe}(\text{btpa})]^{2+}$ (red) in comparison with quantum chemistry calculation (black). The calculations were performed with Gaussian 09 at the B3LYP/cc-pVTZ (H, C, N, O) and Stuttgart ecp effective core potential (Fe) of theory.

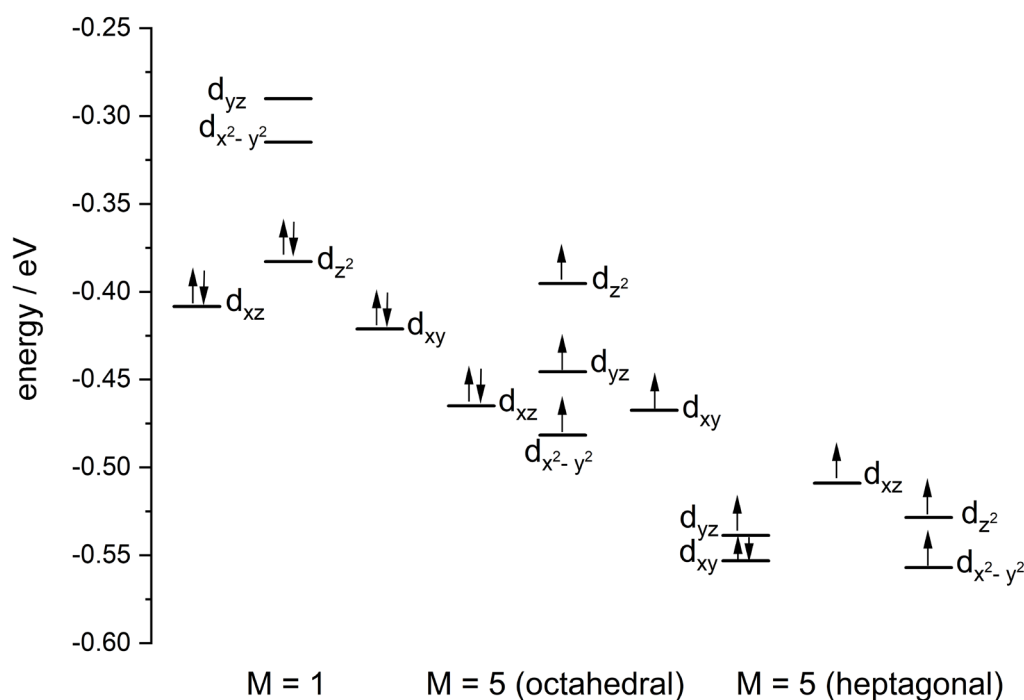


Fig. S26: Calculated orbital energies and spin occupation of the orbitals of [Fe(btpa)]²⁺ with M = 1, 5 in octahedral coordination and M = 5 in quasi seven coordination. The calculations were performed at the B3LYP/cc-pVTZ (H, C, N, O) and Stuttgart ecp effective core potential (Fe) level of theory with a high spin state for the Fe center.

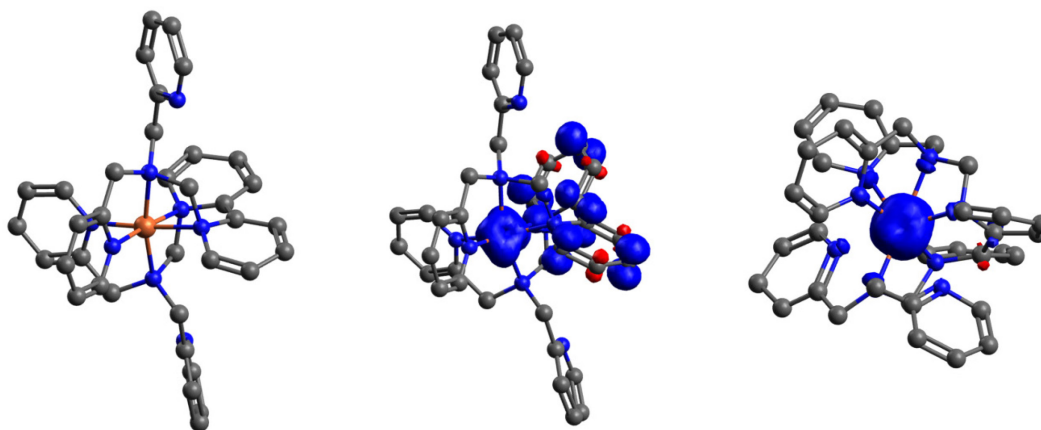


Fig. S27: Calculated Spin densities of [Fe(btpa)]²⁺ for the multiplicities M = 1, M = 5 (octahedral), and M = 5 (heptagonal). The calculations were performed at the B3LYP-Gaussian/cc-pVTZ (H, C, N, O) and Stuttgart ecp effective core potential (Fe) level of theory with six unpaired electrons on the Fe center for M= 5 (octahedral), M = 5 (heptagonal) and no unpaired electron for M=1 corresponding to the minimum structures.

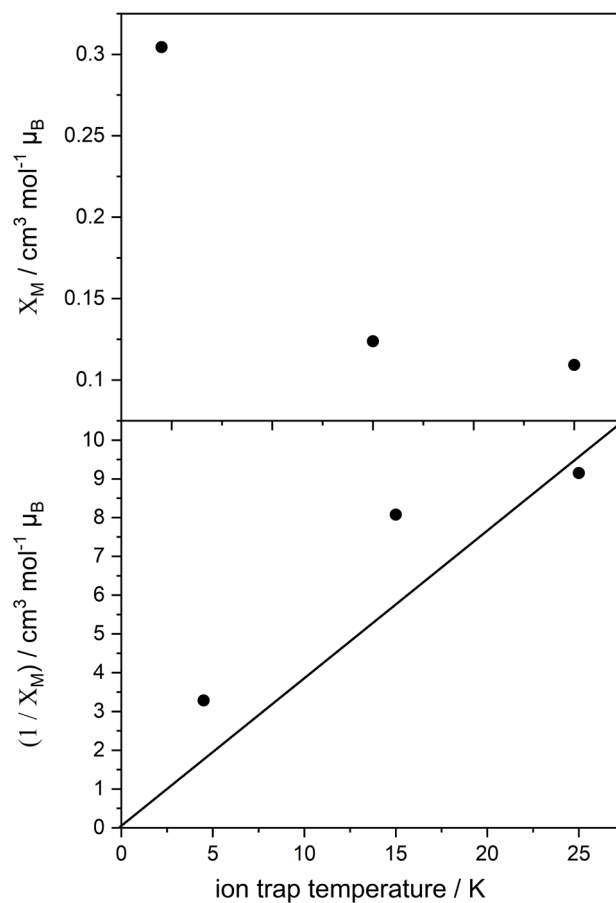


Fig. S28: Calculated susceptibility of $[\text{Fe}(\text{btpa})]^{2+}$ with obtained magnetic moments from the XA spectra and their corresponding ion trap temperature, which was set.

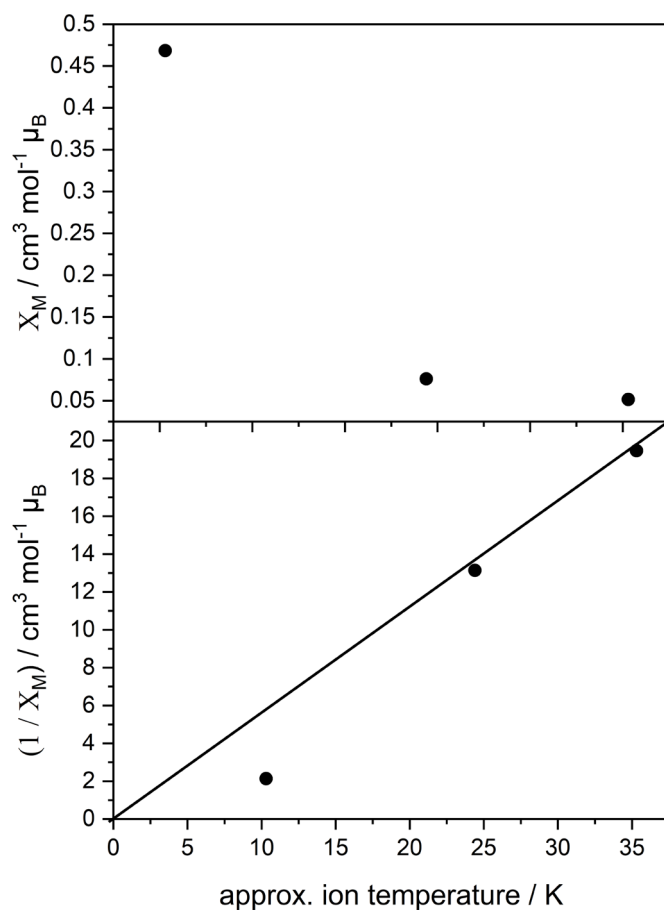


Fig. S29: Calculated susceptibility of $[\text{Fe}(\text{btpa})]^{2+}$ with obtained magnetic moments from the XA spectra and their approximated ion temperature, derived by fitting the Brillouin function.

8 Temperature dependent X-ray magnetic circular dichroic studies of a trinuclear Manganese SMM complex in isolation

Michael Lembach^a, Maximilian Luczak^a, Yannick Mees^a, Vicente Zamudio-Bayer^{b,c}, Martin Timm^b, Markus Kubin^b, Bernd von Issendorff^c, Akira Terasaki^d, Euan Brechin^e, Tobias Lau^{b,c} and Gereon Niedner-Schatteburg^a

^a*Fachbereich Chemie and Forschungszentrum OPTIMAS,
Technische Universität Kaiserslautern,
67663 Kaiserslautern, Germany*

^b*Helmholtz-Zentrum für Materialien und Energie
BESSY II,
14109 Berlin, Germany*

^c*Physikalisches Institut,
Universität Freiburg,
79104 Freiburg, Germany*

^d*Department of Chemistry,
Kyushu University,
Fukuoka, Japan*

^e*University of Edinburgh
Edinburgh, Scotland*

8.1 Preamble

The following chapter is prepared as manuscript for publication. I performed and managed the XMCD experiments, data evaluation, quantum chemical calculations, and XA simulations. I received experimental support from Maximilian Luczak, Yannick Mees, Vicente Zamudio-Bayer, and Markus Kubin to record the presented XA spectra. Tobias Lau, Bernd von Issendorf and Akira Terasaki operate the Ion Trap experimental setup at the Helmholtz Zentrum BESSY II in Berlin. Euan Brechin synthesized the samples in his group and kindly provided the complex for the experiments presented in this chapter. I wrote the chapter in form of a draft manuscript.

8.2 Abstract

Single Molecule Magnets (SMM) reveal magnetic properties, which do not emerge from macroscopic bulk ordering but from individual properties of the molecule itself. Much effort has been spent combining a high spin ground state with a large anisotropy barrier in this kind of complexes. We investigate a trimetallic complex with the general structure $[\text{Mn}_3(\text{Hcht})_2(\text{bipy})_4]^{3+}$ (H_3cht = cis, cis 1,3,5-cyclohexanetriol, bipy = bipyrimidyl) by X-ray Magnetic Circular Dichroism (XMCD) in gas phase. The combination of temperature dependent XMCD spectroscopy and sum rule analysis allows the determination of magnetic moments of transition metal complexes. These results reveal a decline of the magnetic moments by raise of temperature. The presented results help gain a fundamental insight into the molecular structure of single molecule magnets void of any external effects such as crystal packing or solvation.

8.3 Introduction

Transition Metal (TM) complexes with paramagnetic transition metal ions have grown to a fascinating field of research because of their access to a wide variety in medical^[1-5], technical^[6-9], and industrial^[10-12] applications. The high potential of paramagnetic transition metal complexes leads to a broad research field to design and model complexes with enhanced properties in the last decades. Therefore, complexes with magnetic properties like spin-crossover^[13-17] or single molecule magnets^[18-21] (SMM) seem promising candidates for data storage^[22] or quantum computing^[23-26]. Single molecule magnets exhibit remarkable magnetic properties by combining a high spin ground state with a large anisotropy barrier, resulting in slow relaxation of the spins after magnetization and a long living magnetism from the molecule itself^[27-31].

The first archetypical SMM $[\text{Mn}_{12}\text{O}_{12}(\text{CH}_3\text{COO})_{16}(\text{H}_2\text{O})_4]$ was synthesized by Lis^[20] and investigated by many groups^[27-35]. The complex stipulates high magnetization^[30] in cold conditions with a reduced anisotropic barrier^[29]. Besides complexes containing transition metal ions, the research of single molecule magnets has been expanded by including Lanthanides^[18, 36-44]. The high availability of earlier transition metal ions leads to a higher interest in designing SMM complexes containing early transition metals than rare earth

metals. The complex with the structure $[\text{Mn}^{\text{III}}_2(5\text{-Brsalen})_2(\text{MeOH})_2\text{M}^{\text{III}}(\text{CN})_6]\text{NEt}_4$ ($\text{M} = \text{Os, Ru}$; 5-Brsalen = N, N'-ethylene bis(5-bromosalicylidene)iminate)^[18] reveals a ferromagnetic exchange coupling with an extended living magnetization in one specific direction. In all other directions, the transition metal ions point out an antiferromagnetic exchange coupling. Changing the oxidation state in the Manganese SMM complex with the structure $[\text{Mn}^{\text{II}}(\text{tmphen})_2]_3[\text{Mn}^{\text{III}}(\text{CN})_6]_2$ (tmphen = 3, 4, 7, 8-tetramethyl-1, 10-phenanthroline)^[21] points out that a change in the crystal field splitting leads to an antiferromagnetic exchange coupling resulting in a barrier, which inhibits the relaxation of the magnetization.

All these complexes provide Mn^{2+} , Mn^{3+} atoms, or a combination of both oxidation states, and they are almost similar to the presented complex in this work. These complexes show single molecular magnetic behavior with a ferromagnetic or antiferromagnetic exchange coupling for the high spin Mn atoms.

The investigated complex with the general structure $[\text{Mn}_3(\text{Hcht})_2(\text{bipy})_4]^{3+}$ ($\text{H}_3\text{cht} = \text{cis, cis 1, 3, 5-cyclohexanetriol}$, bipy = bipyrimidyl) synthesized by Brechin^[45], achieves three linear arranged Manganese atoms with one Mn^{3+} ion in the center and two Mn^{2+} as neighbors (cf. Fig. 1) by deprotonated Hcht ligands, which provides a μ -oxo bridge between the metal ions. Two bipyrimidyl ligands coordinate to the Mn^{2+} ions to establish an octahedral coordination. The Hcht ligands lead to octahedral coordination in the Mn^{3+} ion. Long bonding distances of the Mn ions of more than 3 Å do not feature a direct metal-metal interaction. Previously X-ray diffraction and high-pressure superconducting quantum interference device (SQUID) measurements of the complex were performed. The high-pressure X-ray diffraction experiments revealed a contracted Mn-Mn core as a result of the shortened Mn^{3+} -O bondings with lower pressure. Pressure and temperature dependent Squid measurements showed almost similar magnetic behavior for different set pressure but a decreasing susceptibility with higher temperature^[45].

All previous experiments were performed in solid state or thin films. Therefore, the exclusion of external effects as crystal packing effects or solvation effects is not possible. Investigation in gas phase seems necessary to determine the magnetic properties from the molecule itself void of external effects.

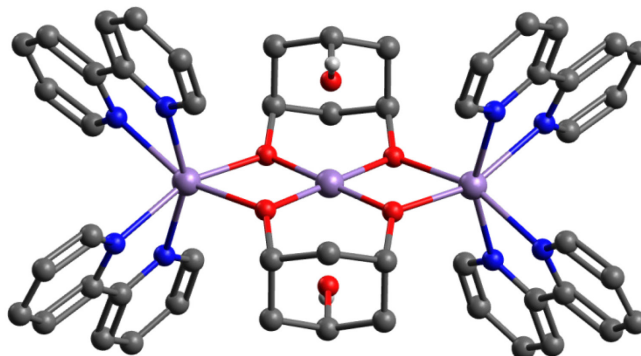


Fig. 1: Calculated geometry of $[\text{Mn}_3(\text{Hcht})_2(\text{bipy})_4]^{3+}$. The calculations were performed with Gaussian 09 at the unrestricted B3LYP/cc-pVTZ and Stuttgart ecp effective core potential (Mn) level of theory. Hydrogen atoms are omitted for clarity except for the two hydroxyl groups (C: grey, O: red, N: blue, Mn: violet).

Electrospray ionization^[46, 47] (ESI) enables mass spectrometric investigations of ionic complexes in gas phase and their activation by photons or collisions. Tandem-MS-based methods like X-ray magnetic circular dichroism (XMCD) and Collision Induced Dissociation (CID) have helped elucidate the molecular structure and their corresponding electronics void from external effects. The CID experiments were performed at room temperature and helped determine the molecular structure by observing the investigated complex's characteristic fragments. In combination with X-ray photons, a determination of the electronic structure and their resulting magnetic properties is possible. For the element selective XMCD experiments, cold conditions and an applied magnetic field (5 T) are necessary to orient the unpaired spins in molecules with magnetic properties^[48-51]. This spectroscopic approach allows the investigation of magnetic properties of surfaces^[52, 53], thin films^[54], deposited nanoparticles^[55], or clusters^[56]. Applying sum rule analysis^[49-51, 57, 58] allows determining the spin, orbital, and total magnetic moment of the investigated complex.

We combine experimental XMCD investigations of isolated $[\text{Mn}_3(\text{Hcht})_2(\text{bipy})_4]^{3+}$ (H_3cht = cis, cis 1, 3, 5-cyclohexanetriol, bipy = bipyrimidyl)^[45] with quantum chemical calculations by Density Functional Theory (DFT), Broken symmetry, Time Dependent Density Functional Theory (TD-DFT), XA simulations and determine the fragmentation pathways of the complex with collision-induced dissociation (CID).

8.4 Experimental Setup and Methods

Collision Induced Dissociation

For ESI mass spectrometric and Collision Induced Dissociation (CID) measurements, we used a quadrupole mass spectrometer (amazon ETD, bruker daltonics) with a three-dimensional Paul trap. A sample solution of $[\text{Mn}_3(\text{Hcht})_2(\text{bipy})_4](\text{ClO}_4)_3$ ^[45] ($c \sim 1 \cdot 10^{-6}$ mol/L) in acetonitrile was constantly infused into the spray chamber by a syringe pump with a flow rate of 180 $\mu\text{L}/\text{h}$. Losing three perchlorates formed the investigated cationic species as counter ions during the ESI process Nitrogen was used as a drying gas with a flow rate of 9 L/min at 200 °C. The nebulizer pressure was set to 280 mbar (4 psi) for spraying the sample solution, and the spray needle was kept at 4.5 kV. The Paul trap comprises a ring electrode and two end caps forming a nearly hyperbolic inner profile. Those end caps possess pinholes that allow them to enter or exit the ions in the trap. The ring electrode is powered with a high voltage RF (radio frequency) potential (781 kHz) while the end caps are grounded. Ions are accumulated in this resulting oscillating quadrupolar electric field generated from the three electrodes. An auxiliary dipolar voltage is fed to either the exit cap or both end caps for ion isolation and fragmentation. A proportional integral derivative (PID) gas controller set a constant partial Helium buffer gas pressure to 10^{-3} mbar inside the trap by a proportional integral derivative (PID) gas controller. CID breakdown curves were recorded by stepwise variation of the excitation amplitudes (Amp_{exp}) from 0.0 V–2.0 V while monitoring the extend of fragmentation and relative abundances of fragments for the isolated complex of interest. The excitation amplitudes determine the internal scale of the mass spectrometer E_{lab} in V. Relative abundances were calculated according to

$$I_{\text{tot}}^{\text{fr}}(E_{\text{lab}}) = \left(\frac{\sum_i I_i^{\text{fr}}(E_{\text{lab}})}{\sum_i I_i^{\text{fr}}(E_{\text{lab}}) + \sum_i I_i^{\text{p}}(E_{\text{lab}})} \right) \quad (1)$$

where I_i^{fr} = intensity of the fragment ion and I_i^{p} = intensity of the parent ions. Center of mass transferred fragmentation energies (E_{com}) were calculated from internal energies by:

$$E_{\text{com}} = \left(\frac{m_{\text{He}}}{m_{\text{He}} + m_{\text{ion}}} \right) \cdot E_{\text{lab}} \quad (2)$$

where m_{ion} stands for the isotopically averaged mass of the molecular ion. Note that the current application of the CID technique by RF excitation in the presence of multiple collisions results in a so called “slow multi-collision heating” mode of operation^[59].

Fragmentation amplitude dependent CID spectra were modeled and fitted by sigmoidal functions of the type

$$I_{\text{fit}}^{\text{fr}}(E_{\text{com}}) = \left(\frac{1}{1 + e^{(E_{\text{com}}^{50} - E_{\text{com}}) B}} \right) \quad (3)$$

Using a least-squares criterion. The E_{com}^{50} fit parameter is the amplitude at which the sigmoid function is at half maximum value, whereas B describes the rise of the sigmoid curve. Because of the correlation between fragmentation amplitude and appearance energy, it is feasible to assume that the appearance curves can be associated with the relative stability of the isolated complexes^[60-62].

For the experiments, via Electron Transfer Dissociation (ETD), we admitted methane in the ETD cell as a mediator to create low energy electrons. Inside the ETD cell, methane is oxidized to a methane radical cation ($\text{CH}_4^{*\cdot} + 2e^-$) via electron impact ionization. The collision of the methane radical cation with the Flouranthene ($\text{C}_{16}\text{H}_{10}$) leads to an electron capture of the low-energy electrons by the Flouranthene. Afterward, the Flouranthene radical anion ($\text{C}_{16}\text{H}_{10}^-$) is guided into the Paul trap, and collisions with the complex of interest lead to an anion-cation electron transfer reaction resulting in a reduction of the complex.

X-ray magnetic circular dichroism

For the presented polarization dependent gas-phase X-ray Absorption (XA) spectra, we used the “Ion Trap” coupled to the UE52-PGM beamline at BESSY II synchrotron facility of the Helmholtz Zentrum Berlin^[51, 56, 57, 63-66]. The Ion Trap is a home built time of flight combined ion trap mass spectrometer to record Total Ion Yield (TIY) gas-phase XA spectra^[51, 56, 64-66]. To transfer the ions into gas phase, we used a custom-built Electrospray Ionization (ESI) source, kindly provided by the Lau (HZB) group. The sample preparation follows the same as for the Collision Induced Dissociation experiments described above. The investigated cationic species were formed by losing three perchlorates as counter ions during the ESI process.

Ions are transferred via an RF Hexapole into a linear quadrupole mass filter (Extrel, 40-4000 amu). After the mass selection, the selected ions are guided into a linear quadrupole ion trap within the high field region (5 T) of a superconducting solenoid. The trap is operated at a frequency of 3.82 MHz. Evaporative liquid He cools down the ion trap to 4 K, 10 K, and 20 K. A constant He backing pressure of $1 \cdot 10^{-6}$ mbar cools down the trapped ions by collisional cooling. A continuous infusion of the ions into the ion trap serves for a stable ion signal. The ions are ejected into the time of flight area with a repetition rate of 120 Hz to record the mass spectra. For the XA spectra recorded by TIY spectroscopy, the ions are irradiated for 10 to 15s at set photon energy. Therefore, we recorded mass spectra as a function of the X-ray energy, with the quantization axis projected to the z- axis. A GaAs-diode records the X-ray intensity from the undulator beamline used for photon flux normalization of the recorded spectra. Spectra on the Mn absorption edges were taken with an exit slit size of 200 μm , a respective resolution of 400 meV from 635 eV to 665 eV for the L_3 and L_2 absorption edges.

XA spectra are recorded with positive and negative polarization in an alternating manner. The subtraction of the polarized dependent spectra leads to the corresponding XMCD spectrum and the addition to the sum spectrum, which is necessary to apply the sum rule analysis (cf. Fig. S1). The color-coded elements **A**, **B**, and **C**, are extracted from the XMCD spectra's integrals and the sum of polarization-dependent XA spectra (**C**). We extract the projections ($m_s^{(z)}$ and $m_L^{(z)}$) of the intrinsic spin (m_s) and orbital (m_L) magnetic moments per atom onto the quantization axis by sum rule analysis. The quantization axis coincides with the magnetic field axis of the surrounding solenoid and the X-ray propagation direction. Under the given experimental conditions, a scaling of the molecule's total magnetic moment must be performed. Therefore, knowledge of all contributing magnetic centers' exact coupling is needed, which we do not know presently. Therefore, we omit such a scaling and present magnetizations at the given experimental conditions ($B= 5 \text{ T}$; $T= 4 \text{ K}, 10 \text{ K}, 20 \text{ K}$). The resulting XMCD spectra were analyzed with sum analysis^[67].

$$m_S^{(z)} = g_S \mu_B \frac{(A - bB)}{c \frac{3}{2} C} n_h - g_S \mu_B \frac{d}{c} \langle T_z \rangle \quad (4)$$

$$m_L^{(z)} = -g_L \mu_B \frac{A + B}{a \frac{3}{2} C} n_h \quad (5)$$

With n_h being the number of holes per Manganese atom in the final state, g_S and g_L the Landé factors for the electron spin and orbital angular momentum ($g_S = 2.0$, $g_L = 1$), μ_B the Bohr magneton and a , b , c , and d are the sum rule related prefactors. We anticipate the containing Mn^{2+} ions to be in a $3d^5$ high spin state and the Mn^{3+} ions in a $3d^4$ high spin state. Therefore, we chose the number of unoccupied valence orbitals n_h as $n_h = 5$ resp. 4 for species. The sum rule related prefactors are $1/2$, 2 , $2/3$, and $7/3$ for investigations on the Mn $L_{3,2}$ absorption edges.

8.5 Computational methods

Minimum energy structures with different multiplicities were calculated with Density Functional Theory (DFT) using the B3LYP^[68-70] functional and cc-pVTZ basis sets^[71-75] (C, H, N, O) in combination with the Stuttgart ecp effective core potential (Mn) with Gaussian 09^[76, 77]. Broken symmetry calculations were performed with the minimum structure with a multiplicity of 15 (cf. Tab. S1). For these calculations, we used similar modeling parameters as described above in a local, customized TURBOMOLE 7.0 program package^[78-80]. With the custom program CANOSSA^[81], localization of the anti-parallel, unpaired spins on each metal center in the complex is possible. Unfortunately, Gaussian does not separate the different spins into “spin up” and “spin down” electrons. It just locates the unpaired electrons in the investigated complex, which is mostly enough to explain certain data types. A broken symmetry state is constructed from a single determinant wave function that reflects the antiferromagnetic coupling. Structures with one “spin up” electron on atom A and one “spin down” electron on atom B exhibit positive (atom A) and negative (atom B) spin density regions. The orbitals in the broken symmetry states are optimized by applying the variational principle.

8.6 Results and Discussion

8.6.1 Collision Induced Dissociation (CID)

The overview mass spectrum reveals distinct masses in the area from 100 to 600 m/z (cf. Fig. S2 a)). Almost every peak can be assigned as fragments of the complex (cf. Tab. S2). Two mass peaks appear after isolation of the complex. The mass peak at 349 m/z belongs to the bare $[\text{Mn}_3(\text{Hcht})_2(\text{bipy})_4]^{3+}$ complex, and the small mass peak at 446 m/z belongs to a monocationic fragment with one perchlorate counter ion.

We investigate the relative gas phase stability of this complex after isolating the parent ion by recording Collision Induced Dissociation (CID) breakdown curves and their corresponding appearance curves of the associated fragments (cf. Fig. 2). The breakdown curves reveal the loss of one protonated bipyrimidyl ligand with a change of the charge from +3 to +2 as primary fragment at an excitation amplitude of 0.8 V. By increasing the fragmentation amplitude to 0.9-1.2 V, a protonated $[\text{Mn}^{2+}(\text{bipy})_2\text{H}]^{2+}$ unit is lost and a $[\text{Mn}^{2+}(\text{bipy})_2]^+$ unit appears as a fragmentation channel. All other fragments appear with high fragmentation amplitudes of 2 Volts (Tab. S3). We observe only primary fragmentation products without a MS^2 step in this complex.

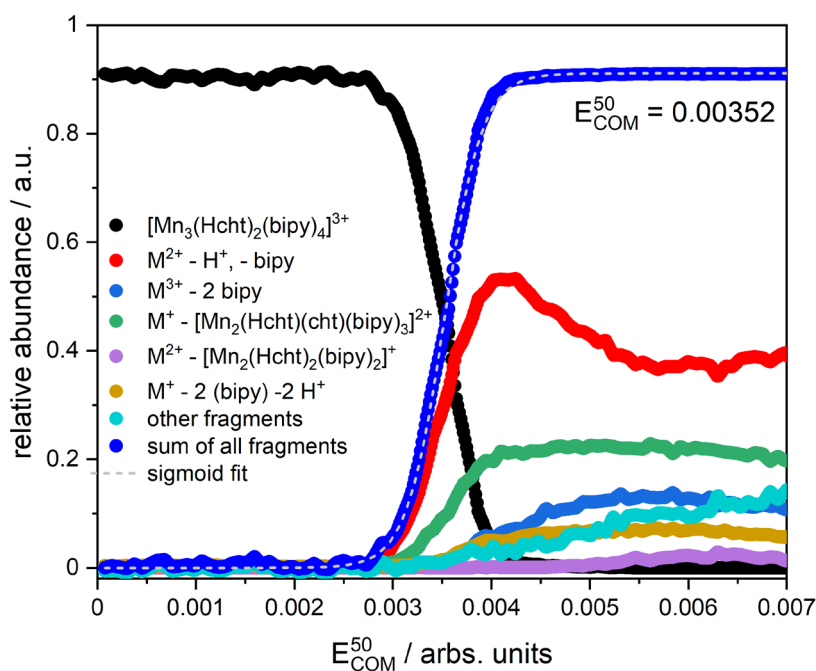


Fig. 2: CID breakdown curves of $[\text{Mn}_3(\text{Hcht})_2(\text{bipy})_4]^{3+}$ and appearance curves of the associated fragments.

The CID experiments point out that the complex is present in the sample solution and the trinuclear arrangement has an intense bonding situation, indicating that CID techniques cannot determine strong covalent or non covalent interactions in this complex.

Calculated covalent and non covalent interactions in the complex

Electron Field Localized (ELF) plots^[82] describe the covalent bonding situation of the Mn centers to the ligands (cf. Fig. S4). For the Mn²⁺ ions, the covalent bonding is very weak, and the influence of the ligands seems negligible. In the case of the Mn³⁺, we observe non spherical electron density. The covalent bondings from the ligand to the Mn²⁺ ions are stronger than the covalent bondings from the ligands to the Mn³⁺ ion (cf. Fig. 3). So-called non covalent interactions (NCI) represent weak van der Waals interactions in a complex. There are strong non covalent interactions between the Mn ions and the ligands. Besides the covalent interaction, non covalent interactions seem to play a significant role in this complex.

The Density Overlap Regions Indicator (DORI) compares the interplay of noncovalent and covalent interactions, indicating that both interactions are necessary for the stability in the complex. Also, these plots reveal that neither covalent nor non covalent interactions in the complex significantly influence the magnetism in this complex.

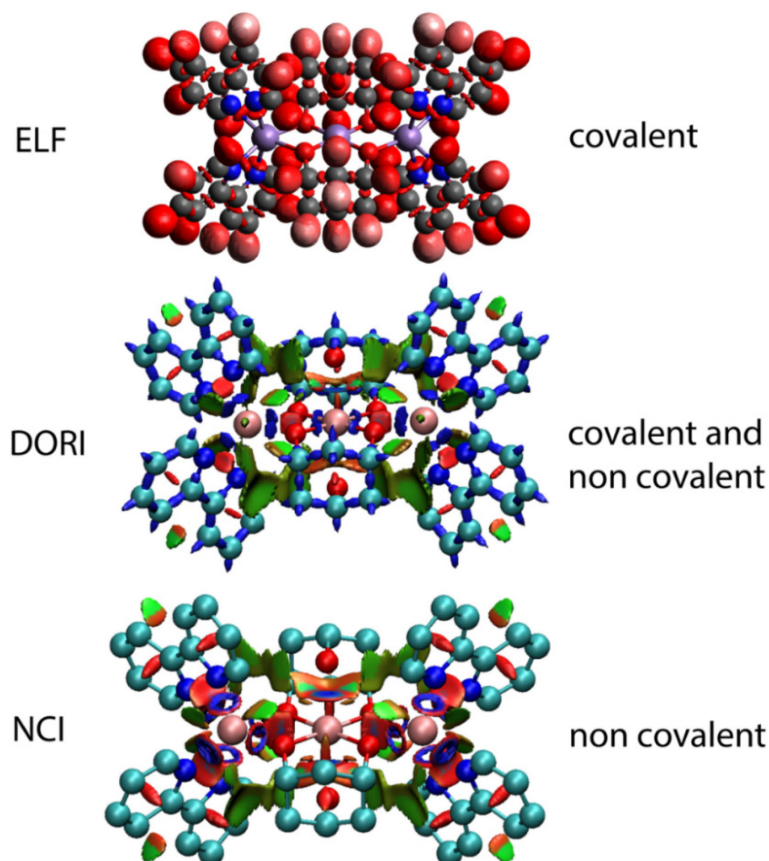


Fig. 3: Electron Field Localization (ELF), Density Orbital Region Indicator (DORI), and Non covalent Interaction (NCI) plots of $[\text{Mn}_3(\text{Hcht})_2(\text{bipy})_4]^{3+}$. The calculations were performed with Gaussian 09 at the B3LYP/cc-pVTZ (H, C, N, O) and Stuttgart ecp effective core potential (Mn) level of theory. Hydrogen is omitted for clarity.

Comparison of the experimental data from the CID experiments with the theoretical results

Weak interactions analysis of the complex points out strong non covalent interactions between the Hcht ligand and the bipyrimidyl ligands. Also, strong interactions between the Mn^{2+} ions and the μ -oxo bridged atoms are predicted. This is consistent with the fragmentation patterns observed. Because there are no covalent or noncovalent interactions between two bipyrimidyl ligands, losing a protonated bipyrimidyl ligand as the main fragmentation channel results in the weakest bonding in the complex. The collision energy overcomes the non covalent interactions with higher excitation amplitudes, and the complex starts its fragmentation by the loss of the two $[\text{Mn}^{2+}(\text{bipy})_2]^+$.

8.6.2 X-ray magnetic dichroism (XMCD)

The cations with the structure $[\text{Mn}_3(\text{Hcht})_2(\text{bipy})_4]^{3+}$ were created within the electrospray process and mass-selected at the mass of 349 m/z (cf. Fig. S5). We obtained the polarized dependent XA spectra and their corresponding XMCD spectra at different ion trap temperatures ($T = 4 \text{ K}$, 10 K , and 20 K) after selecting the complex and optimizing the fragments with X-ray light irradiation (cf. Fig. 4).

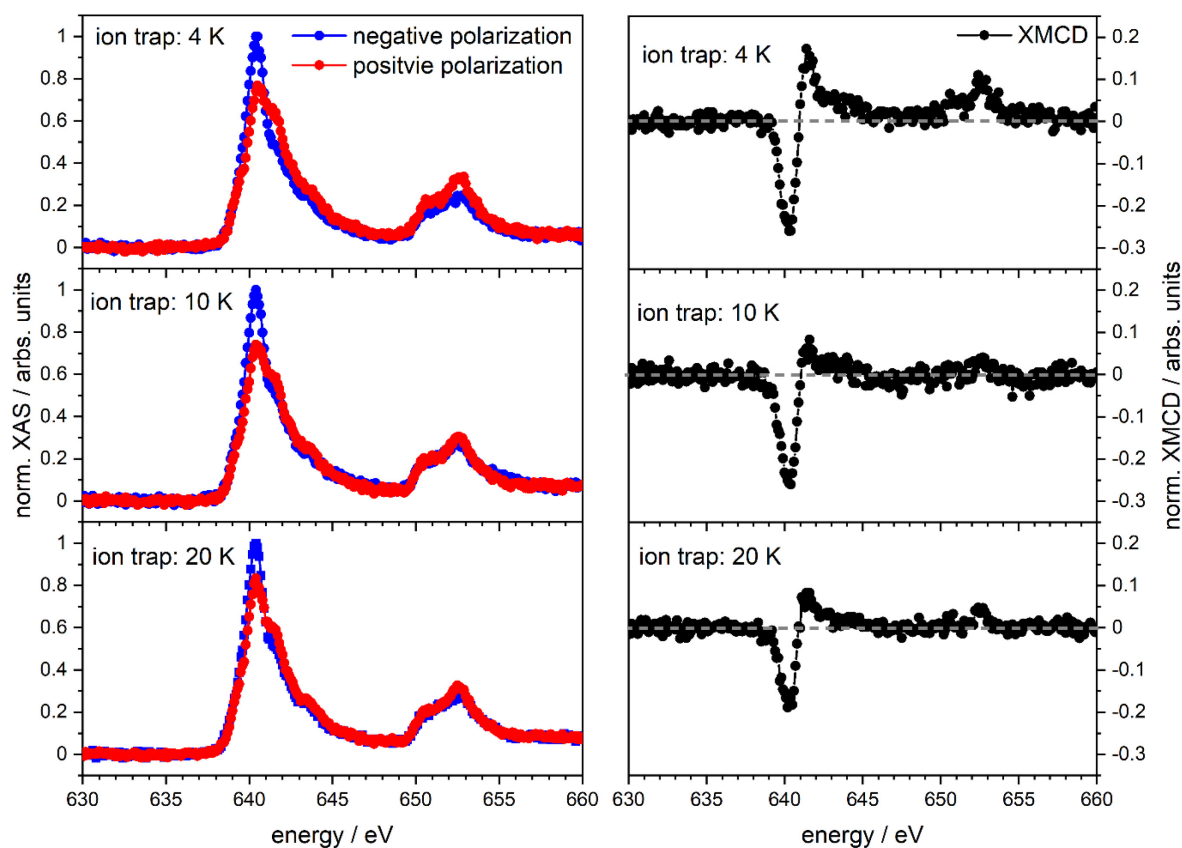


Fig. 4: polarized dependent XA spectra of $[\text{Mn}_3(\text{Hcht})_2(\text{bipy})_4]^{3+}$ (left) and their corresponding XMCD spectra (right) at different ion trap temperatures.

Polarized dependent XA spectra exhibit distinct spectral shapes at each temperature for negative and positive polarized spectra. We observe a dichroic effect for every temperature, but with higher temperatures, the dichroic effect decreases on both edges (cf. Fig. 4). XMCD spectra better visualize the decreasing dichroic effect as a function of the ion trap temperature (cf. Fig. 4). We observe a decreasing effect at the L_2 edge with rising ion trap temperature from 4 K to 10 K. After the effect at the L_2 edge is vanished, a decrease of the L_3 edge takes part from 10 K to 20 K, resulting in lower magnetic values due to minor dichroic effects at higher temperatures.

With the above described sum rule analysis, we obtain the average intrinsic magnetic moments per Manganese atom (cf. Tab. 1). We assume uncertainties of 5% for the presented magnetic values derivate from the sum rule analysis and consider the transition from the 2p core to a 3d valence state in the Mn atoms. The valence states are not always completely separated, resulting in inaccuracies in the magnetic moments determined by sum rule analysis, particularly for spin sum rule analysis^[88]. Teramura et al. developed correction factors for sum rule analysis based on atomic model systems as a result. They also involve the Coulomb interaction and the magnetic dipole operator expectation in the $L_{3,2}$ absorption edges, which is not accessible in our experiments^[83-88]. The suggested procedure of Teramura corrects the presented magnetizations in this work. By raising the temperature, we observe a decreasing trend for the spin magnetic moment in this complex. The magnetization slowly decreases with the temperature variation, as observed by the group of Brechin^[45].

Tab. 1: Experimental magnetic values projected on the z-axis for m_S , m_L , m_J , and m_L/m_S for $[\text{Mn}_3(\text{Hcht})_2(\text{bipy})_4]^{3+}$ at given temperatures and with the correction of 4.5%^[87, 88].

	exp.			corrected		
	4 K	10 K	20 K	4 K	10 K	20 K
$m_S^{(z)}$	0.88(4)	0.28(1)	0.22(1)	0.84(4)	0.27(1)	0.21(1)
$m_L^{(z)}$	0.27(1)	0.23(1)	0.03(1)	0.26(1)	0.22(1)	0.03(1)
$m_J^{(z)}$	1.15(5)	0.51(3)	0.25(1)	1.10(5)	0.49(2)	0.24(1)
$m_L^{(z)}/m_S^{(z)}$	0.31(2)	0.80(2)	0.12(2)	0.31(2)	0.82(2)	0.14(2)

At 4 K, we observe the highest spin magnetic and also angular orbital magnetic moments. The total spin magnetic moments reveal reduced values for every configuration, e.g., Mn^{2+} , Mn^{3+} or mixed valence (cf. Tab. 2). These values decrease as temperature rises, indicating a transition from a ferromagnetic coupling scheme to an antiferromagnetic coupling scheme caused by a spin flip on the Mn^{3+} ion. We assume that there must be an antiferromagnetic coupling between the Mn^{2+} ions and the Mn^{3+} ion, and that the antiferromagnetic coupling becomes more favorable at higher temperatures.

Tab. 2: Experimental total magnetic values of m_S for different oxidation states for the Manganese atoms in $[\text{Mn}_3(\text{Hcht})_2(\text{bipy})_4]^{3+}$ at given temperatures with a correction of 4.5% and in comparison, with the theoretically spin ground states.

	$S_{\text{exp.}}/\text{Mn}^{2+}$	$S(\text{Mn}^{2+})$	$S_{\text{exp.}}/\text{Mn}^{3+}$	$S(\text{Mn}^{3+})$	$S_{\text{exp.}}/(2\text{Mn}^{2+}+\text{Mn}^{3+})$	$S(2\text{Mn}^{2+}+\text{Mn}^{3+})$
4 K	2.20	2.5	1.76	2	6.16	7
10 K	0.63	2.5	0.56	2	1.96	7
20K	0.55	2.5	0.44	2	1.54	7

Theoretical calculations of the electronics and simulation of the XA spectra

To determine the absorption bands for the various oxidation states of Manganese atoms and their corresponding excited core orbitals, we used a projected Density of States (pDOS) calculation to get a better approximation of the involved transitions in the XA spectra (cf. Fig. 5). At slightly higher absorption energies with less intensity, the L_3 absorption edge reveals a small shoulder. In comparison with the pDOS spectra, we observe the p_y orbital excitation into a valence shell for the Mn^{2+} ions at lower absorption energies and the p_z orbital excitation into the valence shell for the Mn^{3+} ion at higher absorption energies.

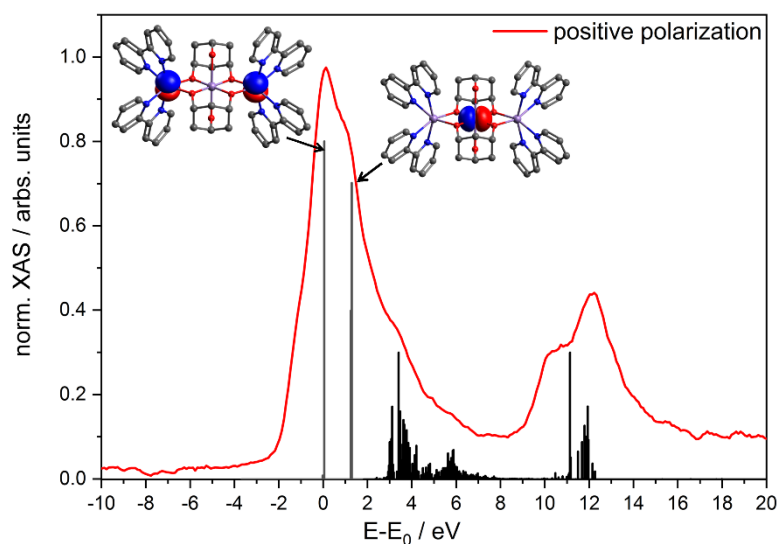


Fig. 5: Calculated density of states spectrum and experimental positively polarized XA spectrum of $[\text{Mn}_3(\text{Hcht})_2(\text{bipy})_4]^{3+}$. The calculations were performed with Gaussian 09 at the B3LYP/cc-pVTZ (H, C, N, O) and Stuttgart ecp effective core potential (Mn) level of theory.

The calculated orbital energies with -63.56 eV for the Mn^{2+} ions and -65.78 eV for the Mn^{3+} are slightly different. Assuming the same energy levels for the d orbitals, more energy is

required for core electron excitation into the valence-shell, resulting in higher absorption energies. We assume that the Jahn Teller distortion leads to a p_z orbital rise at Mn^{3+} . The lowest p orbital is the p_y orbital. In Mn^{2+} , the Jahn Teller distortion is low, and excitation from the core electron into the valence-shell occurs via the p_z orbital (cf. Fig. 5). To better visualize the influence of the different oxidation states in the XA spectra, we convoluted the first derivation of the experimental XA spectra. First of all, negative and positive polarized spectra do not feature a change in their spectral shape by varying their temperature. The XA spectra only reveal a change in their spectral features by switching from negative circular polarized photons to positive circular polarized photons (cf. Fig. 6a)). There are features at 642 eV and 653 eV in the positive polarized XA spectra that do not appear in the negative polarized ones, indicating polarized dependent absorption for the different oxidation states in the Manganese atoms in this complex.

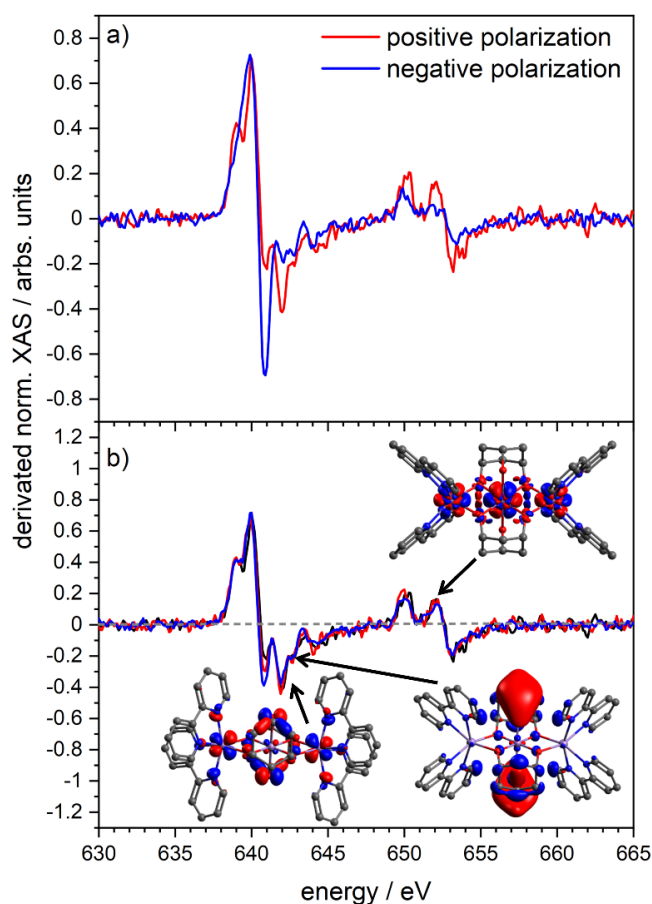


Fig. 6: First derivation of the experimental polarized dependent XA spectra of $[Mn_3(Hcht)_2(bipy)_4]^{3+}$ at different temperatures in comparison with pDOS calculated transition orbitals. The calculations were performed with Gaussian 09 at the B3LYP/cc-pVTZ (H, C, N, O) and Stuttgart ecp effective core potential (Mn) level of theory

Compared with the pDOS calculation and their resulting orbitals, the features at 642 eV and 653 eV belong to the absorption of the Mn²⁺ ions with the Mn³⁺ ion together (cf. Fig. 6b)). The calculated orbitals feature a pure Mn³⁺ absorption at both absorption edges, as expected. In the core-level spectroscopy theory, a positively polarized X-ray beam leads mainly to an excitation of a “spin up” electron into the valence shell. This is impossible with the Pauli rules if every d orbital is occupied with electrons in the same spin state as Mn²⁺. Therefore, the small amount of excited “spin down” electrons into the valence shell leads to the absorption of the Mn²⁺ ions in the complex. The “spin up” electrons only can be absorbed by the empty valence shell in the Mn³⁺ ion.

Determination of the crystal field splittings on the different oxidation states

To determine the crystal field splittings in the Mn centers, we performed simulations of the Mn²⁺ and Mn³⁺ ions and compared them with both polarized XA spectra (cf. Fig. S10). For the first assumption, the simulations do not include crystal field splitting to determine which peaks on the absorption edges belong to the Mn²⁺ and Mn³⁺ cores. Positive polarized XA spectra provide the most information, and the main L₃ edge and L₂ edge clearly belong to the Mn²⁺ ion and the shoulder at the L₃ edge, therefore, belongs to the Mn³⁺ edge. Because of the overlap of the Mn²⁺ ions, the composition of two Mn²⁺ ions and one Mn³⁺ ion causes a slight change in the spectral shape of the XA spectra. Simulation of Mn²⁺ fits well with the experimental negative polarized XA spectra, pointing out that the ligand system does not affect the Mn²⁺ ion strongly. In the Mn³⁺ ion, the spectra fit not well at around 638 eV - 645 eV. This designates that the ligands have more influence on the spectra than with Mn²⁺. The shifts at 640 eV absorption edges are in good agreement with the experimental XA spectra.

Natural Bond Order (NBO) analysis reveals geometrical distortions on every Manganese center (cf. Fig. S9). The Mn³⁺ center in the middle of the linear arrangement has a strong distortion in the z-direction, resulting in a higher energy gap between the d_z² orbital and the d_{x²-y²} orbital. Therefore, the strong distortion of the Mn³⁺ must lead to the angular orbital momentum. The Mn²⁺ ions have a minor Jahn Teller distortion in all dimensions, leading to a slight increase in the energy of the d_z² orbital, resulting in a minor change in the octahedral crystal field splitting of Mn²⁺. Also, minor distortions at the Mn²⁺ ions result in a more spherical electron density with an angular orbital momentum of zero. Orbital energies reveal different energy levels for

the d orbitals (cf. Fig. 7). As mentioned above, the Mn^{3+} ion in the complex has a higher orbital splitting than the Mn^{2+} ions. A closer examination of the orbitals reveals that the energies for the d_{xz} orbitals for all Mn centers in different oxidation states are nearly identical. Also, the d_{xy} orbital could couple with each other, but the energy difference is higher than the d_{xz} orbitals. So, the main overlap of these orbitals should be the d_{xz} orbitals.

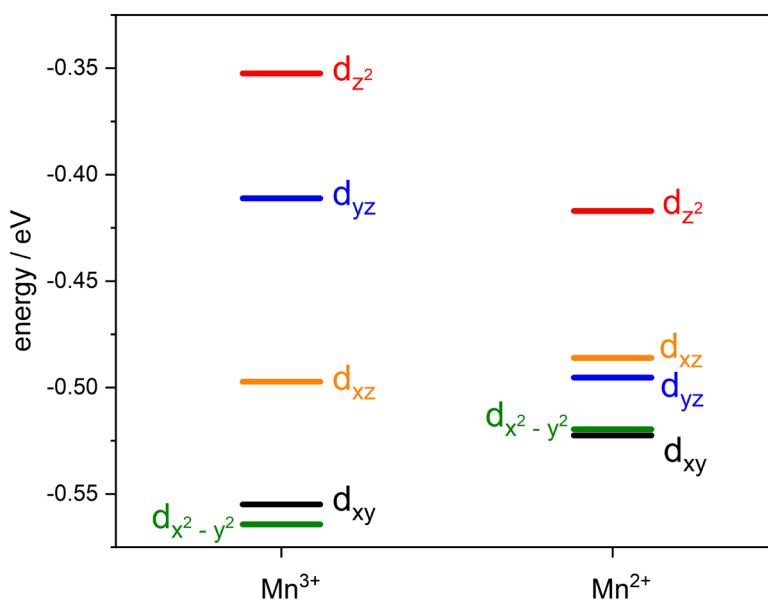


Fig. 7: Calculated energies of the d orbitals of $[\text{Mn}_3(\text{Hcht})_2(\text{bipy})_4]^{3+}$. The calculations were performed with Gaussian 09 at the B3LYP/cc-pVTZ (H, C, N, O) and Stuttgart ecp effective core potential (Mn) level of theory.

The experimental crystal field splittings for the Mn centers reveal a higher crystal field splitting for Mn^{3+} (2.10 eV) than for Mn^{2+} (1.15 eV) (cf. Fig. S11) and is in good agreement with the observed Jahn Teller distortions. For the Mn^{3+} ion, the Jahn Teller distortion leads to a high lying d_{z^2} orbital and a low lying $d_{x^2-y^2}$ orbital. In the case of Mn^{2+} ion, the electron density is more spherical, and therefore the Jahn Teller distortion is minor than in the Mn^{3+} case.

With the experimental crystal field splittings, further simulations were performed for better agreement between simulation and experiment. Simulations with the experimental crystal field splittings reveal a better agreement with experimental XA spectra. The simulation of the Mn^{2+} ion appears to be a little broader than the experimental spectra, but all of the spectral features are present and match the experimental spectra very well (cf. Fig. 8). Also, the Mn^{3+} simulation fits better with the experimental spectra. Therefore, the approximation of the crystal field splittings seems to be conclusive with the Jahn Teller distortions of Mn^{3+} ion in

this complex. Furthermore, the smaller crystal field splitting for Mn^{2+} than for Mn^{3+} is consistent with the fact that the electron density of Mn^{2+} is more spherical than that of Mn^{3+} , resulting in smaller crystal field splittings.

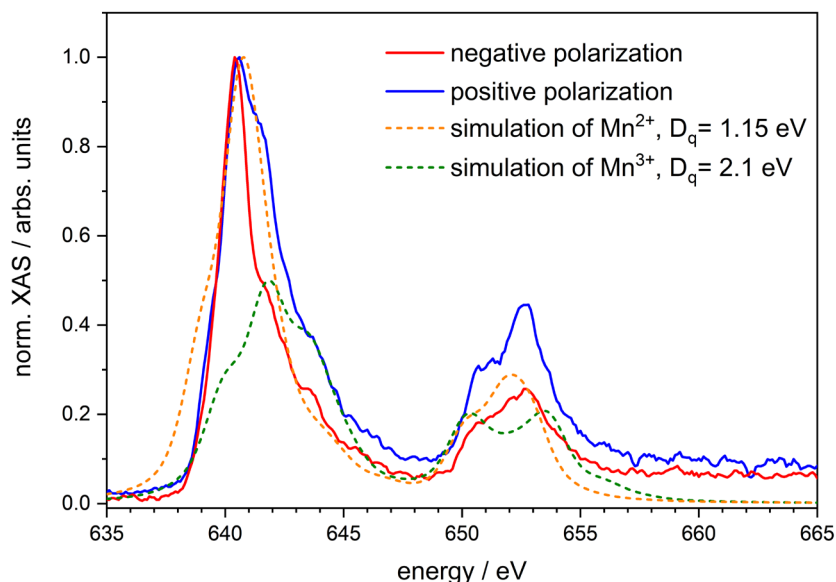


Fig. 8: Polarized dependent XAS spectra of $[\text{Mn}_3(\text{Hcht})_2(\text{bipy})_4]^{3+}$ in blue and red for the positive and negative polarization at 4 K in comparison with gauss folded (broadening 0.2) simulated XAS spectra of an Mn^{2+} atom in orange and Mn^{3+} atom in green with octahedral coordination ($\text{Mn}^{2+} = 1.15$ eV, $\text{Mn}^{3+} = 2.10$ eV). CTM4XAS performed simulated spectra with Cowan batch files^[89].

The first derivation also reveals a higher energy difference at the L_3 edge by changing the polarization (cf. Fig. S12). With the above described absorptions, these broader energy shifts occur by mixing two different oxidation states in an amount of 2:1, and results in a distinct influence of the crystal field splittings as for the negative polarized ones. Also, the absorption energy shifts to lower energies by raising the temperature. We consider a “spin flip” from “spin up” in cold conditions and “spin down” in warmer conditions, leading to smaller bonding distances and shift to lower energies in the XAS spectra absorption edges.

Determination of the Spin orbit couplings in the complex

The difference between the L_2 edge and the L_3 edge represents the spin-orbit coupling of the core electron into the valence shell. The Spin-orbit coupling for the Mn^{2+} ion is higher than for the Mn^{3+} ion (cf. Fig. S13) because Mn^{2+} does not have an orbital momentum by cause of its spherical and more compact spin density. Therefore, more energy is needed to induce a spin-orbit coupling. The Mn^{3+} itself obtains a spin-orbit coupling, and therefore, less energy is

required to generate a spin-orbit coupling from the core electron to the valence-shell. Branching ratio analysis makes it possible to calculate approximated spin-orbit coupling constants of the metal center itself.

We analyzed the spin-orbit sum rule because of the strong core-valence interaction described above [90-92]. This method yields very accurate values for the spin-orbit interactions per hole. For p → d transitions, the branching ratio is defined as

$$BR = \frac{I(L_3)}{I(L_3) + I(L_2)} \quad (4)$$

Where I are the intensities of the transition metal edges. The sum rule [78, 90-92] gives the relation for the spin-orbit interactions per hole

$$SOC = n_{j_2} - \frac{l+1}{l} n_{j_1} \quad (5)$$

n_{j_1} and n_{j_2} represent the occupation number per hole, where $j_1 = l - 0.5$ and $j_2 = l + 0.5$. At least the branching ratio without a spin-orbit interaction can be derived with

$$B = B_0 - \frac{c}{2c+1} \frac{SOC}{n_h} \quad (6)$$

B_0 is the branching ratio without spin-orbit interactions, $\frac{c}{2c+1}$ is a statistical value, and for d^5 it is $\frac{2}{5}$ and n_h represent the holes in the valence shell^[93].

Tab. 3: Branching ratio values with spin-orbit interaction (BR), terms of occupation numbers (n_{j_1} , n_{j_2}), spin-orbit expectation (SOC), branching ratio without spin-orbit interaction (B_0), and the difference of the branching ratios (ΔB)

T / K	BR	statistical value	n_{j_1}	n_{j_2}	SOC	B_0	ΔB
4	0.77	0.60	-0.23	0.77	-3.85(2)	0.31	0.46
10	0.78	0.60	-0.27	0.73	-4.17(2)	0.27	0.51
20	0.78	0.60	-0.47	0.53	-18.67(10)	-1.46	2.24

The branching ratios for the different temperatures are almost equal for every temperature. As a result, the ligands have no effect on the spin-orbit couplings or the resulting magnetic moments. The magnetic properties arise from the intrinsic orbital and spin arrangement in the Manganese centers. The calculated spin-orbit coupling constants point out a downward

trend to lower values, implying that the Mn ions have a stronger antiferromagnetic coupling at higher temperatures. The spin-orbit coupling constant cannot be determined at the highest temperature of 20 K. The deviation of the spin-orbit coupling is strongly dependent (eq. 5) on the angular orbital momentum. At 20 K, almost no angular orbital momentum is present to apply branching ratio analysis, resulting in inaccuracies in determining the spin-orbit coupling. Assuming an antiferromagnetic exchange coupling, the spin orbit coupling must be lower than in ferromagnetically coupled systems.

Broken symmetry calculations

We assume a change in the exchange coupling scheme as a result of the XMCD experiments' reduced spin magnetic and orbital magnetic moments, which do not result from structural changes in the complex caused by temperature variation. Therefore, we performed quantum chemical calculations with the broken symmetry approach. The analyses reveal similar energies for the ferromagnetic coupled (UUU) and the antiferromagnetic coupled (DUU, UDU, UUD) complex (cf. Fig. 9) with an uncertainty of 5 kJ/mol.

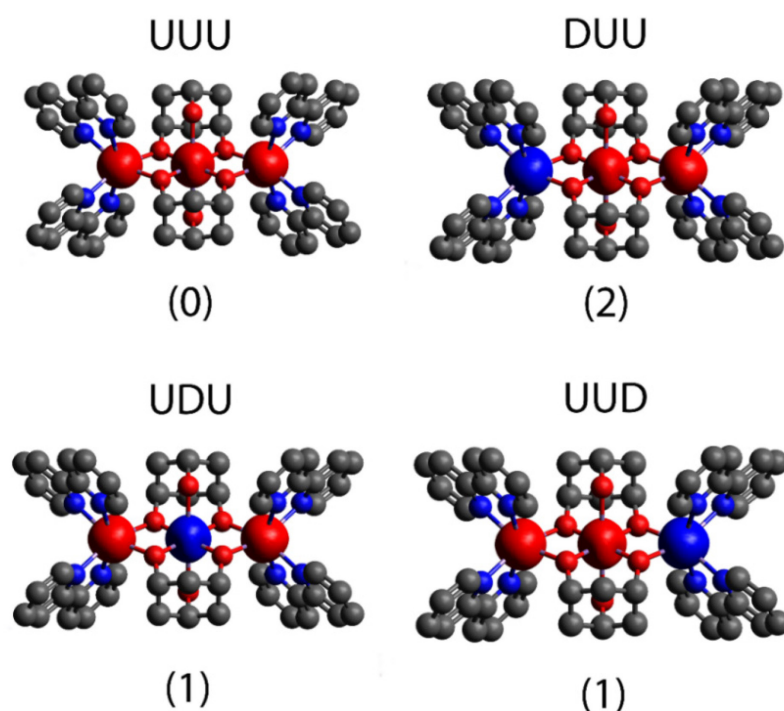


Fig. 9: Spin density isosurfaces (Iso = 0.01) of $[\text{Mn}_3(\text{Hcht})_2(\text{bipy})_4]^{3+}$ in one ferromagnetic and the three broken symmetry configurations. red and blue surfaces indicate alpha and beta spin, respectively. The relative energies in paratheses are given in kJ/mol. The calculations were performed at the B3LYP_Gaussian/cc-pVTZ (H, C, N, O) and Stuttgart 1997 ECP (Mn) level of theory.

The different coupling constants of the metal centers in the complex can be calculated using the broken symmetry calculated energies from these structures. A positive coupling constant represents a ferromagnetic coupling scheme, and a negative coupling constant represents antiferromagnetic coupling schemes. J_1 and J_2 represent the coupling constants for the Mn^{2+} ions, and J_3 is the coupling constant for Mn^{3+} . Every assumption from pure Mn^{2+} to pure Mn^{3+} or a mixed-valence configuration shows the same trend (cf. Tab. 4). The calculations show that J_1 has a varying coupling constant, J_2 has a constant value, and J_3 has a negative value in all cases. J_2 has a constant coupling constant for the different oxidation states but does not have an exchange coupling between one Mn^{2+} ion and the central Mn^{3+} ion. The other coupling constants, J_1 and J_3 , vary with oxidation state, implying an exchange coupling between one Mn^{2+} ion and one Mn^{3+} ion. A calculated mixed-valence state reveals enhanced coupling constants for both Manganese centers. Mn^{3+} has the lowest antiferromagnetic coupling in this complex series, which is not achieved by metals in the same oxidation states. Total coupling constant calculations also reveal the highest value for the mixed valence complex for better visualization, indicating that antiferromagnetic exchange is very weak in this complex.

Tab. 4: Calculated coupling constants of each electron and their total coupling constants of $[Mn_3(Hcht)_2(bipy)_4]^{3+}$.

	J_1/cm^{-1}	J_2/cm^{-1}	J_3/cm^{-1}	J_{total}/cm^{-1}	J^*/cm^{-1}	J/J^*
Mn^{2+}	7.14	2.11	-1.52	7.73	-1.52	-3.04
Mn^{3+}	6.08	2.11	-2.37	5.83	-2.37	-1.73
$Mn^{2+/3+}$	9.01	2.11	-0.93	10.20	-0.93	-6.01

The calculated anisotropic tensors for the different spin configurations reveal the highest tensor for the UUU (195.11) configuration and the lowest tensor for the UDU (194.80) configuration (cf. Fig. S15). We consider that the complex with a UUD/DUU configuration can be excluded because the one Mn^{2+} seems not to participate in the exchange coupling and the higher anisotropic tensor from the calculations, suggesting a “spin flip” from cold conditions to warmer conditions resulting from a ferromagnetic exchange coupling to an antiferromagnetic coupling. Raising the temperature causes a reduction in spin orientation due to rising entropic effects, resulting in tunneling processes and antiferromagnetic exchange coupling of the different oriented spins from the Mn^{2+} and Mn^{3+} ions. Lower temperatures

reduce entropy and increase the possibility of the spins orientation into a UUU configuration, resulting in fewer tunneling processes and a long-living magnetism.

Comparison of the experimental and calculated coupling schemes

By increasing the temperature, we observe lower spin orbit couplings via branching ratio analysis, assuming a stronger antiferromagnetic exchange coupling in warmer conditions. This is in good agreement with the experimental magnetic values, decreasing with rising temperature (cf. Tab. 5).

Tab. 5: Comparison of the Branching ratio analysis spin orbit couplings, experimental magnetic moments, and total magnetic moments in the complex.

	4 K	10 K	20 K
$m_S^{(z)}$	0.88	0.28	0.22
$m_L^{(z)}$	0.27	0.23	0.03
$m_J^{(z)}$	1.15	0.51	0.25
S	6.16	1.96	1.54
L	0.27	0.23	0.03
J	6.43	2.19	1.57
SOC	-3.85	-4.17	-18.67

The broken symmetry calculated coupling constants also reveal an antiferromagnetic exchange coupling for one Mn^{2+} and the central Mn^{3+} ion, so the spin orbit coupling from the branching ratio analysis points out a weak antiferromagnetic exchange coupling because of the reduced spin and orbital magnetic moments, which gains more favorably with higher temperatures. The spin magnetic values do not change drastically from 10 K to 20 K, agreeing with the broken symmetry calculated coupling constants for the Mn ions. In the calculations, one Mn^{2+} ion does couple with the other metal ions by cause of the constant coupling constants, resulting in a ferromagnetic proportion in this complex. The experimental magnetic moments represent a ferromagnetic exchange coupling for cold conditions. In warmer conditions, these values seem to represent a spin magnetic reduced value without an orbital magnetic momentum, which can only occur from a ferromagnetic coupled Mn^{2+} due to the spherical electron distribution.

XMCD UV/VIS correlation

With the experimental crystal field splittings and the normalization with the Racah parameter $B^{[94]}$, we are able to approximate the Manganese centered absorption band in the UV spectra. By putting the data into the Tanabe Sugano diagram, we may identify the ground state and its matching excited state (cf. Fig. S16). With this approximation, the Mn^{2+} ion reveals an excitation from a ${}^6A_{1g}$ state to a ${}^4T_{1g}$ with the corresponding normalized absorption energy of 15.66. The Mn^{3+} ion instead has an excitation from the 5E_g to a ${}^3T_{1g}$ state with the normalized energy of 9.68. This implies that the absorption energy of a metal-centered transition in the UV/VIS spectra should be at a lower wavelength for the Mn^{2+} ions in the complex than for the Mn^{3+} ion. We anticipate an absorption band for the Mn^{2+} ion and no absorption band for the Mn^{3+} ion using the Tanabe-Sugano diagram approximation and renormalization of the absorption energy with the particular Racah parameter $B^{[103]}$.

Tab. 9: Normalized crystal field splittings from the XA spectra, normalized absorption energies from the Tanabe-Sugano diagram, and renormalized wavelength for $[Mn_3(Hcht)_2(bipy)_4]^{3+}$.

	E/B (exp)	E/cm⁻¹ (TS)	E/nm (TS)
Mn^{2+}	9.68	24605	406
Mn^{3+}	15.66	12483	801

To confirm this assumption, we computed the UV spectra of this compound and found a strong band at 414 nm that matches the anticipated Mn^{2+} absorption band (cf. Fig. 10). The absorption band can be determined to MLCT transitions of the Mn^{2+} ions into the bipyrimidyl ligands.

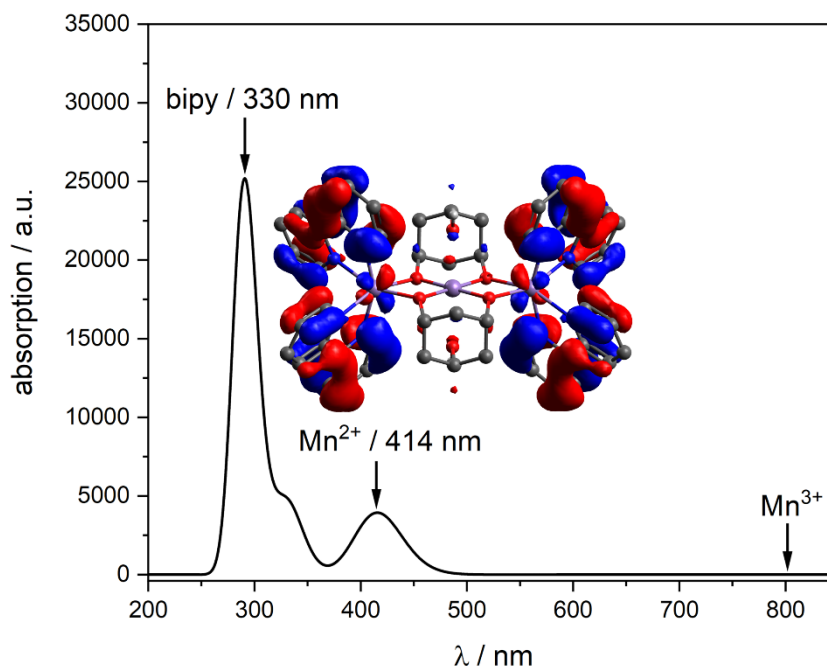


Fig. 10: Calculated UV/VIS spectrum of $[\text{Mn}_3(\text{Hcht})_2(\text{bipy})_4]^{3+}$ with 100 calculated excited states. The calculations were performed at the TD-DFT/UB3LYP/cc-pVTZ (H, C, N, O) and Stuttgart 1997 ECP (Mn) level of theory.

8.7 Conclusion

In the presented work, we investigate the bonding situation of the complex with the structure $[\text{Mn}_3(\text{Hcht})_2(\text{bipy})_4]^{3+}$ via mass spectrometry and CID. We observe the loss of one protonated bipyrimidyl ligand as the main fragmentation channel. Also, no secondary fragmentation appears in the mass spectrum. There is no Hcht ligand loss detected, indicating a strong bonding state. The reduction of the complex via ETD leads to a mono cationic fragment by losing two bipyrimidyl ligands. Calculations of weak interactions reveal more vital non covalent interactions between the Hcht ligand and the bipyrimidyl ligands. Furthermore, significant noncovalent interactions between the Hcht ligand and the Mn^{3+} ion do not result in Hcht ligand loss.

Temperature dependent XMCD spectra of the complex were recorded in gas phase at 4 K, 10 K, and 20 K. The dichroic effect decreases with rising temperature, suggesting a switch from a ferromagnetic exchange coupled system at 4 K to an antiferromagnetic exchange coupled system at 20 K.

The projected density of states illustrates the influence of the Mn^{3+} ion in the complex. The determination of transition orbitals is achievable, indicating that the characteristics of the XA spectra correspond to the Mn^{3+} ion complex in the positive polarized XA spectra. The determined orbitals also show an excitation of the Mn^{2+} ion because of a small amount of excited “spin down” electrons from the core-shell into the valence shell.

Experimental crystal field splittings reveal a higher splitting for the Mn^{3+} than for the Mn^{2+} ions. XA simulations with the applied crystal field splittings agree with the experimental XA spectra. Also, the NBO analysis reveals higher ligand field splittings for the d orbitals in the Mn^{3+} than for the Mn^{2+} .

Branching ratio analysis reveals decreasing values by raising the temperature, hinting a weak antiferromagnetic exchange coupling constant at lower temperatures and a stronger ferromagnetic exchange coupling at higher temperatures.

Broken symmetry calculations reveal an antiferromagnetic coupled Mn^{3+} to one ferromagnetic coupled Mn^{2+} . Also, the other Mn^{2+*} seems not to be influenced by the Mn^{3+} ion. An enhancement of the coupling constant in the mixed-valence system is observed, which is not given all Manganese centers in the same oxidation state. The calculated anisotropic barriers for the different spin configurations reveal the highest anisotropy with a UUU configuration and the lowest anisotropic barrier for the UDU configuration, suggesting a single molecule magnetic behavior if the UUU configuration is established in cold conditions.

In summary, we have shown that gas-phase XMCD investigations add valuable additional insight into single molecule magnets' fascinating magnetic properties.

8.8 Acknowledgment

The German research foundation DFG supported this work within the transregional collaborative research center SFB/TRR 88 “Cooperative effects in homo and heterometallic complexes” (3MET) and by the state research center OPTIMAS.

8.9 References

- [1] M. Frezza, S. Hindo, D. Chen, A. Davenport, S. Schmitt, D. Tomco, and Q. P. Dou, Novel metals and metal complexes as platforms for cancer therapy, *Curr Pharm Des*, 16, 1813-1825, 2010.
- [2] U. Ndagi, N. Mhlongo, and M. E. Soliman, Metal complexes in cancer therapy - an update from drug design perspective, *Drug Des Devel Ther*, 11, 599-616, 2017.
- [3] A. T. Odularu, P. A. Ajibade, J. Z. Mbese, and O. O. Oyedeji, Developments in Platinum-Group Metals as Dual Antibacterial and Anticancer Agents, *J. Chem.*, 2019, 5459461, 2019.
- [4] R. Wai-Yin Sun, D.-L. Ma, E. L.-M. Wong, and C.-M. Che, Some uses of transition metal complexes as anti-cancer and anti-HIV agents, *Dalt. Trans.*, 4884-4892, 2007.
- [5] P. Zhang, and P. J. Sadler, Redox-Active Metal Complexes for Anticancer Therapy, *Europ. J. Inorg. Chem.*, 2017, 1541-1548, 2017.
- [6] C. D. Falk, and J. J. Mooney, "Three-Way Conversion Catalysts: Effect of Closed-Loop Feed-Back Control and Other Parameters on Catalyst Efficiency," 1980.
- [7] J. Kalinowski, V. Fattori, M. Cocchi, and J. Williams, Light-emitting devices based on organometallic platinum complexes as emitters, *Coord. Chem. Rev.*, 255, 2401-2425, 2011.
- [8] B. Ozdemir, and V. Barone, Thickness dependence of solar cell efficiency in transition metal dichalcogenides MX₂ (M: Mo, W; X: S, Se, Te), *Solar Energy Materials and Solar Cells*, 212, 110557, 2020.
- [9] H. Yersin, A. F. Rausch, R. Czerwieniec, T. Hofbeck, and T. Fischer, The triplet state of organo-transition metal compounds. Triplet harvesting and singlet harvesting for efficient OLEDs, *Coord. Chem. Rev.*, 255, 2622-2652, 2011.
- [10] H. Kumobayashi, Industrial application of asymmetric reactions catalyzed by BINAP-metal complexes, *Recueil des Travaux Chimiques des Pays-Bas*, 115, 201-210, 1996.
- [11] K. Matyjaszewski, Atom Transfer Radical Polymerization (ATRP): Current Status and Future Perspectives, *Macromolecules*, 45, 4015-4039, 2012.
- [12] K. Schröder, D. Konkolewicz, R. Poli, and K. Matyjaszewski, Formation and Possible Reactions of Organometallic Intermediates with Active Copper(I) Catalysts in ATRP, *Organometallics*, 31, 7994-7999, 2012.
- [13] Y. Garcia, P. J. van Koningsbruggen, E. Codjovi, R. Lapouyade, O. Kahn, and L. Rabardel, Non-classical FeII spin-crossover behaviour leading to an unprecedented extremely large apparent thermal hysteresis of 270 K: application for displays, *Journal of Materials Chemistry*, 7, 857-858, 1997.
- [14] P. Gütllich, Y. Garcia, and H. A. Goodwin, Spin crossover phenomena in Fe(I) complexes, *Chem. Soc. Rev.*, 29, 419-427, 2000.
- [15] H.-J. Krüger, Spin transition in octahedral metal complexes containing tetraazamacrocyclic ligands, *Coord. Chem. Rev.*, 253, 2450-2459, 2009.
- [16] V. Niel, J. M. Martinez-Agudo, M. C. Muñoz, A. B. Gaspar, and J. A. Real, Cooperative Spin Crossover Behavior in Cyanide-Bridged Fe(II)-M(II) Bimetallic 3D Hofmann-like Networks (M = Ni, Pd, and Pt), *Inorg. Chem.*, 40, 3838-3839, 2001.
- [17] M. Schmitz, M. Seibel, H. Kelm, S. Demeshko, F. Meyer, and H.-J. Krüger, How Does a Coordinated Radical Ligand Affect the Spin Crossover Properties in an Octahedral Iron(II) Complex?, *Angew. Chem. Int. Ed.*, 53, 5988-5992, 2014.
- [18] J. Dreiser, K. S. Pedersen, A. Schnegg, K. Holldack, J. Nehr Korn, M. Sigrist, P. Tregenna-Piggott, H. Mutka, H. Weihe, V. S. Mironov, J. Bendix, and O. Waldmann, Three-Axis Anisotropic Exchange Coupling in the Single-Molecule Magnets NEt₄[MnIII₂(5-Brsalen)₂(MeOH)₂MIII(CN)₆] (M=Ru, Os), *Chemistry – A European Journal*, 19, 3693-3701, 2013.
- [19] B. Kintzel, M. Böhme, J. Liu, A. Burkhardt, J. Mrozek, A. Buchholz, A. Ardavan, and W. Plass, Molecular electronic spin qubits from a spin-frustrated trinuclear copper complex, *Chemical Communications*, 54, 12934-12937, 2018.
- [20] T. Lis, Preparation, structure, and magnetic properties of a dodecanuclear mixed-valence manganese carboxylate, *Acta Crystallographica Section B*, 36, 2042-2046, 1980.
- [21] A. V. Pali, S. M. Ostrovsky, S. I. Klokishner, B. S. Tsukerblat, C. P. Berlinguette, K. R. Dunbar, and J. R. Galán-Mascarós, Role of the Orbitally Degenerate Mn(III) Ions in the Single-Molecule Magnet Behavior of the Cyanide Cluster {[MnII(tmphen)₂]₃[MnIII(CN)₆]₂} (tmphen = 3,4,7,8-tetramethyl-1,10-phenanthroline), *J. Am. Chem. Soc.*, 126, 16860-16867, 2004.

8. Temperature dependent X-ray magnetic circular dichroic studies of a trinuclear Manganese SMM complex in isolation

- [22] R. W. volume editor, and G. A. with contributions by, *Single-molecule magnets and related phenomena*: Berlin ; New York : Springer, [2006] ©2006, 2006.
- [23] G. Aromí, D. Aguilà, P. Gamez, F. Luis, and O. Roubeau, Design of magnetic coordination complexes for quantum computing, *Chem. Soc. Rev.*, 41, 537-546, 2012.
- [24] M. N. Leuenberger, and D. Loss, Quantum computing in molecular magnets, *Nature*, 410, 789-793, 2001.
- [25] M. Mannini, F. Pineider, P. Sainctavit, C. Danieli, E. Otero, C. Sciancalepore, A. M. Talarico, M.-A. Arrio, A. Cornia, D. Gatteschi, and R. Sessoli, Magnetic memory of a single-molecule quantum magnet wired to a gold surface, *Nature Materials*, 8, 194-197, 2009.
- [26] K. V. Raman, A. M. Kamerbeek, A. Mukherjee, N. Atodiresei, T. K. Sen, P. Lazić, V. Caciuc, R. Michel, D. Stalke, S. K. Mandal, S. Blügel, M. Münzenberg, and J. S. Moodera, Interface-engineered templates for molecular spin memory devices, *Nature*, 493, 509-513, 2013.
- [27] J. M. Clemente-Juan, E. Coronado, A. Forment-Aliaga, A. Gaita-Ariño, C. Giménez-Saiz, F. M. Romero, W. Wernsdorfer, R. Biagi, and V. Corradini, Electronic and Magnetic Study of Polycationic Mn₁₂ Single-Molecule Magnets with a Ground Spin State S = 11, *Inorg. Chem.*, 49, 386-396, 2010.
- [28] K. Kim, A. Ford, V. Meenakshi, W. Teizer, H. Zhao, and K. R. Dunbar, Nanopatterning of Mn₁₂-acetate single-molecule magnet films, *J. Appl. Phys.*, 102, 094306, 2007.
- [29] M. Mannini, F. Pineider, P. Sainctavit, L. Joly, A. Fraile-Rodríguez, M.-A. Arrio, C. Cartier dit Moulin, W. Wernsdorfer, A. Cornia, D. Gatteschi, and R. Sessoli, X-Ray Magnetic Circular Dichroism Picks out Single-Molecule Magnets Suitable for Nanodevices, *Advanced Materials*, 21, 167-171, 2009.
- [30] K. M. Mertes, Y. Suzuki, M. P. Sarachik, Y. Myasoedov, H. Shtrikman, E. Zeldov, E. M. Rumberger, D. N. Hendrickson, and G. Christou, Mn₁₂-acetate: a prototypical single molecule magnet, *Solid State Comm.*, 127, 131-139, 2003.
- [31] J. A. A. J. Perenboom, J. S. Brooks, S. Hill, T. Hathaway, and N. S. Dalal, Relaxation of the magnetization of Mn_{12} acetate, *Phys. Rev. B*, 58, 330-338, 1998.
- [32] G. Rogez, B. Donnio, E. Terazzi, J.-L. Gallani, J.-P. Kappler, J.-P. Bucher, and M. Drillon, The Quest for Nanoscale Magnets: The example of [Mn₁₂] Single Molecule Magnets, *Adv. Mat.*, 21, 4323-4333, 2009.
- [33] D. M. Seo, V. Meenakshi, W. Teizer, H. Zhao, and K. R. Dunbar, Enhanced magnetic anisotropy of Mn₁₂-acetate, *J. Magn. and Magnetic Materials*, 301, 31-36, 2006.
- [34] S. Voss, M. Fonin, U. Rüdiger, M. Burgert, U. Groth, and Y. S. Dedkov, Electronic structure of Mn₁₂ derivatives on the clean and functionalized Au surface, *Phys. Rev. B*, 75, 045102, 2007.
- [35] H. Zhao, C. P. Berlinguette, J. Bacsá, A. V. Prosvirin, J. K. Bera, S. E. Tichy, E. J. Schelter, and K. R. Dunbar, Structural Characterization, Magnetic Properties, and Electrospray Mass Spectrometry of Two Jahn-Teller Isomers of the Single-Molecule Magnet [Mn₁₂O₁₂(CF₃COO)₁₆(H₂O)₄], *Inorg. Chem.*, 43, 1359-1369, 2004.
- [36] P.-E. Car, M. Perfetti, M. Mannini, A. Favre, A. Caneschi, and R. Sessoli, Giant field dependence of the low temperature relaxation of the magnetization in a dysprosium(iii)-DOTA complex, *Chem. Comm.*, 47, 3751-3753, 2011.
- [37] G. Cucinotta, M. Perfetti, J. Luzon, M. Etienne, P.-E. Car, A. Caneschi, G. Calvez, K. Bernot, and R. Sessoli, Magnetic Anisotropy in a Dysprosium/DOTA Single-Molecule Magnet: Beyond Simple Magneto-Structural Correlations, *Angew. Chem. Int. Ed.*, 51, 1606-1610, 2012.
- [38] A. Dey, S. Das, V. Mereacre, A. K. Powell, and V. Chandrasekhar, Butterfly-shaped, heterometallic, hexanuclear, [Fe₁₂Ln₁₂] (Ln^{III} = Gd^{III}, Tb^{III}, Dy^{III} and Ho^{III}) Complexes: Syntheses, structure and magnetism, *Inorganica Chimica Acta*, 486, 458-467, 2019.
- [39] Y.-N. Guo, G.-F. Xu, P. Gamez, L. Zhao, S.-Y. Lin, R. Deng, J. Tang, and H.-J. Zhang, Two-Step Relaxation in a Linear Tetranuclear Dysprosium(III) Aggregate Showing Single-Molecule Magnet Behavior, *J. Am. Chem. Soc.*, 132, 8538-8539, 2010.
- [40] P. Hahn, S. Ullmann, J. Klose, Y. Peng, A. K. Powell, and B. Kersting, Dinuclear Tb and Dy complexes supported by hybrid Schiff-base/calixarene ligands: synthesis, structures and magnetic properties, *Dalt. Trans.*, 2020.
- [41] I. J. Hewitt, J. Tang, N. T. Madhu, C. E. Anson, Y. Lan, J. Luzon, M. Etienne, R. Sessoli, and A. K. Powell, Coupling Dy₃ Triangles Enhances Their Slow Magnetic Relaxation, *Angew. Chem. Int. Ed.*, 49, 6352-6356, 2010.
- [42] N. Ishikawa, M. Sugita, T. Ishikawa, S.-y. Koshihara, and Y. Kaizu, Lanthanide Double-Decker Complexes Functioning as Magnets at the Single-Molecular Level, *J. Am. Chem. Soc.*, 125, 8694-8695, 2003.

8. Temperature dependent X-ray magnetic circular dichroic studies of a trinuclear Manganese SMM complex in isolation

- [43] R. Modak, Y. Sikdar, A. E. Thuijs, G. Christou, and S. Goswami, Coll4, Coll7, and a Series of Coll2LnIII (LnIII = NdIII, SmIII, GdIII, TbIII, DyIII) Coordination Clusters: Search for Single Molecule Magnets, *Inorg. Chem.*, 55, 10192-10202, 2016.
- [44] E. Moreno-Pineda, C. Godfrin, F. Balestro, W. Wernsdorfer, and M. Ruben, Molecular spin qubits for quantum algorithms, *Chem. Soc. Rev.*, 47, 501-513, 2018.
- [45] A. Prescimone, J. Sanchez-Benitez, K. V. Kamenev, S. A. Moggach, A. R. Lennie, J. E. Warren, M. Murrie, S. Parsons, and E. K. Brechin, High pressure effects on a trimetallic MnII/III SMM, *Dalt. Trans.*, 7390-7395, 2009.
- [46] R. Colton, A. D'Agostino, and J. C. Traeger, Electrospray mass spectrometry applied to inorganic and organometallic chemistry, *Mass Spectrom. Rev.*, 14, 79-106, 1995.
- [47] J. B. Fenn, Electrospray Wings for Molecular Elephants (Nobel Lecture), *Angew. Chem. Int. Ed.*, 42, 3871-3894, 2003.
- [48] K. Hirsch, J. T. Lau, P. Klar, A. Langenberg, J. Probst, J. Rittmann, M. Vogel, V. Zamudio-Bayer, T. Möller, and B. von Issendorff, X-ray spectroscopy on size-selected clusters in an ion trap: from the molecular limit to bulk properties, *Journal of Physics B: Atomic, Molecular and Optical Physics*, 42, 154029, 2009.
- [49] J. Meyer, M. Tombers, C. van Wüllen, G. Niedner-Schatteburg, S. Peredkov, W. Eberhardt, M. Neeb, S. Palutke, M. Martins, and W. Wurth, The spin and orbital contributions to the total magnetic moments of free Fe, Co, and Ni clusters, *J. Chem. Phys.*, 143, 104302, 2015.
- [50] M. Niemeyer, K. Hirsch, V. Zamudio-Bayer, A. Langenberg, M. Vogel, M. Kossick, C. Ebrecht, K. Egashira, A. Terasaki, T. Möller, B. v. Issendorff, and J. T. Lau, Spin Coupling and Orbital Angular Momentum Quenching in Free Iron Clusters, *Phys. Rev. Lett.* 108, 057201, 2012.
- [51] V. Zamudio-Bayer, L. Leppert, K. Hirsch, A. Langenberg, J. Rittmann, M. Kossick, M. Vogel, R. Richter, A. Terasaki, T. Möller, B. v. Issendorff, S. Kümmel, and J. T. Lau, Coordination-driven magnetic-to-nonmagnetic transition in manganese-doped silicon clusters, *Phys. Rev. B*, 88, 115425, 2013.
- [52] K. Baberschke, The magnetism of nickel monolayers, *Appl. Phys. A*, 62, 417-427, 1996.
- [53] M. Tischer, O. Hjortstam, D. Arvanitis, J. Hunter Dunn, F. May, K. Baberschke, J. Trygg, J. M. Wills, B. Johansson, and O. Eriksson, Enhancement of Orbital Magnetism at Surfaces: Co on Cu(100), *Phys. Rev. Lett.*, 75, 1602-1605, 1995.
- [54] S. Bornemann, O. Šipr, S. Mankovsky, S. Polesya, J. B. Staunton, W. Wurth, H. Ebert, and J. Minár, Trends in the magnetic properties of Fe, Co, and Ni clusters and monolayers on Ir(111), Pt(111), and Au(111), *Phys. Rev. B*, 86, 104436, 2012.
- [55] J. Bansmann, A. Kleibert, M. Getzlaff, A. F. Rodríguez, F. Nolting, C. Boeglin, and K.-H. Meiwes-Broer, Magnetism of 3d transition metal nanoparticles on surfaces probed with synchrotron radiation – from ensembles towards individual objects, *physica status solidi (b)*, 247, 1152-1160, 2010.
- [56] J. T. Lau, A. Föhlich, R. Nietubyċ, M. Reif, and W. Wurth, Size-Dependent Magnetism of Deposited Small Iron Clusters Studied by X-Ray Magnetic Circular Dichroism, *Phys. Rev. L*, 89, 057201, 2002.
- [57] A. Langenberg, K. Hirsch, A. Ławicki, V. Zamudio-Bayer, M. Niemeyer, P. Chmiela, B. Langbehn, A. Terasaki, B. v. Issendorff, and J. T. Lau, Spin and orbital magnetic moments of size-selected iron, cobalt, and nickel clusters, *Phys. Rev. B*, 90, 184420, 2014.
- [58] S. Peredkov, A. Savci, S. Peters, M. Neeb, W. Eberhardt, H. Kampschulte, J. Meyer, M. Tombers, B. Hofferberth, F. Menges, and G. Niedner-Schatteburg, X-ray absorption spectroscopy of mass-selected transition metal clusters using a cyclotron ion trap: An experimental setup for measuring XMCD spectra of free clusters, *Journal of Electron Spectroscopy and Related Phenomena*, 184, 113-118, 2011.
- [59] S. A. McLuckey, and D. E. Goeringer, SPECIAL FEATURE: TUTORIAL Slow Heating Methods in Tandem Mass Spectrometry, *J. Mass Spectrom.*, 32, 461-474, 1997.
- [60] E.-L. Zins, C. Pepe, D. Rondeau, S. Rochut, N. Galland, and J.-C. Tabet, Theoretical and experimental study of tropylium formation from substituted benzylpyridinium species, *J. Mass Spectrom.*, 44, 12-17, 2009.
- [61] E.-L. Zins, C. Pepe, and D. Schröder, Energy-dependent dissociation of benzylpyridinium ions in an ion-trap mass spectrometer, *J. Mass Spectrom.*, 45, 1253-1260, 2010.
- [62] E.-L. Zins, D. Rondeau, P. Karoyan, C. Fosse, S. Rochut, and C. Pepe, Investigations of the fragmentation pathways of benzylpyridinium ions under ESI/MS conditions, *J. Mass Spectrom.*, 44, 1668-1675, 2009.
- [63] A. Langenberg, "Magnetische Momente freier, massenselektierter Eisen-, Cobalt- und Nickelcluster," Doctoral Thesis, Technische Universität Berlin, Fakultät II - Mathematik und Naturwissenschaften, Technische Universität Berlin, Berlin, 2013.
- [64] J. T. Lau, A. Achleitner, H. U. Ehrke, U. Langenbuch, M. Reif, and W. Wurth, Ultrahigh vacuum cluster deposition source for spectroscopy with synchrotron radiation, *Rev. Sci. Instrum.*, 76, 063902, 2005.

8. Temperature dependent X-ray magnetic circular dichroic studies of a trinuclear Manganese SMM complex in isolation

- [65] V. Zamudio-Bayer, K. Hirsch, A. Langenberg, A. Ławicki, A. Terasaki, B. v. Issendorff, and J. T. Lau, Electronic ground states of Fe²⁺ and Co²⁺ as determined by x-ray absorption and x-ray magnetic circular dichroism spectroscopy, *J. Chem. Phys.*, 143, 244318, 2015.
- [66] V. Zamudio-Bayer, R. Lindblad, C. Bülow, G. Leistner, A. Terasaki, B. V. Issendorff, and J. T. Lau, Electronic ground state of Ni²⁺, *J. Chem. Phys.*, 145, 2016.
- [67] P. Carra, B. T. Thole, M. Altarelli, and X. Wang, X-ray circular dichroism and local magnetic fields, *Phys. Rev. Lett.*, 70, 694-697, 1993.
- [68] A. D. Becke, Density-functional exchange-energy approximation with correct asymptotic behavior, *Phys. Rev. A*, 38, 3098-3100, 1988.
- [69] A. D. Becke, Density-functional thermochemistry. III. The role of exact exchange, *J. Chem. Phys.*, 98, 5648-5652, 1993.
- [70] B. Miehlich, A. Savin, H. Stoll, and H. Preuss, Results obtained with the correlation energy density functionals of Becke and Lee, Yang and Parr, *Chem. Phys. Lett.*, 157, 200-206, 1989.
- [71] E. R. Davidson, Comment on "Comment on Dunning's correlation-consistent basis sets", *Chem. Phys. Lett.*, 260, 514-518, 1996.
- [72] T. H. Dunning, Gaussian basis sets for use in correlated molecular calculations. I. The atoms boron through neon and hydrogen, *J. Chem. Phys.*, 90, 1007-1023, 1989.
- [73] R. A. Kendall, T. H. Dunning, and R. J. Harrison, Electron affinities of the first-row atoms revisited. Systematic basis sets and wave functions, *J. Chem. Phys.*, 96, 6796-6806, 1992.
- [74] A. K. Wilson, T. van Mourik, and T. H. Dunning, Gaussian basis sets for use in correlated molecular calculations. VI. Sextuple zeta correlation consistent basis sets for boron through neon, *J. Molecular Structure: THEOCHEM*, 388, 339-349, 1996.
- [75] D. E. Woon, and T. H. Dunning, Gaussian basis sets for use in correlated molecular calculations. III. The atoms aluminum through argon, *J. Chem. Phys.*, 98, 1358-1371, 1993.
- [76] D. Andrae, U. Häußermann, M. Dolg, H. Stoll, and H. Preuß, Energy-adjusted ab initio pseudopotentials for the second and third row transition elements: Molecular test for M2 (M=Ag, Au) and MH (M=Ru, Os), *Theoretica chimica acta*, 78, 247-266, 1991.
- [77] M. Dolg, H. Stoll, H. Preuss, and R. M. Pitzer, Relativistic and correlation effects for element 105 (hahnium, Ha): a comparative study of M and MO (M = Nb, Ta, Ha) using energy-adjusted ab initio pseudopotentials, *J. Phys. Chem.*, 97, 5852-5859, 1993.
- [78] R. Ahlrichs, M. Bär, M. Häser, H. Horn, and C. Kölmel, Electronic structure calculations on workstation computers: The program system turbomole, *Chem. Phys. Lett.*, 162, 165-169, 1989.
- [79] O. Treutler, and R. Ahlrichs, Efficient molecular numerical integration schemes, *The Journal of Chemical Physics*, 102, 346-354, 1995.
- [80] M. Von Arnim, and R. Ahlrichs, Performance of parallel TURBOMOLE for density functional calculations, *J. Comp. Chem.*, 19, 1746-1757, 1998.
- [81] S. Schmitt, "Berechnung der Magnetischen Anisotropie mit Hilfe von ein- und zweikomponentigen dichtefunktionaltheoretischen Rechnungen: Weiterentwicklung vorhandener Methoden und Anwendung auf mehrkernige Übergangsmetallkomplexe," 2015.
- [82] R. F. W. Bader, A quantum theory of molecular structure and its applications, *Chem. Rev.*, 91, 893-928, 1991.
- [83] F. Bondino, C. Cepek, N. Tagmatarchis, M. Prato, H. Shinohara, and A. Goldoni, Element-Specific Probe of the Magnetic and Electronic Properties of Dy-incar-Fullerenes, *J. Phys. Chem. B*, 110, 7289-7295, 2006.
- [84] T. Jo, The 3d-4f exchange interaction, X-ray second-order optical processes and the magnetic circular dichroism (MCD) spin sum rule in rare earths, *Journal of Electron Spectroscopy and Related Phenomena*, 86, 73-82, 1997.
- [85] S. Qiao, A. Kimura, H. Adachi, K. Iori, K. Miyamoto, T. Xie, H. Namatame, M. Taniguchi, A. Tanaka, T. Muro, S. Imada, and S. Suga, Direct evidence of ferromagnetism without net magnetization observed by x-ray magnetic circular dichroism, *Phys. Rev. B*, 70, 134418, 2004.
- [86] S. Qiao, A. Kimura, H. Adachi, K. Iori, K. Miyamoto, T. Xie, H. Namatame, M. Taniguchi, A. Tanaka, T. Muro, S. Imada, and S. Suga, Temperature dependence of spin and orbital magnetic moments of Sm 4f electrons in (Sm, Gd)Al₂, *Journal of Electron Spectroscopy and Related Phenomena*, 144-147, 749-752, 2005.
- [87] Y. Teramura, A. Tanaka, and T. Jo, Effect of Coulomb Interaction on the X-Ray Magnetic Circular Dichroism Spin Sum Rule in 3d Transition Elements, *J. Phys. Soc. of Japan*, 65, 1053-1055, 1996.

8. Temperature dependent X-ray magnetic circular dichroic studies of a trinuclear Manganese SMM complex in isolation

- [88] Y. Teramura, A. Tanaka, B. T. Thole, and T. Jo, Effect of Coulomb Interaction on the X-Ray Magnetic Circular Dichroism Spin Sum Rule in Rare Earths, *J. Phys. Soc. of Japan*, 65, 3056-3059, 1996.
- [89] E. Stavitski, and F. M. F. de Groot, The CTM4XAS program for EELS and XAS spectral shape analysis of transition metal L edges, *Micron*, 41, 687-694, 2010.
- [90] B. T. Thole, and G. van der Laan, Branching ratio in x-ray absorption spectroscopy, *Phys. Rev. B*, 38, 3158-3171, 1988.
- [91] G. van der Laan, K. T. Moore, J. G. Tobin, B. W. Chung, M. A. Wall, and A. J. Schwartz, Applicability of the Spin-Orbit Sum Rule for the Actinide $5f$ States, *Phys. Rev. Lett.*, 93, 097401, 2004.
- [92] G. van der Laan, and B. T. Thole, Strong magnetic x-ray dichroism in 2p absorption spectra of 3d transition-metal ions, *Phys. Rev. B*, 43, 13401-13411, 1991.
- [93] M. Barysz, and Y. Ishikawa, *Relativistic Methods for Chemists*: Springer Netherlands, 2010.
- [94] G. B. Kaufman, Inorganic chemistry: principles of structure and reactivity, 4th ed. (Huheey, James E.; Keiter, Ellen A.; Keiter, Richard L.), *J. Chem. Educ.*, 70, A279, 1993.

8.10 Supplementary material

Temperature dependent X-ray magnetic circular dichroic studies on a trimetallic manganese SMM complex in isolation

Michael Lembach^a, Maximilian Luczak^a, Yannick Mees^a, Vicente Zamudio-Bayer^{b,c}, Martin Timm^b, Markus Kubin^b, Bernd von Issendorff^c, Akira Terasaki^d, Euan Brechin^e, Tobias Lau^{b,c} and Gereon Niedner-Schatteburg^a

(a) Fachbereich Chemie and Forschungszentrum OPTIMAS, Kaiserslautern, Germany

(b) Institut für Methoden und Instrumentierung der Forschung mit Synchrotronstrahlung, Helmholtz-Zentrum Berlin für Materialien und Energie, Berlin, Germany

(c) Physikalisches Institut, Universität Freiburg, Germany

(d) Department of Chemistry, Kyushu University, Fukuoka, Japan

(e) University of Edinburgh, Edingburgh, Scotland

Content

Fig. S1: (a) Example of an XMCD spectrum and its integral over both $L_{3,2}$ absorption (b) Integrated sum of both XA spectra for both photon helicities in the case of $[\text{Mn}_3(\text{Hcht})_2(\text{bipy})_4]^{3+}$ at 20 K.

Tab. S1: Calculated energies for $[\text{Mn}_3(\text{Hcht})_2(\text{bipy})_4]^{3+}$ in different multiplicities. The calculations were performed at the B3LYP/cc-pVTZ (H, C, N, O) and Stuttgart ecp effective core potential (Mn) level of theory with a high spin state for each Mn center.

Fig. S2: a) Mass spectrum of $[\text{Mn}_3(\text{Hcht})_2(\text{bipy})_4]^{3+}$ without isolation and b) with isolation of the complex of interest.

Tab. S2: Mass peaks in the overview mass spectrum of $[\text{Mn}_3(\text{Hcht})_2(\text{bipy})_4]^{3+}$ at the Paul trap mass spectrometer.

Tab. S3: Fragment peaks from the CID breakdown curves of $[\text{Mn}_3(\text{Hcht})_2(\text{bipy})_4]^{3+}$.

Fig.S3: ETD reduced mass spectrum of $[\text{Mn}_3(\text{Hcht})_2(\text{bipy})_4]^{3+}$ without isolation measured at the Paul trap mass spectrometer.

Fig. S4: Electron field localization (ELF) plot of $[\text{Mn}_3(\text{Hcht})_2(\text{bipy})_4]^{3+}$. The calculation was performed with Gaussian 09 at the B3LYP/cc-pVTZ (H, C, N, O) and Stuttgart ecp effective core potential (Mn) level of theory.

Fig. S5: Mass spectrum of $[\text{Mn}_3(\text{Hcht})_2(\text{bipy})_4]^{3+}$ at 17 K with an applied magnetic field of 5 T and mass selection of the mass 349 amu. Mass spectrum was recorded at the Ion Trap at Helmholtz Zentrum Berlin.

Fig. S6: Experimental polarized depended XA Spectra (top), sum XA spectra with integral (middle) and XMCD spectra with integral (Bottom) for $[\text{Mn}_3(\text{Hcht})_2(\text{bipy})_4]^{3+}$ at 4 K, 10 K, and 20 K.

Fig. S7: Sum of positive and negative XA spectra (black) of $[\text{Mn}_3(\text{Hcht})_2(\text{bipy})_4]^{3+}$ at 4 K, 10 K, and 20 K. The shaded areas represent the two-step functions subtracted after normalization, approximating the direct 2p photo ionization and $2p \rightarrow nd$ ($n > 3$) contributions.

Fig. S8: Spin magnetic moments (blue), orbital magnetic moments (red), total magnetic moments (orange), and the spin-orbital ratio (green) per atom of $[\text{Mn}_3(\text{Hcht})_2(\text{bipy})_4]^{3+}$ with given spectra from the sum rule analysis and uncertainties of 5 %.

Tab. S4: Atom coordinates for $[\text{Mn}_3(\text{Hcht})_2(\text{bipy})_4]^{3+}$. The calculation was performed at the B3LYP/cc-pVTZ (H, C, N, O) and Stuttgart ecp effective core potential (Mn) level of theory with a high spin state for each Mn center.

Fig. S9: Calculated bonding distances of $[\text{Mn}_3(\text{Hcht})_2(\text{bipy})_4]^{3+}$. The calculation was performed with Gaussian 09 at the B3LYP/cc-pVTZ (H, C, N, O) and Stuttgart ecp effective core potential (Mn) level of theory. Ligand has been omitted for clarity.

Fig. S10: Normalized negative polarized XA spectra of $[\text{Mn}_3(\text{Hcht})_2(\text{bipy})_4]^{3+}$ in blue and black for the positive and negative polarization at 4 K in comparison with gauss folded (broadening 0.2) simulated XA spectra of an Mn^{2+} atom in orange and Mn^{3+} atom in green without coordination. Simulated spectra were performed by CTM4XAS with Cowan batch files.

Fig. S11: Determination of the crystal field splittings for the Mn^{2+} and Mn^{3+} of $[\text{Mn}_3(\text{Hcht})_2(\text{bipy})_4]^{3+}$ at different temperatures.

Fig. S12: First derivation of the positive polarized XA spectra of $[\text{Mn}_3(\text{Hcht})_2(\text{bipy})_4]^{3+}$ at 4 K ion trap temperature in comparison of simulated XA spectra of $\text{Mn}^{2+/3+}$ and the mixture. Simulated spectra were performed by CTM4XAS with Cowan batch files.

Fig. S13: Determination of the spin-orbit coupling from the core to electron into the valence shell of $[\text{Mn}_3(\text{Hcht})_2(\text{bipy})_4]^{3+}$ at different temperatures.

Fig. S14: First derivation of the polarized dependent XA spectra of $[\text{Mn}_3(\text{Hcht})_2(\text{bipy})_4]^{3+}$ at different temperatures and their corresponding absorption maxima.

Fig. S15: Calculated anisotropy tensors of $[\text{Mn}_3(\text{Hcht})_2(\text{bipy})_4]^{3+}$ in different spin configurations (UUU, UUD, UDU). The calculations were performed at the B3LYP_Gaussian/cc-pVTZ (H, C, N, O) and Stuttgart 1997 ECP (Mn) level of theory.

Fig. S16: Tanabe Sugano diagram of a d^5 HS transition metal with the normalized crystal field energy for Mn^{2+} ion (top) and a d^4 HS transition metal with the normalized crystal field energy for the Mn^{3+} ion (bottom) of $[\text{Mn}_3(\text{Hcht})_2(\text{bipy})_4]^{3+}$ for the approximation of absorption energy in the UV spectrum.

Fig. S17: Calculated susceptibilities for $[\text{Mn}_3(\text{Hcht})_2(\text{bipy})_4]^{3+}$ at different temperatures with experimental spin magnetic moment and error bars of 20%.

Fig. S18: Calculated susceptibilities for $[\text{Mn}_3(\text{Hcht})_2(\text{bipy})_4]^{3+}$ at different temperatures with experimental total magnetic moment and error bars of 20%.

Fig. S19: Integrated intensities of the experimental XMCD spectra and their corresponding derivated 3d holes for $[\text{Mn}_3(\text{Hcht})_2(\text{bipy})_4]^{3+}$.

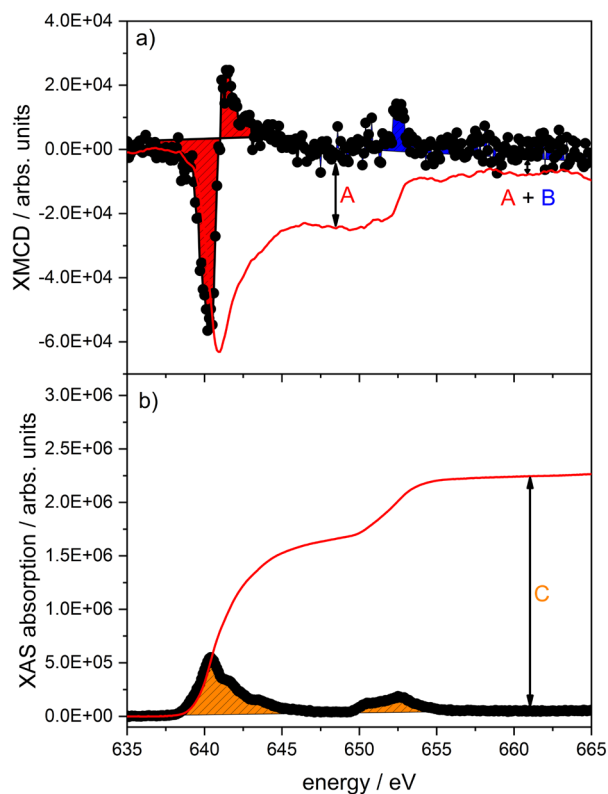


Fig. S1: (a) Example of an XMCD spectrum and its integral over both $L_{3,2}$ absorption (b) Integrated sum of both XA spectra for both photon helicities in the case of $[\text{Mn}_3(\text{Hcht})_2(\text{bipy})_4]^{3+}$ at 20 K.

Tab. S1: Calculated energies for $[\text{Mn}_3(\text{Hcht})_2(\text{bipy})_4]^{3+}$ in different multiplicities. The calculations were performed at the B3LYP/cc-pVTZ (H, C, N, O) and Stuttgart ecp effective core potential (Mn) level of theory with a high spin state for each Mn center.

m	SCF/Hartree	$\Delta\text{SCF}/\text{Hartree}$	$\Delta E/\text{kJ/mol}$
1	-3213.76629125	0.363409830	954
3	-3213.903567020	0.226134060	594
5	-3213.956415140	0.173285940	455
7	-3213.932327240	0.197373840	518
9	-3214.085680300	0.044020780	116
11	-3214.008134630	0.121566450	319
13	-3214.025809140	0.103891940	273
15	-3214.129701080	0.000000000	0
17	-3213.980795810	0.148905270	391
19	-3213.858845150	0.270855930	711

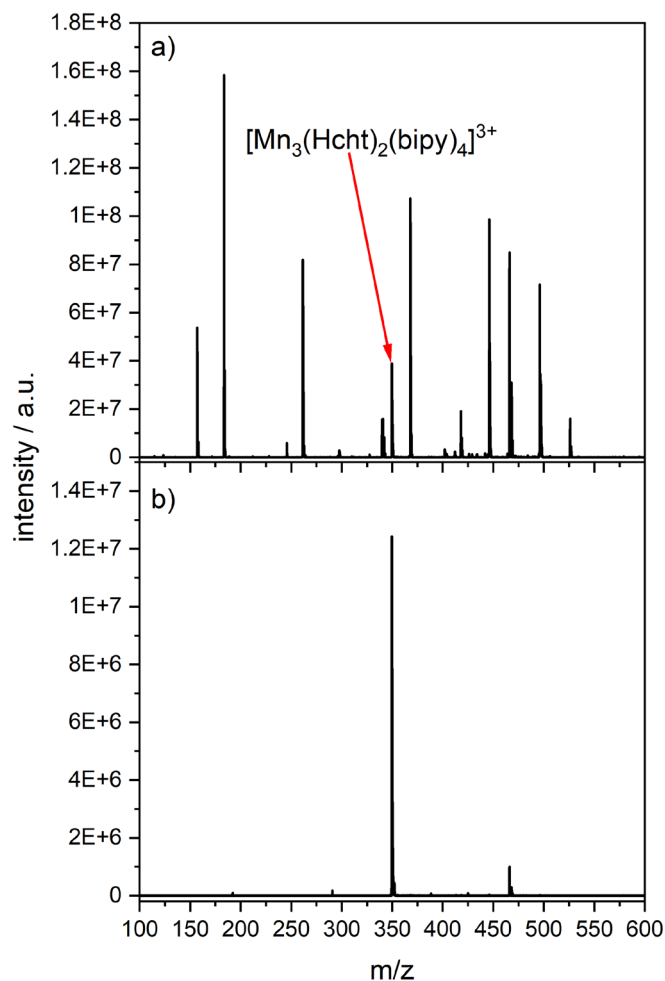


Fig. S2: a) Mass spectrum of $[\text{Mn}_3(\text{Hcht})_2(\text{bipy})_4]^{3+}$ without isolation and b) with isolation of the complex of interest.

Tab. S2: Mass peaks in the overview mass spectrum of $[\text{Mn}_3(\text{Hcht})_2(\text{bipy})_4]^{3+}$

Mass m/z	Fragment
496.1	$[\text{Mn}_3(\text{Hcht})_2(\text{bipy})_3]^+(\text{ClO}_4)$
466.1	$[\text{Mn}(\text{bipy})_2]^+(\text{ClO}_4)$
418.0	$[\text{Mn}_2(\text{Hcht})_2(\text{bipy})_2]^{2+}(\text{ClO}_4)$
368.0	$[\text{Mn}_2(\text{Hcht})(\text{cht})(\text{bipy})_2]^{2+}$
183.5	$[\text{Mn}(\text{bipy})_2]^{2+}$
157.1	$[\text{bipyH}]^+$

Tab. S3: Fragment peaks from the CID breakdown curves of $[\text{Mn}_3(\text{Hcht})_2(\text{bipy})_4]^{3+}$.

Mass m/z	Fragment
466.1	$[\text{Mn}_3(\text{Hcht})(\text{cht})(\text{bipy})_3]^{2+}$
368.0	$[\text{Mn}_3(\text{Hcht})_2(\text{bipy})_2]^{3+}$
183.5	$[\text{Mn}(\text{bipy})_2]^{2+}$
157.1	$[\text{bipyH}]^+$

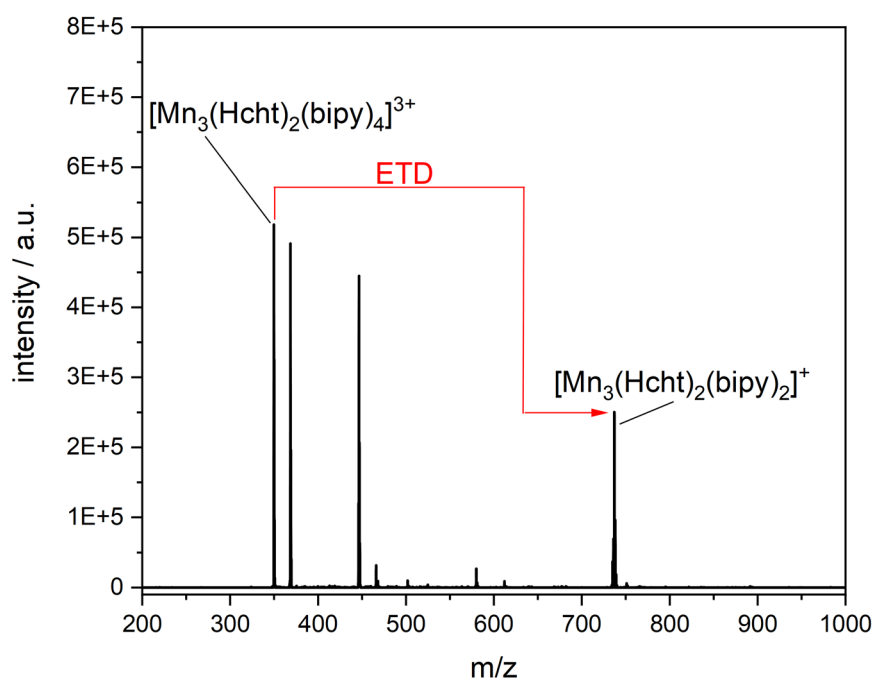


Fig. S3: ETD reduced mass spectrum of $[\text{Mn}_3(\text{Hcht})_2(\text{bipy})_4]^{3+}$ without isolation measured at the Paul trap mass spectrometer.

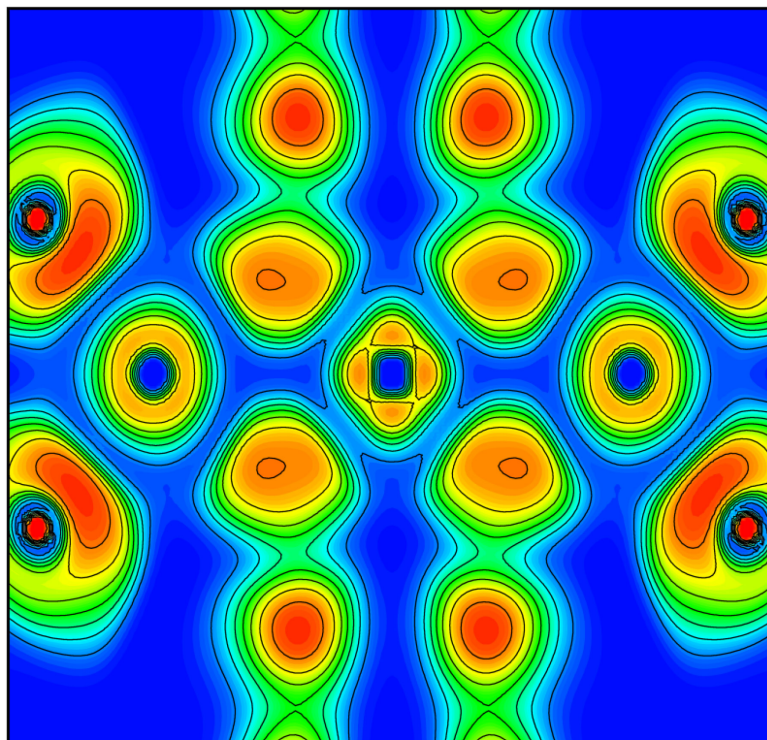


Fig. S4: Electron field localization (ELF) plot of $[\text{Mn}_3(\text{Hcht})_2(\text{bipy})_4]^{3+}$. The calculation was performed with Gaussian 09 at the B3LYP/cc-pVTZ (H, C, N, O) and Stuttgart ecp effective core potential (Mn) level of theory.

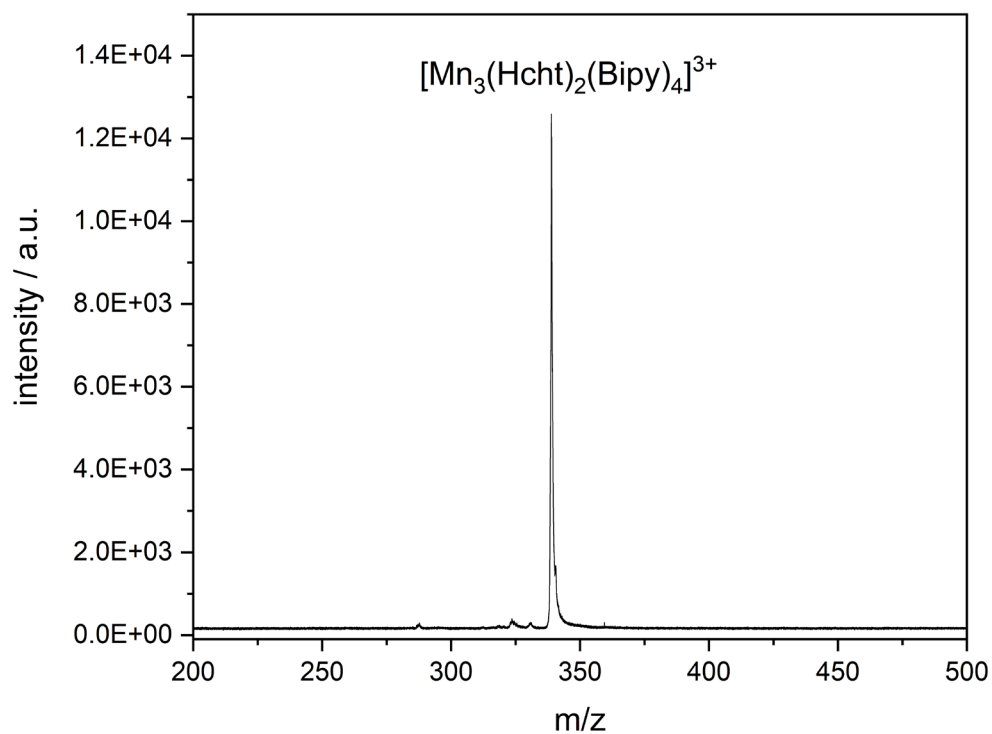


Fig. S5: Mass spectrum of $[\text{Mn}_3(\text{Hcht})_2(\text{Bipy})_4]^{3+}$ at 17 K with an applied magnetic field of 5 T and mass selection of the mass 349 amu. Mass spectrum was recorded at the Ion Trap at Helmholtz Zentrum Berlin.

8. Temperature dependent X-ray magnetic circular dichroic studies of a trinuclear Manganese SMM complex in isolation

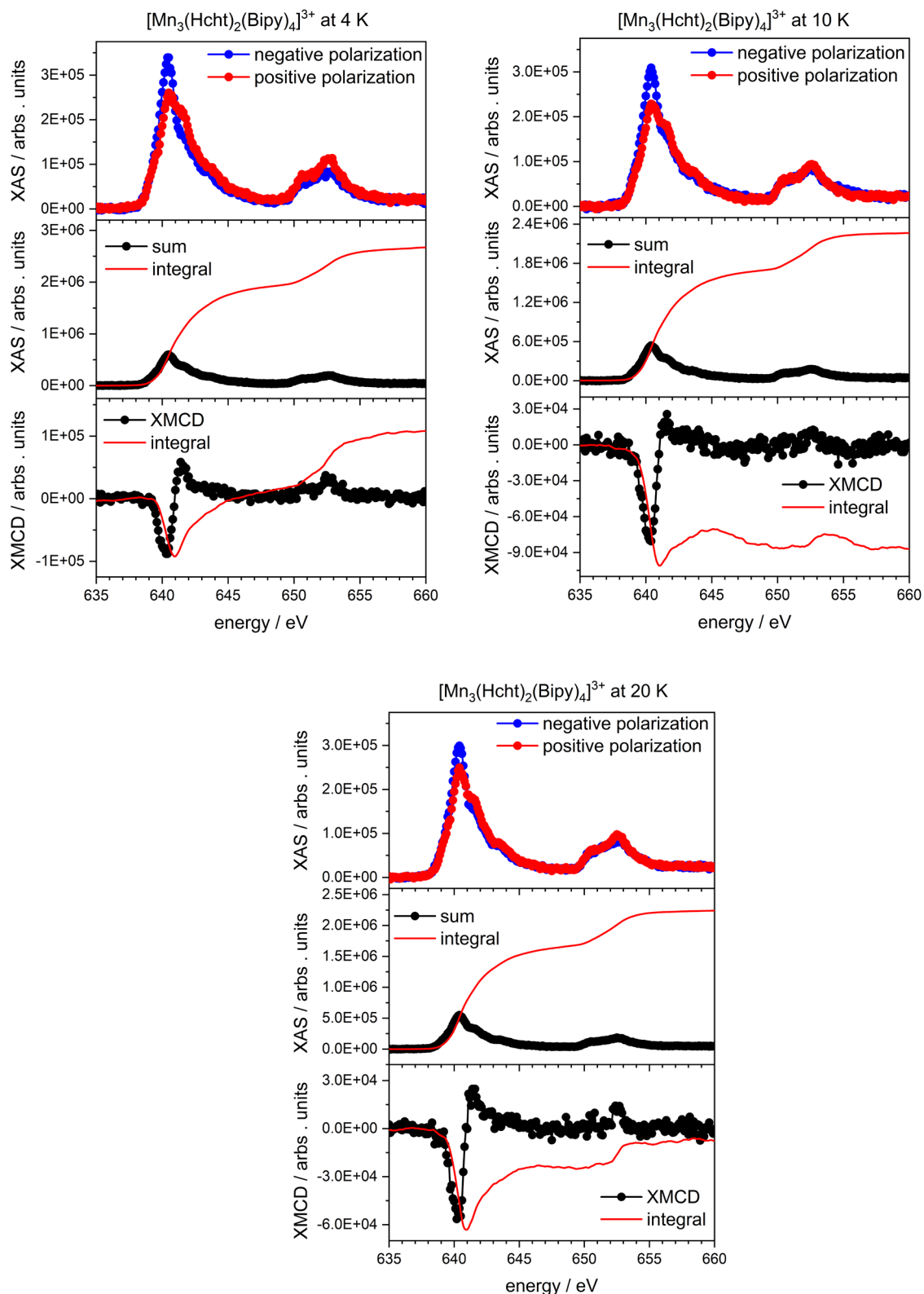


Fig. S6: Experimental polarized depended XA Spectra (top), sum XA spectra with integral (middle) and XMCD spectra with integral (Bottom) for $[\text{Mn}_3(\text{Hcht})_2(\text{bipy})_4]^{3+}$ at 4 K, 10 K, and 20 K.

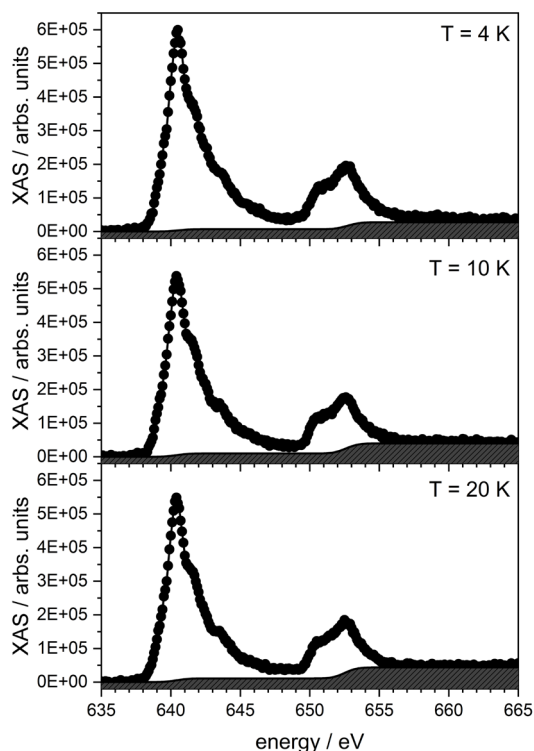


Fig. S7: Sum of positive and negative XA spectra (black) of $[\text{Mn}_3(\text{Hcht})_2(\text{bipy})_4]^{3+}$ at 4 K, 10 K, and 20 K. The shaded areas represent the two-step functions subtracted after normalization, approximating the direct 2p photo ionization and $2p \rightarrow nd$ ($n > 3$) contributions.

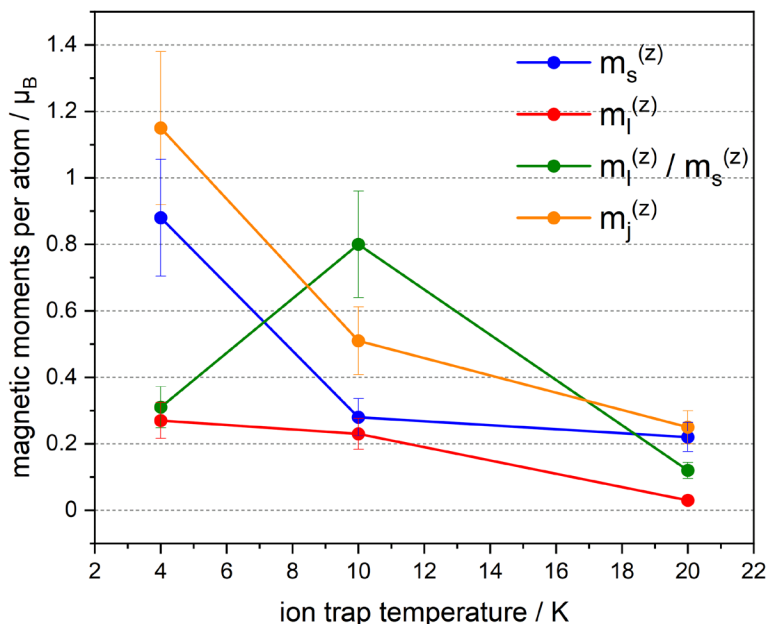


Fig. S8: Spin magnetic moments (blue), orbital magnetic moments (red), total magnetic moments (orange) and the spin-orbital ratio (green) per atom of $[\text{Mn}_3(\text{Hcht})_2(\text{bipy})_4]^{3+}$ with given spectra from the sum rule analysis and uncertainties of 5 %.

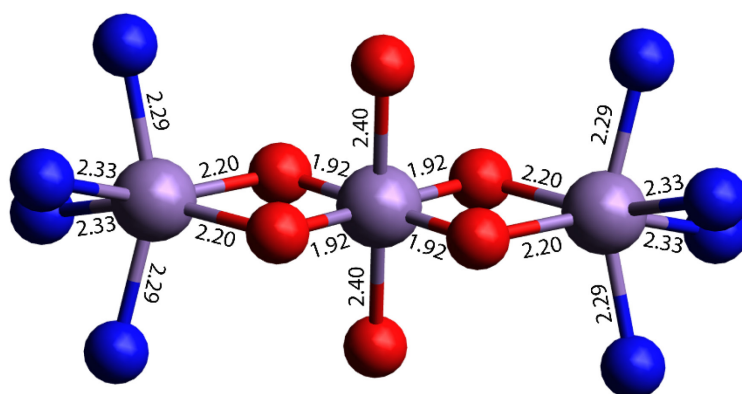


Fig.S9: Calculated bonding distances of $[\text{Mn}_3(\text{Hcht})_2(\text{bipy})_4]^{3+}$. The calculation was performed with Gaussian 09 at the B3LYP/cc-pVTZ (H, C, N, O) and Stuttgart ecp effective core potential (Mn) level of theory. Ligand has been omitted for clarity.

Tab. S4: atom coordinates for $[\text{Mn}_3(\text{Hcht})_2(\text{bipy})_4]^{3+}$. The calculation was performed at the B3LYP/cc-pVTZ (H, C, N, O) and Stuttgart ecp effective core potential (Mn) level of theory with a high spin state for each Mn center.

atom	x	y	z
Mn	0.00000	0.000200	0.000000
O	0.23259	-1.259100	1.428620
C	1.00233	-2.460930	1.273150
C	0.58936	-3.213370	0.000000
C	2.51213	-2.165470	1.265500
C	2.96551	-1.431250	0.000000
O	2.40214	-0.080600	0.000000
N	-2.05267	-0.899280	3.683350
C	-2.51955	-1.994320	3.058420
C	-3.73441	-2.595990	3.382790
C	-4.50296	-2.022660	4.398270
C	-4.03127	-0.878680	5.040730
C	-2.79364	-0.333990	4.665440
C	-2.22538	0.888940	5.303630
C	-2.86615	1.549700	6.360710
C	-2.29254	2.699160	6.904320
C	-1.08755	3.164330	6.378390
C	-0.50559	2.447560	5.333350
N	-1.04875	1.339120	4.802180
H	0.77603	-3.097560	2.146750
H	-0.49964	-3.381520	0.000000
H	1.07045	-4.205700	0.000000
H	3.05928	-3.122050	1.322940
H	2.78629	-1.582130	2.156760
H	4.06237	-1.338520	0.000000

8. Temperature dependent X-ray magnetic circular dichroic studies of a trinuclear Manganese SMM complex in isolation

H	-1.87555	-2.387140	2.268730
H	-4.06492	-3.492550	2.856710
H	-5.46060	-2.458690	4.688930
H	-4.62931	-0.421530	5.827090
H	-3.80490	1.177880	6.767860
H	-2.78274	3.221090	7.728120
H	-0.60200	4.059630	6.768240
H	0.44276	2.771620	4.900690
H	3.11368	0.571660	0.000000
O	0.23259	-1.259100	-1.428620
C	1.00233	-2.460930	-1.273150
C	2.51213	-2.165470	-1.265500
H	0.77603	-3.097560	-2.146750
H	3.05928	-3.122050	-1.322940
H	2.78629	-1.582130	-2.156760
Mn	0.00000	0.000001	-3.212240
O	-0.23258	1.259060	-1.428620
C	-1.00228	2.460920	-1.273140
C	-0.58926	3.213340	0.000000
C	-2.51211	2.165610	-1.265510
C	-2.96563	1.431480	0.000000

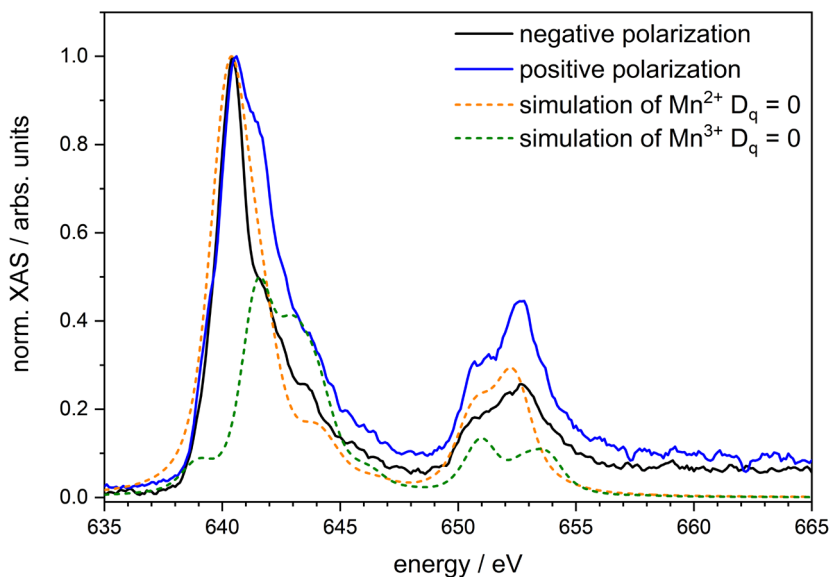


Fig. S10: Normalized negative polarized XA spectra of $[\text{Mn}_3(\text{Hcht})_2(\text{bipy})_4]^{3+}$ in blue and black for the positive and negative polarization at 4 K in comparison with gauss folded (broadening 0.2) simulated XA spectra of an Mn^{2+} atom in orange and Mn^{3+} atom in green without coordination. Simulated spectra were performed by CTM4XAS with Cowan batch files.

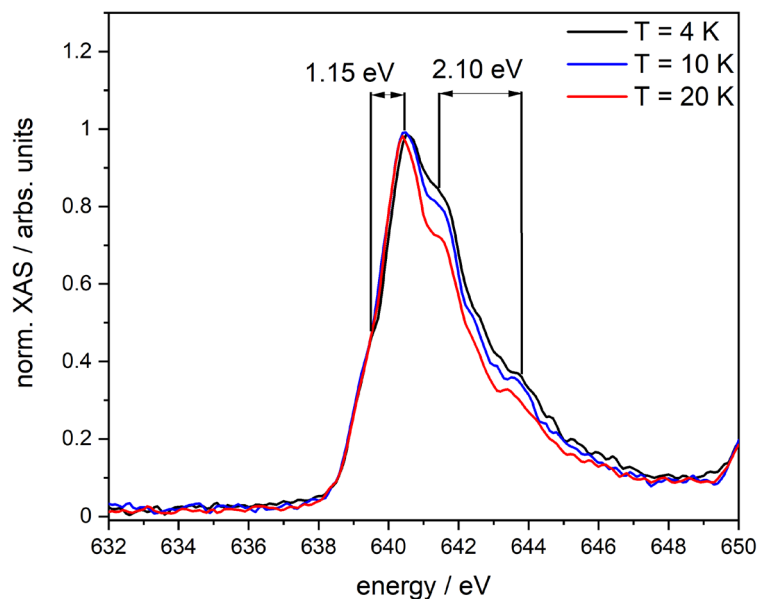


Fig. S11: Determination of the crystal field splittings for the Mn^{2+} and Mn^{3+} of $[\text{Mn}_3(\text{Hcht})_2(\text{bipy})_4]^{3+}$ at different temperatures.

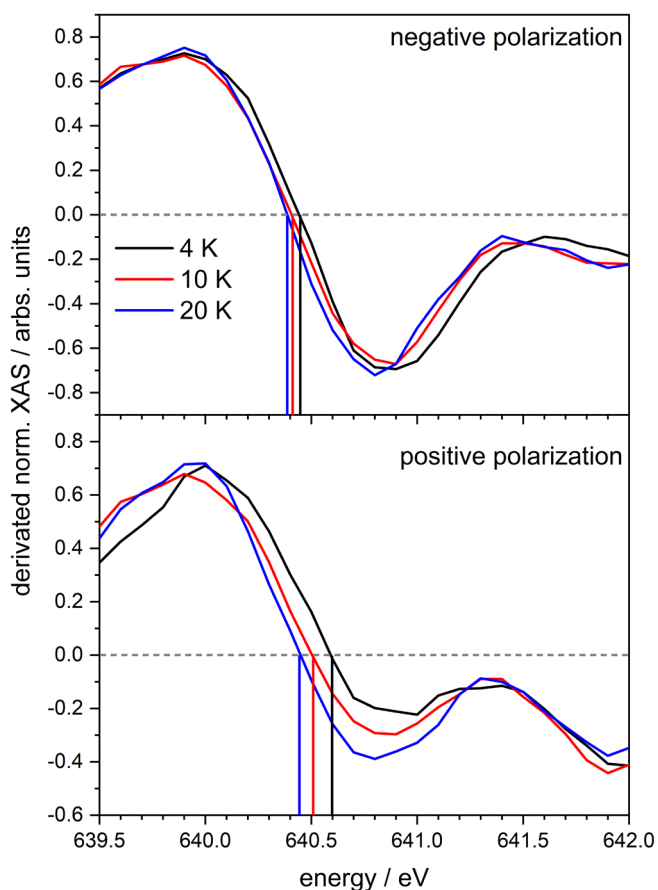


Fig. S12: First derivation of the polarized dependent XA spectra of $[\text{Mn}_3(\text{Hcht})_2(\text{bipy})_4]^{3+}$ at different temperatures and their corresponding absorption maxima.

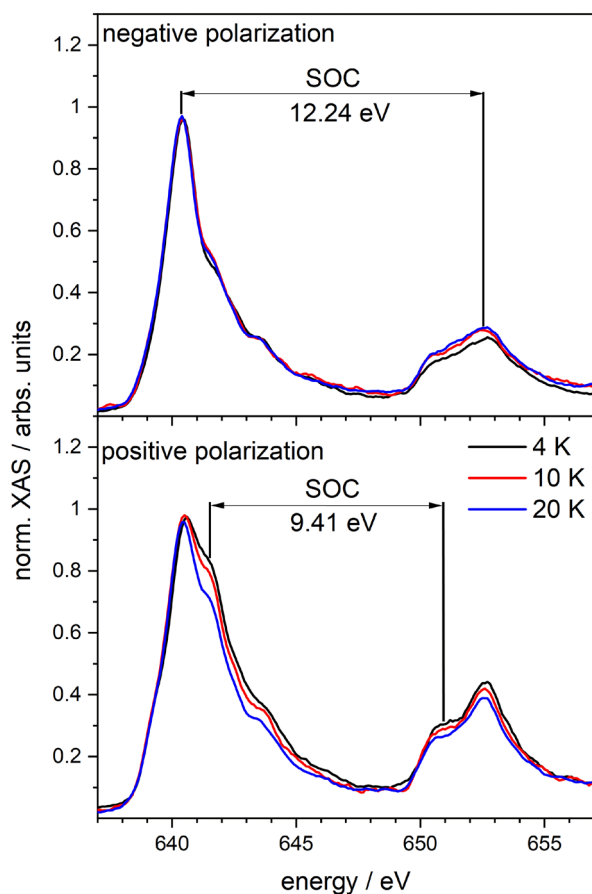


Fig. S13: Determination of the spin-orbit coupling from the core to electron into the valence shell of $[\text{Mn}_3(\text{Hcht})_2(\text{bipy})_4]^{3+}$ at different temperatures.

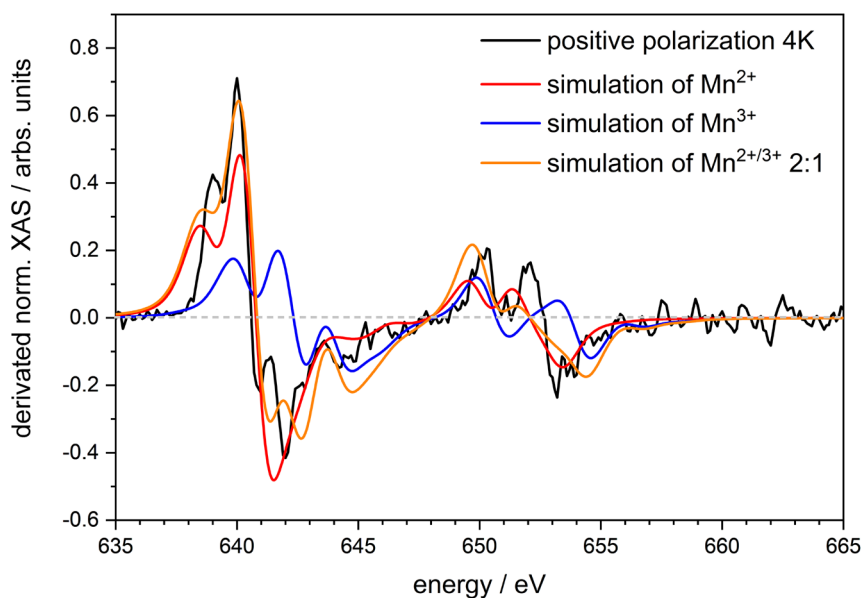


Fig. S14: First derivation of the positive polarized XA spectra of $[\text{Mn}_3(\text{Hcht})_2(\text{bipy})_4]^{3+}$ at 4 K ion trap temperature in comparison of simulated XA spectra of $\text{Mn}^{2+/3+}$ and the mixture. Simulated spectra were performed by CTM4XAS with Cowan batch files.

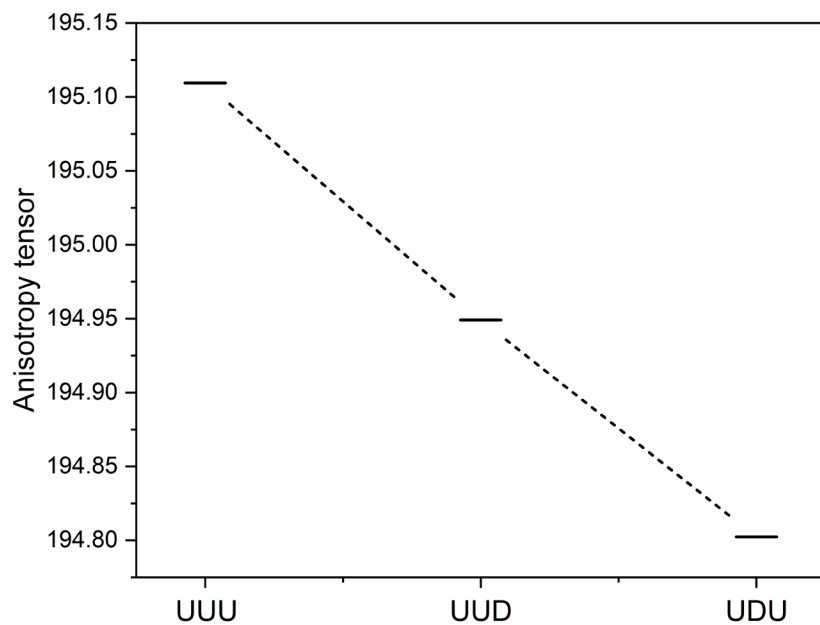


Fig. S15: Calculated anisotropy tensors of $[\text{Mn}_3(\text{Hcht})_2(\text{bipy})_4]^{3+}$ in different spin configurations (UUU, UUD, UDU). The calculations were performed at the B3LYP_Gaussian/cc-pVTZ (H, C, N, O) and Stuttgart 1997 ECP (Mn) level of theory.

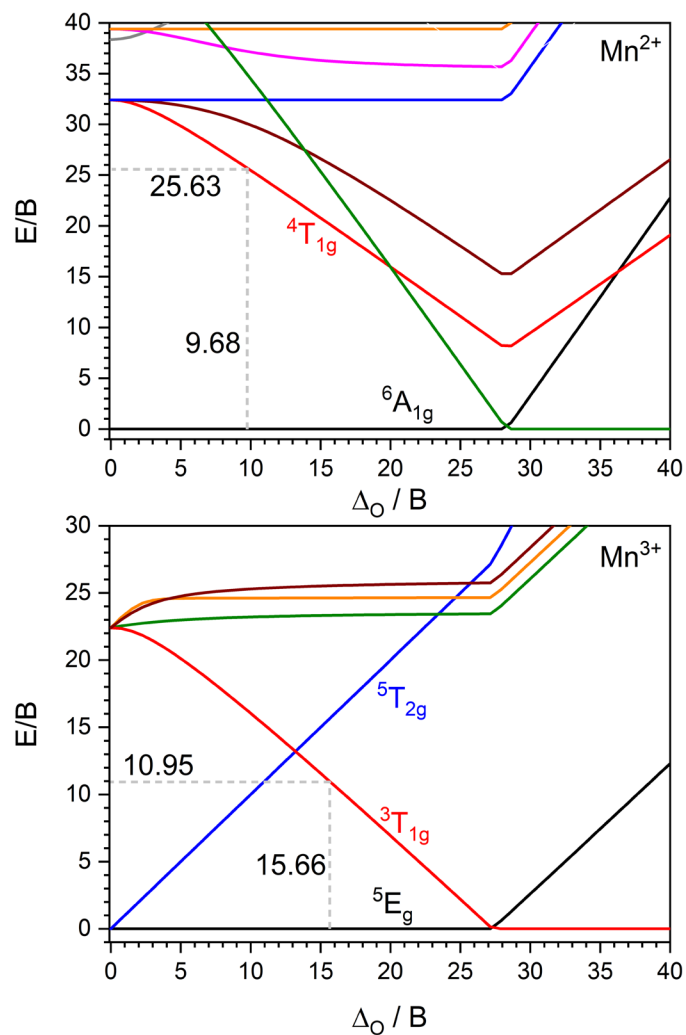


Fig. S16: Tanabe Sugano diagram of a d^5 HS transition metal with the normalized crystal field energy for Mn^{2+} ion (top) and a d^4 HS transition metal with the normalized crystal field energy for the Mn^{3+} ion (bottom) of $[Mn_3(Hcht)_2(bipy)_4]^{3+}$ for the approximation of absorption energy in the UV spectrum.

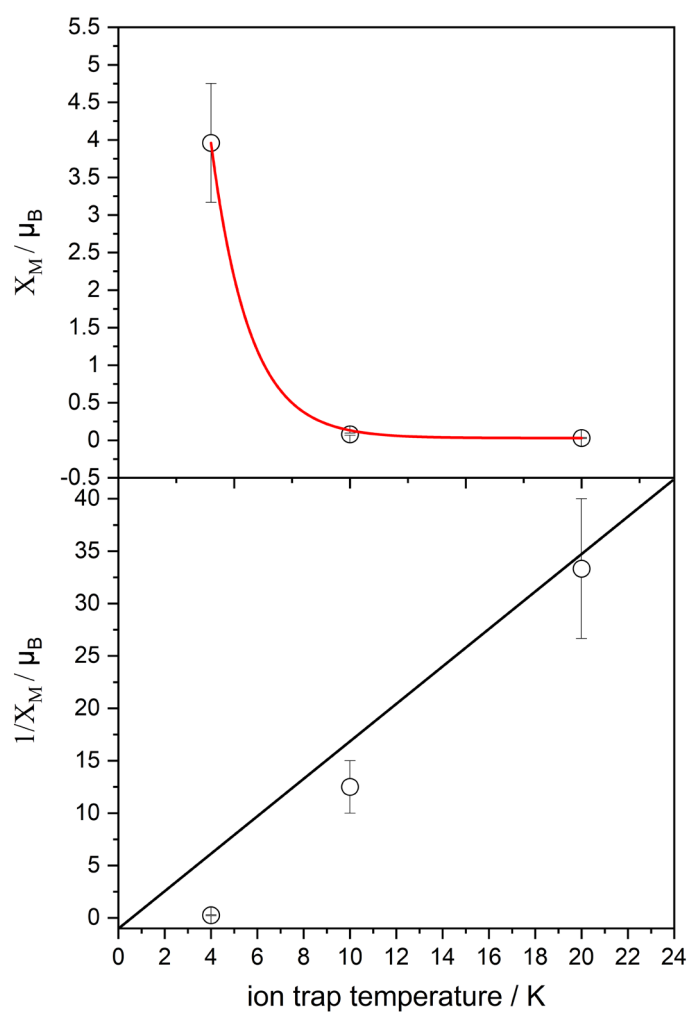


Fig. S17: Calculated susceptibilities for $[\text{Mn}_3(\text{Hcht})_2(\text{bipy})_4]^{3+}$ at different temperatures with experimental spin magnetic moment and error bars of 20%.

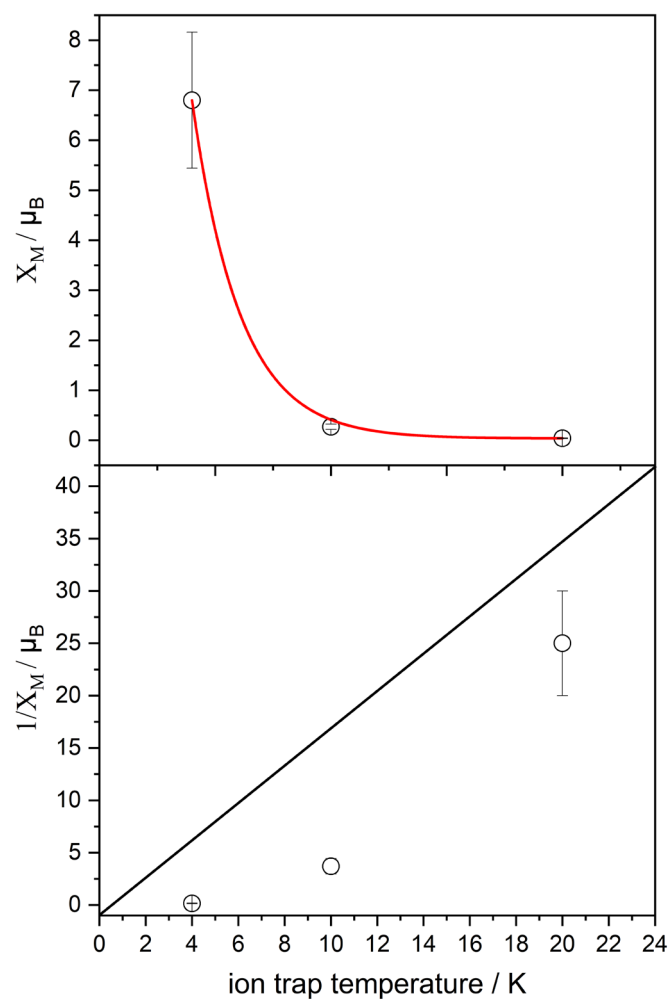


Fig. S18: Calculated susceptibilities for $[\text{Mn}_3(\text{Hcht})_2(\text{bipy})_4]^{3+}$ at different temperatures with experimental total magnetic moment and error bars of 20%.

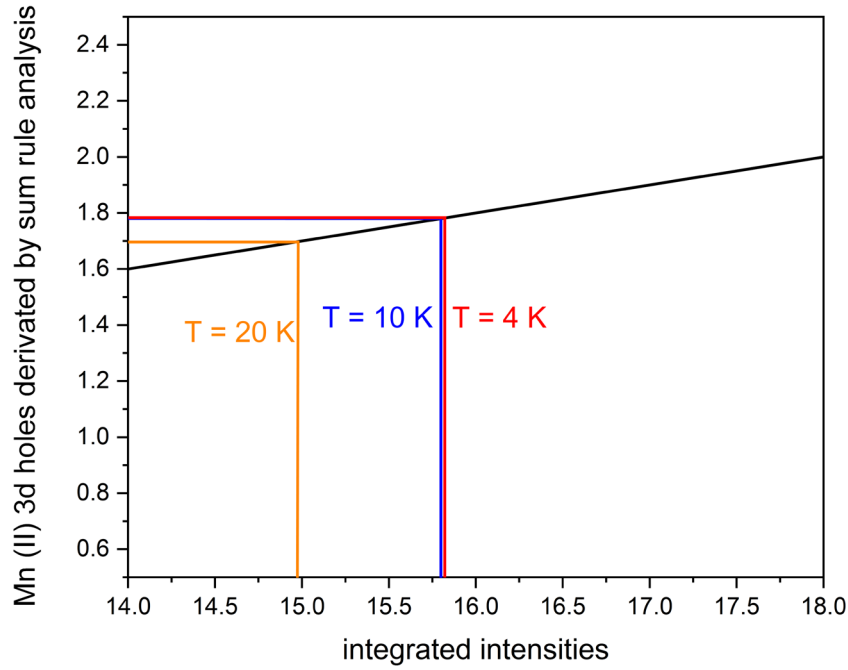


Fig. S19: Integrated intensities of the experimental XMCD spectra and their corresponding derived 3d holes for $[\text{Mn}_3(\text{Hcht})_2(\text{bipy})_4]^{3+}$.

Correction of the spin sum rules by Takeo Jo et al.

The S_z sum rule for the $L_{2,3}$ edge in **3d transition metal** systems is expressed as:

$$X_I = X_E.$$

The relative integrated magnetic circular dichroism (MCD) intensity is defined as

$$X_E = \frac{\int_{L_3} (\mu_+(\omega) - \mu_-(\omega)) d\omega - 2 \int_{L_2} (\mu_+(\omega) - \mu_-(\omega)) d\omega}{\int_{L_3+L_2} (\mu_+(\omega) + \mu_0(\omega) + \mu_-(\omega)) d\omega}$$

And the expectation value is given by

$$X_E = \frac{2}{3(10-n)} \langle S_z \rangle + \frac{7}{3(10-n)} \langle T_z \rangle.$$

The absorption spectra with positive and negative light helicity are given by $\mu_{\pm}(\omega)$, with linearly polarized light by $\mu_0(\omega)$ along the z direction. L_3 and L_2 denote the integrated region with respect to ω , the number of 3d electrons is given by n.

9 IR(M)PD studies on a series of isolated trimetallic single molecule magnets containing 3d metals and Lanthanides

Michael Lembach, Marcel Lechner and Gereon Niedner-Schatteburg

*Fachbereich Chemie and Forschungszentrum OPTIMAS,
Technische Universität Kaiserslautern,
67663 Kaiserslautern, Germany*

9.1 Preamble

The following chapter elucidates the structure determination of a group of complexes with single molecule magnetic behavior. I performed and managed CID, IR(M)PD experiments, data evaluation, quantum chemical calculations, and XA simulations. I received experimental support from Marcel Lechner to synthesize the complexes to record CID breakdown curves and IR(M)PD spectra. I wrote this chapter for detailed documentation.

9.2 Abstract

Single Molecule Magnets (SMM) reveal extraordinary magnetic properties as their magnetic moments do not arise from macroscopic bulk ordering but from the individual properties of the molecule itself. Much effort has been expended on synthesizing complexes that combine a high spin ground state with a large anisotropy barrier. We elucidate a series of complexes with the general structure $[M_2Ln(HVab)_4(NO_3)]^{2+}$ ($M = Co, Cu; Ln = Dy, Gd, Sm, Tb, Nd, Tb$) ($HVab = (2-[(2\text{-hydroxymethyl-phenylimino)-methyl]-6\text{-methoxy-phenol})$) via Collision Induced Dissociation (CID), InfraRed (Multiple) Photon Dissociation (IR(M)PD) and quantum chemical calculations in gas phase. The presented results help gain a fundamental insight into the molecular structure and stabilities of these complexes, void of any external effects such as crystal packing or solvation.

9.3 Introduction

Single molecule magnets (SMM) are a fascinating research field for the development of magnetic materials, such for example data storage^[1] or quantum computing^[2-5]. Molecules that combine a high spin ground state with a significant anisotropy barrier result in a high magnetic moment and slow magnetization relaxation. The first single molecule magnet $[Mn_{12}O_{12}(CH_3COO)_{16}(H_2O)_4]$ synthesized by Lis^[6] is a well investigated molecule given single molecule magnetic behavior^[7-14]. The research of single molecule magnets has been extended with the Lanthanide ions^[15-18].

Slow relaxation in complexes with the general structure $[Ln(Pc)_2]^-$ ($Pc = \text{phthalocyanine}$, $Ln = Tb, Dy, Ho, Er, Tm, Yb$) were observed with temperature dependent squid measurements^[19]. Further investigations on $[Tb(Pc)_2]^-$ via μ squid measurements revealed well defined spin states by changing the applied magnetic field^[20]. These spin states can be determined as $\pm 1/2$ and $\pm 3/2$. The switch of these spin states is possible because of quantum tunneling of the magnetization. Investigations on a trinuclear SMM complex $[Mn^{III}_2(5\text{-Brsalen})_2(MeOH)_2M^{III}(CN)_6]NEt_4$ ($M = Os, Ru$; $5\text{-Brsalen} = N, N'\text{-ethylene bis}(5\text{-bromosalicylidene)iminato}$)^[21] points out a ferromagnetic Ising type exchange coupling between the manganese and the ruthenium or Osmium center. The coupling constants are antiferromagnetically coupled for J_{xx} and J_{zz} , but ferromagnetic coupled to J_{yy} and the resulting

anisotropy is maximal with this configuration. Therefore, much effort has been spent to design SMM complexes containing transition metal complexes and lanthanides to enhance the magnetic properties. Investigations of the complex $[\text{HNEt}_3][\text{Ln}_2(\text{HL}^1)(\text{L}^1)]$ ($\text{L}^1 = 25\text{-}[2\text{-}((2\text{-methyl phenol})\text{imino})\text{ethoxyl-}26, 27, 28\text{-trihydroxy-calix[4]arene)}$; $\text{Ln} = \text{Sm, Eu, Gd, Tb, Dy}$)^[22]. SQUID measurements on these complexes revealed a higher magnetization than expected in higher temperatures, resulting in a slow relaxation. In other studies of a series of complexes $[\text{Fe}_2\text{Ln}_4(\text{L}'\text{H})_2(\text{L})_2(\mu\text{-Piv})_4(\eta^2\text{-Piv})_2(\mu_2\text{-}\eta^2\text{-Piv})_2(\mu^3\text{-OMe})_2]$ ($\text{Ln} = \text{Gd, Tb, Dy, Ho}$), an increasing magnetization without saturation by increasing the external magnetic field up to 7 T^[23] was found.

Earlier studies of the presented complexes with the general structure $[\text{Co}_2\text{Ln}(\text{HVab})_4(\text{NO}_3)](\text{NO}_3)_2 \cdot \text{MeOH} \cdot \text{H}_2\text{O}$ ($\text{Ln} = \text{Dy, Gd, Sm, Tb, Nd, Tb}$) for its characterization were performed^[24, 25]. With the exception of the combination containing Neodymium, temperature dependent Squid measurements of these complexes demonstrate single molecule magnetic behavior. They also recorded FT-IR spectra in solid state for this series and observed a broad band for the Hydrogen bonded OH groups. The elemental analysis appears to support a pure complex void free of impurities.

Unfortunately, the studies of complexes with the structure $[\text{Co}_2\text{Ln}(\text{HVab})_4(\text{NO}_3)](\text{NO}_3)_2 \cdot \text{MeOH} \cdot \text{H}_2\text{O}$ are performed in solid state, and a hydrogen bonded hydroxyl group cannot be eliminated by methanol or water, which are likewise coordinated to the complex. Modak et al. also displayed ESI MS spectra that did not show these compounds. External effects such as crystal packing effects and/or solvation cannot be excluded but seem mandatory.

We synthesized a series of complexes with the general structure $[\text{M}_2\text{Ln}(\text{HVab})_4(\text{NO}_3)](\text{NO}_3)_2$ ($\text{M} = \text{Co, Cu}$; $\text{Ln} = \text{Dy, Gd, Sm, Tb, Nd, Tb}$) ($\text{HVab} = (2\text{-}[(2\text{-hydroxymethyl-phenylimino})\text{-methyl}]\text{-6-methoxy-phenol})$) (cf. Fig. 1)^[25].

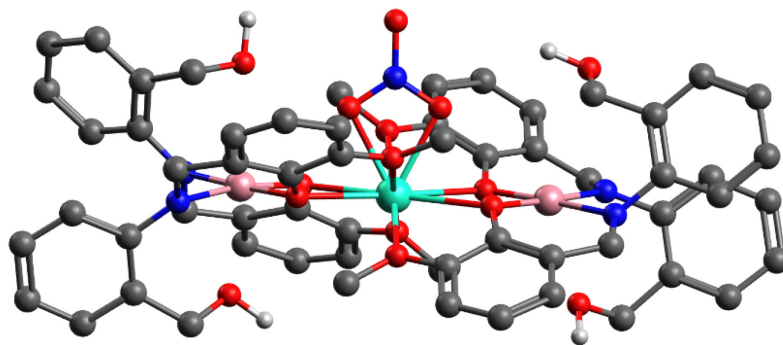


Fig. 1: Calculated minimum structures of $[M_2Ln(HVab)_4(NO_3)]^{2+}$ ($M = Co, Cu$; $Ln = Dy, Gd, Sm, Tb, Nd, Tb$). The calculations were performed with Gaussian 09 at the B3LYP/ cc-pVDZ (H, C, N, O) and ecp-mdf (Co, Cu, Ln) level of theory. Hydrogen is omitted for clarity.

Electrospray ionization^[26, 27] enables mass spectrometric investigations of transition metal complexes and their study of the geometrical structure by irradiation with IR photons. Tandem-based methods helped to investigate molecules and transition metal complexes void from external and/or solvation effects.

We combine experimental CID, ETD reduced CID, and IR(M)PD investigations of isolated $[M_2Ln(HVab)_4(NO_3)]^{2+}$ ($M = Co, Cu$; $Ln = Dy, Gd, Sm, Tb, Nd, Tb$) with quantum chemical calculations by Density Functional Theory (DFT) to gain a better understanding of isolated single molecule magnets void from external effects such as crystal packing or solvation.

9.4 Experimental setup and methods

The general procedure for the synthesis of the complexes was performed as follows^[24, 25]. The used materials for the synthesis were commercially bought at Sigma Aldrich. All reactions were performed under aerobic conditions.

Synthesis of the Ligand (H₂Vab)^[24]: 2-Hydroxy-3-methoxy benzaldehyde (4.5 g) were dissolved in methanol (100 mL). This mixture was stirred, and 2-Aminobenzyl-alcohol (4 g) was added. The mixture was stirred and heated for 6 h at 60 °C. After 6 h, the solution was cooled to room temperature, and a yellow solution was obtained (H₂Vab).

Synthesis of $[\text{Co}_2\text{Ln}(\text{Vab})_3(\text{HVab})(\text{NO}_3)]^{2+}$ (Ln = Dy, Gd, Sm, Tb, Nd, Tb)^[25]: H_2Vab (780 mg, 30 mL) was stirred at room temperature. Sodium methanolate (162 mg) was dissolved in methanol (30 mL). The sodium methanolate solution was dropwise added to the ligand solution and stirred for 15 min. $\text{Ln}(\text{NO}_3)_2 \cdot \text{H}_2\text{O}$ (520 mg) were dissolved in methanol (30 mL) and dropwise added. The mixture was stirred at room temperature for 4 h. $\text{Co}(\text{OAc})_2 \cdot \text{H}_2\text{O}$ (370 mg) was added to the mixture and stirred for 12 h. The solvent was slowly removed in vacuum (950 mbar). The resulting powder was dried in vacuum.

Synthesis of $[\text{Cu}_2\text{Ln}(\text{Vab})_3(\text{HVab})(\text{NO}_3)]^{2+}$ (Ln = Dy, Gd, Sm, Tb, Nd, Tb)^[25]: H_2Vab (780 mg, 30 mL) was stirred at room temperature. Sodium methanolate (162 mg) was dissolved in methanol (30 mL). The sodium methanolate solution was dropwise added to the ligand solution and stirred for 15 min. $\text{Ln}(\text{NO}_3)_2 \cdot \text{H}_2\text{O}$ (520 mg) were dissolved in methanol (30 mL) and dropwise added. The mixture was stirred at room temperature for 4 h. $\text{Cu}(\text{OAc})_2 \cdot \text{H}_2\text{O}$ (370 mg) was added to the mixture and stirred for 12 h. The solvent was slowly removed in vacuum (950 mbar). The resulting powder was dried in vacuum.

Collision Induced Dissociation (CID)

For the ESI MS and CID measurements, we used a quadrupole mass spectrometer (amazon ETD, Bruker daltonics) with a paul trap. The ions of interest are transferred into gas phase by electrospray ionization. The sample solution of $[\text{M}_2\text{Ln}(\text{HVab})_4(\text{NO}_3)]^{2+}$ ($c \sim 1 \cdot 10^{-6}$ mol/L) in acetonitrile as solvent was constantly infused into the ESI chamber by a syringe pump with a flow rate of 180 $\mu\text{L}/\text{h}$. Nitrogen was used as a drying gas with a flow rate of 12 L/min at 180 °C. The nebulizer pressure was set to 280 mbar (4 psi) for spraying the sample solution, and the spray needle was held at 4.5 kV. The Paul trap comprises a ring electrode and two end caps forming a nearly hyperbolic inner profile. The end caps possess pinholes that allow them to enter or exit the ions in the trap. The ring electrode is powered with a high voltage RF (radio frequency) potential (781 kHz) while the end caps are grounded. The ions are accumulated in this resulting oscillating quadrupolar electric field generated from the three electrodes. An auxiliary dipolar voltage is fed to either the exit cap or both end caps for ion isolation and fragmentation. For providing a constant partial Helium buffer gas pressure of ca. 10^{-3} mbar inside the trap, a proportional integral derivative (PID) gas controller is used.

Collision Induced Dissociation (CID) curves varied the excitation voltages (0.0 V–2.5 V). These voltages determine the internal energy scale of the mass spectrometer (E_{lab} in V). Relative abundances were calculated according to:

$$I_{tot}^{fr}(E_{lab}) = \left(\frac{\sum_i I_i^{fr}(E_{lab})}{\sum_i I_i^{fr}(E_{lab}) + \sum_i I_i^p(E_{lab})} \right) \quad (1)$$

where I_i^{fr} = intensity of the fragment ions and I_i^p = intensity of the parent ions. Center of mass transferred fragmentation amplitudes (E_{com}) were calculated from internal amplitudes by:

$$E_{com} = \left(\frac{m_{He}}{m_{He} + m_{ion}} \right) \cdot E_{lab} \quad (2)$$

where m_{ion} stands for the isotopically averaged mass of the molecular ion. Note that the current application of the CID technique by RF excitation in the presence of multiple collisions results in a so called “slow multi collision heating” mode of operation^[28].

Fragmentation amplitude dependent CID spectra were modeled and fitted by sigmoidal functions of the type

$$I_{fit}^{fr}(E_{com}) = \left(\frac{1}{1 + e^{(E_{com}^{50} - E_{com})/B}} \right) \quad (3)$$

using a least-squares criterion. The E_{com}^{50} fit parameter is the amplitude at which the sigmoid function is at half maximum value, whereas B describes the rise of the sigmoid curve. Due to the correlation of fragmentation amplitude and appearance energy, it is feasible to assume that the appearance curves can be associated with the relative stability of the isolated complexes^[29-32].

For the experiments, via Electron Transfer Dissociation (ETD), we admitted methane in the ETD cell as a mediator to create low energy electrons. Inside the ETD cell, methane is oxidized to a methane radical cation ($\text{CH}_4^{\bullet+} + 2e^-$) via electron impact ionization. The collision of the methane radical cation with the Fluoranthene ($\text{C}_{16}\text{H}_{10}$) leads to an electron capture of the low-energy electrons by the Fluoranthene. Afterward, the Fluoranthene radical anion ($\text{C}_{16}\text{H}_{10}^-$) is guided into the Paul trap, and collisions with the complex of interest lead to an anion-cation electron transfer reaction resulting in a reduction of the complex.

InfraRed (Multiple) Photon Dissociation (IR(M)PD)

InfraRed (Multiple) Photon Dissociation (IR(M)PD) experiments were performed using a modified Paul-type quadrupole ion trap mass spectrometer (Amazon SL, Bruker Daltonics) at room temperature. The ions of interest are transferred into gas phase by electrospray ionization. The sample solution of $[M_2Ln(HVab)_4(NO_3)]^{2+}$ ($c \sim 1 \cdot 10^{-6}$ mol/L) in acetonitrile was constantly infused into the ESI chamber by a syringe pump with a flow rate of 180 μ L/h. Nitrogen was used as a drying gas with a flow rate of 12 L/min at 180 °C. The nebulizer pressure was set to 280 mbar (4 psi) for spraying the sample solution, and the spray needle was held at 4.5 kV. The Paul trap consists of a ring electrode and two end caps forming a nearly hyperbolic inner profile. The end caps possess pinholes that allow them to enter or exit the ions in the trap. The ring electrode is powered with a high voltage RF (radio frequency) potential (781 kHz) while the end caps are grounded. The ions are accumulated in this resulting oscillating quadrupolar electric field generated from the three electrodes. An auxiliary dipolar voltage is fed to either the exit cap or both end caps for ion isolation and fragmentation. For providing a constant partial Helium buffer gas pressure of ca. 10^{-3} mbar inside the trap, a proportional integral derivative (PID) gas controller is used.

Laser system

The laser pulses were generated using a KTP/KTA optical parametric oscillator/amplifier (OPO/OPA, LaserVision) system. A pulsed 10 Hz injection seeded Nd³⁺ Yag laser (PL 8000, Continuum) pumps the system and serves as source for tunable IR radiation. The difference frequency (DF) between the OPA signal and idler waves is generated within an AgGaSe₂ crystal, applied for the range between 1000 cm^{-1} and 2000 cm^{-1} . The IR beam is guided into the ion trap by a 90° off axis parabolic silver mirror with a focal length of 15 cm. After passing the Paul-trap, the IR beam was guided to a power meter (Maestro, Gentech) to monitor the laser power. IR(M)PD spectra are obtained by plotting the fragment yield as a function of the laser frequency (ν). The fragment yield is defined as:

$$Y(\nu) = \left(\frac{\sum_i I_i^{fr}(\nu)}{\sum_i I_i^{fr}(\nu) + \sum_i I_i^p(\nu)} \right) \quad (4)$$

Calibration of the IR frequency is done by a wavemeter (821B-NIR, Bristol instruments). The resulting power curves are recorded parallel to the IR(M)PD experiments by digitizing the analog output of the laser power meter through an ADC input of the Amazon SL mass spectrometer. No normalization of the recorded spectra was done because there is an intrinsically nonlinear power dependence of the IR(M)PD fragmentation efficiencies.

9.5 Computational methods

For the calculation of the optimized minimum energy structures and linear absorption spectra, we performed DFT calculations at the B3LYP^[33, 34] level of theory using cc-pVDZ^[35] basis sets (C, H, N, O) and Stuttgart ecp effective core potential^[36] (Co, Cu, Dy, Gd, Nd, Sm, Tb) with the Gaussian 09 program package^[37]. We calculated the different multiplicities in the different geometries to gain the most stable isomers as a function of multiplicities. For the calculation, the standard convergence criteria were applied. Harmonic vibrational frequencies were scaled with 0.9641 to account for prevailing anharmonicity. The scaling factor was derived by matching the calculated accessible OH stretching mode of the experimental spectra with the calculated OH stretching modes. The projected Density of States spectra was also performed at the B3LYP^[33, 34] level using cc-pVDZ^[35] with the Gaussian 09 program package^[37]. To calculate weak interactions of these complexes, we performed single-point calculations at the same Level as above to obtain wfn data for further treatment in multiwfn^[38]. The presented XA simulations were performed with CTM4XAS and batch files from cowan^[39].

9.6 Results

9.6.1 Collision Induced Dissociation (CID)

With the above described sample solution, we recorded mass spectra via electrospray process. The ions of interest are stored and isolated in a Paul trap. We monitor a variety of isotopic peaks ranging from 670 m/z to 700 m/z in this series of complexes, depending on the Lanthanide and transition metal ions (cf. Tab S1). The recorded masses are 1.5 m/z lower than predicted, implying that three hydrogen atoms were lost during the ESI process in this set of complexes or that four hydroxyl groups were never obtained as planned. Furthermore, the masses are half of the real masses, indicating that the complexes under consideration in this case are dicationic ones (cf. Fig. 2).

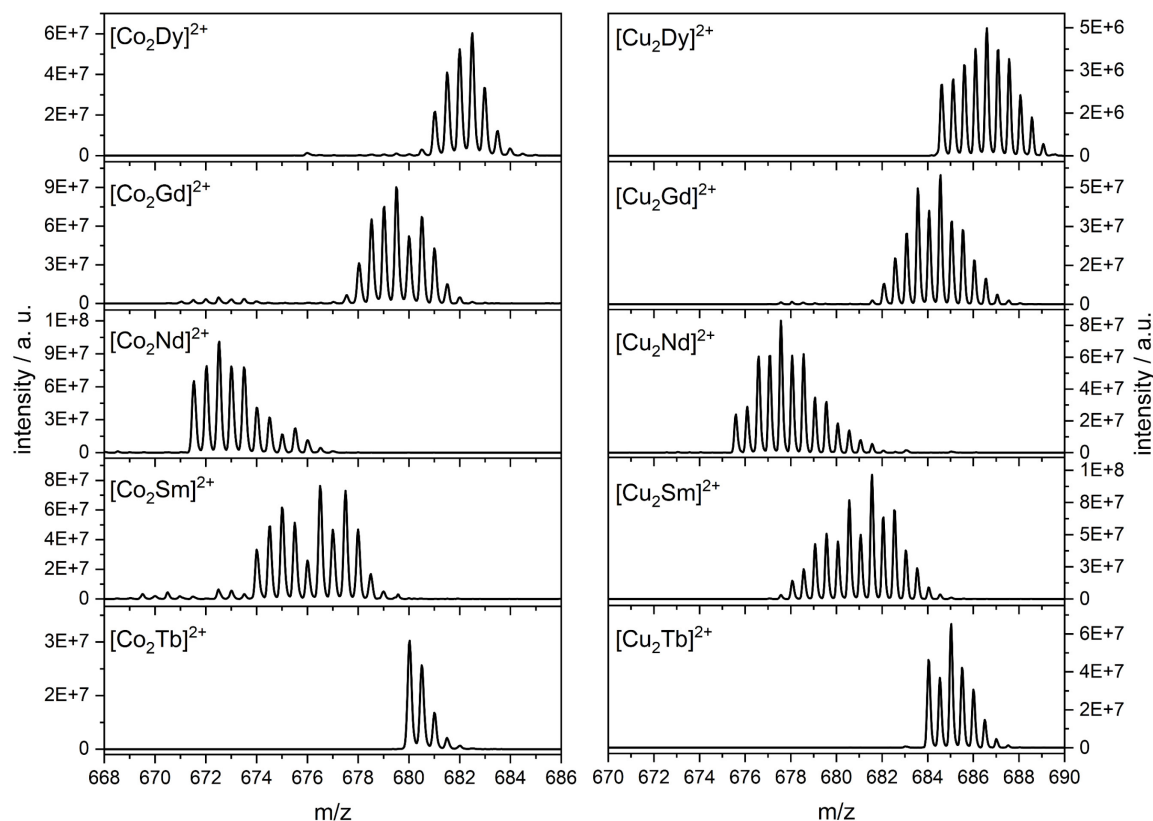


Fig. 2: ESI mass spectra of isolated $[M_2Ln(HVab)(Vab)_3]^{2+}$ ($M = Co, Cu$; $Ln = Dy, Gd, Nd, Sm, Tb$) in a paul type ion trap mass spectrometer.

To verify the above mentioned assumption, we prepared the sample as described above with deuterated acetonitrile to exchange the Hydrogen in the hydroxyl groups with deuterium (cf. Fig. S1). Deuteration results in a mass spectrum that is just 0.5 m/z heavier than the initial mass, implying that the complex seizes only one hydroxyl group rather than four, as previously reported^[25]. We observe a similar trend by changing the transition metal from Cobalt to Copper. The ligand thus offers different possibilities to establish coordination to the corresponding transition metals (c.f. Fig. 3). This results in only one possible composition for cobalt and copper, respectively, to generate a complex with a netto charge of 2+ (c.f. Fig. 3).

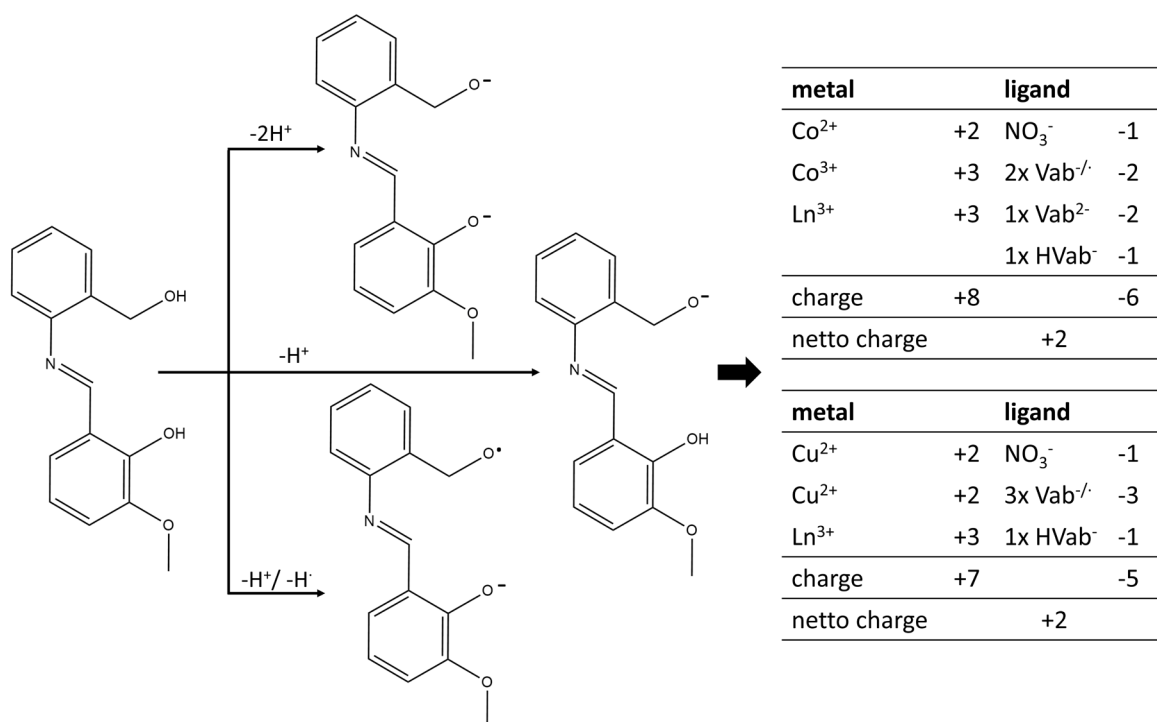


Fig. 3: Possible coordination of the ligands and their formal charges for the construction of the complex while maintaining the net charge +2.

We recorded Collision Induced Dissociation (CID) breakdown curves to determine the bonding strengths in these complexes (cf. Fig. 4) and observe a nearly identical fragmentation pattern for all complexes, regardless of Lanthanide or transition metal exchange. The main fragmentation channel is the loss of the nitrate group with the addition of molecular Hydrogen. With rising excitation amplitude, losing molecular Hydrogen and one deprotonated ligand (Vab) is observed. At the same excitation amplitude as second fragmentation channel, that loses the nitrate group to a mono cationic complex appears. The third fragmentation channel to a mono cationic complex is observed in all complexes but significantly lower in the Copper complexes (cf. Tab. S2).

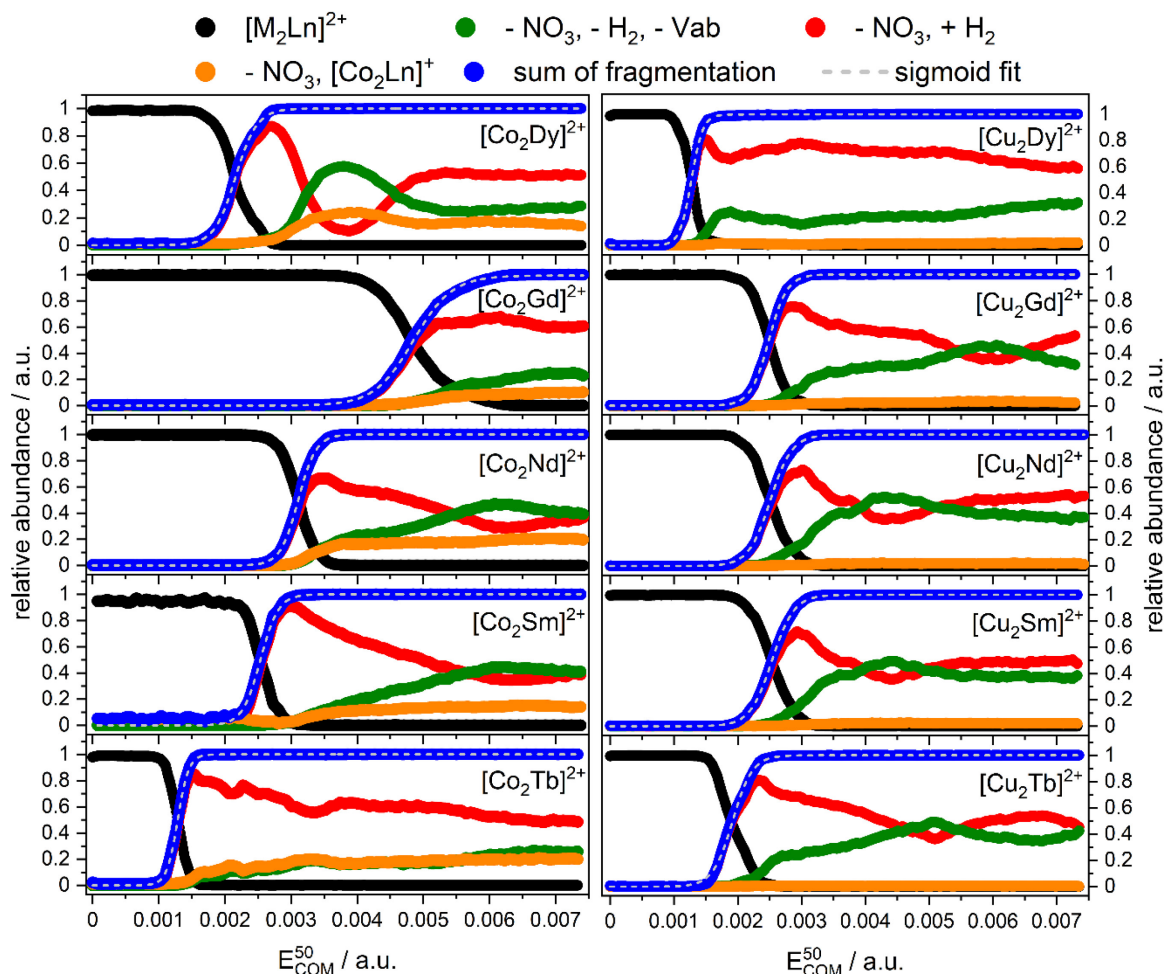


Fig. 4: CID breakdown curves of $[\text{Co}_2\text{Ln}(\text{HVab})(\text{Vab})_3]^{2+}$ (left) and $[\text{Cu}_2\text{Ln}(\text{HVab})(\text{Vab})_3]^{2+}$ ($\text{Ln} = \text{Dy}, \text{Gd}, \text{Nd}, \text{Sm}, \text{Tb}$) with their corresponding appearance curves of the associated fragments and sigmoid fits.

We recorded Electron Transfer Dissociation (ETD) break down curves (cf. Fig. 5) and observe only two fragmentation channels for all complexes. The main fragmentation channel is the loss of the nitrate group and the addition of molecular Hydrogen as observed in the dicationic species. At higher excitation amplitudes, the second fragmentation channel still relates to the loss of the molecular Hydrogen and one ligand. The loss of the nitrate group without the addition of molecular Hydrogen is not monitored, indicating that the third fragmentation channel in the dications results in a monocation, which can only be obtained by an isomer that does not exhibit an intensive bonding condition of the nitrate group.

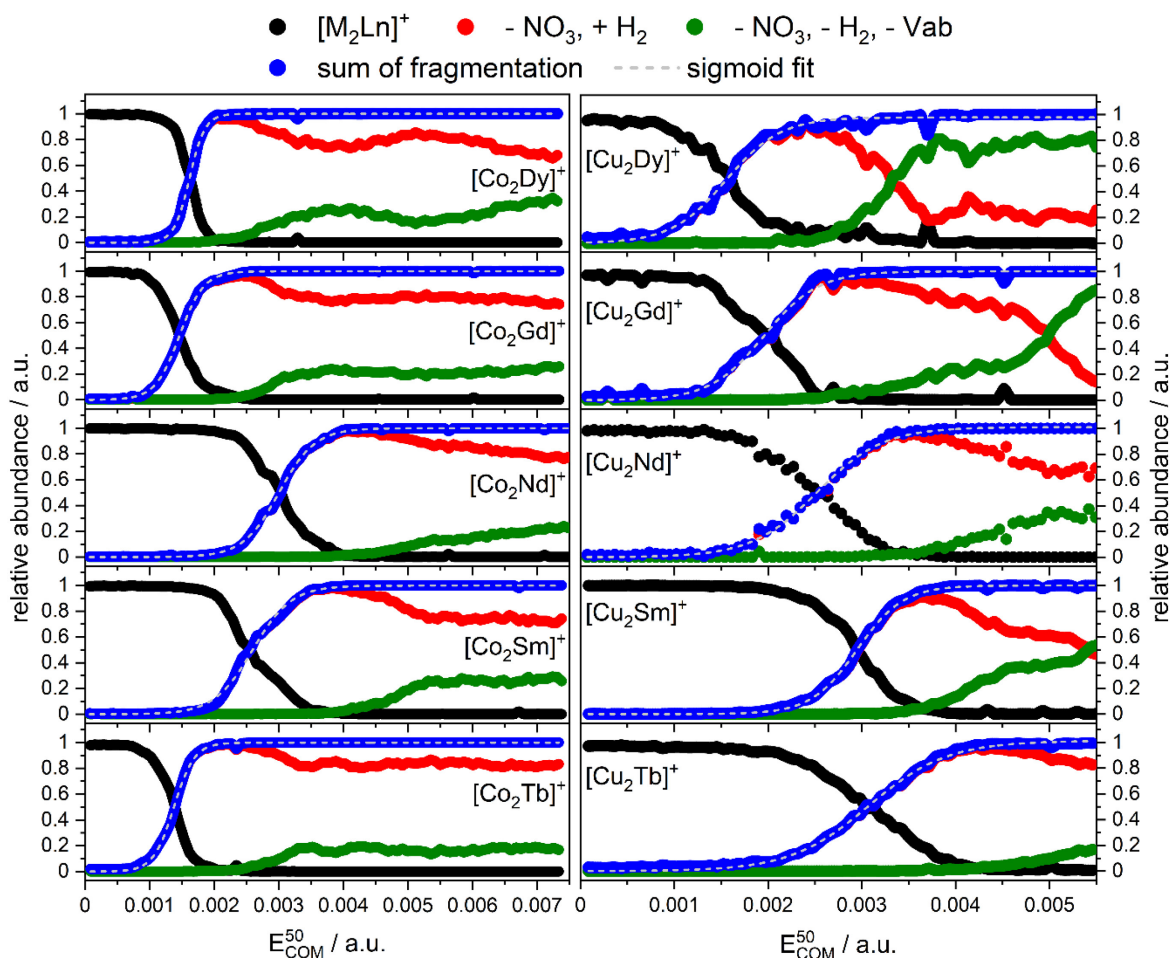


Fig. 5: ETD breakdown curves of $[\text{Co}_2\text{Ln}(\text{HVab})(\text{Vab})_3]^{2+}$ (left) and $[\text{Cu}_2\text{Ln}(\text{HVab})(\text{Vab})_3]^{2+}$ (right) ($\text{Ln} = \text{Dy}, \text{Gd}, \text{Nd}, \text{Sm}, \text{Tb}$) with their corresponding appearance curves of the associated fragments and sigmoid fits.

The resulting gas phase stabilities reveal a change in their stabilities as a function of the Lanthanides, transition metals, and the netto charge of the complex. Gas phase stabilities for the dicationic Cobalt complexes point out an increasing trend with the change from Dysprosium to Gadolinium afterward, a decreasing trend is observed. The gas phase stabilities of the dicationic Copper complexes are lower than those of the Cobalt analoga, and their behavior differs. An increase in the gas phase stability is observed, by changing from Dysprosium to Gadolinium. Then, the gas phase stabilities seem to be equal until a change to Terbium is performed. The ETD reduced gas phase stabilities show different behavior than their dicationic analoga. We monitor an increasing tendency from the Gadolinium complex to the Samarium complex, and the transition to the Terbium complex causes considerable instability for the complexes containing Cobalt. For Copper complexes, we observe an increasing trend by the exchange of Dysprosium to Neodymium.

The complex containing Samarium is the least stable of the three, and the exchange to a Terbium ion results in the maximum gas phase stability. We assume that the gas phase stabilities highly depend on the change of the Lanthanide. The reduced complexes point out that the exchange of the transition metal also affects the gas phase stabilities. Considering that the electron from the ETD process is not delocalized over the ligands since this would not have a major effect on the observed gas phase stabilities. Therefore, the electron might be located near the transition metal and/or the Lanthanide, resulting in a stabilization or destabilization in these complexes.

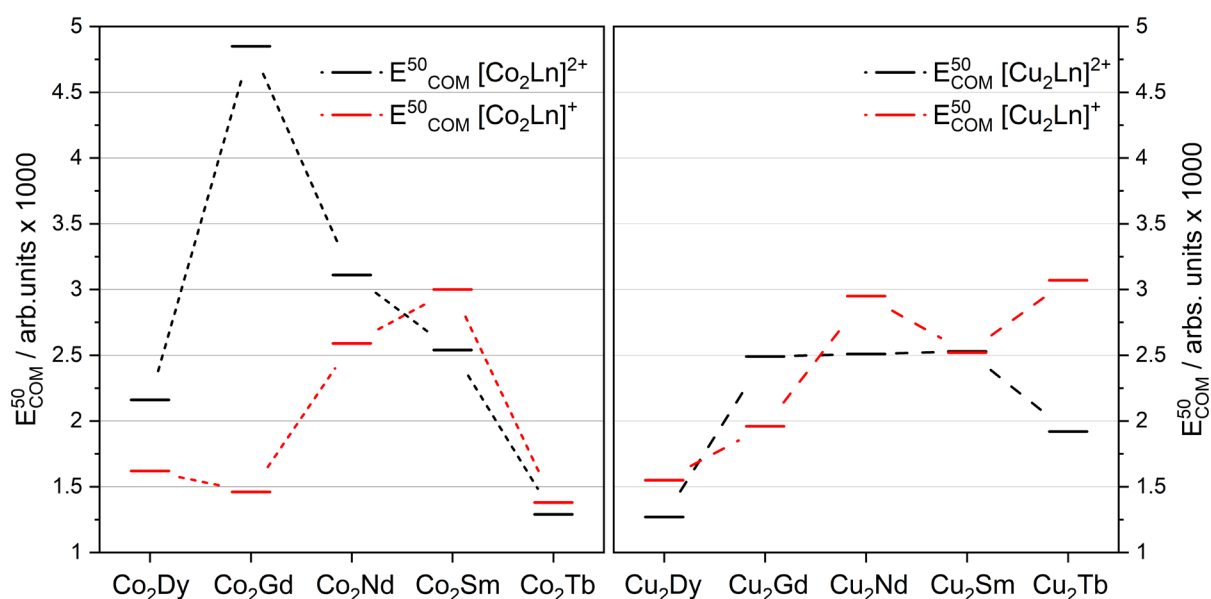


Fig. 6: Approximated gas phase stabilities of $[\text{Co}_2\text{Ln}(\text{HVab})(\text{Vab})_3]^{2+/+}$ (left) and $[\text{Cu}_2\text{Ln}(\text{HVab})(\text{Vab})_3]^{2+/+}$ (right) (Ln = Dy, Gd, Nd, Sm, Tb).

As previously stated, deuteration of these compounds only results in the exchange of one Hydrogen atom for a deuterium atom on the hydroxyl group, suggesting four separate potential isomers in these complexes. The calculated non covalent interactions of these isomers reveal similar interactions for all complexes and all possible isomers (cf. Fig. 7). These noncovalent interactions, on the other hand, contribute to explain the observed fragmentation pattern in this sequence of complexes.

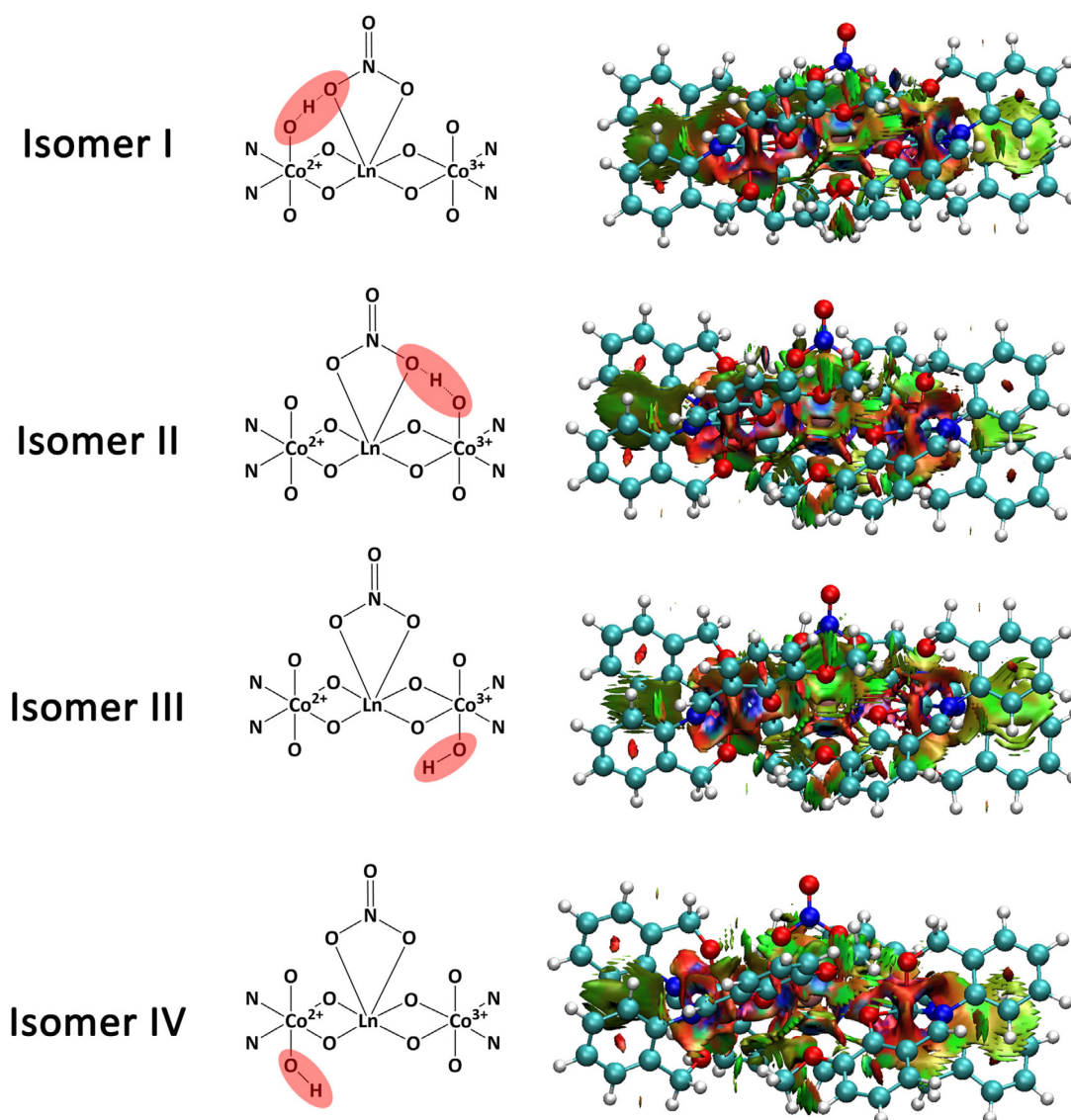


Fig. 7: Calculated non covalent interactions for $[M_2Ln(HVab)(Vab)_3]^{2+}$ (Ln = Dy, Gd, Nd, Sm, Tb) of the central oxygen atom. The calculations were performed with Gaussian 09 at the B3LYP/cc-pVTZ (H, C, N, O) and Stuttgart ecp effective core potential (Co, Dy, Gd, Nd, Sm, Tb) level of theory.

The non covalent interactions in the nitrate group are weak, leading to the lowest bonding strength, resulting in the main fragment of these complexes. The non covalent interactions are more vulnerable on that side where the transition metal with a higher oxidation state is located, leading to the fragmentation of a Vab ligand in this series of complexes, as observed. It is impossible to determine which isomer of these complexes is present with CID/ETD techniques because of their same masses.

9.6.2 InfraRed (Multiple) Photon Dissociation (IR(M)PD)

First, we recorded ATR spectra of the complex series in the range 700-4000 cm^{-1} and found comparable vibrational spectra to the Modak group^[25] (cf. Fig. S2). The recorded ATR spectra reveal the same spectral pattern by variation of the Lanthanide ions. We observe a broad band from 2000-3700 cm^{-1} , which must occur from the Hydrogen bonded hydroxyl groups. We also monitor the same trend by changing the transition metal from Cobalt to Copper. In solid state, weak coordination of methanol from the reaction solvent cannot be excluded. In the area from 700-2000 cm^{-1} , no changes in the spectral pattern appear. The ATR spectra reveal more bands than expected as a result of the high symmetry of the complexes. A high symmetry should result in fewer vibrational modes because most of the vibrational modes degenerate. In combination with the above discussed mass spectra, gas phase investigations seem necessary because the assumption of four hydroxyl groups in this series of complexes cannot be confirmed. The absence of at least three hydroxyl groups must change the oxidation state for one Cobalt, resulting in a change of the IR(M)PD spectra and their magnetism.

The recorded IR(M)PD spectra of these complexes reveal similar vibrational modes with the exchange of the Lanthanides (cf. Fig. 8). The most significant differences to the ATR spectra are reduced vibrational bands between 1000-1800 cm^{-1} by the cause of the high symmetry in the complexes. Also, the broad vibrational band in the region 2000-3700 cm^{-1} reveals more structure in the gas phase than in the solid phase. The change of the transition metal leads to significant changes in the IR(M)PD spectra (cf. Fig. 7). We assume that the methanol coordinates to the complex in solid state and leads to the broad Hydrogen bonded hydroxyl band in the ATR spectra.

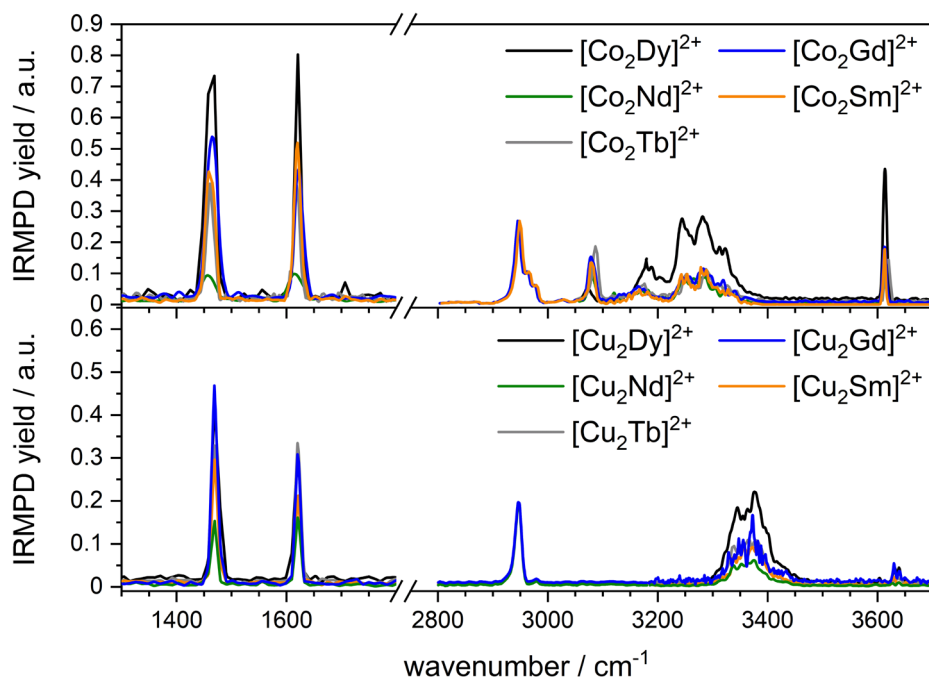


Fig. 8: Experimental IR(M)PD spectra of $[\text{Co}_2\text{Ln}(\text{HVab})(\text{Vab})_3]^{2+}$ (top) and $[\text{Cu}_2\text{Ln}(\text{HVab})(\text{Vab})_3]^{2+}$ (bottom) (Ln = Dy, Gd, Nd, Sm, Tb).

The IR(M)PD spectra of these complexes reveal just two vibrational bands between 1400 cm^{-1} and 1700 cm^{-1} , suggesting a high symmetry of the complex due to degenerated vibrational modes in this series of complexes. The crystal structure of this complex also points out a high symmetry of these complexes. The area between 2800 cm^{-1} and 3700 cm^{-1} reveals almost similar vibrational modes with the exchange of the Lanthanide considering contracted f orbitals in the Lanthanides, a significant energy shift is not expected in the vibrational modes. The change of the transition metal leads to a considerable difference in the vibrational modes of the IR(M)PD spectra in the area of $2800\text{--}3700\text{ cm}^{-1}$ (cf. Fig. 8).

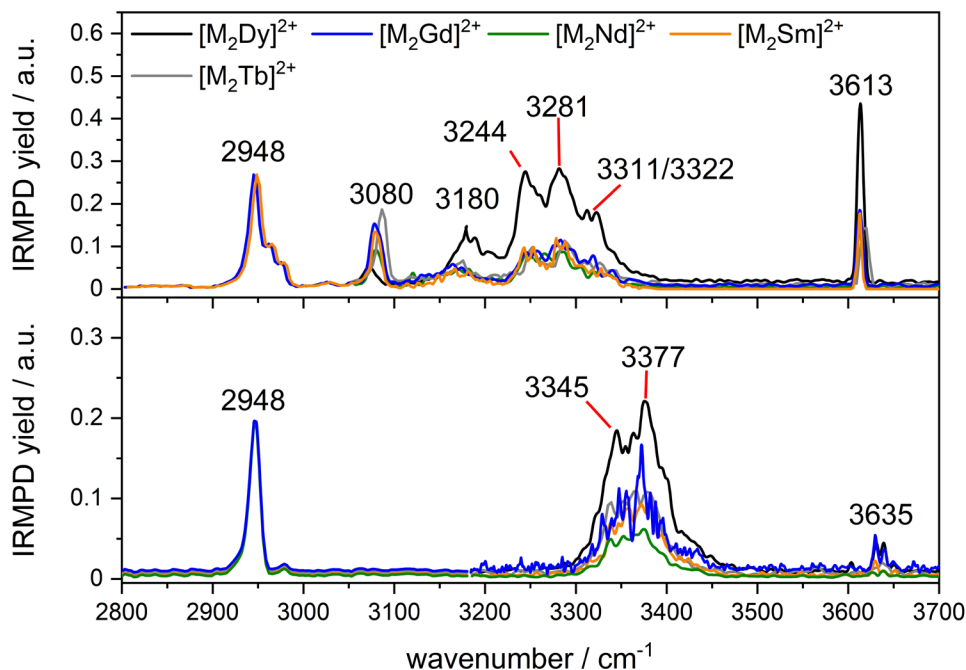


Fig. 9: Experimental IR(M)PD spectra of $[\text{Co}_2\text{Ln}(\text{HVab})(\text{Vab})_3]^{2+}$ (top) and $[\text{Cu}_2\text{Ln}(\text{HVab})(\text{Vab})_3]^{2+}$ (bottom) ($\text{Ln} = \text{Dy}, \text{Gd}, \text{Nd}, \text{Sm}, \text{Tb}$) in the area between 2800 cm^{-1} and 3700 cm^{-1} .

At around 3600 cm^{-1} belongs to the accessible OH stretching mode and obtains higher intensity in the Cobalt complexes than in the Copper complexes. Compared with the broad bands around $3250 \text{ cm}^{-1}/3350 \text{ cm}^{-1}$, which belong to Hydrogen bonded OH stretching modes, assuming that the Hydrogen bonding is stronger in the Cobalt complexes than in the Copper complexes. The presence of the additional bands in the Cobalt complexes hints different isomers of the complex. There may be one isomer with the same structure as in the Copper complexes and at least one isomer, resulting in a little symmetry distortion and non-degenerated vibrational modes of the methyl groups in the ligands. Also, the intensity of the vibrational stretching modes for the free OH group is higher in the Cobalt complex than in the Copper complex. There is also a free hydroxyl group isomer and a hydrogen bound hydroxyl group isomer. The band at around 2950 cm^{-1} belongs to alkyl C-H stretching modes and reveal a minor splitting into three vibrational bands in the Cobalt complexes, which is not observed in the Copper complexes. The splitting of this band also leads to the assumption of an isomer that does not attain a high symmetry in its structure in the Cobalt complexes.

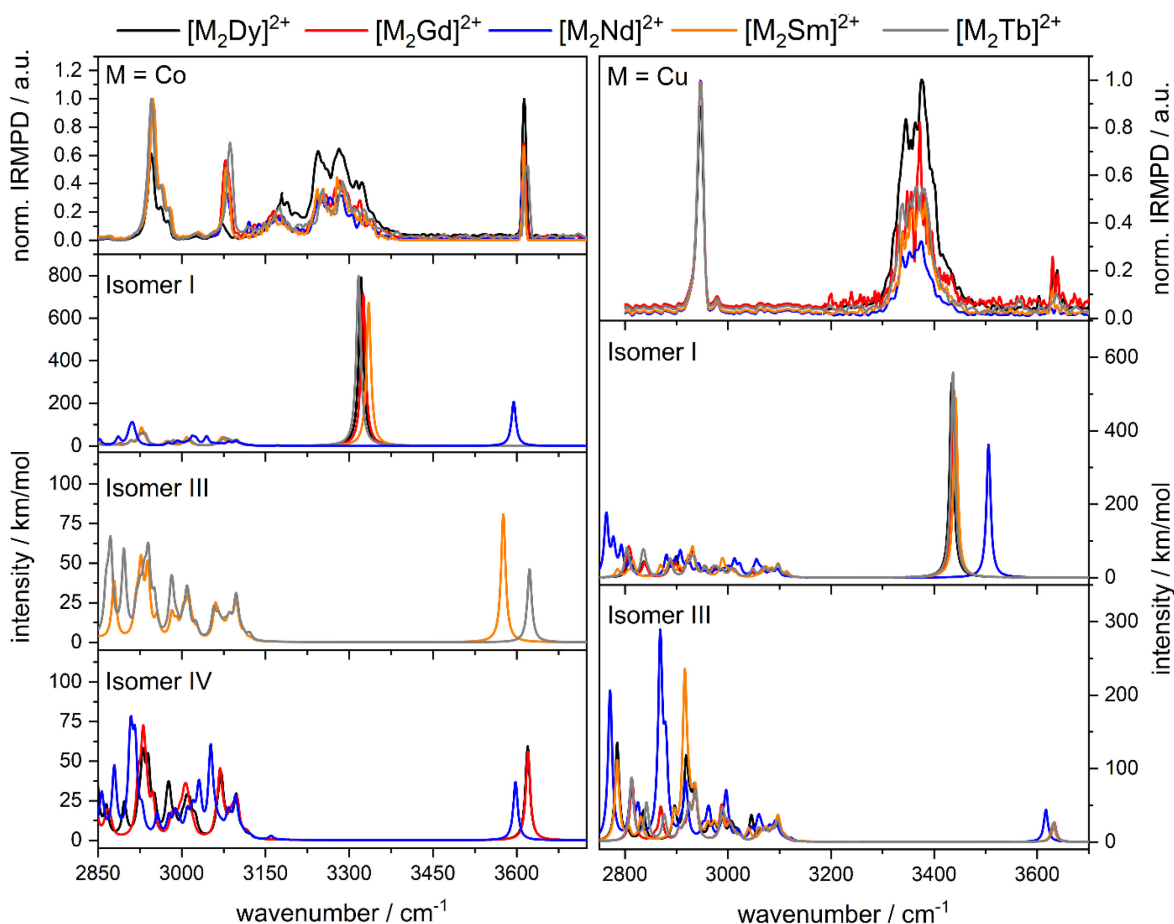


Fig. 10: Experimental IR(M)PD spectra of $[M_2Ln(HVab)(Vab)_3]^{2+}$ ($M = Co$ (left), Cu (right); $Ln = Dy, Gd, Nd, Sm, Tb$) in the area between 2800 cm^{-1} and 3700 cm^{-1} with the calculated possible isomers. The calculations were performed with Gaussian 09 at the B3LYP/cc-pVDZ (H, C, N, O) and Stuttgart ecp effective core potential (Co, Cu, Dy, Gd, Nd, Sm, Tb) level of theory. The spectra were scaled with 0.9641 to compensate anharmonicity in these complexes.

The calculated spectra for the different possible isomers are in good agreement with the experimental spectra (cf. Fig. 10). These complexes reveal a mixed valence state for the Cobalt complexes (e.g., $Co^{3+/2+}$) and for the copper complexes the transition metal ions remain in the same oxidation state (e.g., Cu^{2+}). As a result of the Lanthanide exchange, four distinct isomers can arise in these compounds. The calculated complexes point out two different isomers (I, II) with Hydrogen bonded OH vibrational modes, resulting in a strong redshift in the vibrational spectra. The isomer III and IV obtain a free hydroxyl group on the Co ions resulting in a vibrational mode at around 3600 cm^{-1} . As previously stated, only isomers III and IV exhibit non degenerated C-H stretching modes, indicating the presence of separate isomers in this series of complexes (cf. Fig. S3-S12).

Compared with the calculated vibrational spectra, we observe two isomers in a different composition in every complex. The complexes containing Copper reveal the isomers I and III in every spectrum. The isomer with a free vibrational hydroxyl group has a lower intensity and suggests that there is less of this isomer than the isomer with a hydrogen bound hydroxyl group. Also, the calculations point out that the free OH group is located at the Cu^{2+} ion because the ligand coordinates radically on the other Cu ion. Changing the location of the free OH group results in a spectral pattern that differs from the experimental pattern. Because of the little quantity of the isomer with a free OH group and its decreased symmetry, the band at approximately 3080 cm^{-1} in spectra containing Co ions is not visible in Cu complexes. The band is assigned as an asymmetric C-H stretching mode of the methyl group on the opposite side of the ligand, which is directly coordinated to the Lanthanide (cf. Fig. S13). The second band, at roughly 3150 cm^{-1} , is from another asymmetric C-H stretching mode of a different methyl group in these compounds. The difference between those C-H vibrational modes is that only two Hydrogens in the energetic lower vibrational mode are involved in the energetic higher mode. In all isomers without a hydrogen bonding, the asymmetric CH stretching mode at roughly 2990 cm^{-1} is neighbored to the free hydroxyl group. The determination of the isomers in Cobalt complexes is slightly more difficult than in the Copper complexes. We observe different pairs of isomers by variation of the Lanthanides.

The experimental spectra of the Cobalt complexes seem to be the same. According to the computations, the isomer I with a hydrogen-bonded OH group is present in all complexes. The complexes containing Sm^{3+} and Tb^{3+} the isomer III match the best to the experimental spectra. As a result, the free OH group is found on the Co^{3+} ion, and the splitting of the C-H groups at 2900 cm^{-1} more accurately depicts the spectral pattern than isomer IV. The Gadolinium complex indicates the second isomer IV, which has a free OH group on the Co^{2+} ion. The spectra for complexes containing Neodymium as Lanthanide do not match the calculated vibrational spectra in the same geometry (cf. Fig. 9 and Fig. S3-S12). The nitrate groups rotate more orthogonally in isomer I, resulting in a free hydroxyl vibrational mode for the Cobalt complexes. When the transition metal is changed to Copper, we monitor a hydrogen-bonded OH group towards the nitrate ligand. Still, this vibrational mode is also predicted to be less red shifted than the experimental IR(M)PD spectrum.

We assume that the Hydrogen bond observed in the experimental spectrum belongs to the structure of isomer I. Still, the Hydrogen bonding is weaker than in the other complexes and appears as a free OH group in the Cobalt complexes. Therefore, the change of the Lanthanides leads to different locations of the free OH group on the Co ions resulting in different isomers with minor changes in the spectral pattern of the vibrational spectra. The complex containing Dysprosium is the only complex where the low spin configuration for the isomer I is preferred over a high spin complex (cf. Tab. 1). The isomer IV is the second isomer in the dysprosium complex and also points out an excellent agreement with the experimental spectra.

Tab. 1: Relative energies (kJ/mol) of the spin configurations in the complex $[M_2Ln(HVab)(Vab)_3]^{2+}$ ($M = Co$; $Ln = Dy, Gd, Nd, Sm, Tb$). The calculations were performed with Gaussian 09 at the B3LYP/cc-pVDZ (H, C, N, O) and Stuttgart ecp effective core potential (Co, Dy, Gd, Nd, Sm, Tb) level of theory.

	Isomer I		Isomer II		Isomer III		Isomer IV	
	LS	HS	LS	HS	LS	HS	LS	HS
$[Co_2Dy]^{2+}$	0	75	0	20	2	0	25	0
$[Co_2Gd]^{2+}$	323	0	25	0	71	0	29	0
$[Co_2Nd]^{2+}$	140	0	175	0	281	0	275	0
$[Co_2Sm]^{2+}$	178	0	175	0	219	0	31	0
$[Co_2Tb]^{2+}$	16	0	63	0	44	0	31	0

In the complexes with Copper, a change in the spin configuration is not possible. A Cu^{2+} ion leads to a single unpaired electron in one d orbital and all other electrons remain in spin pairing, where also no change in the spin configuration is expected. Instead, the Cobalt ions can change from a low spin to a high spin state if the spin pairing energy is higher than the crystal field energy. Furthermore, a Co^{3+} stays diamagnetic, which should have an effect on the spectrum pattern of the vibrational spectra. The Cobalt complexes reveal a systematic pattern for the Hydrogen bonded OH group. Therefore, we cannot exclude isomer II, where the vibrational mode is slightly higher than isomer I, by changing the OH group from the Co^{2+} to the Co^{3+} ion (cf. Fig. 10). By including the spectral pattern, we exclude the third isomer for the Cobalt complexes.

Also, one isomer with free OH groups can be excluded from the spectral pattern of the CH stretching modes, where more calculated modes are observed. Still, because of symmetry, most of these bands degenerate, and a determination of the characteristic pattern around 2900 cm^{-1} leads to the observed isomer in the experimental spectra.

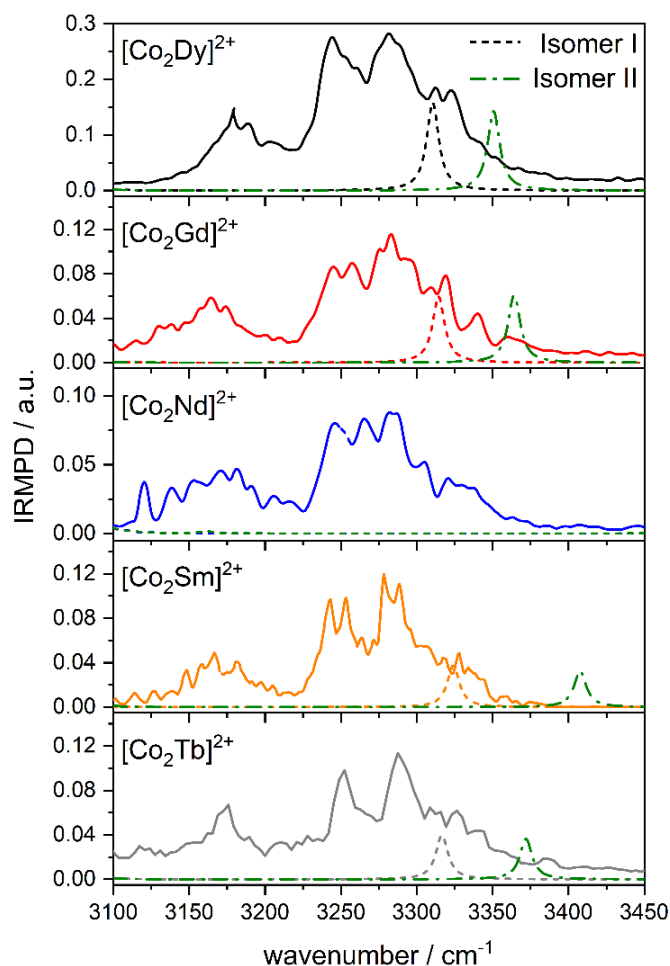


Fig. 11: Experimental IR(M)PD spectra of $[\text{Co}_2\text{Ln}(\text{HVab})(\text{Vab})_3]^{2+}$ ($\text{Ln} = \text{Dy}, \text{Gd}, \text{Nd}, \text{Sm}, \text{Tb}$) in the area between 3100 cm^{-1} and 3450 cm^{-1} with the calculated possible isomers I and II. The calculations were performed with Gaussian 09 at the B3LYP/cc-pVDZ (H, C, N, O) and Stuttgart ecp effective core potential (Co, Dy, Gd, Nd, Sm, Tb) level of theory. The spectra were scaled with 0.9641 to compensate anharmonicity in these complexes.

Unfortunately, the determination of the different isomers cannot be understated by the bands in the fingerprint area because of the high symmetry of the complex. We only observe two bands in the experimental spectra but more predicted bands in the calculations (cf. Fig. 12).

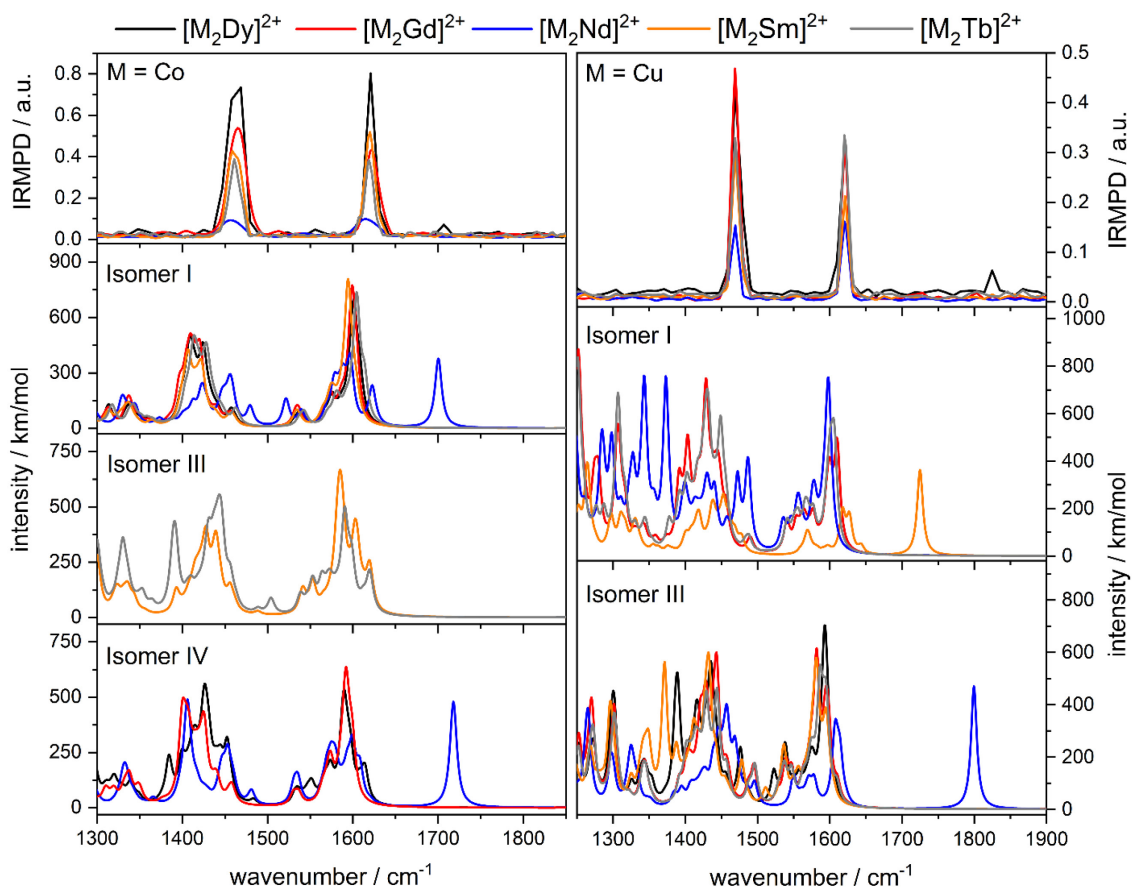


Fig. 12: Experimental IR(M)PD spectra of $[M_2Ln(HVab)(Vab)_3]^{2+}$ ($M = Co$ (left), Cu (right); $Ln = Dy, Gd, Nd, Sm, Tb$) in the area between 1300 cm^{-1} and 1800 cm^{-1} with the calculated possible isomers. The calculations were performed with Gaussian 09 at the B3LYP/cc-pVDZ (H, C, N, O) and Stuttgart ecp effective core potential (Co, Dy, Gd, Nd, Sm, Tb) level of theory. The spectra were scaled with 0.9641 to compensate anharmonicity in these complexes.

The band at 1619 cm^{-1} can be assigned to the N-O stretching mode of the nitrate group in combination with C-C benzyl stretching modes. The second vibrational band at 1466 cm^{-1} belongs to the isomers of the C-H bending modes methyl groups with a free hydroxyl group. For the Hydrogen bonded isomer, these bands can be assigned to N-O stretching mode at 1619 cm^{-1} , and the band at 1466 cm^{-1} still belongs to the methyl groups of the ligand. Both isomers highlight these characteristic bands, and no further differentiation of the distinct isomers in this series of compounds is feasible. However, it is evident that two different isomers are present in the complexes, and every mode is present to determine the structure of these complexes. We also observe bands in the calculated vibrational spectra, which do not agree with the other computed Lanthanide complexes. In the Cobalt/Neodymium complexes, we observe one band at around 1700 cm^{-1} for both isomers. These bands belong to the nitrate

stretching mode as in the other isomers. Still, the nitrate Hydrogen bonding in the isomer I is weakened by a rotation of the nitrate group, resulting in a more extended Hydrogen nitrate bonding. In the other isomer (IV), the calculated band also belongs to the nitrate group but without a Hydrogen bonding resulting in a shift to higher wavenumbers of the vibrational mode. We observe the same trend for the Copper complexes containing Samarium and Neodymium as Lanthanide. In all these complexes, we observe a slight rotation of the nitrate group in the complexes. We applied for all the calculations the same scaling factor for better comparability. Using a scaling factor of 0.8941 instead of 0.9641, these spectra match the others. Therefore, we assume higher anharmonicities in these complexes than in the other ones. The experimental IR(M)PD spectra reveal a less red shifted Hydrogen bonded hydroxyl group in the Copper complexes than in the Cobalt complexes (cf. Tab. 2). Also, the vibrational stretching mode of the free hydroxyl group is less red shifted than in the Cobalt analoga.

Tab. 2: Experimental IR(M)PD vibrational modes and their corresponding shifts relative to the $[\text{Co}_2\text{Ln}(\text{HVab})(\text{Vab})_3]^{2+}$ vibrational modes.

	$\nu_{(\text{OH bond})}/\text{cm}^{-1}$	$\nu_{(\text{Free OH})}/\text{cm}^{-1}$	$\Delta\nu/\text{cm}^{-1}$	$\Delta\nu/\text{cm}^{-1}$
$[\text{Co}_2\text{Ln}]^{2+}$	3281	3613	0	0
$[\text{Cu}_2\text{Ln}]^{2+}$	3376	3628	95	15

We assume that the unpaired electrons in the Cobalt ions lead to a more vital bonding situation than the Copper ions, resulting in a higher redshift of the OH stretching modes. The averaged bonding length for the Hydrogen bond is 1.81 Å for the Cobalt complexes and 1.83 Å for the Copper complexes, indicating a weaker bonding, resulting in a less redshift of the vibrational bands. Also, in the isomer III, the bonding length for the coordination of the hydroxyl groups elongates from Co with 2.22 Å to Cu with 2.34 Å, which weakens the bonding strength and results in a less redshifted stretching mode of the free OH group.

9.6.3 Theoretical approximation of the XA spectra and UV correlation

We performed XA simulations for the Cobalt ions in different oxidation states (cf. Fig. 13) and observe a significant energy shift with the oxidation state change by 2.24 eV, leading to a change in the spectral pattern of the XA spectra and pointing out a mixed valence configuration in the Cobalt complexes. The involving ligand field is not included because the influence of the ligand on the transition metal should be more negligible than 1 eV^[40-45].

Also, the spin orbit coupling constants from the core-shell to the valence hole reveal a higher value for the Co^{2+} ion than for the Co^{3+} ion. An open shell system must lead to a lower spin pairing energy than in a closed shell complex. The Co^{2+} ion has one unpaired electron in the low spin configuration and three unpaired electrons in the high spin configuration, resulting in a higher SOC because the orbital momentum must be higher than in transition metal ions with an even number of electrons due to a homogeneous electron distribution resulting in a spherical electron density. As previously stated, the effect of organic ligand coordination is not included in these simulations, although it can influence the SOC through charge transfer, Jahn Teller distortions, and exchange coupling of the Lanthanide in this series of complexes.

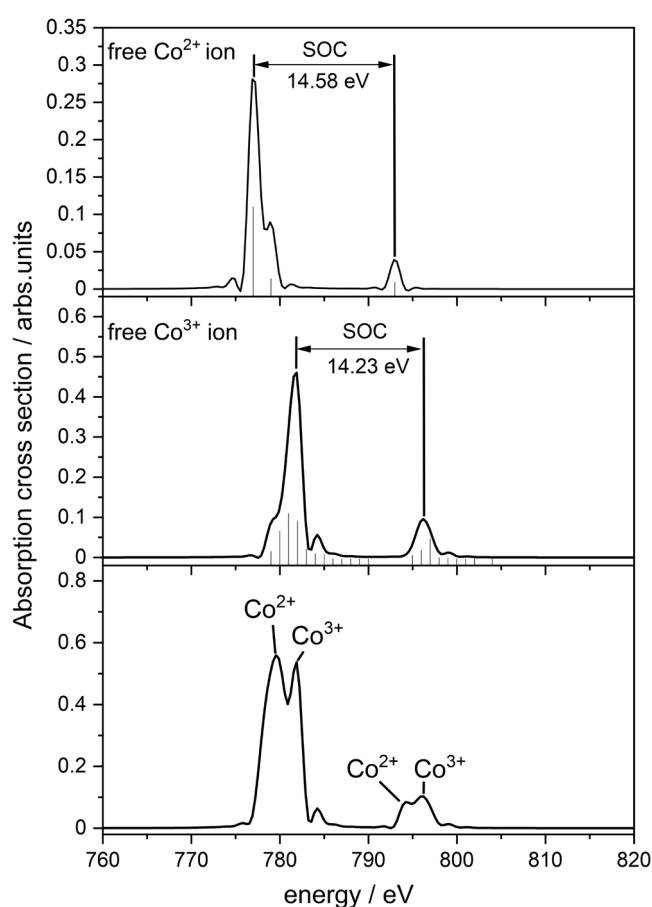


Fig. 13: Simulated XA spectra of free $\text{Co}^{2+/3+}$ atoms at 4.5 K by CTM4XAS and Cowan batch files with corresponding spin orbit coupling constants.

The Copper $\text{L}_{3,2}$ absorption edges simulation does not point out any detail for determining the crystal field splitting (cf. Fig. S14). Therefore, a correlation between the XA spectra and UV/VIS absorptions is not possible. A SOC value for the Cu^{2+} ion is higher than in the Cobalt analoga. The higher SOC occurs from more electrons in the Copper ion than in the Cobalt ion.

There is no possibility for a low spin or high spin composition, resulting in a fixed spin and orbital magnetic moment for the complex. The magnetism only changes by variation of the Lanthanides. For the Cu^{2+} ion in the complex, the unpaired electron should not affect the significant magnetic properties in the complexes, obtaining Cobalt as transition metal complexes.

The XA simulations of the Lanthanides in the $M_{4,5}$ edges reveal almost similar spectral patterns for the investigated Lanthanides presented in this work. The major difference between these spectra is the absorption energy and the spin orbit couplings (cf. Fig. S15). We observe broad absorption bands in all simulated XA spectra for this series of Lanthanides. The neodymium ion has the lowest SOC, and as previously stated, the complex containing Neodymium does not exhibit single-molecule magnetic behavior^[25]. Neodymium achieves the lowest number of unpaired electrons in this series of Lanthanides. A high spin ground state defines a single molecule magnetic behavior in combination with a high anisotropic barrier. The lowest spin orbit coupling of Neodymium hints no SMM behavior in these complexes. We assume that the complex containing Neodymium points out the lowest anisotropic barrier resulting in inefficient SMM behavior. With the simulated XA spectra, we can determine the crystal field splitting for the different transition metal and Lanthanide ions (cf. Tab. 2). We observe a higher crystal field splitting in the Co^{3+} ion than in the Co^{2+} ion. Higher crystal field splitting results in more intense spin pairing energy, resulting in no unpaired electrons in the Co^{3+} ion, implying that no exchange coupling between the Lanthanide and the Co^{3+} ion is provided. This expresses that the magnetic behavior of these complexes mainly occurs from the Lanthanide ions themselves and not from a strong exchange coupling between the transition metal ions and the Lanthanides. Except for the neodymium ion, the crystal field splitting of the Lanthanides displays virtually identical crystal field splittings in this sequence of complexes. According to the same reasoning as for transition metal ions, the crystal field energy is higher than the spin pairing energy, resulting in fewer unpaired electrons and lower magnetic behavior.

Tab. 2: Approximated crystal field splittings of the different transition metals from the simulated XA spectra and their normalization with the Racah parameter $B^{[46]}$ for Cobalt and the Racah parameter $E^{[47]}$ for Ln.

	CF/eV	CF/cm ⁻¹	CF/B
Co ²⁺	1.99	16050	16.83
Co ³⁺	2.56	20648	18.77
Dy ³⁺	5.23	42183	48.53
Gd ³⁺	4.85	39118	46.89
Nd ³⁺	5.56	44844	61.06
Sm ³⁺	4.01	32343	41.22
Tb ³⁺	5.52	44522	51.32

We utilized the Racah parameter B normalized crystal field splittings with the matching Tanabe Sugano diagram to approximate the UV/VIS absorption bands (cf. Fig. 14). This approximation covers weak spin prohibited MLCT transitions for distinct transition metal UV/VIS absorption spectra. For the Co²⁺, we predict a ⁵T_{2g} to a ¹A_{1g} transition and a ⁴T_{1g} to a ²E_g transition for the Co³⁺ ion and observe very low energies for the UV/VIS absorptions. This hints that, in this series of complexes, no MLCT transitions are present, and absorption bands mainly occur from the benzyl rings of the ligand.

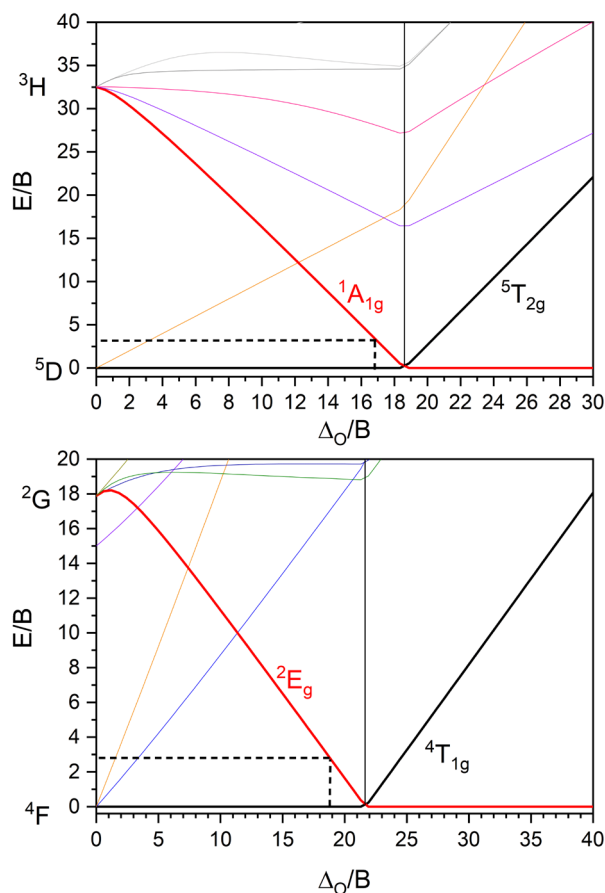


Fig. 14: Tanabe Sugano diagram for free Co^{2+} (top) and Co^{3+} (bottom) with the simulated crystal field splittings from the XA spectra and their associated transition energies in the UV/VIS spectra.

The renormalization of the approximated absorption energies results in energies in the mid-IR region (cf. Tab. 3), which suggests to low-lying electronic transitions for Cobalt and may be noticed in the provided IR(M)PD spectra^[48-53] associated with a Hydrogen bound hydroxyl group as stated above. The Cobalt complexes only have one hydroxyl group, but the spectral pattern in the IR(M)PD spectra reveals three different peaks that are not present in the Copper analoga. Also, one hydroxyl cannot establish three different vibrational modes to generate a spectral pattern of three distinct peaks.

Tab. 3: Approximated normalized crystal field splittings, normalized absorption energies, and renormalized absorption energies with the Racah parameter $B^{[46]}$ for Cobalt in different oxidation states.

	CF/B	E/B	E/cm ⁻¹	E/nm
Co^{2+}	16.83	3.35	3253	3074
Co^{3+}	18.77	2.99	3289	3040

As observed before, the approximation of the UV/VIS absorption bands might lead to low-lying electronic transitions in the IR(M)PD spectra. Therefore, we compared the approximated transitions with the experimental normalized and averaged IR(M)PD spectra of the Cobalt/Lanthanide complexes (cf. Fig. 15).

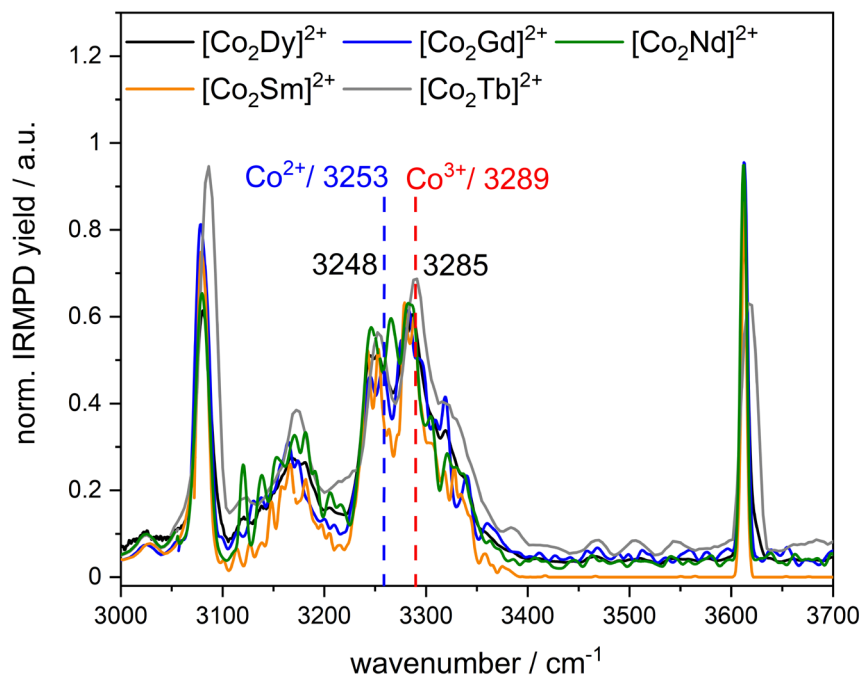


Fig. 15: Experimental IR(M)PD spectrum of $[\text{Co}_2\text{Ln}(\text{HVab})(\text{Vab})_3]^{2+}$ ($\text{Ln} = \text{Dy}, \text{Gd}, \text{Nd}, \text{Sm}, \text{Tb}$) in the area between 3000 cm^{-1} and 3700 cm^{-1} in comparison with the approximated transitions from the Tanabe Sugano diagram.

The observed band around 3300 cm^{-1} is broad and points out a splitting into three vibrational modes. Usually, Hydrogen bonded OH stretching vibrations are red shifted and broadened but mostly did not show any other feature than a broad distribution^[48-54] because of their weak bonding situation. The bonding distances of the Cobalt complexes are, on average, 1.81 \AA for the Hydrogen bonding and almost similar to the averaged bonding distance of 1.83 \AA in the Copper complexes. We assume that the Hydrogen bonding strength in all complexes is identical, and the splitting may occur from electronic transitions. Also, Electronic Localized Field (ELF) plots point out almost similar electron distribution in this series of complexes (cf. Fig. 16).

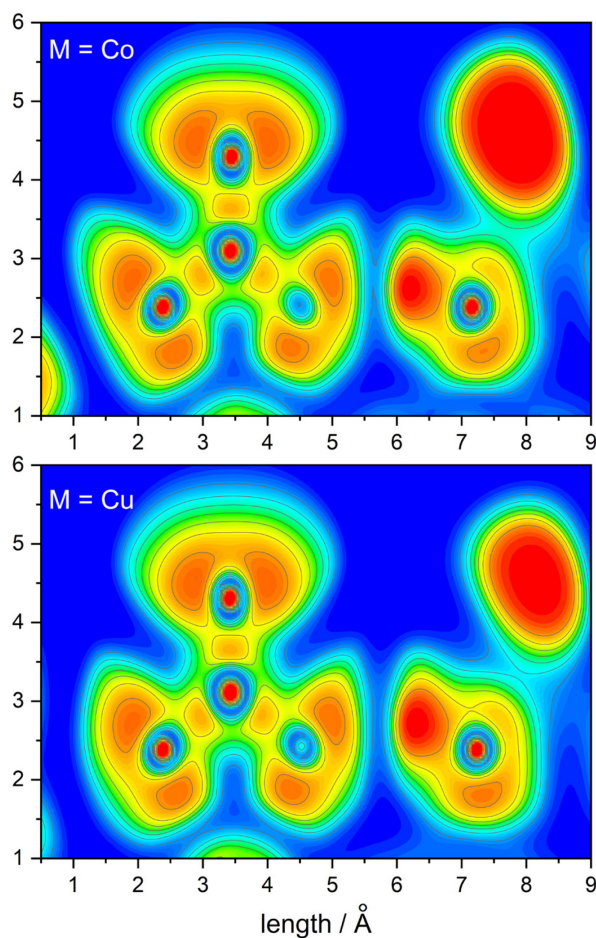


Fig. 16: Electron Localized Field (ELF) of $[M_2Ln(HVab)(Vab)_3]^{2+}$ ($M = Co, Cu$; $Ln = Dy, Gd, Nd, Sm, Tb$). The calculations were performed with Gaussian 09 at the B3LYP/cc-pVDZ (H, C, N, O) and Stuttgart ecp effective core potential (Co, Dy, Gd, Nd, Sm, Tb) level of theory.

As expected, the ELF plots reveal weak covalent interactions for the Hydrogen bonding in this series of complexes. Combined with the knowledge of only one hydroxyl group in these complexes, only two vibrational modes can occur. One vibrational mode is the stretching mode around $3200-3400\text{ cm}^{-1}$, and the other is the bending mode around 1800 cm^{-1} . With the exclusion of another Hydrogen bound isomer, we consider that the spectrum pattern in Cobalt complexes results from an overlay of Hydrogen bonding and low-lying electronic transitions from Cobalt atoms in different oxidation states. Copper does not exhibit low lying electronic transitions, and the IR(M)PD spectra of the complexes do not suggest such characteristics. We can neither confirm nor deny the presence of low-lying electronic transitions with the above performed technique. Still, the approximation of the UV/VIS transitions strongly gives hints to such transitions in the IR(M)PD spectra.

9.7 Conclusion

In the presented work, we investigate the structural properties of a series of complexes with the general structure $[M_2Ln(HVab)(Vab)_3]^{2+}$ ($M = Co, Cu$; $Ln = Dy, Gd, Nd, Sm, Tb$) via mass spectrometry, CID and IR(M)PD. We observe complexes with masses that lead to a loss of three protons than the predicted complex with the same netto charge, indicating mixed valence complexes. Deuteration of the complexes results in the substitution of only one Hydrogen for Deuterium, assuming only one hydroxyl group is present.

Collision Induced Dissociation breakdown curves reveal that losing a nitrate group and the addition of molecular Hydrogen simultaneously represent the main fragmentation channel. The second fragmentation channel is the loss of one tetradentate ligand (Vab). The CID breakdown curves of the ETD reduced complexes reveal similar fragmentation behavior with different gas phase stabilities.

IR(M)PD studies reveal two different isomers for all complexes compared with calculated linear absorption spectra. In the Cobalt complexes, two isomers are more prominent, with a complex obtaining a Hydrogen bonded hydroxyl group and one with a free hydroxyl group. The Copper complexes instead show a lower intensity of the stretching mode for a free hydroxyl group. The exchange of the Lanthanides does not affect the vibrational modes in any way. The isomer composition changes as the transition metal is switched from Cobalt to Copper, and the Hydrogen bound vibrational modes become less red shifted. The complexes containing Neodymium should not show any single molecule magnetic behavior. Also, the calculations point out that the nitrate group is more twisted than in the other complexes, resulting in weaker bonding strength of the Hydrogen bonded hydroxyl group. The experimental spectra instead show no difference to the other complexes. Strong anharmonicities in the complex cannot be excluded, but it is necessary for better comparing to apply the same scaling factor.

Simulation of the XA spectra indicates that a mixed valence state in these complexes would be easily observed in experimental XA spectra. Different spin orbit constants from the core to the valence hole are less for Neodymium than for all other Lanthanides, indicates that the

magnetic behavior of a single molecule is solely due to the intrinsic features of the Lanthanides.

Also, a mixed valence state suggests that only a Co^{2+} ion can perform an exchange coupling with the Lanthanide, where the Co^{3+} remains in a diamagnetic configuration.

Determining the crystal field splitting in the simulations approximates the possible UV/VIS absorptions within a Tanabe Sugano diagram. As a result, no UV/VIS excitation is predicted, but probable absorptions in the IR(M)PD spectra where the hydrogen bound hydroxyl group absorbs are expected. The IR(M)PD spectra for the Cobalt complexes show a pattern with three possible absorption bands, and one can be determined to the hydroxyl group in one isomer. The bonding distances for the Copper and Cobalt complexes are almost similar. ELF plots also show equal electron distribution between the Hydrogen and the nitrate group in all complexes. They can be attributed to low-lying electronic transitions of certain Cobalt ions. Furthermore, the Copper complexes hint to such a transition since these patterns are not seen with Copper ions, revealing low-lying electronic transitions in the Cobalt complexes.

In summary, CID and IR(M)PD studies of this series of complexes reveal a slightly different structure as already published by Modak. The absence of three Hydrogen atoms leads to a mixed valence complex instead of complexes with the same oxidation state in the transition metal ions with the same netto charge.

9.8 Acknowledgment

The German research foundation DFG supported this work within the transregional collaborative research center SFB/TRR 88 "Cooperative effects in homo and heterometallic complexes" (3MET) and by the state research center OPTIMAS.

9.9 References

- [1] R. Winnpenny volume editor, and G. Aromi with contributions by, *Single-molecule magnets and related phenomena*: Berlin ; New York : Springer, 2006.
- [2] G. Aromí, D. Aguilà, P. Gamez, F. Luis, and O. Roubeau, Design of magnetic coordination complexes for quantum computing, *Chem. Soc. Rev.*, 41, 537-546, 2012.
- [3] M. N. Leuenberger, and D. Loss, Quantum computing in molecular magnets, *Nature*, 410, 789-793, 2001.
- [4] M. Mannini, F. Pineider, P. Sainctavit, C. Danieli, E. Otero, C. Sciancalepore, A. M. Talarico, M.-A. Arrio, A. Cornia, D. Gatteschi, and R. Sessoli, Magnetic memory of a single-molecule quantum magnet wired to a gold surface, *Nature Materials*, 8, 194-197, 2009.

9. IR(M)PD studies on a series of isolated trimetallic single molecule magnets containing 3d metals and Lanthanides

- [5] K. V. Raman, A. M. Kamerbeek, A. Mukherjee, N. Atodiresei, T. K. Sen, P. Lazić, V. Caciuc, R. Michel, D. Stalke, S. K. Mandal, S. Blügel, M. Münzenberg, and J. S. Moodera, Interface-engineered templates for molecular spin memory devices, *Nature*, 493, 509-513, 2013.
- [6] T. Lis, Preparation, structure, and magnetic properties of a dodecanuclear mixed-valence manganese carboxylate, *Acta Crystallographica Section B*, 36, 2042-2046, 1980.
- [7] J. M. Clemente-Juan, E. Coronado, A. Forment-Aliaga, A. Gaita-Ariño, C. Giménez-Saiz, F. M. Romero, W. Wernsdorfer, R. Biagi, and V. Corradini, Electronic and Magnetic Study of Polycationic Mn₁₂ Single-Molecule Magnets with a Ground Spin State $S = 11$, *Inorg. Chem.*, 49, 386-396, 2010.
- [8] K. Kim, A. Ford, V. Meenakshi, W. Teizer, H. Zhao, and K. R. Dunbar, Nanopatterning of Mn₁₂-acetate single-molecule magnet films, *J. Appl. Phys.*, 102, 094306, 2007.
- [9] M. Mannini, F. Pineider, P. Sainctavit, L. Joly, A. Fraile-Rodríguez, M.-A. Arrio, C. Cartier dit Moulin, W. Wernsdorfer, A. Cornia, D. Gatteschi, and R. Sessoli, X-Ray Magnetic Circular Dichroism Picks out Single-Molecule Magnets Suitable for Nanodevices, *Adv. Mat.*, 21, 167-171, 2009.
- [10] K. M. Mertes, Y. Suzuki, M. P. Sarachik, Y. Myasoedov, H. Shtrikman, E. Zeldov, E. M. Rumberger, D. N. Hendrickson, and G. Christou, Mn₁₂-acetate: a prototypical single molecule magnet, *Solid State Comm.*, 127, 131-139, 2003.
- [11] J. A. A. J. Perenboom, J. S. Brooks, S. Hill, T. Hathaway, and N. S. Dalal, Relaxation of the magnetization of Mn₁₂ acetate, *Phys. Rev. B*, 58, 330-338, 1998.
- [12] G. Rogez, B. Donnio, E. Terazzi, J.-L. Gallani, J.-P. Kappler, J.-P. Bucher, and M. Drillon, The Quest for Nanoscale Magnets: The example of [Mn₁₂] Single Molecule Magnets, *Adv. Mat.*, 21, 4323-4333, 2009.
- [13] S. Voss, M. Fonin, U. Rüdiger, M. Burgert, U. Groth, and Y. S. Dedkov, Electronic structure of Mn₁₂ derivatives on the clean and functionalized Au surface, *Phys. Rev. B*, 75, 045102, 2007.
- [14] H. Zhao, C. P. Berlinguette, J. Bacsá, A. V. Prosvirin, J. K. Bera, S. E. Tichy, E. J. Schelter, and K. R. Dunbar, Structural Characterization, Magnetic Properties, and Electrospray Mass Spectrometry of Two Jahn-Teller Isomers of the Single-Molecule Magnet [Mn₁₂O₁₂(CF₃COO)₁₆(H₂O)₄], *Inorg. Chem.*, 43, 1359-1369, 2004.
- [15] P.-E. Car, M. Perfetti, M. Mannini, A. Favre, A. Caneschi, and R. Sessoli, Giant field dependence of the low temperature relaxation of the magnetization in a dysprosium(iii)-DOTA complex, *Chem. Comm.*, 47, 3751-3753, 2011.
- [16] G. Cucinotta, M. Perfetti, J. Luzon, M. Etienne, P.-E. Car, A. Caneschi, G. Calvez, K. Bernot, and R. Sessoli, Magnetic Anisotropy in a Dysprosium/DOTA Single-Molecule Magnet: Beyond Simple Magneto-Structural Correlations, *Angew. Chem. Int. Ed.*, 51, 1606-1610, 2012.
- [17] Y.-N. Guo, G.-F. Xu, P. Gamez, L. Zhao, S.-Y. Lin, R. Deng, J. Tang, and H.-J. Zhang, Two-Step Relaxation in a Linear Tetranuclear Dysprosium(III) Aggregate Showing Single-Molecule Magnet Behavior, *J. Am. Chem. Soc.*, 132, 8538-8539, 2010.
- [18] I. J. Hewitt, J. Tang, N. T. Madhu, C. E. Anson, Y. Lan, J. Luzon, M. Etienne, R. Sessoli, and A. K. Powell, Coupling Dy₃ Triangles Enhances Their Slow Magnetic Relaxation, *Angew. Chem. Int. Ed.*, 49, 6352-6356, 2010.
- [19] N. Ishikawa, M. Sugita, T. Ishikawa, S.-y. Koshihara, and Y. Kaizu, Lanthanide Double-Decker Complexes Functioning as Magnets at the Single-Molecular Level, *Journal of the American Chemical Society*, 125, 8694-8695, 2003.
- [20] E. Moreno-Pineda, C. Godfrin, F. Balestro, W. Wernsdorfer, and M. Ruben, Molecular spin qubits for quantum algorithms, *Chem. Soc. Rev.*, 47, 501-513, 2018.
- [21] J. Dreiser, K. S. Pedersen, A. Schnegg, K. Holldack, J. Nehr Korn, M. Sigrist, P. Tregenna-Piggott, H. Mutka, H. Weihe, V. S. Mironov, J. Bendix, and O. Waldmann, Three-Axis Anisotropic Exchange Coupling in the Single-Molecule Magnets NEt₄[Mn^{III}₂(5-Brsalen)₂(MeOH)₂M^{III}(CN)₆] (M=Ru, Os), *Chemistry – A European Journal*, 19, 3693-3701, 2013.
- [22] P. Hahn, S. Ullmann, J. Klose, Y. Peng, A. K. Powell, and B. Kersting, Dinuclear Tb and Dy complexes supported by hybrid Schiff-base/calixarene ligands: synthesis, structures and magnetic properties, *Dalt. Trans.*, 2020.
- [23] A. Dey, S. Das, V. Mereacre, A. K. Powell, and V. Chandrasekhar, Butterfly-shaped, heterometallic, hexanuclear, [Fe^{III}₂Ln^{III}₄] (Ln^{III} = Gd^{III}, Tb^{III}, Dy^{III} and Ho^{III}) Complexes: Syntheses, structure and magnetism, *Inorganica Chimica Acta*, 486, 458-467, 2019.
- [24] J.-W. Lu, Y.-H. Huang, S.-I. Lo, and H.-H. Wei, New μ -oxo-bridged tetranuclear Cu(II) complex with Schiff-base ligand: Synthesis, crystal structure and magnetic properties, *Inorganic Chemistry Communications*, 10, 1210-1213, 2007.

- [25] R. Modak, Y. Sikdar, A. E. Thuijs, G. Christou, and S. Goswami, Coll4, Coll7, and a Series of Coll2LnIII (LnIII = NdIII, SmIII, GdIII, TbIII, DyIII) Coordination Clusters: Search for Single Molecule Magnets, *Inorg. Chem.*, 55, 10192-10202, 2016.
- [26] R. Colton, A. D'Agostino, and J. C. Traeger, Electrospray mass spectrometry applied to inorganic and organometallic chemistry, *Mass Spectrom. Rev.*, 14, 79-106, 1995.
- [27] J. B. Fenn, Electrospray Wings for Molecular Elephants (Nobel Lecture), *Angew. Chem. Int. Ed.*, 42, 3871-3894, 2003.
- [28] S. A. McLuckey, and D. E. Goeringer, SPECIAL FEATURE: TUTORIAL Slow Heating Methods in Tandem Mass Spectrometry, *J. Mass Spectrom.*, 32, 461-474, 1997.
- [29] J. Lang, J. M. Hewer, J. Meyer, J. Schuchmann, C. van Wüllen, and G. Niedner-Schatteburg, Magnetostructural correlation in isolated trinuclear iron(III) oxo acetate complexes, *Phys. Chem. Chem. Phys.*, 20, 16673-16685, 2018.
- [30] E.-L. Zins, C. Pepe, D. Rondeau, S. Rochut, N. Galland, and J.-C. Tabet, Theoretical and experimental study of tropylium formation from substituted benzylpyridinium species, *J. Mass Spectrom.*, 44, 12-17, 2009.
- [31] E.-L. Zins, C. Pepe, and D. Schröder, Energy-dependent dissociation of benzylpyridinium ions in an ion-trap mass spectrometer, *J. Mass Spectrom.*, 45, 1253-1260, 2010.
- [32] E.-L. Zins, D. Rondeau, P. Karoyan, C. Fosse, S. Rochut, and C. Pepe, Investigations of the fragmentation pathways of benzylpyridinium ions under ESI/MS conditions, *J. Mass Spectrom.*, 44, 1668-1675, 2009.
- [33] A. D. Becke, Density-functional exchange-energy approximation with correct asymptotic behavior, *Phys. Rev. A*, 38, 3098-3100, 1988.
- [34] B. Miehlich, A. Savin, H. Stoll, and H. Preuss, Results obtained with the correlation energy density functionals of Becke and Lee, Yang and Parr, *Chem. Phys. Lett.*, 157, 200-206, 1989.
- [35] T. H. Dunning, Gaussian basis sets for use in correlated molecular calculations. I. The atoms boron through neon and hydrogen, *J. Chem. Phys.*, 90, 1007-1023, 1989.
- [36] M. Dolg, H. Stoll, H. Preuss, and R. M. Pitzer, Relativistic and correlation effects for element 105 (hahnium, Ha): a comparative study of M and MO (M = Nb, Ta, Ha) using energy-adjusted ab initio pseudopotentials, *J. Phys. Chem.*, 97, 5852-5859, 1993.
- [37] M. J. Frisch et. al, "Gaussian 16 Rev. C.01," 2016.
- [38] R. F. W. Bader, A quantum theory of molecular structure and its applications, *Chem. Rev.*, 91, 893-928, 1991.
- [39] E. Stavitski, and F. M. F. de Groot, The CTM4XAS program for EELS and XAS spectral shape analysis of transition metal L edges, *Micron*, 41, 687-694, 2010.
- [40] J. Everett, E. Céspedes, L. R. Shelford, C. Exley, J. F. Collingwood, J. Dobson, G. van der Laan, C. A. Jenkins, E. Arenholz, and N. D. Telling, Ferrous iron formation following the co-aggregation of ferric iron and the Alzheimer's disease peptide β -amyloid (1-42), *J. Royal Soc. Interface*, 11, 20140165, 2014.
- [41] W. Gu, H. Wang, and K. Wang, Nickel L-edge and K-edge X-ray absorption spectroscopy of non-innocent Ni[S₂C₂(CF₃)₂]_{2n} series (n = -2, -1, 0): direct probe of nickel fractional oxidation state changes, *Dalt. Trans.*, 43, 6406-6413, 2014.
- [42] G. S. Henderson, F. M. F. de Groot, and B. J. A. Moulton, X-ray Absorption Near-Edge Structure (XANES) Spectroscopy, *Reviews in Mineralogy and Geochemistry*, 78, 75-138, 2014.
- [43] R. K. Hocking, S. DeBeer George, K. N. Raymond, K. O. Hodgson, B. Hedman, and E. I. Solomon, Fe L-edge X-ray absorption spectroscopy determination of differential orbital covalency of siderophore model compounds: electronic structure contributions to high stability constants, *J. Am. Chem. Soc.*, 132, 4006-4015, 2010.
- [44] J. K. Kowalska, A. W. Hahn, A. Albers, C. E. Schiewer, R. Bjornsson, F. A. Lima, F. Meyer, and S. DeBeer, X-ray Absorption and Emission Spectroscopic Studies of [L₂Fe₂S₂]_n Model Complexes: Implications for the Experimental Evaluation of Redox States in Iron-Sulfur Clusters, *Inorg. Chem.*, 55, 4485-4497, 2016.
- [45] J. K. Kowalska, B. Nayyar, J. A. Rees, C. E. Schiewer, S. C. Lee, J. A. Kovacs, F. Meyer, T. Weyhermüller, E. Otero, and S. DeBeer, Iron L_{2,3}-Edge X-ray Absorption and X-ray Magnetic Circular Dichroism Studies of Molecular Iron Complexes with Relevance to the FeMoco and FeVco Active Sites of Nitrogenase, *Inorg. Chem.*, 56, 8147-8158, 2017.
- [46] G. B. Kaufman, Inorganic chemistry: principles of structure and reactivity, 4th ed. (Huheey, James E.; Keiter, Ellen A.; Keiter, Richard L.), *J. Chem. Educ.*, 70, A279, 1993.
- [47] W. U. M. S. Arya, P. Vasudevan, H. S. Nalwa, The double-double effect in Racah parameters of lanthanides(III) ions, *J. inorg. nucl. Chem.*, 43, 3381-3383, 1981.

- [48] R. Cheng, E. Loire, and T. D. Fridgen, Hydrogen bonding in alkali metal cation-bound i-motif-like dimers of 1-methyl cytosine: an IRMPD spectroscopic and computational study, *Phys. Chem. Chem. Phys.*, 21, 11103-11110, 2019.
- [49] J. A. Fournier, C. T. Wolke, M. A. Johnson, T. T. Odbadrakh, K. D. Jordan, S. M. Kathmann, and S. S. Xantheas, Snapshots of Proton Accommodation at a Microscopic Water Surface: Understanding the Vibrational Spectral Signatures of the Charge Defect in Cryogenically Cooled $H+(H_2O)_n=2-28$ Clusters, *J. Phys. Chem. A*, 119, 9425-9440, 2015.
- [50] J. Hewer, "Magnetic and Structural Characterization of Isolated Gaseous Ions by XMCD and IRMPD Spectroscopy," 2017.
- [51] H. Kagi, R. Lu, P. Davidson, A. F. Goncharov, H. Mao, and A. Hemley, Evidence for ice VI as an inclusion in cuboid diamonds from high PT near infrared spectroscopy, *Mineralogical Magazine - MINER MAG*, 64, 2000.
- [52] C. Merkert, "Metal cluster aggregates of the composition $Fen^{+/-}$, $Con^{+/-}$, $Nin^{+/-}$ and $[ConMm]^{+/-}$ (M: Au, Rh and Pt) as model systems for catalytic C-H activation and structural determination of ionic dicarboxylic acids as model system for intramolecular hydrogen bonding," 2014.
- [53] E. Nibbering, J. Dreyer, O. Kühn, J. Bredenbeck, P. Hamm, and T. Elsaesser, "Vibrational dynamics of hydrogen bonds," pp. 619-687, 2007.
- [54] Y. Yang, G. Liao, and X. Kong, Charge-state Resolved Infrared Multiple Photon Dissociation (IRMPD) Spectroscopy of Ubiquitin Ions in the Gas Phase, *Scientific Reports*, 7, 16592, 2017.

9.10 Supplementary material

IR(M)PD studies on a series of trimetallic single molecule magnets containing 3d metals and lanthanides in gas phase

Michael Lembach^a, Marcel Lechner and Gereon Niedner-Schatteburg^a

(a) Fachbereich Chemie and Forschungszentrum OPTIMAS, Kaiserslautern, Germany

Content

Tab. S1: Experimental masses and their corresponding calculated masses of $[M_2Ln(HVab)(Vab)_3]^{2+}$ (M = Co, Cu; Ln = Dy, Gd, Nd, Sm, Tb).

Fig. S1: ESI mass spectra of isolated $[Co_2Dy(HVab)(Vab)_3]^{2+}$ and deuterated $[Co_2Dy(HVab)(Vab)_3]^{2+}$.

Tab. S2: Experimental masses and their corresponding calculated masses of the fragments in the complexes $[M_2Ln(HVab)(Vab)_3]^{2+}$ (M = Co, Cu; Ln = Dy, Gd, Nd, Sm, Tb).

Fig. S2: Experimental ATR spectra of $[Co_2Ln(HVab)(Vab)_3]^{2+}$ (top) and $[Cu_2Ln(HVab)(Vab)_3]^{2+}$ (bottom) (Ln = Dy, Gd, Nd, Sm, Tb).

Fig. S3: Experimental IR(M)PD spectra of $[Co_2Dy(HVab)(Vab)_3]^{2+}$ between 2800 cm^{-1} and 3700 cm^{-1} with the calculated possible isomers. The calculations were performed with Gaussian 09 at the B3LYP/cc-pVDZ (H, C, N, O) and Stuttgart ecp effective core potential (Co, Dy) level of theory. The spectra were scaled with 0.9641 to compensate anharmonicity in these complexes.

Fig. S4: Experimental IR(M)PD spectra of $[Co_2Gd(HVab)(Vab)_3]^{2+}$ between 2800 cm^{-1} and 3700 cm^{-1} with the calculated possible isomers. The calculations were performed with Gaussian 09 at the B3LYP/cc-pVDZ (H, C, N, O) and Stuttgart ecp effective core potential (Co, Gd) level of theory. The spectra were scaled with 0.9641 to compensate anharmonicity in these complexes.

Fig. S5: Experimental IR(M)PD spectra of $[\text{Co}_2\text{Nd}(\text{HVab})(\text{Vab})_3]^{2+}$ between 2800 cm^{-1} and 3700 cm^{-1} with the calculated possible isomers. The calculations were performed with Gaussian 09 at the B3LYP/cc-pVDZ (H, C, N, O) and Stuttgart ecp effective core potential (Co, Nd) level of theory. The spectra were scaled with 0.9641 to compensate anharmonicity in these complexes.

Fig. S6: Experimental IR(M)PD spectra of $[\text{Co}_2\text{Sm}(\text{HVab})(\text{Vab})_3]^{2+}$ between 2800 cm^{-1} and 3700 cm^{-1} with the calculated possible isomers. The calculations were performed with Gaussian 09 at the B3LYP/cc-pVDZ (H, C, N, O) and Stuttgart ecp effective core potential (Co, Sm) level of theory. The spectra were scaled with 0.9641 to compensate anharmonicity in these complexes.

Fig. S7: Experimental IR(M)PD spectra of $[\text{Co}_2\text{Tb}(\text{HVab})(\text{Vab})_3]^{2+}$ between 2800 cm^{-1} and 3700 cm^{-1} with the calculated possible isomers. The calculations were performed with Gaussian 09 at the B3LYP/cc-pVDZ (H, C, N, O) and Stuttgart ecp effective core potential (Co, Tb) level of theory. The spectra were scaled with 0.9641 to compensate anharmonicity in these complexes.

Fig. S8: Experimental IR(M)PD spectra of $[\text{Cu}_2\text{Dy}(\text{HVab})(\text{Vab})_3]^{2+}$ between 2800 cm^{-1} and 3700 cm^{-1} with the calculated possible isomers. The calculations were performed with Gaussian 09 at the B3LYP/cc-pVDZ (H, C, N, O) and Stuttgart ecp effective core potential (Cu, Dy) level of theory. The spectra were scaled with 0.9641 to compensate anharmonicity in these complexes.

Fig. S9: Experimental IR(M)PD spectra of $[\text{Cu}_2\text{Gd}(\text{HVab})(\text{Vab})_3]^{2+}$ between 2800 cm^{-1} and 3700 cm^{-1} with the calculated possible isomers. The calculations were performed with Gaussian 09 at the B3LYP/cc-pVDZ (H, C, N, O) and Stuttgart ecp effective core potential (Cu, Gd) level of theory. The spectra were scaled with 0.9641 to compensate anharmonicity in these complexes.

Fig. S10: Experimental IR(M)PD spectra of $[\text{Cu}_2\text{Nd}(\text{HVab})(\text{Vab})_3]^{2+}$ between 2800 cm^{-1} and 3700 cm^{-1} with the calculated possible isomers. The calculations were performed with Gaussian 09 at the B3LYP/cc-pVDZ (H, C, N, O) and Stuttgart ecp effective core potential (Cu, Nd) level of theory. The spectra were scaled with 0.9641 to compensate anharmonicity in these complexes.

Fig. S11: Experimental IR(M)PD spectra of $[\text{Cu}_2\text{Sm}(\text{HVab})(\text{Vab})_3]^{2+}$ between 2800 cm^{-1} and 3700 cm^{-1} with the calculated possible isomers. The calculations were performed with Gaussian 09 at the B3LYP/cc-pVDZ (H, C, N, O) and Stuttgart ecp effective core potential (Cu, Sm) level of theory. The spectra were scaled with 0.9641 to compensate anharmonicity in these complexes.

Fig. S12: Experimental IR(M)PD spectra of $[\text{Cu}_2\text{Tb}(\text{HVab})(\text{Vab})_3]^{2+}$ between 2800 cm^{-1} and 3700 cm^{-1} with the calculated possible isomers. The calculations were performed with Gaussian 09 at the B3LYP/cc-pVDZ (H, C, N, O) and Stuttgart ecp effective core potential (Cu, Tb) level of theory. The spectra were scaled with 0.9641 to compensate anharmonicity in these complexes.

Fig. S13: Experimental IR(M)PD spectra of $[\text{Co}_2\text{Ln}(\text{HVab})(\text{Vab})_3]^{2+}$ (Ln = Dy, Gd, Nd, Sm, Tb) in the area between 3040 cm^{-1} and 3080 cm^{-1} .

Fig. S14: Simulated XA spectra of a free Cu^{2+} atom at 4.5 K by CTM4XAS and Cowan batch files with the corresponding spin orbit coupling constant.

Tab. S3: Atom coordinates for $[\text{M}_2\text{Ln}(\text{HVab})(\text{Vab})_3]^{2+}$ (M = Co, Cu; Ln = Dy, Gd, Nd, Sm, Tb) for isomer I. The calculations were performed at the B3LYP/cc-pVTZ (H, C, N, O) and Stuttgart ecp effective core potential (Co, Cu, Dy, Gd, Nd, Sm, Tb) level of theory.

Tab. S4: Atom coordinates for $[\text{M}_2\text{Ln}(\text{HVab})(\text{Vab})_3]^{2+}$ (M = Co, Cu; Ln = Dy, Gd, Nd, Sm, Tb) for isomer II. The calculations were performed at the B3LYP/cc-pVTZ (H, C, N, O) and Stuttgart ecp effective core potential (Co, Cu, Dy, Gd, Nd, Sm, Tb) level of theory.

Tab. S5: Atom coordinates for $[\text{M}_2\text{Ln}(\text{HVab})(\text{Vab})_3]^{2+}$ (M = Co, Cu; Ln = Dy, Gd, Nd, Sm, Tb) for isomer III. The calculations were performed at the B3LYP/cc-pVTZ (H, C, N, O) and Stuttgart ecp effective core potential (Co, Cu, Dy, Gd, Nd, Sm, Tb) level of theory.

Tab. S6: Atom coordinates for $[M_2Ln(HVab)(Vab)_3]^{2+}$ (M = Co, Cu; Ln = Dy, Gd, Nd, Sm, Tb) for isomer IV. The calculations were performed at the B3LYP/cc-pVTZ (H, C, N, O) and Stuttgart ecp effective core potential (Co, Cu, Dy, Gd, Nd, Sm, Tb) level of theory.

Tab. S1: Experimental masses and their corresponding calculated masses of $[\text{M}_2\text{Ln}(\text{HVab})(\text{Vab})_3]^{2+}$ ($\text{M} = \text{Co}, \text{Cu}$; $\text{Ln} = \text{Dy}, \text{Gd}, \text{Nd}, \text{Sm}, \text{Tb}$).

Complex	m/z_{exp}	m/z_{calc}
$[\text{Co}_2\text{Dy}]^{2+}$	682.49	682.57
$[\text{Co}_2\text{Gd}]^{2+}$	679.51	679.57
$[\text{Co}_2\text{Nd}]^{2+}$	672.52	672.56
$[\text{Co}_2\text{Sm}]^{2+}$	676.51	676.57
$[\text{Co}_2\text{Tb}]^{2+}$	680.01	680.07
$[\text{Cu}_2\text{Dy}]^{2+}$	686.60	686.60
$[\text{Cu}_2\text{Gd}]^{2+}$	684.56	684.57
$[\text{Cu}_2\text{Nd}]^{2+}$	677.57	677.56
$[\text{Cu}_2\text{Sm}]^{2+}$	681.56	681.57
$[\text{Cu}_2\text{Tb}]^{2+}$	685.03	685.07

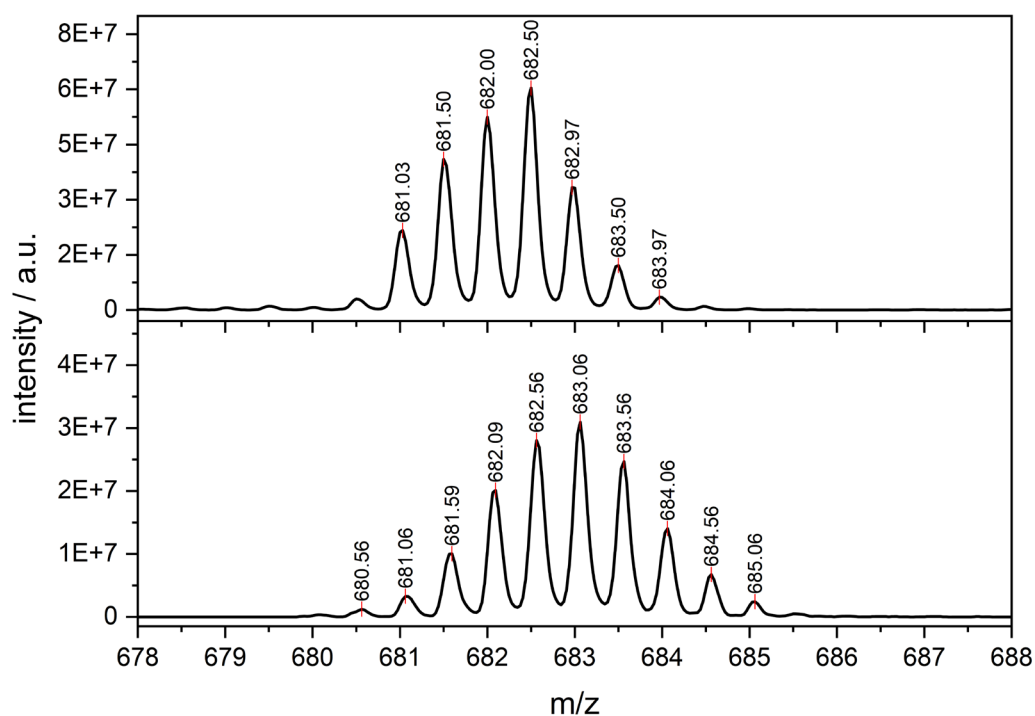


Fig. S1: ESI mass spectra of isolated $[\text{Co}_2\text{Dy}(\text{HVab})(\text{Vab})_3]^{2+}$ and deuterated $[\text{Co}_2\text{Dy}(\text{HVab})(\text{Vab})_3]^{2+}$.

Tab. S2: Experimental masses and their corresponding calculated masses of the fragments in the complexes $[M_2Ln(HVab)(Vab)_3]^{2+}$ ($M = Co, Cu; Ln = Dy, Gd, Nd, Sm, Tb$).

Fragment	m/z_{exp}	m/z_{calc}
$M_2Ln(C_{15}H_{13}NO_3)_3(C_{15}H_{14}NO_3)(H_2)$	642.49-656.03	642.57-656.08
$M_2Ln(C_{15}H_{13}NO_3)_3(C_{15}H_{14}NO_3)$	641.49-655.03	641.57-655.08
$M_2Ln(C_{15}H_{13}NO_3)_3$	513.98-529.00	513.01-529.07

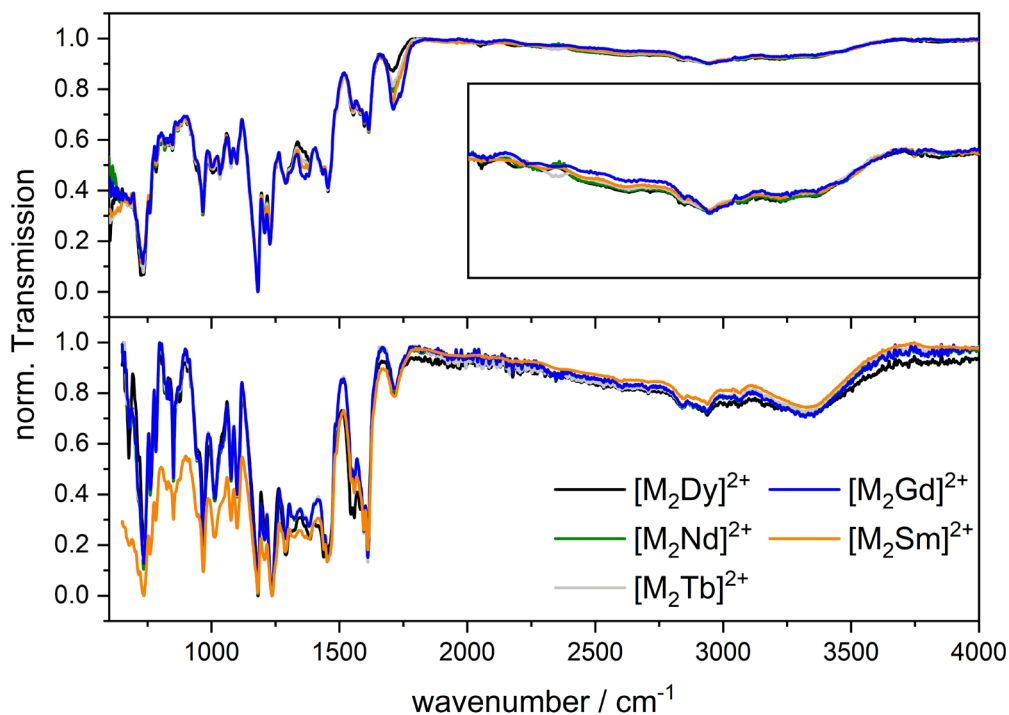


Fig. S2: Experimental ATR spectra of $[Co_2Ln(HVab)(Vab)_3]^{2+}$ (top) and $[Cu_2Ln(HVab)(Vab)_3]^{2+}$ (bottom) ($Ln = Dy, Gd, Nd, Sm, Tb$).

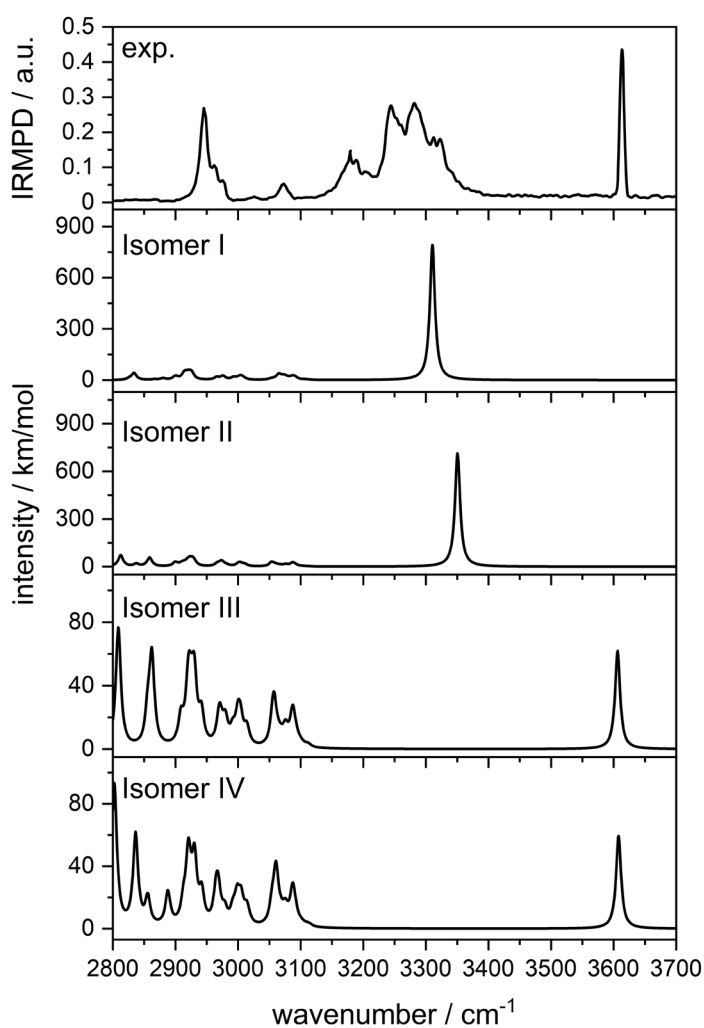


Fig. S3: Experimental IR(M)PD spectra of $[\text{Co}_2\text{Dy}(\text{HVab})(\text{Vab})_3]^{2+}$ between 2800 cm^{-1} and 3700 cm^{-1} with the calculated possible isomers. The calculations were performed with Gaussian 09 at the B3LYP/cc-pVDZ (H, C, N, O) and ecp-mdf (Co, Dy) level of theory. The spectra were scaled with 0.9641 to compensate anharmonicity in these complexes.

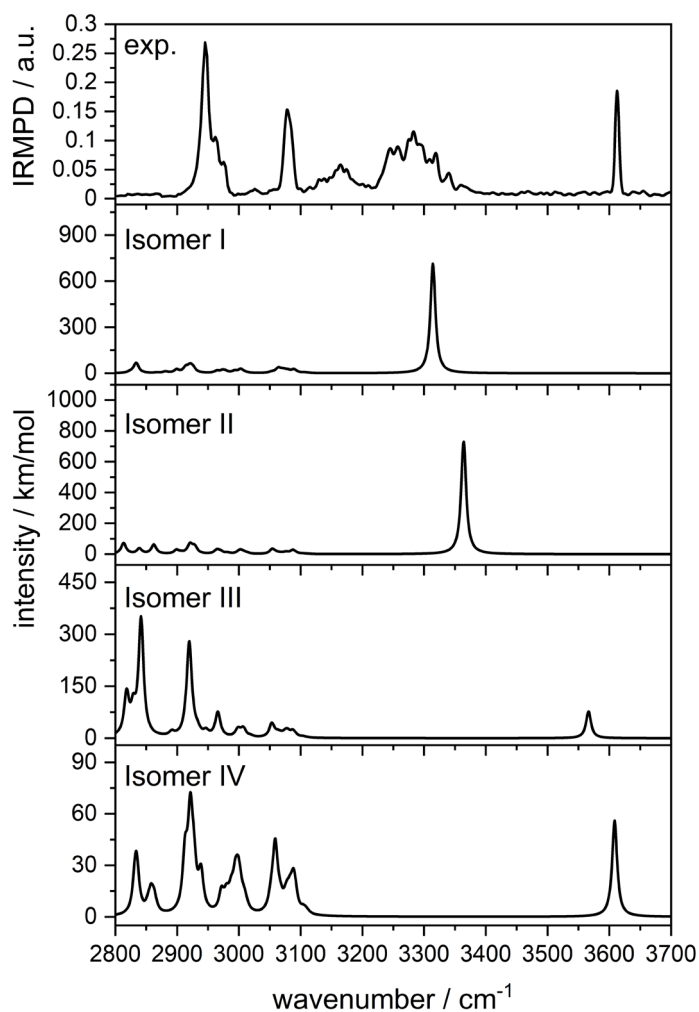


Fig. S4: Experimental IR(M)PD spectra of $[\text{Co}_2\text{Gd}(\text{HVab})(\text{Vab})_3]^{2+}$ between 2800 cm^{-1} and 3700 cm^{-1} with the calculated possible isomers. The calculations were performed with Gaussian 09 at the B3LYP/cc-pVDZ (H, C, N, O) and ecp-mdf (Co, Gd) level of theory. The spectra were scaled with 0.9641 to compensate anharmonicity in these complexes.

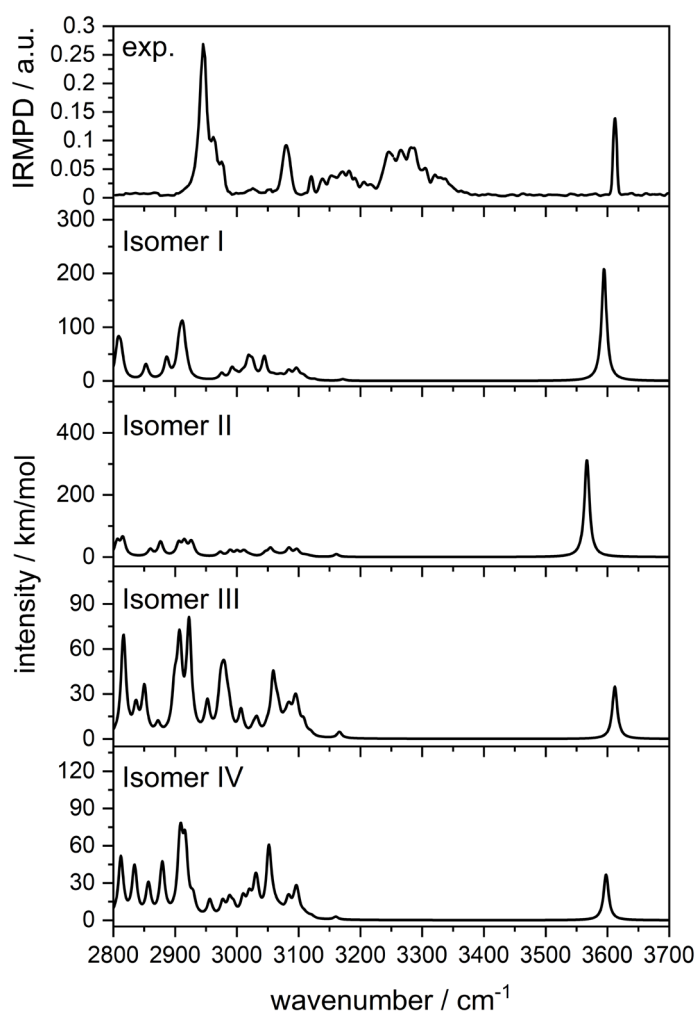


Fig. S5: Experimental IR(M)PD spectra of $[\text{Co}_2\text{Nd}(\text{HVab})(\text{Vab})_3]^{2+}$ between 2800 cm^{-1} and 3700 cm^{-1} with the calculated possible isomers. The calculations were performed with Gaussian 09 at the B3LYP/cc-pVDZ (H, C, N, O) and ecp-mdf (Co, Nd) level of theory. The spectra were scaled with 0.9641 to compensate anharmonicity in these complexes.

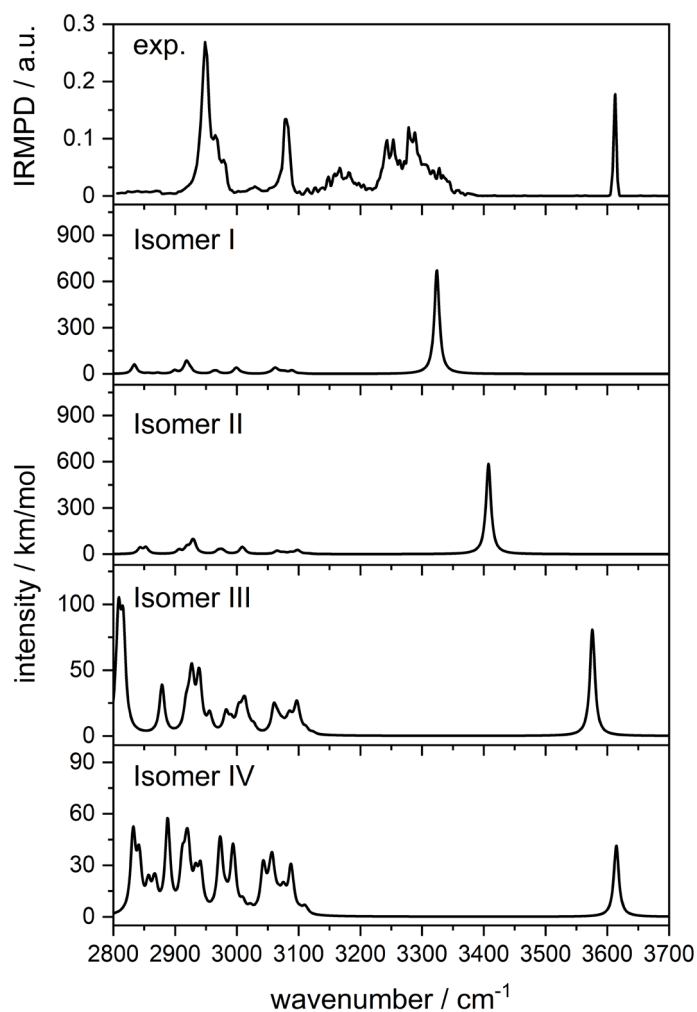


Fig. S6: Experimental IR(M)PD spectra of $[\text{Co}_2\text{Sm}(\text{HVab})(\text{Vab})_3]^{2+}$ between 2800 cm^{-1} and 3700 cm^{-1} with the calculated possible isomers. The calculations were performed with Gaussian 09 at the B3LYP/cc-pVDZ (H, C, N, O) and ecp-mdf (Co, Sm) level of theory. The spectra were scaled with 0.9641 to compensate anharmonicity in these complexes.

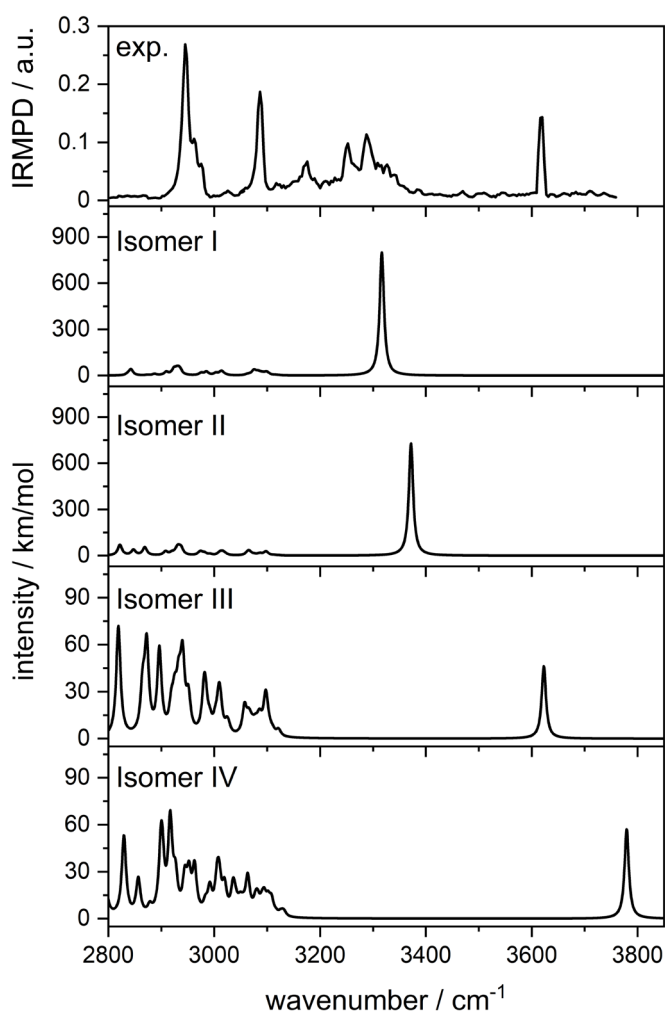


Fig. S7: Experimental IR(M)PD spectra of $[\text{Co}_2\text{Tb}(\text{HVab})(\text{Vab})_3]^{2+}$ between 2800 cm^{-1} and 3700 cm^{-1} with the calculated possible isomers. The calculations were performed with Gaussian 09 at the B3LYP/cc-pVDZ (H, C, N, O) and ecp-mdf (Co, Tb) level of theory. The spectra were scaled with 0.9641 to compensate anharmonicity in these complexes.

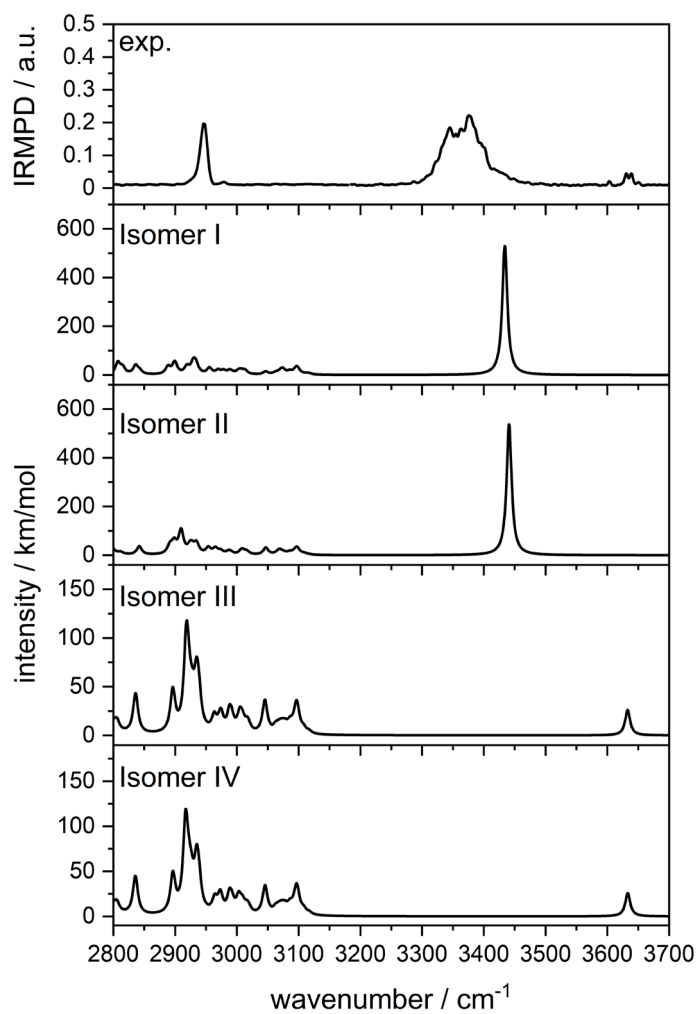


Fig. S8: Experimental IR(M)PD spectra of $[\text{Cu}_2\text{Dy}(\text{HVab})(\text{Vab})_3]^{2+}$ between 2800 cm^{-1} and 3700 cm^{-1} with the calculated possible isomers. The calculations were performed with Gaussian 09 at the B3LYP/cc-pVDZ (H, C, N, O) and ecp-mdf (Cu, Dy) level of theory. The spectra were scaled with 0.9641 to compensate anharmonicity in these complexes.

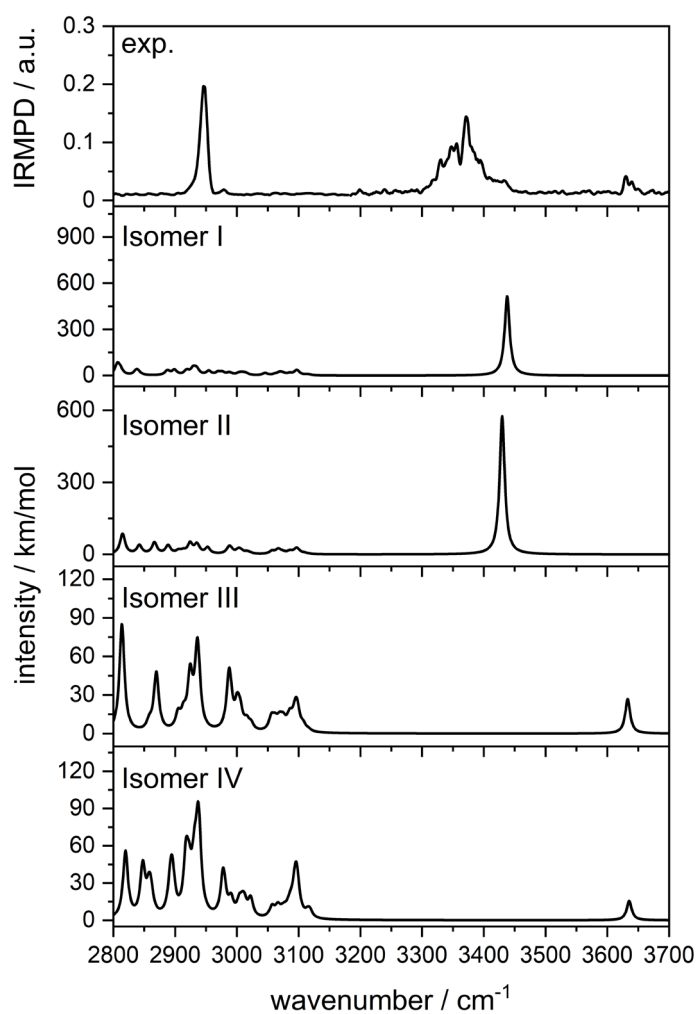


Fig. S9: Experimental IR(M)PD spectra of $[\text{Cu}_2\text{Gd}(\text{HVab})(\text{Vab})_3]^{2+}$ between 2800 cm^{-1} and 3700 cm^{-1} with the calculated possible isomers. The calculations were performed with Gaussian 09 at the B3LYP/cc-pVDZ (H, C, N, O) and ecp-mdf (Cu, Gd) level of theory. The spectra were scaled with 0.9641 to compensate anharmonicity in these complexes.

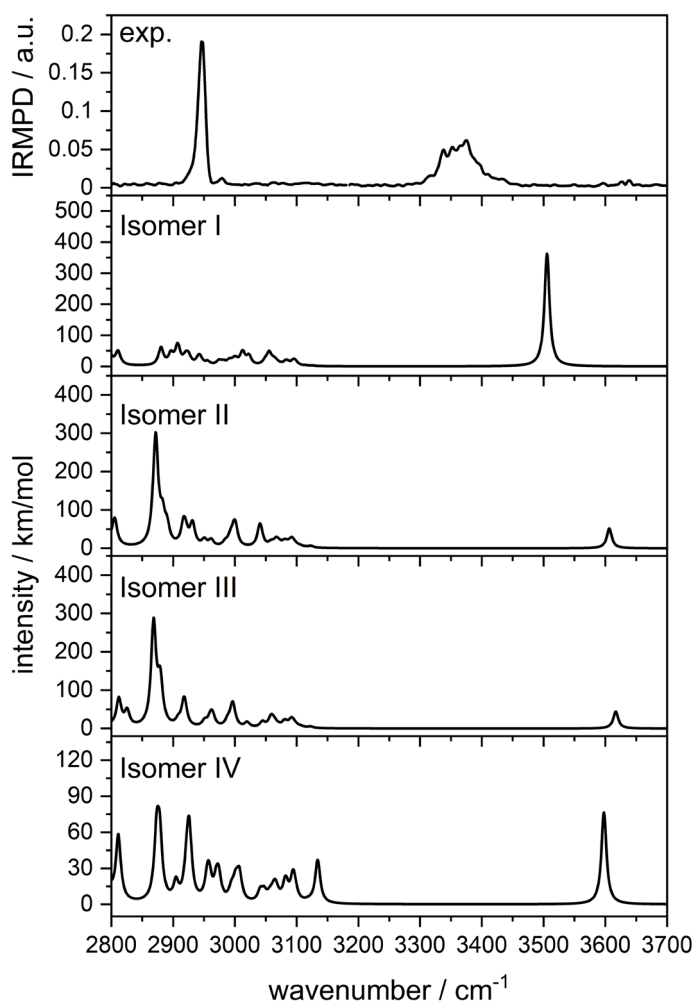


Fig. S10: Experimental IR(M)PD spectra of $[\text{Cu}_2\text{Nd}(\text{HVab})(\text{Vab})_3]^{2+}$ between 2800 cm^{-1} and 3700 cm^{-1} with the calculated possible isomers. The calculations were performed with Gaussian 09 at the B3LYP/cc-pVDZ (H, C, N, O) and ecp-mdf (Cu, Nd) level of theory. The spectra were scaled with 0.9641 to compensate anharmonicity in these complexes.

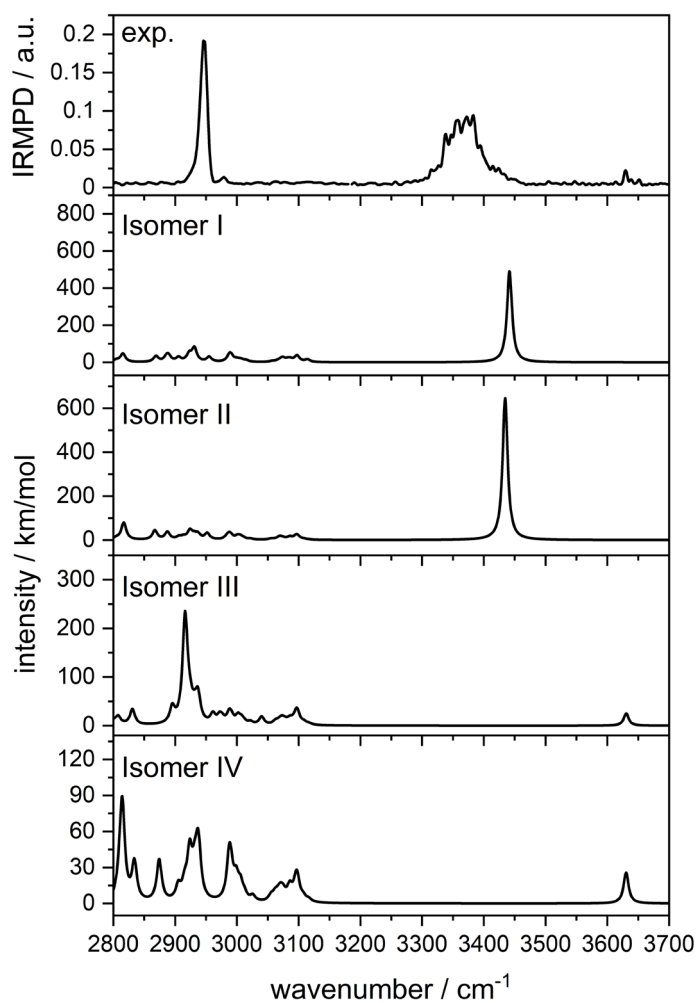


Fig. S11: Experimental IR(M)PD spectra of $[\text{Cu}_2\text{Sm}(\text{HVab})(\text{Vab})_3]^{2+}$ between 2800 cm^{-1} and 3700 cm^{-1} with the calculated possible isomers. The calculations were performed with Gaussian 09 at the B3LYP/cc-pVDZ (H, C, N, O) and ecp-mdf (Cu, Sm) level of theory. The spectra were scaled with 0.9641 to compensate anharmonicity in these complexes.

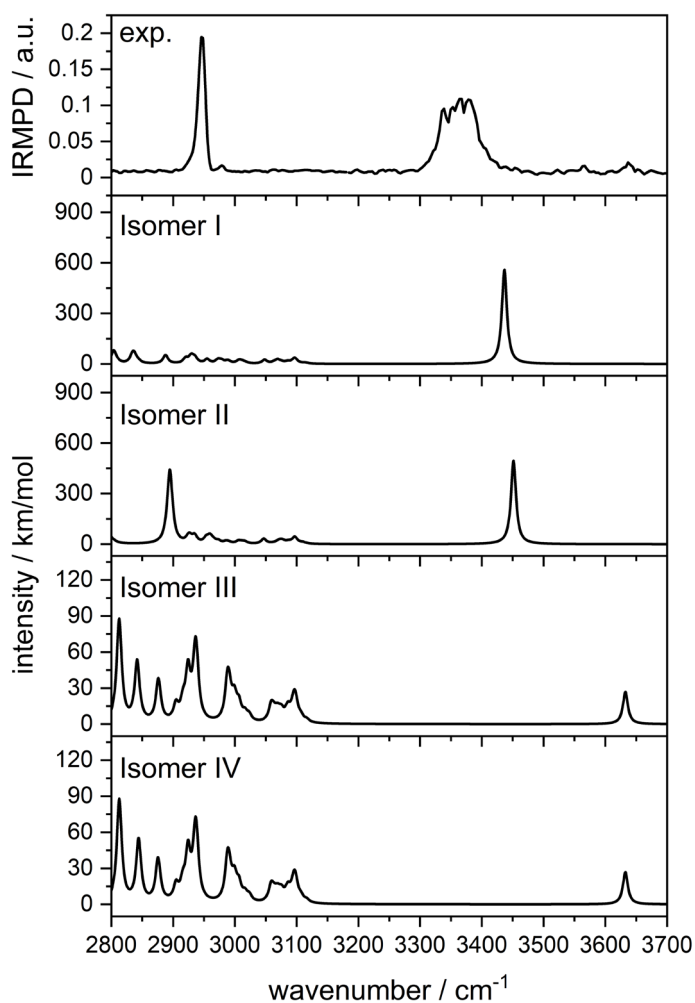


Fig. S12: Experimental IR(M)PD spectra of $[\text{Cu}_2\text{Tb}(\text{HVab})(\text{Vab})_3]^{2+}$ between 2800 cm^{-1} and 3700 cm^{-1} with the calculated possible isomers. The calculations were performed with Gaussian 09 at the B3LYP/cc-pVDZ (H, C, N, O) and ecp-mdf (Cu, Tb) level of theory. The spectra were scaled with 0.9641 to compensate anharmonicity in these complexes.

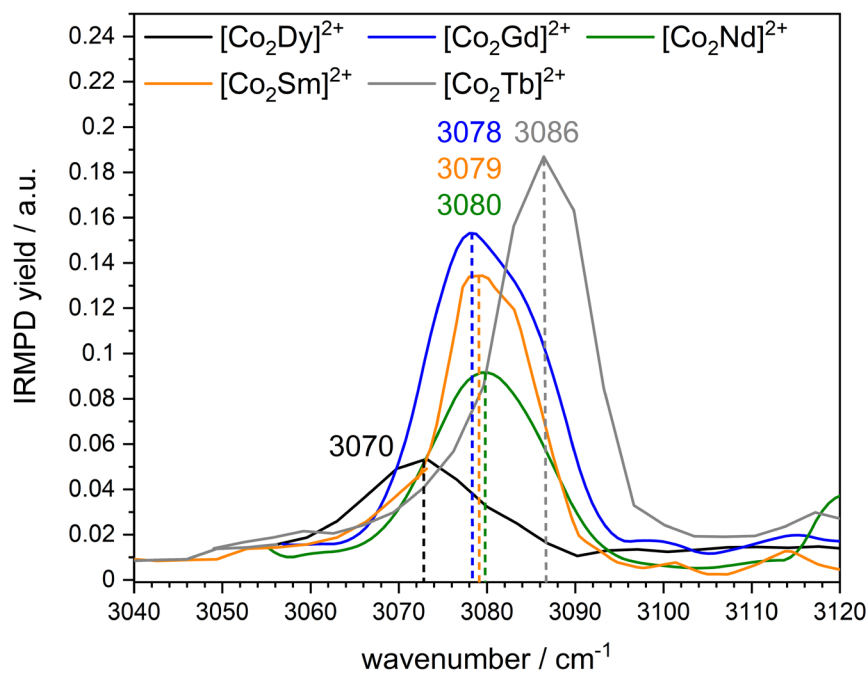


Fig. S13: Experimental IR(M)PD spectra of $[\text{Co}_2\text{Ln}(\text{HVab})(\text{Vab})_3]^{2+}$ (Ln = Dy, Gd, Nd, Sm, Tb) in the area between 3040 cm^{-1} and 3080 cm^{-1} .

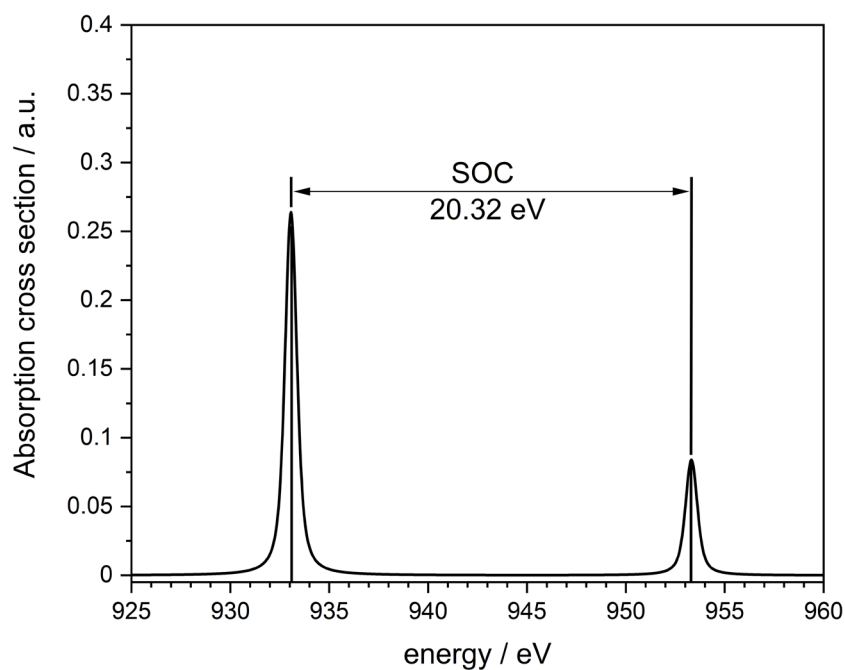


Fig. S14: Simulated XA spectra of a free Cu^{2+} atom at 4.5 K by CTM4XAS and Cowan batch files with the corresponding spin orbit coupling constant.

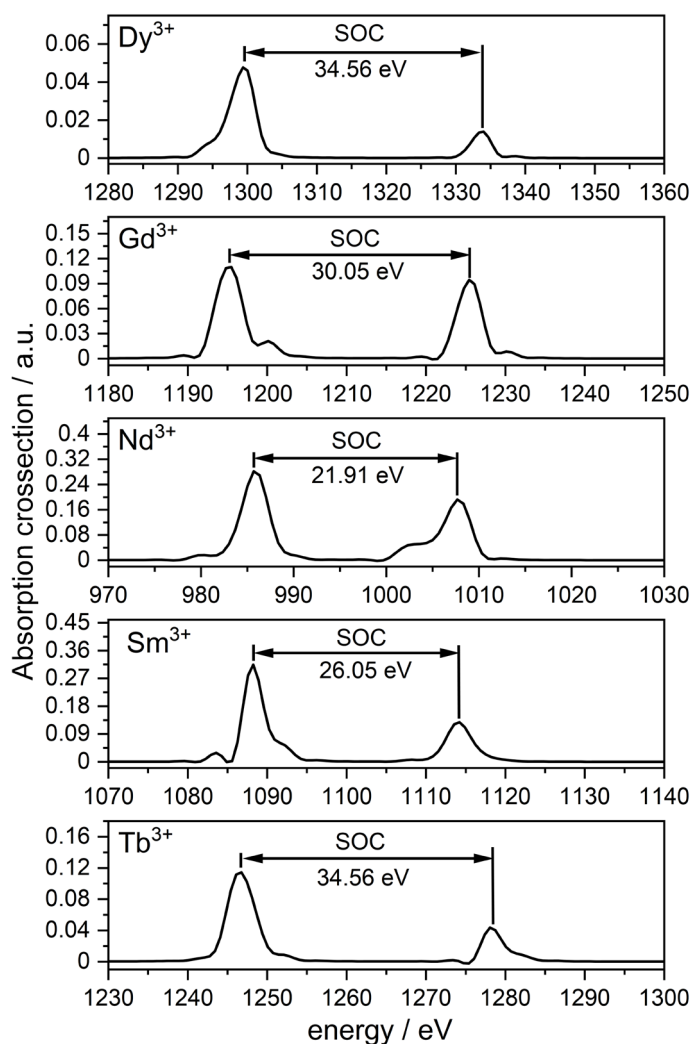


Fig. 13: Simulated XA spectra of a free Ln^{3+} ($\text{Ln} = \text{Nd}, \text{Sm}, \text{Gd}, \text{Tb}, \text{Dy}$) atom at 4.5 K by CTM4XAS and Cowan batch files with their corresponding spin orbit coupling constants.

Tab. S3: Atom coordinates for $[\text{M}_2\text{Ln}(\text{HVab})(\text{Vab})_3]^{2+}$ ($\text{M} = \text{Co}, \text{Cu}$; $\text{Ln} = \text{Dy}, \text{Gd}, \text{Nd}, \text{Sm}, \text{Tb}$) for isomer I. The calculations were performed at the B3LYP/cc-pVTZ (H, C, N, O) and Stuttgart ecp effective core potential (Co, Cu, Dy, Gd, Nd, Sm, Tb) level of theory.

atom	x	Y	z
Ln	-0.00547	0.13095	-0.22761
M	3.62033	-0.15150	0.22828
M	-3.63321	0.04377	0.14432
O	-0.14407	-2.13536	-1.49416
O	2.03911	-1.33259	-0.27928
O	3.84938	-0.09841	-1.97381
O	2.03896	1.10167	0.54366
O	-0.01577	1.59580	2.03213
O	3.93023	-0.21911	2.04731

9. IR(M)PD studies on a series of isolated trimetallic single molecule magnets containing 3d metals
and Lanthanides

O	-2.20987	1.41036	0.03155
O	-3.64319	0.03032	1.97692
O	-0.07194	2.66967	-0.92371
O	-2.05227	-1.08156	0.33138
O	0.01570	-1.45399	1.87484
N	-4.78480	-1.52215	-0.01699
O	-3.50938	-0.00569	-1.66447
O	-0.86567	0.43838	-2.54392
O	1.26694	0.44914	-2.27386
O	0.43575	0.59406	-4.29728
N	4.89331	-1.81894	0.13836
C	-2.41970	2.55103	-0.61445
C	-1.30431	3.27169	-1.12249
C	-1.31701	-2.52262	-2.24597
H	-1.05984	-2.62263	-3.31116
H	-2.04684	-1.72025	-2.10996
H	-1.71107	-3.47516	-1.85952
C	0.96438	-2.96422	-1.60462
C	2.12823	-2.48289	-0.95042
C	4.65118	0.83487	-2.73299
H	4.08484	1.77721	-2.84484
H	4.81590	0.41875	-3.73853
C	5.97006	1.09455	-2.05922
C	6.01616	1.53331	-0.72003
N	4.78950	1.61380	0.00526
C	4.53100	2.68167	0.69321
H	5.26441	3.50223	0.67927
C	3.34457	2.91749	1.49269
C	2.17249	2.12356	1.39285
C	1.06435	2.44104	2.21160
C	-1.10887	1.73987	2.95900
H	-0.74203	1.61052	3.98950
H	-1.83816	0.96589	2.70252
H	-1.57648	2.73075	2.84872
C	1.10728	3.50926	3.10120
H	0.25400	3.74491	3.73540
C	2.26528	4.30327	3.18185
H	2.29129	5.14442	3.87527
C	3.36000	4.01782	2.38340
H	4.25831	4.63571	2.44436
C	7.24204	1.84564	-0.11686
H	7.26863	2.13294	0.93579
C	8.42634	1.74937	-0.85071
H	9.37773	1.99266	-0.37436
C	8.39162	1.32762	-2.18143
H	9.31508	1.24710	-2.75742

9. IR(M)PD studies on a series of isolated trimetallic single molecule magnets containing 3d metals and Lanthanides

C	7.16875	0.99747	-2.77397
H	7.14180	0.66989	-3.81601
C	4.87385	-0.94567	2.80073
C	6.18387	-1.20160	2.08634
C	6.16797	-1.68564	0.76382
C	4.57576	-2.93703	-0.43140
H	5.32656	-3.74163	-0.44036
C	3.30869	-3.27621	-1.04497
C	3.27352	-4.50903	-1.74191
H	4.18472	-5.10895	-1.78901
C	2.12073	-4.95264	-2.36221
H	2.10678	-5.89928	-2.90274
C	0.95627	-4.17203	-2.29456
H	0.05335	-4.52485	-2.78912
C	7.36148	-1.99603	0.10094
H	7.33358	-2.33013	-0.93805
C	8.58203	-1.84333	0.76402
H	9.51187	-2.08438	0.24566
C	8.61064	-1.37254	2.07890
H	9.56326	-1.25105	2.59767
C	7.41513	-1.05052	2.73090
H	7.43865	-0.68843	3.76188
C	-4.76394	0.14162	2.81123
C	-6.11737	0.39054	2.17880
C	-6.24809	1.01458	0.92930
C	-7.51161	1.31682	0.40211
H	-7.59151	1.76282	-0.59081
C	-8.65888	1.01735	1.13502
H	-9.64124	1.25595	0.72414
C	-8.54570	0.39631	2.38362
H	-9.44087	0.15205	2.95832
C	-7.28430	0.08283	2.89299
H	-7.19902	-0.39537	3.87245
N	-5.05130	1.34376	0.21362
C	-4.88853	2.56096	-0.21400
H	-5.74291	3.23920	-0.09315
C	-3.70359	3.14319	-0.77689
C	1.07130	3.36881	-1.46014
H	0.96300	3.50017	-2.54767
H	1.93487	2.73620	-1.24765
H	1.18077	4.34588	-0.96650
C	-1.46730	4.49528	-1.76095
H	-0.60579	5.03351	-2.15116
C	-2.74416	5.06549	-1.91320
H	-2.84879	6.02735	-2.41520

9. IR(M)PD studies on a series of isolated trimetallic single molecule magnets containing 3d metals and Lanthanides

C	-3.84515	4.40365	-1.41232
H	-4.84177	4.83983	-1.50471
C	-2.13142	-2.08798	1.19689
C	-1.01372	-2.36223	2.01679
C	1.10221	-1.54941	2.81847
H	0.70890	-1.47866	3.84424
H	1.77785	-0.71762	2.60470
H	1.64144	-2.49857	2.68120
C	-1.00778	-3.45722	2.87457
H	-0.14291	-3.66952	3.50129
C	-2.12724	-4.30749	2.93791
H	-2.10794	-5.16845	3.60677
C	-3.24363	-4.04833	2.15933
H	-4.11770	-4.70050	2.21421
C	-3.27133	-2.92135	1.30568
C	-4.44940	-2.65912	0.51555
H	-5.11388	-3.51259	0.33068
C	-5.93112	-1.46457	-0.87526
C	-7.12206	-2.11584	-0.50654
H	-7.18955	-2.61168	0.46329
C	-8.22325	-2.09575	-1.35657
H	-9.14358	-2.60351	-1.06338
C	-8.14774	-1.41089	-2.57555
H	-9.00708	-1.38913	-3.24809
C	-6.97416	-0.74483	-2.92373
H	-6.91895	-0.20792	-3.87453
C	-5.84976	-0.75485	-2.08343
C	-4.60176	-0.01978	-2.53292
N	0.26939	0.49842	-3.11051
H	2.92689	-0.03493	-2.31740
H	-4.55443	0.97241	3.52030
H	-4.82038	-0.77057	3.43889
H	5.05893	-0.39466	3.73997
H	4.41713	-1.91644	3.08927
H	-4.88597	1.02128	-2.79562
H	-4.24344	-0.47268	-3.47834

Tab. S4: Atom coordinates for $[M_2Ln(HVab)(Vab)_3]^{2+}$ (M = Co, Cu; Ln = Dy, Gd, Nd, Sm, Tb) for isomer II. The calculations were performed at the B3LYP/cc-pVTZ (H, C, N, O) and Stuttgart ecp effective core potential (Co, Cu, Dy, Gd, Nd, Sm, Tb) level of theory.

atom	x	Y	z
Ln	0.01735	-0.16097	-0.18458
M	-3.74602	0.10804	0.17112
M	3.60007	-0.14604	0.27195
O	0.03517	2.60336	-1.30659
O	-2.03455	1.60632	-0.04243
O	-3.86875	0.45263	-1.61777
O	-2.05686	-1.15156	0.30805
O	-0.00302	-1.71252	1.81207
O	-3.85837	-0.18460	1.99564
O	2.09658	-1.42291	-0.20477
O	3.70824	-0.01891	2.08084
O	-0.00103	-2.50995	-1.32792
O	2.03020	1.07023	0.38107
O	-0.00933	1.28048	1.97733
N	4.71347	1.71147	-0.05078
O	3.78514	-0.14376	-1.92262
O	1.14449	0.13037	-2.32423
O	-1.00135	0.02460	-2.41921
O	0.14762	0.19372	-4.27552
N	-4.94189	1.74610	0.44232
C	2.29341	-2.58868	-0.81341
C	1.18352	-3.22361	-1.42437
C	1.21639	3.16947	-1.91866
H	1.11949	3.14992	-3.01462
H	2.03736	2.52638	-1.59488
H	1.36450	4.19855	-1.55946
C	-1.13373	3.24401	-1.48038
C	-2.25089	2.63975	-0.74626
C	-4.38031	-0.43708	-2.58447
H	-3.71036	-1.31036	-2.71462
H	-4.38940	0.09921	-3.54941
C	-5.77985	-0.90728	-2.24551
C	-5.98146	-1.53031	-0.99784
N	-4.83010	-1.64396	-0.16777
C	-4.53653	-2.77270	0.38608
H	-5.22693	-3.61954	0.25085
C	-3.33864	-3.04629	1.15769
C	-2.18193	-2.22404	1.10220
C	-1.08094	-2.58967	1.90946

9. IR(M)PD studies on a series of isolated trimetallic single molecule magnets containing 3d metals
and Lanthanides

C	1.06793	-1.87774	2.76382
H	0.66179	-1.84228	3.78617
H	1.76809	-1.05236	2.59718
H	1.58235	-2.83610	2.59581
C	-1.09658	-3.72160	2.71700
H	-0.23608	-3.98497	3.33045
C	-2.23531	-4.54182	2.73714
H	-2.24633	-5.43537	3.36185
C	-3.33378	-4.20893	1.96024
H	-4.22387	-4.84172	1.97359
C	-7.24532	-1.99618	-0.61667
H	-7.38895	-2.44012	0.37057
C	-8.32113	-1.86000	-1.49856
H	-9.30974	-2.21761	-1.20473
C	-8.13276	-1.25837	-2.74587
H	-8.97393	-1.15157	-3.43342
C	-6.86747	-0.78298	-3.11272
H	-6.72377	-0.31411	-4.08940
C	-4.62876	0.55783	2.90894
C	-6.02082	0.88012	2.41080
C	-6.14767	1.51727	1.16074
C	-4.73363	2.89263	-0.10988
H	-5.51467	3.66176	-0.01945
C	-3.54425	3.31227	-0.83567
C	-3.65284	4.47605	-1.58971
H	-4.61450	4.99061	-1.63905
C	-2.56208	4.99792	-2.30837
H	-2.69562	5.89630	-2.91300
C	-1.30431	4.38985	-2.25119
H	-0.47486	4.82211	-2.80737
C	-7.40269	1.88901	0.65773
H	-7.48395	2.33199	-0.33669
C	-8.54657	1.63553	1.41603
H	-9.52736	1.90871	1.02307
C	-8.43472	1.01742	2.66549
H	-9.32977	0.81785	3.25765
C	-7.17797	0.64183	3.15505
H	-7.09598	0.16195	4.13318
C	4.69078	-0.64492	2.88380
C	6.06337	-0.76381	2.25607
C	6.16726	-1.26761	0.94808
C	7.41348	-1.48463	0.34969
H	7.46958	-1.84196	-0.68015
C	8.57712	-1.21400	1.07348
H	9.55146	-1.38278	0.61176
C	8.49109	-0.71395	2.37559

9. IR(M)PD studies on a series of isolated trimetallic single molecule magnets containing 3d metals and Lanthanides

H	9.40008	-0.49451	2.93866
C	7.23923	-0.48823	2.95938
H	7.17589	-0.10642	3.98126
N	4.94197	-1.54721	0.26651
C	4.74954	-2.72089	-0.26056
H	5.59246	-3.42320	-0.20469
C	3.55458	-3.24228	-0.87436
C	-1.14838	-3.06404	-2.00776
H	-0.93554	-3.16939	-3.08241
H	-1.95803	-2.34814	-1.85109
H	-1.41042	-4.03843	-1.56943
C	1.31240	-4.45308	-2.05903
H	0.45375	-4.93023	-2.52851
C	2.56184	-5.09862	-2.10157
H	2.65097	-6.06437	-2.59935
C	3.66099	-4.50592	-1.51152
H	4.63236	-5.00395	-1.53619
C	2.08711	2.05933	1.27859
C	0.98323	2.23519	2.14090
C	-1.07156	1.25993	2.95460
H	-0.64841	1.09211	3.95694
H	-1.74615	0.44558	2.66946
H	-1.62584	2.20983	2.93276
C	0.94058	3.28371	3.05514
H	0.08969	3.41141	3.72277
C	2.01283	4.18925	3.12256
H	1.97385	5.01349	3.83551
C	3.11481	4.02854	2.29452
H	3.95433	4.72411	2.35912
C	3.18321	2.95219	1.38299
C	4.38572	2.79062	0.58418
H	5.05279	3.66558	0.53241
C	5.92136	1.67725	-0.80304
C	7.13878	2.12211	-0.26983
H	7.17545	2.49267	0.75619
C	8.30575	2.04854	-1.03353
H	9.25064	2.39445	-0.61043
C	8.26424	1.51801	-2.32476
H	9.17479	1.45303	-2.92285
C	7.05022	1.06437	-2.85032
H	7.01665	0.65986	-3.86487
C	5.86767	1.13781	-2.10568
C	4.54998	0.77582	-2.73576
N	0.08595	0.11570	-3.07792
H	4.34225	-1.66092	3.16523

9. IR(M)PD studies on a series of isolated trimetallic single molecule magnets containing 3d metals and Lanthanides

H	4.76530	-0.05800	3.81584
H	-4.70716	-0.03961	3.83532
H	-4.12182	1.50945	3.18267
H	4.72059	0.31014	-3.71852
H	3.94863	1.68906	-2.89559
H	2.87248	-0.16120	-2.28860

Tab. S5: Atom coordinates for $[M_2Ln(HVab)(Vab)_3]^{2+}$ (M = Co, Cu; Ln = Dy, Gd, Nd, Sm, Tb) for isomer III. The calculations were performed at the B3LYP/cc-pVTZ (H, C, N, O) and Stuttgart ecp effective core potential (Co, Cu, Dy, Gd, Nd, Sm, Tb) level of theory.

atom	x	Y	z
Ln	-0.10954	0.21778	-0.17370
M	-3.66264	0.11817	0.07710
M	3.69588	-0.19781	0.15033
O	-0.11563	2.40360	-1.38039
O	-2.25635	1.47054	-0.12736
O	-3.64427	0.08700	-1.73830
O	-2.09945	-1.00477	0.44427
O	0.02167	-1.27957	1.91987
O	-3.79770	0.31913	2.22276
O	2.16371	-1.60356	0.37221
O	3.75607	0.02596	1.98223
O	-0.01595	-2.59314	-0.76299
O	2.02981	1.05595	0.31136
O	0.00481	1.77167	1.79089
N	4.83424	1.56636	-0.26884
O	3.83183	-0.49626	-1.64627
O	1.15513	-0.20903	-2.14052
O	-0.96889	-0.55735	-2.28339
O	0.33622	-1.15142	-3.93996
N	-5.06546	1.46957	0.03831
C	2.31500	-2.61225	-0.36980
C	1.13563	-3.22045	-1.01687
C	1.04071	2.86046	-2.12580
H	0.87016	2.71989	-3.20318
H	1.87300	2.23591	-1.79295
H	1.23251	3.91822	-1.89534
C	-1.33163	3.01374	-1.67341
C	-2.44952	2.46197	-1.00477
C	-4.21341	-0.95218	-2.48553
H	-3.59508	-1.87472	-2.44053
H	-4.18750	-0.61316	-3.53670
C	-5.63959	-1.29313	-2.10488

9. IR(M)PD studies on a series of isolated trimetallic single molecule magnets containing 3d metals and Lanthanides

C	-5.92450	-1.56490	-0.75668
N	-4.81554	-1.47494	0.15492
C	-4.51062	-2.54030	0.83130
H	-5.19017	-3.40017	0.75950
C	-3.32167	-2.71790	1.64064
C	-2.16610	-1.93521	1.39485
C	-1.01781	-2.15676	2.19017
C	1.13125	-1.27801	2.85480
H	0.75499	-1.04575	3.86291
H	1.84020	-0.51903	2.50742
H	1.62868	-2.25835	2.84660
C	-0.99671	-3.15486	3.15697
H	-0.11046	-3.32131	3.76755
C	-2.13371	-3.96103	3.36002
H	-2.10319	-4.74830	4.11370
C	-3.27916	-3.74823	2.61313
H	-4.16323	-4.37004	2.76873
C	-7.19780	-1.96475	-0.33956
H	-7.39652	-2.14676	0.71870
C	-8.21520	-2.10136	-1.28753
H	-9.21187	-2.41371	-0.97083
C	-7.95355	-1.83366	-2.63452
H	-8.74833	-1.93587	-3.37590
C	-6.67433	-1.43158	-3.03581
H	-6.47194	-1.23242	-4.09098
C	-4.76899	1.24296	2.80488
C	-6.13603	1.13087	2.18862
C	-6.26984	1.29169	0.79560
C	-4.91221	2.58679	-0.60806
H	-5.76478	3.27923	-0.62041
C	-3.71893	3.04044	-1.26854
C	-3.83668	4.14393	-2.14741
H	-4.82307	4.57891	-2.32050
C	-2.72596	4.65370	-2.79169
H	-2.81564	5.49231	-3.48222
C	-1.46478	4.08252	-2.55247
H	-0.59528	4.49056	-3.06450
C	-7.53197	1.31352	0.19749
H	-7.61616	1.41880	-0.88541
C	-8.67454	1.18304	0.99316
H	-9.66082	1.21151	0.52657
C	-8.55580	1.00823	2.37403
H	-9.44849	0.90536	2.99329
C	-7.28853	0.97574	2.96622
H	-7.19698	0.86524	4.04975

9. IR(M)PD studies on a series of isolated trimetallic single molecule magnets containing 3d metals and Lanthanides

C	4.74135	-0.30707	2.92035
C	6.11561	-0.54268	2.33013
C	6.23352	-1.26283	1.12969
C	7.49378	-1.53770	0.57499
H	7.56368	-2.02984	-0.39679
C	8.64812	-1.12868	1.24384
H	9.62777	-1.33106	0.80732
C	8.54379	-0.44209	2.46063
H	9.44406	-0.12194	2.98856
C	7.28276	-0.15005	2.99215
H	7.20369	0.38988	3.93922
N	5.01189	-1.64958	0.52564
C	4.84220	-2.81182	0.00521
H	5.65984	-3.54964	0.02796
C	3.60383	-3.26587	-0.61160
C	-1.21862	-3.09182	-1.38156
H	-1.12468	-3.07177	-2.47726
H	-2.01152	-2.40488	-1.07161
H	-1.43445	-4.11247	-1.02921
C	1.25991	-4.35177	-1.82871
H	0.39004	-4.78371	-2.31955
C	2.51166	-4.93907	-2.01612
H	2.60010	-5.82297	-2.64983
C	3.66212	-4.40907	-1.39686
H	4.62358	-4.90423	-1.54930
C	2.17955	2.19379	1.00400
C	1.10197	2.63723	1.80860
C	-1.03211	2.00792	2.75634
H	-0.60401	2.00311	3.77079
H	-1.75372	1.19524	2.63945
H	-1.52979	2.97016	2.56201
C	1.13887	3.81852	2.53950
H	0.29255	4.12612	3.15174
C	2.27953	4.63515	2.47733
H	2.31173	5.56907	3.03874
C	3.34661	4.24526	1.68572
H	4.23432	4.87789	1.61877
C	3.33007	3.02696	0.96559
C	4.51276	2.72971	0.17843
H	5.16912	3.58676	-0.03913
C	6.01717	1.40378	-1.04703
C	7.24763	1.94416	-0.64793
H	7.32274	2.47616	0.30237
C	8.37869	1.76394	-1.44668
H	9.33567	2.18433	-1.13207
C	8.28412	1.03805	-2.63718

9. IR(M)PD studies on a series of isolated trimetallic single molecule magnets containing 3d metals and Lanthanides

H	9.16563	0.89653	-3.26535
C	7.05796	0.48401	-3.02003
H	6.98449	-0.08080	-3.95290
C	5.91263	0.65542	-2.23574
C	4.56399	0.11844	-2.67319
N	0.17994	-0.66330	-2.85215
H	4.42692	-1.22364	3.46690
H	4.81133	0.48992	3.68466
H	-4.80054	1.07763	3.89152
H	-4.33582	2.23676	2.62053
H	4.70768	-0.60544	-3.49499
H	3.95732	0.94959	-3.09149
H	-3.96383	-0.56652	2.58848

Tab. S5: Atom coordinates for $[M_2Ln(HVab)(Vab)_3]^{2+}$ ($M = Co, Cu$; $Ln = Dy, Gd, Nd, Sm, Tb$) for isomer IV. The calculations were performed at the B3LYP/cc-pVTZ (H, C, N, O) and Stuttgart ecp effective core potential (Co, Cu, Dy, Gd, Nd, Sm, Tb) level of theory.

atom	x	Y	z
Ln	-0.00208	0.13634	-0.30874
M	3.62636	-0.16348	-0.06358
M	-3.62998	0.04604	0.11766
O	-0.11134	-2.12746	-1.65448
O	2.02112	-1.36964	-0.32377
O	3.99387	-0.14743	-1.85026
O	2.08357	1.04194	0.52437
O	0.02398	1.50093	2.02563
O	3.95631	-0.13262	2.32823
O	-2.19614	1.39693	0.08596
O	-3.56705	-0.08538	1.94553
O	-0.07705	2.70866	-0.85307
O	-2.06128	-1.11918	0.14983
O	-0.01210	-1.56704	1.70768
N	-4.80525	-1.49456	-0.13307
O	-3.58627	0.21687	-1.68859
O	-0.93795	0.51262	-2.50608
O	1.21270	0.57327	-2.33583
O	0.27341	0.94687	-4.27685
N	4.78318	-1.86884	0.28537
C	-2.41519	2.58077	-0.47142
C	-1.31138	3.32636	-0.97221
C	-1.24856	-2.48298	-2.46987
H	-0.94098	-2.56911	-3.52308
H	-1.96611	-1.66720	-2.35585

9. IR(M)PD studies on a series of isolated trimetallic single molecule magnets containing 3d metals
and Lanthanides

H	-1.68073	-3.43297	-2.11943
C	0.97786	-2.97720	-1.70146
C	2.11223	-2.51725	-0.97795
C	4.71787	0.74375	-2.65822
H	4.08634	1.63478	-2.85088
H	4.87730	0.25962	-3.63761
C	6.04436	1.14636	-2.05201
C	6.09566	1.58555	-0.71387
N	4.87450	1.59683	0.02980
C	4.57075	2.66068	0.70550
H	5.27385	3.50778	0.69255
C	3.37197	2.86192	1.50303
C	2.20794	2.05433	1.38430
C	1.09587	2.35128	2.21151
C	-1.07449	1.63189	2.95171
H	-0.70979	1.48261	3.98039
H	-1.80936	0.86881	2.67742
H	-1.53642	2.62682	2.85793
C	1.12773	3.40822	3.11490
H	0.27041	3.62438	3.75030
C	2.27496	4.21689	3.20947
H	2.28847	5.05056	3.91220
C	3.37261	3.95362	2.41017
H	4.26293	4.58273	2.47683
C	7.31081	1.98559	-0.14115
H	7.34542	2.28056	0.90965
C	8.47972	1.97202	-0.90555
H	9.42456	2.27985	-0.45405
C	8.43772	1.55340	-2.23756
H	9.34914	1.54035	-2.83798
C	7.22582	1.13830	-2.79963
H	7.19455	0.80877	-3.84106
C	4.82672	-1.08908	2.98918
C	6.11629	-1.30443	2.24489
C	6.06620	-1.72958	0.90189
C	4.49724	-3.00001	-0.28704
H	5.24920	-3.80192	-0.24255
C	3.27869	-3.33901	-0.98084
C	3.26520	-4.57859	-1.66796
H	4.16254	-5.20040	-1.64881
C	2.14769	-4.99369	-2.36602
H	2.14860	-5.94165	-2.90457
C	0.99571	-4.18629	-2.38478
H	0.12382	-4.52324	-2.94270
C	7.24755	-1.98053	0.19428
H	7.19732	-2.27000	-0.85700

9. IR(M)PD studies on a series of isolated trimetallic single molecule magnets containing 3d metals and Lanthanides

C	8.48434	-1.83031	0.82893
H	9.40242	-2.02806	0.27268
C	8.54481	-1.41997	2.16215
H	9.50975	-1.30278	2.65832
C	7.36229	-1.15494	2.86171
H	7.40858	-0.84296	3.90835
C	-4.68199	-0.29784	2.76408
C	-6.03552	0.17281	2.26618
C	-6.19435	0.96711	1.12130
C	-7.46933	1.39481	0.71398
H	-7.57771	1.96932	-0.20760
C	-8.59120	1.05916	1.46646
H	-9.57870	1.39626	1.14714
C	-8.44681	0.27855	2.61975
H	-9.32206	0.00861	3.21337
C	-7.18143	-0.16218	3.00435
H	-7.07160	-0.77143	3.90563
N	-5.03048	1.34166	0.37586
C	-4.86402	2.58672	0.04328
H	-5.69158	3.26987	0.27292
C	-3.69869	3.19335	-0.53901
C	1.05151	3.42349	-1.40337
H	0.90067	3.60254	-2.47867
H	1.91660	2.77367	-1.25883
H	1.18917	4.37587	-0.87003
C	-1.48832	4.58813	-1.52685
H	-0.63804	5.14305	-1.91834
C	-2.76521	5.17516	-1.59095
H	-2.88072	6.16704	-2.02810
C	-3.85199	4.49301	-1.08492
H	-4.84635	4.94353	-1.10638
C	-2.13697	-2.18079	0.94814
C	-1.02638	-2.50230	1.75954
C	1.04837	-1.69937	2.67003
H	0.62796	-1.71735	3.68770
H	1.69639	-0.82916	2.53897
H	1.62354	-2.61868	2.48178
C	-1.01175	-3.66124	2.52947
H	-0.14971	-3.90900	3.14750
C	-2.11972	-4.52804	2.51796
H	-2.09403	-5.43878	3.11682
C	-3.23730	-4.21623	1.76086
H	-4.10892	-4.87382	1.76736
C	-3.27215	-3.02528	0.99902
C	-4.47007	-2.68320	0.27284

9. IR(M)PD studies on a series of isolated trimetallic single molecule magnets containing 3d metals and Lanthanides

H	-5.15857	-3.50515	0.03870
C	-5.98984	-1.34012	-0.92505
C	-7.19130	-1.95335	-0.53541
H	-7.23732	-2.50282	0.40630
C	-8.32992	-1.82513	-1.32730
H	-9.26093	-2.30300	-1.01817
C	-8.27818	-1.06832	-2.50321
H	-9.16776	-0.95854	-3.12591
C	-7.08798	-0.44186	-2.87267
H	-7.04991	0.14928	-3.79155
C	-5.92729	-0.56570	-2.09397
C	-4.64656	0.07628	-2.58093
N	0.18685	0.68899	-3.10456
H	-4.47351	0.21478	3.72545
H	-4.76264	-1.37684	3.01518
H	5.01269	-0.76090	4.02290
H	4.24070	-2.01934	3.03155
H	-4.87817	1.07904	-2.99800
H	-4.25642	-0.50183	-3.44590
H	4.23269	0.76014	2.58821

10 Comment: X-ray Magnetic Circular Dichroism Spectroscopy Applied to Nitrogenase and Related Models: Experimental Evidence for a Spin-Coupled Molybdenum(III) Center

Michael Lembach, Marcel Schmitt, and Gereon Niedner-Schatteburg

*Fachbereich Chemie and Forschungszentrum OPTIMAS,
Technische Universität Kaiserslautern,
67663 Kaiserslautern, Germany*

10.1 Preamble

The following chapter is prepared as a comment to the earlier published paper of Kowalska et al. and serves better to interpret the presented data in the recent paper. I performed the quantum chemical calculations and XA simulations. I thank Marcel Schmitt for giving this publication to my attention, and I wrote this comment.

10.2 Introduction

A spin-coupled Mo^{3+} atom inside a nitrogenase-like complex was explored in recent articles^[1, 2] by Kowalska et al. and Bjornson et al. A delocalized electron between two Fe^{2+} centers is anticipated for the $[\text{MoFe}_3\text{S}_4]^-$ core, and the Molybdenum atom should follow a spin configuration against the Hund'sche rule with a total spin of $3/2$. A reference complex containing a Molybdenum atom shows a total spin of $1/2$. Unfortunately, no magnetic data are supplied in the current publication by Kowalska^[2] et al. to understand the magnetic coupling scheme of the Fe center in the $[\text{MoFe}_3\text{S}_4]^-$ core. A reduced spin and orbital magnetic momentum would hint an antiferromagnetic exchange coupling scheme of the different Fe centers. Because of the increased spin magnetic value, this would also hint at the delocalized electron in the complex. The orbital magnetic values would also improve since the delocalized electron should result in higher orbital momenta in the Fe^{2+} atoms in this complex. No spin and orbital magnetic values for the Molybdenum atom are presented in this work. With these values it should be possible to approximate the total spin configuration of the different Molybdenum complexes. A spin-coupled Molybdenum center reveals a significant change in the spin, orbital, and total magnetic values for the metal centers and would lead to reduced magnetic values. Also, it is not stated which charge the $[\text{MoFe}_3\text{S}_4]^-$ complex obtains. The complex in the recent paper is abbreviated as $[\text{MoFe}_3\text{S}_4]^{3+}$, suggesting a tricationic species. However, the presented complex has a counterion with a positive netto charge, resulting in a mono anionic complex. In the paper of Bjornson^[1], TD-DFT calculations of the complex $[\text{MoFe}_3\text{S}_4]^{3+}$ were performed. Also, here is not pointed out which netto charge this complex obtain. Furthermore, it is unclear if the calculations were conducted for the ground state or the excited states as a result of the TD-DFT computation. The publication does not specify which excited state is addressed when the excited state is discussed. The mentioned Mössbauer spectra are not given in the paper or the supplement, only the calculations suggest a delocalized electron between two Fe^{2+} centers in this combination.

10.3 Results

DFT calculations of the $[\text{MoFe}_3\text{S}_4]^-$ complex reveal a minimum structure with a multiplicity of 16. This verifies the presence of a delocalized electron between two of the three iron atoms (cf. Fig. 1).

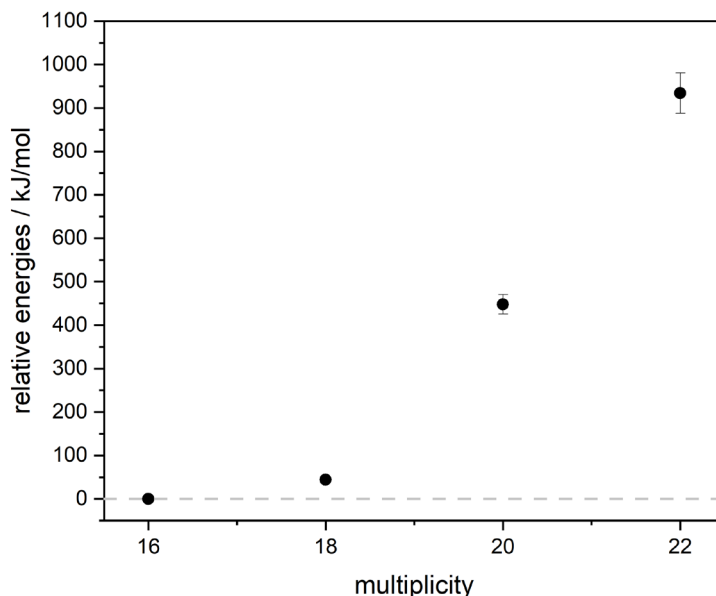


Fig. 1: Relative energies of the $[\text{MoFe}_3\text{S}_4]^-$ complex with different multiplicities with uncertainties of 5%. The calculations were performed with Gaussian 09 at the B3LYP/cc-pVTZ (H, C, N, B, Cl) and ecp-(10, 28)-mdf (Fe, Mo) level of theory.

In the complex, a Fe^{2+} atom in a low spin conformation would decimate the spin magnetic values. The LS configuration does not have any magnetic values to feature an exchange coupling to the other metal center. A delocalized electron should have a higher impact on the spin and orbital magnetic moments. The extra electron between two Fe^{2+} would formal lead to a Fe^{3+} atom in the cubane system. Here, a significant change in the orbital magnetic values should be expected.

The spin density of this complex demonstrates localized spin density on the metal centers (cf. Fig. 2), which does not hint a delocalized electron in the first place.

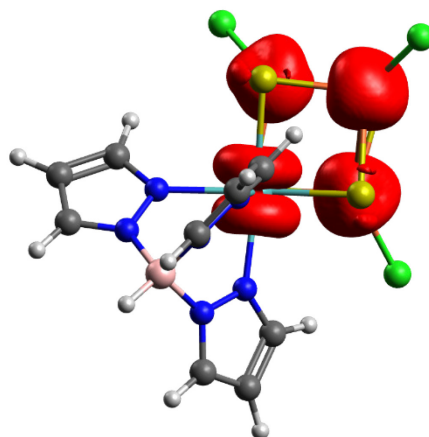


Fig. 2: Calculated spin density of $[\text{MoFe}_3\text{S}_4]$. The calculation was performed with Gaussian 09 at the B3LYP/cc-pVTZ (H, C, N, B, Cl) and ecp-(10, 28)-mdf (Fe, Mo) level of theory.

Electron localized field plots^[2] (ELF) of the Fe₂S₂ sides did not reveal a delocalized electron in between any Fe atoms in the complex (cf. Fig.3). There are weak electronic interactions between the very diffuse sulfur atoms in this complex. However, there is a lack of electron density in the direction of the Fe centers, indicating that the delocalized electron is not between two iron atoms and is more centered in the cubane system due to the extensively diffuse sulfur atoms. As in the spin density, the electron density is also firmly located to the metal center and has a more spherical electron distribution, resulting in a reduced orbital magnetic momentum.

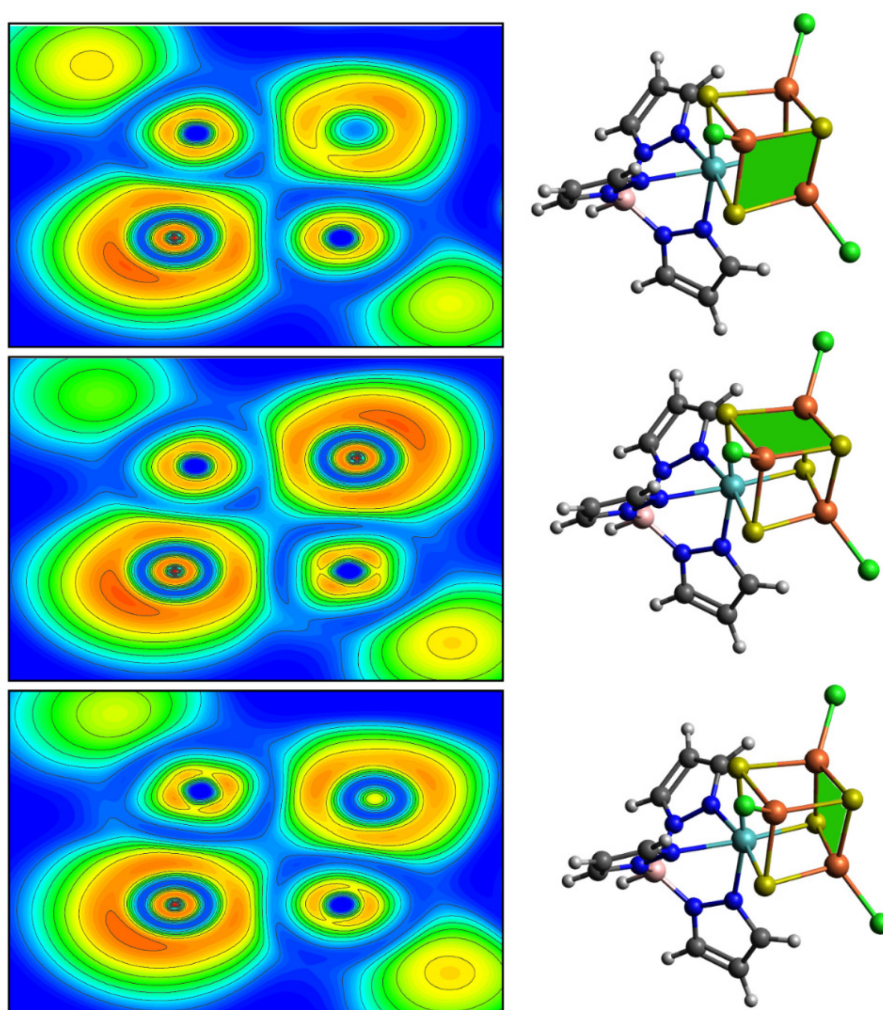


Fig. 3: Electron localized field plots of the Fe₂S₂ sides. ELF plots represent the green planes in the structure. The calculation was performed with Gaussian 09 at the B3LYP/cc-pVTZ (H, C, N, B, Cl) and ecp-(10, 28)-mdf (Fe, Mo) level of theory.

The composition of a Fe^{2+,2+;3+} oxidation state in the complex XA simulations reveals the possible spectral pattern of the L_{3,2} edges (cf. Fig. 4).

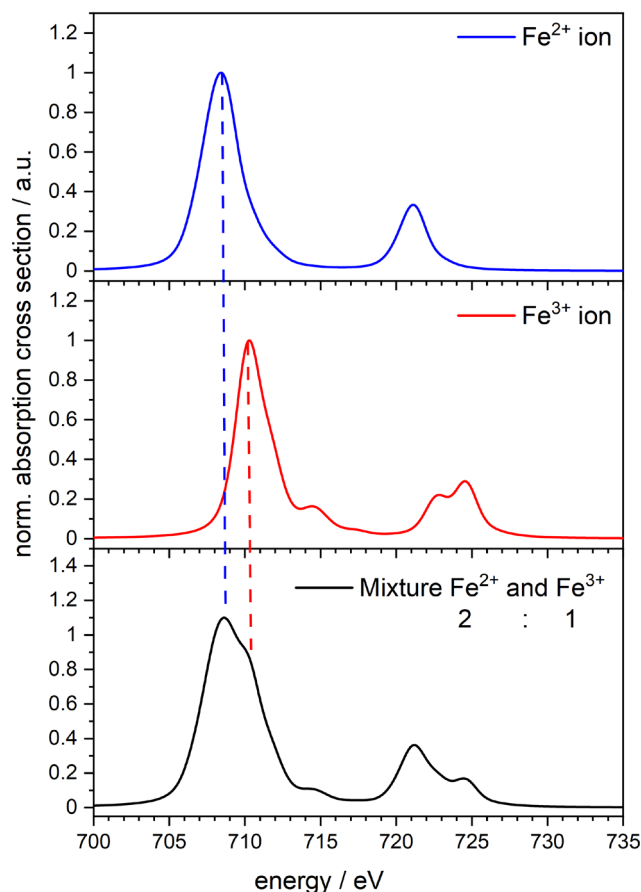


Fig. 4: Normalized XA spectra of a Fe^{2+} ion (blue), Fe^{3+} (red) ion and the mixture of $\text{Fe}^{2+,2+,3+}$ (black) with gauss folded (broadening 0.3) simulated XA spectra by CTM4XAS^[3] and Cowan batch file.

By assuming a 2:1 concentration of $\text{Fe}^{2+/3+}$, the spectral pattern does not match the experimental spectra from Kowalska^[4]. We do not observe the appearance of a Fe^{3+} ion in the experimental XA spectra. Absorptions of Fe^{3+} on the L_3 edge are typically around 710 eV; previous Fe^{3+} investigations have also revealed absorptions in this region^[5-7]. Earlier studies on siderophore side effects have shown higher absorption energy for Fe^{3+} ions^[5]. A slight shoulder on the L_2 edge should arise, however it is not seen in the experimental spectra from the current study. Simulations with other combinations of the oxidation state like a $\text{Fe}^{2+,3+,3+}$ configuration leads to slightly different spectral patterns (cf. Fig. 5), matching the experimental XA spectra better than in the other case. Still, the L_3 absorption edge does not feature such a configuration because the energy is much higher than in the experimental XA spectra.

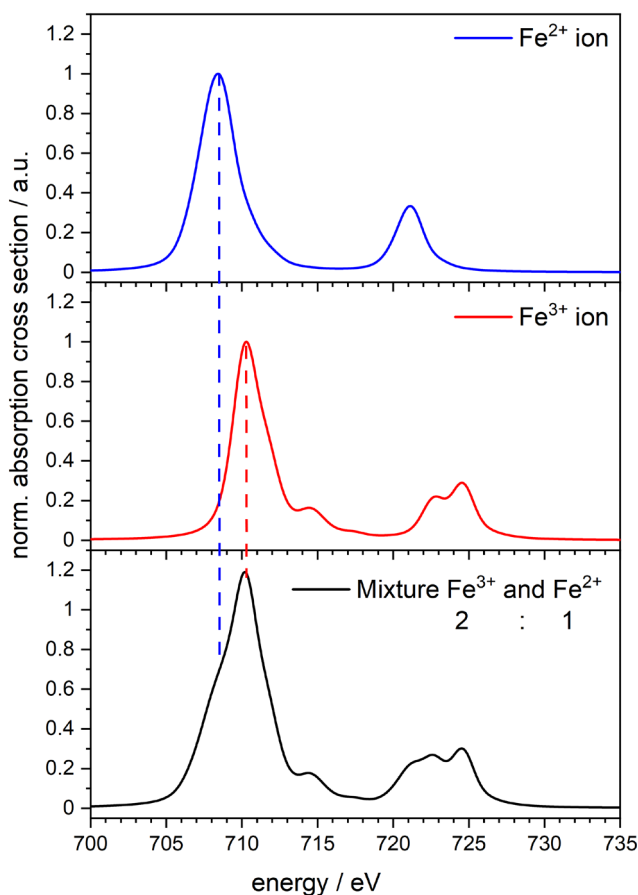


Fig. 5: Normalized XA spectra of a Fe^{2+} ion (blue), Fe^{3+} (red) ion, and the mixture of $\text{Fe}^{2+,3+,3+}$ (black) with gauss folded (broadening 0.3) simulated XA spectra by CTM4XAS^[3] and Cowan batch file.

This hints at the first assumption that no Fe^{3+} atom is present in the experimental spectra of Kowalska. The shape of the spectrum does not show any features of a Fe^{3+} atom, which is assumed in the cubane complex. We do not contradict that a Fe^{3+} ion has to be a presence in this complex. Calculations of the complex confirm that one iron atom has to be in the Fe^{3+} oxidation state. The change in their oxidation state would lead to a difference of 1.88 eV for the L_3 edge and 3.51 eV for the L_2 edge (cf. Fig. 6). Therefore, we expect a change in the spectral pattern of the experimental XA spectra.

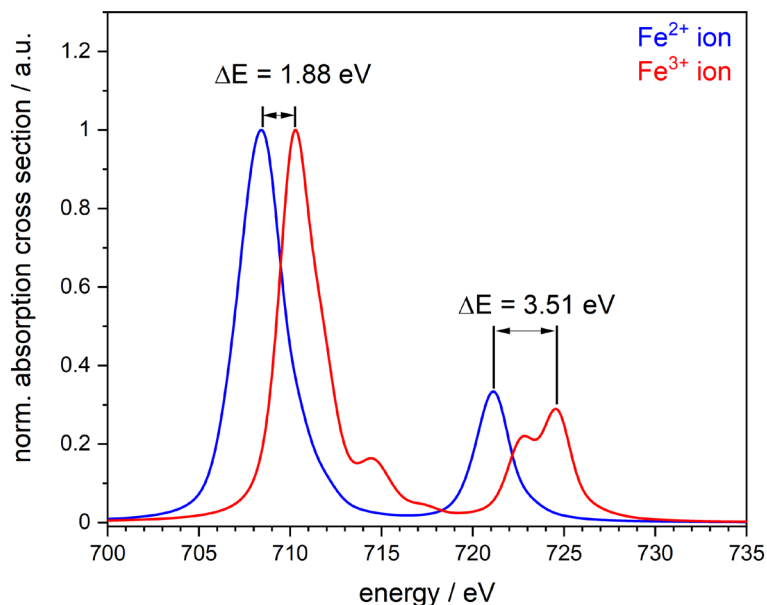


Fig. 6: Normalized simulated XA spectra of a Fe^{2+} ion (blue) and Fe^{3+} (red) ion with gauss folded (broadening 0.3) by CTM4XAS^[3] and Cowan batch file with the resulting energy difference between their absorption maxima.

We assume that the delocalized electron in such complexes has a major influence on the oxidation state of the iron atoms and the resulting XA spectra presented in the recent paper^[4]. A good hint would be the spin-orbit coupling from the core to the hole, which also can be extracted from the XA spectra (cf. Fig. 7). If there is a mixture of different oxidation states, a significant change should be observed. The spin-orbit coupling from a Fe^{3+} ion has to be higher because of the higher orbital momentum.

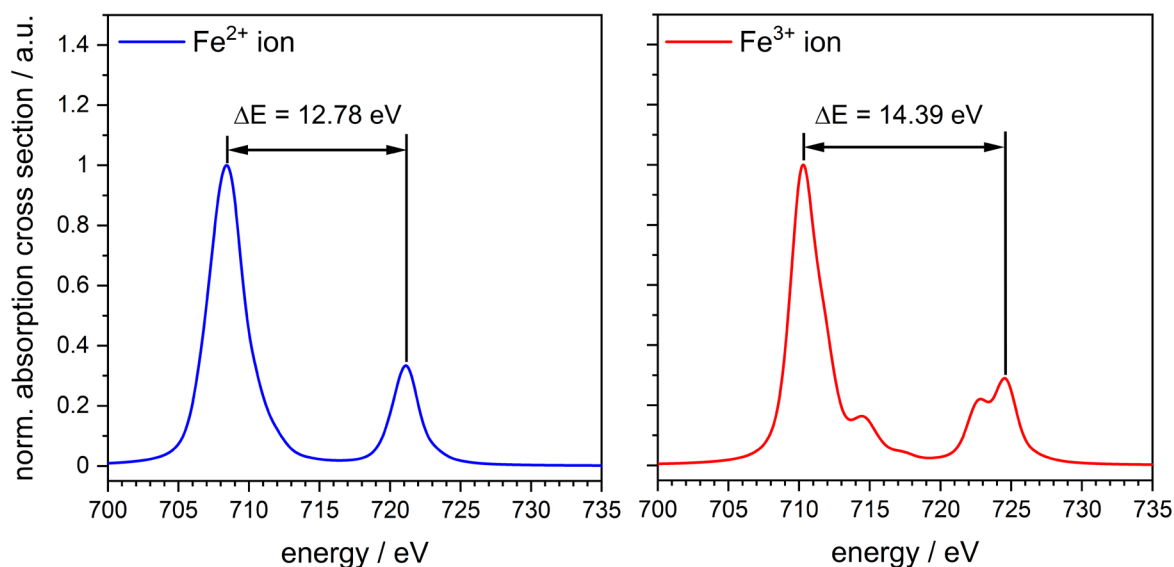


Fig. 7: Normalized simulated XA spectra of a Fe^{2+} ion (blue) and Fe^{3+} (red) ion with gauss folded (broadening 0.3) by CTM4XAS^[3] and Cowan batch file with the resulting spin-orbit coupling from the core to the hole.

The derived spin-orbit coupling constants for various cubane complex structures show fascinating values when compared to the experimental spin-orbit coupling constant from their XA spectra (cf. Tab. 1). The SOC values for a pure Fe³⁺ ion are excessively high, and the SOC values for simulated mixtures are higher than the observed spin-orbit coupling constant. Only the pure Fe²⁺ matches the experimental values by a deviation of 0.03 eV. This also is in good agreement with the above discussed simulated XA spectra and the *Abinitio* calculations. We are confident that with the irradiation with X-ray light and their resulting XA spectra, no Fe³⁺ ion is observed.

Tab. 1: Spin-orbit coupling constants for different oxidation states of iron and their possible mixtures in the cubane complex compared to the experimental approximated spin-orbit coupling constant from the paper^[4].

Configuration	L ₃ edge / eV	L ₂ edge / eV	SOC / eV
Fe ²⁺	708.41	721.19	12.78
Fe ³⁺	710.21	724.60	14.39
Fe ^{2+,2+3+}	708.63	721.95	13.32
Fe ^{3+,3+2+}	710.12	723.97	13.85
Exp.	707.25	720.5	12.75

We suppose that the delocalized electron is somewhere between one Fe²⁺ center and the Fe³⁺ center, rather than between two Fe²⁺ ions. We do not contradict a delocalized electron, but we assume that the delocalized electron must be near the Fe³⁺ center and lead by absorption of the X-ray light to a formal Fe²⁺ ion. This explains why no features of Fe³⁺ are present in the XA spectra, and the SOC values are precise as the pure Fe²⁺ ion.

A totally ferromagnetic exchange coupled complex (UUUU) destabilizes by 58 kJ/mol in comparison to an antiferromagnetically coupled complex (DUUD). Broken symmetry calculations of the complex reveal a favored minimum structure with pairwise antiferromagnetic exchange coupling of the transition metal ions in this complex (cf. Fig. 8). First, this verifies the idea that the spin coupled Molybdenum atom in this combination is related by antiferromagnetic exchange with the neighboring "spin up" iron atoms. Therefore, the experimental spin and orbital magnetic moments must be reduced by the antiferromagnetic exchange coupling. In addition, the third Fe atom acquires a "spin down"

configuration, which may result in even lower magnetic moments. The experimental XAS and their corresponding XMCD spectrum point out a dichroic effect, considering a ferromagnetic exchange coupling in this complex. In combination with the presented broken symmetry calculation, we assume that both “spin down” metals (Mo^{3+} , Fe^{2+}) establish an antiferromagnetic exchange coupling, which reduces the ferromagnetic exchange coupling of the “spin up” metals but not in a way that no magnetic effects are observed. Unfortunately, no magnetic values are presented in the recent paper to evaluate this assumption.

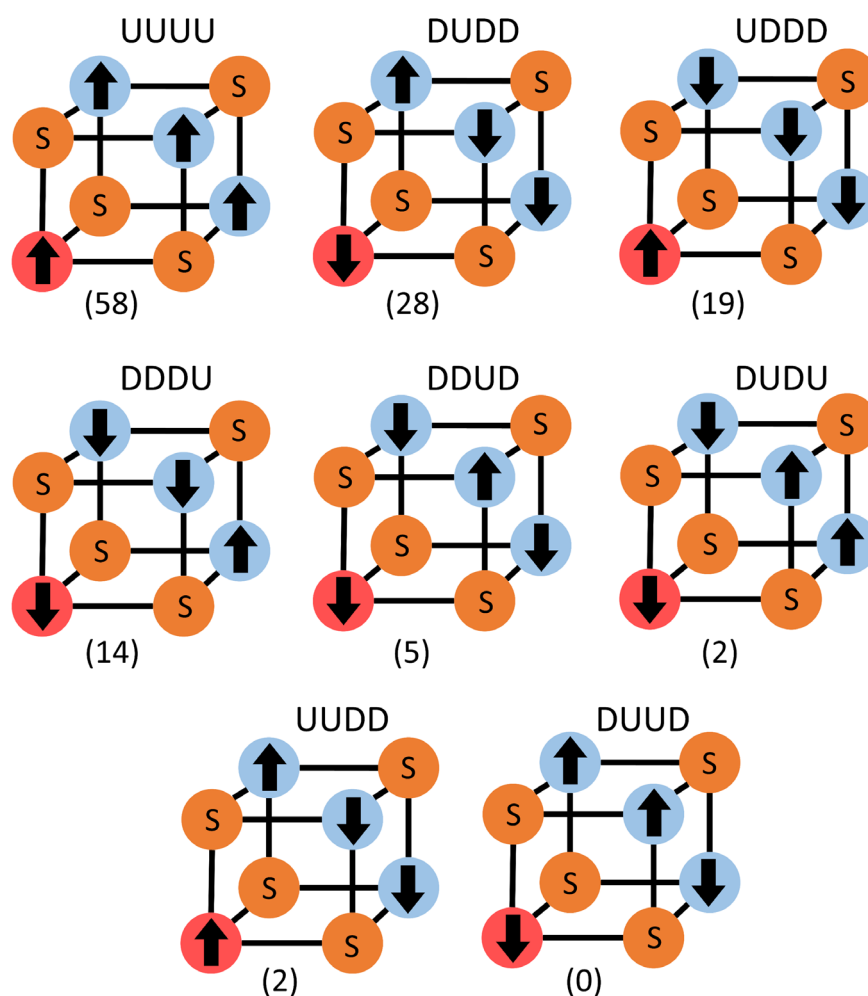


Fig. 8: Possible spin orientations in the $[\text{MoFe}_3\text{S}_4]^-$ complex with one ferromagnetic (UUUU) and seven broken symmetry configurations. The blue circles represent the iron atoms, and the red circle represents the Molybdenum atom in this complex. The relative energies in parentheses are given in kJ/mol. The calculations were performed at the b3-lyp/cc-pVDZ (H, C, N, O) and Stuttgart 1997 ECP (Fe, Mo) level of theory.

The calculated coupling constants from the broken symmetry calculations reveal two negative values for the Molybdenum and one Fe^{2+} ion (cf. Tab. 2). A positive coupling constant represents a ferromagnetic exchange coupling and a negative one, an antiferromagnetic one. The Molybdenum atom points out an antiferromagnetic exchange coupling, such as one iron atom. The Fe^{3+} and Fe^{2+} ions are still in a ferromagnetic exchange coupling, which dominates the XAS described in the latest research. Therefore, we assume that the delocalized electron must be more located between the ferromagnetic coupled Fe^{3+} and Fe^{2+} ions. A delocalized electron between the Mo^{3+} ion and the Fe^{2+} ion would not result in an antiferromagnetic exchange coupling, where the magnetic moments are not zero. Between two ferromagnetic Fe^{2+} , the delocalized electron would enhance the spin magnetic momentum per Fe atom, but the antiferromagnetic coupled Fe atom reduces the spin magnetic moment in a higher amount, where the delocalized electron is flagged.

Tab. 2: Calculated exchange coupling constants of $[\text{MoFe}_3\text{S}_4]^-$ with the spin configuration of the minimum structure. The calculations were performed with Turbomole 7.0 at the b3-lyp/cc-pVDZ (H, C, N, O) and Stuttgart 1997 ECP (Fe, Mo) level of theory.

	$\text{J} / \text{cm}^{-1}$
Mo	-38.76
Fe₁	10.16
Fe₂	15.47
Fe₃	-28.48

No spin and orbital magnetic momenta are shown for the presented XA spectra of the Molybdenum in these complexes. As a result, it is impossible to argue that the Molybdenum atom is spin-coupled with the iron atoms that surround it. A spin-coupled Molybdenum atom should exhibit large fluctuations in magnetization in both directions. Also, it is not mentioned if there is a ferromagnetic exchange coupling or an antiferromagnetic exchange coupling, which would be seen in the spin, orbital, and total magnetic moments from the XMCD data. Also, no L_2 edge is shown and no change in the spectral shape of the XA spectra can be observed (cf. Fig. 8). The experimental XMCD spectra and approximated crystal field splitting serves for the XA simulations (cf. Fig. 9).

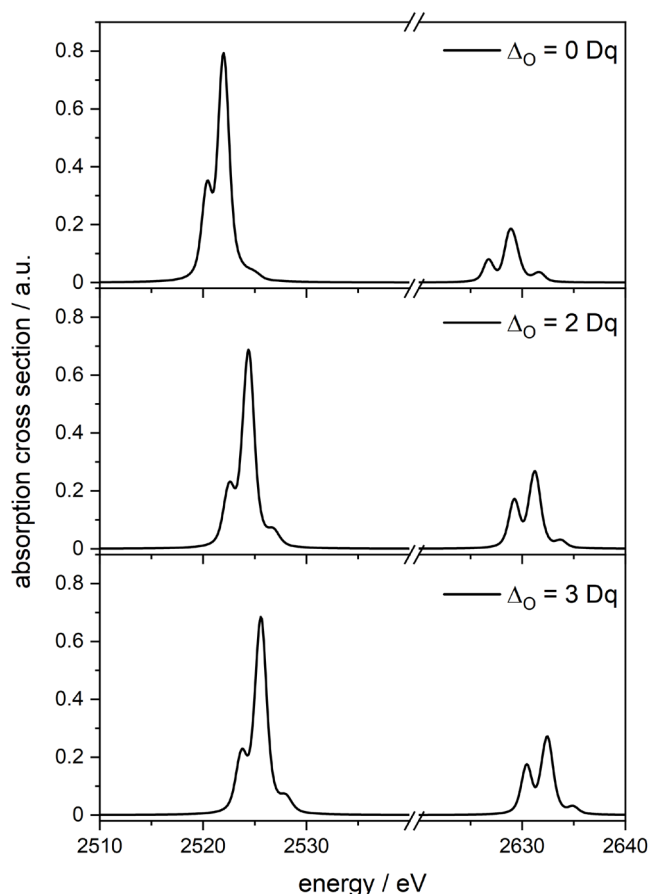


Fig. 9: Normalized simulated XA spectra of a Mo³⁺ ion with gauss folded (broadening 0.3) by CTM4XAS^[3] and Cowan batch file with different crystal field splittings (atomic = 0 Dq, Mo(ttcn)Cl₃ = 2 Dq and [MoFe₃S₄]⁻ = 3 Dq).

Both spectra simulated and experimental reveal a change in the crystal field splittings for the different complexes. The higher crystal field splitting leads to a higher shift in the L3 edge of the absorption energy in Molybdenum. The Molybdenum XA spectra simulation agrees with the experimental XA spectra from the recent paper. For the XA spectra simulation, a less broadening than in the experimental spectra is given, and therefore, the shift of the absorption edges is shown better (cf. Fig. 10).

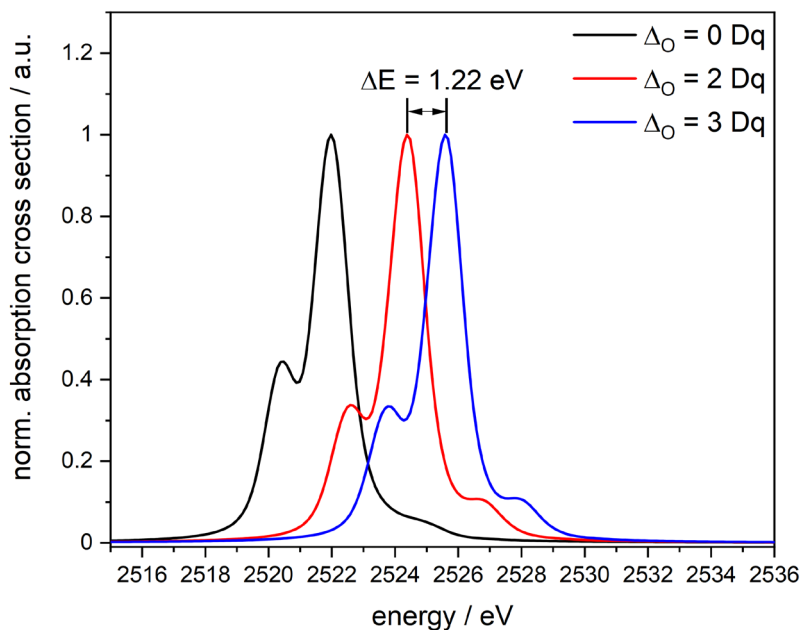


Fig. 10: Normalized simulated XA spectra of a Mo^{3+} ion with gauss folded (broadening 0.3) by CTM4XAS^[3] and Cowan batch file with different crystal field splittings (atomic = 0 Dq, $\text{Mo}(\text{ttcn})\text{Cl}_3 = 2$ Dq and $[\text{MoFe}_3\text{S}_4]^- = 3$ Dq).

Natural bond order analysis reveals elongated bondings for the d_z^2 and $d_{x^2-y^2}$ orbitals in the complex $[\text{Mo}(\text{ttcn})\text{Cl}_3]$. For the corresponding $[\text{MoFe}_3\text{S}_4]^-$, only one bonding in the z-direction is elongated. The other bondings are shortened compared to the $[\text{Mo}(\text{ttcn})\text{Cl}_3]$ complex. Furthermore, the bonding distances in the x and y directions are shorter in the $[\text{MoFe}_3\text{S}_4]^-$ complex than in the $[\text{Mo}(\text{ttcn})\text{Cl}_3]^-$ complex (cf. Fig. 11). Because of the ligand alteration, the crystal field splittings in these complexes change significantly. Chloride establishes weak crystal field splittings observed in the bonding distances by not changing the distance in any position where chloride coordinates are ligand. Chloride is a hard donor that prefers a complex with a high spin. A nitrogen ligand serves as a donor and leads to a higher crystal field splitting. Therefore, a low spin complex is more favored than in the chloride species. The Mo^{3+} ion is higher charged than the Fe atoms in the $[\text{MoFe}_3\text{S}_4]^-$ complex, resulting in higher crystal field splittings and favors Low spin complexes than high spin complexes.

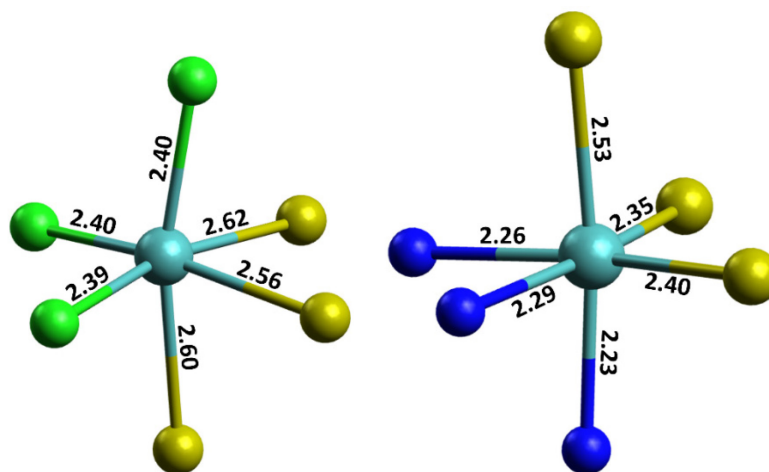


Fig.11: Bonding distances of [Mo(ttcn)Cl₃] (left) and [MoFe₃S₄]⁻ (right). The calculation was performed with Gaussian 09 at the B3LYP/cc-pVTZ (H, C, N, B, Cl) and ecp-mdf (Fe, Mo) level of theory. The ligand is omitted for clarity.

The calculated orbital energies of the d orbital in both complexes confirm the assumed crystal field splittings as discussed before (cf. Fig. 12). The Jahn Teller distortion leads to higher orbital energies of the d_{z^2} orbital in both complexes. The smaller elongation in the [MoFe₃S₄]⁻ complex results in stronger bondings, and therefore the $d_{x^2-y^2}$ orbital is more lowered as in the [Mo(ttcn)Cl₃] complex. Following the Hund'sche rule in [Mo(ttcn)Cl₃] all orbitals with almost equal energies will be filled by one electron, yielding a complex with a total spin of $S=3/2$. Because the $d_{x^2-y^2}$ orbital is lowered in the [MoFe₃S₄]⁻ complex, the second Hund'sche rule must be used, which states that if all orbitals with nearly identical energies are filled with one unpaired electron, then a spin pairing of the lowest orbital takes place. In the [MoFe₃S₄]⁻ complex, the $d_{x^2-y^2}$ orbital has to be doubly occupied, and then the next energetic higher orbital is occupied, leading to the observed total spin of $S=1/2$.

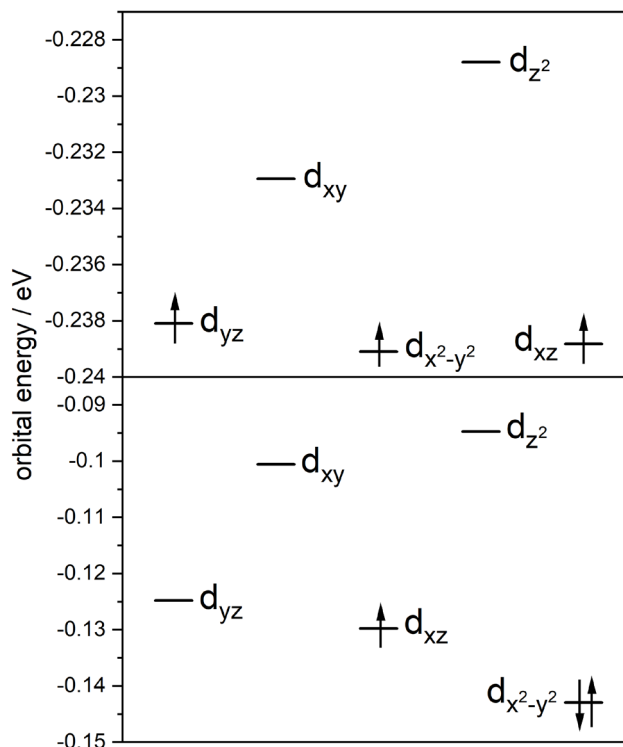


Fig. 12: Calculated d orbital energies of [Mo(ttcn)Cl₃] (top) and [MoFe₃S₄] (bottom). The calculations were performed with Gaussian 09 at the B3LYP/cc-pVTZ (H, C, N, B, Cl) and ecp-(10, 28)-mdf (Fe, Mo) level of theory.

We do not expect a Molybdenum ion, which does not follow the Hund'sche rule only by determining the total spin. It more seems like the Molybdenum ion has a low spin configuration induced by the ligand. This also may be seen by the spin magnetic moments from the XMCD spectra, which are not presented. Therefore, the presented cubane system illustration needs to be modified at some points (cf. Fig. 13).

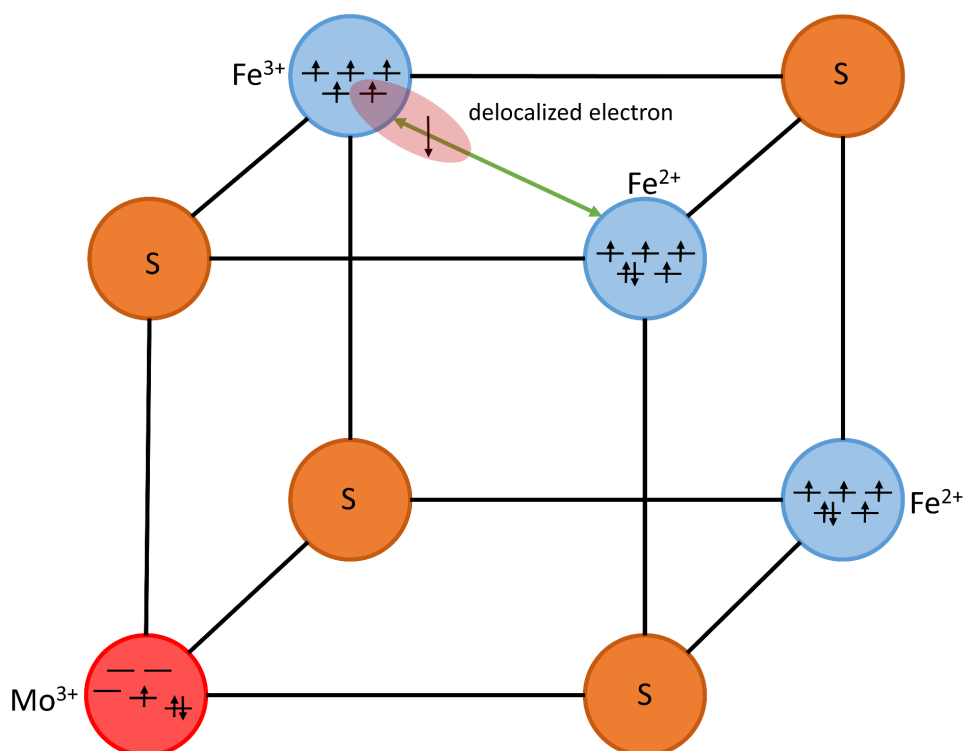


Fig. 13: Electronic structure in the cubane system of $[\text{MoFe}_3\text{S}_4]^-$ with the delocalized electron and the crystal field splitting of the different metal ions.

We do not doubt the experimental results with all the assumptions discussed, but the interpretation is highly questionable in the recent paper^[4]. We assume that the delocalized electron must be near the Fe^{3+} ion because the experimental XA spectra do not show any feature of the Fe^{3+} ion. Moreover, the Fe^{3+} and the delocalized electron lead to a XA absorption of a “formal” Fe^{2+} ion. The Molybdenum ion in the $[\text{MoFe}_3\text{S}_4]^-$ complex does not behave against the Hund’sche rule as assumed. The ligand leads to a different crystal field splitting than in the $[\text{Mo}(\text{ttcn})\text{Cl}_3]$ complex and forces the Mo^{3+} in a low spin configuration with a total Spin $S=1/2$.

10.4 Acknowledgment

The German research foundation DFG supported this work within the transregional collaborative research center SFB/TRR 88 “Cooperative effects in homo and heterometallic complexes” (3MET) and by the state research center OPTIMAS.

10.5 References

- [1] R. Bjornsson, F. A. Lima, T. Spatzal, T. Weyhermüller, P. Glatzel, E. Bill, O. Einsle, F. Neese, and S. DeBeer, Identification of a spin-coupled Mo(iii) in the nitrogenase iron–molybdenum cofactor, *Chem. Science*, 5, 3096-3103, 2014.
- [2] R. F. W. Bader, A quantum theory of molecular structure and its applications, *Chem. Rev.*, 91, 893-928, 1991.
- [3] E. Stavitski, and F. M. F. de Groot, The CTM4XAS program for EELS and XAS spectral shape analysis of transition metal L edges, *Micron*, 41, 687-694, 2010.
- [4] J. K. Kowalska, J. T. Henthorn, C. Van Stappen, C. Trncik, O. Einsle, D. Keavney, and S. DeBeer, X-ray Magnetic Circular Dichroism Spectroscopy Applied to Nitrogenase and Related Models: Experimental Evidence for a Spin-Coupled Molybdenum(III) Center, *Angew. Chem. Int. Ed.*, 58, 9373-9377, 2019.
- [5] R. K. Hocking, S. DeBeer George, K. N. Raymond, K. O. Hodgson, B. Hedman, and E. I. Solomon, Fe L-Edge X-ray Absorption Spectroscopy Determination of Differential Orbital Covalency of Siderophore Model Compounds: Electronic Structure Contributions to High Stability Constants, *J. Am. Chem. Soc.*, 132, 4006-4015, 2010.

11 First Investigations of a heptanuclear homoleptic Manganese complex with single molecular magnetic behavior

Michael Lembach, Marcel Lechner, and Gereon Niedner-Schatteburg

*Fachbereich Chemie and Forschungszentrum OPTIMAS,
Technische Universität Kaiserslautern,
67663 Kaiserslautern, Germany*

11.1 Preamble

The following chapter represents the first investigation and calculations of a single molecule magnet. I managed the Mass spectrometric experiments, XA simulations, and quantum chemical calculations. I received experimental support from Marcel Lechner in the synthesis of the complex. I wrote this chapter for detailed documentation.

11.2 Abstract

Compounds with magnetic properties are fascinating and might lead to access to a new application in technology. Single Molecule Magnets (SMM) show extraordinary magnetic properties which arise from the molecule itself. Such molecules combine a large spin ground state with a high anisotropic barrier. In this chapter, a seven metallic complex with the general structure $[\text{Mn}_7(\text{Vab})_6]^{2+}$ (Vab = 2-[(2-hydroxymethyl-phenylimino)-methyl]-6-methoxy-phenol) is investigated theoretically to its magnetic properties and structure determination via Mass spectrometry (MS) in comparison with Collision Induced Dissociation (CID). The calculations suggest single molecule magnetic behavior in the investigated complex.

11.3 Introduction

In the last decades, transition metal (TM) complexes have become a highly fascinating field of research for many applications^[1-13]. The wide variety in the use of transition metal complexes enables access to research in their molecular magnetism. Much effort is spent in the design, modeling, and synthesis of transition metal complexes with a spin frustrated^[14-18] ground state, spin-crossover^[19-23] (SCO) behavior, or single molecule magnetic^[24-31] (SMM) behavior. Single molecule magnets seem promising for quantum computing applications^[32-35] or data storage^[36]. Compounds with single molecule magnetic behavior combine a large spin ground state with a high anisotropic barrier^[37, 38] and result in a long living magnetization with a slow relaxation of the magnetism. The archetypical single molecule magnet was first synthesized by Lis^[28] and investigated by many groups^[24, 39-46]. The research is also expended on rare earth metals^[26, 27, 30, 47-52], but also investigations of early transition metals, especially Manganese, seem to be prominent candidates for single molecule magnets^[53-58].

All these studies were performed in solid state or thin films, and therefore minor influence of external effects such as crystal packing effects or solvation effects cannot be excluded. Previous investigations on $[\text{Mn}_{12}\text{O}_{12}(\text{OAc})_{15}(\text{CH}_3\text{CN})]^+$ in gas phase via XMCD^[59, 60] revealed a shift in the primary absorption edge of around 2 eV in comparison with the bulk XA investigations by Mannini^[34, 40, 59, 60].

However, the magnetic properties seem to be almost the same, indicating that the magnetic properties arise from the molecule itself and are not or very weak affected by external effects.

The presented complex (cf. Fig. 1) is synthesized to obtain seven Manganese ions which are μ oxo bridged over the ligand (Vab)^[29, 30]. They build up an almost in plane star-shaped arrangement of the Mn²⁺ ions. Six Manganese ions build a ring around one central Manganese ion. With an averaged distance of 3.35 Å, no direct metal-metal interaction is expected. Each Manganese ion is in octahedral coordination by the coordination of two tridentate ligands. Seven Mn²⁺ ions in a high spin configuration lead to an electronic spin ground state with $S = 35$. The homoleptic heptanuclear Manganese complex serves as a model complex to investigate its single molecular magnetic behavior.

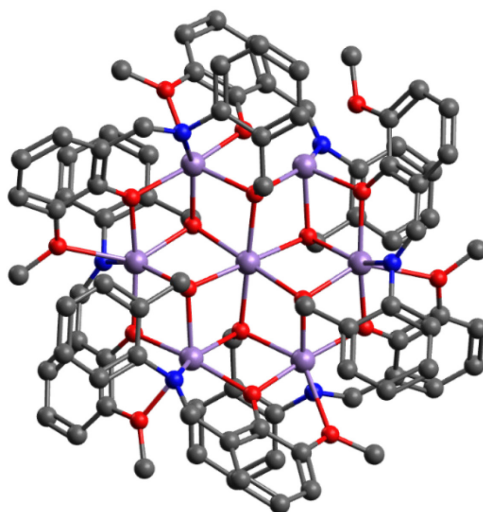


Fig. 1: Calculated minimum structure of $[\text{Mn}_7(\text{Vab})_6]^{2+}$. The calculations were performed with Gaussian 09 at the B3LYP/ cc-pVTZ (H, C, N, O) and Stuttgart RSC ecp effective core potential (Mn) level of theory. Hydrogen atoms are omitted for clarity.

Electrospray ionization^[61, 62] enables mass spectrometric investigations of ionic complexes in gas phase and allows the determination of the structure via CID. In combination with different light sources, the determination of the structure^[63-67], electronic ground state^[68-72], and magnetic moments^[73-79] are possible with such tandem-based methods. The CID experiments were performed at room temperature and helped determine the molecular structure by observing the investigated characteristic fragments of the complex. First mass spectra, CID breakdown curves, and abinitio calculation for this complex were performed to gain the first hints for the structure, stability, and magnetic exchange coupling.

11.4 Experimental setup and methods

The mass spectrometric and Collision Induced Dissociation (CID) experiments were performed with a quadrupole mass spectrometer (amazon ETD, Bruker daltonics) containing a three dimensional Paul trap. For the ESI process, a sample solution of $[\text{Mn}_7(\text{Vab})_6]^{2+}$ ($c \sim 1 \cdot 10^{-6} \text{ mol/L}$) in acetonitrile was prepared and constantly infused into the spray chamber by a syringe pump with a constant flow rate of $140 \mu\text{L/h}$. Nitrogen was used as a drying gas with a flow rate of 9 L/min at $180 \text{ }^\circ\text{C}$. The nebulizer pressure to spray the sample solution was set to 280 mbar (4psi), and the voltage of the spray needle was kept at 4.5 kV . The Paul trap consists of a ring electrode and two end caps forming a nearly hyperbolic inner profile. The end caps possess pinholes that allow to enter or exit the ions in the trap. The ring electrode is powered with a high voltage RF (radio frequency) potential (781 kHz) while the end caps are grounded. The ions are accumulated in this resulting oscillating quadrupolar electric field generated from the three electrodes. An auxiliary dipolar voltage is fed to either the exit cap or both end caps for ion isolation and fragmentation. For providing a constant partial Helium buffer gas pressure of ca. 10^{-3} mbar inside the trap, a proportional integral derivative (PID) gas controller is used.

CID breakdown curves were recorded by varying the excitation amplitudes (0.0 V – 3.0 V). The excitation amplitudes determine the internal scale of the mass spectrometer (E_{lab} in V).

Relative abundances were calculated according to

$$I_{\text{tot.}}^{\text{fr.}}(E_{\text{lab}}) = \left(\frac{\sum_i I_i^{\text{fr.}}(E_{\text{lab}})}{\sum_i I_i^{\text{fr.}}(E_{\text{lab}}) + \sum_i I_i^{\text{p.}}(E_{\text{lab}})} \right) \quad (1)$$

The relative abundance is the quotient of the sum of the intensity of the fragments ($I_i^{\text{fr.}}$) over the sum of the intensity of the fragments ($I_i^{\text{fr.}}$) and the intensity of the parents ($I_i^{\text{p.}}$). Center of mass corrected fragmentation amplitudes (E_{com}) can be calculated from the internal amplitudes

$$E_{\text{com}} = \left(\frac{m_{\text{He}}}{m_{\text{He}} + m_{\text{ion}}} \right) \cdot E_{\text{lab}} \quad (2)$$

The fragmentation amplitude dependent CID breakdown curves were modeled and fitted by a sigmoidal function

$$I_{\text{fit}}^{\text{fr}}(E_{\text{com}}) = \left(\frac{1}{1 + e^{(E_{\text{com}}^{50} - E_{\text{com}}) B}} \right) \quad (3)$$

The investigated complex was synthesized in our group in a workplace kindly provided by Thiel et al. The synthesis was performed under aerobic conditions with chemicals purchased from Sigma Aldrich without further purifications.

Synthesis of 2-[(2-hydroxymethyl-phenylimino)-methyl]-6-methoxy-phenol^[29]: 2-Hydroxy-3-methoxy benzaldehyde (4.5. g) were dissolved in methanol (100 mL). This mixture was stirred, and 2-Aminobenzyl-alcohol (4 g) was added). The mixture was stirred and heated for 6 h at 60 C. After 6 h, the solution was cooled to room temperature, and a yellow solution was obtained (H₂Vab).

Synthesis of [Mn₇(Vab)₆](NO₃)₂^[30]: H₂Vab (780 mg, 30 mL) was stirred at room temperature. Sodium methanolate (162 mg) was dissolved in methanol (30 mL). The sodium methanolate solution was dropwise, added to the ligand solution, and stirred for 15 min. Ln(NO₃)₂·H₂O (520 mg) were dissolved in methanol (30 mL) and dropwise added. The mixture was stirred at room temperature for 4 h. Mn(OAc)₂·H₂O (370 mg) was added to the mixture and stirred for 12 h. The solvent was slowly removed in vacuum (950 mbar). The resulting powder was dried in vacuum.

This synthesis gives two types of complexes in this chapter, the heptanuclear complex is in focus. The other transition metal – Lanthanide complexes are discussed in chapter 9 and serve as a model system for single molecule magnets.

11.5 Computational methods

Minimum structure with different multiplicities, electronics, and also weak interactions were calculated with Density Functional Theory (DFT) using B3LYP^[80-82] functional, cc-pVTZ basis sets^[83-87] (C, H, N, O) and the Stuttgart ecp effective core potential (Mn) with Gaussian 09^[88]. The calculation of the UV/VIS spectrum was performed by using the minimum structure and performing TD-DFT using UB3LYP^[89] with cc-pVTZ basis sets^[83-87] (C, H, N, O) and the Stuttgart RSC ecp effective core potential (Mn) with the Gaussian 09 package^[88]. Broken symmetry calculations were performed by Density Functional Theory (DFT) with B3LYP_Gaussian^[81, 82] functional, cc-pVTZ basis set^[84] (C, H, N, O) in combination with the ecp-10-mdf^[89] effective

core potential (Mn) as implemented in a local, customized Turbomole 7.0 program package^[90-92]. We studied the antiferromagnetic couplings between the seven Manganese centers in the complex with our custom CANOSSA program. This program makes it possible to localize anti-parallel, unpaired spins separately on the metal centers in the system. A broken symmetry state is constructed from a single determinant wave function that reflects the antiferromagnetic coupling. The orbitals in the broken symmetry states are optimized by applying the variational principle. Data evaluation of weak interaction was performed using Multiwfn^[93] combined with VMD graphical user interface. The simulations of the XA spectra were performed with a Mathematica based program package CTM4XAS^[94] in combination with batch files from Cowan, attaining orca calculated parameters for the simulation of the XA spectra.

11.6 Results and Discussion

The Mass spectrum reveals an isotropic peak at 957.5 m/z with a characteristic pattern for Manganese (cf. Fig. 2). Thus, the simulation fits very well with the experimental mass spectrum.

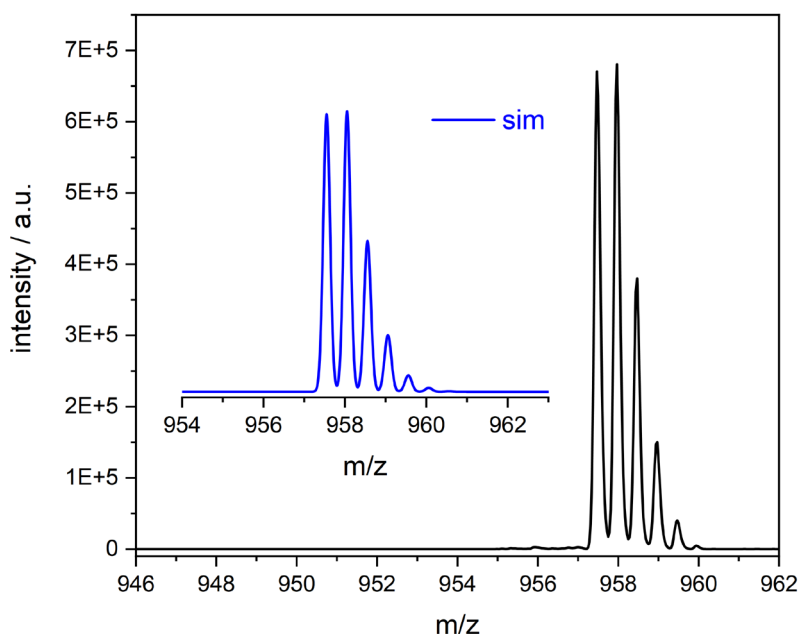


Fig. 2: Isolated mass spectrum of $[\text{Mn}_7(\text{Vab})_6]^{2+}$ (black) and the simulated mass spectrum (blue).

We observe the loss of one methyl group as main fragmentation channel by applying a fragmentation amplitude (cf. Fig. 3).

Higher fragmentation amplitudes result in the loss of a second methyl group and the whole ligand. In addition, minor fragments occur that have yet to be attributed to the complex. Losing the first methyl groups starts with the fragmentation amplitude of 0.6 V. Afterwards. We observe the loss of the other fragments. Finally, with the fragmentation amplitude of 1.8 V, the complex is entirely in fragmentation.

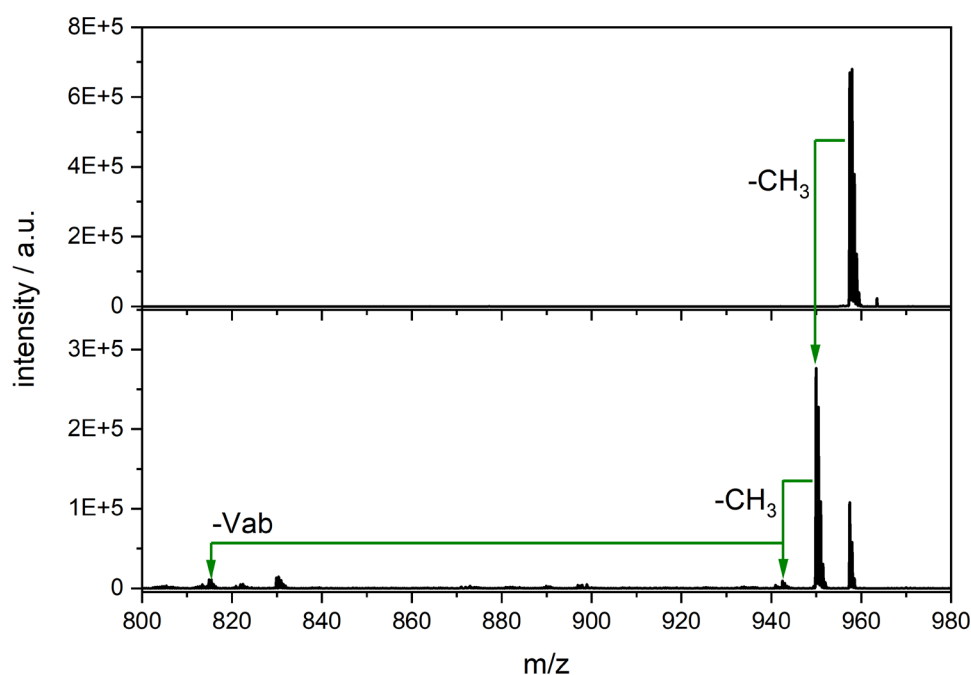


Fig. 3: Isolated spectrum (top) and the corresponding CID spectrum (bottom) of $[\text{Mn}_7(\text{Vab})_6]^{2+}$.

The CID breakdown curves also show that the predominant fragmentation route is the loss of one methyl group (cf. Fig. 4). Afterward, the loss of a second methyl group appears with a lower intensity than the first one. The last fragment detected with increased fragmentation amplitude represents the loss of a complete ligand. By raising the amplitude, the complex fragments into the main fragmentation channel. With a range from 0 V to 2 V and a complete fragmentation, this complex shows very high stability, and therefore strong bondings in the complex can be assumed when the main fragment is the loss of one methyl group.

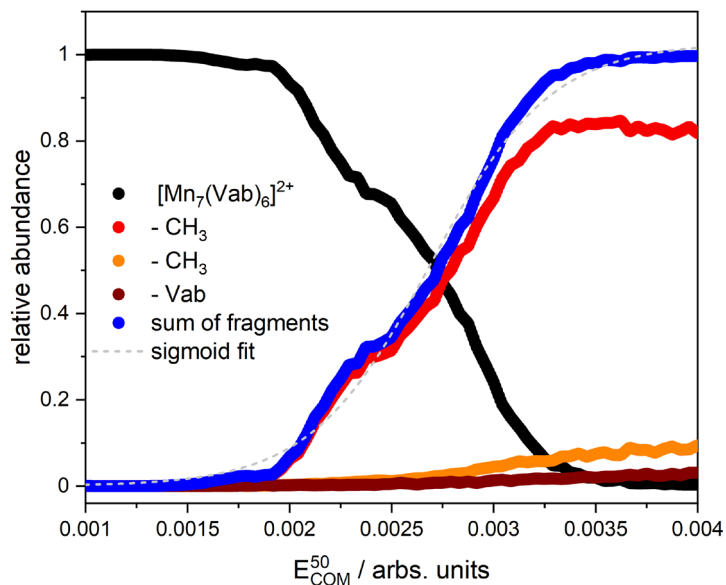


Fig. 4: CID breakdown curves of the $[\text{Mn}_7(\text{Vab})_6]^{2+}$ complexes and their appearance curves of the associated fragments.

The determination of the minimum structure calculations in different multiplicities was performed (cf. Fig. 5). The most stable complex has a multiplicity of 36, leading to a complex containing seven Mn^{2+} ions with a high spin configuration in all metal centers, which agrees with one part for defining a complex with single molecule magnetic behavior. All other spin configurations seem not favored because their relative energies are at least 100 kJ/mol higher than the minimum structure. Therefore, we can exclude any different spin configurations in this complex.

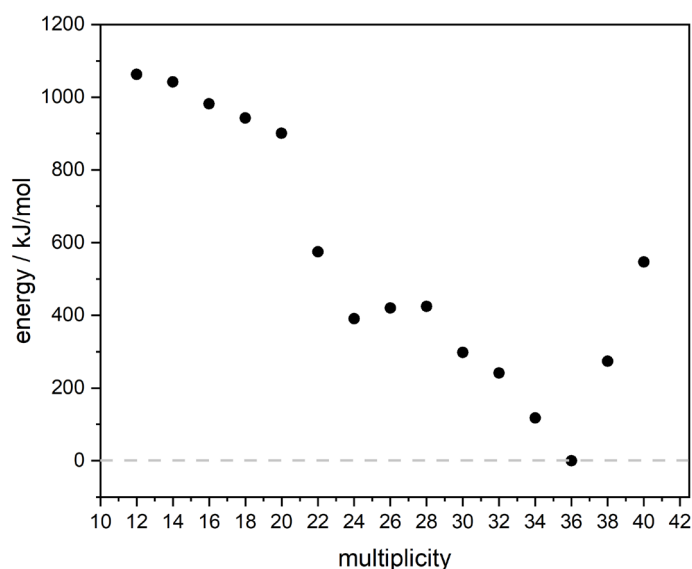


Fig. 5: Calculated energies for different multiplicities of $[\text{Mn}_7(\text{Vab})_6]^{2+}$. The calculations were performed with Gaussian 09 at the B3LYP/cc-pVTZ (H, C, N, O) and Stuttgart RSC ecp effective core potential (Mn) level of theory.

The bonding distances of the seven Manganese centers reveal six distorted Manganese ions, and only the central Manganese atom does not show a Jahn Teller distortion (cf. Fig. 6). Because the bonding lengths of all six distorted Manganese ions are equivalent, the crystal field splitting for the six Mn^{2+} ions should be comparable. The central Mn^{2+} does not distort the octahedral coordination and should lead to a different crystal field splitting than the other metal centers. All Mn^{2+} coordinated bondings are shortened in at least one z-direction and point towards the neighboring metal center, suggesting strong exchange couplings between the metal centers. The central Mn^{2+} ion shows no distortion and the most extended bonding distances to the bridging oxygen atoms than the other metal ions. Also, it might hint a change in the exchange coupling between the central Mn^{2+} and their surrounding Mn^{2+} ions.

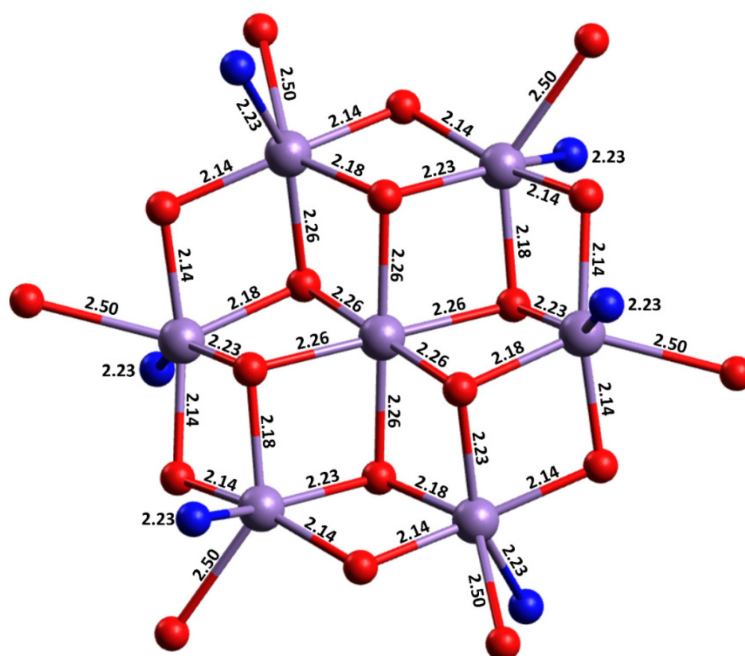


Fig. 6: Calculated bonding distances of $[\text{Mn}_7(\text{Vab})_6]^{2+}$. The calculations were performed with Gaussian 09 at the B3LYP/cc-pVTZ (H, C, N, O) and Stuttgart RSC ecp effective core potential (Mn) level of theory.

The simulated XA spectra with different crystal field splittings illustrate a change in the spectral pattern by raising the crystal field splitting from an atomic ion to a complex with high crystal field splittings (cf. Fig. 7). A high crystal field splitting would lead to a shift in the L_3 absorption edge to higher energies. Besides the energy shift, a splitting of the e_g and t_{2g} orbitals will become more present in the XA spectra because the e_g and t_{2g} orbital energy levels are more separated in high crystal field split complexes than in atomic ions.

The complex itself shows distortions in six of the seven Mn^{2+} ions, which hints at least a spectral pattern of the XA spectra as for the simulations for $\Delta_o = 2 - 3$ eV. A higher crystal field splitting would favor Mn^{2+} ions in a low configuration, which is not expected for a single molecule magnet.

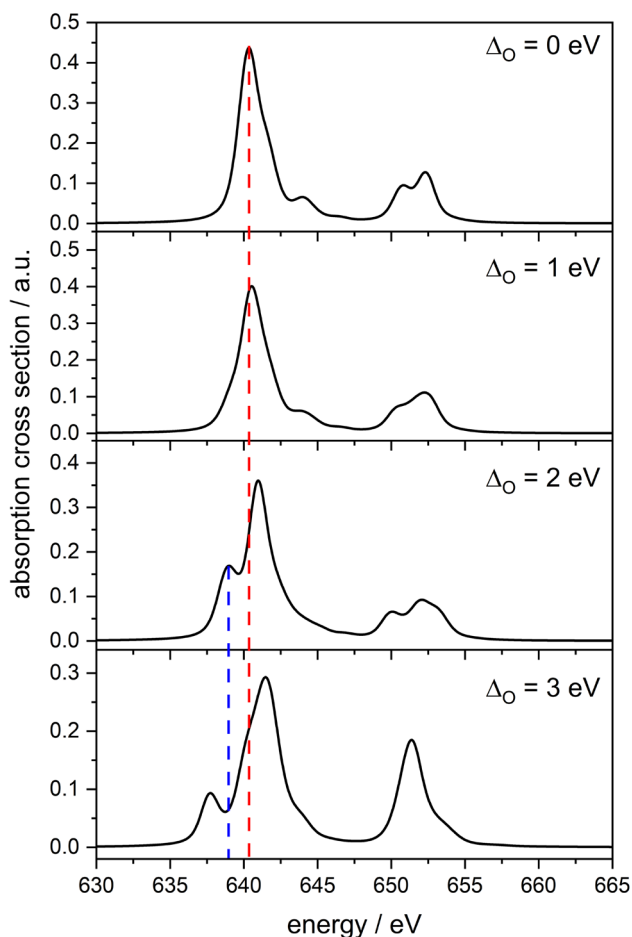


Fig. 7: Simulated XA spectra of $[\text{Mn}_7(\text{Vab})_6]^{2+}$ with different crystal field splittings of the metal centers in the complex. CTM4XAS performed the simulations with Cowan Batch files^[94].

The XA spectrum with a crystal field splitting of $\Delta_o = 2$ eV agrees well with the pDOS spectra (cf. Fig. 8), implying that the Mn^{2+} must be in a high spin state, as anticipated by the computations.

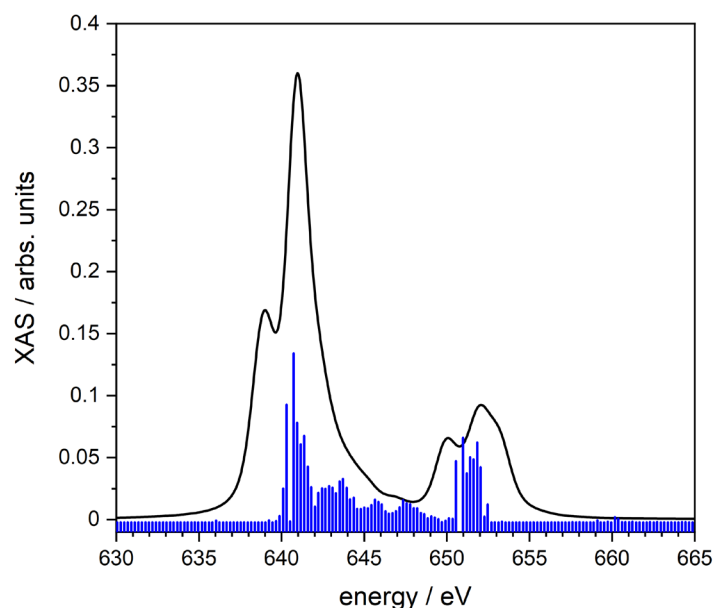


Fig. 8: Simulated XAS spectra with a crystal field splitting of 2 eV (black) and the calculated pDOS spectrum of [Mn₇(Vab)₆]²⁺. CTM4XAS performed the simulations with Cowan Batch files^[94]. The calculations were performed with Gaussian 09 at the B3LYP/cc-pVTZ (H, C, N, O, Mn) level of theory.

The approximated crystal field splitting from the simulated XAS spectra leads to possible transitions in the UV/VIS spectrum by normalization with the Racah parameter $B^{[95]}$ and approximation in a Tanabe Sugano diagram. The calculated UV/VIS spectrum reveals three absorption bands in the area between 500 nm and 800 nm (cf. Fig. 9). All these transitions are very weak and spin forbidden metal to ligand charge transfer (MLCT) transitions. Therefore, the approximation of different Jahn Teller distorted Mn²⁺ ions in the various complex bands in the UV/VIS spectrum seems reasonable.

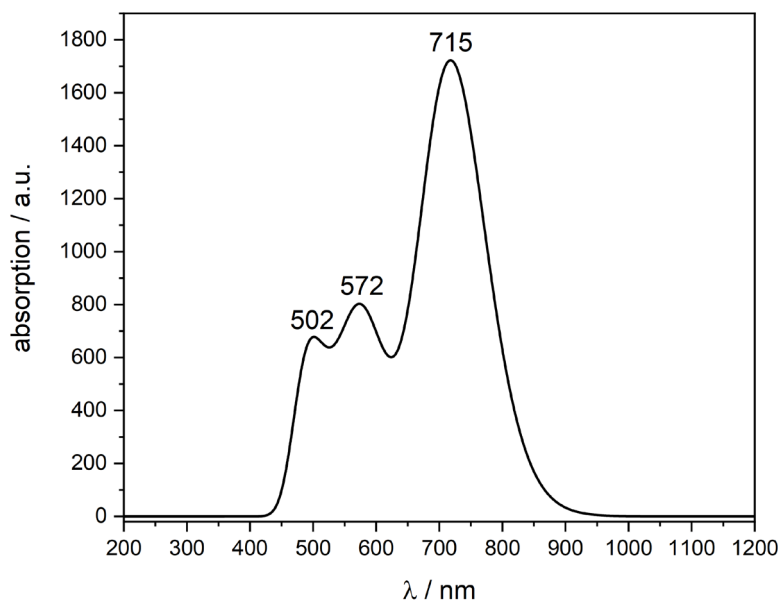


Fig. 9: Calculated UV/VIS spectrum of $[\text{Mn}_7(\text{Vab})_6]^{2+}$. The calculations were performed with Gaussian 09 at the TD-DFT B3LYP/ cc-pVTZ (H, C, N, O) and Stuttgart RSC ecp effective core potential (Mn) level of theory.

The calculated absorption energies can be normalized with the Racah parameter $B^{[95]}$, leading to a more precise approximation of the crystal field splitting in this complex (cf. Fig. 10). We observe two different crystal field splittings agreeing with one symmetric Mn^{2+} ion and six distorted Mn^{2+} ions in the complex compared with the structure determination. The predicted UV/VIS spectra reveal a higher intensity absorption band at 715 nm than at 572 nm, indicating distinct Mn^{2+} ions with a considerable shift in crystal field splittings. Unfortunately, only one crystal field splitting can be determined in the XA spectra. The resonant absorption energy is almost similar for all Manganese cores, assuming that the approximated crystal field splitting in the XA spectrum represents the six distorted Mn^{2+} ions because they build the main absorption edge in the spectrum.

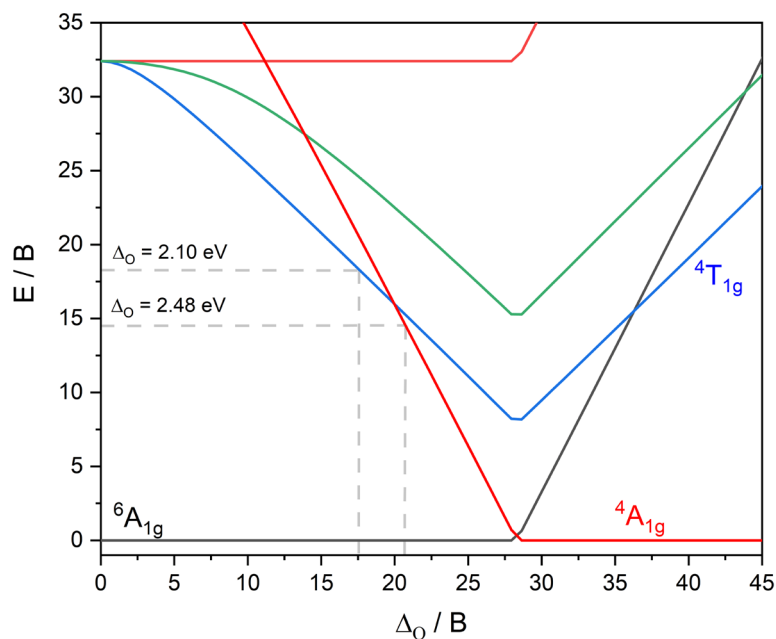


Fig. 10: Tanabe Sugano diagram of a d^5 atom with the approximated crystal field splittings from the XA simulations.

The normalized crystal field splittings lead to different absorption energies in the UV/VIS spectrum (cf. Fig. 10 and Tab. 1). The assumption of a crystal field splitting with 3 eV seems impossible because Mn^{2+} should show an absorption band in the UV/VIS spectra^[96]. Therefore, two crystal field splittings of 2.10 eV and 2.48 eV seem suitable for this complex. Absorptions at 550 nm also suggest an MLCT absorption, which is also conceivable with the electron-rich ligand surrounding the Mn^{2+} ions, showing an exchange coupling constant between the Mn^{2+} ions and the oxygen atoms. The transitions in the simulated spectra hint a ${}^6A_{1g}$ to ${}^4T_{1g}$ transition for six Mn^{2+} ions and a ${}^6A_{1g}$ to ${}^4A_{1g}$ transition for the central Mn^{2+} ion.

Tab.1: Approximated crystal field splittings in eV and cm^{-1} , normalized crystal field splittings, corresponding normalized UV/VIS energies, and the absorption energies in cm^{-1} and nm.

Δ_o/eV	Δ_o/cm^{-1}	Δ_o/B	E/B	E/cm^{-1}	$E_{(calc)}/nm$
2.10	16937.55	17.64	18.24	17512.72	572
2.48	20002.44	20.83	14.43	13848.43	715

Density Overlap Region Indicator (DORI) plots reveal strong non covalent interactions in the complex. The high stability observed in the MS studies discussed above is mainly induced by more vital dispersion and/or van der Waals interactions in the molecule (cf. Fig. 11).

These interactions strengthened the bonding situation in the complex and leads to a stiffer Mn^{2+} coordination. We assume that an excited state does not change its geometrical structure, and therefore no change in the UV/VIS or the XA spectra is considered. Thus, the exchange coupling scheme in this complex would be the same in both states. Temperature dependent XA experiments seem necessary for this complex because this also includes the assumption of a high anisotropic barrier.

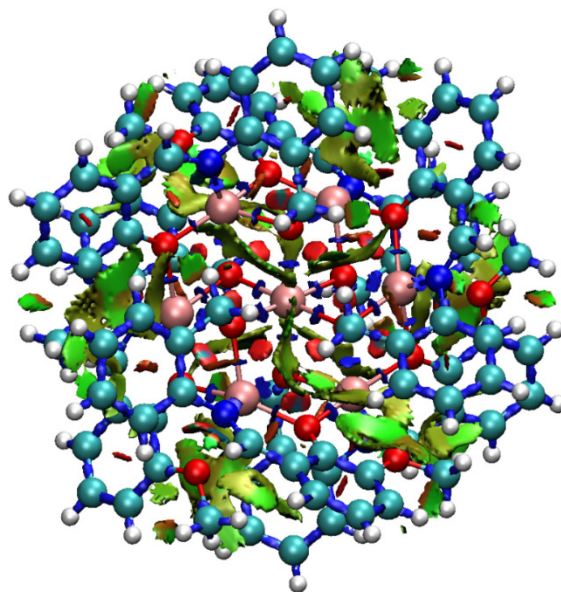


Fig. 11: Calculated Density overlap region indicator (DORI) of $[\text{Mn}_7(\text{Vab})_6]^{2+}$. The calculations were performed with Gaussian 09 at the B3LYP/cc-pVTZ (H, C, N, O) and Stuttgart RSC ecp effective core potential (Mn) level of theory.

The calculated spin density for this combination reveals localized spin density of the Manganese ions with a minor amount on the oxygen bridging atoms between the Mn^{2+} ions, indicating that there is no direct metal-metal contact between the Manganese ions. However, as shown, a ferromagnetically coupled system would lead to a high spin magnetic ground state with $S = 35$. Therefore, an antiferromagnetic exchange coupling cannot be excluded.

Broken symmetry calculations for all possible spin configurations were performed to gain the minimum structure with their corresponding spin state. (cf. Tab. 2). The 64 possible spin configurations reveal slightly different energies relative to the minimum structure. The energies differ from 0 – 1.5 kJ/mol, suggesting a compassionate spin state influences the structure and corresponding exchange coupling scheme. The minimum structure with three spin down electrons and four spin up electrons on each Mn^{2+} seems to be favored.

Tab. 2: Possible spin configurations with their calculated energies (SCF) and relative energies corresponding to their minimum structure. The calculations were performed with Turbomole 7.0 at the Gaussian_B3LYP/ cc-pVTZ (H, C, N, O) and ecp-10-mdf (Mn) level of theory.

Spin configuration	SCF/Hartree	SCF/kJ/mol	ΔE /kJ/mol
UUUUUUU	-13213.76266	-3469272.700	2.94208936
UUUUUUD	-13213.76304	-34692728.69	1.95349899
UUUUUDD	-13213.76342	-34692729.69	0.94781740
UUUUDDD	-13213.76339	-34692729.62	1.02340948
UUUDDDD	-13213.76355	-34692730.03	0.61339755
UUDDDDD	-13213.76370	-34692730.43	0.20768305
UDDDDDD	-13213.76365	-34692730.30	0.34463619
DDDDDDD	-13213.76266	-34692727.70	2.94209041
1 spin down			
DUUUUUU	-13213.76365	-34692730.30	0.34463882
UDUUUUU	-13213.76304	-34692728.70	1.94262259
UUDUUUU	-13213.76304	-34692728.69	1.95582228
UUUDUUU	-13213.76304	-34692728.69	1.94738394
UUUUUUU	-13213.76310	-34692728.84	1.80124442
UUUUUDU	-13213.76304	-34692728.70	1.94376285
UUUUUUD	-13213.76304	-34692728.69	1.95348140
2 spin down			
DDUUUUU	-13213.76370	-34692730.43	0.20761348
DUDUUUU	-13213.76371	-34692730.44	0.20078717
DUUDUUU	-13213.76371	-34692730.44	0.19878654
DUUUUUU	-13213.76370	-34692730.43	0.21401339
DUUUUDU	-13213.76371	-34692730.44	0.20143935
DUUUUUD	-13213.76370	-34692730.44	0.20600378
UDDUUUU	-13213.76323	-34692729.18	1.45683061
UDUDUUU	-13213.76323	-34692729.18	1.45720606
UDUUDUU	-13213.76342	-34692729.68	0.95782502
UDUUUDU	-13213.76342	-34692729.70	0.94505170
UDUUUUD	-13213.76342	-34692729.69	0.94673307
UUDUDUU	-13213.76342	-34692729.70	0.94414800
UUDUUDU	-13213.76341	-34692729.68	0.96463871
UUDUUUD	-13213.76322	-34692729.17	1.46744524
UUUDUDU	-13213.76322	-34692729.18	1.46642078
UUUDUUD	-13213.76341	-34692729.67	0.96989654
UUUUDDU	-13213.76323	-34692729.19	1.45471342
UUUUUDU	-13213.76323	-34692729.19	1.45393285

11. First Investigations of a heptanuclear homoleptic Manganese complex with single molecular magnetic behavior

3 spin down			
DDUUUU	-13213.76355	-34692730.03	0.61334583
DDUDUU	-13213.76355	-34692730.03	0.61422170
DDUUDU	-13213.76373	-34692730.51	0.12837248
DDUUUD	-13213.76374	-34692730.54	0.10181922
DDUUUD	-13213.76374	-34692730.54	0.10242441
DUDDUU	-13213.76375	-34692730.55	0.09077454
DUDUDU	-13213.76374	-34692730.54	0.10274472
DUDUUD	-13213.76374	-34692730.53	0.10854943
DUDUUUD	-13213.76355	-34692730.03	0.61126354
DUUDDU	-13213.76374	-34692730.54	0.10297629
DUUDUD	-13213.76374	-34692730.53	0.10914543
DUUDUUD	-13213.76374	-34692730.53	0.10915015
DUUUDD	-13213.76355	-34692730.02	0.61873572
DUUUUD	-13213.76355	-34692730.02	0.61669859
DUUUUD	-13213.76375	-34692730.55	0.09518617
UDDUUU	-13213.76339	-34692729.61	1.02882010
UDDUDU	-13213.76358	-34692730.12	0.52368502
UDDUUD	-13213.76358	-34692730.11	0.52811188
UDDUUUD	-13213.76339	-34692729.61	1.03328529
UUDDDU	-13213.76378	-34692730.64	0.00000000
UUDDUD	-13213.76358	-34692730.10	0.53712836
UUDDUUD	-13213.76358	-34692730.10	0.54032071
UUUDDU	-13213.76339	-34692729.61	1.03077506
UUUDDUD	-13213.76358	-34692730.11	0.52697635
UUUUDD	-13213.76339	-34692729.62	1.02353103
4 spin down			
DDDUUU	-13213.76339	-34692729.62	1.02344361
DDUDUU	-13213.76358	-34692730.10	0.53740850
DDUUDU	-13213.76358	-34692730.11	0.52685846
DDUUUD	-13213.76339	-34692729.61	1.03078057
DUDUDD	-13213.76375	-34692730.55	0.09518538
DUDUDU	-13213.76339	-34692729.61	1.02926696
UDDDDU	-13213.76375	-34692730.55	0.09518538
UDDUDU	-13213.76355	-34692730.02	0.61668809
UDDUUD	-13213.76355	-34692730.02	0.61873361
UDUDDD	-13213.76375	-34692730.55	0.09081156
UUDDDU	-13213.76374	-34692730.54	0.10244016
UUDDUD	-13213.76374	-34692730.54	0.10179219

11. First Investigations of a heptanuclear homoleptic Manganese complex with single molecular magnetic behavior

5 spin down			
DDDDDUU	-13213.76342	-34692729.69	0.94781714
DDDDUDU	-13213.76332	-34692729.44	1.20595048
DDDDUUD	-13213.76323	-34692729.19	1.45466248
UDDDDDU	-13213.7637	-34692730.44	0.20599774
UDDDDUD	-13213.76371	-34692730.44	0.20142805
UDDUDDD	-13213.76371	-34692730.44	0.19881174
6 spin down			
DDDDDDU	-13213.76304	-34692728.69	1.95347955
DDDDUDU	-13213.76304	-34692728.7	1.94376417
DDDDUUD	-13213.76304	-34692728.69	1.94957387
DDUDDDD	-13213.76304	-34692728.69	1.94738340
DDDUDDD	-13213.76304	-34692728.69	1.95582150
DUDDDDD	-13213.76304	-34692728.70	1.94262128

The spin configuration with three “spin down” electrons reveal almost similar energies relative to the minimum structure (cf. Fig. 12).

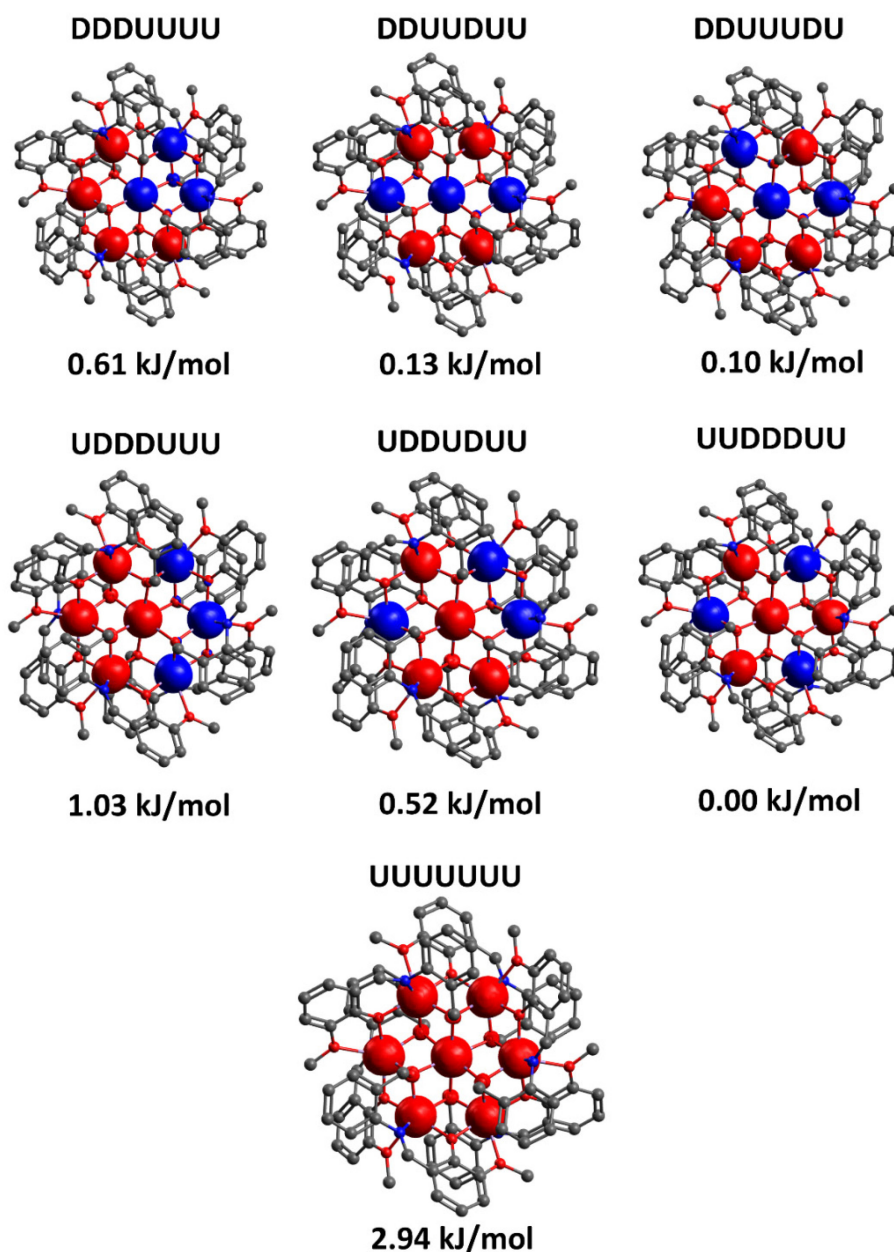


Fig. 12: Broken symmetry calculated spin densities of $[\text{Mn}_7(\text{Vab})_6]^{2+}$ in different spin configurations. The calculations were performed with Turbomole 7.0 at the B3LYP_Gaussian/cc-pVTZ (H, C, N, O) and ecp-10-mdf (Mn) level of theory.

The estimated anisotropic tensors of these distinct spin configurations show that the predicted minimum structure in this series of spin configurations has the largest anisotropic tensor (cf. Fig. 13). The highest anisotropic tensor is only reached when the central Mn^{2+} ion has a spin-up configuration. The ferromagnetically coupled complex has the lowest anisotropic tensor. Together with the definition of single molecule magnets, the calculated results are in good agreement. Therefore, this complex minimum structure has the highest anisotropic tensor and a central Mn^{2+} with a “spin up” configuration.

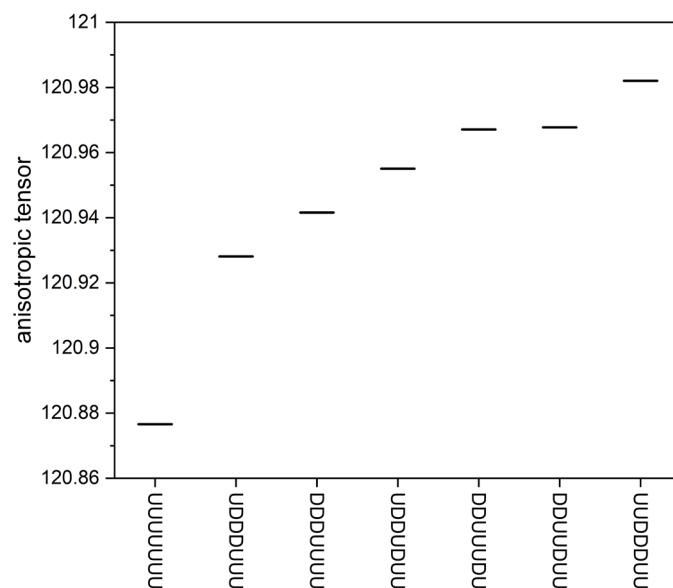


Fig. 13: Broken symmetry calculated anisotropic tensors of $[\text{Mn}_7(\text{Vab})_6]^{2+}$ in different spin configurations. The calculations were performed with Turbomole 7.0 at the Gaussian_ B3LYP/cc-pVTZ (H, C, N, O) and ecp-10-mdf (Mn) level of theory.

The configuration UDDUUU is the minimum structure for all these calculations. The spin density reveals an alternating spin down and “spin up” arrangement in the outer ring (cf. Fig. 14).

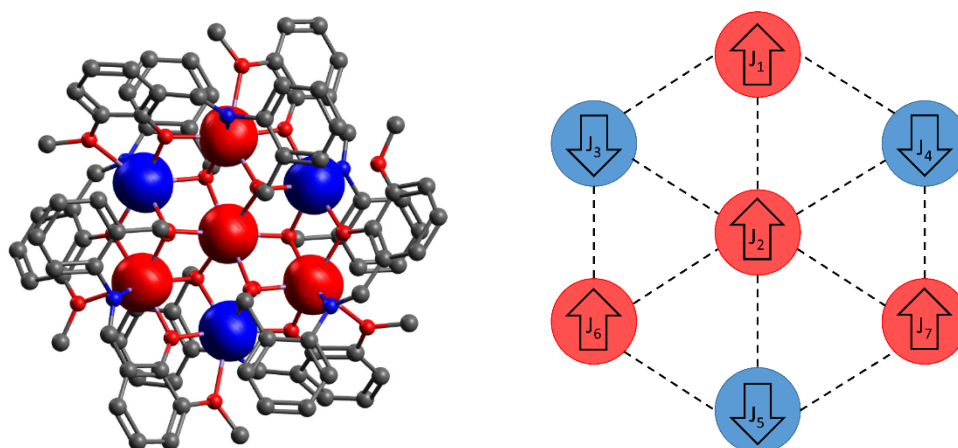


Fig. 14: Broken symmetry calculated spin density of $[\text{Mn}_7(\text{Vab})_6]^{2+}$ (left) and their corresponding exchange coupling scheme (right). The calculations were performed with Turbomole 7.0 at the Gaussian_ B3LYP/cc-pVTZ (H, C, N, O) and ecp-10-mdf (Mn) level of theory.

This complex obtains seven coupling constants for each Mn^{2+} ion, calculated by its energy differences^[63, 64]. A positive J value would represent a ferromagnetic exchange coupling and a negative one, an antiferromagnetic exchange coupling (cf. Fig. 14, Tab. 3). The calculated exchange coupling constant reveals a ferromagnetic coupled central Mn^{2+} ion surrounded by three spin up Mn^{2+} ions (cf. Fig. 14, Tab. 3). The other three Mn^{2+} ions are antiferromagnetically coupled, assuming that the spin magnetic value has to be significantly reduced in this complex, resulting in a complex, which does not have a single molecule magnetic behavior. With antiferromagnetically coupled Manganese cores, the contribution of these cores must be zero. For a high magnetization, a completely ferromagnetic coupled system would be best for single molecule magnets.

Tab. 3: Calculated exchange coupling constants of $[\text{Mn}_7(\text{Vab})_6]^{2+}$ with the minimum structure's spin configuration. The calculations were performed with Turbomole 7.0 at the Gaussian_B3LYP/cc-pVTZ (H, C, N, O) and ecp-10-mdf (Mn) level of theory.

	J/kJ/mol	J/cm ⁻¹
Mn₁	0.037	3.10
Mn₂	0.031	2.63
Mn₃	-0.020	-1.70
Mn₄	-0.042	-3.54
Mn₅	-0.013	-1.10
Mn₆	0.044	3.70
Mn₇	0.038	3.23

Compared with the completely ferromagnetic coupled complex, the energy difference is only 3 kJ/mol, and the calculations were performed at room temperature. Maybe the complex has a ferromagnetic coupling scheme at lower temperatures, favoring a single molecule magnetic behavior. The anisotropic tensor of the ferromagnetically coupled complex is 120.87 and lower than the antiferromagnetically coupled complex of 120.98. The possibility of a spin flip is not excluded, but to prove this temperature dependent XMCD experiments are necessary.

11.7 Conclusion

CID experiments have shown that the complex is very stable, and the ligand bonding strengths to the metal atoms are stronger than a methyl group of the ligand. With higher fragmentation amplitudes, the loss of a complete ligand is observed after losing one methyl group. We do not observe the splitting of the star-shaped Mn^{2+} core with any fragmentation amplitude in this complex.

Calculation of the minimum structure revealed different Mn^{2+} coordination patterns. Six manganese ions are Jahn Teller distorted, while the core Mn^{2+} ion has virtually symmetrical bonding, resulting in two distinct crystal field splittings in the complex. Simulated XA spectra with different crystal field splittings reveal a rising splitting of the e_g and t_{2g} absorption edges with higher crystal field splittings. Future experimental XA spectra might lead to a pattern as the simulated XA spectra with a crystal field splitting of 2 eV.

The UV/VIS spectrum calculation reveals two bands in the area of 500 nm to 800 nm. Normalization of these energies using the Racah parameter B and approximation in the Tanabe Sugano Diagram provide crystal field splittings of 2.10 eV and 2.55 eV, which are consistent with the simulated XA spectra. Electron localized field plots show spherical Mn^{2+} , assuming that the orbital magnetic moment must be close to zero. Also, the DORI plot points out that non covalent interactions in the complex establish high stability in this complex. Therefore, no change in the geometry is expected and leads to the assumption that the magnetic behavior in this complex has to change by thermally induced properties and not with geometrical properties.

According to broken symmetry calculations, an antiferromagnetically coupled spin configuration is preferred over a ferromagnetically coupled one. Also, the anisotropic tensor in the antiferromagnetically coupled spin isomer is higher than in the ferromagnetic isomer. The relative energies are almost similar for the antiferromagnetically coupled complexes and slightly higher in the ferromagnetically coupled system, which hints that the antiferromagnetically coupled complex might be degenerated.

We assume that the complex might be in a ferromagnetic spin configuration with lower temperatures. A “spin flip” takes part to establish a higher anisotropic barrier by raising the temperature, inducing a long living magnetization.

With all these assumptions, temperature-dependent XMCD studies seem necessary for this complex to verify these assumptions.

11.8 Acknowledgment

The German research foundation DFG supported this work within the transregional collaborative research center SFB/TRR 88 “Cooperative effects in homo and heterometallic complexes” (3MET) and by the state research center OPTIMAS.

11.9 References

- [1] B. Akermark, B. C. Soederberg, and S. S. Hall, The mechanism of the Wacker process. Corroborative evidence for distal addition of water and palladium, *Organometallics*, 6, 2608-2610, 1987.
- [2] C. Bizzarri, E. Spuling, D. Knoll, D. Volz, and S. Bräse, Sustainable metal complexes for organic light-emitting diodes (OLEDs), *Coord. Chem. Rev.*, 373, 2017.
- [3] G. W. Brudvig, Catalysing water oxidation using nature’s metal, *Nature Catalysis*, 1, 10-11, 2018.
- [4] W. C. H. Choy, W. K. Chan, and Y. Yuan, Recent Advances in Transition Metal Complexes and Light-Management Engineering in Organic Optoelectronic Devices, *Adv. Mat.*, 26, 5368-5399, 2014.
- [5] M. J. Cleare, Transition metal complexes in cancer chemotherapy, *Coord. Chem. Rev.*, 12, 349-405, 1974.
- [6] M. Hartings, Reactions coupled to palladium, *Nature Chemistry*, 4, 764-764, 2012.
- [7] Y. Ishii, K. Miyashita, K. Kamita, and M. Hidai, Selective Hydroformylation of Internal Acetylenes by PdCl₂(PCy₃)₂: Remarkable Synergistic Effect of Cobalt¹, *J. Am. Chem. Soc.*, 119, 6448-6449, 1997.
- [8] M. D. Kärkäs, and B. Åkermark, Water oxidation using earth-abundant transition metal catalysts: opportunities and challenges, *Dalt. Trans.*, 45, 14421-14461, 2016.
- [9] G. Palermo, A. Magistrato, T. Riedel, T. von Erlach, C. A. Davey, P. J. Dyson, and U. Rothlisberger, Fighting Cancer with Transition Metal Complexes: From Naked DNA to Protein and Chromatin Targeting Strategies, *Chem. Med. Chem.*, 11, 1199-1210, 2016.
- [10] L. Pereira, *Organic Light Emitting Diodes: The Use of Rare Earth and Transition Metals*, 2012.
- [11] S. Qin, L. Dong, Z. Chen, S. Zhang, and G. Yin, Non-redox metal ions can promote Wacker-type oxidations even better than copper(ii): a new opportunity in catalyst design, *Dalt. Tran.*, 44, 17508-17515, 2015.
- [12] F. Ungváry, Application of transition metals in hydroformylation, *Coord. Chem. Rev.*, 251, 2072-2086, 2007.
- [13] R. Wai-Yin Sun, D.-L. Ma, E. L.-M. Wong, and C.-M. Che, Some uses of transition metal complexes as anti-cancer and anti-HIV agents, *Dalt. Trans.*, 4884-4892, 2007.
- [14] B. Kintzel, M. Böhme, J. Liu, A. Burkhardt, J. Mrozek, A. Buchholz, A. Ardavan, and W. Plass, Molecular electronic spin qubits from a spin-frustrated trinuclear copper complex, *Chem. Comm.*, 54, 12934-12937, 2018.
- [15] D. Maspocho, D. Ruiz-Molina, K. Wurst, C. Rovira, and J. Veciana, A very bulky carboxylic perchlorotriphenylmethyl radical as a novel ligand for transition metal complexes. A new spin frustrated metal system, *Chem. Comm.*, 2958-2959, 2002.
- [16] R. Shaw, R. H. Laye, L. F. Jones, D. M. Low, C. Talbot-Eeckelaers, Q. Wei, C. J. Milios, S. Teat, M. Helliwell, J. Raftery, M. Evangelisti, M. Affronte, D. Collison, E. K. Brechin, and E. J. L. McInnes, 1,2,3-Triazolate-Bridged Tetradecametallic Transition Metal Clusters [M₁₄(L)₆O₆(OMe)₁₈X₆] (M = Fe^{III}, Cr^{III} and V^{III/IV}) and Related Compounds: Ground-State Spins Ranging from S = 0 to S = 25 and Spin-Enhanced Magnetocaloric Effect, *Inorg. Chem.*, 46, 4968-4978, 2007.

11. First Investigations of a heptanuclear homoleptic Manganese complex with single molecular magnetic behavior

- [17] P. Zhang, and P. J. Sadler, Redox-Active Metal Complexes for Anticancer Therapy, *European Journal of Inorg. Chem.*, 2017, 1541-1548, 2017.
- [18] W.-X. Zhang, W. Xue, J.-B. Lin, Y.-Z. Zheng, and X.-M. Chen, 3D geometrically frustrated magnets assembled by transition metal ion and 1,2,3-triazole-4,5-dicarboxylate as triangular nodes, *Cryst. Eng. Comm.*, 10, 1770-1776, 2008.
- [19] Y. Garcia, P. J. van Koningsbruggen, E. Codjovi, R. Lapouyade, O. Kahn, and L. Rabardel, Non-classical FeII spin-crossover behaviour leading to an unprecedented extremely large apparent thermal hysteresis of 270 K: application for displays, *J. Materials Chemistry*, 7, 857-858, 1997.
- [20] P. Gütllich, Y. Garcia, and H. A. Goodwin, Spin crossover phenomena in Fe(I) complexes, *Chem. Soc. Rev.*, 29, 419-427, 2000.
- [21] P. Gütllich, H. A. Goodwin, and Y. Garcia, *Spin Crossover in Transition Metal Compounds I*: Springer, 2004.
- [22] H.-J. Krüger, Spin transition in octahedral metal complexes containing tetraazamacrocyclic ligands, *Coord. Chem. Rev.*, 253, 2450-2459, 2009.
- [23] M. Schmitz, M. Seibel, H. Kelm, S. Demeshko, F. Meyer, and H.-J. Krüger, How Does a Coordinated Radical Ligand Affect the Spin Crossover Properties in an Octahedral Iron(II) Complex?, *Angew. Chem. Int. Ed.*, 53, 5988-5992, 2014.
- [24] J. M. Clemente-Juan, E. Coronado, A. Forment-Aliaga, A. Gaita-Ariño, C. Giménez-Saiz, F. M. Romero, W. Wernsdorfer, R. Biagi, and V. Corradini, Electronic and Magnetic Study of Polycationic Mn₁₂ Single-Molecule Magnets with a Ground Spin State $S = 11$, *Inorg. Chem.*, 49, 386-396, 2010.
- [25] A. Dey, S. Das, V. Mereacre, A. K. Powell, and V. Chandrasekhar, Butterfly-shaped, heterometallic, hexanuclear, [FeII₂LnIII₄] (LnIII = GdIII, TbIII, DyIII and HoIII) Complexes: Syntheses, structure and magnetism, *Inorganica Chimica Acta*, 486, 458-467, 2019.
- [26] J. Dreiser, K. S. Pedersen, A. Schnegg, K. Holldack, J. Nehr Korn, M. Sigrist, P. Tregenna-Piggott, H. Mutka, H. Weihe, V. S. Mironov, J. Bendix, and O. Waldmann, Three-Axis Anisotropic Exchange Coupling in the Single-Molecule Magnets NEt₄[MnIII₂(5-Brsalen)₂(MeOH)₂MIII(CN)₆] (M=Ru, Os), *Chemistry – A European Journal*, 19, 3693-3701, 2013.
- [27] P. Hahn, S. Ullmann, J. Klose, Y. Peng, A. K. Powell, and B. Kersting, Dinuclear Tb and Dy complexes supported by hybrid Schiff-base/calixarene ligands: synthesis, structures and magnetic properties, *Dalt. Trans.*, 2020.
- [28] T. Lis, Preparation, structure, and magnetic properties of a dodecanuclear mixed-valence manganese carboxylate, *Acta Crystallographica Section B*, 36, 2042-2046, 1980.
- [29] J.-W. Lu, Y.-H. Huang, S.-I. Lo, and H.-H. Wei, New μ -oxo-bridged tetranuclear Cu(II) complex with Schiff-base ligand: Synthesis, crystal structure and magnetic properties, *Inorg. Chem. Comm.*, 10, 1210-1213, 2007.
- [30] R. Modak, Y. Sikdar, A. E. Thuijs, G. Christou, and S. Goswami, Coll₄, Coll₇, and a Series of Coll₂LnIII (LnIII = NdIII, SmIII, GdIII, TbIII, DyIII) Coordination Clusters: Search for Single Molecule Magnets, *Inorg. Chem.*, 55, 10192-10202, 2016.
- [31] A. V. Palii, S. M. Ostrovsky, S. I. Klokishner, B. S. Tsukerblat, C. P. Berlinguette, K. R. Dunbar, and J. R. Galán-Mascarós, Role of the Orbitally Degenerate Mn(III) Ions in the Single-Molecule Magnet Behavior of the Cyanide Cluster {[MnII(tmphen)₂]₃[MnIII(CN)₆]₂} (tmphen = 3,4,7,8-tetramethyl-1,10-phenanthroline), *J. Am. Chem. Soc.*, 126, 16860-16867, 2004.
- [32] G. Aromí, D. Aguilà, P. Gamez, F. Luis, and O. Roubeau, Design of magnetic coordination complexes for quantum computing, *Chem. Soc. Rev.*, 41, 537-546, 2012.
- [33] M. N. Leuenberger, and D. Loss, Quantum computing in molecular magnets, *Nature*, 410, 789-793, 2001.
- [34] M. Mannini, F. Pineider, P. Saintavirt, C. Danieli, E. Otero, C. Sciancalepore, A. M. Talarico, M.-A. Arrio, A. Cornia, D. Gatteschi, and R. Sessoli, Magnetic memory of a single-molecule quantum magnet wired to a gold surface, *Nature Materials*, 8, 194-197, 2009.
- [35] K. V. Raman, A. M. Kamerbeek, A. Mukherjee, N. Atodiresei, T. K. Sen, P. Lazić, V. Caciuc, R. Michel, D. Stalke, S. K. Mandal, S. Blügel, M. Müntenberg, and J. S. Moodera, Interface-engineered templates for molecular spin memory devices, *Nature*, 493, 509-513, 2013.
- [36] R. W. volume editor, and G. A. with contributions by, *Single-molecule magnets and related phenomena*: Berlin ; New York : Springer, 2006.
- [37] G. Christou, D. Gatteschi, D. N. Hendrickson, and R. Sessoli, Single-Molecule Magnets, *MRS Bulletin*, 25, 66-71, 2011.
- [38] D. Gatteschi, and R. Sessoli, Quantum Tunneling of Magnetization and Related Phenomena in Molecular Materials, *Angew. Chem. Int. Ed.*, 42, 268-297, 2003.

11. First Investigations of a heptanuclear homoleptic Manganese complex with single molecular magnetic behavior

- [39] K. Kim, A. Ford, V. Meenakshi, W. Teizer, H. Zhao, and K. R. Dunbar, Nanopatterning of Mn₁₂-acetate single-molecule magnet films, *J. Appl. Phys.*, 102, 094306, 2007.
- [40] M. Mannini, F. Pineider, P. Sainctavit, L. Joly, A. Fraile-Rodríguez, M.-A. Arrio, C. Cartier dit Moulin, W. Wernsdorfer, A. Cornia, D. Gatteschi, and R. Sessoli, X-Ray Magnetic Circular Dichroism Picks out Single-Molecule Magnets Suitable for Nanodevices, *Adv. Mat.*, 21, 167-171, 2009.
- [41] K. M. Mertes, Y. Suzuki, M. P. Sarachik, Y. Myasoedov, H. Shtrikman, E. Zeldov, E. M. Rumberger, D. N. Hendrickson, and G. Christou, Mn₁₂-acetate: a prototypical single molecule magnet, *Solid State Communications*, 127, 131-139, 2003.
- [42] J. A. A. J. Perenboom, J. S. Brooks, S. Hill, T. Hathaway, and N. S. Dalal, Relaxation of the magnetization of Mn₁₂ acetate, *Phys. Rev. B*, 58, 330-338, 1998.
- [43] G. Rogez, B. Donnio, E. Terazzi, J.-L. Gallani, J.-P. Kappler, J.-P. Bucher, and M. Drillon, The Quest for Nanoscale Magnets: The example of [Mn₁₂] Single Molecule Magnets, *Adv. Mat.*, 21, 4323-4333, 2009.
- [44] D. M. Seo, V. Meenakshi, W. Teizer, H. Zhao, and K. R. Dunbar, Enhanced magnetic anisotropy of Mn₁₂-acetate, *J. Magn. and Magnetic Materials*, 301, 31-36, 2006.
- [45] S. Voss, M. Fonin, U. Rüdiger, M. Burgert, U. Groth, and Y. S. Dedkov, Electronic structure of Mn₁₂ derivatives on the clean and functionalized Au surface, *Physical Review B*, 75, 045102, 2007.
- [46] H. Zhao, C. P. Berlinguette, J. Bacsá, A. V. Prosvirin, J. K. Bera, S. E. Tichy, E. J. Schelter, and K. R. Dunbar, Structural Characterization, Magnetic Properties, and Electrospray Mass Spectrometry of Two Jahn–Teller Isomers of the Single-Molecule Magnet [Mn₁₂O₁₂(CF₃COO)₁₆(H₂O)₄], *Inorg. Chem.*, 43, 1359-1369, 2004.
- [47] P.-E. Car, M. Perfetti, M. Mannini, A. Favre, A. Caneschi, and R. Sessoli, Giant field dependence of the low temperature relaxation of the magnetization in a dysprosium(iii)–DOTA complex, *Chem. Comm.*, 47, 3751-3753, 2011.
- [48] G. Cucinotta, M. Perfetti, J. Luzon, M. Etienne, P.-E. Car, A. Caneschi, G. Calvez, K. Bernot, and R. Sessoli, Magnetic Anisotropy in a Dysprosium/DOTA Single-Molecule Magnet: Beyond Simple Magneto-Structural Correlations, *Angew. Chem. Int. Ed.*, 51, 1606-1610, 2012.
- [49] Y.-N. Guo, G.-F. Xu, P. Gamez, L. Zhao, S.-Y. Lin, R. Deng, J. Tang, and H.-J. Zhang, Two-Step Relaxation in a Linear Tetranuclear Dysprosium(III) Aggregate Showing Single-Molecule Magnet Behavior, *J. Am. Chem. Soc.*, 132, 8538-8539, 2010.
- [50] I. J. Hewitt, J. Tang, N. T. Madhu, C. E. Anson, Y. Lan, J. Luzon, M. Etienne, R. Sessoli, and A. K. Powell, Coupling Dy₃ Triangles Enhances Their Slow Magnetic Relaxation, *Angew. Chem. Int. Ed.*, 49, 6352-6356, 2010.
- [51] N. Ishikawa, M. Sugita, T. Ishikawa, S.-y. Koshihara, and Y. Kaizu, Lanthanide Double-Decker Complexes Functioning as Magnets at the Single-Molecular Level, *J. Am. Chem. Soc.*, 125, 8694-8695, 2003.
- [52] E. Moreno-Pineda, C. Godfrin, F. Balestro, W. Wernsdorfer, and M. Ruben, Molecular spin qubits for quantum algorithms, *Chem. Soc. Rev.*, 47, 501-513, 2018.
- [53] G. Arom, S. M. J. Aubin, M. A. Bolcar, G. Christou, H. J. Eppley, K. Folting, D. N. Hendrickson, J. C. Huffman, R. C. Squire, H.-L. Tsai, S. Wang, and M. W. Wemple, Manganese carboxylate clusters: from structural aesthetics to single-molecule magnets, Dedicated to Professor Jack Lewis on the occasion of his 70th birthday, *Polyhedron*, 17, 3005-3020, 1998.
- [54] M. Murugesu, M. Habrych, W. Wernsdorfer, K. A. Abboud, and G. Christou, Single-Molecule Magnets: A Mn₂₅ Complex with a Record S = 51/2 Spin for a Molecular Species, *J. Am. Chem. Soc.*, 126, 4766-4767, 2004.
- [55] C. Rojas-Dotti, N. Moliner, F. Lloret, and J. Martínez-Lillo, Hexanuclear manganese(III) single-molecule magnets based on oxime and azole-type ligands, *Polyhedron*, 170, 223-231, 2019.
- [56] C.-I. Yang, W. Wernsdorfer, G.-H. Lee, and H.-L. Tsai, A Pentanuclear Manganese Single-Molecule Magnet with a Large Anisotropy, *J. Am. Chem. Soc.*, 129, 456-457, 2007.
- [57] J. Yoo, E. K. Brechin, A. Yamaguchi, M. Nakano, J. C. Huffman, A. L. Maniero, L.-C. Brunel, K. Awaga, H. Ishimoto, G. Christou, and D. N. Hendrickson, Single-Molecule Magnets: A New Class of Tetranuclear Manganese Magnets, *Inorg. Chem.*, 39, 3615-3623, 2000.
- [58] F. Liedy, J. Eng, R. McNab, R. Inglis, T. J. Penfold, E. K. Brechin, and J. O. Johansson, Vibrational coherences in manganese single-molecule magnets after ultrafast photoexcitation, *Nature Chemistry*, 12, 452-458, 2020.
- [59] J. Meyer, "Spin and orbital contributions to the magnetic moment of isolated transition metal clusters and complexes," 2014.

11. First Investigations of a heptanuclear homoleptic Manganese complex with single molecular magnetic behavior

- [60] M. Tombers, "Spin and orbital magnetic moments of isolated single molecule magnets and transition metal clusters," 2015.
- [61] R. Colton, A. D'Agostino, and J. C. Traeger, Electro spray mass spectrometry applied to inorganic and organometallic chemistry, *Mass Spectrom. Rev.*, 14, 79-106, 1995.
- [62] J. B. Fenn, Electro spray Wings for Molecular Elephants (Nobel Lecture), *Angew. Chem. Int. Ed.*, 42, 3871-3894, 2003.
- [63] J. Lang, "Characterization of Structures, Fragmentation Pathways and Magnetism of Mononuclear and Oligonuclear Transition Metal Complexes in Isolation," 2017.
- [64] J. Lang, J. M. Hewer, J. Meyer, J. Schuchmann, C. van Wüllen, and G. Niedner-Schatteburg, Magnetostructural correlation in isolated trinuclear iron(III) oxo acetate complexes, *Phys. Chem. Chem. Phys.*, 20, 16673-16685, 2018.
- [65] J. Lang, J. Mohrbach, S. Dillinger, J. M. Hewer, and G. Niedner-Schatteburg, Vibrational blue shift of coordinated N₂ in [Fe₃O(OAc)₆(N₂)_n]⁺: "non-classical" dinitrogen complexes, *Chem. Comm.*, 53, 420-423, 2017.
- [66] J. Meyer, "Fragmentation and Infrared Spectroscopy of oxo-centered Homo- and Heterotrimetallic Carboxylate Bridged Transition Metal Complexes," 2018.
- [67] J. Roithová, Characterization of reaction intermediates by ion spectroscopy, *Chemical Society Reviews*, 41, 547-559, 2012.
- [68] D. Imanbaew, "Time-resolved pump-probe action spectroscopy on isolated organic dyes and supramolecular photocatalysts," 2017.
- [69] D. Imanbaew, J. Lang, M. F. Gelin, S. Kaufhold, M. G. Pfeffer, S. Rau, and C. Riehn, Pump-Probe Fragmentation Action Spectroscopy: A Powerful Tool to Unravel Light-Induced Processes in Molecular Photocatalysts, *Angew. Chem. Int. Ed.*, 56, 5471-5474, 2017.
- [70] S. V. Kruppa, F. Böppler, C. Holzer, F. Dietrich, R. Diller, W. Klopper, and C. Riehn, Excited state vibrational coherence in a binuclear metal adduct: wave packet phase dependant molecular fragmentation under variation of ligand size, *EPJ Web Conf.*, 205, 2019.
- [71] S. V. Kruppa, F. Böppler, C. Holzer, W. Klopper, R. Diller, and C. Riehn, Vibrational Coherence Controls Molecular Fragmentation: Ultrafast Photodynamics of the [Ag₂Cl]⁺ Scaffold, *J. Phys. Chem. Lett.*, 9, 804-810, 2018.
- [72] S. V. Kruppa, Y. Nosenko, M.-O. Winghart, S. P. Walg, M. M. Kappes, and C. Riehn, Fragmentation pathways of dianionic [Pt₂(μ-P₂O₅H₂)₄X₂Y]²⁻ (X,Y=H, K, Ag) species in an ion trap induced by collisions and UV photoexcitation, *Int. J. Mass spectrom.*, 395, 7-19, 2016.
- [73] A. Langenberg, "Magnetische Momente freier, massenselektierter Eisen-, Cobalt- und Nickelcluster," Doctoral Thesis, Technische Universität Berlin, Fakultät II - Mathematik und Naturwissenschaften, Technische Universität Berlin, Berlin, 2013.
- [74] A. Langenberg, K. Hirsch, A. Ławicki, V. Zamudio-Bayer, M. Niemeyer, P. Chmiela, B. Langbehn, A. Terasaki, B. v. Issendorff, and J. T. Lau, Spin and orbital magnetic moments of size-selected iron, cobalt, and nickel clusters, *Phys. Rev. B*, 90, 184420, 2014.
- [75] J. T. Lau, A. Achleitner, H. U. Ehrke, U. Langenbuch, M. Reif, and W. Wurth, Ultrahigh vacuum cluster deposition source for spectroscopy with synchrotron radiation, *Rev. Sci. Instrum.*, 76, 063902, 2005.
- [76] J. T. Lau, A. Föhlich, R. Nietubyċ, M. Reif, and W. Wurth, Size-Dependent Magnetism of Deposited Small Iron Clusters Studied by X-Ray Magnetic Circular Dichroism, *Phys. Rev. L*, 89, 057201, 2002.
- [77] V. Zamudio-Bayer, K. Hirsch, A. Langenberg, A. Ławicki, A. Terasaki, B. v. Issendorff, and J. T. Lau, Electronic ground states of Fe²⁺ and Co²⁺ as determined by x-ray absorption and x-ray magnetic circular dichroism spectroscopy, *J. Chem. Phys.*, 143, 244318, 2015.
- [78] V. Zamudio-Bayer, L. Leppert, K. Hirsch, A. Langenberg, J. Rittmann, M. Kossick, M. Vogel, R. Richter, A. Terasaki, T. Möller, B. v. Issendorff, S. Kümmel, and J. T. Lau, Coordination-driven magnetic-to-nonmagnetic transition in manganese-doped silicon clusters, *Physical Review B*, 88, 115425, 2013.
- [79] V. Zamudio-Bayer, R. Lindblad, C. Bülow, G. Leistner, A. Terasaki, B. V. Issendorff, and J. T. Lau, Electronic ground state of Ni²⁺, *J. Chem. Phys.*, 145, 2016.
- [80] A. D. Becke, Density-functional exchange-energy approximation with correct asymptotic behavior, *Phys. Rev. A*, 38, 3098-3100, 1988.
- [81] A. D. Becke, Density-functional thermochemistry. III. The role of exact exchange, *J. Chem. Phys.*, 98, 5648-5652, 1993.
- [82] B. Miehlich, A. Savin, H. Stoll, and H. Preuss, Results obtained with the correlation energy density functionals of Becke and Lee, Yang and Parr, *Chemical Physics Letters*, 157, 200-206, 1989.

11. First Investigations of a heptanuclear homoleptic Manganese complex with single molecular magnetic behavior

- [83] E. R. Davidson, Comment on "Comment on Dunning's correlation-consistent basis sets", *Chem. Phys. Letters*, 260, 514-518, 1996.
- [84] T. H. Dunning, Gaussian basis sets for use in correlated molecular calculations. I. The atoms boron through neon and hydrogen, *J. Chem. Phys.*, 90, 1007-1023, 1989.
- [85] R. A. Kendall, T. H. Dunning, and R. J. Harrison, Electron affinities of the first-row atoms revisited. Systematic basis sets and wave functions, *J. Chem. Phys.*, 96, 6796-6806, 1992.
- [86] A. K. Wilson, T. van Mourik, and T. H. Dunning, Gaussian basis sets for use in correlated molecular calculations. VI. Sextuple zeta correlation consistent basis sets for boron through neon, *Journal of Molecular Structure: THEOCHEM*, 388, 339-349, 1996.
- [87] D. E. Woon, and T. H. Dunning, Gaussian basis sets for use in correlated molecular calculations. III. The atoms aluminum through argon, *J. Chem. Phys.*, 98, 1358-1371, 1993.
- [88] M. J. Frisch et. al, "Gaussian 16 Rev. C.01," 2016.
- [89] M. Dolg, H. Stoll, H. Preuss, and R. M. Pitzer, Relativistic and correlation effects for element 105 (hahnium, Ha): a comparative study of M and MO (M = Nb, Ta, Ha) using energy-adjusted ab initio pseudopotentials, *J. Phys. Chem.*, 97, 5852-5859, 1993.
- [90] R. Ahlrichs, M. Bär, M. Häser, H. Horn, and C. Kölmel, Electronic structure calculations on workstation computers: The program system turbomole, *Chem. Phys. Lett.*, 162, 165-169, 1989.
- [91] O. Treutler, and R. Ahlrichs, Efficient molecular numerical integration schemes, *J. Chem. Phys.*, 102, 346-354, 1995.
- [92] M. Von Arnim, and R. Ahlrichs, Performance of parallel TURBOMOLE for density functional calculations, *J. Comp. Chem.*, 19, 1746-1757, 1998.
- [93] T. Lu, and F. Chen, Multiwfn: A multifunctional wavefunction analyzer, *J. Comp. Chem.*, 33, 580-592, 2012.
- [94] E. Stavitski, and F. M. F. de Groot, The CTM4XAS program for EELS and XAS spectral shape analysis of transition metal L edges, *Micron*, 41, 687-694, 2010.
- [95] G. B. Kaufman, Inorganic chemistry: principles of structure and reactivity, 4th ed. (Huheey, James E.; Keiter, Ellen A.; Keiter, Richard L.), *J. Chem. Ed.*, 70, A279, 1993.
- [96] X. Yang, G. Li, X. Yang, Z. Jia, and N. Luo, *Determination of Manganese in Environmental Samples by UV-Vis after Cloud Point Extraction*, 2015.

12 Development of a new ion source for aggregation of small molecules on cluster surfaces

12.1 Preamble

This chapter provides the first mass spectra with a new ion source for the aggregation of small molecules onto transition metal clusters at room temperature. This ion source enables access to co-adsorbed molecules onto cluster surfaces to investigate catalytic properties of transition metal clusters, e.g., ammonia synthesis.

12.2 Introduction

Transition metal (TM) clusters serve as model systems in fundamental processes achieving high relevance in heterogeneous catalysis^[1, 2]. This type of catalyst is made up of numerous metal components or simply one type of metal. These metals can be separated or settled together as an alloy to catalyze various chemical reactions^[3]. Such catalysts are widely used in a variety of applications, including vehicle three-way catalysts^[4-6] and the most well-known processes, such as the Haber-Bosch process^[7] or the Fischer Tropsch process^[8]. The adsorption and their corresponding activation are a fascinating field of research^[4, 5]. Transition metal clusters serve as a model system for investigating the catalytic activity as a function of their cluster size^[6, 7] and their corresponding structure^[8]. The splitting of molecular Nitrogen is an essential step in the Haber process. For the activation of molecular Nitrogen, transition metals such as Fe, Ni, Ru, and other metals are used^[9]. As a result, various studies of such transition metal cluster adsorbates were carried out under cryogenic circumstances in conjunction with IR(M)PD experiments in order to define the structure of these clusters and obtain further information about the cluster surface^[15-19].

Different methods to produce such clusters are established. One way to aggregate small molecules onto cluster surfaces is by using a mixture of the carrier gas with molecules of interest^[10-13]. Infusing gaseous molecules into an ion trap where the clusters are kept is another method for adding molecules to cluster surfaces^[15, 17-19, 24]. This chapter represents a new ion source that allows aggregation of small molecules before the ion cloud condenses into different clusters by entering the vacuum chamber. We modified a home built Laser vaporization source^[14-17] (LVAP) with a so called “pick up” block to add small molecules to the clusters (cf. chapter 2.3).

12.3 Results

With this improved setup, we attempt to record spectra of metal clusters without the addition of gas in order to optimize the bare clusters, which should adsorb molecules to their surface. The first spectrum displays a high amount of contaminants onto the clusters (cf. Fig. 1).

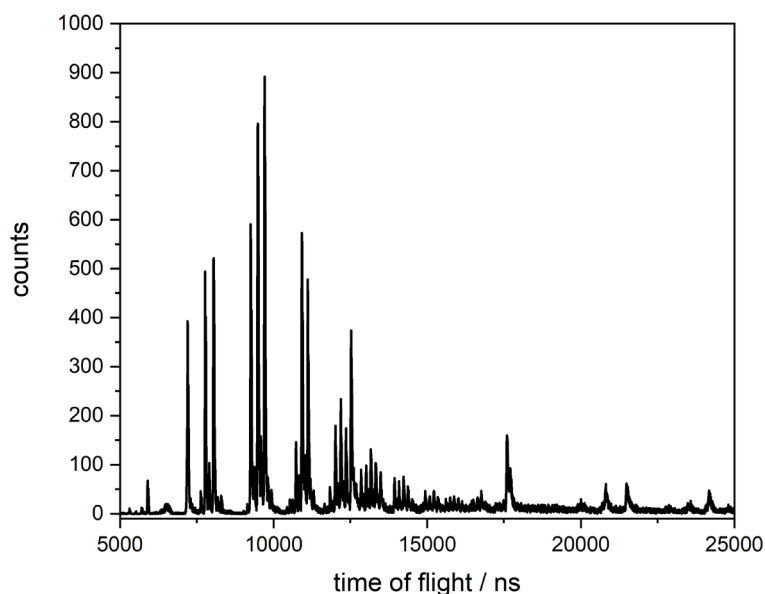


Fig. 1: Time of flight spectrum of Nb cluster with the modified ion source.

We switched to Rhodium, and we observed the same impurities in the spectrum, which are Hydroxyl, Oxygen, and water adsorbed onto the metal clusters. We assumed impurities in the gas inlets respective lines for the carrier gas and the ion source chamber itself. The gas inlets and lines were heated under vacuum to get rid of the impurities. During the piezo ventile restoration, we did a residual gas examination of the ion source chamber to determine where the contaminants emerged. We recorded mass spectra of the residual gas background in the chamber when the gate valve of the oil diffusion pump is opened and closed (cf. Fig. 2). The results show that the contaminants originate from the oil diffusion pump, and so we were unable to acquire spectra of bare clusters under these conditions. The most prominent peaks are water with a mass of 18 amu, molecular Nitrogen with 28 amu, and molecular Oxygen with 32 amu. We assume the ion cloud expands into the vacuum, and the condensation directly involves the impurities to clusters.

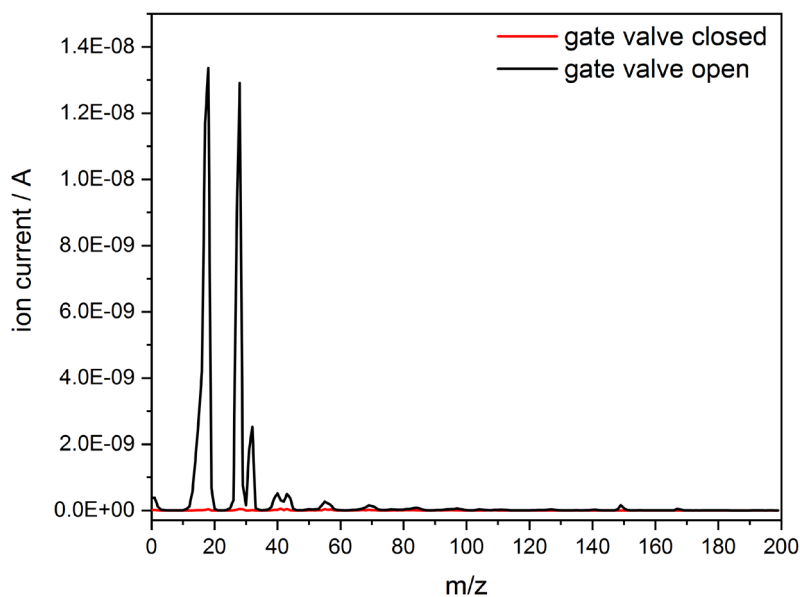


Fig. 2: Residual gas analysis of the ion source chamber with the gate valve for the oil diffusion pump opened (black) and closed (red)

We also observed a decreasing trend for the ion source chamber impurities (cf. Fig. 3). By opening the gate valve, the pollutants rise, indicating that the oil condenses on the cooling baffle and returns to the diffusion pump. The oil gets heated again and can pass the cooling baffle. This would also explain the decreasing trend of the impurities after some time.

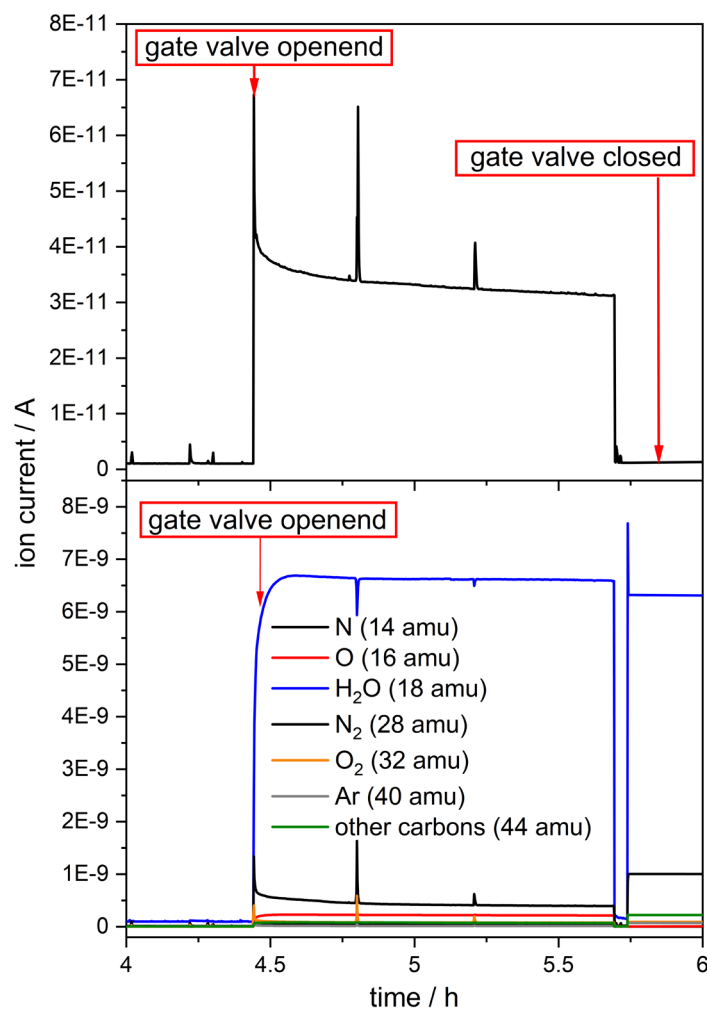


Fig. 3: Residual gas analysis as time dependent function recorded over one hour (top) and corresponding impurity traces (bottom).

As mentioned above, one of the primary impurities is water. Therefore, we recorded time dependent residual gas analysis for every mass we observed (cf. Fig. 3). The experimental data leads to the same results for each impurity trace. When the gate valve is opened, we monitor an instantaneous spike in contaminants and a slow decline in these impurities after a while. When the gate valve is closed, the impurities decrease rapidly, and there is only the residual gas left in the chamber. To calculate the impurity decrease, we compute the ion current difference at the beginning and the end (see Fig. 4), which results in a drop of 1×10^{-10} A per hour. To obtain pure mass spectra of transition metal clusters, background contaminants should show at ion currents less than 10^{-11} A. With this assumption, the decrease to a practical background value would take around 266 hours, respective 12 days with an open gate valve, which is not an option because of the safety aspects of the oil diffusion pump.

We shut down the oil diffusion pump and replaced it with a molecular turbopump to obtain a better vacuum and reduce the impurity background. The installed pump reaches a vacuum of 2.6×10^{-6} mbar without Helium background pressure. After reaching the vacuum, we recorded time of flight spectra with Rhodium to verify that the ion source chamber background is better (cf. Fig. 4 (top)). The problem is that the intensity is minimal, and recording spectra takes about 45 min. We observe a broad cluster distribution with a small amount of impurities.

To transform the time of flights into masses, we perform a cubic fit of the correlated theoretical masses and the experimental time of flights. The fit function exhibits a perfect match between the assumed masses and their related flight times (see Fig. 4 (middle)). The χ^2 value is almost one that expresses a good fit. The mass spectra reveal Rhodium clusters up to a size of $n = 46$ (cf. Fig. 4 (bottom)) with a typical cluster distribution. The resolution of the mass peaks is meager because of the low intensity in the recorded time of flight spectra, resulting in a broadening of the peaks because the ions arrive with a slight time delay on the detector. Furthermore, the ions do not arrive continuously, resulting in a reduced signal-to-noise ratio and, as a result, more intense contaminants. If the cluster is not intensive and there is an adsorption of oxygen, the peaks become more broadened because of the overlay of those two peaks. The other case is that the ion package is not very compressed and leads to a broadening because of local errors in the clusters.

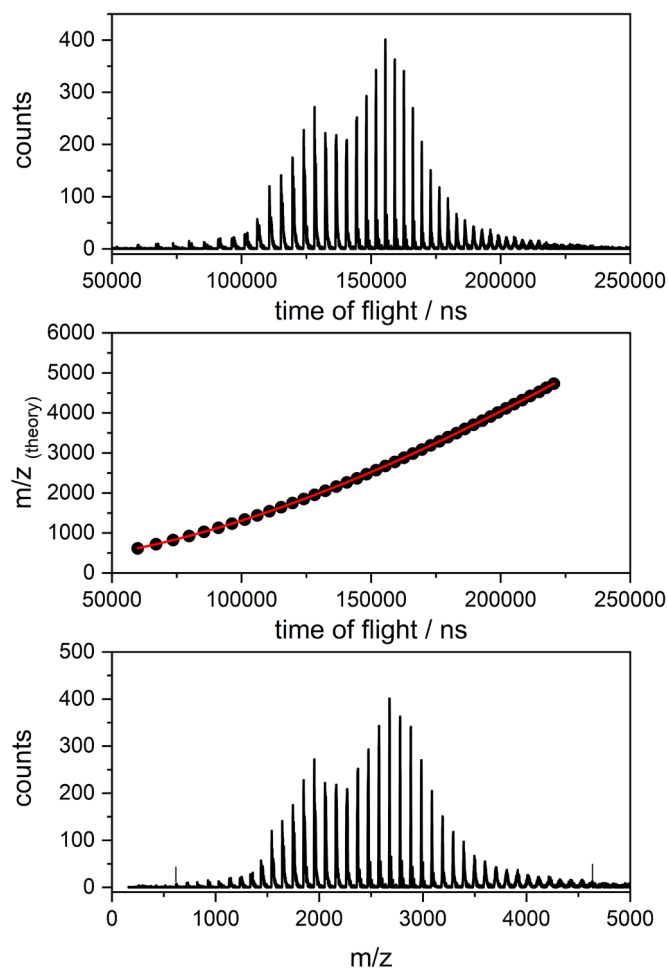


Fig. 4: Time of flight spectrum of Rhodium clusters (top), Fit function for the mass transformation (middle), and mass spectrum (bottom).

The spectrum reveals that the ion package is not compressed (cf. Fig. 5). We observe more sharpened peaks for the optimized clusters than those appearing in the mass spectrum because the ions enter the Wiley McLaren arrangement and then accelerate into the time of flight region at a particular time. The smaller clusters are long through the Wiley McLaren arrangement, and the bigger clusters have not entered the acceleration area. The acceleration leads to a smear of the not optimized cluster sizes due to an inefficient space focus.

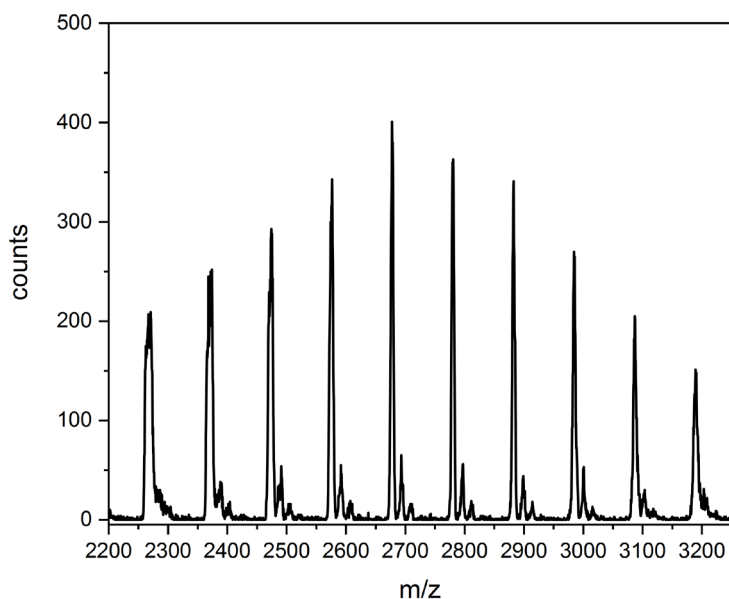


Fig. 5: Mass spectra of $[\text{Rh}]_n^+$ clusters with $n = 22-31$.

The transformed masses from the fit agree with the common masses (cf. Tab. 2). Also, the variations for the small and huge clusters are minimal. We assume that the change from the oil diffusion pump to the molecular turbopump leads to a better background of the vacuum, resulting in better expansion conditions of the clusters and fewer underlying impurities that can broaden the mass peaks.

Tab. 2: Expected masses in comparison with the masses from the Fit of $[\text{Rh}]_n^+$ clusters

Cluster	expected mass m/z	masses from Fit m/z
$[\text{Rh}_6]^+$	617.43	618.68
$[\text{Rh}_7]^+$	720.33	720.76
$[\text{Rh}_8]^+$	823.24	823.60
$[\text{Rh}_9]^+$	926.14	926.42
$[\text{Rh}_{10}]^+$	1029.06	1029.01
$[\text{Rh}_{11}]^+$	1131.96	1132.70
$[\text{Rh}_{12}]^+$	1234.87	1235.60
$[\text{Rh}_{13}]^+$	1337.77	1336.13
$[\text{Rh}_{14}]^+$	1440.67	1438.76
$[\text{Rh}_{15}]^+$	1543.58	1541.86
$[\text{Rh}_{16}]^+$	1646.49	1642.77
$[\text{Rh}_{17}]^+$	1749.39	1745.85
$[\text{Rh}_{18}]^+$	1852.30	1849.06
$[\text{Rh}_{19}]^+$	1955.20	1951.72
$[\text{Rh}_{20}]^+$	2058.11	2054.77
$[\text{Rh}_{21}]^+$	2161.01	2164.67
$[\text{Rh}_{22}]^+$	2263.93	2270.64
$[\text{Rh}_{23}]^+$	2366.83	2373.98

[Rh ₂₄] ⁺	2469.73	2474.39
[Rh ₂₅] ⁺	2572.64	2576.50
[Rh ₂₆] ⁺	2675.54	2677.54
[Rh ₂₇] ⁺	2778.45	2780.58
[Rh ₂₈] ⁺	2881.35	2882.80
[Rh ₂₉] ⁺	2984.26	2984.56
[Rh ₃₀] ⁺	3087.16	3086.70
[Rh ₃₁] ⁺	3190.07	3189.16
[Rh ₃₂] ⁺	3292.98	3292.35
[Rh ₃₃] ⁺	3395.88	3393.28
[Rh ₃₄] ⁺	3498.78	3495.80
[Rh ₃₅] ⁺	3601.69	3597.37
[Rh ₃₆] ⁺	3704.60	3704.05
[Rh ₃₇] ⁺	3807.50	3810.23
[Rh ₃₈] ⁺	3910.41	3913.79
[Rh ₃₉] ⁺	4013.31	4007.25
[Rh ₄₀] ⁺	4116.22	4110.42
[Rh ₄₁] ⁺	4219.13	4214.96
[Rh ₄₂] ⁺	4322.03	4318.71
[Rh ₄₃] ⁺	4424.94	4423.25
[Rh ₄₄] ⁺	4527.84	4538.91
[Rh ₄₅] ⁺	4630.75	4634.05
[Rh ₄₆] ⁺	4733.65	4733.62

As mentioned above, the intensity of the clusters is very weak. We made minor changes to the mass spectrometer and fixed some problems to obtain a better cluster signal.

Change of the angle in the acceleration area to the time of flight region

By changing the angle in the acceleration area, ions have different velocity components in a three-dimensional room, e.g., the ions may not be straight accelerated into the time of the flight region and still has a velocity component, leading to desorption onto the vacuum chamber and a loss of the intensity (cf. Fig. 6).

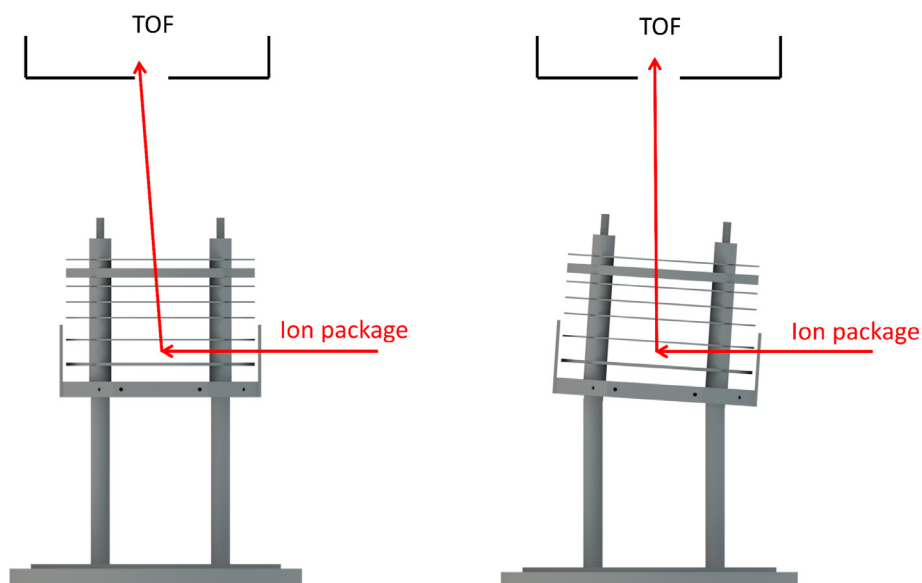


Fig. 6: Scheme of the ion package acceleration without an angle (left) and an angle (right).

We calculated an approximated ion velocity for the ion package before the acceleration and after acceleration into the TOF region with Cobalt clusters to determine the theoretical angle needed to gain a straight acceleration (cf. Fig. 17). The calculation of these velocities can be achieved with the following equations:

$$v(\text{TOF, package}) = 2 * E_{\text{Kin}} * e^{-} \quad (1)$$

$$\frac{v_m}{z}(\text{TOF, package}) = \sqrt{\frac{2 * v(\text{TOF, package})}{\frac{M}{1000}}} \quad (2)$$

With this approximation, we observe a higher velocity for the ions into the time of flight region as the velocity from the package itself (cf. Fig. 7), leading to the assumption that a velocity component hinders a straight acceleration into the time of flight region with the current system.

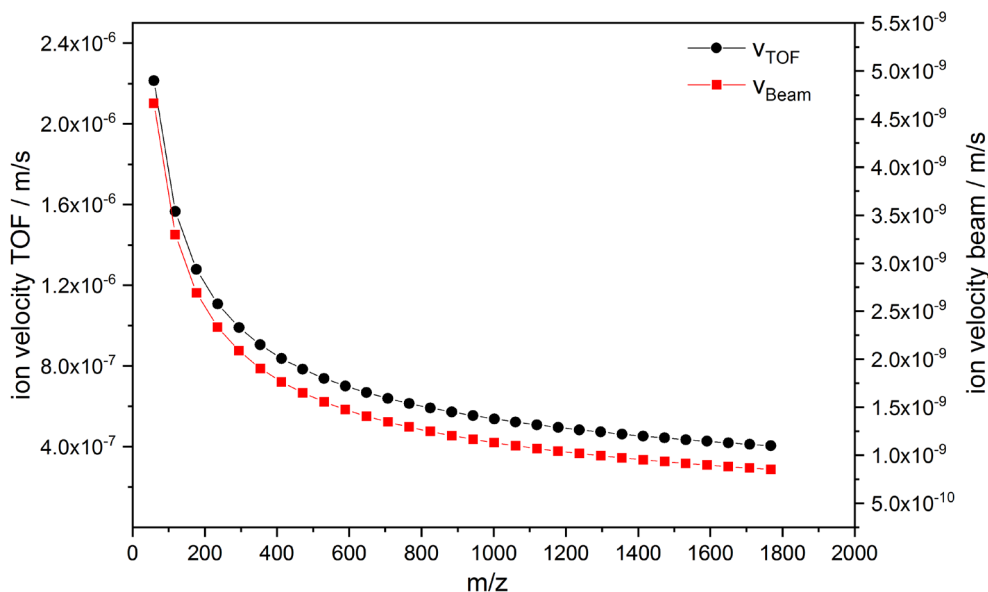


Fig. 7: Calculated ion velocities for the ion package before (red) and after (black) acceleration into the time of flight region for cobalt with $n = 1 - 30$.

The approximated angle which has to be set up can be calculated with the following equation:

$$\theta = \arctan\left(\frac{v\left(\frac{m}{z}\right)(TOF)}{v\left(\frac{m}{z}\right)(package)}\right) \quad (3)$$

For a straight acceleration into the time of flight area, this calculation yields an angle of 1.56° .

There are two methods to include an angle into the Wiley McLaren layout.

1. Elongation of two rods for placing the Wiley McLaren arrangement into the ion pathway. This would mean that the whole setup must be removed and rewired to change the rods made in the local machine workshop.
2. Loose the screws on top of the setup and bring some washers between the rods and the arrangement to gain the calculated angle.

For a quick check up we decided on the alternative two. We removed the screws on top of the setup and brought three washers between the rods and the arrangement and obtained an angle of 1.6° with this method.

Change of a broken RF generator with a minimum frequency of 2 MHz to a generator with a maximum frequency of 1 MHz

We operated a radiofrequency generator with 2–20 MHz at 2.2 MHz. Most mass spectrometers are operating their ion guides between several kHz to 1 MHz. The electronic workshop built a generator in this region, and we tested it. The first test went very well, but we recognized a loss of the signal and checked the RF voltages. We observed different amplitudes for the octupole rod pairs (cf. Fig. 8).

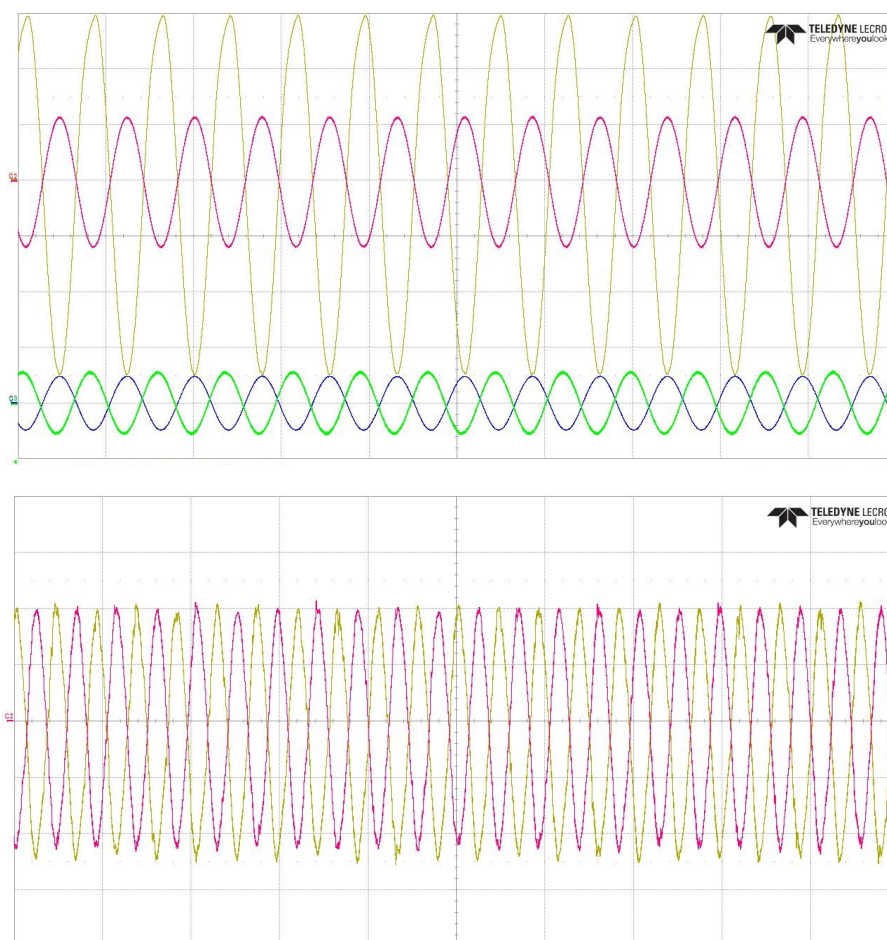


Fig. 8: RF amplitudes and frequencies of the octupole rod pairs. 180° (yellow), 0° (pink), Monitor output 180° (green) and Monitor output 0° (blue) with the broken RF generator (top) and the new RF generator (bottom).

The monitor output seems to be the same for both amplitudes, but the amplitudes measured directly on the octupole rods are asymmetric by a factor of two (cf. Fig. 8 (top)), indicating that the ions are not properly directed in the field free zone. Here, there is a high possibility that the ions are desorbed to the octupole rods or at the vacuum chamber. We changed the generator with a similar one and observed symmetric phase shifted frequencies with the same amplitudes for the octupole rod pairs (cf. Fig. 8 (bottom)).

This leads to optimal ion guide because the ions are in a field free region where there is no possibility to desorb on the octupole rods or elsewhere.

Rewiring of the Reflectron

There are two different versions of the reflectron used in time of flight technology. One is a one staged assembly, and the other one is a two-staged assembly. Two separate pairs of rings are present in the two staged cases, and a high voltage is applied to each pair of rings. As in the one staged reflectron resistor chains, establish a voltage gradient for each pair of rings. Only one high voltage is applied in the one staged reflectron, and the resistor chain leads to a voltage gradient with lower voltage at the reflectron entrance.

Here, a one staged reflectron was wired as a two-staged one. Therefore, the cables were rewired so that only one high voltage was applied, and the other end of the resistor chain was grounded (cf. Fig. 9).

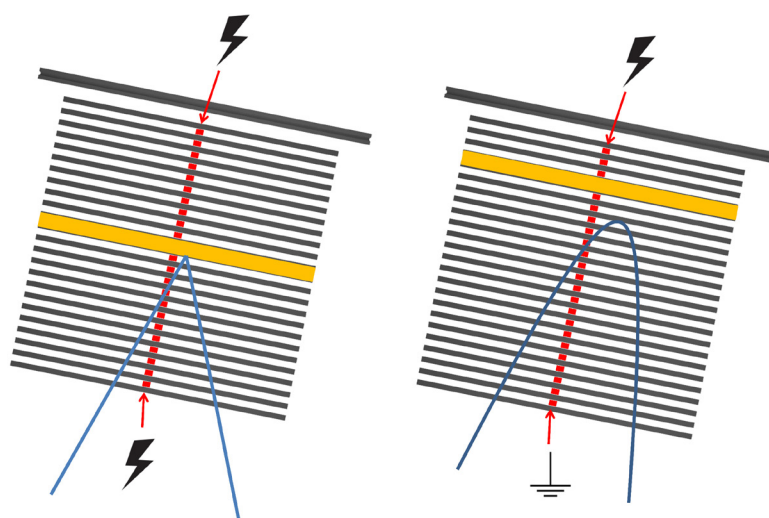


Fig. 9: Schematic description of the reflectron, including the old wiring (left) and the new wiring (right).

After rewiring of the reflectron, exchange of the MCP detectors, and an exchange of the ground plug to avoid a DC floated detector, a tantalum target was built in the modified LVAP source, and a time of flight spectrum was recorded (cf. Fig. 10 (top))

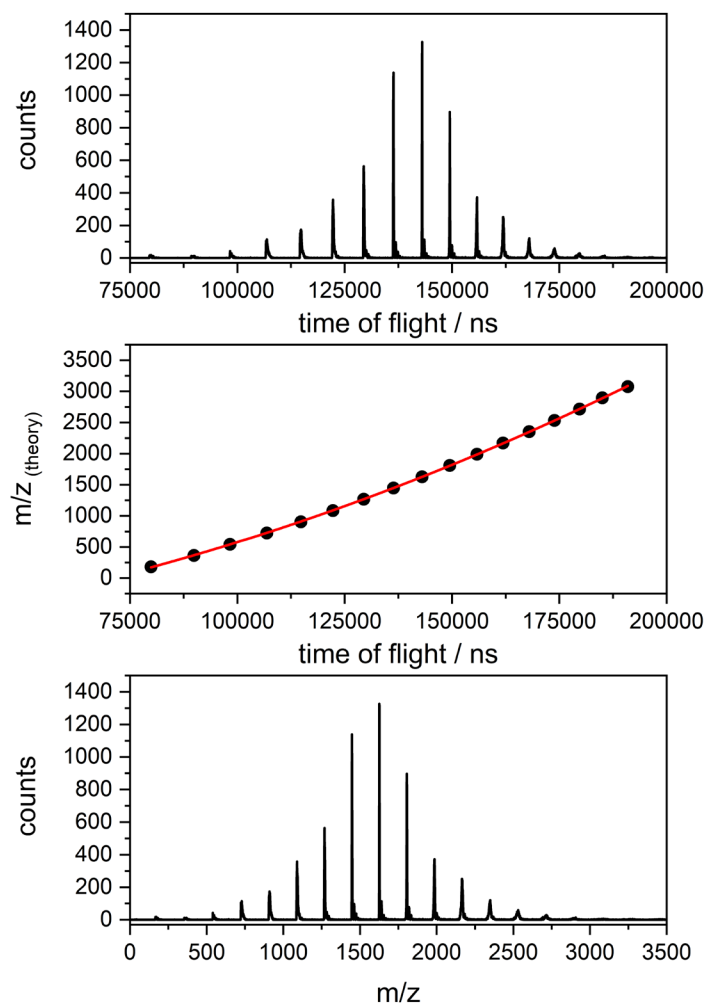


Fig. 10: Time of flight spectrum of different Tantalum cluster ($n = 1-17$) (top), fit function for mass transformation (middle) and mass spectrum (bottom).

To transform the time of flight spectrum into a mass spectrum, we correlate the theoretical masses of the different Tantalum clusters to their assumed time of flights (cf. Fig. 10 (middle)). The correlation leads to an almost linear progression, indicating that the theoretical masses are the time of flights of the different cluster sizes. The fit was performed with a parabola function (cf. eq. 4).

$$m = A + Bx + Cx^2 \quad (4)$$

To transform the time of flight spectra to a mass spectrum, all time of flights in the time flight spectrum is set into the parabola fit from above for the accuracy of the fit the R square value hint a good or less fit for the transformation into a mass spectrum. In this case, the value is almost one, indicating a good transformation from the flight time into a mass spectrum, leading to the mass spectra in good agreement with the theoretically calculated masses (cf. Fig. 10 (bottom)).

It is possible to test the gas inlet of the “pick up” source in the ion source with the clusters. Therefore, we applied different gas pressures to prove an aggregation of N₂ to the tantalum clusters and a change of the aggregation with higher gas pressure (cf. Fig. 11). The recorded spectra reveal more peaks in the TOF area, and with higher pressure, these peaks vanish again. Maybe the background pressure of the vacuum chamber is too high for N₂ adsorbed transition metal clusters condensation, resulting in less intensity of the ions of interest. The higher background pressure may also change the optimal conditions for the set parameters. Still, we wanted the same conditions for all pressure-dependent mass spectra for these tests.

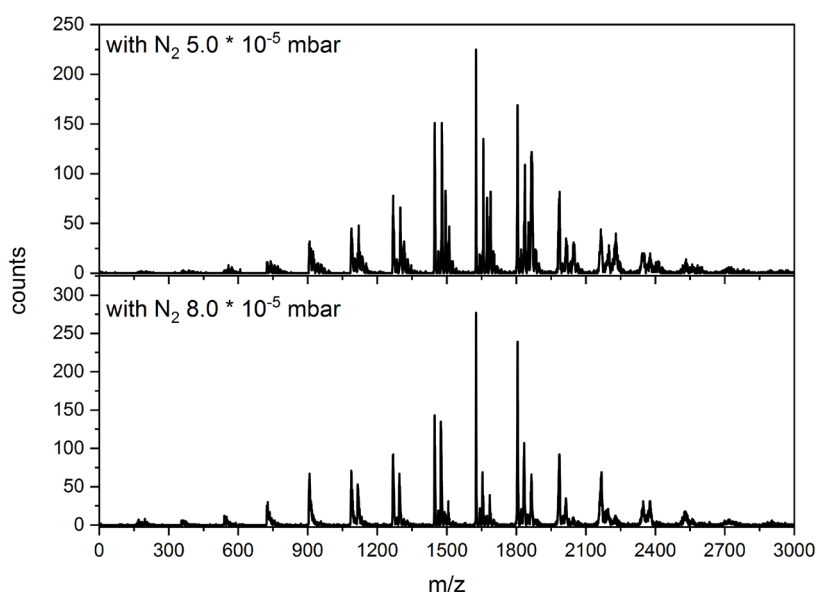


Fig. 11: Mass spectra of N₂ adsorbed Tantalum clusters with a cluster size of 1-17 and different N₂ background pressures.

For small clusters, we observe an aggregation of one Nitrogen (cf. Fig. 12). This is not that much as expected, but optimization of the clusters was performed for larger clusters, meaning some peaks may not have been detected because of the not optimized parameters for these clusters. These spectra are recorded at room temperature, and molecular Nitrogen is an inert gas, which does not feature a covalent exchange with the transition metal clusters. In cold conditions, the adsorption of more Nitrogen is possible^[18-23]. Also, the condensation of the clusters leads to a cooling effect, which is not cold enough to bond the Nitrogen to the clusters. The spectra clearly show that Nitrogen is adsorbed to the cluster, and the first tests went pretty well.

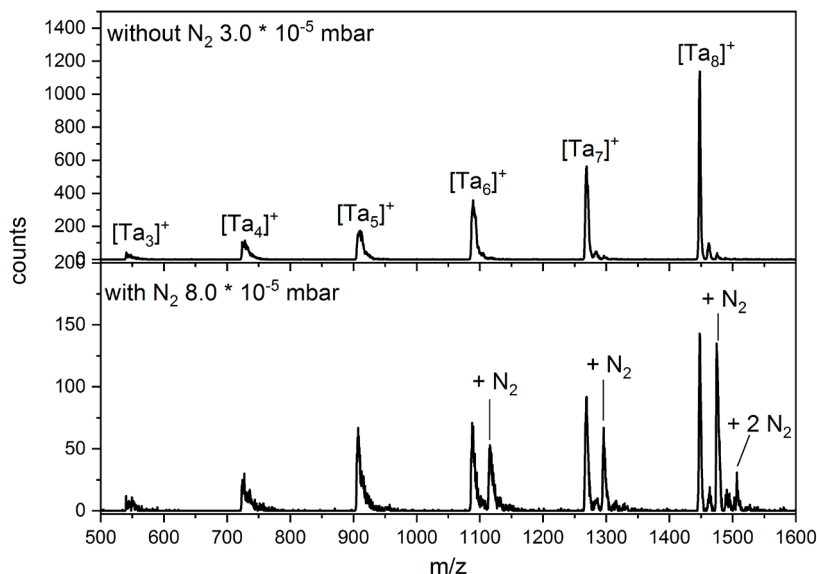


Fig. 12: Comparison of the bare clusters (top) and the Nitrogen adsorbed nitrogen clusters (bottom) for small clusters 3-8.

For larger clusters, at least the absorption of two molecular Nitrogen atoms is observed (cf. Fig. 13), where the cluster distribution was optimized. Further optimization of these cluster sizes may lead to more adsorbed cluster peaks in the spectra. We do not change any set parameter in the first test and just let Nitrogen leak into the ion source. This setup does not feature a mass selection of specific masses. Isolating one peak might lead to more adsorption of Nitrogen because of a change in their intensities. With this ion source, it is impossible to store the ions and serve for more aggregation as a function of the storage time.

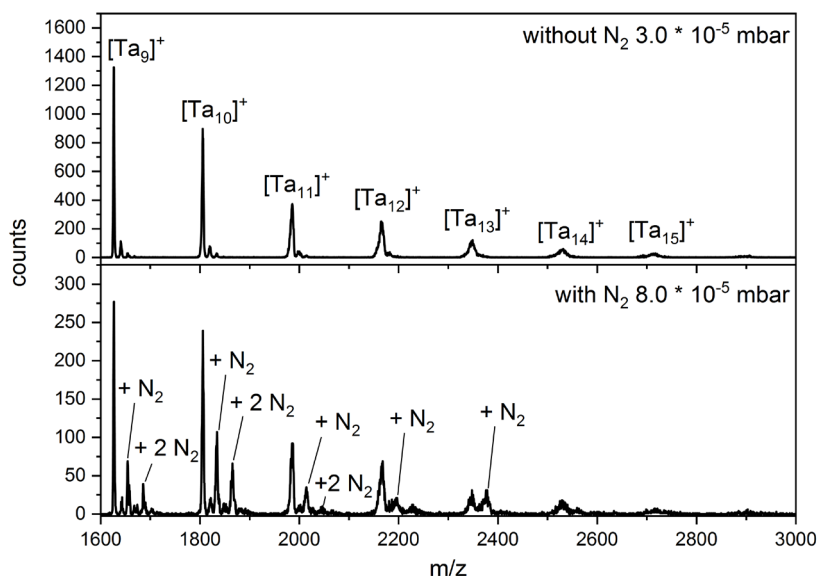


Fig. 13: Comparison of the bare clusters (top) and the Nitrogen adsorbed nitrogen clusters (bottom) for small clusters 9-15.

A closer look at the different cluster sizes compared with earlier measurements of the FRITZ instrument reveals a good agreement of the mass spectra in different mass spectrometers (cf. Fig. 14). The mass spectra of the FRITZ experiment show a few more adsorbed Nitrogen molecules than the mass spectra of the GERTI experiment. One of the most significant differences in both mass spectra is the temperature. The mass spectrum taken from the FRITZ apparatus is under cryogenic conditions, and the GERTI spectrum is recorded at room temperature. Both spectra show at least one adsorbed Nitrogen for the Tantalum ($n = 4$) cluster. The Mass spectrum of the FRITZ MS is represented in a semi-logarithm plot, indicating weak adsorption of the Nitrogen. For better comparability, both spectra are recorded without further optimization of the cluster size and their adsorption. We observe the adsorption of atomic Oxygen in both spectra, which belongs to residual gas in the gas lines.

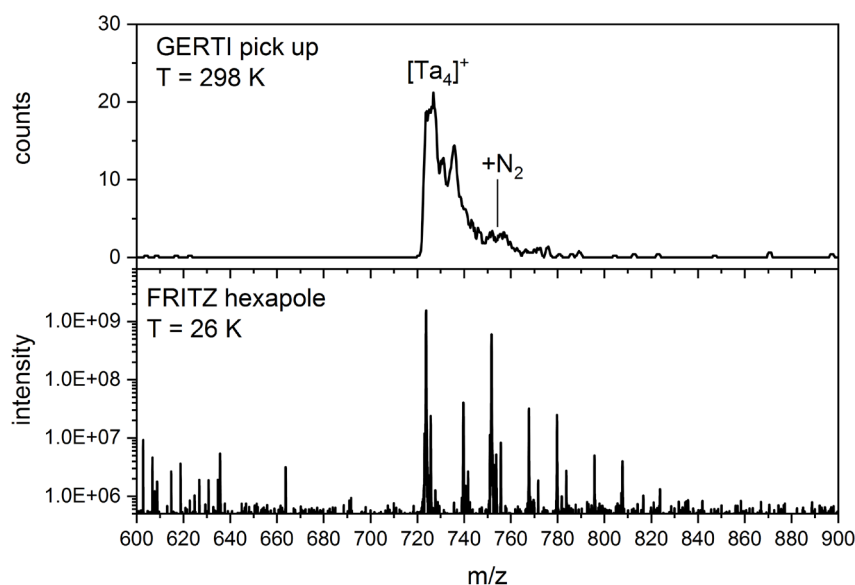


Fig. 14: Comparison of the mass spectra of Tantalum cluster ($n = 4$) with nitrogen adsorption in the GERTI MS (top) and FRITZ FTMS (bottom).

A more precise effect appears for larger clusters with better cluster size optimization (cf. Fig. 15). In comparison with the FRITZ FTMS spectrum, three adsorbed nitrogen molecules occur in both mass spectra. It seems like cryogenic conditions for this cluster size are unnecessary to adsorb Nitrogen onto the cluster surface. Adsorption of atomic oxygen is not present in the GERTI mass spectrum as in the FRITZ mass spectrum, pointing out that the impurities in the GERTI Mass spectrometer are getting better.

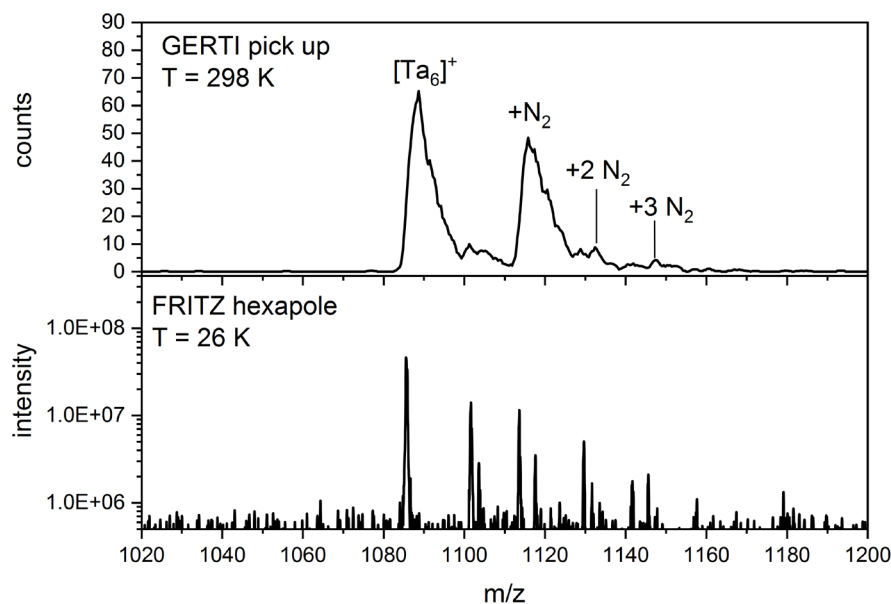


Fig. 15: Comparison of the mass spectra of Tantalum cluster ($n = 6$) with nitrogen adsorption in the GERTI MS (top) and FRITZ FTMS (bottom).

Both spectra of the FRITZ FTMS are shown semi logarithm and indicate the negligible adsorption of Nitrogen in the FRITZ mass spectra. In the other case of the GERTI mass spectra, no semi-logarithm plot is needed to point out the nitrogen adsorption. It also must be noted that the intensity in the GERTI mass spectrometer is much lower than the FRITZ FTMS mass spectrometer because of higher resolution and ion detection in the mass spectrometer.

12.4 Conclusion

We successfully get a home built mass spectrometer operable and produce mass spectra of transition metal clusters. Further optimization of the mass spectrometer leads to a reduction of the impurities in the observed cluster distribution.

The Elimination of electronic problems and their corresponding short circuits enhance the intensity of the cluster distribution in the mass spectrometer.

The installation of the new ion source revealed a cluster distribution with fewer impurities. By entering Nitrogen into the ion source, an aggregation of Nitrogen onto these clusters is observed.

Compared with the FRITZ FTMS spectrum, the same adsorbed clusters are observed with the ion source in warm conditions.

12.5 References

- [1] G. A. Somorjai, Introduction to Surface Chemistry and Catalysis, *John Wiley & Sons*, 1994.
- [2] J. K. N. T. Bligaard, Heterogeneous Catalysis, in *Chemical Bonding at Surfaces and Interfaces*, Elsevier: Amsterdam, chapter 4, 255-321, 2008.
- [3] O. Deutschmann, H. Knözinger, K. Kochloefl, and T. Turek, "Heterogeneous Catalysis and Solid Catalysts," *Ullmann's Encyclopedia of Industrial Chemistry*.
- [4] S. Brunauer, P. H. Emmett, and E. Teller, Adsorption of Gases in Multimolecular Layers, *J. Am. Chem. Soc.*, 60, 309-319, 1938.
- [5] I. Langmuir, THE ADSORPTION OF GASES ON PLANE SURFACES OF GLASS, MICA AND PLATINUM, *J. Am. Chem. Soc.*, 40, 1361-1403, 1918.
- [6] M. B. Knickelbein, REACTIONS OF TRANSITION METAL CLUSTERS WITH SMALL MOLECULES, *An. Rev. Phys. Chem.*, 50, 79-115, 1999.
- [7] Z. Luo, A. W. Castleman, and S. N. Khanna, Reactivity of Metal Clusters, *Chem. Rev.*, 116, 14456-14492, 2016.
- [8] W. Han, H. Yan, H. Tang, Y. Li, and H. Liu, Preparation of efficient ruthenium catalysts for ammonia synthesis via high surface area graphite dispersion, *Reaction Kinetics, Mechanisms and Catalysis*, 113, 361-374, 2014.
- [9] R. Schlögl, Heterogeneous Catalysis, *Angew. Chem. Int. Ed.*, 54, 3465-3520, 2015.
- [10] R. C. Bell, K. A. Zemski, D. R. Justes, and A. W. Castleman, Formation, structure and bond dissociation thresholds of gas-phase vanadium oxide cluster ions, *J. Chem. Phys.*, 114, 798-811, 2000.
- [11] F. Mafuné, Y. Tawarayama, and S. Kudoh, Nitrogen Molecule Adsorption on Cationic Tantalum Clusters and Rhodium Clusters and Desorption from Their Nitride Clusters Studied by Thermal Desorption Spectrometry, *J. Phys. Chem. A*, 120, 4089-4095, 2016.
- [12] M. Takenouchi, S. Kudoh, K. Miyajima, and F. Mafuné, Adsorption and Desorption of Hydrogen by Gas-Phase Palladium Clusters Revealed by In Situ Thermal Desorption Spectroscopy, *J. Phys. Chem. A*, 119, 6766-6772, 2015.
- [13] S. Yin, Z. Wang, and E. R. Bernstein, Formaldehyde and methanol formation from reaction of carbon monoxide and hydrogen on neutral Fe₂S₂ clusters in the gas phase, *Phys. Chem. Chem. Phys.*, 15, 4699-4706, 2013.
- [14] C. Berg, T. Schindler, G. Niedner-Schatteburg, and V. E. Bondybey, Reactions of simple hydrocarbons with Nb_n: Chemisorption and physisorption on ionized niobium clusters, *J. Chem. Phys.*, 102, 4870-4884, 1995.
- [15] V. E. Bondybey, and J. H. English, Laser induced fluorescence of metal clusters produced by laser vaporization: Gas phase spectrum of Pb₂, *J. Chem. Phys.*, 74, 6978-6979, 1981.
- [16] T. G. Dietz, M. A. Duncan, D. E. Powers, and R. E. Smalley, Laser production of supersonic metal cluster beams, *J. Chem. Phys.*, 74, 6511-6512, 1981.
- [17] S. Maruyama, L. R. Anderson, and R. E. Smalley, Direct injection supersonic cluster beam source for FT-ICR studies of clusters, *Rev. Sci. Instrum.*, 61, 3686-3693, 1990.
- [18] S. Dillinger, M. P. Klein, A. Steiner, D. C. McDonald, M. A. Duncan, M. M. Kappes, and G. Niedner-Schatteburg, Cryo IR Spectroscopy of N₂ and H₂ on Ru₈⁺: The Effect of N₂ on the H-Migration, *J. Phys. Chem. Lett.*, 9, 914-918, 2018.
- [19] S. Dillinger, J. Mohrbach, J. Hewer, M. Gaffga, and G. Niedner-Schatteburg, Infrared spectroscopy of N₂ adsorption on size selected cobalt cluster cations in isolation, *Phys. Chem. Chem. Phys.*, 17, 10358-10362, 2015.
- [20] S. Dillinger, J. Mohrbach, and G. Niedner-Schatteburg, Probing cluster surface morphology by cryo spectroscopy of N₂ on cationic nickel clusters, *J. Chem. Phys.*, 147, 184305, 2017.
- [21] J. Mohrbach, S. Dillinger, and G. Niedner-Schatteburg, Probing cluster surface morphology by cryo kinetics of N₂ on cationic nickel clusters, *J. Chem. Phys.*, 147, 184304, 2017.
- [22] J. Mohrbach, S. Dillinger, and G. Niedner-Schatteburg, Cryo Kinetics and Spectroscopy of Cationic Nickel Clusters: Rough and Smooth Surfaces, *J. Phys. Chem. C*, 121, 10907-10918, 2017.
- [23] J. Mohrbach, S. Dillinger, and G. Niedner-Schatteburg, Probing cluster surface morphology by cryo kinetics of N(2) on cationic nickel clusters, *J Chem Phys*, 147, 184304, 2017.

Summary and outlook

The presented work comprises of several investigations of various transition metal complexes with respect to their magnetic, electronic, and structural properties when held as isolated species and as prepared by electrospray ionization (ESI). Isolation of samples within an ion trap enables the exploration of various intrinsic properties of these complexes void from external effects such as, e.g., crystal packing, bulk, and solvation effects.

Magnetic moments of isolated complexes that reveal magnetic effects, e.g., spin frustration, spin-crossover, and single molecule magnetic behavior, were investigated by gas phase X-ray magnetic circular dichroism (XMCD) combined with sum rule analysis. Thereby total magnetic moments can be separated into their spin and orbital magnetic contributions. All XMCD experiments were performed at the "Ion Trap" endstation connected to the UE52-PGM soft X-ray beamline at BESSY II synchrotron facility of the Helmholtz-Zentrum für Materialien und Energie GmbH in Berlin. X-ray absorption (XA) simulations, density functional theory (DFT) combined with Broken symmetry calculations augment the experiments and help achieve a better understanding of the magnetic properties.

The investigation of the vibrational properties was performed with InfraRed (Multiple) Photon Dissociation (IR(M)PD) spectroscopy. The experiments were conducted with a modified Amazon SL Paul trap mass spectrometer combined with a broadband Laservision OPO/OPA laser system, which provides a tunable infrared light covering a spectral region from 1000-4000 cm^{-1} . DFT calculations serve to determine the minimum structure and further calculations of the linear harmonic absorption spectra.

The electronic properties of isolated complexes were performed with Ultraviolet Photon Dissociation (UVPD) spectroscopy. These experiments were performed with a modified Amazon Speed instrument combined with a diode pumped Wyvern laser system (KMLabs). The experimental setup is similar to the IR(M)PD experiments. TD-DFT calculations serve for the determination of the electronics in transition metal complexes.

XMCD studies on spin frustrated trinuclear 3d metal complexes with the structure $[\text{Fe}_3\text{O}(\text{OAc})_6(\text{py})_{0-3}]^+$ served as model systems and provided insight into their spin and orbital contributions by coordination of pyridine to the complex. For symmetric complexes ($n = 0,3$),

an antiferromagnetic exchange coupling is observed with the distortion of the triangular Fe_3O core an increasing ferromagnetic exchange coupling resulting from rising distortion of the Fe_3O core. By coordinating pyridine, the crystal field splittings of these complexes rise until the symmetry is restored. The calculated density of states reveals coordination dependent absorption edges. Pyridine coordination raises orbital energies, resulting in a higher ferromagnetic exchange coupling until symmetry is restored. The change in magnetic coupling scheme results as a change in the Fe-O-Fe-pyn angle, although bonding lengths are unaffected. Gas phase UVPD experiments on the complexes with the structure $[\text{Fe}_3\text{O}(\text{OAc})_6(\text{py})_{0-3}]^+$ reveal a strong red shift in comparison to the liquid phase spectra. This points out that solvation effects take a significant part in the condensed phase.

A correlation between the change in angle and absorption energies results in a nearly linear dependency until the coordination of the third pyridine takes place. All transitions in the UVPD spectra are determined as HOMO-LUMO transitions. A non-classical bonding coordination can explain the change in the UVPD spectra caused by non-covalent pyridine interactions with the complex. From the presented XA and UVPD spectra of $[\text{Fe}_3\text{O}(\text{OAc})_6(\text{py})_{0-3}]^+$ a correlation of the crystal field splittings and the absorption energies within a Tanabe Sugano diagram is possible. Both spectra reveal the same trend in their energy shift respective to the spectroscopic approach. The shifts in both spectroscopic approaches directly reveal a linear dependency due to its ground state. The relative shift in the UVPD spectra compared to the total magnetic momenta of the complex also points out an almost linear correlation for $n = 0 - 2$. DFT calculations with a different axial ligand show no changes in the distortion of the Fe_3O core but a change in non covalent interactions, which are weak for small molecules like nitrogen but become stronger with bigger molecules like pyridine. Changing the bridging ligand from acetate to benzoate has no effect on the geometrical structure of the Fe_3O core. The substitution of Sulfur for the central Oxygen atom causes a substantial change in the complex.

The structural characterisation of complexes with the structure $[\text{Ru}_3\text{O}(\text{OAc})_6(\text{py})_{0-3}]^+$ serves as a starting point for further research by switching the metal from Fe^{3+} (HS) to Ru^{3+} (LS). The impact in these complexes differs markedly from that seen in previous experiments with $[\text{Fe}_3\text{O}(\text{OAc})_6(\text{py})_{0-3}]^+$. We observe a high symmetric complex for the bare complex with rising pyridine coordination, two additional asymmetric CO stretching are monitored. For the

coordination of three pyridines to the complex, we detect a somewhat deformed complex with a weak asymmetric CO stretching mode. Calculations are in good agreement with experimental R(M)PD spectra. Theoretical UV spectra result in absorption bands, which result in estimated crystal field splittings of these complexes that are smaller than in the iron analogs. Broken symmetry calculations reveal no change in the antiferromagnetic exchange coupling in any coordination.

Investigating spin-crossover events in isolated transition metal complexes using XMCD helps to better understand the molecular changes in their orbital occupancy. $[\text{Fe}(\text{btpa})]^{2+}$ served as a model system in this work. Temperature dependent XMCD experiments reveal decreasing spin-, orbital-, and total magnetic moments per Fe atom with rising temperature. The declining effect is weaker from an ion trap temperature of 15 K to 25 K than it is from 4 K to 15 K. The approximation onto the Brillouin function leads in much warmer ions of around 10 K and may be used to calculate an approximation of a high spin/low spin combination. The spectra reveal different crystal field splittings for a set temperature. DFT calculations also predict three minimum structures, e.g., two octahedral complexes and one quasi seven coordinated structure. For the evidence of three different isomers in $[\text{Fe}(\text{btpa})]^{2+}$, gas phase IR(M)PD spectra and CID breakdown curves were recorded. The three predicted minimum structures can be assigned to the IR(M)PD spectrum compared to DFT calculated linear absorption spectra. According to transition state calculations, the quasi heptagonal coordinated high spin complex is produced from the octahedral high spin complex rather than directly from the low spin complex. Aggregation of metal acetates to the complex is conceivable, implying the presence of the heptagonal coordinated complex. In comparison with CID curves, we were able to determine their gas phase stabilities for this series of complexes. The comparison of the gas phase XA spectra with the UV/VIS spectra in solvents phase reveals two different absorption edges and two different absorption bands in the UV/VIS for $[\text{Fe}(\text{btpa})]^{2+}$. A correlation within a Tanabe Sugano diagram points out that there have to be two different isomers. TD-DFT calculations reveal that there are no low spin absorptions in the examined region of the UV/VIS spectrum, providing strong evidence that the observed MLCT transitions correspond to two distinct high spin complexes. Orbital energies reveal a stabilization from the low spin complex to the heptagonal coordinated high

spin complex. Comparing XA, IR(M)PD, and UV/VIS investigations reveal that the heptagonal coordinated complex always obtains the highest shift in each spectroscopic approach.

Temperature dependent XMCD studies of a complex with the structure $[\text{Mn}_3(\text{Hcht})_2(\text{bipy})_4]^{3+}$ reveal decreasing spin-, orbital- and total magnetic moments per Mn atom with rising temperature. The density of states calculations of the minimum structure show absorption edges for manganese ions in two different oxidation states. The first derivation of the XA spectra reveals polarized dependent absorption for different oxidation states in this complex. Broken symmetry calculations reveal almost identical energy for antiferromagnetically coupled and ferromagnetically coupled complexes. The calculations show an antiferromagnetic coupled Mn^{3+} ion and two ferromagnetic coupled Mn^{2+} ions, as well as one Mn^{2+} anticipated with a constant total magnetic coupling constant, implying an exchange coupling between just one Mn^{2+} ion and the Mn^{3+} ion in this combination. The calculated anisotropic tensors indicate a diminishing trend from a ferromagnetically coupled complex to an antiferromagnetically coupled complex. Therefore, a thermally induced spin-flip to an antiferromagnetically coupled complex can explain a lower orbital magnetic momentum by rising temperature. The crystal field splitting delivers possible absorption bands of this complex in the UV/VIS spectrum, which are in good agreement with the calculated UV/VIS spectrum.

Mass spectra of the complexes with the structure $[\text{M}_2\text{Ln}(\text{HVab})(\text{Vab})_3(\text{NO}_3)]^{2+}$ ($\text{M} = \text{Co}^{2+}, \text{Cu}^{2+}$, $\text{Ln} = \text{Dy}^{3+}, \text{Gd}^{3+}, \text{Nd}^{3+}, \text{Sm}^{3+}, \text{Tb}^{3+}$) reveal a mass, which is three mass units lower than expected. Deuteration of the complex leads to mass spectra, pointing out a mass that is only one mass unit heavier than without deuteration. The characterization of this complex series via CID reveals different gas phase stabilities by variation of the lanthanides with constant transition metals. Also, the change of the transition metal from Cobalt to Copper leads to a variation of the gas phase stabilities. Electron Transfer Dissociation (ETD) changes the gas phase stabilities but not the fragmentation pattern. IR(M)PD studies of this series of complexes point out two different isomers in complexes containing Cobalt as transition metals. We can assign the isomers in a mixed-valence state ($\text{Co}^{2+/3+}$) compared with calculated linear absorption spectra. Copper complexes leads to two isomers, however the isomer with a free hydroxyl group is less abundant than in the Cobalt analoga. DFT calculations reveal complexes with mixed-valence

states as minimum structure. The various isomers of these complexes can only be formed by changing the location of the hydrogen in order to form an O-H bonding condition. Simulation of the XA spectra for the Cobalt complexes results in approximated crystal field splitting, suggesting approximated electronic transitions for the UV/VIS spectra. These low lying electronic transitions might be present by overlaying the hydrogen bonded hydroxyl group in one isomer. These electronic transitions are not observed in the Cooper complexes.

Theoretical investigations of a model complex for nitrogenase activities, abbreviated [MoFe], published by Kowalska, raise concerns. DFT calculations reveal a cubane system with two Fe²⁺ ions and one Fe³⁺ in a high spin state, but the published XA spectra did not feature an absorption pattern of a Fe³⁺ ion. Together with electron localized field plots, a delocalized electron between two Fe²⁺ can be excluded. Simulations of the XA spectra with iron in different oxidation states indicate that the published XA spectrum should show features of the different iron atoms in this complex. The calculated spin-orbit couplings (SOC) from the core to the valence hole match the observed SOC well. The delocalized electron seems to be more positioned between one Fe²⁺ and one Fe³⁺ ion, and resonant absorption of x-ray photons results in a spectral pattern of a Fe²⁺ ion. An anti Hund'sche rule at the Mo³⁺ ion does not apply, other than predicted before. Natural bond order calculations of the cubane system and the symmetric model system reveal a lowered dx²-y² orbital of the Mo³⁺ ion in the cubane system. By applying the Hund'sche rules, the energetic lowest orbital has to be doubly occupied.

In the described CID studies, preliminary examinations of the complex with the structure [Mn₇(Vab)₆]²⁺ suggest the loss of a methyl group as the predominant fragmentation route. Calculating non covalent interactions reveal strong van der Waals interaction in the star-shaped Mn₇ core, which explains the high stability in the complex. Broken symmetry calculations reveal an antiferromagnetic exchange coupling for three manganese ions, suggesting a reduced spin magnetic exchange coupling. The calculated minimum structure has the largest anisotropic tensor compared to the ferromagnetically coupled complex. Also, the relative energies are within the typical uncertainties of DFT calculations. Therefore, no determination of the favored spin configuration is possible. The calculations hint a possible "spin flip" from an antiferromagnetically coupled complex to a ferromagnetic coupled one.

The development of a novel ion source to facilitate the adsorption of small molecules onto cluster surfaces proceeded successfully. A broad cluster distribution was reported once the home-built mass spectrometer was operational again and contaminants were removed. By leaking Nitrogen into the ion source, the adsorption of these molecules onto tantalum clusters is observed. Compared with earlier experiments from the FRITZ FTMS setup, we observe the same amount of Nitrogen adsorbed to the different clusters.

The presented work shows that gas phase investigations are good techniques for magnetic, structural, or electronics in transition metal complexes void from external effects such as packing or solvation.

In future experiments for the μ -oxo bridged complexes, a variation of the metal atoms in the M_3O core seems necessary. Because of the effect of their magnetic behavior and electronic ground state, heteroleptic compounds, in addition to homoleptic compounds, are a field of high interest for all various spectroscopic methods. Further IR(M)PD investigations using a free electron laser (FEL) in the 400-1200 cm^{-1} range are essential for the complexes given in this study to further identify the distortion in the M_3O core. Also, the investigation of the spin and orbital magnetic moments per atom in different homo- and heteroleptic metal complexes could reveal a better insight into the magnetic exchange coupling of such spin frustrated complexes. Temperature dependent measurements of these complexes would also be relevant in order to rule out a thermal influence of the exchange coupling via increasing entropy.

Regarding spin-crossover complexes magnetic field dependent, XMCD experiments would be helpful to determine the spin orientation change and the effect of the observed spin-crossover in the complex. The presented IR(M)PD spectra of the complex presented in this work are recorded at room temperature. IR(M)PD spectra cold conditions would reduce the high spin complex, and a better determination of the low spin complex would be possible. Temperature-dependent IR(M)PD spectra would also lead to an approximated temperature where the spin-crossover occurs. UV/VIS spectra in gas phase would also help gain a better insight into the different isomers in the spin forbidden area due to higher laser power. Furthermore, the investigation of spin-crossover complexes could be expanded from mononuclear complexes to di- and trinuclear complexes with such unique magnetic behavior.

The investigation of complexes with single molecule magnetic behavior is fascinating. The complex with the structure $[\text{Mn}_3(\text{Hcht})_2(\text{bipy})_4]^{3+}$ seems to be a good candidate for field dependent XMCD experiments due to its thermal induced spin flip. A different magnetic field could result in a slightly different spin- and orbital magnetic moments of this complex by changing the orientation of the unpaired electrons in the external applied magnetic field. Furthermore, structural determination of the complex in gas phase via IR(M)PD has not been performed yet. The structural properties may lead to further insight into the magnetic properties related to their structural properties. Gas phase UV/VIS experiments are necessary to determine the electronic ground state in this complex.

The complexes with the general structure $[\text{M}_2\text{Ln}(\text{HVab})(\text{Vab})_3(\text{NO}_3)]^{2+}$ ($\text{M} = \text{Co}, \text{Cu}$; $\text{Ln} = \text{Dy}, \text{Gd}, \text{Nd}, \text{Sm}, \text{Tb}$) presented in this work were characterized by their structural properties. The region between 1000 and 2000 cm^{-1} reveals only two bands, and further two color IR(M)PD measurements seem to be necessary for this complex series. The calculated IR spectra reveal more bands, which might assist in a better determination of the structure in these complexes. In the cobalt complexes also the determination of the different isomers is more proficient. This series of complexes should obtain single molecule magnetic behavior. Therefore temperature and field dependent XMCD experiments need to be performed. In combination with UV/VIS experiments, the determination of the magnetism with their corresponding ground state might lead to a better insight into the single molecule magnetic behavior in such complexes. Also, calculations including anharmonicity seem necessary for these complexes to precisely determine the energy and vibrational modes in the IR(M)PD spectra. Broken symmetry calculations of these complexes will lead to an approximation of the magnetic exchange coupling and their anisotropic barriers in the minimum structure. Combining the magnetic moments per atom with the broken symmetry calculated structures, a better explanation of the SMM behavior should be possible.

In the comment of the nitrogenase complex structural characterization via CID and IR(M)PD seems necessary. The exchange of the chloride ligands to a hydroxyl or acetate ligand would lead to an antenna, and a change in the Oxidation state should lead to a change in their vibrational modes. Investigations of the model complex with UVPD can help to determine the electronic ground state and also confirm the position of the delocalized electron near the Fe^{3+} ion. Further femtosecond experiments may help to understand the dynamic processes by

absorption of photons to such complexes. Also, field and temperature dependent XA experiments to determine the magnetic properties in such cubane complexes and their changes could help gain a better insight into nitrogenase-like complexes.

A repeated synthesis of the complex with the structure $[\text{Mn}_7(\text{Vab})_6](\text{NO}_3)_2$ seems mandatory to reproduce and confirm the current findings. IR(M)PD investigations were performed, but the complex did not start fragmentation due to efficient IVR processes. In the future, two color IR(M)PD investigations seem necessary to investigate the structure. Also, UVPD spectra can help to determine the electronic ground state of this complex. The calculations reveal a broad MLCT transition with a single main peak and two small shoulders. Also, temperature and field dependent XMCD studies must be performed to confirm the predicted exchange coupling in the complex. Also, the change of the transition metal to Cobalt or iron could be interesting for determining the magnetic properties in such complexes. The mixture of different transition metals with a combination of ferromagnetic and diamagnetic metal ions would inhibit the predicted exchange coupling as a reference system.

The modified laser vaporization ion source with a pick-up unit must be mounted to our FT-ICR mass spectrometer to verify the presented results within the instrument. This would enable the coadsorption of small molecules onto the cluster surface of interest, e.g., ammonia synthesis. Also, it would be possible to adsorb three different molecules onto different transition metal clusters. One of these molecules could adsorb directly by letting gas into the pick-up, the other one in the hexapole ion trap, and the last molecule could be adsorbed in the Infinity cell of the modified FT-ICR. IR(M)PD experiments and kinetic studies of the adsorbates seem necessary and could give a deeper insight into the surface of transition metal clusters.

The present work documents multiple studies of mono- and multinuclear transition metal complexes in terms of their magnetic, electronic, and structural properties. A good progress has been made in their characterization and paves the way for a better understanding of further studies of complexes with similar properties as described in this work.

Zusammenfassung und Ausblick

Die vorliegende Arbeit umfasst Untersuchungen von Übergangsmetallkomplexen im Hinblick auf ihre magnetischen, elektronischen und strukturellen Eigenschaften, wenn sie als isolierte Spezies durch Elektrospray-Ionisation (ESI) hergestellt werden. Die Fixierung der Proben in einer Ionenfalle ermöglicht die Erforschung verschiedener intrinsischer Eigenschaften dieser Komplexe, die von externen Effekten wie z.B. Kristallpackung, Volumen- und Solvatationseffekten unabhängig sind.

Magnetische Momente isolierter Komplexe, die magnetische Effekte, wie z.B. Spinfrustration, Spin-Crossover und magnetisches Einzelmolekülverhalten, zeigen, wurden mittels Röntgenmagnetischer Zirkulardichroismus (XMCD) in der Gasphase in Kombination mit Summenregelanalyse untersucht. Dadurch können die gesamten magnetischen Momente in ihre spin- und orbitalmagnetischen Beiträge getrennt werden. Alle XMCD-Experimente wurden an der "Ion Trap" Apparatur durchgeführt, die an die UE52-PGM Soft X-ray Beamline an der Synchrotronanlage BESSY II des Helmholtz-Zentrums für Materialien und Energie GmbH in Berlin angeschlossen ist. Röntgenabsorptionssimulationen (XA), Dichtefunktionaltheorie (DFT) kombiniert mit Broken-Symmetrieberechnungen ergänzen die Experimente und tragen zu einem besseren Verständnis der magnetischen Eigenschaften bei.

Die Untersuchung der Schwingungseigenschaften erfolgte mit Infrarot (Mehrfach) Photonendissoziation (IR(M)PD) Spektroskopie. Die Experimente wurden mit einem modifizierten Amazon SL Paul-Fallen Massenspektrometer in Kombination mit einem breitbandigen Laservision OPO/OPA-Lasersystem durchgeführt, das einen Spektralbereich von 1000-4000 cm^{-1} abdeckt. DFT-Berechnungen dienen der Bestimmung der Minimumstruktur und weiteren Berechnungen der linearen harmonischen Absorptionsspektren.

Die elektronischen Eigenschaften der isolierten Komplexe wurden mit Ultraviolett-Photodissoziations-Spektroskopie (UVPD) untersucht. Diese Experimente wurden mit einem modifizierten Amazon Speed Instrument in Kombination mit einem diodengepumpten Wyvern-Lasersystem (KMLabs) durchgeführt. Der Versuchsaufbau ist ähnlich wie bei den

IR(M)PD-Experimenten. TD-DFT Berechnungen dienen zur Bestimmung der elektronischen Struktur in Übergangsmetallkomplexen.

XMCD Untersuchungen an spinfrustrierten dreikernigen 3d-Metallkomplexen mit der Struktur $[\text{Fe}_3\text{O}(\text{OAc})_6(\text{py})_{0-3}]^+$ dienen als Modellsysteme und lieferten Einblicke in ihre Spin- und Orbitalbeiträge durch die Koordination von Pyridin an den Komplex. Bei symmetrischen Komplexen ($n = 0, 3$) wird eine antiferromagnetische Austauschkopplung beobachtet und eine zunehmende ferromagnetische Austauschkopplung mit steigender Verzerrung des Fe_3O -Kerns beobachtet. Durch die Koordination von Pyridin steigen die Kristallfeldaufspaltungen dieser Komplexe, bis die Symmetrie wiederhergestellt ist. Die berechnete Zustandsdichte zeigt koordinationsabhängige Absorptionskanten. Die Pyridin Koordination führt zu höheren Orbitalenergien und damit zu einer höheren ferromagnetischen Austauschkopplung, bis die Symmetrie wiederhergestellt ist. Die Änderung des magnetischen Kopplungsschemas geht mit einer Änderung des Fe-O-Fe-py_n Winkels einher, während die Bindungsabstände nicht beeinflusst werden. Gasphasen-UVPD-Experimente an den Komplexen mit der Struktur $[\text{Fe}_3\text{O}(\text{OAc})_6(\text{py})_{0-3}]^+$ zeigen eine starke Rotverschiebung im Vergleich zu den Spektren der Lösungsmittelphase. Dies weist darauf hin, dass Solvatationseffekte in der kondensierten Phase eine wichtige Rolle spielen.

Eine Korrelation mit der Änderung des Winkels und der Absorptionsenergien ergibt eine nahezu lineare Abhängigkeit, bis die Koordination des dritten Pyridins hinzukommt. Alle Übergänge in den UVPD-Spektren werden als HOMO-LUMO-Übergänge bestimmt. Eine nicht-klassische Bindungssituation kann die Verschiebung in den UVPD-Spektren aufgrund der nicht-kovalenten Pyridin Wechselwirkungen mit dem Komplex erklären. Aus den vorgestellten XA- und UVPD-Spektren von $[\text{Fe}_3\text{O}(\text{OAc})_6(\text{py})_{0-3}]^+$ ist eine Korrelation der Kristallfeldaufspaltungen und der Absorptionsenergien innerhalb eines Tanabe-Sugano-Diagramms möglich. Beide Spektren zeigen den gleichen Trend in ihrer Energieverschiebung je nach spektroskopischem Ansatz. Die Verschiebungen in beiden spektroskopischen Ansätzen zeigen direkt eine lineare Abhängigkeit von seinem Grundzustand. Die relative Verschiebung in den UVPD-Spektren im Vergleich zu den magnetischen Gesamtmomenten des Komplexes weist ebenfalls auf eine fast lineare Korrelation für $n = 0-2$ hin. DFT-Berechnungen mit einer Variation des axialen Liganden zeigen keine Veränderungen in der Verzerrung des Fe_3O -Kerns,

aber eine Veränderung der nicht-kovalenten Wechselwirkungen, die bei kleinen Molekülen, z. B. Stickstoff, schwach sind und bei größeren Molekülen wie Pyridin an Stärke gewinnen. Der Wechsel des verbrückenden Liganden von Acetat zu Benzoat führt nicht zu einer Veränderung der geometrischen Struktur des Fe₃O-Kerns. Der Wechsel des zentralen Sauerstoffatoms zu Schwefel führt zu einer deutlichen Veränderung des Komplexes.

Die strukturelle Charakterisierung von Komplexen mit der Struktur [Ru₃O(OAc)₆(py)₀₋₃]⁺ dient als weitere Untersuchung, indem das Metall von Fe³⁺ (HS) zu Ru³⁺ (LS) ausgetauscht wird. Der Einfluss in diesen Komplexen unterscheidet sich deutlich von dem in den früheren Studien mit [Fe₃O(OAc)₆(py)₀₋₃]⁺. Wir beobachten einen hochsymmetrischen Komplex für den nackten Komplex und mit steigender Pyridinkoordination werden zwei zusätzliche asymmetrische CO-Streckungen beobachtet. Wir beobachten einen leicht verzerrten Komplex mit einem schwachen asymmetrischen CO-Streckschwingungs moden für die Koordination von drei Pyridinen an den Komplex. Die Berechnungen stehen in guter Übereinstimmung mit den experimentellen R(M)PD-Spektren. Theoretische UV Spektren führen zu Absorptionsbanden, die zu angenäherten Kristallfeldaufspaltungen dieser Komplexe führen, die kleiner sind als bei den Eisen analoga. Berechnungen mittels Broken Symmetry zeigen keine Änderung der antiferromagnetischen Austauschkopplung in jeder Koordination.

Die Untersuchung von Spin-Crossover-Prozessen in isolierten Übergangsmetallkomplexen mittels XMCD hilft, den molekularen Übergang in ihrer Orbitalbesetzung besser zu verstehen. [Fe(btppa)]²⁺ diene in dieser Arbeit als Modellsystem. Temperaturabhängige XMCD-Experimente zeigen, dass die Spin-, Orbital- und Gesamtmagnetmomente pro Fe-Atom mit steigender Temperatur abnehmen. Der Effekt ist von einer Ionenfallentemperatur von 15 K bis 25 K schwächer als der Effekt von 4 K bis 15 K. Die Annäherung an die Brillouin-Funktion führt zu signifikant wärmeren Ionen von etwa 10 K und es kann eine Annäherung an ein High-Spin/Low-Spin-Gemisch bestimmt werden. Die Spektren zeigen unterschiedliche Kristallfeldaufspaltungen für eine bestimmte Temperatur. DFT Berechnungen sagen auch drei Minimalstrukturen voraus, zwei oktaedrische Komplexe und eine quasi siebenfach koordinierte Struktur. Zum Nachweis von drei verschiedenen Isomeren in [Fe(btppa)]²⁺ wurden Gasphasen-IR(M)PD-Spektren und CID Zerfallskurven aufgenommen. Die drei vorhergesagten Minimalstrukturen können dem IR(M)PD-Spektrum zugeordnet werden, verglichen mit den mit DFT berechneten linearen Absorptionsspektren der entsprechenden Minimalstruktur.

Übergangszustandsberechnungen deuten darauf hin, dass der quasi heptagonal koordinierte high spin komplex aus dem oktaedrischen high spin komplex und nicht direkt aus dem low spin komplex gebildet wird. Eine Aggregation von Metallacetaten zum Komplex ist möglich, was bedeutet, dass der heptagonal koordinierte Komplex vorhanden sein muss. Durch den Vergleich mit CID-Kurven konnten wir die Gasphasenstabilität für diese Komplexreihe bestimmen. Der Vergleich der XA-Spektren in der Gasphase mit den UV/VIS-Spektren in der Lösungsmittelphase zeigt unterschiedliche Absorptionskanten bzw. zwei unterschiedliche Absorptionsbanden im UV/VIS für $[\text{Fe}(\text{btpa})]^{2+}$. Eine Korrelation innerhalb eines Tanabe Sugano Diagramms weist darauf hin, dass es sich um zwei verschiedene Isomere handeln muss. TD-DFT Berechnungen bestätigen, dass es im untersuchten Bereich des UV/VIS Spektrums keine Absorptionen des low spin Komplex gibt, was ein starker Beweis dafür ist, dass die beobachteten MLCT-Übergänge zu zwei verschiedenen high spin Komplexen gehören. Die Orbitalenergien zeigen eine Stabilisierung von dem low spin Komplex zu dem heptagonal koordinierten high spin Komplex. Der Vergleich von XA-, IR(M)PD- und UV/VIS-Untersuchungen zeigt, dass der heptagonal koordinierte Komplex bei jedem spektroskopischen Ansatz die höchste Verschiebung aufweist.

Temperaturabhängige XMCD-Studien eines Komplexes mit der Struktur $[\text{Mn}_3(\text{Hcht})_2(\text{bipy})_4]^{3+}$ zeigen mit steigender Temperatur abnehmende Spin-, Orbital- und Gesamtmagnetmomente pro Mn Atom. Die Zustandsdichteberechnungen der Minimumstruktur zeigen Absorptionskanten für Mangan Ionen in zwei verschiedenen Oxidationsstufen. Die erste Ableitung der XA Spektren zeigt eine polarisationsabhängige Absorption für verschiedene Oxidationszustände in diesem Komplex. Broken Symmetry Berechnungen zeigen fast ähnliche Energien für die antiferromagnetisch gekoppelten und ferromagnetisch gekoppelten Komplexe. Die Berechnungen zeigen auch ein antiferromagnetisch gekoppeltes Mn^{3+} Ion und zwei ferromagnetisch gekoppelte Mn^{2+} Ionen. Außerdem wird ein Mn^{2+} mit einer konstanten magnetischen Gesamtkopplungskonstante vorhergesagt, was auf eine Austauschkopplung nur zwischen einem Mn^{2+} Ion und dem Mn^{3+} Ion in diesem Komplex hindeutet. Die berechneten anisotropen Tensoren zeigen einen abnehmenden Trend vom ferromagnetisch gekoppelten Komplex zu einem antiferromagnetisch gekoppelten Komplex. Daher kann ein thermisch induzierter Spin-Flip zu einem antiferromagnetisch gekoppelten Komplex mit einem geringeren magnetischen Bahnmoment bei steigender Temperatur erklären. Die

Kristallfeldaufspaltung liefert mögliche Absorptionsbanden dieses Komplexes im UV/VIS-Spektrum, die in guter Übereinstimmung mit dem berechneten UV/VIS-Spektrum sind.

Massenspektren der Komplexe mit der Struktur $[M_2Ln(HVab)(Vab)_3(NO_3)]^{2+}$ ($M = Co^{2+}, Cu^{2+}$; $Ln = Dy^{3+}, Gd^{3+}, Nd^{3+}, Sm^{3+}, Tb^{3+}$) zeigen eine Masse, die drei Massen niedriger ist als erwartet. Die Deuterierung des Komplexes führt zu Massenspektren, die auf eine Masse hinweisen, die nur eine Masse schwerer ist als ohne Deuterierung. Die Charakterisierung dieser Komplexreihe mittels CID zeigt unterschiedliche Gasphasenstabilitäten durch Variation der Lanthanid Ionen mit konstanten Übergangsmetallen. Auch der Wechsel des Übergangsmetalls von Kobalt zu Kupfer führt zu einer Variation der Gasphasenstabilitäten. Die Elektronentransferdissoziation führt zu unterschiedlichen Gasphasenstabilitäten, verändert aber nicht das Fragmentierungsmuster. IR(M)PD-Studien dieser Komplexreihe weisen auf zwei verschiedene Isomere in Komplexen hin, die Kobalt als Übergangsmetall enthalten. Im Vergleich zu den berechneten linearen Absorptionsspektren können wir die Isomere einem gemischt-valenten Zustand ($Co^{2+/3+}$) zuordnen. Die kupferhaltigen Komplexe führen ebenfalls zu zwei verschiedenen Isomeren, aber das Isomer mit einer freien Hydroxylgruppe ist weniger präsent als in den Kobalt-Analoga. DFT-Berechnungen aller Komplexe zeigen Komplexe mit gemischt-valenten Zuständen als Minimumstruktur. Die verschiedenen Isomere dieser Komplexe entstehen nur durch Änderung der Wasserstoffposition, um eine O-H-Bindung aufzubauen. Die Simulation der XA-Spektren für die Kobaltkomplexe ergibt eine angenäherte Kristallfeldaufspaltung, was auf angenäherte elektronische Übergänge für die UV/VIS-Spektren schließen lässt. Diese tief liegenden elektronischen Übergänge könnten durch Überlagerung der wasserstoffgebundenen Hydroxylgruppe in einem Isomer vorhanden sein. Diese elektronischen Übergänge werden in den Cooper-Komplexen nicht beobachtet.

Theoretische Untersuchungen eines Modellkomplexes für die Nitrogenase-Prozesse mit dem Kürzel [MoFe], veröffentlicht von Kowalska, führen zu Fragen. DFT-Berechnungen zeigen ein kubisches System mit zwei Fe^{2+} Ionen und einem Fe^{3+} Ion im high spin Zustand, aber die veröffentlichten XA-Spektren zeigten kein Absorptionsmuster eines Fe^{3+} Ions. Zusammen mit den Darstellungen des lokalen Elektronenfelds kann ein delokalisiertes Elektron zwischen zwei Fe^{2+} Ionen ausgeschlossen werden. Simulationen der XA-Spektren mit Eisen in verschiedenen Oxidationsstufen deuten darauf hin, dass das veröffentlichte XA-Spektrum Merkmale der verschiedenen Eisenatome in diesem Komplex zeigen sollte. Die berechneten Spin Orbit

Kopplungen (SOC) vom Kern zum Valenzloch zeigen eine gute Übereinstimmung mit den experimentellen SOC. Es scheint, dass sich das delokalisierte Elektron eher zwischen einem Fe^{2+} und einem Fe^{3+} Ion befindet, und die resonante Absorption der Röntgenphotonen dazu führt, dass das Spektrum einem Fe^{2+} Ion ähnelt. Eine Anti-Hund'sche Regel am Mo^{3+} Ion ist nicht wie vorhergesagt gegeben. NBO Rechnungen des Cuban-Systems und des symmetrischen Modellsystems zeigen ein abgesenktes $d_{x^2-y^2}$ Orbital des Mo^{3+} Ions im Cuban-System. Unter Anwendung der Hund'schen Regeln muss das energetisch niedrigste Orbital doppelt besetzt sein.

Erste Untersuchungen des Komplexes mit der Struktur $[\text{Mn}_7(\text{Vab})_6]^{2+}$ zeigen in den vorgestellten CID-Experimenten den Verlust einer Methylgruppe als Hauptfragmentierungskanal. Berechnungen nicht kovalenter Wechselwirkungen zeigen eine starke van der Waals Wechselwirkung im sternförmigen Mn_7 Kern, was die hohe Stabilität des Komplexes erklärt. Broken Symmetry Berechnungen zeigen eine antiferromagnetische Austauschkopplung für drei Mangan Ionen, was auf eine reduzierte Spin magnetische Austauschkopplung hindeutet. Die berechnete Minimumstruktur weist auf den höchsten anisotropen Tensor im Vergleich zum ferromagnetisch gekoppelten Komplex auf. Auch die relativen Energien liegen innerhalb der typischen Unsicherheiten von DFT Berechnungen. Daher ist keine Bestimmung der bevorzugten Spin Konfiguration möglich. Die Berechnungen deuten auf einen möglichen "Spin-Flip" von einem antiferromagnetisch gekoppelten Komplex zu einem ferromagnetisch gekoppelten Komplex hin.

Die Entwicklung einer neuen Ionenquelle, die einen leichteren Zugang für die Adsorption kleiner Moleküle an Clusteroberflächen ermöglicht, verlief gut. Nachdem das selbstgebaute Massenspektrometer wieder funktionsfähig und von Verunreinigungen befreit war, wurde eine breite Clusterverteilung aufgezeichnet. Durch Einleiten von Stickstoff in die Ionenquelle wird die Adsorption dieser Moleküle an Tantal Cluster beobachtet. Im Vergleich zu früheren Experimenten mit dem FRITZ FTMS beobachten wir die gleiche Menge an Stickstoff, die an den verschiedenen Clustern adsorbiert wird.

Die vorgestellten Arbeiten zeigen, dass Gasphasenuntersuchungen gute Techniken für magnetische, strukturelle oder elektronische Untersuchungen von

Übergangsmetallkomplexen sind, die von externen Effekten wie Packung oder Solvation unabhängig sind.

In zukünftigen Experimenten für die μ -Oxo-verbrückten Komplexe scheint eine Variation der Metallatome im M_3O -Kern notwendig. Neben homoleptischen Verbindungen sind auch heteroleptische Verbindungen aufgrund des Einflusses ihres magnetischen Verhaltens und ihres elektronischen Grundzustandes von großem Interesse für alle verschiedenen spektroskopischen Ansätze. Für die in dieser Arbeit vorgestellten Komplexe scheinen weitere IR(M)PD-Experimente im Bereich von $400\text{-}1200\text{ cm}^{-1}$ mit einem Freie-Elektronen-Laser (FEL) notwendig, um die Verzerrung im M_3O Kern besser zu bestimmen. Auch die Untersuchung der magnetischen Spin- und Bahnmomente pro Atom in verschiedenen homo- und heteroleptischen Metallkomplexen könnte einen besseren Einblick in die magnetische Austauschkopplung solcher Spin frustrierter Komplexe geben. Temperaturabhängige Messungen dieser Komplexe wären ebenfalls interessant, um einen thermischen Effekt der Austauschkopplung durch Erhöhung der Entropie auszuschließen.

Im Hinblick auf magnetfeldabhängige Spin-Crossover-Komplexe wären XMCD Experimente interessant, um die Änderung der Spin Orientierung und die Auswirkungen des beobachteten Spin-Crossover im Komplex zu bestimmen. Die IR(M)PD Spektren des in dieser Arbeit vorgestellten Komplexes wurden bei Raumtemperatur aufgenommen. IR(M)PD-Spektren unter kalten Bedingungen würden den Komplex mit hohem Spin reduzieren, und eine bessere Bestimmung des Komplexes mit niedrigem Spin wäre möglich. Temperaturabhängige IR(M)PD-Spektren würden auch zu einer angenäherten Temperatur führen, bei der der Spin-Crossover stattfindet. UV/VIS-Spektren in der Gasphase würden aufgrund der höheren Laserleistung ebenfalls einen besseren Einblick in die verschiedenen Isomere im Spin verbotenen Bereich ermöglichen. Darüber hinaus könnte die Untersuchung von Spin-Crossover Komplexen von einkernigen Komplexen auf zwei- und dreikernige Komplexe mit diesem einzigartigen magnetischen Verhalten ausgeweitet werden. Die Untersuchung von Komplexen mit magnetischem Einzelmolekülverhalten ist faszinierend. Der Komplex mit der Struktur $[Mn_3(Hcht)_2(bipy)_4]^{3+}$ scheint ein guter Kandidat für feldabhängige XMCD-Experimente zu sein, da er einen thermisch induzierten Spin-Flip aufweist. Ein anderes Magnetfeld könnte zu leicht veränderten Spin- und Bahnmomenten dieses Komplexes führen, indem die Orientierung der ungepaarten Elektronen im externen Magnetfeld verändert wird.

Darüber hinaus ist die Strukturbestimmung des Komplexes in der Gasphase mittels IR(M)PD noch nicht durchgeführt worden. Die strukturellen Eigenschaften könnten zu weiteren Erkenntnissen über die magnetischen Eigenschaften führen, die mit ihren strukturellen Eigenschaften zusammenhängen. UV/VIS-Experimente in der Gasphase sind notwendig, um den elektronischen Grundzustand in diesem Komplex zu bestimmen.

Die in dieser Arbeit vorgestellten Komplexe mit der allgemeinen Struktur $[M_2Ln(HVab)(Vab)_3(NO_3)]^{2+}$ ($M = Co, Cu$; $Ln = Dy, Gd, Nd, Sm, Tb$) werden durch ihre strukturellen Eigenschaften charakterisiert. Der Bereich zwischen 1000 und 2000 cm^{-1} zeigt nur zwei Banden, so dass für diese Komplexreihe zwei Farben IR(M)PD-Messungen erforderlich zu sein scheinen. Die berechneten IR Spektren zeigen mehr Banden, was zu einer besseren Bestimmung der Struktur in diesen Komplexen führt.

Die Reihe von Komplexen sollte ein magnetisches Einzelmolekülverhalten aufweisen. Daher müssen temperatur- und feldabhängige XMCD Experimente durchgeführt werden. In Kombination mit UV/VIS Experimenten führt die Bestimmung des Magnetismus mit dem entsprechenden Grundzustand zu einem besseren Einblick in das magnetische Einzelmolekülverhalten in solchen Komplexen. Außerdem scheinen Berechnungen unter Einbeziehung der Anharmonizität für diese Komplexe notwendig zu sein, um die Energie und die Schwingungsmoden in den IR(M)PD Spektren genau zu bestimmen. Broken Symmetry Berechnungen dieser Komplexe führen zu einer Annäherung an die magnetische Austauschkopplung und ihre anisotropen Barrieren in der Minimumstruktur. Kombiniert man die magnetischen Momente pro Atom mit den berechneten Broken Symmetry Strukturen, sollte eine bessere Erklärung des SMM-Verhaltens möglich sein.

In der Stellungnahme zum Nitrogenase-Komplex wird eine strukturelle Charakterisierung mittels CID und IR(M)PD für notwendig erachtet. Der Austausch der Chlorid Liganden gegen einen Hydroxyl- oder Acetat-Liganden würde zu einer Antenne führen, und eine Änderung des Oxidationszustandes sollte zu einer Änderung ihrer Schwingungsmoden führen. Untersuchungen des Modellkomplexes mit UVPD können helfen, den elektronischen Grundzustand zu bestimmen und auch die Position des delokalisierten Elektrons in der Nähe des Fe^{3+} -Ions zu bestätigen. Weitere Femtosekunden Experimente können helfen, die dynamischen Prozesse bei der Absorption von Photonen in solchen Komplexen zu verstehen.

Auch feld- und temperaturabhängige XA-Experimente zur Bestimmung der magnetischen Eigenschaften in solchen Cuban Komplexen und ihrer Veränderungen könnten dazu beitragen, einen besseren Einblick in nitrogenaseartige Komplexe zu gewinnen.

Die Synthese des Komplexes mit der Struktur $[\text{Mn}_7(\text{Vab})_6](\text{NO}_3)_2$ muss erneut durchgeführt werden. IR(M)PD Untersuchungen wurden durchgeführt, aber der Komplex begann aufgrund effizienter IVR Prozesse nicht zu fragmentieren. In Zukunft scheinen zweifarbige IR(M)PD Untersuchungen notwendig, um die Struktur zu untersuchen. Auch UVPD Spektren können helfen, den elektronischen Grundzustand dieses Komplexes zu bestimmen. Die Berechnungen zeigen einen breiten MLCT Übergang mit einem Hauptpeak und zwei kleinen Schultern. Außerdem müssen temperatur- und feldabhängige XMCD Studien durchgeführt werden, um die vorhergesagte Austauschkopplung im Komplex zu bestätigen. Auch der Wechsel des Übergangsmetalls zu Kobalt oder Eisen könnte für die Bestimmung der magnetischen Eigenschaften in solchen Komplexen interessant sein. Die Mischung verschiedener Übergangsmetalle mit einer Kombination aus ferromagnetischen und diamagnetischen Metallionen würde die vorhergesagte Austauschkopplung als Referenzsystem hemmen.

Die modifizierte Laser-Vaporisations-Ionenquelle mit einer Pick-up-Einheit muss an unser FT-ICR Massenspektrometer montiert werden, um die präsentierten Ergebnisse innerhalb des Instruments zu verifizieren. Dies würde die Koadsorption kleiner Moleküle auf der Clusteroberfläche von Interesse ermöglichen, z. B. die Ammoniaksynthese. Außerdem wäre es möglich, drei verschiedene Moleküle an verschiedene Übergangsmetallcluster zu adsorbieren. Eines dieser Moleküle könnte direkt adsorbiert werden, indem Gas in den Pick-up geleitet wird, das andere in der Hexapol-Ionenfalle, und das letzte Molekül könnte in der Infinity-Zelle des modifizierten FT-ICR adsorbiert werden. IR(M)PD-Experimente und kinetische Untersuchungen der Adsorbate scheinen notwendig und könnten einen tieferen Einblick in die Oberfläche von Übergangsmetallclustern geben.

Die vorliegende Arbeit dokumentiert mehrere Studien von mono- und multinukleare Übergangsmetall Komplexen in Bezug auf ihre magnetischen, elektronischen und strukturellen Eigenschaften. Hierbei konnten sehr gute Fortschritte in deren Charakterisierung erzielt werden und ebnet den Weg für ein besseres Verständnis für weitere Untersuchungen von Komplexen mit ähnlichen Eigenschaften, wie in dieser Arbeit beschrieben wurden.

Appendices

Appendix I: IR(M)PD and CID investigations on a trimetallic Rhodium complex in isolation

Transition metal (TM) complexes have become a research field with high interest in different areas such as magnetism^[1-9], catalysis^[10-15], or biochemistry^[16-20]. In this case, fluoro complexes combined with late transition metals in low oxidation states show features that have attracted growing attention in the last few years^[21-25]. The presented complex obtains a triangular rhodium core. Two hydroxyl groups coordinate above and underneath to build up a trigonal bipyramidal structure. On each rhodium ion, a bidentate cyclooctadiene ligand coordinates to transition metal core. The netto charge is +1 and neutralizes by hydrofluoric acid (HF_2^-) as a counterion^[26].

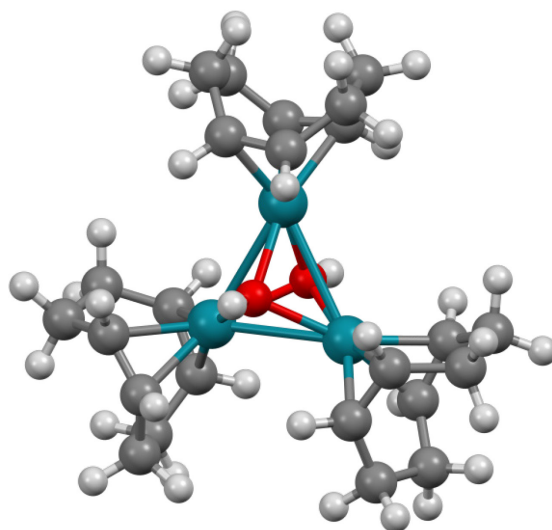


Fig. 1: Calculated minimum structure of $[\text{Rh}_3(\mu\text{-OH})_2(\text{COD})_3]^+$. The calculations were performed with Gaussian 09 at the B3LYP/cc-pVTZ (H, C, N, O) and ecp-28-mdf (Rh) level of theory.

Schwartzburd prepared a complex with the general structure $[\text{Rh}(\text{6-NHC})-(\text{PPh}_3)_2\text{H}]$ and performed catalytic hydrodefluorination of octafluorotoluene^[27]. They found a catalytic reaction at room temperature for this compound to afford cis and trans isomers of these fluoride complexes. This reformation is observed by heating the complex solution with protonated triethyl silane to triethylsilanefluorid.

Masciocchi synthesized the complex with the general structure $[\text{Rh}_3(\mu\text{-OH})_2(\text{COD})_3](\text{HF}_2)$, and this complex serves as starting point for further catalysis with Rh(I) and hydrofluoric acid^[26].

They performed *abinitio* X-ray powder diffraction methods for this complex and determined strong $\mu\text{-OH-HF}_2$ hydrogen bonding in the 1D chain. They also performed ^1H NMR spectroscopy and found three multiplets for the COD ligands but no peaks for the hydroxyl group in this complex. However, a broad peak is observed with lower temperatures, and they assume that this peak belongs to the hydrogen-bonded hydroxyl group.

Unfortunately, no further complex characterization was performed in solid state, solution, or gas phase. Masciocchi kindly provided the complex $[\text{Rh}(\mu\text{-OH})_2(\text{COD})_3](\text{HF}_2)$ for the characterization of the structure and their electronics in gas phase.

Electrospray ionization^[28, 29] gives access to mass spectrometric investigations of complexes in isolation and their geometrical structure by irradiation with IR photons. Tandem MS based methods have helped investigate complexes void from external effects, e.g., packing and solvation effects.

We combine experimental CID and IR(M)PD investigations of isolated $[\text{Rh}_3(\mu\text{-OH})_2(\text{COD})_3]^+$, $[\text{Rh}_3(\mu\text{-OD})_2(\text{COD})_3]^+$ and $[\text{Rh}_3(\mu\text{-OH})(\mu\text{-Cl})(\text{COD})_3]^+$ with quantum chemical calculations by Density Functional Theory (DFT).

Experimental setup and methods

ESI MS and CID measurements were performed with a quadrupole mass spectrometer (amazon ETD, Bruker daltonics), obtaining a Paul trap. The ions of interest are transferred into gas phase by electrospray ionization. The sample solution of $[\text{Rh}_3\text{O}(\mu\text{-OH})_2(\text{COD})_3](\text{HF}_2)$ ($c \sim 1 \cdot 10^{-6}$ mol/L) acetonitrile was constantly infused into the ESI chamber by a syringe pump with a flow rate of 180 $\mu\text{L/h}$. The deuterated and chloride complexes were prepared using 10 μL deuterated water or tetrabutylammonium chloride solution in the same concentration as the sample solution. Nitrogen was used as a drying gas with a flow rate of 12 L/min at 180 °C. The nebulize pressure was set to 280 mbar (4 psi) for spraying the sample solution, and the spray needle was held at 4.5 kV. The Paul trap consists of a ring electrode and two end caps forming a nearly hyperbolic inner profile. The end caps possess pinholes that allow to enter or exit the ions in the trap. The ring electrode is powered with a high voltage RF (radio frequency) potential (781 kHz) while the end caps are grounded.

The ions are accumulated in this resulting oscillating quadrupolar electric field generated from the three electrodes. An auxiliary dipolar voltage is fed to either the exit cap or both end caps for ion isolation and fragmentation. For providing a constant partial Helium buffer gas pressure of ca. 10^{-3} mbar inside the trap, a proportional integral derivative (PID) gas controller is used.

The recorded Collision Induced Dissociation (CID) breakdown curves were recorded by varying the excitation amplitudes (0.0 V–1.5 V). These amplitudes determine the internal energy scale of the mass spectrometer (E_{lab} in V). Relative abundances were calculated according to:

$$I_{tot}^{fr}(E_{lab}) = \left(\frac{\sum_i I_i^{fr}(E_{lab})}{\sum_i I_i^{fr}(E_{lab}) + \sum_i I_i^p(E_{lab})} \right) \quad (1)$$

where I_i^{fr} = intensity of the fragment ions and I_i^p = intensity of the parent ions. Center of mass transferred fragmentation amplitudes (E_{com}) were calculated from internal amplitudes by:

$$E_{com} = \left(\frac{m_{He}}{m_{He} + m_{ion}} \right) \cdot E_{lab} \quad (2)$$

where m_{ion} stands for the isotopically averaged mass of the molecular ion. Note that the current application of the CID technique by RF excitation in the presence of multiple collisions results in a so called “slow multi collision heating” mode of operation.

Fragmentation amplitude dependent CID spectra were modeled and fitted by sigmoidal functions of the type

$$I_{fit}^{fr}(E_{com}) = \left(\frac{1}{1 + e^{(E_{com}^{50} - E_{com}) B}} \right) \quad (3)$$

Using a least-squares criterion. The E_{com}^{50} fit parameter is the amplitude at which the sigmoid function is at half maximum value, whereas B describes the rise of the sigmoid curve. Due to the correlation of fragmentation amplitude and appearance energy, it is feasible to assume that the appearance curves can be associated with the relative stability.

InfraRed (Multiple) Photon Dissociation (IR(M)PD) experiments were performed using a modified Paul-type quadrupole ion trap mass spectrometer (Amazon SL, Bruker Daltonics) at room temperature. The ions of interest are transferred into gas phase by electrospray ionization. The sample solution was constantly infused into the ESI chamber by a syringe pump with a flow rate of 180 μ L/h. Nitrogen was used as a drying gas with a flow rate of 12 L/min at

180°C. The nebulize pressure was set to 280 mbar (4 psi) for spraying the sample solution, and the spray needle was held at 4.5 kV. The Paul trap consists of a ring electrode and two end caps forming a nearly hyperbolic inner profile. The end caps possess pinholes that allow to enter or exit the ions in the trap. The ring electrode is powered with a high voltage RF (radio frequency) potential (781 kHz) while the end caps are grounded. The ions are accumulated in this resulting oscillating quadrupolar electric field generated from the three electrodes. An auxiliary dipolar voltage is fed to either the exit cap or both end caps for ion isolation and fragmentation. For providing a constant partial Helium buffer gas pressure of ca. 10^{-3} mbar inside the trap, a proportional integral derivative (PID) gas controller is used.

Laser system

The laser pulses were generated using a KTP/KTA optical parametric oscillator/amplifier (OPO/OPA, LaserVision) system. A pulsed 10 Hz injection pumps the system seeded Nd³⁺:Yag laser (PL 8000, Continuum) and serves as source for tunable IR radiation. The difference frequency (DF) between the OPA signal and idler waves is generated within an AgGaSe₂ crystal, applied for the range between 1000 cm⁻¹ and 2000 cm⁻¹. The IR beam was guided and focused by 90° off-axis parabolic silver mirror with a focal length of 15 cm through the modified Paul-trap. After passing the Paul-trap, the IR beam was guided to a powermeter (Maestro, Gentech) to provide a constant laser power measurement. The experimental gained IR(M)PD spectra arise from the plot of the fragment yield as a function of the laser frequency (ν). The fragment yield is defined as:

$$Y(\nu) = \left(\frac{\sum_i I_i^{fr}(\nu)}{\sum_i I_i^{fr}(\nu) + \sum_i I_i^p(\nu)} \right) \quad (4)$$

Calibration of the IR frequency is done by a wavemeter (821B-NIR, Bristol instruments). The resulting power curves of the Laser are recorded parallel to the IR(M)PD experiments by digitizing the analog output of the laser power meter through a ADC input of the Amazon SL mass spectrometer. No normalization of the recorded spectra was done because there is an intrinsically nonlinear power dependence of the IR(M)PD fragmentation efficiencies.

Computational methods

Crystal structures of the complex with the structure $[\text{Rh}_3(\mu\text{-OH})_2(\text{COD})_3]^+$ serve as starting point for further calculations^[26]. For multiplicity dependent determination of the minimum structure, linear absorption spectra, and their corresponding weak interactions, we performed Density Functional Theory (DFT) calculations with B3LYP^[30, 31] functional and cc-pVTZ^[32] basis sets in combination with ecp-28-mdf^[33] core potential (Rh) in Gaussian 09 program package^[34]. The linear absorption spectra were scaled with 0.948. The line spectra were convoluted by GaussSum using a Lorentzian function with a full width of half maximum of 10 cm^{-1} .

Results and discussion

ESI mass spectra and Collision Induced Dissociation (CID)

The ESI mass spectra of these complexes reveal different masses at 667, 669, and 685 m/z (cf. Fig. 1). The complexes, which do not contain chloride, do not feature any isotopic pattern other than the carbon isotopes. With the change of one hydroxyl group, a characteristic isotope pattern for chloride is observed. The intensity decreased from the original complex with the change of the hydroxyl groups to deuterated or chloride groups. We do not observe an exchange from two hydroxyl groups to two chloride ligands. We assume that the exchange of chloride is not that efficient and leads to less intensity.

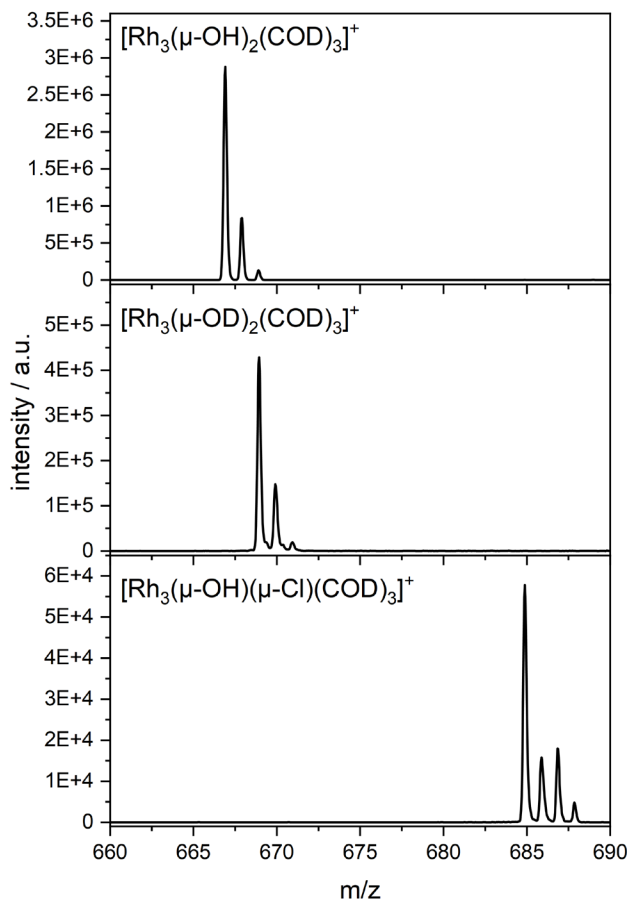


Fig. 2: ESI mass spectra of $[\text{Rh}_3(\mu\text{-OH})_2(\text{COD})_3]^+$ (top), $[\text{Rh}_3(\mu\text{-OD})_2(\text{COD})_3]^+$ (middle) and $[\text{Rh}_3(\mu\text{-OH})(\mu\text{-Cl})(\text{COD})_3]^+$ (bottom).

After isolation of the parent ion, we recorded Collision Induced Dissociation (CID) breakdown curves and their corresponding appearance curves of the fragments (cf. Fig. 2). The recorded CID breakdown curves reveal the loss of water as main fragmentation channel. After water loss, the complex starts deprotonating molecular hydrogen from the cyclooctadiene (COD) to cyclooctatriene (COT). Another deprotonation of the COD ligand takes part, and with higher excitation amplitudes, the loss of the second water appears. The last fragmentation channel observed in higher excitation amplitudes is the loss of one COT ligand in this complex. By exchanging the hydroxyl groups to deuterated groups or a chloride ligand, similar fragmentation channels are observed. With chloride, the primary fragmentation channel is not water loss but a loss of hydrochloric acid.

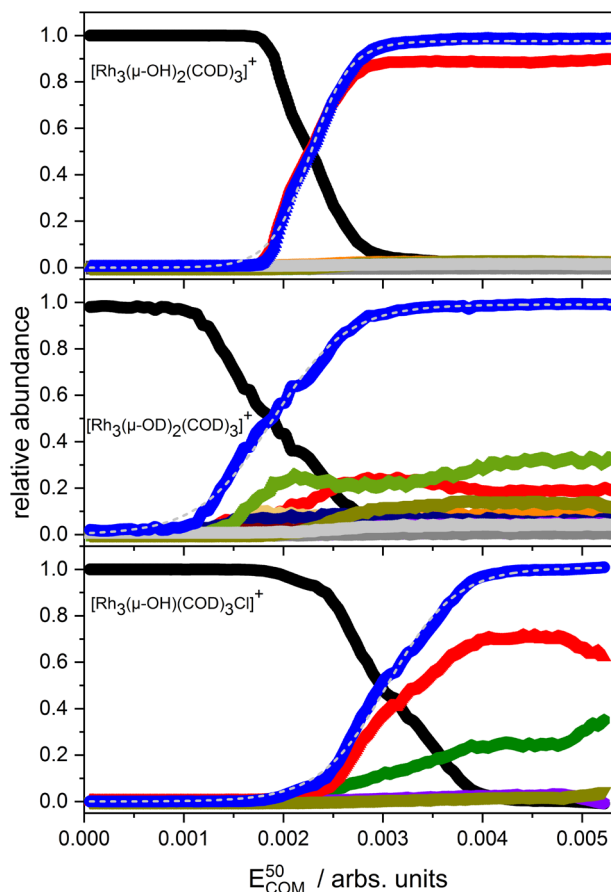


Fig. 3: CID breakdown curves of $[\text{Rh}_3(\mu\text{-OH})_2(\text{COD})_3]^+$, $[\text{Rh}_3(\mu\text{-OD})_2(\text{COD})_3]^+$ and $[\text{Rh}_3(\mu\text{-OH})(\mu\text{-Cl})(\text{COD})_3]^+$ and their appearance curves of the associated fragments.

The cross-section of the CID breakdown curves represents the relative gas phase stabilities of these complexes. We observe the highest stability with the exchange of a hydroxyl group (0.00227) to a chloride ligand (0.00305) and the lowest stability for the deuterated complex (0.00189) (cf. Fig. 2). Therefore, an exchange to a chloride ligand might lead to stronger bondings in the complex, enhancing the stability of the complex. On the other hand, the deuterated complex obtains the lowest gas phase stability because of the exchange with hydrogen in the complex.

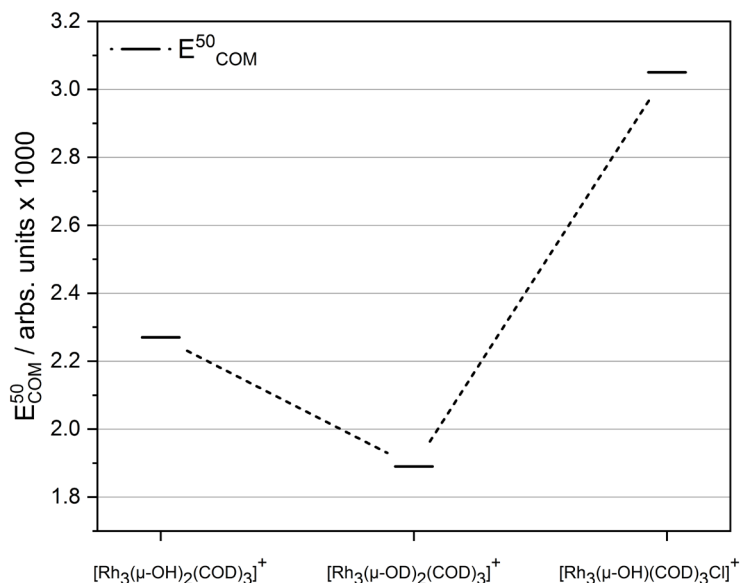


Fig. 4: Determined E_{COM}^{50} values of $[\text{Rh}_3(\mu\text{-OH})_2(\text{COD})_3]^+$, $[\text{Rh}_3(\mu\text{-OD})_2(\text{COD})_3]^+$ and $[\text{Rh}_3(\mu\text{-OH})(\mu\text{-Cl})(\text{COD})_3]^+$.

To better interpret the different gas phase stabilities, we performed calculations of the weak interactions^[35] in these complexes (cf. Fig. 5). Electron localized field (ELF) plots point out covalent bonding situations, and we observe stronger covalent bondings for the chloride complex than for the hydroxyl complexes. The chloride atom obtains a more diffuse electron distribution than the oxygen atoms. The non covalent interactions (NCI) point out non covalent interactions instead. The chloride complex also brings the highest non covalent interactions, leading to stronger bonding situations. The hydroxyl groups in the other complexes reveal similar covalent and non covalent interactions. The differential orbital covalency (DORI) plots show the interplay between the covalent and non covalent interactions. These plots reveal an attractive interplay between covalent and non covalent interactions. This is in good agreement with the experimental gas phase stabilities.

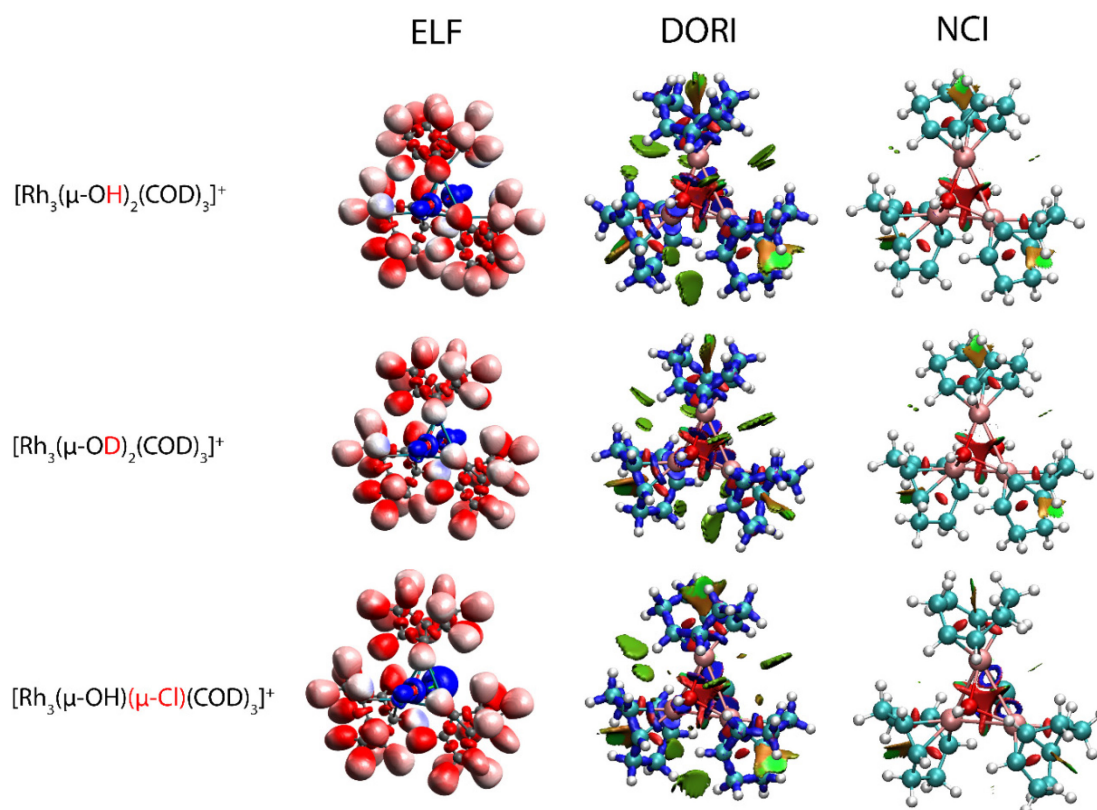


Fig. 5: Electron field localization (ELF), density orbital regions indicator (DORI), and non covalent interaction (NCI) plots of $[\text{Rh}_3(\mu\text{-OH})_2(\text{COD})_3]^+$, $[\text{Rh}_3(\mu\text{-OD})_2(\text{COD})_3]^+$ and $[\text{Rh}_3(\mu\text{-OH})(\mu\text{-Cl})(\text{COD})_3]^+$. The calculations were performed with Gaussian 09 at the B3LYP/cc-pVTZ (H, C, N, O) and ecp-28-mdf (Rh) level of theory. Hydrogen is omitted for clarity.

The exchange of the hydroxyl group leads to a change of the non covalent bonding situation, resulting in a higher gas phase stability. Electron localized field plots also reveal a stronger covalent bonding situation for the chloride complex than for the hydroxyl complex (cf. Fig. 6). These plots point out that the chloride obtains a broader and more diffuse electron density than the hydroxyl groups.

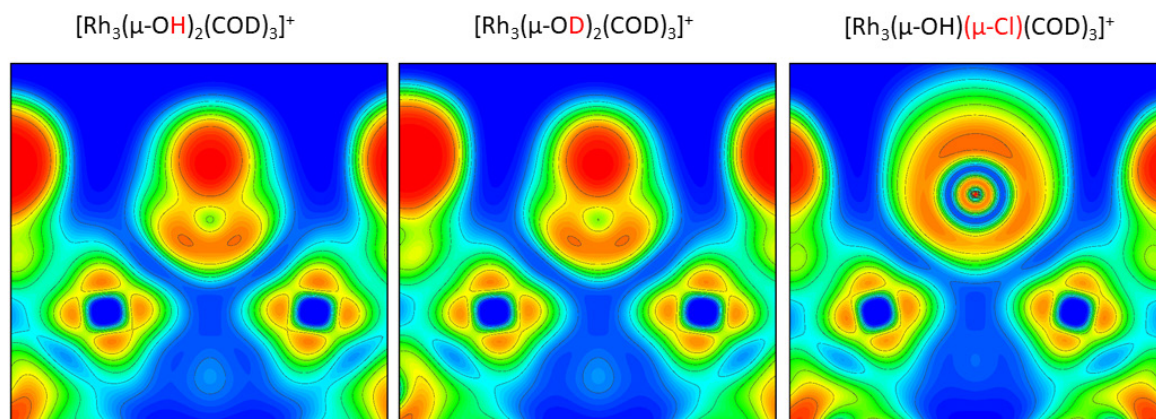


Fig. 6: Electron field localization (ELF) plots of $[\text{Rh}_3(\mu\text{-OH})_2(\text{COD})_3]^+$, $[\text{Rh}_3(\mu\text{-OD})_2(\text{COD})_3]^+$ and $[\text{Rh}_3(\mu\text{-OH})(\mu\text{-Cl})(\text{COD})_3]^+$ for the exchange of the ligand in these complexes. The calculations were performed with Gaussian 09 at the B3LYP/cc-pVTZ (H, C, N, O) and ecp-28-mdf (Rh) level of theory.

We do not observe a fragmentation of the rhodium triangle in these complexes. Therefore, we calculated two dimensional electronic localized field plots to determine the bonding situation of the rhodium triangle (cf. Fig. 6). These plots reveal similar stabilities for the different coordination of the ligands to the triangle. Therefore, we assume that the triangle's bondings are intense that no dissociation appears in the experiment. This also means that the different ligands' coordination does not affect the electron density in the transition metals.

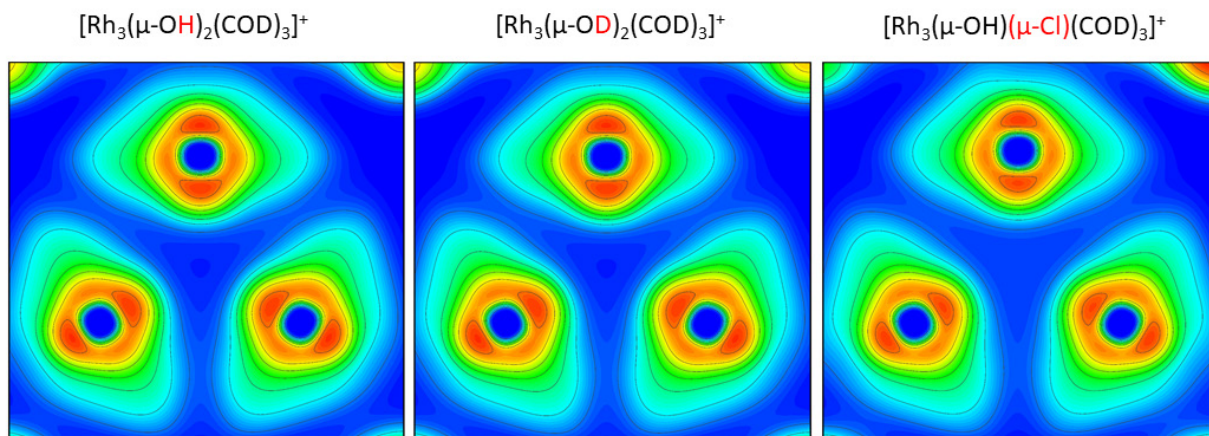


Fig. 7: Electron field localization (ELF) plots of $[\text{Rh}_3(\mu\text{-OH})_2(\text{COD})_3]^+$, $[\text{Rh}_3(\mu\text{-OD})_2(\text{COD})_3]^+$ and $[\text{Rh}_3(\mu\text{-OH})(\mu\text{-Cl})(\text{COD})_3]^+$. The calculations were performed with Gaussian 09 at the B3LYP/cc-pVTZ (H, C, N, O) and ecp-28-mdf (Rh) level of theory.

InfraRed (Multiple) Photon Dissociation (IR(M)PD)

We recorded an IR(M)PD spectrum of $[\text{Rh}_3(\mu\text{-OH})_2(\text{COD})_3]^+$ in comparison with calculated linear absorption spectra for all complexes (cf. Fig. 7). The minimum structure of these complexes predicts that all Rhodium ions in the complex are in a Low spin configuration without unpaired electrons resulting in a multiplicity of 1. We observe one band at 3621 cm^{-1} which belongs to the free OH stretching modes in the complex. This reveals a high symmetry in the complex due to degenerated hydroxyl stretching modes in the complex. The area between 2900 cm^{-1} and 3000 cm^{-1} belongs to the C-H stretching modes in the cyclooctadiene ligands. The vibrational mode at 2988 cm^{-1} belongs to the double-bonded carbon atom's symmetric C-H stretching modes in the COD ligands. The asymmetric stretching C-H modes of these double-bonded carbon atoms are at 2943 cm^{-1} . At 2925 cm^{-1} belongs to the asymmetric C-H stretching modes of the CH_2 units in the COD ligands. The symmetric C-H stretching modes of these CH_2 units are found at 2900 cm^{-1} . We also observe a vibrational mode at 2852 cm^{-1} which belongs to symmetric C-H stretching modes of the CH_2 units in just one COD ligand. We can exclude a rhodium triangle with a high spin configuration because the experimental IR(M)PD spectral pattern on the spectrum does not fit the calculated spectrum (cf. Fig. 7) in the C-H stretching modes.

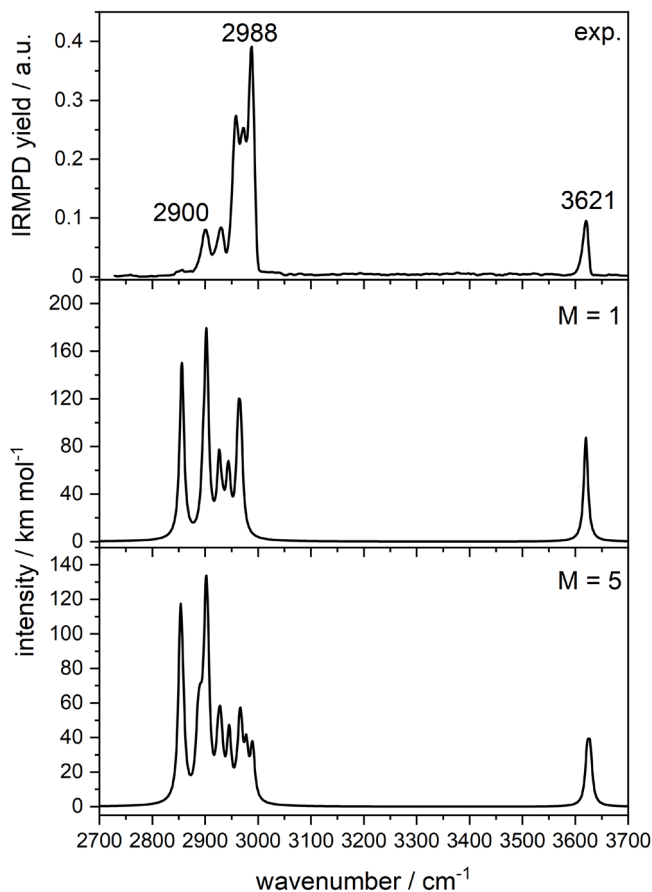


Fig. 8: IR(M)PD spectra (top) in comparison with calculated linear absorption spectra of $[\text{Rh}_3(\mu\text{-OH})_2(\text{COD})_3]^+$. The calculations were performed with Gaussian 09 at the B3LYP/cc-pVTZ (H, C, N, O) and ecp-28-mdf (Rh) level of theory.

With higher multiplicity, a degeneration of the C-H stretching modes is not given anymore, and more vibrational modes should be present in the experimental gained IR(M)PD spectrum. In addition, a small shoulder appears in the vibrational band at 2900 cm^{-1} , indicating a repeal of degeneration in the C-H stretching modes of the CH₂ units in the COD ligands, which is also not observed in the experimental spectrum.

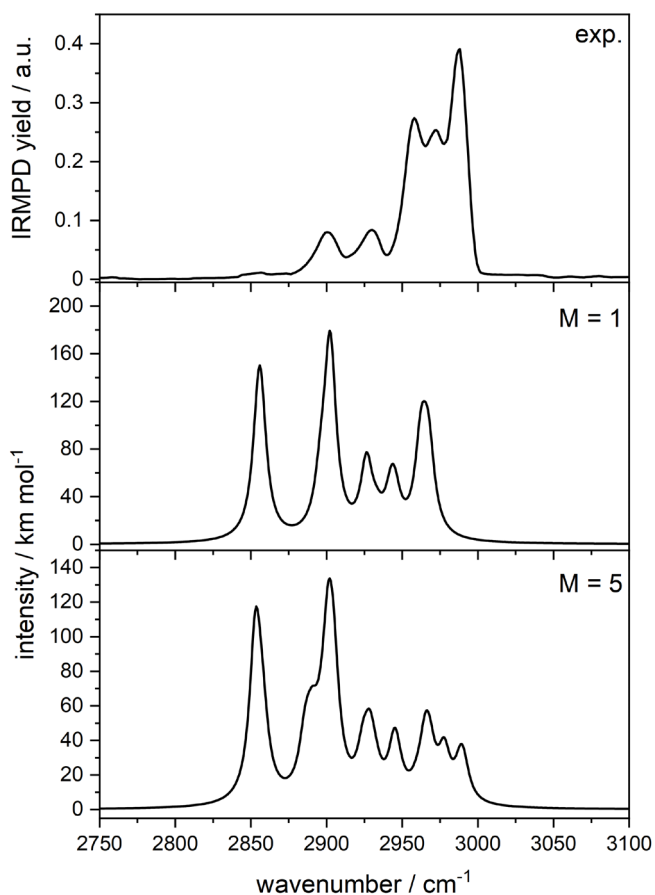


Fig. 9: IR(M)PD spectra (top) in comparison with calculated linear absorption spectra of $[\text{Rh}_3(\mu\text{-OH})_2(\text{COD})_3]^+$ in the region between 2750 cm^{-1} and 3100 cm^{-1} . The calculations were performed with Gaussian 09 at the B3LYP/cc-pVTZ (H, C, N, O) and ecp-28-mdf (Rh) level of theory.

The calculated spectra of the chloride complex reveal almost similar vibrational modes as the hydroxyl complex (cf. Fig. 9). The main difference is that the degeneration of C-H stretching modes is not given because the complex is not symmetric anymore. The deuterated complex reveals a band underneath 2800 cm^{-1} for the free O-D stretching modes. This band is also degenerated due to the symmetry of the complex. The band is more than 1000 cm^{-1} red shifted relative to the free O-H stretching modes but earlier studies observed similar behavior in nonmetallic investigations^[36, 37]. We assume a higher force constant in the O-D stretching mode induced by the reduced masses leads to the observed redshift in the spectra.

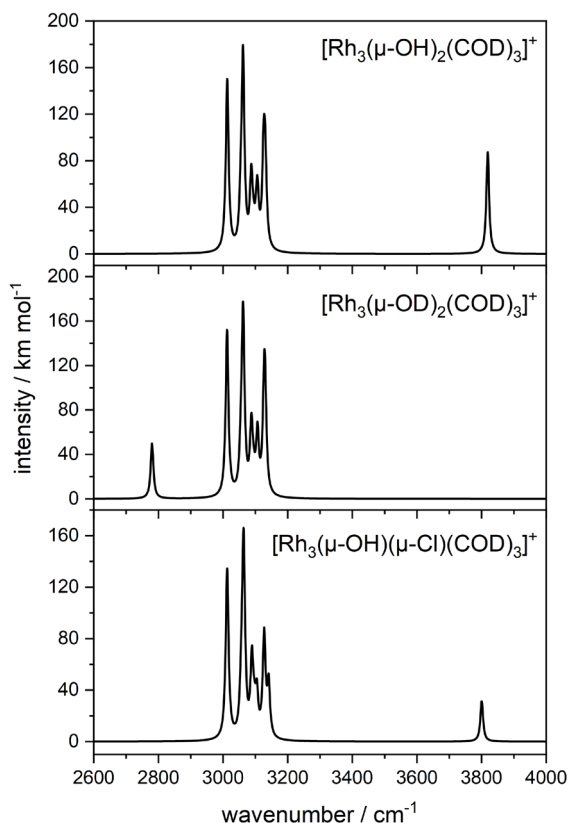


Fig. 10: Calculated linear absorption spectra of $[\text{Rh}_3(\mu\text{-OH})_2(\text{COD})_3]^+$ (top), $[\text{Rh}_3(\mu\text{-OD})_2(\text{COD})_3]^+$ (middle) and $[\text{Rh}_3(\mu\text{-OH})(\mu\text{-Cl})(\text{COD})_3]^+$. The calculations were performed with Gaussian 09 at the B3LYP/cc-pVTZ (H, C, N, O) and ecp-28-mdf (Rh) level of theory.

Conclusion

In the presented work, we investigated the bonding situation of the complex with the structure $[\text{Rh}_3(\mu\text{-OH})_2(\text{COD})_3]^+$ by the exchange of the hydroxyl groups by chloride and deuterated OH groups. The fragmentation patterns are almost similar in every complex and lead to the same results that the rhodium triangle does not start a fragmentation. However, the gas phase stabilities are slightly different for these complexes. Calculated weak interactions reveal strong covalent and non covalent interactions in all complexes. Still, the chloride complex obtains the highest covalent and also non covalent interactions in this complex series. This points out the high gas phase stability in the chloride complex. Also, the deuterated complex has the lowest gas stability, which is given by two reasons.

On the one hand, there are almost the same interactions as in the original hydroxyl complex, which does not favor higher stability than the original complex. On the other hand, a constant exchange from the deuterium to a more available hydrogen atom leads to a decreased gas

phase stability. The Electron localized field plots reveal similar covalent interactions of the rhodium triangle in these complexes, pointing out high stability in the triangle with a good agreement in the experimental data where no fragments with one rhodium are observed.

The recorded IR(M)PD spectrum of the complex reveals a highly symmetric complex. Both hydroxyl groups degenerate in one vibrational stretching mode. The C-H stretching modes in this complex are degenerated, not observed in the calculated chloride complex. The deuterated complex calculation reveals a vibrational stretching mode at around 2800 cm^{-1} due to the change of the force constants.

References

- [1] G. Christou, D. Gatteschi, D. N. Hendrickson, and R. Sessoli, "Single-Molecule Magnets," *MRS Bulletin*, 25, 11, 66-71, 2000.
- [2] G. Filoti, J. Bartolome, D. P. E. Dickson, C. Rillo, I. Prisecaru, T. Jovmir, V. Kuncser, and C. Turta, "Intermediate frustration in $[\text{Fe}_3\text{O}(\text{CH}_3\text{COO})_6(\text{H}_2\text{O})_3]\text{NO}_3 \cdot 4(\text{H}_2\text{O})$ trinuclear cluster," *J. Magnetism and Magnetic Materials*, 196-197, 561-563, 1999.
- [3] A. N. Georgopoulou, Y. Sanakis, and A. K. Boudalis, "Magnetic relaxation in basic iron(III) carboxylate $[\text{Fe}_3\text{O}(\text{O}_2\text{CPh})_6(\text{H}_2\text{O})_3]\text{ClO}_4 \cdot \text{py}$," *Dalt. Trans.*, 40, 24, 6371-6374, 2011.
- [4] K. Kim, A. Ford, V. Meenakshi, W. Teizer, H. Zhao, and K. R. Dunbar, "Nanopatterning of Mn₁₂-acetate single-molecule magnet films," *J. Appl. Phys.*, 102, 9, 094306, 2007.
- [5] H.-J. Krüger, "Spin transition in octahedral metal complexes containing tetraazamacrocyclic ligands," *Coord. Chem. Rev.*, 253, 19, 2450-2459, 2009.
- [6] J. A. A. J. Perenboom, J. S. Brooks, S. Hill, T. Hathaway, and N. S. Dalal, "Relaxation of the magnetization of Mn_{12} acetate," *Phys. Rev. B*, 58, 1, 330-338, 1998.
- [7] M. Schmitz, "Spincrossover-Prozesse und π -Radikalliganden," 2016.
- [8] M. Schmitz, M. Seibel, H. Kelm, S. Demeshko, F. Meyer, and H.-J. Krüger, "How Does a Coordinated Radical Ligand Affect the Spin Crossover Properties in an Octahedral Iron(II) Complex?," *Angew. Chem. Int. Ed.*, 53, 23, 5988-5992, 2014.
- [9] T. C. Stamatatos, D. Foguet-Albiol, C. C. Stoumpos, C. P. Raptopoulou, A. Terzis, W. Wernsdorfer, S. P. Perlepes, and G. Christou, "New Mn₃ structural motifs in manganese single-molecule magnetism from the use of 2-pyridyloximate ligands," *Polyhedron*, 26, 9, 2165-2168, 2007.
- [10] D. E. De Vos, M. Dams, B. F. Sels, and P. A. Jacobs, "Ordered Mesoporous and Microporous Molecular Sieves Functionalized with Transition Metal Complexes as Catalysts for Selective Organic Transformations," *Chem. Rev.*, 102, 10, 3615-3640, 2002.
- [11] A. Fröscher, K. Langenbach, E. von Harbou, W. R. Thiel, and H. Hasse, "NMR Spectroscopic Study of Chemical Reactions in Mixtures Containing Oleic Acid, Formic Acid, and Formoxystearic Acid," *Industrial & Engineering Chemistry Research*, 58, 14, 5622-5630, 2019.
- [12] H. B. Kagan, and T.-P. Dang, "Asymmetric catalytic reduction with transition metal complexes. I. Catalytic system of rhodium(I) with (-)-2,3-O-isopropylidene-2,3-dihydroxy-1,4-bis(diphenylphosphino)butane, a new chiral diphosphine," *J. Am. Chem. Soc.*, 94, 18, 6429-6433, 1972.
- [13] C. K. Prier, D. A. Rankic, and D. W. C. MacMillan, "Visible Light Photoredox Catalysis with Transition Metal Complexes: Applications in Organic Synthesis," *Chem. Rev.*, 113, 7, 5322-5363, 2013.
- [14] F. Schön, M. Leist, A. Neuba, J. Lang, C. Braun, Y. Sun, G. Niedner-Schatteburg, S. Bräse, and W. R. Thiel, "A direct access to heterobimetallic complexes by roll-over cyclometallation," *Chem. Comm.*, 53, 88, 12016-12019, 2017.
- [15] C. Zhong, and X. Shi, "When Organocatalysis Meets Transition-Metal Catalysis," *European Journal of Organic Chemistry*, 2010, 16, 2999-3025, 2010.
- [16] D. Kovala-Demertzi, "Transition metal complexes of diclofenac with potentially interesting anti-inflammatory activity," *J. Inorg. Biochem.*, 79, 1, 153-157, 2000.

- [17] C. S. Müller, H. Auerbach, K. Stegmaier, J. A. Wolny, V. Schünemann, and A. J. Pierik, "Mössbauer spectroscopy and DFT calculations on all protonation states of the 2Fe-2S cluster of the Rieske protein," *Hyperfine Interactions*, 238, 1, 102, 2017.
- [18] D. Sanz, J. L. García, and E. Díaz, "Expanding the current knowledge and biotechnological applications of the oxygen-independent ortho-phthalate degradation pathway," *Environmental Microbiology*, 22, 8, 3478-3493, 2020.
- [19] P. E. M. Siegbahn, and M. R. A. Blomberg, "Transition-Metal Systems in Biochemistry Studied by High-Accuracy Quantum Chemical Methods," *Chem. Rev.*, 100, 2, 421-438, 2000.
- [20] Y. Z. Voloshin, O. A. Varzatskii, and Y. N. Bubnov, "Cage complexes of transition metals in biochemistry and medicine," *Russian Chemical Bulletin*, 56, 4, 577-605, 2007.
- [21] N. M. Doherty, and N. W. Hoffmann, "Transition-metal fluoro compounds containing carbonyl, phosphine, arsine, and stibine ligands," *Chem. Rev.*, 91, 4, 553-573, 1991.
- [22] J. H. Holloway, and E. G. Hope, "Novel synthesis using inorganic fluorides," *Journal of Fluorine Chemistry*, 76, 2, 209-212, 1996.
- [23] E. F. Murphy, R. Murugavel, and H. W. Roesky, "Organometallic Fluorides: Compounds Containing Carbon-Metal-Fluorine Fragments of d-Block Metals," *Chem. Rev.*, 97, 8, 3425-3468, 1997.
- [24] H. W. Roesky, I. Leichtweis, and M. Noltemeyer, "Oxo fluorides of titanium and vanadium. Preparation and crystal structures of [Cp*TiF(.mu.-O)]₄ and OVF₂N:PPh₃," *Inorg. Chem.*, 32, 23, 5102-5104, 1993.
- [25] H. W. Roesky, and I. Haiduc, "Fluorine as a structure-directing element in organometallic fluorides: discrete molecules, supramolecular self-assembly and host-guest complexation †," *J. Chem. Soc., Dalton Trans.*, 14, 2249-2264, 1999.
- [26] J. Vicente, J. Gil-Rubio, D. Bautista, A. Sironi, and N. Masciocchi, "Synthesis and Reactivity of Fluoro Complexes: Part 2.1 Rhodium(I) Fluoro Complexes with Alkene and Phosphine Ligands. Synthesis of the First Isolated Rhodium(I) Bifluoride Complexes. Structure of [Rh₃(μ₃-OH)₂(COD)₃](HF₂) by X-ray Powder Diffraction," *Inorg. Chem.*, 43, 18, 5665-5675, 2004.
- [27] L. Schwartsburd, M. F. Mahon, R. C. Poulten, M. R. Warren, and M. K. Whittlesey, "Mechanistic Studies of the Rhodium NHC Catalyzed Hydrodefluorination of Polyfluorotoluenes," *Organometallics*, 33, 21, 6165-6170, 2014.
- [28] R. Colton, A. D'Agostino, and J. C. Traeger, "Electrospray mass spectrometry applied to inorganic and organometallic chemistry," *Mass Spectrom. Rev.*, 14, 2, 79-106, 1995.
- [29] J. B. Fenn, "Electrospray Wings for Molecular Elephants (Nobel Lecture)," *Angew. Chem. Int. Ed.*, 42, 33, 3871-3894, 2003.
- [30] A. D. Becke, "Density-functional thermochemistry. III. The role of exact exchange," *J. Chem. Phys.*, 98, 7, 5648-5652, 1993.
- [31] B. Miehlich, A. Savin, H. Stoll, and H. Preuss, "Results obtained with the correlation energy density functionals of Becke and Lee, Yang and Parr," *Chemical physics letters*, vol. 157, no. 3, pp. 200-206, 1989.
- [32] T. H. Dunning, "Gaussian basis sets for use in correlated molecular calculations. I. The atoms boron through neon and hydrogen," *J. Chem. Phys.*, 90, 2, 1007-1023, 1989.
- [33] M. Dolg, H. Stoll, H. Preuss, and R. M. Pitzer, "Relativistic and correlation effects for element 105 (hahnium, Ha): a comparative study of M and MO (M = Nb, Ta, Ha) using energy-adjusted ab initio pseudopotentials," *J. Phys. Chem.*, 97, 22, 5852-5859, 1993.
- [34] M. J. Frisch et. al, "Gaussian 16 Rev. C.01," 2016.
- [35] R. F. W. Bader, "A quantum theory of molecular structure and its applications," *Chem. Rev.*, 91, 5, 893-928, 1991.
- [36] K. Ishida, D. M. Jenkins, and F. C. Hawthorne, "Mid-IR bands of synthetic calcic amphiboles of tremolite-pargasite series and of natural calcic amphiboles," *American Mineralogist*, 93, 7, 1112-1118, 2008.
- [37] S. Sabbatini, C. Conti, G. Orilisi, and E. Giorgini, "Infrared spectroscopy as a new tool for studying single living cells: Is there a niche?," *Biomedical Spectroscopy and Imaging*, 6, 85-99, 2017.

Appendix II: Investigation of the auto oxidation in a neutral trinuclear palladium complex to a monocationic complex in isolation

Transition metal complexes have become a fascinating field in research for many applications such as magnetism^[1-8], photoluminescent processes^[9, 10], or catalysis^[11-16]. Much effort has been spent synthesizing polynuclear transition metal complexes for homogeneous^[17-19] and heterogeneous^[20, 21] catalysis. In terms of the catalytic behavior of transition metal complexes, the coordination of the ligand is an essential factor for the efficiency of the catalytic cycle. Therefore, tetradentate ligands seem suitable for the stabilization of small transition metal clusters^[22-25].

The presented complex obtains a triangular palladium core with two μ^3 -capping tris(methimazolyl)silanide (Si(mt^{Me})) ligands in trans position^[26]. The silicium and palladium ions build up a trigonal bipyramidal configuration (cf. Fig.1).

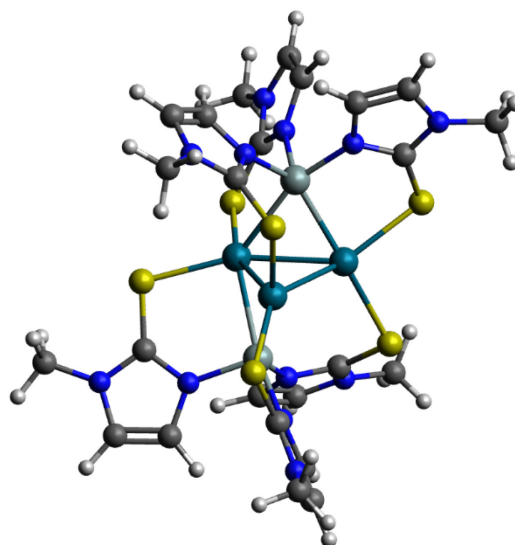


Fig.1: Calculated minimum structure of $[\text{Pd}_3(\text{Si}(\text{mt}^{\text{Me}})_3)_2]$. The calculations were performed at the B3LYP/cc-pVTZ (H, C, N, O) and ecp-28-mdf (Pd) level of theory with no unpaired electrons on the Pd ions.

Gerhards et al. performed time-resolved step scan Fourier transform infrared spectroscopy (FTIR), UV/VIS, and lifetime experiments of the presented complex^[27]. They found a ^1A ground state and a long living ^3A excited state in this complex. They assume that the ^3A state is populated in less than 400 fs. The long living excited state is formed by the interaction of the

three palladium ions in the complex. They also observe a change of the symmetry from a D_3 symmetry into a C_2 symmetry by excitation of the electronic ground state.

These experiments were performed in solid state or solvation where external effects such as packing and solvation cannot be excluded. Breher kindly provided the complex for gas phase experiments.

Electrospray ionization^[28, 29] gives access for mass spectrometric investigations of complexes in isolation and their bonding strengths in the complex by Collision Induced Dissociation (CID). Tandem MS based methods have helped investigate complexes void from external effects, e.g., packing and solvation effects.

Experimental setup and methods

ESI MS and CID measurements were performed with a quadrupole mass spectrometer (amazon ETD, Bruker daltonics), obtaining a Paul trap. The ions of interest are transferred into gas phase by electrospray ionization. The sample solution of the complex $[Pd_3(Si(mt^{Me})_3)_2]$ ($c \sim 1 \cdot 10^{-6}$ mol/L) in acetonitrile was constantly infused into the ESI chamber by a syringe pump with a flow rate of 180 μ L/h. Nitrogen was used as a drying gas with a flow rate of 12 L/min at 180 °C. The nebulize pressure was set to 280 mbar (4 psi) for spraying the sample solution, and the spray needle was held at 4.5 kV. The Paul trap consists of a ring electrode and two end caps forming a nearly hyperbolic inner profile. The end caps possess pinholes that allow to enter or exit the ions in the trap. The ring electrode is powered with a high voltage RF (radio frequency) potential (781 kHz) while the end caps are grounded. The ions are accumulated in this resulting oscillating quadrupolar electric field generated from the three electrodes. An auxiliary dipolar voltage is fed to either the exit cap or both end caps for ion isolation and fragmentation. For providing a constant partial Helium buffer gas pressure of approx. 10^{-3} mbar inside the trap, a proportional integral derivative (PID) gas controller is used. The recorded Collision Induced Dissociation (CID) breakdown curves were recorded by varying the excitation amplitudes (0.0 V–3.0 V). These amplitudes determine the internal energy scale of the mass spectrometer (E_{lab} in V). Relative abundances were calculated according to:

$$I_{tot}^{fr}(E_{lab}) = \left(\frac{\sum_i I_i^{fr}(E_{lab})}{\sum_i I_i^{fr}(E_{lab}) + \sum_i I_i^p(E_{lab})} \right) \quad (1)$$

where I_i^{fr} = intensity of the fragment ions and I_i^p = intensity of the parent ions. Center of mass transferred fragmentation amplitudes (E_{com}) were calculated from internal amplitudes by:

$$E_{com} = \left(\frac{m_{He}}{m_{He} + m_{ion}} \right) \cdot E_{lab} \quad (2)$$

where m_{ion} stands for the isotopically averaged mass of the molecular ion. Note that the current application of the CID technique by RF excitation in the presence of multiple collisions results in a so called “slow multi collision heating” mode of operation.

Fragmentation amplitude dependent CID spectra were modeled and fitted by sigmoidal functions of the type

$$I_{fit}^{fr}(E_{com}) = \left(\frac{1}{1 + e^{(E_{com}^{50} - E_{com}) B}} \right) \quad (3)$$

using a least-squares criterion. The E_{com}^{50} fit parameter is the amplitude at which the sigmoid function is at half maximum value, whereas B describes the rise of the sigmoid curve. Due to the correlation of fragmentation amplitude and appearance energy, it is feasible to assume that the appearance curves can be associated with relative stability.

Computational methods

Crystal structures of the neutral complex with the structure $[\text{Pd}3(\text{Si}(\text{mt}^{\text{Me}})_3)_2]$ ^[27] serve as starting point for further calculations. For multiplicity dependent determination of the minimum structures for the neutral and the cationic complexes and their corresponding weak interactions, we performed Density Functional Theory (DFT) calculations with B3LYP^[30, 31] functional and cc-pVTZ^[32] basis sets in combination with ecp-28-mdf^[33] core potential (Pd) in a local installed Gaussian 09 program package^[34].

Results and discussion

Usually, the complex should not be observed in the mass spectrum. However, spraying the sample solution, an isotropic peak with a characteristic isotope pattern is observed at a mass of 1053 m/z (cf. Fig. 1). Comparing the simulated isotope pattern with the experimental mass peak, we observe a good agreement with the intact cationic complex.

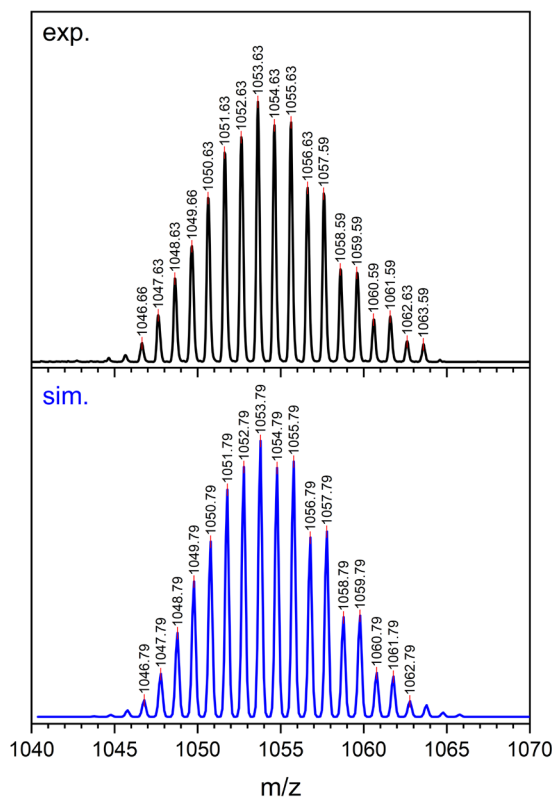


Fig. 1: ESI mass spectrum of $[\text{Pd}_3\{\text{Si}(\text{mt}^{\text{Me}})_3\}_2]^+$ (top) and the simulated isotope pattern within a Paul type trap.

We recorded Collision Induced Dissociation (CID) breakdown curves of the cationic complex and their corresponding appearance curves of the fragments (cf. Fig. 2). We observe the loss of one methimazole (mt^{Me}) ligand and molecular hydrogen aggregation as main fragmentation channel. With higher excitation amplitude, the loss of another methimazole ligand and three methyl groups appears. The aggregation of molecular hydrogen leads to the assumption that the catalytic reaction in such complexes starts when the ligand of the complex at least rotates, and one of the palladium ions reveals a free coordination sphere to perform a possible catalytic reaction.

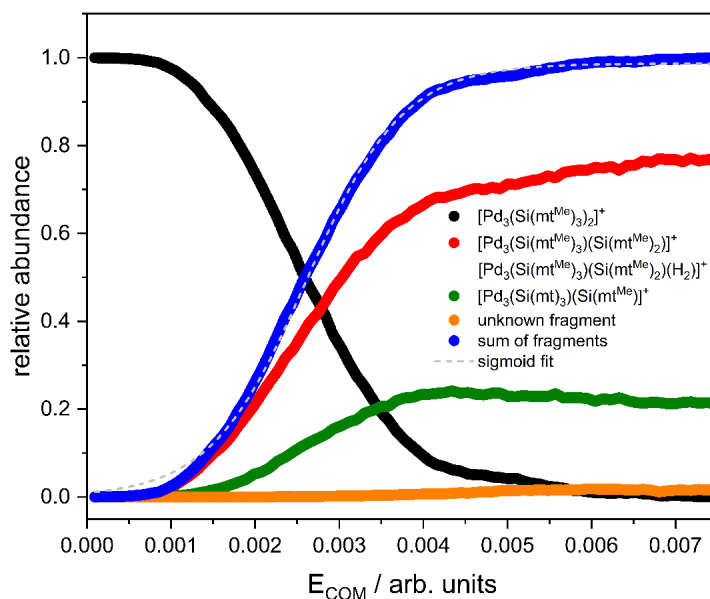


Fig. 2: CID breakdown curves of $[\text{Pd}_3\{\text{Si}(\text{mt}^{\text{Me}})_3\}_2]^+$ and their appearance curves of the associated fragments.

The non covalent interactions (NCI) determination reveals similar interactions for the neutral as for the cationic complex (cf. Fig. 3). Therefore, we assume that a similar fragmentation behavior occurs for the neutral complex than for the cationic complex. The loss of one electron does not change the structural properties nor the non covalent interactions of the complex resulting in similar gas phase stabilities for the complex. Also, a loss of an electron must occur from the palladium ions rather than from the ligand.

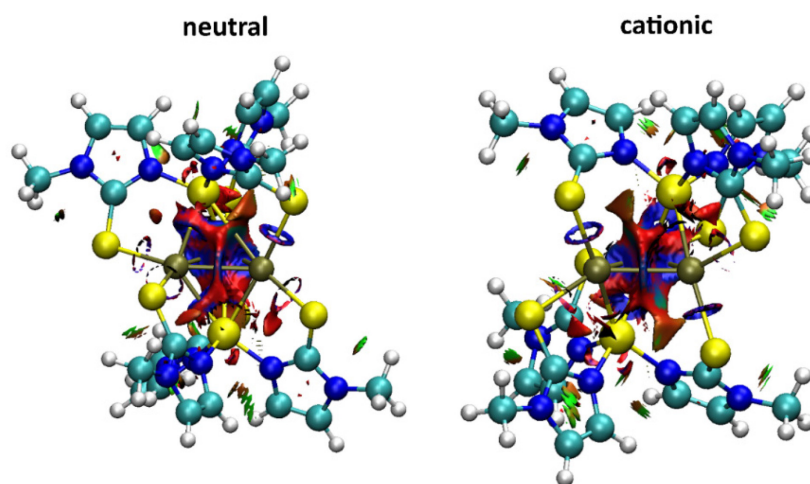


Fig. 3: Non covalent interactions in neutral complex (left) and in the cationic complex (right) with the structure $[\text{Pd}_3\{\text{Si}(\text{mt}^{\text{Me}})_3\}_2]^+$. The calculations were performed at the B3LYP/cc-pVTZ (H, C, N, O) and ecp-28-mdf (Pd) level of theory with no unpaired electrons on the Pd ions for the neutral complex and one unpaired electron on each Pd ion in the cationic complex.

Multiplicity dependent calculations of the minimum structure for both complexes reveal a minimum structure with no unpaired electrons for the neutral complex and three unpaired electrons for the cationic complex (cf. Fig. 4). Higher multiplicities for the cationic complexes are all lower in their relative energies than in the neutral complex. This hints that a cationic complex is more favored due to higher stability than in the neutral complex.

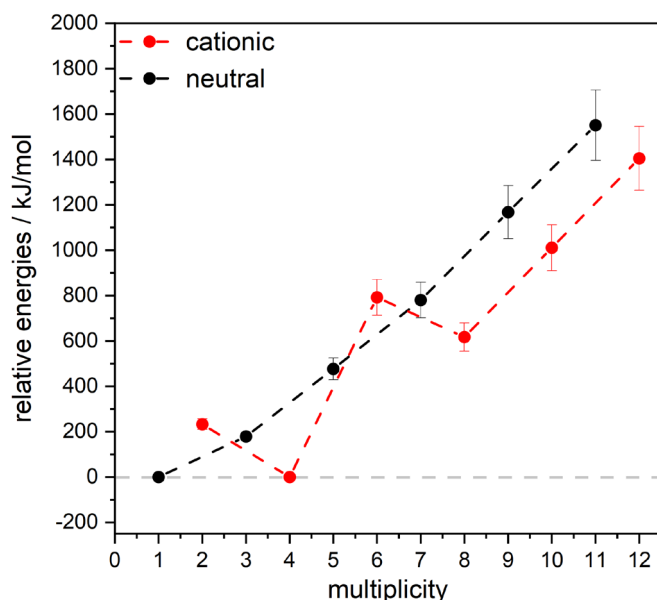


Fig. 4: Multiplicity dependent energies of the minimum structures of the neutral complex and the cationic complex. The calculations were performed at the B3LYP/cc-pVTZ (H, C, N, O) and ecp-28-mdf (Pd) level of theory with no unpaired electrons on the Pd ions the neutral complex and one unpaired electron on each Pd ion in the cationic complex.

Comparing the relative minimum energies from the neutral complex with the first ionization energy for palladium, we observe lower energy for the cationic complex than the ionization energy, suggesting that the complex reduces the d orbital levels in the Pd ions by coordinating the ligands compared to the ESI process where the high voltage is set to 4.5 kV a redox reaction of the Pd ions cannot be excluded. Therefore, we assume that the complex performed a redox reaction within the ESI process to a cationic complex by losing one electron on each palladium ion in the complex.

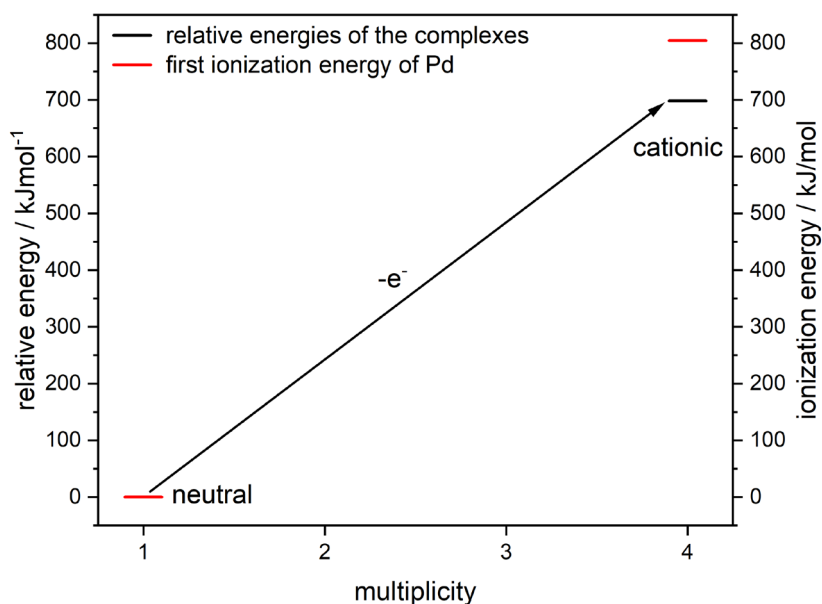


Fig. 5: Relative energies of the neutral and the cationic complex compared with the palladium's first ionization energy. The calculations were performed at the B3LYP/cc-pVTZ (H, C, N, O) and ecp-28-mdf (Pd) level of theory with no unpaired electrons on the Pd ions the neutral complex and one unpaired electron on each Pd ion in the cationic complex.

The calculated spin density indicates that the unpaired electrons are strongly localized on the Pd ions (cf. Fig. 6). This leads to excluding the ionization of the Silicon ions or the organic ligands in the complex. Moreover, this indicates that the ligands change their coordination from a radical anion to an anion to establish a netto charge of +1 in this complex.

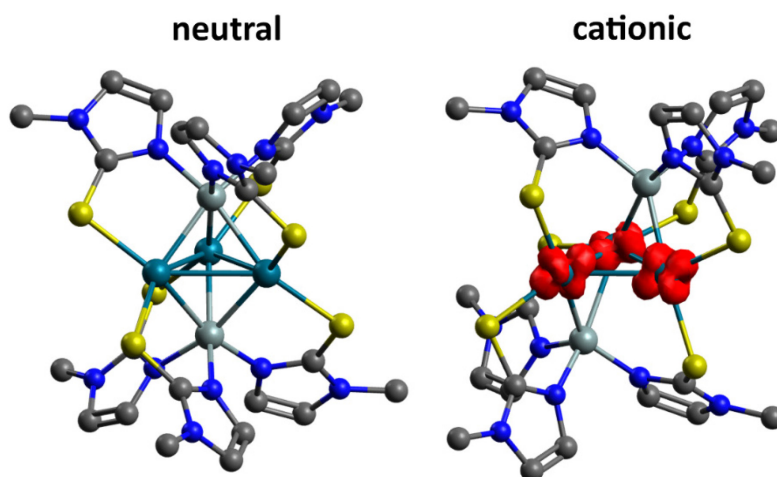


Fig. 6: Spin densities of the neutral and the cationic complex. The calculations were performed at the B3LYP/cc-pVTZ (H, C, N, O) and ecp-28-mdf (Pd) level of theory with no unpaired electrons on the Pd ions the neutral complex and one unpaired electron on each Pd ion in the cationic complex.

Electron localized field plots^[35] reveal stronger covalent interactions for the cationic complex than for the neutral complex (cf. Fig. 7), leading to the assumption that the cationic complex obtains higher stability due to stronger covalent interactions in the palladium triangle. Covalent interactions are getting stronger in the 4d orbitals with unpaired electrons because they are more diffuse than in the neutral complex without unpaired electrons. These unpaired electrons overlap into the other 4d orbitals of the neighboring palladium ions, resulting in a stronger bonding situation than in the neutral complex.

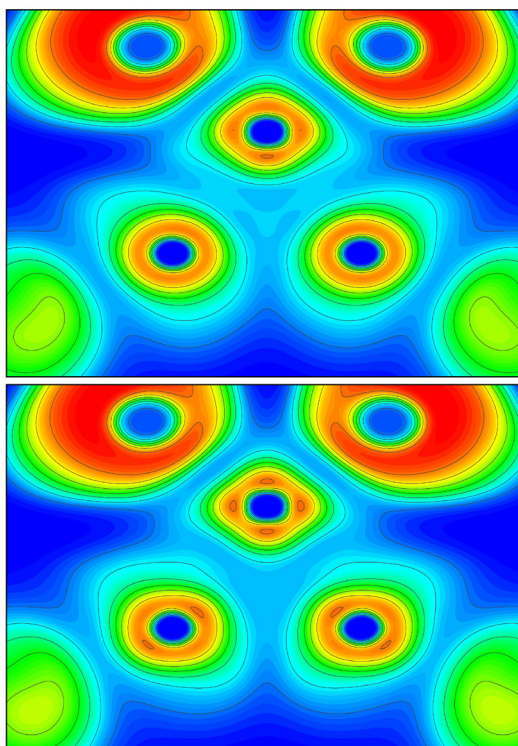


Fig. 7: Electron localized field plots of the neutral (top) and the cationic (bottom) complex. The calculations were performed at the B3LYP/cc-pVTZ (H, C, N, O) and ecp-28-mdf (Pd) level of theory with no unpaired electrons on the Pd ions the neutral complex and one unpaired electron on each Pd ion in the cationic complex.

Conclusion

We observe auto oxidation of the neutral complex to a mono cationic complex without any fragmentation. CID break down curves reveal the loss of a mt^{Me} ligand as the main fragmentation channel, indicating a possible way to perform catalytic reactions. We do not observe a fragmentation of the palladium triangle at any excitation amplitude. The ligand does not feature the possibility of losing electrons for the observed auto oxidation.

The calculations of the non covalent interactions in the complex reveal almost similar interactions for the complex in the neutral and the cationic state. In both oxidation states, the complex shows strong non covalent interactions in the palladium core, explaining the high stability of the transition metal core observed in the CID experiments.

Multiplicity-dependent calculations to determine the minimum structure in the neutral and the cationic complex reveal a minimum structure with no unpaired electrons in the neutral complex and three unpaired electrons in the cationic complex. Also, the different multiplicities point out that the cationic complex obtains higher stabilities by lower energies. This leads to the assumption that the cationic complex is preferred in gas phase rather than the neutral complex.

The relative energies of the minimum structures are lower than the first ionization energy of palladium, which hints that auto oxidation occurs because the energy in the complex is lower than in the free ion. Also, a static high voltage of 4.5 kV is kept on the spray needle during the ESI process, and we assume that a Redox reaction is observed, leading to the cationic complex as follows.

The calculated spin densities reveal localized electrons on the palladium ions. Therefore, the loss of the electrons does not occur from the ligand instead from the Pd ions themselves. The ligand coordinates radically, leading to a netto charge of +1.

Electron localized field plots reveal intense covalent bonding situation in the neutral complex. The oxidation of the palladium ions enhancing the covalent bonding situation in the palladium triangle, resulting in higher stability.

References

- [1] G. Aromí, D. Aguilà, P. Gamez, F. Luis, and O. Roubeau, "Design of magnetic coordination complexes for quantum computing," *Chem. Soc. Rev.*, 41, 2, 537-546, 2012.
- [2] G. Filoti, J. Bartolome, D. P. E. Dickson, C. Rillo, I. Prisecaru, T. Jovmir, V. Kuncser, and C. Turta, "Intermediate frustration in $[\text{Fe}_3\text{O}(\text{CH}_3\text{COO})_6(\text{H}_2\text{O})_3] \text{NO}_3 \cdot 4(\text{H}_2\text{O})$ trinuclear cluster," *J. Magn. and Magnetic Materials*, 196-197, 561-563, 1999.
- [3] A. N. Georgopoulou, Y. Sanakis, and A. K. Boudalis, "Magnetic relaxation in basic iron(III) carboxylate $[\text{Fe}_3\text{O}(\text{O}_2\text{CPh})_6(\text{H}_2\text{O})_3]\text{ClO}_4 \cdot \text{py}$," *Dalt. Trans.*, 40, 24, 6371-6374, 2011.
- [4] K. Kim, A. Ford, V. Meenakshi, W. Teizer, H. Zhao, and K. R. Dunbar, "Nanopatterning of Mn_{12} -acetate single-molecule magnet films," *J. Appl. Phys.*, 102, 9, 094306, 2007.
- [5] M. N. Leuenberger, and D. Loss, "Quantum computing in molecular magnets," *Nature*, 410, 6830, 789-793, 2001.

- [6] M. Mannini, F. Pineider, P. Saintavitt, C. Danieli, E. Otero, C. Sciancalepore, A. M. Talarico, M.-A. Arrio, A. Cornia, D. Gatteschi, and R. Sessoli, "Magnetic memory of a single-molecule quantum magnet wired to a gold surface," *Nature Materials*, 8, 3, 194-197, 2009.
- [7] K. V. Raman, A. M. Kamerbeek, A. Mukherjee, N. Atodiresei, T. K. Sen, P. Lazić, V. Caciuc, R. Michel, D. Stalke, S. K. Mandal, S. Blügel, M. Müntenberg, and J. S. Moodera, "Interface-engineered templates for molecular spin memory devices," *Nature*, 493, 7433, 509-513, 2013.
- [8] R. W. volume editor, and G. A. with contributions by, *Single-molecule magnets and related phenomena*: Berlin ; New York : Springer, 2006.
- [9] J. A. Faiz, R. M. Williams, M. J. J. P. Silva, L. De Cola, and Z. Pikramenou, "A Unidirectional Energy Transfer Cascade Process in a Ruthenium Junction Self-Assembled by α - and β -Cyclodextrins," *J. Am. Chem. Soc.*, 128, 14, 4520-4521, 2006.
- [10] S. Serroni, S. Campagna, F. Puntoriero, F. Loiseau, V. Ricevuto, R. Passalacqua, and M. Galletta, "Dendrimers made of Ru(II) and Os(II) polypyridine subunits as artificial light-harvesting antennae," *Comptes Rendus Chimie*, 6, 8, 883-893, 2003.
- [11] D. E. De Vos, M. Dams, B. F. Sels, and P. A. Jacobs, "Ordered Mesoporous and Microporous Molecular Sieves Functionalized with Transition Metal Complexes as Catalysts for Selective Organic Transformations," *Chem. Rev.*, 102, 10, 3615-3640, 2002.
- [12] A. Fröscher, K. Langenbach, E. von Harbou, W. R. Thiel, and H. Hasse, "NMR Spectroscopic Study of Chemical Reactions in Mixtures Containing Oleic Acid, Formic Acid, and Formoxystearic Acid," *Industrial & Engineering Chemistry Research*, 58, 14, 5622-5630, 2019.
- [13] H. B. Kagan, and T.-P. Dang, "Asymmetric catalytic reduction with transition metal complexes. I. Catalytic system of rhodium(I) with (-)-2,3-O-isopropylidene-2,3-dihydroxy-1,4-bis(diphenylphosphino)butane, a new chiral diphosphine," *J. Am. Chem. Soc.*, 94, 18, 6429-6433, 1972.
- [14] C. K. Prier, D. A. Rankic, and D. W. C. MacMillan, "Visible Light Photoredox Catalysis with Transition Metal Complexes: Applications in Organic Synthesis," *Chem. Rev.*, 113, 7, 5322-5363, 2013.
- [15] F. Schön, M. Leist, A. Neuba, J. Lang, C. Braun, Y. Sun, G. Niedner-Schatteburg, S. Bräse, and W. R. Thiel, "A direct access to heterobimetallic complexes by roll-over cyclometallation," *Chem. Comm.*, 53, 88, 12016-12019, 2017.
- [16] C. Zhong, and X. Shi, "When Organocatalysis Meets Transition-Metal Catalysis," *European Journal of Organic Chemistry*, 2010, 16, 2999-3025, 2010.
- [17] A. Behr, "Angewandte homogene Katalyse," *Wiley-VCH*, 2008.
- [18] J. Falbe, and H. Bahrmann, "Homogene Katalyse in der Technik," *Chemie in unserer Zeit*, 15, 2, 37-45, 1981.
- [19] M. Röper, "Homogene Katalyse in der Chemischen Industrie. Selektivität, Aktivität und Standzeit," *Chemie in unserer Zeit*, 40, 2, 126-135, 2006.
- [20] M. E. Dry, "The Fischer-Tropsch process: 1950-2000," *Catalysis Today*, 71, 3, 227-241, 2002.
- [21] G. Ertl, "Reactions at Surfaces: From Atoms to Complexity (Nobel Lecture)," 47, 19, 3524-3535, 2008.
- [22] S. Akine, T. Taniguchi, and T. Nabeshima, "Cooperative Formation of Trinuclear Zinc(II) Complexes via Complexation of a Tetradentate Oxime Chelate Ligand, Salamo, and Zinc(II) Acetate," *Inorg. Chem.*, 43, 20, 6142-6144, 2004.
- [23] W.-K. Dong, Y.-X. Sun, X.-N. He, J.-F. Tong, and J.-C. Wu, "Trinuclear and mononuclear copper(II) complexes incorporating tetradentate 2,2'-[1,1'-(ethylenedioxydinitrilo)diethylidene]diphenol ligand: Syntheses, crystal structures, spectral and thermal behaviors," *Spectrochimica Acta Part A: Molecular and Biomolecular Spectroscopy*, 76, 5, 476-483, 2010.
- [24] S. Mukhopadhyay, D. Mandal, P. B. Chatterjee, C. Desplanches, J.-P. Sutter, R. J. Butcher, and M. Chaudhury, "Bi- and Trinuclear Copper(II) Complexes of a Sterically Constrained Phenol-Based Tetradentate Ligand: Syntheses, Structures, and Magnetic Studies," *Inorg. Chem.*, 43, 26, 8501-8509, 2004.
- [25] X.-X. Zhou, H.-C. Fang, Y.-Y. Ge, Z.-Y. Zhou, Z.-G. Gu, X. Gong, G. Zhao, Q.-G. Zhan, R.-H. Zeng, and Y.-P. Cai, "Assembly of a Series of Trinuclear Zinc(II) Compounds with N₂O₂ Donor Tetradentate Symmetrical Schiff Base Ligand," *Crystal Growth & Design*, 10, 9, 4014-4022, 2010.
- [26] F. Armbruster, J. Meyer, A. Baldes, P. O. Burgos, I. Fernández, and F. Breher, "A triangulopalladium cluster consisting of μ ₃-capping silyl ligands," *Chem. Comm.*, 47, 1, 221-223, 2011.
- [27] M. Zimmer, F. Rupp, P. Singer, F. Walz, F. Breher, W. Klopfer, R. Diller, and M. Gerhards, "Time-resolved IR spectroscopy of a trinuclear palladium complex in solution," *Phys. Chem. Chem. Phys.*, 17, 21, 14138-14144, 2015.

-
- [28] R. Colton, A. D'Agostino, and J. C. Traeger, "Electrospray mass spectrometry applied to inorganic and organometallic chemistry," *Mass Spectrom. Rev.*, 14, 2, 79-106, 1995.
- [29] J. B. Fenn, "Electrospray Wings for Molecular Elephants (Nobel Lecture)," *Angew. Chem. Int. Ed.*, 42, 33, 3871-3894, 2003.
- [30] A. D. Becke, "Density-functional thermochemistry. III. The role of exact exchange," *J. Chem. Phys.*, 98, 7, 5648-5652, 1993.
- [31] B. Miehlich, A. Savin, H. Stoll, and H. Preuss, "Results obtained with the correlation energy density functionals of Becke and Lee, Yang and Parr," *Chem. phy. lett.*, 157, 3, 200-206, 1989.
- [32] T. H. Dunning, "Gaussian basis sets for use in correlated molecular calculations. I. The atoms boron through neon and hydrogen," *J. Chem. Phys.*, 90, 2, 1007-1023, 1989.
- [33] M. Dolg, H. Stoll, H. Preuss, and R. M. Pitzer, "Relativistic and correlation effects for element 105 (hahnium, Ha): a comparative study of M and MO (M = Nb, Ta, Ha) using energy-adjusted ab initio pseudopotentials," *J. Phys. Chem.*, 97, 22, 5852-5859, 1993.
- [34] M. J. Frisch et. al, "Gaussian 16 Rev. C.01," 2016.
- [35] R. F. W. Bader, "A quantum theory of molecular structure and its applications," *Chem. Rev.*, 91, 5, 893-928, 1991.

Appendix III: Repairing an RF contact failure in an Amazon Paul trap mass spectrometer

One of the most common errors in the mass spectrometer of the Amazon series is a power supply failure for the RF voltage to transfer the ions through the mass spectrometer into the Paul trap. Therefore, a screen appears in the trap control program where no RF voltages are found (cf. Fig. 1).

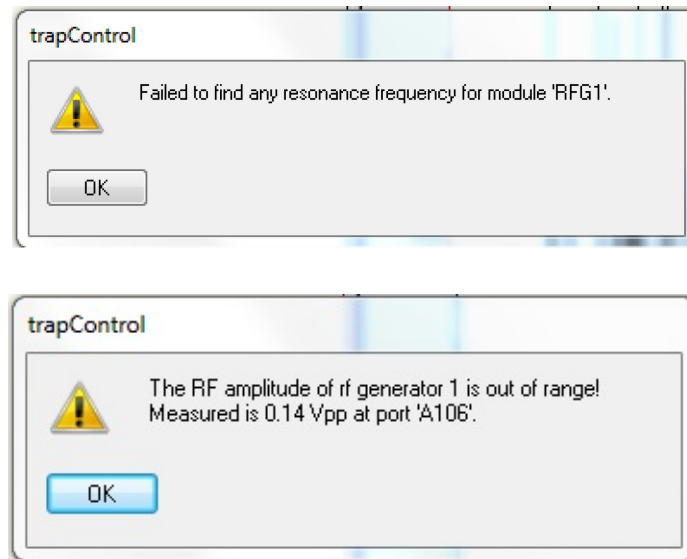


Fig. 1: Error message for the power supply failure to provide RF voltage to the ion funnels in the trap control program.

A closer look at the Power Communication Frontend indicates that no RF voltages are applied to the ion funnel 2 via diagnostic (cf. Fig. 2). All the other voltages seem to be applied to the ion optic. This hints broken cables or a broken RF generator in the mass spectrometer.

Test Funnel2 : FAILED

Result	Value	Range	Unit	Comment	Port
passed	1	1		Vacuum Ready	VACR
passed	31	10:85	°C	Temperature	A107
failed	0	1200:1500	kHz	Resonance Frequency	F2RF
failed	0.1	300.0:900.0	V	Funnel RF	A106
failed	0.1	150.0:450.0	V		
passed	0.05	-100.00:100.00	V		
failed	37	150:300	mA	Funnel DC Current	A108
failed	36	75:150	mA		
passed	36	25:50	mA		
passed	-300.3	-315.0:-285.0	V	Funnel Entrance	A056
passed	-150.1	-157.5:-142.5	V		
passed	-0.26	-5.00:5.00	V		
passed	150.7	142.5:157.5	V		
passed	301.1	285.0:315.0	V		
passed	-298.8	-315.0:-285.0	V	Funnel Exit	A057
passed	-149.1	-157.5:-142.5	V		
passed	-0.15	-5.00:5.00	V		
passed	149.9	142.5:157.5	V		
passed	299.7	285.0:315.0	V		
passed	-299.0	-315.0:-285.0	V	Funnel Lens	A058
passed	-149.2	-157.5:-142.5	V		
passed	-0.04	-5.00:5.00	V		
passed	150.0	142.5:157.5	V		
passed	299.7	285.0:315.0	V		

Fig. 2: Error message for the power supply failure to provide RF voltage to the ion funnels.

In both cases, the Mass spectrometer must be opened and controlled. First, the mass spectrometer's cover must be removed to see the electronic power supplies for the different ion optics. On the right side of the mass spectrometer is the RF power supply for the ion funnels mounted. The cover must be carefully removed (cf. Fig. 3).



Fig. 3: RF generator for the ion funnels in the Amazon mass spectrometer. The cover is removed for clarity.

On the different circuit boards are LED lights installed. These LED light serves as control lights if the RF generator works or if there is a failure. In the best case, all lights are green. If not, then a failure in the power supply is present. Before the mass spectrometer needs to be vented, a service switch at the top back of the mass spectrometer can be flipped, and all power supplies are shut down, except the vacuum system (cf. Fig. 4). **Flip the switch is important** because the RF generator needs to be unmounted to check the power supply contacts.



Fig. 4: Service switch on the top back of the mass spectrometer to cut all power supplies.

To unmount the RF power supply, all supply cables need to be unplugged and marked for later when the power supplies are plugged in again(cf. Fig. 5).

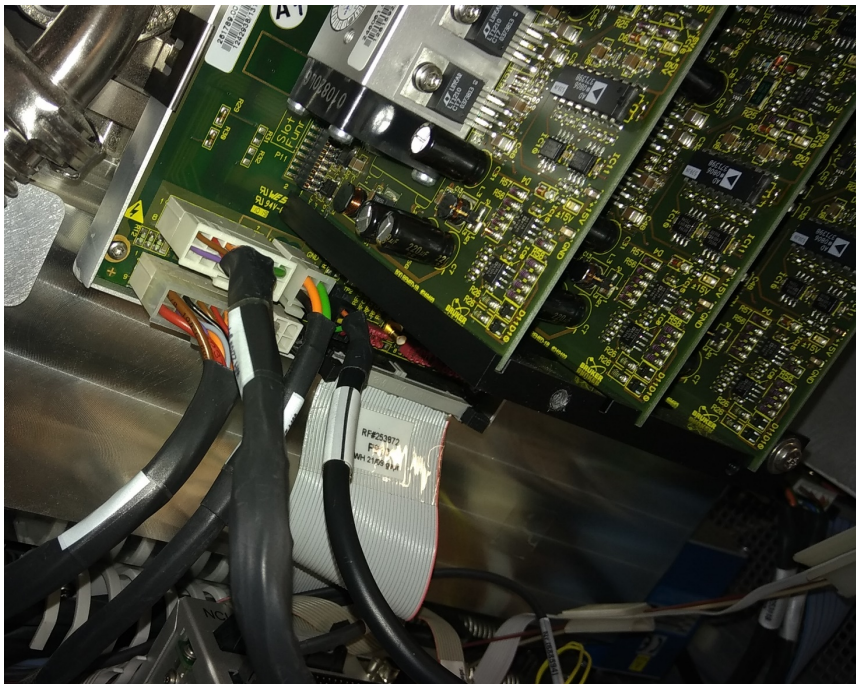


Fig. 5: Power supply plugs to the RF generator in the mass spectrometer.

Then two screws need to be unscrewed, and the RF generator can be carefully unmounted from the slide system (cf. Fig. 6).



Fig. 6: Mass spectrometer without RF power supply.

Now the RF generator can be checked for burned electrical parts on the circuit boards. If no obvious burnt electronic parts are found, a contact failure seems to be the problem. Check and clean the gold pins on the backside of the RF generator with isopropanol and let the pins dry. On the other side, at the mass spectrometer is a pin plate installed, with a multimeter, the electrical continuity, and the applied resistance can be checked. The corresponding contacts can be extracted from the circuit diagram (cf. Fig.7).

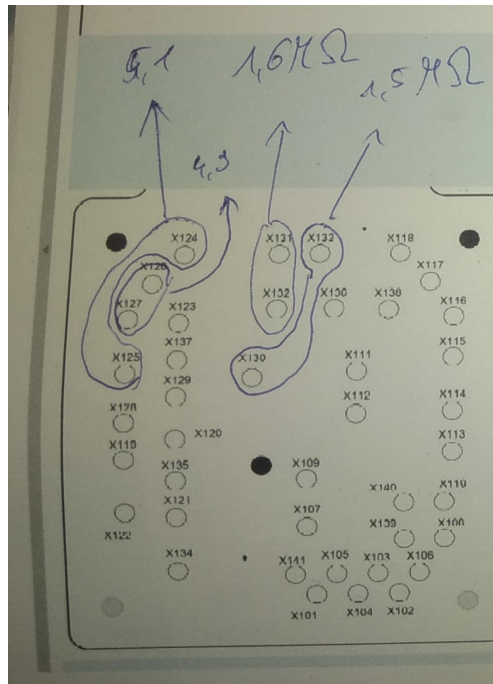


Fig. 7: Circuit diagram for the RF contacts of the mass spectrometer with described resistance between two contacts.

When no electrical continuity or resistance is observed, the contact failure is inside the mass spectrometer. It needs to be vented, and the ion funnel needs to be removed from the mass spectrometer. To vent the mass spectrometer, go to the power PC Communication module Frontend and click on service. Then click on vacuum control and then click on stop continuous. Then click on the vent button and wait approx. 30 minutes. When the mass spectrometer is vented, turn off the main switches of the mass spectrometer and the fore pump (cf. Fig. 8).

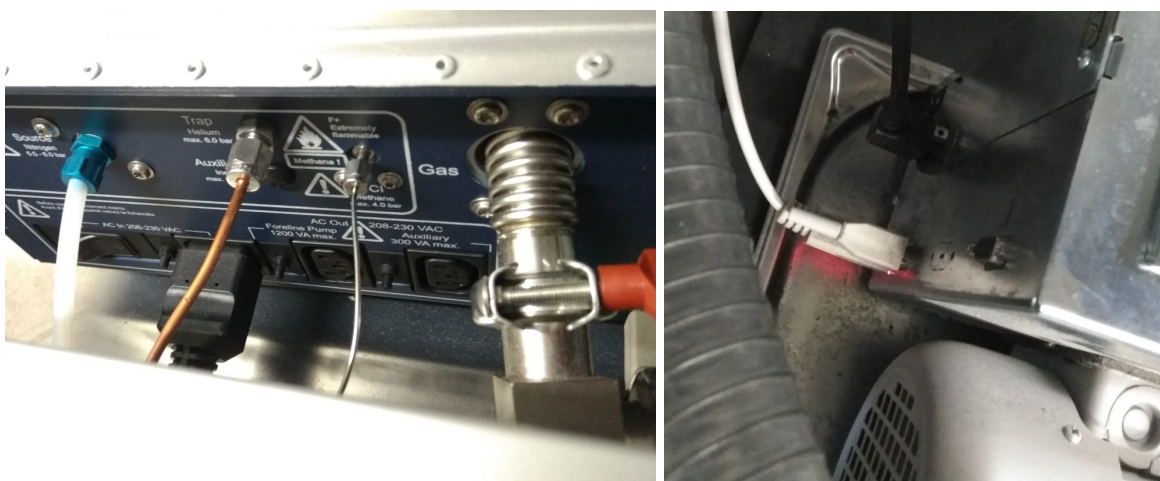


Fig. 8: Main switches of the mass spectrometer (left) and the fore pump (right).

When the mass spectrometer is shut down, close the nitrogen supply. Then remove the ESI spray chamber, the solvent waste hose, all power supply cables, and the nitrogen gas line. (cf. Fig. 9).



Fig. 9: Unplugged transfer capillary unit with spray shield.

Then unscrew the transfer capillary unit, which is mounted on a slide system. Carefully remove the whole unit from the mass spectrometer. When the unit is removed, the ion funnel stack is free to remove out of the mass spectrometer (cf. Fig. 10).

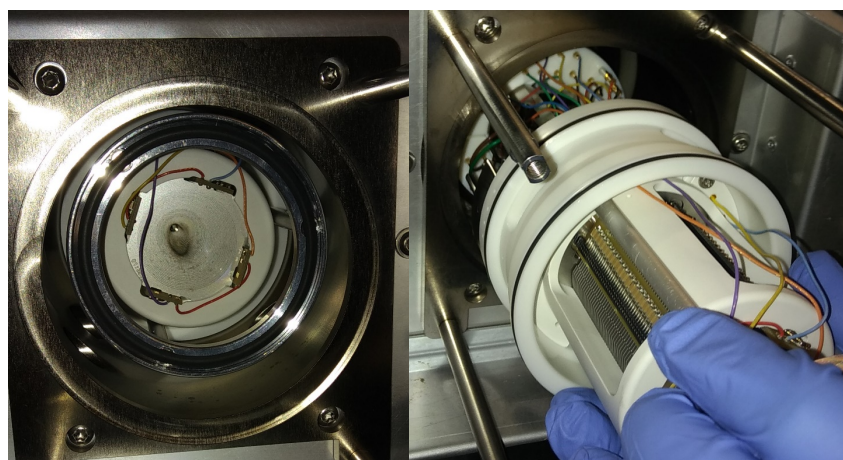


Fig. 10: Ion funnel stack in and out of the mass spectrometer.

With a multimeter, the electrical continuity can be measured from the inside of the gold-coated plates and from the outside where the RF generator usually is mounted (cf. Fig. 11).

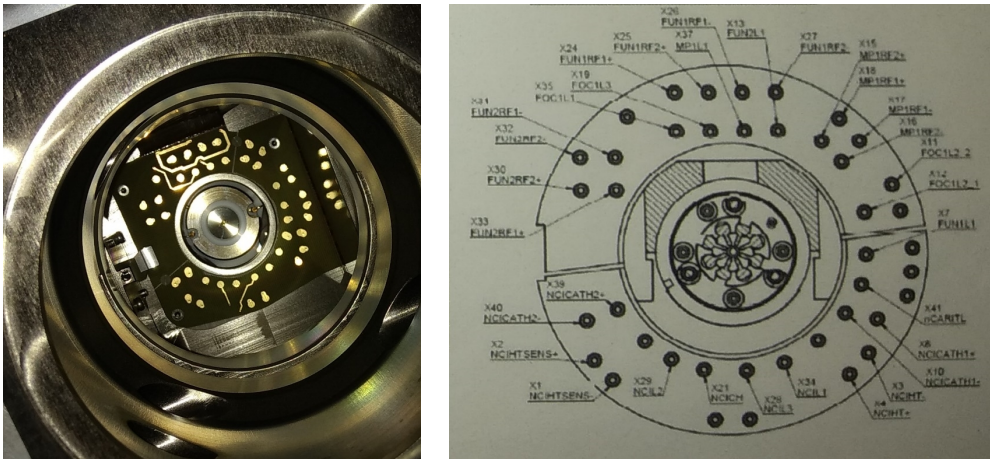


Fig. 11: Gold-coated pin plate inside the mass spectrometer and circuit diagram for the pin position of the RF voltages.

Check the ion funnel stack there are a lot of gold-coated pins with a feather inlay. Sometimes, these feathers get stuck, resulting in contact issues. If one of these pins is lower in height than the others, this must be changed (cf. Fig. 12).

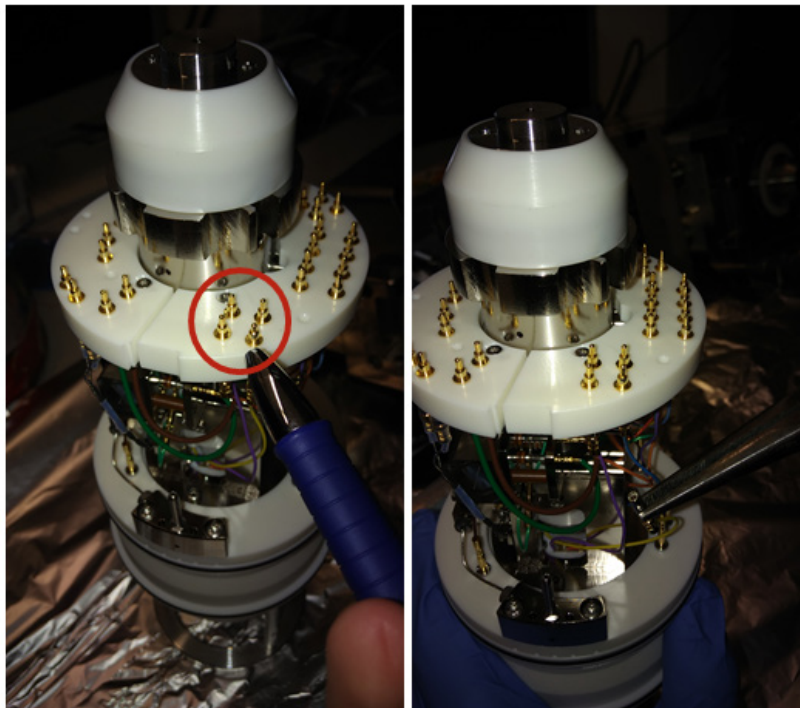


Fig. 12: Ion funnel stack with defect gold-coated pin (left) and unplugged defective pin (right).

After replacing the broken golden pin, take some Q-tips to clean the pins with isopropanol and dry them. When everything is dried, replace the ion funnel stack to the mass spectrometer (cf. Fig. 13). For the correct position of the ion funnel stack, a small block with a small pole must be located on the ion funnel stack's left side.



Fig. 13: Ion funnel stack replacement into the mass spectrometer.

After the ion funnel stack is replaced, check for electrical continuity and resistance as before (cf. Fig. 7). If there is no contact, remove the stack again and carefully pull the gold-coated pin out of the pin holder to guarantee a contact. Repeat this procedure until the electrical continuity and resistance are observed. When the contact is established, replace the transfer capillary unit, connect the gas inlet and the electronic wires. Then replace the ESI chamber and mount the RF generator. Flip the service switch, the fore pump switch, and the main switch of the mass spectrometer. Then go to the Power PC communication Module Frontend and start the vacuum system. Wait until every interlock is passed and start a diagnostic. The failure should vanish when everything is okay, and all results should appear green (cf. Fig. 14).

Test Funnel2 : PASSED

Result	Value	Range	Unit	Comment	Port
passed	1	1		Vacuum Ready	VACR
passed	29	10:85	°C	Temperature	A107
passed	1350	1200:1500	kHz	Resonance Frequency	F2RF
passed	600.3	300.0:900.0	V	Funnel RF	A106
passed	300.8	150.0:450.0	V		
passed	0.18	-100.00:100.00	V		
passed	217	150:300	mA	Funnel DC Current	A108
passed	110	75:150	mA		
passed	36	25:50	mA		
passed	-300.2	-315.0:-285.0	V	Funnel Entrance	A056
passed	-150.0	-157.5:-142.5	V		
passed	-0.19	-5.00:5.00	V		
passed	150.7	142.5:157.5	V		
passed	301.1	285.0:315.0	V		
passed	-298.7	-315.0:-285.0	V	Funnel Exit	A057
passed	-149.0	-157.5:-142.5	V		
passed	-0.04	-5.00:5.00	V		
passed	150.0	142.5:157.5	V		
passed	299.7	285.0:315.0	V		
passed	-298.9	-315.0:-285.0	V	Funnel Lens	A058
passed	-149.1	-157.5:-142.5	V		
passed	-0.03	-5.00:5.00	V		
passed	150.0	142.5:157.5	V		
passed	299.8	285.0:315.0	V		

Fig. 14: Power PC Communication Module Frontend after diagnosis of the ion funnel 2.

Appendix IV: Reanimation of the MALDI ULTRAFLEX TOF mass spectrometer

The commercial bought mass spectrometer MALDI (Ultraflex, bruker daltonics) is essential for analytics for many workings groups, focusing on synthesizing molecules to determine the masses and their fragmentation behavior. Electrospray ionization (ESI) leads to a soft ionization and transfer into the vacuum of molecules, but the mass spectrometer (Amazon, bruker daltonics) is limited by the mass range within a quadrupole ion trap^[1-5]. Usually, such mass spectrometers are used for small organic molecules^[6-8] and transition metal complexes^[9-18] up to 2000 m/z. Matrix assisted laser desorption (MALDI) in combination with a time of flight mass spectrometer enables access to mass spectrometric investigations without a mass range limitation for proteomics^[19-22] and xylomics^[23-26].

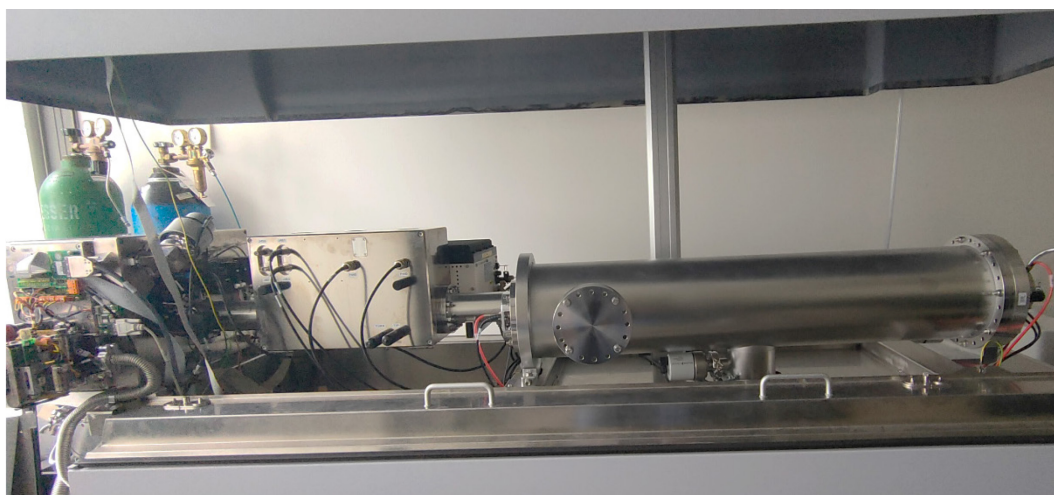


Fig. 1: Experimental Setup of the Ultraflex time of flight mass spectrometer.

After an electrical shutdown of the building, the mass spectrometer broke down, starting with a broken hard drive of the computer, which is needed to operate the mass spectrometer. A new one replaced the hard drive, and a backup of the operating system was installed. In the operation mode, the instrument did not start the turbo molecular pump of the source chamber. The expansion of the vacuum pump did not show damage to the pump itself. Therefore, we exchanged the turbo pump controller (cf. Fig. 2) and started the vacuum system.

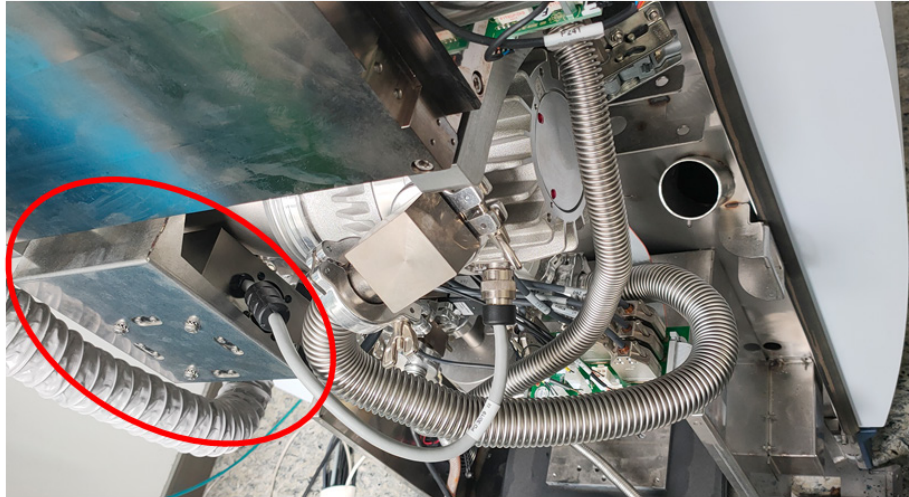


Fig. 2: Turbo molecular pump underneath the source chamber of the Ultraflex time of flight mass spectrometer.

Unfortunately, the vacuum ventiles did not work as expected. Usually, both ventiles for the source chamber and time of flight should open simultaneously to get the rough vacuum in both chambers, and when the vacuum is reached, the ventiles for the turbo molecular pumps should open to get the high vacuum in both chambers. The instrument only opens the ventile for the source chamber to get the rough vacuum and then opens the ventile for the high vacuum for the source chamber. A few seconds later, the ventile for the rough vacuum at the time of flight opens. As a result of this scheme, both turbo molecular pumps have to pump against the atmospheric pressure from the time of flight chamber with their full rotation frequency. Both vacuum pumps are at high risk for a break down due to the rough vacuum. The diagnostics did not show any failure, and therefore we assume a failure on the mainboard of the instrument where the digital logic is installed (cf. Fig. 3). The panel was unscrewed, and as far as the panel was removed, we observed sparks at one of the fuses. The whole mass spectrometer shut down and did not boot up again. The mainboard was extracted and repaired by the local electronic repair shop at the TU Kaiserslautern.

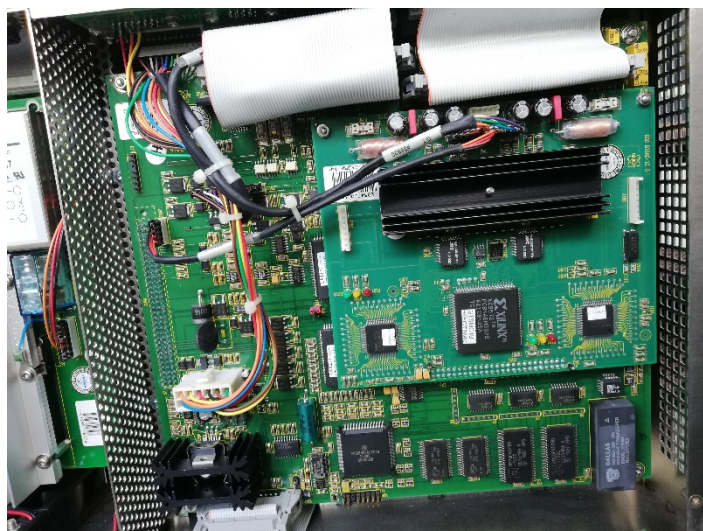


Fig. 3: Mainboard without the panel of the Ultraflex time of flight mass spectrometer.

The electronic repair shop found four defective SMD fuses (cf. Fig. 4) and a preceding resistor at the main fuse, serving as a sacrificial resistor to prevent electrical damage to the mainboard.

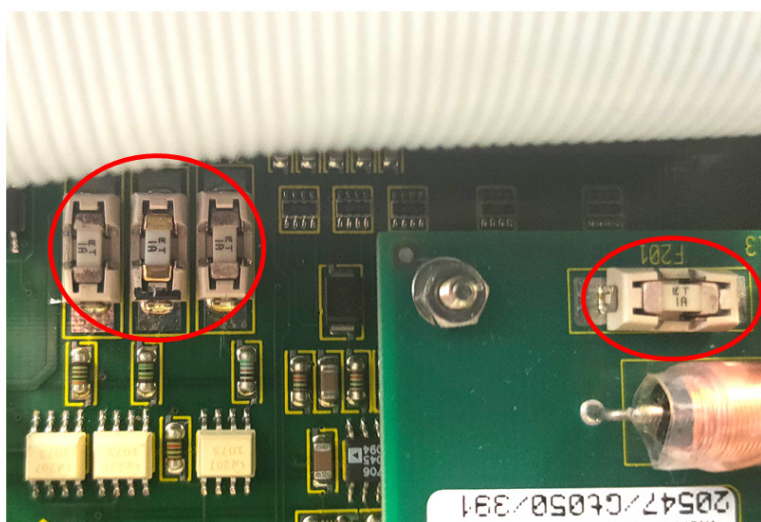


Fig. 4: SMD fuses installed on the mainboard of the Ultraflex time of flight mass spectrometer.

We checked all fuses installed in the mass spectrometer and found 2 more defective fuses in the distribution box for the different electrical parts (cf. Fig. 5). The distribution box obtains three fuses, and two of these 3 fuses were nonexistent and replaced by new fuses.



Fig. 5: Fuses of the distribution box for the electrical parts in the Ultraflex time of flight mass spectrometer.

Also, the oil of the fore pump was renewed, and due to the lack of vacuum, the whole vacuum system needed to be cleaned because the oil got into the vacuum chambers. The mainboard was reinstalled, and the mass spectrometer went operable again, but the communication between the computer and the instrument was not established. After the shutdown of the instrument, we rechecked the mainboard and found a coin cell neighbors to the digital logic. The coin cell is as old as the instrument, and we assume that the reparation of the main board took too long due to the corona pandemic, which the coin cell discharged over that time. The old coin cell was replaced, and the main board was installed again. After installing the backup of the digital logic to the mainboard, communication between the computer and the instrument was established.

When the vacuum in the instrument has reached a failure in the stepper motor for the laser attenuator and focus was displayed in the Flex control operation program. A burnt resistor and diode were detected on the electrical board for the power supply of these Stepper motors, and therefore we removed the electrical board. The electronic repair shop changed the defective parts and checked the whole board. Meanwhile, a loose contact on the six pole platin plug was fixed, and both stepper motors were checked to see if they were working. The repaired electrical board was reinstalled, and the flex control program did not show any failures. By adjusting the zero positions of the different lenses and filters, a defective probe for the laser focus was detected. The defective probe leads to a focus lens position out of the adjustment range, resulting in an error and a defocused laser beam. Because there are no spare parts available, we optimized the laser focus manually and ruled out the laser focus

application from the program in the service mode to prevent defocusing the laser by the defective probe.

We noticed that the lightbulb was broken by transferring the sample plate into the vacuum and switching on the light to see the sample spots. So the lightbulb was replaced by a new one, and the light was adjusted to the sample spots for optimal illumination of the sample. The measurement of the first mass spectra delivered a failure in the trigger setup of the instrument. The master trigger seems to work, but the slave processor does not respond, and data acquisition does not take part. This part was replaced too, and the slave processor started to respond. Therefore, we checked the trigger main board and found nothing defective but the measurements of the inner resistance of the optocoupler was infinity high, indicating that this part is also defective (cf. Fig. 6).

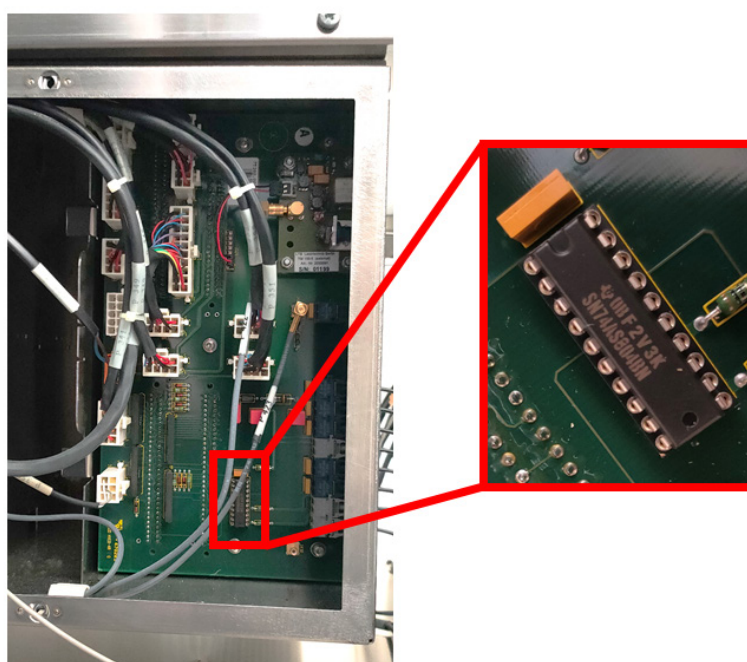


Fig. 6: Trigger main board of the Ultraflex time of flight mass spectrometer.

After booting the instrument, the data acquisition works without any problems, but the vacuum ventiles shut with several shots onto the sample plate. We also installed the newest version for the master and slave triggers and the Flex control program starts the data acquisition. The data acquisition of the test spectra took several shots and then went into longer loops. No errors occurred, therefore the instrument was shut down and all power

supplies were disconnected from electricity. The disconnect leads to a hard reset of all electrical parts and also erases temporarily files written in the random access memory.

A quick check of the vacuum control reveals insufficient pressures near the setpoints of the instruments, which release the interlocks of the mass spectrometer to prevent further damage to other parts (cf. Tab. 1). The high vacuum of the analyzer is only 0.1 underneath the setpoint, leading to the release of the interlock. The old fore pump (Pfeiffer duo 10) was replaced by another fore pump (Edwards, E2M30). Also, the bigger fore pump obtains a higher absorbency than the original one. This should lead to a better vacuum, and the resulting gases can be more efficiently pumped out from the vacuum chamber.

Tab. 1: Setpoint of the instrument and reached pressures with the old and the new fore pump.

	Set point/mbar	old fore pump/mbar	new fore pump/mbar
lock rough	$2.9 \cdot 10^{-1}$	$3.9 \cdot 10^{-2}$	$1.6 \cdot 10^{-2}$
source rough	$2.8 \cdot 10^{-1}$	$6.4 \cdot 10^{-2}$	$1.9 \cdot 10^{-2}$
source high	$3.0 \cdot 10^{-6}$	$2.9 \cdot 10^{-6}$	$1.4 \cdot 10^{-6}$
analyzer rough	$2.9 \cdot 10^{-1}$	$6.2 \cdot 10^{-2}$	$1.8 \cdot 10^{-2}$
analyzer high	$3.0 \cdot 10^{-6}$	$2.9 \cdot 10^{-6}$	$1.2 \cdot 10^{-7}$

Finally, no errors occur, and the mass spectrometer works again. We recorded mass spectra of $[\text{Cs}(\text{Csl})_n]^+$ clusters and Vitamin B12 (VB12) with different laser power (LP) (cf. Fig. 7). The recorded mass spectra reveal that the data acquisition works, and also, the laser attenuator switches the laser power to adjust the laser desorption from a small amount of fragmentation to a high amount of fragmentation. In the Csl sample, we observe a higher Csl cluster with higher laser power and in the Vitamin B12 mass spectra, we observe a higher amount of fragments by adjusting the laser power to higher energies.

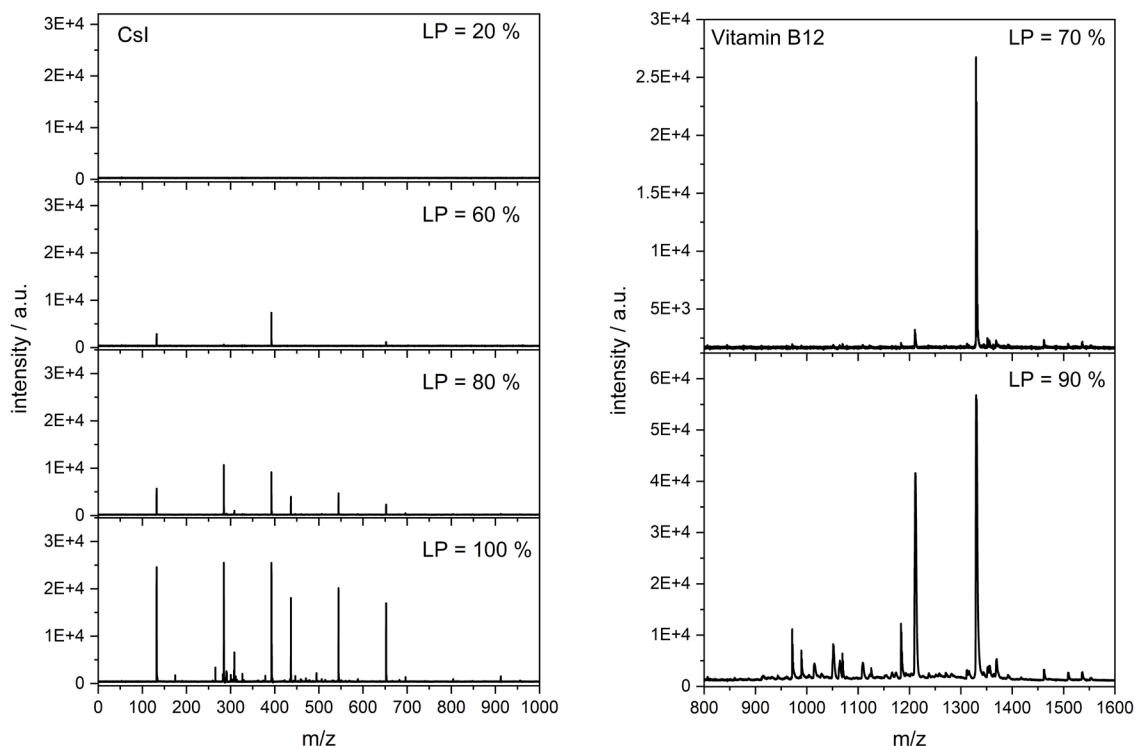


Fig. 7: Recorded mass spectra of $[\text{Cs}(\text{CsI})_n]^+$ clusters and Vitamin B12 (VB12) with different laser power (LP).

References

- [1] E. R. Badman, R. C. Johnson, W. R. Plass, and R. G. Cooks, A Miniature Cylindrical Quadrupole Ion Trap: Simulation and Experiment, *Anal. Chem.*, 1998.
- [2] B. Daltonics, AmaZon SL series user manual.
- [3] J. Martens, G. Berden, C. R. Gebhardt, and J. Oomens, Infrared ion spectroscopy in a modified quadrupole ion trap mass spectrometer at the FELIX free electron laser laboratory, *Rev. Scient. Instrum.*, 2016.
- [4] J. F. J. Todd, and R.E.March, Quadrupole Ion Trap Mass Spectrometry, *John Wiley & Sons, Inc*, 2005.
- [5] G. E. Reid, J. Mitchell Wells, E. R. Badman, and S. A. McLuckey, Performance of a quadrupole ion trap mass spectrometer adapted for ion/ion reaction studies, *International Journal of Mass Spectrometry*, 222, 243-258, 2003.
- [6] B. Andrae, D. Bauer, P. Gaß, M. Koller, F. Worek, and S. Kubik, Influence of cyclic and acyclic cucurbiturils on the degradation pathways of the chemical warfare agent VX, *Organic & Biomolecular Chem.*, 2020.
- [7] J. Bartl, L. Reinke, M. Koch, and S. Kubik, Selective sensing of sulfate anions in water with cyclopeptide-decorated gold nanoparticles, *Chem. Commun.*, 2020.
- [8] D. Mungalpara, S. Stegmüller, and S. Kubik, A neutral halogen bonding macrocyclic anion receptor based on a pseudocyclopeptide with three 5-iodo-1,2,3-triazole subunits, *Chem. Commun.*, 2017.
- [9] Y. Becker, F. Schön, S. Becker, Y. Sun, and W. Thiel, Structure-dependent Regioselectivity of a Roll-Over Cyclopalladation Occuring at 2,2'-Bipyridine-type Ligands, *J. Organomet. Chem.*, 2021.
- [10] C. Groß, Y. Sun, T. Jost, T. Grimm, M. P. Klein, G. Niedner-Schatteburg, S. Becker, and W. R. Thiel, Generation of a zinc and rhodium containing metallomacrocyclic by rearrangement of a six-coordinate precursor complex, *Chem. Commun.*, 2020.
- [11] S. V. Kruppa, F. Böppler, C. Holzer, F. Dietrich, R. Diller, W. Klöpffer, and C. Riehn, Excited state vibrational coherence in a binuclear metal adduct: wave packet phase dependant molecular fragmentation under variation of ligand size, *EPJ Web Conf.*, 2019.

- [12] S. V. Kruppa, F. Bappler, C. Holzer, W. Klopfer, R. Diller, and C. Riehn, Vibrational Coherence Controls Molecular Fragmentation: Ultrafast Photodynamics of the [Ag₂Cl]⁺ Scaffold, *J. Phys. Chem. Lett.*, 2018.
- [13] S. V. Kruppa, Y. Nosenko, M.-O. Winghart, S. P. Walg, M. M. Kappes, and C. Riehn, Fragmentation pathways of dianionic [Pt₂(μ-P₂O₅H₂)₄X,Y]²⁻ (X,Y=H, K, Ag) species in an ion trap induced by collisions and UV photoexcitation, *Int. J. Mass Spectrom.*, 2016.
- [14] J. Lang, M. Cayir, S. P. Walg, P. Di Martino-Fumo, W. R. Thiel, and G. Niedner-Schatteburg, Intermetallic Competition in the Fragmentation of Trimetallic Au–Zn–Alkali Complexes, *Chemistry – A European Journal*, 22, 2345-2355, 2016.
- [15] J. Lang, D. V. Fries, and G. Niedner-Schatteburg, Characterization of Trinuclear Oxo Bridged Cobalt Complexes in Isolation, *Z. Phys. Chem.*, 2018.
- [16] J. Lang, M. Gaffga, F. Menges, and G. Niedner-Schatteburg, Two-color delay dependent IR probing of torsional isomerization in a [AgL₁L₂]⁺ complex, *Phys. Chem. Chem. Phys.*, 2014.
- [17] J. Lang, J. M. Hewer, J. Meyer, J. Schuchmann, C. van Wullen, and G. Niedner-Schatteburg, Magnetostructural correlation in isolated trinuclear iron(iii) oxo acetate complexes, *Phys. Chem. Chem. Phys.*, 2018.
- [18] M. Leist, C. Kerner, L. Taghlizadeh Ghoochany, S. Farsadpour, A. Fizia, J. Neu, F. Schon, Y. Sun, B. Oelkers, J. Lang, F. Menges, G. Niedner-Schatteburg, K. Salih, and W. Thiel, Roll-over cyclometalation: A versatile tool to enhance the catalytic activity of transition metal complexes, *J. Organomet. Chem.*, 2018.
- [19] J. Franck, K. Arafah, M. Elayed, D. Bonnel, D. Vergara, A. Jacquet, D. Vinatier, M. Wisztorski, R. Day, I. Fournier, and M. Salzet, MALDI Imaging Mass Spectrometry: STATE OF THE ART TECHNOLOGY IN CLINICAL PROTEOMICS*, *Molecular & Cellular Proteomics*, 2009.
- [20] J. O. R. Gustafsson, M. K. Oehler, A. Ruzkiewicz, S. R. McColl, and P. Hoffmann, MALDI Imaging Mass Spectrometry (MALDI-IMS)—Application of Spatial Proteomics for Ovarian Cancer Classification and Diagnosis, *Int. J. Molecular Sciences*, 2011.
- [21] L. Putignani, F. Del Chierico, M. Onori, L. Mancinelli, M. Argentieri, P. Bernaschi, L. Coltella, B. Lucignano, L. Pansani, S. Ranno, C. Russo, A. Urbani, G. Federici, and D. Menichella, MALDI-TOF mass spectrometry proteomic phenotyping of clinically relevant fungi, *Molecular BioSystems*, 2011.
- [22] D. Suckau, A. Resemann, M. Schuerenberg, P. Hufnagel, J. Franzen, and A. Holle, A novel MALDI LIFT-TOF/TOF mass spectrometer for proteomics, *Anal. Bioanal. Chem.*, 2003.
- [23] X. Chen, X. Xi, A. Pizzi, E. Fredon, G. Du, C. Gerardin, and S. Amirou, Oxidized demethylated lignin as a bio-based adhesive for wood bonding, *J. Adhesion*, 2021.
- [24] X. Xi, A. Pizzi, C. Gerardin, X. Chen, and S. Amirou, Soy protein isolate-based polyamides as wood adhesives, *Wood Science and Technology*, 2020.
- [25] P. Pristaš, S. Kvasnova, S. Gaperova, T. Gašparcova, and J. Gaper, Application of MALDI-TOF mass spectrometry for in vitro identification of wood decay polypores, *For. Pathol.*, 2017.
- [26] O. Schmidt, and W. Kallow, Differentiation of indoor wood decay fungi with MALDI-TOF mass spectrometry, 2005.

Curriculum Vitae

Personal Data

Name: Michael Lembach

School & Education

2017–today

TU Kaiserslautern

PhD student in the group of Prof. Dr. Dr. Niedner- Schatteburg

- Title of the thesis: „Magnetic, electronic and structural characterization of mass-selected mono and multinuclear transition metal complexes“

2012–2017

TU Kaiserslautern

Studies in Chemistry with specialization in physical chemistry

- Title of the thesis: „Characterization of three different ion sources with a Time of flight mass spectrometer“
- Diploma

2007–2012

TU Kaiserslautern

Studies in industrial engineer with specialization in chemistry

2006–2007

Berufsbildende Schule I

Berufsoberschule II

- General university entrance qualification

2004–2006

Berufsbildende Schule I

Berufsoberschule I

- Subject related higher education entrance qualification

2000–2003

Berufsbildende Schule I

Apprenticeship as painter

- Certificate of apprenticeship
- Middle maturity

1999-2000

Berufsbildende Schule I

1994–1999

Hauptschule Bännjerrück

- Lower secondary school leaving certificate

1990–1994

Grundschule Pestalozzi

Lebenslauf

Persönliche Daten

Name: Michael Lembach

Schule & Ausbildung

2017–Heute

TU Kaiserslautern

Doktorand in der Gruppe von Prof. Dr. Dr. Niedner- Schatteburg

- Titel der Dissertation: „Magnetic, electronic and structural characterization of mass-selected mono and multinuclear transition metal complexes“

2012–2017

TU Kaiserslautern

Studium der Chemie mit Schwerpunkt physikalischen Chemie

- Titel der Diplomarbeit: „Charakterisierung von drei neuen Ionenquellen mit einem Time of flight Massenspektrometer“
- Diplomabschluss

2007-2012

TU Kaiserslautern

Studium Wirtschaftsingenieur mit Schwerpunkt Chemie

2006–2007

Berufsbildende Schule I

Berufsoberschule II

- Allgemeine Hochschulreife

2004–2006

Berufsbildende Schule I

Berufsoberschule I

- Fachgebundene Hochschulreife

2000–2003

Berufsbildende Schule I

Ausbildung zum Maler und Lackierer

- Gesellenbrief
- Abschluss Sekundarstufe II

1999–2000

Berufsbildende Schule I

1994–1999

Hauptschule Bännjerrück

- Hauptschulabschluss

1990–1994

Grundschule Pestalozzi

Contribution to conferences: Oral, Poster Presentations and Beamtime proposals

Oral Presentation

Michael Lembach, Maximilian Luczak, Yannick Mees, Mathias Klein, Daniela Fries, Annika Steiner, Maximilian Huber and Gereon Niedner-Schatteburg, Magnetism of isolated multinuclear transition metal complexes via X-ray Magnetic Circular Dichroism (XMCD) and functional cooperativity of clusters via InfraRed (Multiple) Photon Dissociation (IR(M)PD) within cryo ion traps, Phd Seminar 3MET, virtual, 22.-24.09.2020.

Poster Presentations

Jonathan Meyer, Michael Lembach, Pol Boden and Gereon Niedner-Schatteburg, "Activation of small organic molecules by size selected transition metal clusters (n = 2-8) in the gas phase", 116th Bunsentagung, Kaiserslautern, 25.-27.05.2017.

Michael Lembach, Matthias P. Klein, Joachim Hewer, Julius Wolny, Vicente Zamudio-Bayer, Martin Timm, Christine Bülow, Tobias Lau, Volker Schünemann and Gereon Niedner-Schatteburg, " X-ray magnetic circular dichroic studies on a monometallic spincrossover iron complexes in the gasphase", 117th Bunsentagung, Hannover, 10.5.-12.5.2018.

Michael Lembach, Johannes Lang, Max Luczak, Yannick Mees, Vicente Zamudio-Bayer, Martin Timm, Christine Bülow, Tobias Lau and Gereon Niedner-Schatteburg, " X-ray magnetic circular dichroic studies on spinfrustated trinuclear oxo bridged iron complexes in the gas phase", 4th International Conference on Bimetallic Complexes (3MET), Karlsruhe, 11.10.-12.10.2018.

Michael Lembach, Johannes Lang, Max Luczak, Yannick Mees, Vicente Zamudio-Bayer, Martin Timm, Christine Bülow, Tobias Lau and Gereon Niedner-Schatteburg, " X-ray magnetic circular dichroic studies on spinfrustated trinuclear oxo bridged iron complexes in the gas phase", 118th Bunsentagung, Jena 30.05.-1.06.2019.

Michael Lembach, Matthias P. Klein, Annika Steiner and Gereon Niedner-Schatteburg, "Magnetism and functional cooperativity of isolated oligo-nuclear transition metal complexes within cryo ion traps", Third review of the Collaborative Research Center (3MET), Kaiserslautern 5.06.-6.06.2019.

Felix Nüßlein, Klaus Blaum, Paul Fischer, Sebastian George, Jürgen Göck, Manfred Grieser, Robert von Hahn, Oded Heber, Stav Knaffo, Michael Lembach, Yannick Mees, Damian Müll, Gereon Niedner-Schatteburg, Oldrich Novotny, Israel Rubinstein, Viviane Schmidt, Lutz Schweikhard, Rajeev Singh, Yoni Toker, Andreas Wolf, Amitai Yona, "Delayed electron detachment and fragmentation of laser-excited metal cluster anions", Clustertreffen, Bad Honnef, 30.9-4.10.2019.

Michael Lembach, Johannes Lang, Max Luczak, Yannick Mees, Vicente Zamudio-Bayer, Martin Timm, Christine Bülow, Tobias Lau and Gereon Niedner-Schatteburg, "Magnetic properties and their correlation to the electronic ground states of isolated trinuclear 3d spin frustrated complexes", DPG Tagung der Sektion Atome, Moleküle, Quantenoptik und Plasmen (SAMOP), virtual, 20.09.-24.09.2021.

Beamtime proposals

Michael Lembach, Matthias Klein, Yannick Mees, Christine Bülow, Vicente Zamudio-Bayer, Bernd von Issendorf, Akira Terasaki, Tobias Lau and Gereon Niedner-Schatteburg, Investigation of spin frustrated Homo- and Hetero oxo-centered trinuclear transition metal complexes via X-ray magnetic circular dichroism, (high ranked), 2018.

Michael Lembach, Matthias Klein, Maximilian Luczak, Yannick Mees, Martin Timm, Christine Bülow, Vicente Zamudio-Bayer, Bernd von Issendorf, Akira Terasaki, Tobias Lau and Gereon Niedner-Schatteburg, X-ray magnetic circular dichroism of an isolated 4d homometallic Single Molecule Magnet, dinuclear 3d spin-crossover complex, and spinfrustrated Ruthenium complexes, 2019.

Michael Lembach, Maximilian Luczak, Yannick Mees, Christine Bülow, Vicente Zamudio-Bayer, Tobias Lau and Gereon Niedner-Schatteburg, Spin and Orbital magnetic moments of isolated single molecule magnets and electronic structure determination via X-ray magnetic circular dichroism, (high ranked), 2020.

Michael Lembach, Maximilian Luczak, Christopher Wiehn, Markus Kubin, Vicente Zamudio-Bayer, Tobias Lau and Gereon Niedner-Schatteburg, Temperature dependent determination of magnetic properties and their electronics in isolated single molecule magnets via X-ray magnetic circular dichroism, 2021.

Research visits

Helmholtz Zentrum Berlin für Materialien und Energie (BESSY II):

24.9.2017-30.9.2017: X-ray magnetic circular dichroism of spin frustrated oxo-centered trinuclear iron(III) and cobalt (III) carboxylate complexes in isolation

12.3.2018-18.3.2018: X-ray magnetic circular dichroism of temperature induced spin-crossover in isolated transition metal complexes

11.6.2018-17.6.2018: X-ray magnetic circular dichroism of temperature induced spin-crossover in isolated transition metal complexes

9.3.2020-12.3.2020: Spin and orbital magnetic moments of isolated single molecule magnets and electronic structure determination via X-ray magnetic circular dichroism (shutdown due Corona 9.3.2020-23.3.2020)

Paul Scherrer Institut (PSI):

15.10.2018-5.11.2018: Spin and Orbital moments of isolated transition metal clusters and complexes via X-ray magnetic circular dichroism

21.1.2019-31.1.2019: Replace a new infinity cell into an ICR FT-MS, rewiring of a cryostat in the mass spectrometer and commissioning the cryostat. Maintenance of several parts of the mass spectrometer.

29.3.2019-14.4.2019: Troubleshooting at the electronics of the Apex instrument and refill of the superconducting magnet for the detection of the ions.

Max Planck Institut für Kernphysik Cryo Storage Ring (CSR):

4.3.2019-11.3.2019: Delayed electron detachment and fragmentation of laser excited metal clusters anions

Danksagung

Ich danke Prof. Gereon Niedner-Schatteburg für die Ermöglichung einer Promotion im AK GNS. Weiterhin möchte ich ihm danken für den mir eingeräumten Freiraum in meiner wissenschaftlichen Arbeit. Ebenso wie den stetigen Diskussionen in und vor allem abseits forschungsrelevanter Themen.

Frau Jun. Prof. Jennifer Meyer möchte ich für die Übernahme des Zweitgutachtens, sowie den unterhaltsamen Gesprächen und der stetigen Diskussionen innerhalb und außerhalb forschungsrelevanter Themen danken. Herrn Prof. Antonio Pierik möchte ich für die Übernahme des Prüfungsvorsitzes in der Prüfungskommission danken.

Auch möchte ich mich bei Matthias Tombers, Jonathan Meyer, Johannes Lang und Sebastian Dillinger für die nette Aufnahme im Arbeitskreis bedanken.

Auch bedanken möchte ich mich an die jetzigen Mitarbeiter, Doktoranden und Studenten im AK GNS für eine tolle und angenehme Atmosphäre untereinander.

Besonders möchte ich mich bei meinen Bürokollegen Björn Kwasigroch, Sebastian Kruppa und Marcel Schmitt für die angenehme und teilweise sehr lustige Zeit aber auch bei Problemen und deren Lösungen bedanken.

Auch ein riesen Dank geht an meine Leidensgenossen Maximilian Luczak, Yannick Mees und Matthias Klein, die auf Strahlzeiten in Berlin die ein oder andere Überstunde mir zu liebe geleistet haben. Auch wenn da das ein oder andere Bier im Späti nötig war. Abseits von Berlin wurde aber auch in Heidelberg oder in der Schweiz immer eine tolle und entspannte Atmosphäre mit mehr oder weniger lustigen Erinnerungen geschaffen, es sei da nur erwähnt mit Einkäufen durch die halbe Schweiz zu laufen, da mittags keine Busse mehr gingen.

Bedanken möchte ich mich auch bei Tobias Lau und Team BESSY für die Möglichkeit an ihrer Apparatur Messungen zur Bestimmung magnetischer Momente durchführen zu können. Weiterhin möchte ich mich auch für die Diskussionen und hilfreichen Ratschlägen bezüglich der Auswertung und Interpretation von erhaltenen Daten bedanken. Vicente Zamudio-Bayer, Christine Bülow, Martin Timm und Markus Kubin möchte ich auch für die tatkräftige Unterstützung und der tollen Zusammenarbeit während der Strahlzeiten bei BESSY danken.

Ein großer Dank geht auch an Thomas Schlathölter für die Bereitstellung seiner ESI Quelle, um die Messungen an der Ion Trap durchführen zu können.

Weiterhin möchte ich mich für bei meinen Kooperationspartnern Julius Wolny, Hagen Kämmerer, Annie Powell und Euan Brechin für Bereitstellung verschiedener Komplexe bedanken.

Danken möchte ich auch Roumany Israil und Christoph Riehn für die Möglichkeit meine Messungen zwischen ihren Projekten reinquetschen zu dürfen und mir bei der Durchführung dieser Messungen zur Seite zu stehen.

Christian Malchau möchte ich danken, dass er mir und den Praktikanten erlaubt hat uns in einen seiner Abzüge einzecken zu dürfen, um eigene Komplexe synthetisieren zu können.

Den Mitarbeitern aus den Elektronik und Metallwerkstätten danke ich, da sie meist das unmögliche ganz unkompliziert möglich gemacht haben und mit beratenden Gespräche schnell zum Ziel geführt haben. Vor allem wenn es mal wieder ganz schnell gehen musste.

Vielen Dank auch an Thomas Kolling für die Hilfe bei allen Problemen, die so in der Promotion aufgetaucht sind. Die zielorientierten Problemlösungen wie „weg mit dem Dreck!“ oder „Ist das Kunst oder kann das weg?“ in Verbindung mit einem großen Metallcontainer ließen viel Platz für neues. Auch bei der Verpackung und Umzug für schweres Gerät in die Schweiz war eine lockere und entspannte Atmosphäre immer gegeben, selbst wenn es Zeitdruck gab. AutoCAD und ich werden zwar keine Freunde mehr aber Thomas hat mir bei Problemen auch immer da geholfen wie es nur ging.

Ein besonderer Dank geht an Sybille Heieck, Birgit Harrison-Weber, Petra Wetzels und Bärbel Stemler, die insgeheim den Laden am Laufen halten und uns so gut es geht den bürokratischen Kram abnehmen aber auch immer ein offenes Ohr für jeden haben.

Danken möchte ich auch der Nutzerbetreuung, die Pforte und dem Gästehaus bei BESSY, die fast immer alles möglich gemacht haben, außer die Beton Klötze retten zu können bevor diese verbrannt wurden.

Generell möchte ich den Leuten aus der physikalischen und theoretischen Chemie für die tolle und entspannte Atmosphäre, sei es in Praktika, Seminaren oder generell im Alltag danken. Durch die Seminare sind auch schon die ein oder anderen running gags entstanden, welche mich auch weiterhin begleiten werden.

Ein ganz besonderer Dank geht an meine langjährigen Freunde, die mir in den letzten zwei Jahrzehnten bei allem beigestanden haben. Allem voran möchte ich Steffen dafür danken, dass manches einem auch einfach egal sein sollte und man sich auf das wichtige konzentrieren soll. Deine Ratschläge, Sprüche und Ausraster werden mir fehlen. Aber auch Sibel möchte ich danken, dass sie immer an meiner Seite steht, wenn es Probleme gibt und immer ein offenes Ohr für alle hat (außer wenn wir jetzt gehen müssen ;)). Jermaine danke ich für unglaublich gute Zeit in den letzten Jahren auch wenn es manchmal schwere Zeiten gab die wir irgendwie überlebt haben. In Paris aufwachen ohne Geld muss man mal erlebt haben :). Erol danke ich dafür, dass er alles stehen und liegen lässt, wenn es mal brennt und dringend Hilfe gebraucht wird aber auch für die lustige Zeit um mal nicht an Probleme und Alltag denken zu müssen. Auch Flo möchte ich danken für zahlreiche lustige Momente, die wir so an dem ein oder anderen Wochenende erlebt haben.

Nicht zuletzt möchte ich meiner Mutter, meinem Stiefvater und seiner Familie danken, dass sie immer an mich geglaubt haben auch wenn es andere in der Familie nicht taten. Meinem Vater möchte ich danken, dass er immer für mich da war auch wenn es ihm nicht gut ging. Vielen Dank auch an die Familie meines Stiefvaters, welche mich und meine Mutter so herzlich aufgenommen haben als gehören wir schon immer dazu.

Eidesstattliche Erklärung

Hiermit bestätige ich, Michael Lembach, dass die vorliegende Arbeit mit dem Titel

„Magnetic, electronic and structural characterization of mass-selected mono and multinuclear transition metal complexes“

gemäß der Promotionsordnung des Fachbereichs Chemie der Technischen Universität Kaiserslautern selbstständig und mit keinen anderen als den hier angegebenen Quellen und Hilfsmitteln erstellt wurde. Kooperationsprojekte mit anderen Arbeitskreisen oder Institutionen sowie die beteiligten Mitarbeiter sind ausdrücklich in den entsprechenden Projekten genannt. Die vorliegende Arbeit wurde bei keiner anderen Hochschule als der Technischen Universität Kaiserslautern in ähnlicher oder gleicher Form eingereicht.

Kaiserslautern, den

Michael Lembach